

PHYSICS and CHEMISTRY LABORATORY



# Collected Reprints 1974-75



#### U.S. DEPARTMENT OF COMMERCE

National Oceanic and Atmospheric Administration Environmental Reasearch Laboratories

Boulder, Colorado





## Atmospheric Physics and Chemistry Laboratory

## Collected Reprints 1974-75

Boulder, Colorado

May 1976

U.S. DEPARTMENTOF COMMERCE Elliot Richardson, Secretary



Environmental Research Laboratories Wilmot Hess, Director



For sale by the Superintendent of Documents, U.S. Government Printing Office, Washington, D.C. 20402



#### TABLE OF CONTENTS\*

TABLE OF CONTENTS	Page
Allee, P. A.	1-9
Atmospheric Particulate Concentrations Measured Over the Atlantic Ocean During the 1969 Bomex Experiment, <i>Journal de Recherches Atmos.</i> 8, 947-955, July-Dec. 1974.	
Allee, P. A.	10-13
Ice Nuclei Concentration Measured by a Benchmark Network, Preprint Vol. of 4th Conference on Weather Modification, Ft. Lauderdale, Fla., Amer. Meteorological Society, 242-245, Nov. 1974.	
Barrett, E. W.	14-89
Inadvertent Weather and Climate Modification, CRC Critical Reviews in Environmental Control, 15-90, Dec. 1975.	
Bodhaine, B. A., R. F. Pueschel	90-95
Source of Seasonal Variations in Solar Radiation at Mauna Loa, <i>Journal of Atmospheric Sciences 31</i> , 840-845, Apr. 1974.	
Chappell, C. F.	96-101
Physical Basis For Seeding Cold Orographic Clouds, Preprint Vol. of Special Regional Weather Modification Conf., San Francisco, Cal., 33-38, Nov. 11-13, 1975.	
Chappell, C. F., F. L. Johnson	102-110
Potential for Snow Augmentation in Cold Orographic Clouds, Journal of Appl. Meteorology 13, 374-382, Apr. 1974.	
Chappell, C. F., E. L. Magaziner, J. M. Fritsch	111-113
On the Computation of Isobaric Wet-Bulb Temperature and Saturation Temperature Over Ice, <i>Journal of Appl. Meteor-ology 13</i> , 726-728, Sept. 1974.	
Chappell, C. F., D. R. Smith	114-125
Generation of Available Buoyant Energy by Cloud Glaciation, Pure and Appl. Geophysics 113, Nos. 5/6, 825-836, 1975.	
Cobb, W. E.	126-135
Atmospheric Electrical Conductivity and the Detection of Global Aerosol Pollution, Proceedings of Tech. Conference on Observation and Measurement of Atmospheric Pollution (TECOMAP), Helsinki, WMO-No. 368, 307-315, July 30-	

Eyre, D.	136-137
Wind Tunnel Tests of an Airborne Iso-Kinetic Ice Crystal Decelerator, NOAA Technical Memorandum ERL APCL-18, 65 pages, Sept. 1974. (abstract only)	
Fleischer, R. L., F. P. Parungo	138
Aerosol Particles on Tobacco Trichomes, <i>Nature 250</i> , 158-159, July 1974.	
Fritsch, J. M.	139-146
Synoptic - Meso Scale Budget Relationships for a Tornado Producing Squall Line, <i>Preprint Vol. of Ninth Conference on Severe Local Storms</i> , <i>Norman</i> , <i>Okla.</i> , Amer. Meteorological Society, 165-172, Oct. 21-23, 1975.	
Fritsch, J. M.	147-163
Cumulus Dynamics: Local Compensating Subsidence and Its Implications for Cumulus Parameterization, <i>Pure and Appl. Geophysics</i> 113, Nos. 5/6, 851-867, 1975.	
Gloersen, P., R. Ramseier, W. Campbell, P. Kuhn, W. Webster, Jr.	164-175
Ice Thickness Distribution As Inferred From Infrared and Microwave Remote Sensing During the Bering Sea Experiment, Proceedings of Final Symposium on Results of Joint Soviet-American Expedition, Leningrad, 282-292, May 12-17, 1974.	
Hanson, K. (Ed.), E. Flowers, G. Herbert, D. Hoyt, P. Kuhn, S. Manabe, R. Pueschel, L. Stearns	176-178
Environmental Research Laboratories Radiation Program-Requirements and Recommendations, NOAA Technical Rept. ERL 300-OD12, 22 pages, May 1974. (abstract only)	
Henz, J. F., V. R. Scheetz, J. M. Fritsch	179-184
Use of NMC Numerical Guidance in the Prediction of Severe Downslope Windstorm, Preprint Vol. of Fifth Conference on Weather Forecasting and Analysis, St. Louis, Mo., Amer. Meteorological Society, 136-141, Mar. 4-7, 1974.	
Holitza, F. J., H. W. Kasemir	185-189
Accelerated Decay of Thunderstorm Electric Fields by Chaff Seeding, Journal of Geophysical Research 79, 425-429, Jan. 20, 1974.	
Holitza, F. J., H. W. Kasemir	190-191
Reply, Journal of Geophysical Research 79, 3485-3486,	

Hoxit, L. R.	192-209
Diurnal Variations in Planetary Boundary-Layer Winds Over Land, Boundary Layer Meteorology 8, 21-38, 1975.	
Hoxit, L. R.	210-227
Planetary Boundary Layer Winds in Baroclinic Conditions, Journal of Atmospheric Sciences 31, 1003-1020, May 1974.	
Hoxit, L. R., C. F. Chappell	228-235
An Analysis of the Mesoscale Circulations Which Produced the April 3, 1974 Tornadoes in Northern Indiana, Preprint Vol. of Ninth Conference on Severe Local Storms, Norman, Okla., Amer. Meteorological Society, 256-263, Oct. 21-23, 1975.	
Hoxit, L. R., C. F. Chappell	236-238
Tornado Outbreak of April 3-4, 1974; Synoptic Analysis, NOAA Technical Rept. ERL 338-APCL 37, 48 pages, Oct. 1975. (abstract only)	
Kuhn, P. M.	239-240
Zonal Profiles of Atmospheric Water Vapor, NOAA Technical Rept. ERL 319-APCL 33, 11 pages, Mar. 1975. (abstract only)	
Kuhn, P. M., L. P. Stearns	241
Antarctic Infrared Radiation Budget, Antarctic Journal of the US, IX (5), 211, 1974.	
Kuhn, P. M., L. P. Stearns	242
Changes in the Antarctic Thermal Radiation Budget, <i>Antarctic Journal X</i> (5), 227, Sept Oct. 1975.	
Kuhn, P. M., L. P. Stearns	243-247
Infrared Radiation Observations vs. Calculations in the Atmosphere During Skylab, <i>Preprint Vol. of Sixth Conference on Aerospace and Aeronautical Meteorology, El Paso, Texas</i> , Amer. Meteorology Society, 120-124, Nov. 12-15, 1974.	
Kuhn, P. M., L. P. Stearns, M. S. Lojko	248-251
Latitudinal Profiles of Stratospheric Water Vapor, Geophysical Research Letters 2, 227-230, June 1975.	
Kuhn, P. M., L. P. Stearns, R. O. Ramseier	252-254
Airborne Infrared Imagery of Arctic Sea Ice Thickness,  NOAA Technical Rept. ERL 331-APCL 34, 20 pages, May 1975.  (abstract only)	

Kuhn, P. M., H. K. Weickmann, M. S. Lojko, L. P. Stearns	255-260
Transfer of Infrared Radiation Through Clouds, <i>Appl</i> .  Optics 13, 512-517. Mar. 1974.	
Kuhn, P. M., H. K. Weickmann, L. P. Stearns	261-266
Longwave Radiation Effects of the Harmattan Haze, Journal of Geophysical Research 80, 3419-3424, Aug 20, 1975.	
Kuhn, P. M., V. S. Whitehead, W. E. Marlatt	267-274
The Skylab Concentrated Atmospheric Radiation Project, Proceedings of NASA Earth Resources Survey Symposium, Houston, Texas, 1177-1184, June 1975.	
Langer, G., C. J Garcia, B. G. Mendonca, R. F. Pueschel, C. M. Fullerton	275-277
Hawaiian Volcanos - A Source of Ice Nuclei? Journal of Geophysical Research 79, 873-875, Feb 20, 1974.	
Long, A. B.	278-285
Solutions to the Droplet Collection Equation for Polynomial Kernels, <i>Preprint Vol. of Conference on Cloud Physics, Tucson, Ariz.</i> , Amer. Meteorological Society, 87-94, Oct 21-24, 1974.	
Nickerson, E. C., V. E. Smiley	286-289
Surface Layer and Energy Budget Parameterizations for Mesoscale Models, <i>Journal of Appl. Meteorology 14</i> , 297-300, Apr. 1975.	
Parungo, F. P., E. Ackerman, R. F. Pueschel	290-297
AgI Ice Nuclei: Physical and Chemical Properties Depending on Their Generating Procedure, Preprint Vol. of Fourth Conference on Weather Modification, Ft. Lauderdale, Fla., Amer. Meteorological Society, 165-172, Nov. 18-21, 1974.	
Parungo, F. P., R. F. Pueschel, B. T. Patten, D. Eyre	298-299
Physical and Chemical Properties of AgI Aerosols Formed at Simulated Airborne Conditions, NOAA Technical Rept. ERL 337-APCL 36, 43 pages, Dec. 1975. (abstract only)	
Pueschel, R. F., C. J Garcia, R. T. Hansen	300-304
Solar Radiation: Effects of Atmospheric Water Vapor and Volcano Aerosels, <i>Journal of Appl. Meteorology 13</i> , 397-401, Apr. 1974.	

Pueschel, R. F., P. M. Kuhn	305-307
Infrared Absorption of Ionospheric Aerosols: Urban and Rural Aerosols of Phoenix, Arizona, <i>Journal of Geophysical Research</i> 80, 2960-2962, July 20, 1975.	
Pueschel, R. F., F. P. Parungo, B. T. Patten	308-310
Artificial Ice Nuclei Production by Evaporation and Sublimation of Salts in a Flame, Preprint Vol. of Fourth Conference on Weather Modification, Ft. Lauderdale, Fla., Amer. Meteorological Society, 173-175, Nov. 18-21, 1974.	
Pueschel, R. F., C. C. Van Valin	311-320
The Mixed Nature of Laboratory-Produced Aerosols From Sea- water, <i>Journal de Recherches Atmos. 8</i> , 601-610, July-Dec. 1974.	
Pueschel, R. F., C. C. Van Valin, F. P. Parungo	321-324
Effects of Air Pollutants on Cloud Nucleation, Geophysical Research Letters 1, 51-54, May 1974.	
Thiebaux, M. L.	325-330
Approximations to Diffusion in a Random Velocity Field, The Physics of Fluids 17, 509-514, Mar. 1974.	
Thiebaux, M. L.	331-336
On the Application of Quasi-Lagrangian Coordinates to Random Shear Flows, <i>Journal of Math. Physics 15</i> , 613-618, May 1974.	
Thiebaux, M. L., H. J. Thiebaux	337-343
Radionuclide Decay in Steady State Reservoirs, Water Research 8, 447-453, 1974.	
Van Valin, C. C., R. F. Pueschel, F. P. Parungo	344-347
Formation of Cloud and Ice Nuclei by the Combustion of Crude Oil, <i>Journal of Appl. Meteorology 14</i> , 1200-1203, Sept. 1975.	
Weickmann, H. K.	348-354
Modification of Snow Accumulation by Cloud Seeding, Proceedings of 1972 Intl. Symposia on The Role of Snow and Ice in Hydrology: Measurement and Forecasting, Banff, Alberta, Canada, WMO-5, 6 pages, Dec. 1974.	
Weickmann, H. K., P. V. Hobbs	355-361
International Conference on Weather Modification, Tashkent, USSR, Bull. of the Amer. Meteorological Society 55, 318-323, Apr. 1974.	

Whitehead, Victor S., Peter M. Kuhn, William E. Marlatt, L. Edwin Williamson

362-365

The Skylab Concentrated Atmospheric Radiation Project — An Overview, Preprint Vol. of Sixth Conference on Aerospace and Aeronautical Meteorology, El Paso, Texas, Amer. Meteorological Society, 117-119, Nov 12-15, 1974.

Whiteman, C. D., J. G. Whiteman

366-367

An Historical Climatology of Damaging Downslope Windstorms at Boulder, Colorado, NOAA Technical Rept. ERL 336-APCL 35, 62 pages, Nov. 1974. (abstract only)

<sup>\*</sup>NOAA publications referenced here are obtainable by request from National Technical Information Service Operations Division Springfield, Virginia 22151

## ATMOSPHERIC PARTICULATE CONCENTRATIONS MEASURED OVER THE ATLANTIC OCEAN DURING THE 1969 BOMEX EXPERIMENT

by

#### Paul A. ALLEE

Atmospheric Physics and Chemistry Laboratory Environmental Research Laboratories National Oceanic and Atmospheric Administration Boulder, Colorado, U.S.A.

#### RÉSUMÉ

Les concentrations des noyaux d'Aitken (AN), des noyaux de condensation (CCN) et des noyaux glaçogènes (IN) ont été mesurées. Les concentrations AN, mesurées depuis la surface de l'océan jusqu'à une altitude d'environ 3,7 km, varient peu et sont comprises entre 200 et 350 particules ml-1. Les CCN varient entre 100 et 200 particules ml-1 et IN varient de 0,1 à 0,2 l-1. Les concentrations AN et CCN étaient bien corrélées. Elles étaient plus faibles entre 1,2 et 3 km qu'au-dessus et au-dessous de ces altitudes. Les concentrations IN augmentent avec l'altitude et ne sont apparemment pas corrélées avec AN et CCN. L'atmosphère au-dessus de l'Océan Atlantique à l'Est et au Sud des Barbades apparaît libre de pollution industrielle.

#### ABSTRACT

Concentrations of Aitken nuclei (AN), cloud droplet condensation nuclei (CCN), and ice nuclei (IN) were measured. The AN concentrations measured from the surface of the ocean to an altitude of 12,000 ft ( $\sim$  3.7 km) varied from slightly less than 200 to about 350 particles  $ml^{-1}$ . CCN varied from approximately 100 to 200  $ml^{-1}$ , and IN varied from 0.1 to 0.2  $l^{-1}$ . The AN and CCN concentrations were strongly correlated and were lower between 4000 and 10,000 ft ( $\sim$  1.2 - 3.0 km), than either above or below this altitude range. IN concentrations increased with altitude and were not apparently correlated with AN and CCN. The atmosphere above the Atlantic Ocean east and southeast of Barbados appeared to be free of industrial pollution.

#### Introduction.

During the 1969 BOMEX experiments, the Atmospheric Physics and Chemistry Laboratory of NOAA operated atmospheric particulate sampling equipment on a NOAA Research Flight Facility DC-6 aircraft and on the NOAA Ship DISCOVERER. The BOMEX experimental area was a 500 km square grid in the Western Atlantic, with its center northeast of Barbados at station CHARLIE (15°00'N, 56°30'W). Three types of atmospheric particulate concentrations were measured on most of the DC-6 flights: 1) Aitken nuclei (AN), those particles that serve as condensation nuclei at supersatura-

tions > 300 percent, 2) cloud droplet condensation nuclei (CCN), those particles that serve as condensation nuclei at low water vapor supersaturation and that are active in nature, and 3) ice nuclei (IN), those particles that are active as freezing and deposition nuclei. On the NOAA Ship DISCOVERER only the AN concentration was measured.

#### Instrumentation.

The DC-6 was equipped with an isokinetic sampling intake that brought outside air into the aircraft into a 9.5 mm ID Tygon tube, where the air sample was divided among the three instruments that measured the three nuclei concentrations. The air intake could not accept air when the cabin was pressurized, so that, except for one event, data at altitudes higher than 10,000 ft (3.0 km) were not obtained.

The AN concentrations were measured with a Gardner Small Particle Detector, corrected for altitude, according to Auer [1]. The general operational characteristics of Gardner Small Particle Detectors have been discussed by Hogan [2]. The operational characteristics of the Gardner Small Particle Detector (serial number 911) used for airborne sampling during the BOMEX project have been investigated by Saxena et al. [3]. CCN concentrations at 1 percent water vapor supersaturation were measured with a thermal diffusion chamber similar to that discussed by Twomey [4]. The construction features of the NOAA/APCL thermal diffusion chamber have been described by Allee [5]; a comparison of this instrument with others of the same type has been discussed by Ruskin and Kocmond [6]. The IN concentrations were measured with an NCAR acoustic ice nucleus counter at —20 °C. For the conditions encountered during the BOMEX experiment, the correction factor for loss to the bottom of the continuous cloud chamber would be about 10X, according to Langer [7].

On the NOAA Ship DISCOVERER, AN concentrations were also measured with a Gardner Small Particle Detector.

None of the instruments measuring nuclei concentrations was capable of determining the size distribution of the nuclei.

#### RESULTS.

Only a summary of the results is presented here. Complete documentation of the individual observations will be found in the BOMEX Permanent Archive of NOAA.

The general appearance of the maritime atmosphere was hazy; visibility was sometimes less than 10 miles ( $\sim$  16 km). The concentration of Aitken particles was usually less than 400 ml<sup>-1</sup> at all measured levels, except near a source of atmospheric pollutants, such as ships, other aircraft flying the same flight path, and Barbados. Visual observations from high flying aircraft indicated that the haze layer extended from the ocean surface to about 12,000 ft ( $\sim$  3.7 km).

Figure 1 shows a typical analog summary graph of the altitudes, and the concentrations of AN, CCN and IN during the flight of May 27, 1969. The AN concentration points plotted are the average values of a series of two or three, and sometimes more, individual measurements. The CCN concentration points usually represent only one measurement.

The IN concentration was derived from the analog trace of ice nuclei concentration recorded by the rate meter. Average and maximum concentrations measured for succeeding 12-minute segments are shown. During 12 minutes of flight, approximately 36 miles (58 km) are traversed. The response of the rate meter is such that the maximum IN concentration reached by the analog trace during a 12-minute period represents a flight path of at least 1/2 mile (0.8 km). A « V » at the 0.1 IN l<sup>-1</sup> ordinate position

P.A. ALLEE 949

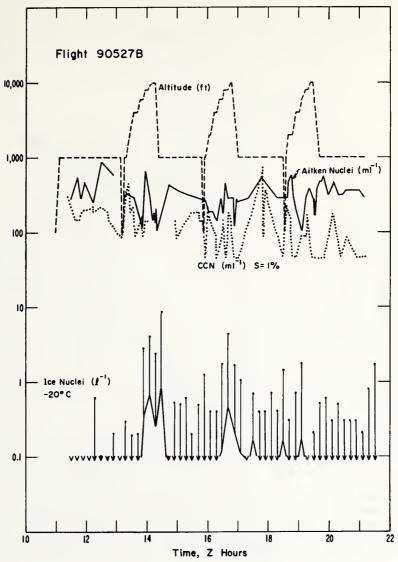


Fig. 1. — AN, CCN, and IN concentrations vs altitude during flight of May 27, 1969.

indicates that the IN concentration is less than 0.1 l<sup>-1</sup> during that 12-minute interval, as measured with a planimeter from the analog graph of the rate meter.

The AN concentrations during the three vertical atmospheric soundings reached minimum values at  $\sim 6000$  ft (1.8 km), but were greater both above and below that altitude. The IN concentration was apparently influenced by altitude, being greater for the higher altitudes.

On June 3, 1969, a satellite picture from Nimbus 3 (picture time 1529.37Z, center point: 14.9°N, 13.5°W) showed plumes originating at the Caribbean Islands and extending downwind. To determine whether an island modified the concentration of CCN, a flight was scheduled to study the nuclei concentrations around, and downwind from, the island of Barbados. The flight path, the latter portion of light 90720B, July 20, 1969, is shown in figure 2. Plotted on the map are the wind speed in knots,

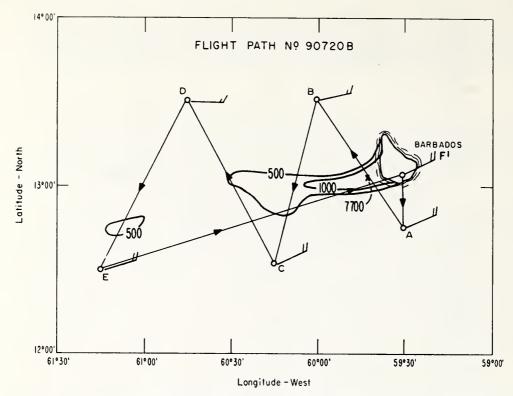
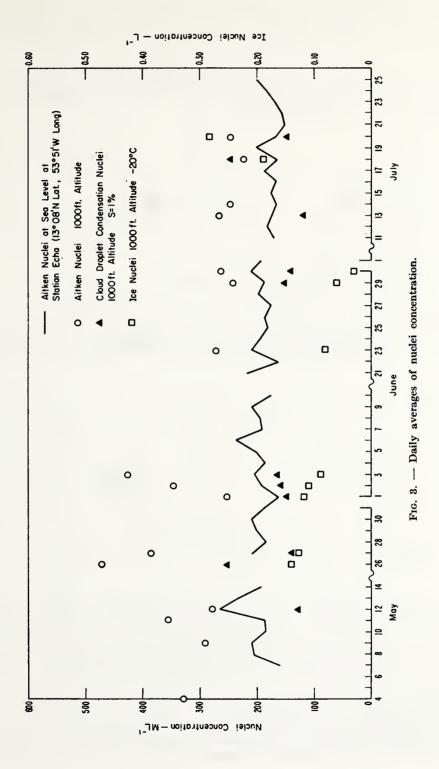


Fig. 2. — Flight path, wind direction, wind speed (knots), and isopleths of AN concentration (ml<sup>-1</sup>) at 1000 ft (0.3 km) in the vicinity of Barbados, July 20, 1969.

wind direction at selected points along the flight path, and isopleths of the AN concentration. The background concentration was about 300 AN ml<sup>-1</sup>, and the variability was such that any concentration less than 500 ml<sup>-1</sup> could not be attributed to a source on the island of Barbados. A binormal continuous plume dispersion model was used to estimate the concentration of the AN. When the appropriate cross section of the dispersion model was matched to the coast of Barbados, the model indicated that at 62 miles (~ 100 km) the AN concentration would be about 100 ml<sup>-1</sup>, which would be indistinguishable from the background concentration of AN free from the influence of Barbados. Coagulation of the nuclei during a 4 hour period would be a minor factor in the reduction of the AN concentration [8], and therefore was not taken into account in the plume model.

No modification of the background concentrations of CCN or IN was found in the plume downwind of Barbados. Observation aircraft near one of the island plumes on June 3, 1969, reported that the «plume» observed by satellite was a cloud. Since CCN and IN concentrations, important to cloud formation and modification, were not modified by the islands, this cloud was probably formed by radiative and or thermodynamic effects on the air temperature of the nearly water vapor-saturated air passing over the islands.

The daily concentration averages obtained with the four nuclei counters are presented in figure 3. They show generally decreasing nuclei concentrations during the period of the BOMEX experiment. The AN concentration at Station ECHO (13°08'N, 53°51'W) aboard the NOAA Ship DISCOVERER decreased about 20 percent. The AN concentration at 1000 ft (0.3 km), determined from measurements aboard the DC-6,



decreased also, although the daily averages varied considerably during May and June. The CCN daily averages at 1000 ft (0.3 km) showed the least variation with time. The IN concentration at 1000 ft (0.3 km) decreased, except for the anomalous data of July 18 and 19.

In contrast, Prospero and Carlson [9] and Carlson and Prospero [10] showed that during the same period the mineral aerosol concentration (µg m<sup>-3</sup>), transported from the deserts of North Africa to the northern equatorial Atlantic, increased both at the surface and at 1000 ft (0.3 km) levels.

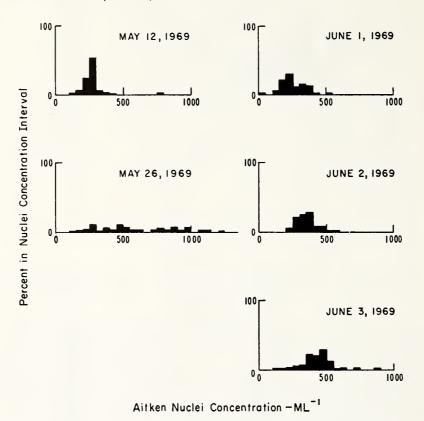


Fig. 4. — Distribution of observations within 50 nuclei ml<sup>-1</sup> concentration intervals for five identical flight paths.

The distribution of AN measurements on five similar flight paths around the northern half of the BOMEX array is shown in figure [4. May 12 had the narrowest distribution, with 250-300 ml<sup>-1</sup> being measured in about 54 percent of the individual measurements, and 200-250 ml<sup>-1</sup> occurring in about 23 percent. Measurements of May 26 had the widest distribution, with measurements ranging from 100 ml<sup>-1</sup> to 1250 ml<sup>-1</sup>. The most frequent concentrations of AN, i.e., 250-300 ml<sup>-1</sup> and 450-500 ml<sup>-1</sup>, occurred only about 12 percent of the time. The three successive flights of June 1, 2 and 3 show an approximate doubling of the average AN concentration from June 1 to June 3. The most frequently occurring concentrations were 250-300 ml<sup>-1</sup>, 350-400 ml<sup>-1</sup> and 450-500 ml<sup>-1</sup>, respectively, on these 3 days.

The AN concentrations averaged from all available data are plotted in figure 5. These concentrations exhibited an inverse relationship to the Saharan dust concentration

P.A. ALLEE 953

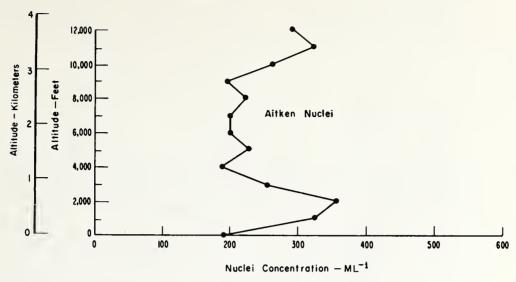


Fig. 5. — Variation of AN concentration with altitude.

noted by Prospero and Carlson [9, 10]. They showed that the higher Saharan dust concentrations were found between 4000 ft (1.2 km) and 10,000 ft (3.0 km). These two altitudes correspond to inversions at the base and top of what they term the Saharan air layer.

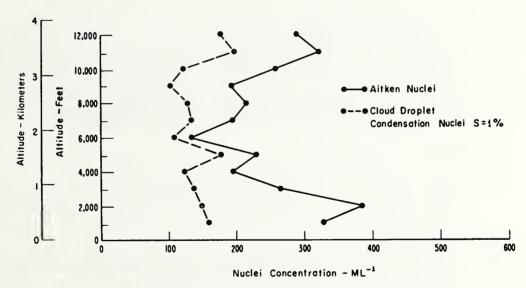


Fig. 6. — Concurrent measurements of AN and CCN concentrations.

A comparison of concurrent measurement of AN and CCN concentrations at several altitudes is shown in figure 6. The correlation coefficient between the average CCN concentration and the average AN concentration is r=0.63. When the average AN concentration increased or decreased with altitude, the average CCN concentration usually changed in the same manner. The values of CCN concentrations at different

altitudes are similar to those measured by Dinger et al. [11] southeast of Puerto Rico.

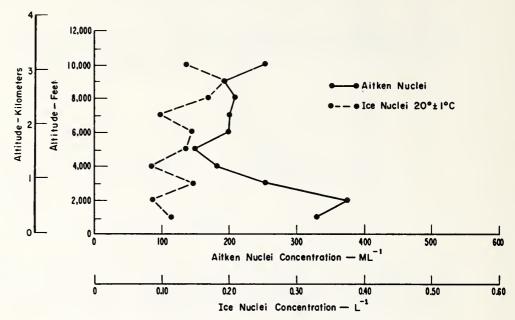


Fig. 7. — Concurrent measurements of AN and IN concentrations.

Figure 7 is a comparison of IN concentrations active at —20 °C with concurrent AN concentrations. There is no apparent correlation between the concentrations of the two types of nuclei. The IN concentration increased with altitude, as does the Saharan dust concentration [9]. Since many of the dry minerals carried into the upper levels of the atmosphere in desert regions are active as ice nuclei [12], it is probable that the increase in IN concentration with altitude during the BOMEX experiment is associated with the increase in Saharan dust concentration with altitude.

#### Conclusions.

The atmosphere above the BOMEX experiment area appeared to fit Junge's definition [8] of the worldwide atmosphere that has an aged average background AN concentration of 200 to 300 ml<sup>-1</sup>. The presence of the Saharan air layer between 4000 ft (1.2 km) and 10,000 ft (3.0 km) appeared to suppress the background concentration to about 200 ml<sup>-1</sup>.

The average background values of CCN varied less with altitude than did the AN concentration, but generally showed the same increasing or decreasing trend with respect to altitude. The average CCN background concentration was between 100 and 200 nuclei ml<sup>-1</sup> at a supersaturation of 1 percent.

The average background value of the IN concentration varied between 0.8 and 2 nuclei l<sup>-1</sup> (corrected) and increased with altitude.

P.A. ALLEE 955

#### REFERENCES

- [1] AUER A. (1965). The vertical distribution of Aitken nuclei in the vicinity of Ft. Collins, Colorado. Tech. Paper No. 6, Dept. of Atmos. Sci., Colorado State University, Ft. Collins, Colorado.
- [2] Hogan A.W. (1971). Three commercial Aitken nuclei counters. The second International Workshop on Condensation and Ice Nuclei, Ft. Collins, Colorado, 5-19 August, 1970. Report... compiled by L.O. Grant, Dept. of Atmos. Sci., Colorado State University, Ft. Collins, Colorado, pp. 33-34.
- [3] SAXENA V.K., ALOFS D.J., TEBELAK A.C. and ALLEE P.A. (1972). A comparative study of Aitken nuclei counters. J. Rech. Atmos., VI, no 1-2-3, pp. 495-505.
- [4] Twomey S. (1963). Measurement of natural cloud nuclei. J. Rech. Atmos., I, no 3, pp. 101-05.
- [5] ALLEE P.A. (1971). A description of the ESSA-APCL portable thermal diffusion cloud chamber. The second International Workshop on Condensation and Ice Nuclei, Ft. Collins, Colorado, 5-19 August, 1970. Report... compiled by L.O. Grant, Dept. of Atmos. Sci., Colorado State University, Ft. Collins, Colorado, pp. 39-40.
- [6] RUSKIN R.E. and KOCMOND W.C. (1971). Summary of condensation nucleus investigations at the 1970 International Workshop on Condensation and Ice Nuclei. The second International Workshop on Condensation and Ice Nuclei, Ft. Collins, Colorado, 5-19 August, 1970. Report... compiled by L.O. Grant, Dept. of Atmos. Sci., Colorado State University, Ft. Collins, Colorado, pp. 92-97.
- [7] LANGER G. and WEICKMANN J. (1973). Ice crystal loss to the bottom of the continuous cloud chamber in the NCAR ice nucleus counter. J. Rech. Atmos., VII, no 2, pp. 77-82.
- [8] JUNGE C. (1963). Air Chemistry and Radioactivity, Academic Press, New York, 382 p.
- [9] PROSPERO J.M. and CARLSON T.N. (1972). Vertical and Areal Distribution of Saharan dust over the western equatorial North Atlantic Ocean. J. Geophys. Res., 77, no 27, pp. 5255-65.
- [10] Carson T.N. and Prospero J.M. (1972). The large-scale movement of Saharan air outbreaks over the northern equatorial Atlantic. J. Appl. Meteor., 11, no 2, pp. 283-97.
- [11] DINGER J.E., HOWELL H.B. and WOJCIECHOWSKI T.A. (1970). On the source and composition of cloud nuclei in a subsident air mass over the North Atlantic. J. Atmos. Sci., 27, no 5, pp. 791-97.
- [12] ROBERTS P. and HALLETT J. (1968). A laboratory study of the ice nucleating properties of some mineral particulates. Quart. J. Roy. Meteor. Soc., 94, no 399, pp. 25-34.

\*

#### ICE NUCLEI CONCENTRATION MEASURED BY A BENCHMARK NETWORK

## Paul A. Allee Atmospheric Physics and Chemistry Laboratory NOAA, Boulder, Colorado 80302

#### 1. INTRODUCTION

It is important for the atmospheric scientist to know the concentration of atmospheric ice nuclei and the variation of concentration with time. Atmospheric ice nuclei are involved in precipitation and in the conversion of supercooled water clouds to ice clouds; any theoretical consideration of weather modification must be concerned with the presence of these nuclei in the atmosphere. Measurements of atmospheric concentrations of ice nuclei have been made at individual sites for varying time periods. However, organized large-scale measurements of atmospheric ice nuclei concentration, covering a number of widespread sites over the same interval of time have been carried out by only a few projects.

Bowen (1958) reported on the results of simultaneous examinations for one month of concentrations of ice nuclei at eight stations, six in Australia, two in the United States. Bigg and Miles (1968) carried out a lengthy experiment in which simultaneous measurements of ice nuclei concentrations were made at 24 locations in eastern Australia. Kline (1963) reported on extensive measurements derived, between 1959 and 1962, from a cooperative ice nuclei observational program at 15 locations in the United States. His results show a geographical difference in ice nuclei concentrations. The most comprehensive survey of global ice nuclei concentration, reported by Bigg and Stevenson (1970), covered 44 locations throughout the world during January, February, and March of 1969. A three-station network in the north Pacific Ocean during portions of 1968 and 1969 detected the advection of enhanced ice nuclei concentrations eastward across the Pacific Ocean (Hobbs et al., 1971).

#### 2. DISCUSSION

An ice nuclei concentration benchmark network has been established in the western United States by the National Oceanic and Atmospheric Administration (Allee, 1973a). The purpose of the network is to determine the climatological mean and variation for ice nuclei concentration throughout the 17 westernmost states and the north Pacific Ocean. The network consists of field monitors at 19 National Weather Service station locations selected as most likely to be free from anthropogenic sources of ice nuclei. The field monitor sites, identified by National Weather Service call letters, are shown in Figure 1.

The instrumentation of the network consists of two parts: (1) The equipment for collecting ice nuclei at the field monitoring site. Its major components are timer, vacuum pump, airflow meter, elapsed time meter, and encapsulated membrane

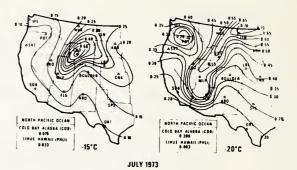


Figure 1. Benchmark network average ice nuclei concentrations for July 1973. (Uncorrected data; actual values of ice nuclei concentrations are about 4x greater.)

filter. (2) An NCAR (National Center for Atmospheric Research) Ice Nucleus Analyzer for the activation and counting of ice nuclei particles on the membrane filter. This equipment is at the Atmospheric Physics and Chemistry Laboratory (APCL) in Boulder, Colorado.

The field monitor filters air through a membrane for a few minutes of each hour 24 hours a day. Thus, the particulate sample obtained on a membrane filter that is changed daily will be representative of the conditions present throughout a 24 hour period. The time intervals of pump operation and air flow are coordinated so that about 300 liters of air per day pass through the filter.

The filters are changed daily as close to midnight, local time, as possible. The daily atmospheric ice nuclei concentration can then be compared with the daily weather records obtained by the cooperating National Weather Service station for any weather-dependent correlations or anomalies. When a number of exposed membrane filter capsules have been collected at the monitor station, they are mailed to APCL for ice nuclei activation and counting. Because of the volume effect associated with the membrane filter method for measuring ice nuclei concentration (Bigg et al., 1963; Gagin and Aroyo, 1969), and flow meter correction, nuclei concentrations are increased by a factor of about four.

The investigation of ice nuclei concentration by Hobbs et al. (1971) indicated that variation of climatological ice nuclei concentration is on a greater-than-one-day time scale. Accordingly, filters from a station are activated at -15°C and

-20°C on alternate days. This gives ice nuclei concentration data for two temperatures without interfering seriously with the expected climatological variation time scale. The first period of operation was from May 1, 1973, to August 31, 1974. The data are now being evaluated and the feasibility of expanding the network to cover the entire United States for an additional operational period is being studied. Modifications to improve the field monitor and to increase the capacity of the nuclei counting equipment have been initiated.

#### 3. RESULTS

A preliminary report on the first few months of operational results has already been given (Allee, 1973b). At that time, no strong correlations between the daily ice nuclei concentrations and local meteorological elements had been found. Since that time the monthly ice nuclei concentration averages for all stations have been analyzed through the end of December 1973.

Between May and December 1973, an annual trend was found in the average monthly ice nuclei concentrations active at  $-15^{\circ}\text{C}$  and  $-20^{\circ}\text{C}$ . A maximum value occurred in either July or August for nearly every station. Analysis of the data has not yet been completed for those months with minimum average ice nuclei concentration for each station.

Figure 1 shows the isopleths of average ice nuclei concentration over the benchmark network at -15°C and -20°C for July. It is apparent that the ice nuclei concentrations are lower along the coastal areas than they are in the continental interior. The high -15°C monthly average of concentration at LND (Lander, Wyoming) is probably due to two anthropogenic factors: a rodeo during the first week of July that generated enough dust to occasionally reduce the visibility to 2 miles, and activities associated with the construction of a new airport terminal building. The -20°C isopleths show a ridge of high ice nuclei concentration from FLC (Flagstaff, Arizona) to ISN (Williston, North Dakota). The reason for a suppressed -20°C ice nuclei concentration at PDT (Pendleton, Oregon) is not known.

Figure 2 shows plots of July 1973 monthly average ice nuclei concentrations (at two temperatures) versus distance from the nearest seashore (either the Pacific Ocean or the Gulf of Mexico).

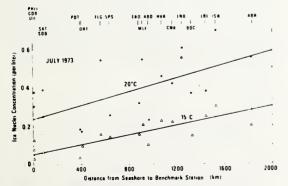


Figure 2. Average ice nuclei concentrations for July 1973. (Uncorrected data; actual values of ice nuclei concentrations are about ix greater.)

Linear regression lines have been calculated for -15°C and -20°C data and drawn on the graph. Except for LND, the regression line fits the -15°C data points very well. The slope of the lines can be interpreted to mean that as the atmosphere crosses the coastline and flows inland, the ice nuclei concentration increases within the atmosphere in direct proportion to the distance from the seashore. If the source of ice nuclei is the surface of the earth and if the ice nuclei are convected throughout the troposphere, it can be shown that there are generated at the earth's surface about 2 ice nuclei m<sup>-2</sup> min<sup>-1</sup> (after a 4x correction).

The  $-20^{\circ}$ C regression line does not match the data as well, but a geographic grouping of the stations is possible, reflecting the path of motion of the atmosphere across various portions of the western United States.

Figure 3 shows the isopleths of average ice nuclei concentration over the benchmark network at -15°C and -20°C for December. The -15°C isopleth gradient is very weak, showing two weak highs of average monthly ice nuclei concentration, the first over Oklahoma and Kansas, the second in northwest Washington. The -20°C isopleths between July and December showed a collapse of the ridge of July. It was replaced by a trough of low monthly average ice nuclei concentration, oriented along essentially the same axis as the ridge of July. The trough values were flanked by higher values of ice nuclei concentration that had a gradient of decreasing ice nuclei concentration toward the seashore.

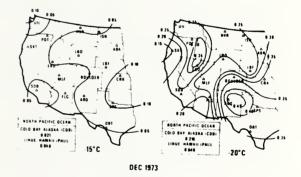


Figure 3. Benchmark network average ice nuclei concentrations for December 1973. (Uncorrected data; actual values of ice nuclei concentrations are about 4x greater.)

Considering the trough delineated by the  $-20^{\circ}\text{C}$  isopleths in Figure 3, we find that the regression line in Figure 4, representing the relationship between the monthly average ice nuclei concentration and distance from the seashore, becomes more representative if it is broken into two parts: one line representing distances less than 1000 km from the seashore; the other line representing distances greater than 1000 km from the seashore. The regression line for -15°C was divided the same way but could have been a single regression line representing the complete range of distance from the seashore up to 2000 km.

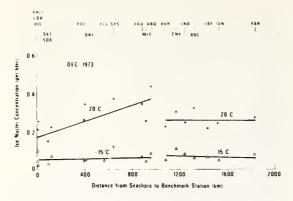


Figure 4. Average ice nuclei concentrations for December 1973. (Uncorrected data; actual values of ice nuclei concentrations are about 4x greater.)

The differences between the July and December sets of ice nuclei concentration data give an insight into the physical characteristics of ice nuclei. During July, the ice nuclei concentration increased monotonically as the air passed over the seashore and moved inland. We conclude from this that the earth's surface is the source of ice nuclei. Whether the -15°C and -20°C ice nuclei are inorganic or organic cannot be inferred. However, it is notable that the -15°C monthly average ice nuclei concentration was greater at LND (Lander, Wyoming) than at any other station, and the ice nuclei were most likely to be an inorganic dust, because of the conditions probably associated with their origin.

During December, the average monthly ice nuclei concentration of the air active at  $-20\,^{\circ}\mathrm{C}$  passing the seashore was less than for July, but it increased with air passage inland at a steady rate (2 ice nuclei  $\mathrm{m}^{-2}$   $\mathrm{min}^{-1}$ ) until 1000 km from the seashore. Beyond that distance the ice nuclei concentration was less and remained constant with increasing distance from the seashore. The area beyond 1000 km from the seashore, where the trough of lower ice nuclei concentration values is located in Figure 3, was the location of most of the snowfall that remained on the ground for any length of time during December 1973. It is quite likely that the snow-covered, and probably frozen, ground surfaces were incapable of generating ice nuclei, either organic or inorganic.

The  $-15\,^{\circ}\text{C}$  regression lines in Figure 4 lead to an interesting speculation. The air that came over the seashore had the same ice nuclei concentration in July and in December. During July the ice nuclei concentration in the atmosphere increased. There was no corresponding increase in December in ice nuclei concentration as there was for the -20°C active ice nuclei. Assuming that the air was, in general, moving inland during December, we are led to the conclusion that, whatever the mechanism is that releases from the earth's surface in July ice nuclei that are active at -15°C, that mechanism is not operative during December. Since this is true for distances of less than 1000 km from the seashore, where the physical conditions of the surface are not modified by a snow cover, it is probable that the

processes for the generation and release of inorganic ice nuclei from the earth's surface are not impaired. This suggests the possibility that during July the increase with distance from the seashore of atmospheric ice nuclei active at -15°C is due to some organic factor, animal or vegetable, or combination thereof, that is suppressed during December. This hypothesis appears to be supported by the considerable increase in concentration of ice nuclei active at -15°C at LND (Lander, Wyoming) during July. The increase was probably due to the added injection of inorganic particles into the air by the rodeo and construction activities.

#### 4. CONCLUSIONS

No strong correlations between the daily ice nuclei concentration and local meteorological elements have been found.

Monthly ice nuclei concentration averages at the network stations sometimes show a monotonic increase when related to the distance of the station from the seashore. This suggests that the earth's surface is a source of ice nuclei. An annual variation of ice nuclei concentration has been found at all stations, with the maximum values occurring during July or August at nearly all stations.

Additional studies are needed: (1) To determine whether an average correction factor for the volume effect can be assigned to the ice nuclei concentration network data on a whole, regional, or seasonal basis. (2) To determine ice nuclei concentration aloft by aircraft measurements simultaneously with ground measurements, to test the extent of possible stratification of ice nuclei concentration within the atmosphere by such meteorological conditions as temperature inversions. (3) To determine ice nuclei chemical and physical characteristics from various portions of the network.

Ice nuclei effective at the warmer temperature of  $-15\,^{\circ}\text{C}$  originating over the continent during July could be predominantly of organic origin. Those effective at  $-20\,^{\circ}\text{C}$  are probably both organic and inorganic.

Whatever the cause, concentrations of -20°C active ice nuclei are lower in December beyond 1000 km from the seashore. Concentrations of -15°C active ice nuclei are lower in December at all distances from the seashore. This lowering of concentration of -15°C and -20°C active ice nuclei indicates that weather modification projects in the interior of the country involving seeding with a specific number of ice nuclei would be more successful in winter than in summer.

#### References

Allee, P. A., 1973a: A benchmark network for ice nucleus counts. Journal of Weather Modification, 5, 217-221.

Allee, P. A., 1973b: An ice nuclei concentration benchmark network. Proceedings of the International Conference on Weather Modification, Tashkent, USSR, 1-7 October 1973.

Bigg, E. K., and G. T. Miles, 1968: The results of

- large-scale measurements of natural ice nuclei. J. Atmos. Sci., <u>21</u>, 396-403.
- Bigg, E. K., S. C. Mossop, R. T. Meade and N. S. Thorndike, 1963: The measurement of ice nucleus concentrations by means of Millipore filters. J. Appl. Meteor., 2, 266-269.
- Bigg, E. K., and C. M. Stevenson, 1970: Comparison of concentrations of ice nuclei in different parts of the world. J. Rech. Atmos., Vol IV, 2<sup>e</sup> annee, no. 2. 41-58.
- Bowen, E. G., 1958: Freezing nucleus measurements in January 1957. Aus. J. Phys., <u>11</u>, 452-455.
- Gagin, A., and M. Aroyo, 1969: A thermal diffusion chamber for the measurement of ice nuclei concentrations. J. Rech. Atmos., Vol. IV, 1<sup>re</sup> annee, no. 3., 115-122.
- Hobbs, P. V., G. C. Bluhm and T. Ohtake, 1971: Transport of ice nuclei over the North Pacific Ocean. Tellus, XXIII, 1, 28-39.
- Kline, D. B., 1963: Evidence of geographical differences in ice nuclei concentrations. Mon. Wea. Rev., 91, 681-686.

### CRITICAL REVIEWS IN ENVIRONMENTAL CONTROL, VOL. 6, NO. 1, PAGES 15-90, DECEMBER 1975.

#### INADVERTENT WEATHER AND CLIMATE MODIFICATION

Author: Earl W. Barrett

National Oceanic and

Atmospheric Administration

Boulder, Colorado

Referee: II. L. Landsberg

University of Maryland College Park, Maryland

#### INTRODUCTION

Out of the total ensemble of environmental factors, the subset which is sensed most immediately and directly by man and which has the greatest integrated impact on human activities is that which is subsumed under the terms weather and climate. Earthquakes may level cities, volcanoes may bury them and their inhabitants under heaps of dust and slag, but reconstruction or relocation is accomplished in a period of months or years; these disasters show up only as minor perturbations in the population statistics. On the other hand, paleoclimatic studies have shown that past fluctuations in the long-term state of the atmosphere have caused drastic alterations in animal and plant populations. It seems probable that the pressure of the extreme climatic oscillations of the Pleistocene contributed heavily to the evolution of modern man and his emphasis on managing the environment rather than accepting it. Examples of far-reaching social consequences of small climatic changes are available within historical times; probably the best documented of these is the "little ice age," lasting roughly from 1300 to 1700 of the present era. This recession put an end

to the westward movement of the Scandinavian peoples across the Atlantic and thus postponed by several centuries the European colonization of North America.

For most of history, the relationship between man and weather has been basically the one stated succinctly by Charles Dudley Warner: Everybody talked about the weather, but nobody did anything about it. In the 1940s, however, the discovery that clouds could be modified by additions of freezing nuclei created a realization that, at some times and places at least, it might be possible to do something about the weather. This entering wedge into the field of intentional weather modification has since been heavily studied and exploited; it had as a by-product the creation of considerable interest in weather modification on the part of both the scientific community and the general population. The possibility that man had, in fact, been doing something about the weather without knowing it became a subject for serious consideration.

Although the possibility of climatic alterations by human activity was hinted at in the scientific literature at the beginning of this century, and again in the late 1930s, it received little serious attention until the 1950s. The first period of thermonuclear testing, 1954 to 1958, generated a great deal of concern about drastic and widespread effects on weather, mostly irrational and without either a sound physical or valid statistical basis. It was felt that anything which liberated such high energies must somehow influence the atmosphere. The fact that a device fired at sea level or under the sea did create a large convective cloud locally was cited as evidence.

By about 1960 it was clear that (with one possible exception to be discussed later in this article) no large-scale or long-term meteorological effects would ensue from nuclear testing at the levels of the 1950s. It had become clear that the inertia of the atmosphere-ocean system was simply too large to be perturbed seriously by the sudden release of any energy man could generate. Instead of the spectacular and violent, it was realized that one would have to look to the realm of the slow and insidious to find evidence of human influences on climate.

As was mentioned above, some evidence (to be discussed in detail later) that man-made carbon dioxide was accumulating in the atmosphere appeared as early as 1938. This, together with some early systematic data from Scandinavia, led to the inclusion of a CO<sub>2</sub> measurement program during the International Geophysical Year (IGY), 1957–1958. This program, which has continued to the present, was the first serious scientific study of a possible man-made climatic influence on a large scale.

As the reality of this effect became established, and as the general mood of increased concern for the environment, and the concept of "spacecraft Earth" developed during the 1960s, more serious scientific effort began to be focused on inadvertent weather and climate modification. It had, of course, been recognized for a long time that the climate of a city differed significantly from its rural environs due to the release of heat and pollutants; it was not until the late 1960s that evidence of urban influence on the climate at considerable distances downwind began to be noticed. The role of pollution aerosols as climate modifiers became a topic of great interest, and it remains so today.

In the United States, the attention of the national government to these problems began with the IGY effort; CO<sub>2</sub> and solar-radiation measurement programs were started in Antarctica and at

the Mauna Loa Observatory in Hawaii, which was established specifically for this program by the U.S. Weather Bureau.<sup>1-4</sup> This station, located at an elevation of 3400 m on the north slope of Mauna Loa, has been improved over the years and remains the prototype "benchmark" station for climatic change monitoring. In 1965, the Environmental Pollution Panel of the U.S. President's Science Advisory Committee made a number of recommendations relative to such monitoring.

The first major meeting devoted exclusively to the inadvertent modification problem was held in Dallas, Texas, in December 1968. The proceedings<sup>5</sup> were subsequently published in hardcover book form. In the following year, a series of discussions between some faculty members of the Massachusetts Institute of Technology and some government officials and other scientists gave rise to the first working conference, the Study of Critical Environmental Problems (SCEP). This meeting, held at Williams College, Williamstown, Massachusetts during July 1970, was devoted to identifying possible global environmental hazards and making recommendations concerning monitoring, abatement, etc. The climatic problem areas which were identified were carbon dioxide and other trace gases that may affect climate; particulate matter in the atmosphere as turbidity and as cloud modifier; waste heat (thermal pollution); changes in the earth's surface (land-use changes); radioactivity in the atmosphere; and jet aircraft pollution of the high troposphere and stratosphere. The proceedings of this meeting were published<sup>6</sup> by the M.1.T. Press. In the present article, these proceedings will be referred to as SCEP, rather than by the numerical superscript.

The working group for SCEP was, with one exception, composed of residents of the United States: scientists, representatives of industrial management, and government officials. Some of the participants felt that a more multinational participation would be essential if standardized global programs were to come into existence as a result of such a meeting. Also, it was felt that the problems of climate modification were complex enough to occupy the entire attention of a working meeting. As a result, a second such meeting was held, this time in Stockholm, with participants from 14 countries, all of whom were scientists. This working meeting was called Study of Man's Impact on Climate (SMIC). The report

prepared by this group, while only ten pages shorter than SCEP, deals entirely with the substantive scientific questions of inadvertent climate modification and does not concern itself with financial and administrative details. The major areas treated by SMIC were previous climatic changes; man's activities influencing climate; theory and models of climatic change; climatic effects of man-made surface change; modification of the troposphere; and modification of the stratosphere. One objective of SMIC was to provide guidelines for the World Meteorological Organization (WMO) and other international agencies to use in establishing monitoring and research programs.

The need for global monitoring was reiterated by various scientists and official bodies during the first two years of the 1970s.8-12 Due to the inevitable lag in planning, financing, and constructing such facilities (which must necessarily be in wilderness areas in order to give representative data not reflecting local effects), the minimum number of benchmark stations (ten) considered necessary has not yet been reached. Four stations are currently in operation. Mauna Loa Observatory (MLO), the oldest, 13,14 was established by the U.S. Weather Bureau, then transferred to the supervision of the Atmospheric Physics and Chemistry Laboratory of the Environmental Science Services Administration in 1966 and finally to the Air Resources Laboratory (ARL) of the National Oceanic and Atmospheric Administration (NOAA) in 1971. In the following year, the NOAA network was officially expanded to four stations: 15 MLO; South Pole; Point Barrow, Alaska; and American Samoa. At the time of writing, the first three are fully equipped and functioning and the fourth is under construction. The other operational station is located at Kislovodsk, North Caucasus, in the U.S.S.R.<sup>16</sup> The government of Canada has plans for three high latitude northern stations; some limited monitoring activities are being conducted in Australia and New Zealand. 17

In addition to the long-term monitoring program, two shorter but highly intensive programs have been devoted to the problem of inadvertent modification. The first of these, the Metropolitan Meteorological Experiment (METROMEX), 18 was directed toward a concentrated investigation of downwind effects of the thermal and particulate emissions from a typical metropolitan area (St. Louis, Missouri). The

project involved an examination of all available climatological data in a circle around the city, plus an extensive field program in which a number of state and federal government agencies and university research groups participated.

The second program was one of the largest efforts directed toward the solution of a single scientific or technological problem since the Manhattan Project of World War II. The final objective of this program was to prepare an authoritative environmental impact statement on the effects of supersonic transport aircraft (SST) for submission to the Congress of the United States for their guidance in making policy decisions. In 1970 the Congress passed legislation requiring the U.S. Department of Transportation to prepare such a statement by the end of 1974. The resulting research activity, the Climatic Impact Assessment Program (CIAP), 19,20 involved nine agencies and departments of the United States Government, seven agencies of other national governments, and over a thousand individual scientists in the U.S. and abroad. The program involved data-collecting activities using aircraft and balloons in the stratosphere, development of new techniques for sampling and measuring stratospheric pollutants, laboratory work in the photochemistry of atmospheric trace gases, measurement of pollutant emission by aircraft engines, mathematical modeling of the stratosphere including simultaneous chemical reactions and transport processes, and modeling of the effects on the planetary ecology and costbenefit relationships. The Report of Findings<sup>21</sup> which was submitted to the Congress and which is essentially a summary of the results plus the conclusions, consists of 153 pages plus 8 appendices totaling 691 pages. Six of these appendices summarize six monographs (now in press) which present in detail the scientific results of the program.

The programs and studies enumerated above have shown that human activities are capable of influencing weather and climate on both the regional and global scale, but that the degree of the global influence is as yet too small to detect relative to the "noise" of natural climate fluctuations. The ongoing long-term monitoring programs will ultimately make possible the separation of the information from the noise as well as provide the data needed for refinement of prognostic mathematical models of climatic change.

The remainder of this article will be devoted to

presentation and discussion of the several ways in which human activities can affect weather and climate. Before proceeding, however, we wish to note that, in addition to SCEP and SMIC, a considerable number of survey, review, and speculative articles relating to inadvertent weather modification has appeared in the scientific and popular literature during the past 25 years. To cite them all individually in this paper would lengthen it excessively; they are listed in the bibliography of articles at the end of this paper for the interested reader.

#### NATURAL CLIMATIC FLUCTUATIONS

In any attempt to assess a man-made climatic effect, it is essential to have a measure of the degree of variability of the various weather elements which may be expected in the absence of human influence. The term "natural," as used here, refers to what would have happened either in the absence of the human species or if that species lived, at a much lower population level, in a primitive state without combustion or agriculture. Obviously, no direct data are available from such remote times; qualitative reports (cold winters, dry summers, etc.) go back only two or three millenia, and quantitative data only begin around the end of the 17th century. However, geological, geochemical and fossil-biological data (isotope ratios, pollens, etc.) do permit estimates of temperatures, precipitation-evaporation ratios, and wind regimes of past eras to be made.

Climate is, by definition, the ensemble of statistics of weather elements as defined over a suitably long period (30 years is taken as a standard climatological epoch). The customary statistics are the means, the extremes, and measures of dispersion and skewness. Higher moments are rarely, if ever, needed. The weather elements considered are primarily, those having a direct and palpable influence on people and other biota, such as temperature, wind, precipitation, evaporation, amount of received solar radiation, and humidity; and secondarily, those which are needed by the atmospheric scientist or forecaster to aid in understanding the variations of the former, such as pressures and winds at many levels in the atmosphere. The chemical composition of the atmosphere can be considered in both categories, since small changes do not impact directly on human perception, but large changes (oxygen

depletion, huge increases in carbon dioxide) obviously would do so.

Since climate is a set of statistics defined over a period of the order of decades, it is evident that, if these statistics are not stationary, the climate may change when considered over periods longer than this. Two conclusions follow from this: that detection of a human influence through statistical analysis alone will require a lapse of time which is inversely related to the magnitude of the postulated change; and as a corollary, that a trend of only a few years' duration in a climatic element following on a change in human activities cannot in confidence be attributed to that change unless a sound causal physical chain can be established. Unfortunately, many doomsayers fall into this ancient trap of the post hoc ergo propter hoc fallacy; those who blame the severe winter of 1962-63 on nuclear weapons testing conveniently ignore the fact that the winter of 1941-42 was nearly as severe.

When assessing a measured trend in a climatic parameter such as temperature, it is necessary to determine whether trends of the observed intensity and duration have a high probability of occurring naturally. In the case of temperature, it is well established that the mean temperature in middle latitudes has oscillated over the range +10° to -2°C with periods of tens of thousands of years during the past 2 megayears (10<sup>6</sup> years). Hence it is very difficult to decide whether a downward trend of, say, 0.01°C/year for 20 years is the result of particulate pollution by man or of some other quite independent cause unless it can be shown that the particulate loading of the atmosphere had an upward trend of the right order of magnitude, and that the solar input had a simultaneous downward trend. As will be shown later, the actual data do not permit any such clear-cut decision.

The primary causes of past climatic fluctuations cannot be established specifically and beyond all doubt or controversy. Various theories have been proposed; most are plausible, some are contradictory. An obvious choice is solar variability;<sup>22,23</sup> reduced solar flux will result in lower terrestrial temperatures unless it is compensated for by a drop in planetary albedo or an increased "greenhouse effect." The major objection is that there is no firm astrophysical evidence for the requisite degree of variability at present; the familiar 11- (or 22-) year cycle does not change the total solar flux appreciably, and there is no

evidence for longer-period variability. A variant of this is the cosmic dust hypothesis;<sup>24</sup> it has the advantage that no astrophysical theory is required and it cannot be disproved by evidence. A third astronomical theory<sup>25</sup> attributes climatic fluctuations to secular changes in the eccentricity of the earth's orbit, precession of the equinoxes, and variations in the tilt of the earth's axis relative to the ecliptic plane. The difficulty with this theory is that these changes are too cyclic, and the periods are too long to account for the more recent rapid fluctuations.

A number of "terrestrial" theories have also been formulated. Fluctuations in atmospheric carbon dioxide concentration can affect the atmospheric heat-storage capacity and thereby change the vertical distribution of temperature and the temperature at the ground. This theory, first put forward in the second half of the last century, 26-30,108 fell into disfavor when it was found that the absorption spectra of CO2 and water vapor in the infrared overlap considerably. However, with better data on the spectra, and with more sophisticated radiative-transfer models, the effect of CO<sub>2</sub> changes is found to be sufficiently large; we shall return to this point in the discussion of man-made CO<sub>2</sub>. To make the theory viable only requires an explanation for natural CO2 variations. The recent observation that CO<sub>2</sub> is the primary constituent of both the thin atmosphere of Mars and the dense one of Venus suggests that the primitive terrestrial atmosphere was in fact much richer in CO<sub>2</sub> than at present. It is difficult, however, to construct a theory for fluctuating rather than steadily decreasing CO<sub>2</sub> concentrations, although it was attempted 28-30 on geochemical grounds before the concept of a terrestrial atmosphere formed by outgassing had been formulated. This theory, like the astronomical and solar theories, can conceivably account for the generally-cold periods separated by 2 × 10<sup>8</sup> years or more, but cannot account (by itself) for the "fine structure" of the Quaternary glaciations and interglacials which involve time scales of 104 to 105 year. The same comment applies to explanations based on continental drift and orogeny.

Volcanic dust has been invoked as an agent of climatic change, <sup>3 1-3 3</sup> and (as will be discussed in more detail later) its effect on received solar energy has been measured extensively during the period since the eruption of Mt. Agung in Bali in

March of 1963. Some evidence<sup>3,3</sup> from measurements of volcanic dust in sea-bottom cores suggests that there was a period of strong dust production lasting 2.5 × 10<sup>5</sup> years about 1.6 to 1.8 million years ago. The atmospheric dust load was estimated to be about 400 times the present level. A very strong criticism<sup>34</sup> of the volcanic dust theory, however, is that, while it explains climates cooler than the present without difficulty, it cannot account for the much warmer Tertiary climate. If all the dust load were removed from the present atmosphere, the mean midlatitude temperature would rise 0.5° to 1°C (depending on the model used to calculate it), whereas a rise of about 9°C is needed to match the Eocene warm period. The only escape from this dilemma is to postulate a large thermal inertia for the earth-atmosphere system, so that the time scale for recovery from a cooling due to volcanic dust is several thousand years after the dust is removed. While this is not inconceivable, it is not supported by strong evidence (except that the turnover time for deep-sea water may be as large as 1000 years).

A major difficulty in any attempt to study the effect of changing a single parameter such as solar radiation on the total climate is the strong degree of coupling between all the climatic parameters. This coupling creates the possibility of multiple feedbacks which may give rise to paradoxical end results. A reduction in solar input to the atmosphere by dust or astronomical causes might reduce the amount of evaporation from the sea, thereby reducing cloudiness, decreasing the earth's albedo, and thus ameliorating the effect of the weaker sunshine by providing more hours of it at any given point on the ground. This is an example of negative feedback. On the other hand, the weaker sunshine would melt less ice from glaciers in the summer; if this effect dominated over the reduced precipitation the glaciers would grow, thereby increasing the planetary albedo and lowering the mean temperature still more. This is an example of positive feedback, which leads to runaway instability until checked by some other factor.

Theories of climatic change involving such feedbacks have been devised. Budyko<sup>3 5-3 7</sup> has advocated the positive feedback mechanism described in the previous paragraph. It can, however, be criticized on the basis of an electrical analog. Electronic circuits incorporating this kind of feedback are in common use for a variety of purposes; they have the property that they spend

most of the time in one or the other of their extreme states (full on or full off) and only change to the other state when triggered by a strong impulse. They then change state very rapidly. The triggering impulse, while it may be of very short duration, must be of the same order of amplitude as the difference between the two extreme states. If the presence of the ice phase on the planet makes it an analog of a "flip-flop" device, then the nature of the sharp triggering impulse is difficult to imagine. Once the entire planet became ice-covered, it should remain so unless a drastic rise in solar output took place.

A theory combining both kinds of feedbacks has been offered by Ewing and Donn, 38-40 in which the peculiar geography of the Arctic Sea plays a vital role. An increase of solar input (from any cause) would melt more of the Arctic Sea ice, decreasing the albedo and giving rise to a positive feedback situation there. Melting of this ice would lead to a higher exchange rate with the North Atlantic, leading to further warming and an ice-free basin year-round. The increased evaporation would lead to increased precipitation over the surrounding land areas, and therefore to increased snow deposition at higher elevations, thus building up ice sheets over land. This would continue until the falling sea level (due to the water storage in the ice sheets) cut off the communication with the Atlantic (this is the negative feedback part of the mechanism). Then the Arctic Sea would refreeze, precipitation over land would decrease, and the glaciers would retreat.

A theory of this kind, combining both types of feedback, also has its analog in any of the varieties of electronic oscillator. The key characteristic of such an oscillator is its strict periodicity. Thus, while the model looks attractive insofar as accounting for the Pleistocene oscillations is concerned, it cannot explain the preceding 200 million years without oscillations. Also, there is no evidence that the Arctic Sea was, in fact, open during the glacial waxing. Finally, the fact that most of the ice mass at the warm peaks is located in the Antarctic speaks against Arctic control; it would be a case of the tail wagging the dog.

A theory which has similar elements, but which gives control to the Antarctic, has been put forth by Wilson.<sup>4</sup> In this case, an initial fall of temperature leads to expansion of the sea ice around the southern continent. This reduces the

20

evaporation and hence the precipitation over the Antarctic interior. This reduces the pressure head for plastic flow of the ice, thereby reducing the amount of sea ice, etc. Wilson claims that deep-sea cores suggest that this does happen with a period of about  $4 \times 10^4$  years. Again, the idea is attractive in accounting for the Quaternary oscillations, but leaves the very long warm eras unexplained.

Two basic defects in all of the theories discussed above is that they rest on qualitative reasoning and that they try to isolate a portion of a complex system. With the arrival on the scene of larger and faster electronic computers, it has become possible to construct models in which quantitative relationships replace verbal ones. The present time is therefore one of transition from easy speculation to more rigorous formulation. Unfortunately, the second defect (incompleteness of the models) still remains; it is beyond the capacity of any foreseeable computer to handle a reasonably complete model of the earth-oceanatmosphere system which can forecast the effect of a change of a parameter for several decades or centuries. However, even the relatively primitive models already in use do provide reasonable numerical values for shorter-term trends. References will be made to these models in the sections which follow.

Natural fluctuations on a shorter time scale are, of course, superimposed on the long-term trends. Adequate global temperature data have only been available since about 1880, so only the trends of the past 90 years are known quantitatively. Figure 1 shows the trend of annual mean temperature for three latitude belts over this time period. It can be noted that the period 1880 to 1940 was characterized by a general upward trend except for a slight recession in the period 1910 to 1920. Since 1940 the trend has been sharply downward. The amplitude of the fluctuation is about 0.6°C for the widest latitude band, 0 to 80°N, smaller for 0 to 60°N, and least for 0 to 60°S (due to the buffering effect of the larger area of ocean in the southern hemisphere). It is thus clear that the oscillation has been felt most strongly in the Arctic.

It is not possible to attribute this fluctuation to any single "forcing function." Figure 2 shows the deviation of annual mean and 10-year running mean temperatures from the period mean (1882 to 1960) and the deviations of annual mean solar flux at the ground from the period mean (1886 to

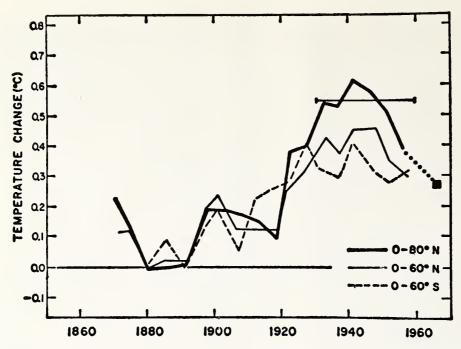


FIGURE 1. Annual mean temperatures for three latitude belts, 1870 to 1967. Data source: Mitchell<sup>4 2</sup> with subsequent updating. The horizontal bar gives the mean temperature in the belt 0° to 80° N for the climatological epoch 1931 to 1960. (From Wilson, C. L., Ed., Study of Man's Impact on Climate (SMIC), Inadvertent Climate Modification, MIT Press, Cambridge, Mass., 1971, 42. With permission.)

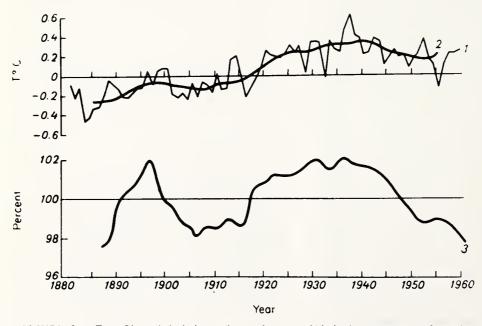


FIGURE 2. (Top) Plot of deviations of annual mean mid-latitude temperatures from the grand mean for the northern hemisphere, 1881 to 1960; Curve 1 is the untreated data while Curve 2 has been smoothed by taking decadal running means. (Bottom) Curve 3 shows the percent deviation of annual mean insolation at the ground from the grand mean 1886 to 1960. Note similarities in fluctuations of Curves 2 and 3. Correlation would be improved if a small upward trend in temperature were subtracted from Curve 2. (From Budyko, M. 1., 43 Climate and Life, Academic Press, New York, 1974, 294. With permission.)

1960). While there are similarities (coincidences of maxima and minima) the variance of even the smoothest temperature curve is not completely accounted for by the solar-radiation curve. In particular, the radiation in 1960 is nearly as low as in 1886, but the temperature is 0.4°C higher. We have made a rough calculation of the correlation coefficient (by scaling data from the figure); the value for zero lag is 0.45, and for a 2-year lag of the temperature behind the solar radiation it increases to 0.51. This leaves more than half the variance of temperature unexplained. Neither cloudiness nor turbidity can be invoked to explain the remainder; the effects of these are included in the measured solar radiation. It is possible that the data for both temperature and solar radiation (taken at discrete points on the globe) are not sufficiently representative, so that sampling errors have biased the results. It is unfortunately true that "global" means are often computed from data collected at rather sparsely distributed stations. Oceanic areas are almost always under-represented: the same is true for the tropics, both on land and sea. Both the quality and quantity of the meteorological data have tended, generally, to increase with time, so that the earlier figures have inherently larger errors than the later ones. None of the authors responsible for Figures 1 and 2 have given any measures of the probable errors associated with the data they have presented. In any case, it is clear that even the best documented climatic trends are very difficult to explain quantitatively, and that the isolation of an anthropogenic component is even more difficult unless it is so strong that it swamps any natural fluctuations. It is possible, for example, that the failure of the temperature curve to drop as much as the radiation curve toward the end of the period is due to increased carbon dioxide (which does not affect incoming solar radiation appreciably). Certainly, if one would subtract an upward trend from the temperature data, the correlation with radiation would improve (we have not done this because of the crudity of the data scaled from the figure).

It might be thought that variations in mean temperature of a few tenths of a degree in 80 years have very little environmental significance; this, however, is not the case. Figure 1 shows that the impact of temperature change is felt most strongly in high latitudes, where the growing season is shortest. A drop in the mean annual temperature

of a degree lasting for several years could cause total crop failure in such marginal regions.

Ecologically important climate fluctuations are of the same order of magnitude as the "noise level" of existing climatological data. Therefore, it is evident that a global monitoring network for climatic change must meet very stringent requirements as to precision and accuracy of data and long-term stability of calibration, as well as immunity from changes due to local human activity.

#### PROBLEMS AND LIMITATIONS OF MATHEMATICAL MODELING OF CLIMATIC CHANGE

In the preceding section a distinction was made between theories and models based on the degree of quantitativeness. A theory establishes a chain of logical connections between events or phenomena; a model is a numerical analog of a system, embodying the theory of the system but as a set of mathematical relationships quantifying the chain of logical connections. By varying the numerical value of a parameter, the response of the system can be calculated. The accuracy of the calculated response obviously depends on the closeness of the analogy between the model and the actual system and on computational limitations such as roundoff error.

Models may be divided into two classes. A diagnostic model is one which is time-independent; it is only of use in describing the state of a system without time lags, or the steady-state condition of a system when one is not concerned about the time required to reach that state. A prognostic model is one which involves the time coordinate explicitly; it is used to forecast the future state of a system from given initial conditions. Most climatic models are necessarily of the second type. since the time needed to achieve a change is an important piece of output information. An example of a diagnostic model is one which relates the amount of solar radiation at the ground to the amount of dust suspended in the air and the elevation angle of the sun. Diagnostic models are often embedded in larger prognostic models, or used to answer questions which arise in the design of prognostic models.

Prognostic models are usually classified according to the number of spatial dimensions along which data are resolved. A global mean, or

zero-dimensional model, is not concerned with any spatial variation. Such a model is usually a special formulation of the first law of thermodynamics, of the form: Power in from sun minus power radiated or scattered back to space equals time rate of change of stored energy. This may be coupled with a statement about the partitioning of the stored energy between various forms inside the earthatmosphere system, and statements about possible feedback effects on the radiative input or output, e.g., an increase in albedo (backscatter to space increases) if the stored energy decreases. The outputs of such models are planetary averages of temperature, precipitation, etc., without regard to latitude, longitude, or altitude. Effects of transport by atmospheric motions are totally parameterized in such models, which are therefore most economical of computer memory and time.

One-dimensional models are used when the details of structure in the vertical or north-south direction are important. In this case, the energy balance equation plus the transport equation (and equations of motion if needed) for the selected direction are used. Transport effects in the other two directions are parameterized or assumed to be zero (axisymmetric models).

Two-dimensional models most commonly assume axial symmetry, e.g., all quantities are taken to be independent of longitude. Solutions are obtained for the vertical-meridional plane. The energy balance equation (which in this and the vertical one-dimensional case must include the equation of radiative transfer) and the dynamical equations in all three component directions (but averaged around the globe in longitude) are needed. Such models can give more realistic results, such as showing the greatest cooling in high latitudes when solar input is reduced, but cannot cope with the obvious differences in longitude which exist in the real world, such as the different thermal, radiative, and mechanical properties of land and water, which are extremely important in determining climate.

Three-dimensional models are obviously the most desirable; they yield distributions of the climatic parameters in latitude, longitude, and altitude. They require the full set of hydrodynamic and thermodynamic equations (conservation of mass, momentum, and energy) and a complete specification of surface boundary conditions. They must allow for interaction with the oceans; in fact, the hydrodynamic equations

for the sea and atmosphere should be coupled. Such models are structurally the same as those used for numerical weather prediction for short periods, but are necessarily more elaborate because phenomena such as air-sea interaction and radiative energy transfer which can usually be treated as constant or zero for short periods become highly important for long-range prediction.

In any model involving one or more space dimensions, data are only specified at a finite number of points in space; spatial derivatives are represented by their finite-difference analogs. The finer the grid of points, the smaller are the errors arising from this incomplete description of reality. Events on a smaller scale than the grid are either ignored or parameterized (motion, for example, is treated as a kind of diffusion). In any global model, the formation of clouds and precipitation must be treated in this way, since clouds are obviously below any reasonable grid scale. Since the number of grid points tends to increase more or less as the power of the number of dimensions and the number of arithmetic operations increases even more strongly, the amount of detail which can be incorporated in a model is ultimately limited by computer memory capacity and speed. If too coarse a grid is used, the model output will be dominated completely by the cumulative effects of roundoff and truncation errors, while if it is made very fine the number of operations becomes astronomical. Since a climate model must be capable of forecasting for decades or centuries, the ratio of forecast time to real time must be very large. A ratio of 144, for example, means that a computer can make a 72-hr forecast in 30 minutes. A 100-year climatic forecast with this model would require that the computer run uninterrupted for about 8.5 months. It is therefore clear why really complete three-dimensional models for long-range prediction are nonexistent; those that have been developed are very highly parameterized and involve "smoothing" the data and the equations by averaging in both time and space so that longer time steps may be used in computation.

Despite these limitations, the models currently in use do respond to changes in initial conditions in reasonable ways, and represent a great improvement over the speculative approaches of the pre-computer era.

A detailed and thorough discussion of the problems and limitations of climatic modeling is available in an article by Smagorinsky.<sup>361</sup>

## CARBON DIOXIDE AND THE TERRESTRIAL HEAT BALANCE

The possible role of carbon dioxide released by fuel combustion as a modifier of the global heat balance is probably the earliest example of largescale inadvertent climate modification to be recognized. After the identification of this gas as a regular constituent of the atmosphere in the middle of the 18th century, many experimenters measured the concentration of CO2 at numerous geographic locations at the ground, in cities and rural sites, in buildings, and in the free atmosphere using manned balloons and aircraft. Prior to the last decades of the 19th century, these measurements were usually directed toward an understanding of the biological carbon cycle in nature or to air pollution studies, both indoors and out. (Because a thorough bibliography covering these early observations is available,45 they will not be referenced in this paper). In 1894, Trabert<sup>46</sup> published early data on the radiation-absorbing properties of this gas; this discovery led to the recognition that CO2 played a significant role in the heat budget of the atmosphere. Since that time, a great deal of laboratory work has been devoted to refining the data on the absorption spectrum of this gas and its dependence on pressure and temperature. It has been found that CO<sub>2</sub> has two very strong but fairly narrow absorption regions centered at 2.8 and 4.3  $\mu$ m, and an exceedingly strong and wide band from 13 to 18  $\mu$ m centered near 15  $\mu$ m, together with a number of weaker bands near 2.1, 4.8, 9.3, 10.3, and 12.5  $\mu$ m. All of these wavelengths are in the near infrared; the 15  $\mu$ m band, in particular, is in the spectral region where the radiation from the surface of the earth is intense. For this reason, the radiation from the surface in this band cannot go directly to space; it is absorbed by the CO<sub>2</sub> in each infinitesimal layer of the atmosphere, which then radiates it back, half upwards to the next layer, but half downwards to the ground or the layer below. The CO<sub>2</sub> thus acts as a resistance to the radiative flux of heat from earth to space. The earth, however, must somehow radiate as much power to space, in the long run, as it receives. In order to do so in the face of this CO<sub>2</sub> resistance, it must raise its "potential," namely the temperature of the surface, which is therefore higher than it would be if the CO2 were absent. On the other hand, solar energy in the 2.8 and 4.3  $\mu$ m bands is impeded from reaching the surface, but this energy is a tiny fraction of the total solar flux. This effect of an infrared-absorbing gas on temperature near the ground is commonly referred to as the "greenhouse effect" although the analogy is not exact; a greenhouse also has the important property of blocking *convective* heat and water vapor transport from the plants by the atmosphere.

The greenhouse effect is complicated by the fact that both ozone and water vapor also absorb in the near infrared. Since there is some overlap between the water and CO<sub>2</sub> band, and since the optical thickness of water vapor at a point on the earth is highly variable and dependent on the circulation of the atmosphere, modeling of the effect is far from simple.

The potential climatic influence of changes in CO<sub>2</sub> concentration is thus a modulation of the greenhouse effect. Since CO2 is a product of the combustion of all common fuels (except hydrogen), and since the rate of use of such fuels has grown steadily since the industrial revolution, the possibility of a climatic effect suggests itself. This question was first investigated by Callendar<sup>47</sup> in 1938. He started from a set of CO<sub>2</sub> measurements taken in England in the "free air" away from local pollution sources which yielded a mean value of 274 parts per million by volume (ppmv). Combining this with the estimated CO<sub>2</sub> production by combustion,  $4.3 \times 10^9$  tons/year, and a loss to the sea based on a turnover time for the total mass of the sea of  $2 \times 10^3$  and  $5 \times 10^3$  years, he extrapolated the CO<sub>2</sub> concentration to about 290 ppmv in 1936, 314 ppmv in 2000, and 346 ppmv in 2100. If the oceanic sink was neglected, the figures were 296, 335, and 396 ppmv. He then compared this extrapolation with the mean of 1156 measurements made in the eastern United States during the period 1930 to 1936, which was 310 ppmv. He also noted that the CO<sub>2</sub> data at Kew Observatory (somewhat affected by urban pollution) from 1898 to 1901 yielded a mean of 292 ppmv. Under the assumption that the American data were biased toward the high side by similar effects, he concluded that his extrapolation of a 6% rise from 1900 to 1936 was supported by the data. He then calculated, by a zerodimensional radiative-transfer model, the magnitude of the temperature increases to be expected from this addition of  $CO_2$ ; it was  $7 \times 10^{-3}$  °C/year for the period 1910 to 1930. From this, one can

calculate the thermal effect of doubling the CO<sub>2</sub> from 300 to 600 ppmv; it amounts to a rise of about 2.4°C. He then cited climatological data demonstrating the temperature rise from 1900 to 1936 (similar to Figure 1) and showed that (for the earth as a whole) the observed trend was somewhat steeper than could be accounted for by the CO<sub>2</sub> increase alone.

This paper received considerable damnation with faint praise when it was read before the Royal Meteorological Society. The use of a zero-dimensional radiative-transfer model was said to be much too inaccurate, the 36-year upward temperature trend could equally well be due to changes in the general circulation, and the CO<sub>2</sub> trend was claimed by one critic to be below the noise level of CO<sub>2</sub> analyses. Another argued that Callendar had grossly underestimated the strength of the oceanic sink; he cited some calculations which showed that if a difference in partial pressure of CO<sub>2</sub> of only  $10^{-5}$  atm between air and sea were maintained, the sea would take up  $3.7 \times 10^9$  tons/year of CO<sub>2</sub> or 86% of the annual production by combustion.

This paper and the criticism it received raised all of the key points of the CO<sub>2</sub> problem. The work of the nearly four decades since has clarified them to varying degrees.

In his second paper 48 Callendar examined what he believed to be the most reliable and representative data sets for CO<sub>2</sub>, with the purpose of seeing whether or not air masses of different latitudes of origins showed differences in CO2 mixing ratios. He argued that the tropical ocean should be supersaturated with CO<sub>2</sub> and act as a source to the tropical air masses, while the water in high latitudes should be undersalurated and function as a sink, so that arctic air masses should be CO<sub>2</sub>-poor. The data tended to give some slight support for this hypothesis, though the correlation with wind direction was weak. Data from Cape Horn and Northern Finland lent stronger support to the idea; it is now known, however, that the very low values from Cape Horn (down to 231 ppmv) must have been in error.

This paper also gives the first estimate of the amplitude of the annual cycle; a peak to trough range of 6.5 ppmv with winter maximum is given for a set of over 1000 measurements in the period 1872 to 1901. Callendar also noted that the data, when plotted against time, showed relative steadiness up to about 1900, and a rising trend thereafter. Unfortunately, as Figure 3 shows, the 20th century data are bunched together in only three groups (1898 to 1901, 1909 to 1912, and

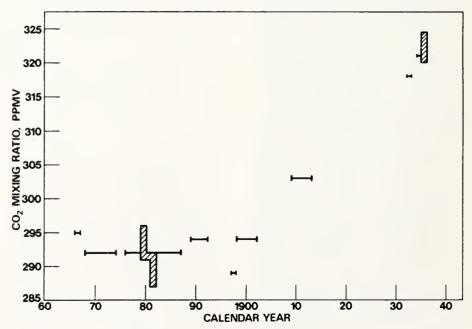


FIGURE 3. Measurements of volume mixing ratio of atmospheric carbon dioxide for the period 1865 to 1935 which were considered to be reliable by Callendar. Solid bars indicate mean of a single set of measurements by a particular experimenter or group during the time interval shown. When more than one data set existed in a given year or period, the upper and lower bounds established by the different data sets are the boundaries of the hatched areas. (From Callendar.<sup>47</sup>)

1932 to 1935), so that the actual behavior up to 1935 is not well represented.

The increase from 1900 to 1935 of about 30 ppmv corresponds to a mass increment of 2 X 10<sup>11</sup> tons; the estimated production by combustion is 1.5 X 10<sup>11</sup> tons. Callendar explained the excess as being due to delayed mixing into the southern hemisphere from the source region in the northern (now known to be incorrect; the mixing time is too rapid to allow this). He concluded that the oceanic sink was very weak, and that essentially all of the combustion product remained in the atmosphere for centuries. His third paper<sup>49</sup> essentially repeats the same data and conclusions.

Interest in CO<sub>2</sub> measurements tended to die out after 1900. Except for the set taken near Boston, Massachusetts from 1909 to 1912, almost all of the measurements until 1954 were taken by the Finnish oceanographer K. Buch<sup>50</sup> (the data for 1932 to 1935 were taken by him). He also published a review<sup>51</sup> (in Swedish) of Callendar's work. Except for Buch's activity, the period 1940 to 1954 was a slack one for research on atmospheric CO<sub>2</sub>.

One possible reason for this is that the collection and analysis of samples was tedious and time-consuming. Also, because a wet-chemical technique was the only one available at the time, systematic errors due to small differences in technique cast some doubts on whether the numbers obtained were accurate enough to give confidence in Callendar's trend. The technique used until the late 1950s involved collecting air in evacuated glass flasks (or pumping it through a reaction vessel) containing carefully measured amounts of standard alkali or alkaline-earth hydroxide solution, allowing the CO2 to react, and then titrating the solution to an indicator endpoint (usually phenolphthalein) with standard hydrochloric acid. (Some early data were obtained by absorbing the CO<sub>2</sub> on alkali or alkaline-earth hydroxide pellets and weighing them, but this method was grossly inaccurate due to water absorption and was soon abandoned.) As every first-year chemistry student knows, both systematic and random errors are very frequent when such a technique is used, regardless of how simple it seems in principle. The stock solution of standard base must be scrupulously protected against premature exposure to atmospheric CO<sub>2</sub>. Burettes must be precisely calibrated rather than relying on the graduation of their barrels. Reproductibility of menisci and drop-splitting on burettes is often imperfect, as is the reading of positions (parallax errors). End-point determinations depend on color judgments; ideally, therefore, all laboratories should use the same normalities of acid and base and add the same quantity of indicator. Filling of the sample flasks also offers opportunity for sampling error, such as not facing into the wind when opening the valve, or opening it too close to vegetation in leaf, etc. In view of all of these opportunities for error, it is not surprising that much of the early to middle 19th century data are totally useless. Reported concentrations in outdoor air covered the range from 100 to over 700 ppmv.

At an informal conference on atmospheric chemistry held in Stockholm in 1954, Professor Buch called the attention of Professor C.-G. Rossby, founder and director of the International Institute of Meteorology, University of Stockholm, to the importance of the study of atmospheric CO<sub>2</sub> and to the way in which it had been neglected for nearly 20 years. As a result of this meeting, a network of 15 stations<sup>52</sup> in the 4 Scandinavian countries (Sweden, Norway, Denmark, and Finland) was established, taking flask samples 3 times per month. These were analyzed partly at Stockholm and partly at Helsinki, with occasional cross-checks (using two flasks filled at the same place and time) to guard against systematic differences in technique. The mean of all observations for the first year, 329 ppm, did lend support to the idea of a secular increase (the 1935 data averaged around 322). The amplitude of the annual cycle was rather large (as much as 40 ppmv) and in Finland showed a reversed phase; attempts were made to account for this on the basis of the atmospheric circulation.

At about this same time, a renewal of interest in modeling the effect of CO<sub>2</sub> on climate took place. Erikson and Welander<sup>5 3</sup> devised a "box" model with four reservoirs: the air, the sea, 'the living biosphere, and the dead biosphere. Reversible exchanges were assumed for the fluxes between the air and the sea, and between the air and the living biosphere (photosynthesis and respiration), while one-way fluxes were assumed to take place from the living to the dead biosphere and from the dead biosphere to the air. No communication between the biosphere and the sea was allowed; biological processes in the sea were considered purely a matter of its internal

26

economy. For purely physical processes, rates of exchange were considered to be proportional to concentration differences. However, the exchange rates between the living biosphere and the other boxes were taken to be empirical functions which were proportional to concentrations when the latter were small, but changed progressively to decreasing functions of concentration when the latter became large (reflecting the fact that land plants grow faster as the available CO2 increases up to a point, after which growth slows down and eventually goes to zero). These assumptions led to a coupled set of three first-order differential equations, of which two are nonlinear, plus one algebraic equation, to be solved for the time dependence of the CO<sub>2</sub> in each reservoir. Because of the nonlinearity of two of the equations, the solution could not be obtained in terms of the usual exponential functions. Some topological properties of the solution were determined, showing that oscillations were possible for some ranges of parameters and initial conditions. Numerical solutions were obtained for a few cases, using a first-generation electronic computer. It was found that introduction of time lags in response of the biosphere and/or the sea tended to encourage oscillations with periods of a few hundred years. Adding CO<sub>2</sub> at a constant rate in their model resulted in most of the addition going into the biosphere with little effect on the atmosphere. They attributed the apparent observed rise of CO<sub>2</sub> after 1860 as perhaps being part of a natural oscillation rather than a sustained increase.

In the same journal issue, Plass<sup>54,55</sup> presented a model combining two boxes (atmosphere and sea) for CO2, two for nongaseous water (sea and ice caps), and a radiative-transfer algorithm to predict temperature. His model had the virtue of permitting oscillations for some ranges of the parameters, because of delay times in the sea, thus accounting for the Pleistocene oscillations. Unfortunately, h wever, he used an early estimate of the pelagic turnover time of 10<sup>4</sup> years, about 10 times longer than later estimates. Since the oscillation period in the model must necessarily be of the same order of magnitude as this turnover time, it does not now appear that the model accounts satisfactorily for the oscillations. The sequence of events giving rise to the oscillation starts with a drop in CO2 reducing mean global temperature and the CO2 in air and sea moving toward equilibrium. Ice begins building on land; the water

tied up in the ice is distilled from the sea, thus increasing the carbon concentrations therein and initiating a flux of CO2 to the air in a move toward equilibrium; this initiates a warming, the ocean and air approach CO<sub>2</sub> equilibrium, but the melting of the ice (after a certain lag time) dilutes the ocean, rendering it undersaturated and thus starting another cycle. He estimates that this oscillatory behavior would ensue if the total air and sea CO<sub>2</sub> content were reduced somehow by about 7%. He ignores the biosphere for long-term trends, arguing that increased respiration and decay oxidation will quickly (on a geologic time scale) balance the increased photosynthesis following an increase in CO<sub>2</sub>. The model predicts a global mean temperature increase of 3.6°C for a doubling of atmospheric CO<sub>2</sub> and a drop of 3.8°C when it is halved (from a base of 300 ppmv) under assumptions of clear skies. With average cloudiness, these changes become 2.5°C and 2.7°C respectively.

One of the main contributions of this work was the refutation of the earlier contention that CO<sub>2</sub> would have little effect on temperature because of the overlap with water absorption; Plass showed that when the fine structure of the absorption spectra was taken into account, the overlap was quite small.

At very nearly this same time, Suess 56 and his co-workers at the Scripps Institute of Oceanography began to apply the technique of radiocarbon dating to the problem of atmospheric CO<sub>2</sub> changes. Because CO<sub>2</sub> from fossil fuels is nearly free of C14 due to radioactive decay, addition of this old carbon to the air should dilute the C14 and result in a lower ratio of C14 to total carbon. It follows that carbon laid down in tree rings prior to 1900 should be richer (after correction for radioactive decay) than more recent tree rings (as long as the recent rings were not laid down after the beginning of thermonuclear testing in the early 1950s). When the analyses were carried out, it was found that recent tree rings were only deficient by about 1% as compared with those laid down around 1900. This indicated that the man-made increase in CO<sub>2</sub> since 1900 was only about 1% instead of Callendar's 10%, and that therefore the sea was taking up about 90% of the combustion CO<sub>2</sub>. Once again, doubt was cast on the reality of the upward CO<sub>2</sub> trend, and at the same time, a turnover time of thousands of years for the sea was apparently excluded from possibility.

Callendar<sup>5 7</sup>, however, again reviewed the data and defended his trend, while conceding that the C<sup>14</sup> analysis was difficult to explain.

This paradox gave rise to a considerable amount of concern about the role of the sea in the carbon cycle. Schloesing<sup>58</sup> had called attention in 1880 to the large storage capacity of the sea for oxidized carbon and the consequent buffering action of the sea on the atmospheric CO<sub>2</sub>. The concept was developed further by Harden<sup>59</sup> and Krogh<sup>60</sup> (the latter was apparently a good theoretical chemist, but a bad experimentalist; some of his atmospheric CO2 analyses near Greenland gave concentrations as high as 700 ppmv). The ideas in these papers were summarized in a short paper by Hann<sup>61</sup> in 1905. These authors note that sea water has an excess of cations, i.e., is basic with respect to neutral water (pH  $\approx$  8.0). This excess alkalinity, which varies somewhat with water mass in the sea, was (by 1905 estimates) equivalent to about 52.8 mg/l or 26.9 cm<sup>3</sup>/l at ntp, i.e., this much CO2 would have to be added to the water to combine with the excess cations to form carbonates (calcium and magnesium). On the other hand, in North Atlantic surface waters, the total dissolved inorganic carbon was equivalent to 49.1 cm<sup>3</sup>/l CO<sub>2</sub> at ntp. Despite this apparent capacity to take up more CO2, experiments involving shaking sea water with air of normal CO2 content resulted in a release of CO2 to the air (probably because the experimental vessel was warmer than the sea temperature). These facts made it clear that the equilibrium between sea and air with respect to CO<sub>2</sub> depended upon the chemical potentials of four species in the sea, namely CO<sub>3</sub><sup>-2</sup>, HCO<sub>3</sub>, dissolved CO<sub>2</sub>, and total excess alkalinity A. The activity of dissolved CO2 may be expressed as a partial pressure; the difference between this pressure and that of the atmospheric CO<sub>2</sub> provides the driving force for air-sea exchange of the gas. However, the change in pCO<sub>2</sub> in the water is not simply proportional to the amount of CO<sub>2</sub> taken up or outgassed, because the other ionic species will change concentration to provide or remove some of the CO<sub>2</sub> involved in the exchange with the air. This buffering action tends to hold pCO<sub>2</sub> in the sea nearly steady when relatively large volumes of gas are exchanged; Hann cites a relationship of a change in pCO2 in the atmosphere of  $\pm 1.45 \times 10^{-4}$  atm causing a transfer to or from the sea of 4.3 cm<sup>3</sup>/l relative to a pre-existing content of 36.7 cm<sup>3</sup>/l. It is also noted that, if the atmospheric mixing ratio is 300 ppmv,

the sea contains about 27 times the amount of  $CO_2$  in the atmosphere (this figure is now known to be too small by more than a factor of 2). It is further calculated that, in order to raise the atmospheric  $CO_2$  content to 400 ppmv at equilibrium, the total atmospheric burden of  $CO_2$  would have to be raised from  $2.4 \times 10^{12}$  tons to  $5.6 \times 10^{12}$  tons.

It is stated without proof (which is really required, since equilibrium constants do not give any information about rates) that the rate of exchange between air and sea is "remarkably fast;" the estimate given is 0.525 cm<sup>3</sup> CO<sub>2</sub>/cm<sup>2</sup> sea surface/year for a  $\Delta pCO_2$  of  $10^{-3}$  atm. This corresponds to a total flux to or from the sea of 3.85 × 10<sup>9</sup> tons/year. Hann thus calculates that, at the 1905 rate of combustion, the doubling time for atmospheric CO2 in the absence of the sea would be about 10<sup>3</sup> years, but that the effect of sea buffering would permit the atmospheric CO<sub>2</sub> to rise only to 350 ppmv in that length of time. He cites as evidence for the reality of this process that in general the measured atmospheric CO2 values are smaller over the (temperate) seas than over land, implying a net flux to the sea.

While the basic concepts of these three pioneering papers remained qualitatively valid during the ensuing 75 years, much effort has gone into refining the quantitative values of the equilibrium and rate constants and insuring that all molecular species involved in the equilibrium chain have been accounted for, as well as accounting for nonchemical parameters of importance (transport processes in the sea, mechanical control of the flux through the air-sea interface, etc.).

One of the first modifications which had to be made was the treatment of the sea as a single reservoir. Over most of the earth, the thermal stratification is such that, while the upper few hundred meters of the sea are often neutrally stable with respect to vertical displacements and can therefore be easily stirred by wind action, at least one layer (the thermocline) is stably stratified and hence is a strong barrier to mixing by stirring. Only in high latitudes in winter (mainly in the Antarctic) does the thermocline disappear (due to strong surface cooling), so as to permit free communication between surface and deep waters for a time each year. It follows that only a fraction of the total sea volume, about 2%, can be involved in the fast equilibration postulated by the early investigators already cited.

Radioisotope dating has confirmed this, and has

provided estimates of the mean lifetime of a particular 66,67 molecule in the waters below the thermocline.62-64 These cover the range from 500 to 3000 years. Radioisotope measurements in the water above the thermocline 64-66,68 and further radiocarbon analyses of tree rings 9,70 give residence times for CO<sub>2</sub> in the atmosphere against uptake by the sea ranging from 20 months to 10 years.

The earlier idea that there is everywhere a flux of CO<sub>2</sub> from air to sea has had to be modified on the basis of data taken on numerous oceanographic cruises: <sup>71-76</sup> These data generally show that the tropical oceans between about 15°S and 15°N are usually supersaturated and acting as a source of CO<sub>2</sub> for the atmosphere. This is also the case in regions of upwelling of deeper waters, such as off the west coasts of the Americas in lower middle latitudes. Otherwise, most middle and high latitude seas are close to equilibrium of are subsaturated (sink for atmospheric CO<sub>2</sub>). Some exceptions occur; the Benguela Current off South Africa's west coast, which is associated with upwelling, tends to be undersaturated, <sup>76</sup> while the

waters of the southeast Bering Sea appear supersaturated when ice leads open and expose water to the air.<sup>75</sup>

The problem of the rate of transport of CO<sub>2</sub> across the sea-air interface has been studied experimentally by several investigators. 64,77-80 Craig 64 reports a (presumably mean) value of about 2 X 10<sup>-3</sup> mole/cm<sup>2</sup>/year, (44.8 cm<sup>3</sup>/cm<sup>2</sup>/year at n.t.p.), while Keeling<sup>79</sup> gives the mean rate constant between 30°N and 30°S latitudes to be 18 moles/cm<sup>2</sup> atm/year. Assuming that these two estimates are compatible, the partial pressure excess in the sea in this latitude band must then be close to 10<sup>-4</sup> atm. Kanwisher<sup>77</sup> points out that, on the basis of aerodynamic boundary layer considerations, the rate constant should depend on the mean squared surface wind speed over the sea, and hence would be different at different latitudes, most likely maximizing in the "roaring forties" of the southern hemisphere.

The four-species chemical equilibrium of 1905 has been expanded to six, and others have been suggested. The set of six can be written schematically as

$$CO_2(g) \rightleftharpoons CO_3(aq) \rightleftharpoons H_2CO_3(aq) \rightleftharpoons HCO_3^-(aq) \rightleftharpoons CO_3^{-2}(aq) \rightleftharpoons MCO_3(s)$$

in which (g) means gaseous, (aq) means in aqueous solution (in the sea), s means solid, and M is a divalent cation (Ca or Mg). Each double arrow implies an equilibrium constant (which in turn depends on the temperature, salinity or, more accurately, the chemical composition of other dissolved solids, and pH of the sea) and a pair of rate constants when the system is out of equilibrium. These constants are affected by the stratification of the sea referred to earlier; if, for example, all or most of the precipitated carbonates are on deep-sea bottoms, the rate constant for the last approach to equilibrium on the right side of the set of equilibria shown above is of the order of several hundred years when referred to the far left side. In practice, it is necessary to write this set of relations for the two marine reservoirs separately, omitting the first equilibrium on the left for the deep layer and (probably) the last equilibrium on the right for the shallow upper layer, and then coupling them with a rate constant of the order of  $2 \times 10^{-3}$ /year when embedding this chemistry in long-term climatic change models. For assessing short-term effects, only the top layer need be considered (possibly corrected by a small constant sink term giving the flux to the deep layer).

There have been several suggestions that the relatively simple chemistry shown above should be modified to take account of the fact that the sea contains living organisms. Alekin and Moricheva<sup>81</sup> pointed out that the marine biological cycle disturbs the simple inorganic equilibria; marine vegetation takes up CO<sub>2</sub> which ultimately ends up as CaCO3 in crustacean shells and coral beds. Thus, the last equilibrium on the right could possibly be important in the upper marine layer, at least near shore, with equilibrium and rate constants which are biologically determined. Eriksson<sup>8 2</sup> has suggested that serious disturbances of the marine biota could result in world-wide changes in the atmospheric CO<sub>2</sub> concentration. More recently, Berger and Libby<sup>83</sup> have called attention to the possibility that enzymes of biological origin (carbonic anhydrases) might affect the rates and equilibria in the sea. They supported their hypothesis by laboratory experiments, but did not show that these enzymes were in fact present in sea water in sufficient concentrations.

Bolin and Eriksson<sup>84</sup> incorporated the chemistry presented above into a non-equilibrium (unsteady) model of the "box" type with one

atmospheric and two marine reservoirs. This model showed, among other things, that it was possible to reconcile the low "Suess effect" (ratio of C<sup>14</sup>/C<sup>12</sup> in recent and 50-year-old tree rings) with Callendar's estimate of a 10% rise in CO<sub>2</sub>. The first and most obvious reason is that only about 2% of the sea is involved in the interaction with the atmosphere on a time scale of decades, and the second is that the hydration and dissociation rates of CO2 and H2CO3 are sensitive to pH in such a way as to give a positive feedback, i.e., addition of CO<sub>2</sub> to the water raises the pH and shifts the dissociation equilibrium with the ionized form to the left, thus further increasing the amount of carbon in the CO<sub>2</sub> (aq) chemical reservoir. Much of the CO2 thus made available is relatively old, hence richer in C14 than the newest CO2 in the atmosphere. Since diffusion of CO<sub>2</sub> at the interface between air and sea is a two-way street, it follows that some of the new atmospheric CO<sub>2</sub> is replaced with older CO<sub>2</sub> whose carbon has spent some time in the ocean as HCO<sub>3</sub> or CO<sub>3</sub><sup>-2</sup> Therefore, the Suess effect (which assumes a steady state of pH) overestimates the flux of CO<sub>2</sub> to the water (because a one-way street is implied). The key result of this model is that, depending on the choice of the model parameters, the fraction of the combustion CO2 which remains in the atmosphere lies between 60 and 75% rather than the 10% implied by the Suess effect considered without regard to the transient behavior of the ocean-atmosphere system. This reconciliation with the Suess effect (which, on the basis of further measurements<sup>85</sup> had been increased to a 3.5% dilution by fossil CO<sub>2</sub> by 1957) was more satisfactory than an earlier attempt by Callendar<sup>86</sup> based on less quantitative considerations of biospheric circulation and possible sea temperature changes. Bolin and Eriksson showed schematically how the biospheric constants could not be estimated as well as those for the sea, and because of the complexity of the resulting system (at least sixth-order), no attempt was made to compute with this model.

In a later paper, Bolin<sup>8 7</sup> studied the details of the transfer of  $CO_2$  across the air-sea interface, and found that the flux of atmospheric  $CO_2$  was controlled principally by the characteristics of a thin (35  $\mu$ m) boundary layer in which the rate of hydration of  $CO_2$  was slow compared to diffusion of the  $CO_2$  (aq). This meant that the flux through this layer was due *only* to the species  $CO_2$  (aq) and not to the total ensemble of dissolved  $CO_2$ ,

H<sub>2</sub>CO<sub>3</sub>, HCO<sub>3</sub><sup>-</sup>, and CO<sub>3</sub><sup>-2</sup>; the flux would be much larger if the equilibrium between species were established before the diffusion (the apparent solubility of CO<sub>2</sub> in the boundary layer would be higher). The result was a further reduction in the estimated buffering action of the sea.

The middle 1950s brought a technological improvement which simplified the measurement of atmospheric  $CO_2$  and increased the accuracy. This was the replacement of the wet-chemical technique of analysis by a physical method, namely measurement of extinction of radiation in the 15  $\mu$ m band by a column of air. The infrared  $CO_2$  analyzer<sup>88</sup> made continuous, unattended measurements possible for the first time, with a relative accuracy of  $\pm 1$  ppmv. It was then possible to obtain better mean values and to avoid sampling biases linked to the time of day and biological activity. <sup>89</sup>

With this new technique available, it was decided that an attempt should be made during the International Geophysical Year to obtain some definitive measurements at sites as unaffected as possible by urban pollution or biological activity. Dr. Harry Wexler of the U.S. Weather Bureau was successful in establishing CO<sub>2</sub> programs in Antarctica and at the Mauna Loa Observatory in Hawaii. The analyzers and their calibration were provided by a group under C. D. Keeling of the Scripps Institution of Oceanography, University of California, 90 who also initiated a measurement program at the Scripps site in La Jolla, California. Data obtained from Antarctica were sporadic due to logistics and maintenance problems. A run of 9 months was obtained in 1958, at Little America; the equipment was then shifted to the Amundsen-Scott station at the South Pole, where good data were obtained for June through August of 1960 and from April 1961 through October 1963. Air samples taken in evacuated glass flasks were, however, taken at weekly intervals during 1963 and later years and shipped to a laboratory where they were measured on the same type of infrared analyzer. The flask samples were processed only at Scripps until 1966, at which time a duplicate facility was established in the Atmospheric Physics and Chemistry Laboratory (APCL) of the Environmental Science Services Administration (ESSA) in Boulder, Colorado and reassigned in 1971 to the Air Resources Laboratory (ARL) of the National Oceanic and Atmospheric Administration (NOAA). Continuous measurement was only resumed at the South Pole in January 1975.

The Mauna Loa record, on the other hand, is very nearly continuous from March 1958 to the time of writing (April 1975), or a period of 17 years. It thus constitutes the most definitive data set in existence for atmospheric CO<sub>2</sub>.

An infrared analyzer was acquired for processing the flask samples from the Scandinavian network and used during 1959. This seems to have been the final year of operation of that network; no data for subsequent years appear in the literature. It is probable that the Scandinavian program, like so many scientific endeavors, died from lack of financial support.

A program of measurement in the Arctic was carried out by Kelley<sup>91,92</sup> from July 1961 through February 1963, also using the infrared analyzer. Bischof, of the Department of Meteorology, University of Stockholm, has collected flask samples on aircraft<sup>93-96</sup> of various types, including commercial transpolar and transatlantic flights (this seems to have been the only surviving part of the Scandinavian program) from 1963 to 1968.

A three-year program of measurements in Italy was carried out by De Maio et al.<sup>97</sup> during 1964 through 1966.

The NOAA-ARL monitoring program has been expanded to include continuous CO<sub>2</sub> analysis at Point Barrow, Alaska (as well as resumption at the South Pole) and a fourth station in the low latitude of the southern hemisphere is expected to be operating within a year (W. D. Komhyr and T. B. Harris of ARL, private communication).

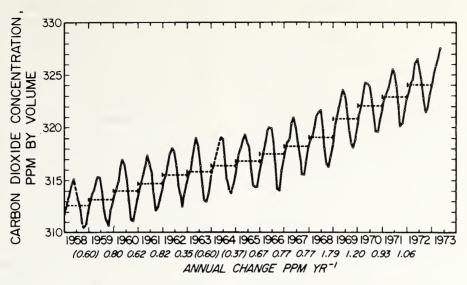
The adoption of the infrared analysis technique greatly reduced the scatter among the data, in part because the continuous record made it possible to eliminate sampling errors (by discarding anomalously high data caused by sporadic pollution), but also because the responsibility for all calibrations has been kept in one laboratory (Keeling, Scripps Institution of Oceanography). The IR technique is not an absolute measurement; the instruments are calibrated several times each hour by passing a reference mixture of CO<sub>2</sub> and dry nitrogen (or N2-O2 mixture in the normal atmospheric proportion) through the instrument. 98,99 The reference gases are prepared by gravimetric or volumetric means and stored in ordinary steel gas cylinders. The references used at each station are checked regularly against "primary" references at Scripps; these in turn are checked against each other (newer against older). Strangely enough, it has been found that such

mixtures, stored in cylinders for some months or years, do exhibit small unexplained variations in mixing ratio with time; also, mixtures of CO<sub>2</sub> with N<sub>2</sub> and of the same volume mixing ratio of CO<sub>2</sub> with N<sub>2</sub>-O<sub>2</sub> blends do not give exactly the same readings on the analyzer. For these reasons, a central calibration authority has been essential.

One point which seems not to have been discussed extensively in the literature is that the CO<sub>2</sub> mixing ratios obtained with the new technique starting in 1958 showed an abrupt drop of about 10 ppmv from all the older data of the Scandinavia network and of Buch. It is not clear whether this is due to a systematic error in the wet-chemical method, or whether it is a result of the location of the newer stations in nearly life-free regions. Bischof<sup>93</sup> did note that aircraft samples tended to be poorer in CO<sub>2</sub> than those taken near the ground in Scandinavia. Whatever the reason may be, this discrepancy makes it impossible to compare data taken before 1958 with the later information.

It will be recalled that, prior to 1958, there was no agreement that Callendar's secular increase was real; the statistical significance of the older data was challenged and defended. By 1971, however, the data from the several programs listed above show a consistent pattern, and this has continued up to the present.

The monthly mean values of CO<sub>2</sub> mixing ratio at Mauna Loa for the period 1958 to 1973 are plotted in Figure 4. The significant features of this curve are (a) an annual cycle with a peak to trough amplitude of about 5 ppmv, with a maximum in late spring and a minimum in late fall; and (b) a smooth upward trend from about 312 ppm in early 1958 to 324 ppm in 1973 when the annual march is removed by numerical filtering. The trend is not linear, but shows changes in slope which vary from about 0.5 to over 1.0 ppm/year; the mean value is close to 0.7 ppmv/year or about 0.2% of the mean concentration each year. One point of interest concerning the annual cycle is its phasing; data taken at stations in close contact with the biosphere in temperate latitudes show the maximum in winter and minimum in summer, due to the high rate of CO<sub>2</sub> removal by photosynthesis during the growing season, Mauna Loa Observatory, however, is situated in the middle of relatively recent lava beds which do not even support lichens, so that no biospheric CO<sub>2</sub> sources (other than station personnel) contribute directly



# MEASUREMENTS OF ATMOSPHERIC CARBON DIOXIDE AT MAUNA LOA OBSERVATORY, HAWAII

FIGURE 4. Plot of monthly mean volume mixing ratio of atmospheric carbon dioxide for the period 1958 to 1973 at Mauna Loa Observatory, Hawaii, at 3.4 km MSL. Annual means are shown as dashed bars. The numbers plotted below the years along the abscissa are the annual increases, i.e., the slope of the curve which would be obtained if the annual marches were removed by numerical filtering. (From C. D. Keeling, private communication via L. Machta and W. D. Komhyr.)

to the CO<sub>2</sub> burden. Air does move upslope from tropical forest regions during the afternoon (this is reflected in the daily cycle as an afternoon minimum) but this vegetation is fairly constant in photosynthethic activity throughout the year. The observed phase shift suggests that the mean time since the air over Mauna Loa was in contact with the temperate biosphere is three to four months.

The short run of continuous data from the Antarctic, 1961 to 1963, is insufficient to determine the amplitude of the annual march there, but it appears that it is smaller than at Mauna Loa (about 2 ppmv), with the maximum in late spring and the minimum in fall or winter (southern hemisphere). The biospheric effects are therefore less strong than at Mauna Loa, although the delay time is about the same; this probably reflects the smaller amount of forested land in the southern hemisphere. The upward trend is 0.72 ppmv/year in good agreement with the Mauna Loa data, although less confidence can be placed in this trend because of the smaller data base. Unfortunately, no CO2 data for Antarctica have been published since 1963 (although flask samples have been taken and sent to Scripps), so that the trend in recent years is not known.

Data from the Arctic 91,92,105 show annual

means about 2 ppmv higher than the Antarctic; the trend is, again, close to 0.7 ppmv/year. The aircraft data of Bischof, 106 when broken down into upper tropospheric and stratospheric data, show an annual cycle of range 8 to 9 ppmv in the troposphere, with spring maximum and summer to early fall minimum, similar to Mauna Loa but with the minimum occurring 2 months earlier. The stratospheric data have a smaller amplitude, comparable to the Antarctic (2 ppmv) and show the maximum in early fall and minimum in late winter. This paper also gives the Antarctic cycle, based on a report (apparently unpublished) of Keeling et al. in 1972, with the 2 ppmv amplitude but having the peak in November and trough in March through April. The stratosphere and the Antarctic thus appear to behave similarly, while the upper troposphere between 50 and 70°N latitude is similar to Mauna Loa. The trend of the aircraft data is shown to have increased from 0.5 ppmv/year in 1963 to 1.3 ppmv in 1971, with an "acceleration" of 0.09 ppmv/year<sup>2</sup>. The mean trend during the period was 0.9 ppmv/year.

The concordance among these data sets has established beyond any question the reality of an increase in atmospheric CO<sub>2</sub> since 1958. Figure 5 summarizes the annual mean data up to 1970; a

world-wide increase of from 312 to 313 ppmv in 1958 to 320 ppmv in 1970 has occurred, with a mean rate of increase of 0.7 ppmv/year or 0.2%/year. The Mauna Loa data indicate that the increase has continued through 1973 to a level of 324 ppmv, and the trend has risen to about 1.06 ppmv/year, or 0.33%/year.

The average rate of increase for the decade 1958 to 1968 is 0.64 ppmv/year, whereas the rate due to combustion would have been 1.24 ppmv/year; about one half of the combustion CO<sub>2</sub> therefore remains in the atmosphere. (SMIC, p. 234.) This is the order of magnitude to be expected on the basis of model of Bolin and Ericksson, <sup>84</sup> indicating that the role of the sea in buffering the atmospheric CO<sub>2</sub> had been represented reasonably well by that model. Recently, several models of the same basic type, but incorporating new data and more reservoirs, have been utilized to predict the future CO<sub>2</sub> trend. Revelle<sup>109</sup> calculates a 30% increase above the 1971 value, or a rise to 416 ppmv, but warns of

even larger rises if positive feedback mechanisms come into play. Machta<sup>110</sup> has devised a seven box model; the atmosphere is divided into two (troposphere and stratosphere), the ocean into two (mixed layer and deep ocean), and the biosphere into three (long-term, short-term, and marine). The exchange coefficients for fluxes between troposphere and mixed layer of the sea are based on measurements by Telegadas 111 of the rate of decrease of C14O2. This model, discussed in more detail in SMIC (p. 235-237), when initialized by conditions prevailing in 1958, agrees well with the smoothed trend at Mauna Loa for the period after 1958. It predicts a concentration of 375 ppmv by the end of this century. Cramer and Myers<sup>112</sup> have also developed a model of similar type which gives a more conservative prediction of 350 ppmv by the year 2000. A general discussion of these zero-dimensional reservoir models has been given by Keeling. 113

The Mauna Loa data show fluctuations in the rate of CO<sub>2</sub> increase from year to year which are

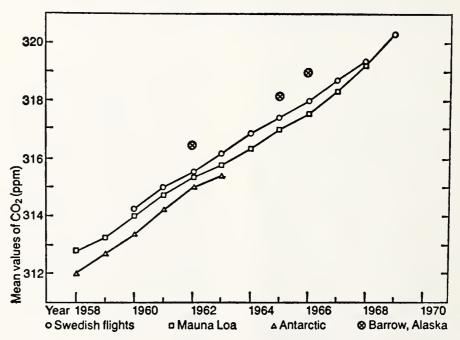


FIGURE 5. Trends of annual mean earbon dioxide volume mixing ratio, 1958 to 1969, from 4 different data sets. While the absolute values obtained by the various observers differ slightly, the trends are highly similar for all sets, thereby establishing beyond question the reality of the secular increase. (Data sources: Bolin and Bischot<sup>9,6</sup> [Swedish flights]; Pales and Keeling<sup>1,2,7</sup> and Bainbridge, private communication to L. Machta 1970 [Mauna Loa]; Brown and Keeling,<sup>1,9,4</sup> [Antarctica], and Kelley<sup>1,9,5</sup> [Alaska]. From Wilson, C. L., Ed., Man's Impact on the Global Environment, Study of Critical Environmental Problems (SCEP), MIT Press, Cambridge, Mass. 1970, 47. With permission.)

considerably larger than fluctuations in the combustion output. These cannot be accounted for by the simple box models with fixed exchange coefficients. Photosynthetic variability, on land at least, is probably too small to account for this; it seems more probable that the cause is to be sought in short-term variability of the general circulation of the atmosphere and the sea. Estimates of the order of magnitude of mean eddy fluxes of CO2 have been made by Bolin and Keeling;114 they deduce a meridional eddy diffusivity of 3 X 10<sup>10</sup> cm<sup>2</sup>/ sec and an eddy flux from low to high latitudes of 2 X 10<sup>10</sup> tons/year. It is well known that the large-scale eddy flux of other physical quantities such as angular momentum, heat, and water vapor vary significantly from year to year, depending on the intensity and structure of the planetary waves; one may thus expect similar variations in the redistribution of CO2.

The net uptake of CO<sub>2</sub> by the biosphere is of the same order of magnitude as the meridional flux. Lieth<sup>115</sup> has estimated an uptake of 1.5 X 10<sup>10</sup> tons/year for the entire land area of the earth, while Bolin and Keeling<sup>114</sup> arrive at the same figure for the land vegetation north of the 45th parallel. Machta assumes a total uptake by the biosphere (but ultimately returned as a result of decay) of 7.6 X 10<sup>10</sup> tons/year at present. It is therefore evident that the quantitative measure of the biospheric role in modulation of the atmospheric CO<sub>2</sub> balance is in need of refinement.

The projections of CO<sub>2</sub> levels at the end of the century cited above assume that the exchange coefficients between the reservoirs are not themselves functions of the atmospheric CO2. If variations in CO<sub>2</sub> are, in fact, reflected in temperature changes in the upper levels of the sea, then the sea-air exchange will be significantly altered. Kanwisher 107 has measured the dependence of pCO<sub>2</sub> on temperature in a sample of natural sea water taken near Woods Hole, Massachusetts. The results are shown in Figure 6. The average temperature coefficient of pCO<sub>2</sub> over the range 11° to 22°C is about 14 ppmv/degree. A warming of only 1°C is sufficient to cause a shift from under to supersaturation. Since the CO<sub>2</sub> reservoir in the mixed layer is estimated at from 2 to 4 times the atmospheric burden, 110,115 it follows that a substantial flux of gas from sea to air would take place during a period of rising sea temperature, giving rise to a positive feedback and "thermal runaway" if not compensated by other factors. It is therefore conceivable that short-term fluctuation in global sea temperatures could account in part for the irregularities in the CO<sub>2</sub> trend observed at Mauna Loa.

Despite an occasional demurrer such as that by Pearman and Garratt 116 the general consensus is that the upward trend in atmospheric CO2 is a direct consequence of human activity in the combustion of fossil fuels; that about one half of the CO<sub>2</sub> generated by combustion remains in the air (at the present rate of combustion); that the trend is of the order of 0.7 to 1.0 ppmv/year but is probably exponential rather than linear in the long run and so is better stated as 0.2%/year; that short-term (2 to 4 year) fluctuations in the trend are observed which are not traceable to a single cause but which are probably associated with fluctuations in the general circulation patterns of the atmosphere and the oceans on the same time scale; and that an atmospheric concentration somewhere between 350 and 415 ppmv should prevail by the year 2000.

Unfortunately, the climatic consequences of this increase cannot be forecast with the same degree of precision or confidence because of the limitations on modeling discussed in an earlier section of this paper. The earliest and simplest models dealt only with the perturbations of the radiative equilibrium caused by CO<sub>2</sub> changes. These models were at most one-dimensional (vertical distribution of global mean temperature as function of CO2) but more often were zerodimensional; they simply equated a change in the net long-wave radiation to a change in ground surface temperature using the Stefan-Boltzmann relationship. The differences were mainly in the modeling of the effect of CO2 on the net radiation. Models derived prior to 1956 generally made very crude approximations to the absorption spectra of the atmospheric gases, and are therefore only of historical interest in that they seemed to indicate that the effect of CO2 on radiation was negligible and so caused the retardation of CO<sub>2</sub> research for some years. Plass<sup>54,55</sup> calculated the net radiation using newer data on the detailed structure of the 15-\mu CO<sub>2</sub> absorption band; he assumed a dry, cloudless atmosphere. He arrived at a drop of 3.8°C in mean global surface temperature when CO<sub>2</sub> was halved (reduced to 150 ppmv) and a rise of 3.6°C for doubled CO<sub>2</sub> (600 ppmv). Kaplan<sup>117,118</sup> made similar calculations using a refined technique for representing the absorption

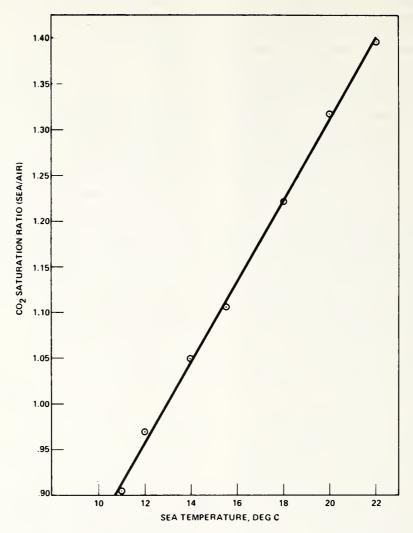


FIGURE 6. Saturation ratio for carbon dioxide in a sample of sea water taken at Woods Hole, Massachusetts, as a function of water temperature, referred to a volume mixing ratio of 315 ppmv in the air. (From Kanwisher.<sup>107</sup>)

spectrum in manageable form. He carried out his calculations for varying amounts of cloud cover and cloud-base heights (but ignored water vapor). For "average cloudiness" he arrived at a temperature decrease of only 1.8°C on halving the CO<sub>2</sub> concentration. He also criticized various details of Plass' model. Plass replied 118 with several criticisms of Kaplan's model, namely, terminating the atmosphere at 100 mbar pressure, using unrealistic temperature profiles, and a number of other details of his modeling of the absorption spectrum. Moller 119 criticized both Plass and Kaplan for their neglect of the water vapor overlap, and calculated with his own model, in which he used an atmosphere with the thermal structure of the

old U.S. Standard Atmosphere (surface temperature 288K, tropospheric lapse rate 6.5/km, stratosphere isothermal at 218K), CO<sub>2</sub> concentrations of 300, 330, 600, and 150 ppmv, and a relative humidity of 75% at all heights. He used generalized absorption coefficients of Elsasser and Culbertson<sup>120</sup> for CO<sub>2</sub> and H<sub>2</sub>O, and divided the atmosphere into 15 slabs in the vertical (using thinner slabs near the ground) for purpose of integrating the radiative-transfer equation. He also noted that it was not correct to adjust the ground temperature so that the black-body radiation from the ground matches the computed flux change due to the change in CO<sub>2</sub>, because the air temperature is also modified. Instead, one must adjust the

surface temperature so that the difference between global absorption of solar radiation and emitted long-wave radiation is constant. Möller's computed global mean temperature decrease when CO2 is halved was 1.5°C; the increase for a doubling of CO<sub>2</sub> was likewise 1.5°C. He pointed out that the change in the vertical temperature structure resulting from CO<sub>2</sub> should really not be ignored, and that it would be most reasonable to keep the relative humidity fixed as these temperatures change. In this case, he arrived at the paradoxical result that an increase in CO2 would cause a decrease in surface temperature (and absolute humidity). He also argued that a climatic effect of CO<sub>2</sub> would be nearly impossible to find, because the effect of doubling the CO2 burden would be cancelled by a decrease of 3% in precipitable water or an increase of 1% in mean cloudiness, and that changes of these magnitudes on a global scale were unmeasurable (this was in 1963, when satellite instrumentation was less sophisticated than at present).

At this point, Kaplan seems to have withdrawn from the controversy, but Plass<sup>121</sup> challenged Möller's conclusion that water vapor changes (at constant relative humidity) would act to cancel or even outweigh the effect of increasing CO<sub>2</sub> after a lapse of time, thus leading to an ultimately lower temperature. Möller, in his reply<sup>121</sup> defends his position but concedes that he has used radiation diagrams to arrive at it, and that he would like to see computations of higher accuracy.

Manabe and Wetherald<sup>122</sup> developed a onedimensional radiative-transfer model (actually, one of a set of models generated by Manabe and co-workers at NOAA's Geophysical Fluid Dynamics Laboratory) with the objective of embedding it in more complete general circulation models. This model has similarities to Möller's, but goes beyond it in several respects. The relative humidity distribution in the vertical is held constant with time. The solar constant, the planetary albedo, and the cloudiness are adjustable input parameters, as are the amounts and height distributions of CO2 and ozone. The temperature distribution in the vertical is not arbitrarily chosen, but is computed by the model as it moves toward equilibrium; the redistribution of heat by convection is included by permitting vertical mixing so as to keep the lapse rate always ≤6.5°C/km. For lower lapse rates, radiative transfer alone controls the temperature. The computations are carried out for 9 to 18 levels in the vertical.

Several interesting results were obtained from this model: (a) the paradoxical effect obtained by Möller did not appear when the equilibrium of the entire atmosphere was considered; the assumption of fixed relative humidity always tended to amplify effects as compared to the assumption of fixed absolute humidity; (b) the time constant of approach to equilibrium with fixed relative humidity was always longer (by about 50%), and was of the order of 100 days for approach from the warm side and 75 days for approach from the cold side (e<sup>-1</sup> time constant is meant); (c) the effect of perturbing the CO2 concentration was felt most strongly in the stratosphere. Doubling of CO<sub>2</sub> with fixed relative humidity gave temperature increases at the ground of 2.36°C with "average cloudiness" and 2.92 with clear sky, as compared to 1.33 and 1.36 respectively with fixed absolute humidity. Halving the CO<sub>2</sub> (to 150 ppmv) produced a drop of 2.28°C with average cloudiness and 2.80°C with clear sky, as against 1.25 and 1.30 respectively when the absolute humidity was fixed. The positive feedback effect of adding more water vapor to the atmosphere when it warms up was clearly demonstrated. The range of temperatures in the high stratosphere (at 2.3 mbar) encountered when going from 150 to 600 ppmv was about 15°C, or three times as great as at the ground, with the colder stratosphere associated with the higher CO<sub>2</sub> concentration.

A great advantage of this model is that very many parameters are adjustable, so that, if other feedbacks from a general circulation model (changes in albedo, cloudiness, CO<sub>2</sub>, etc.) occur, they can react upon the thermal equilibrium in the appropriate way.

Newell and co-workers 1 2 3 ,1 2 4 and Gebhardt 1 2 5 have made calculations of the net heating or cooling rates at various levels of the atmosphere, including the solar heating of CO<sub>2</sub> in the 2.8- and 4.3- $\mu$ m bands. Newell et al. do not try to express their results in terms of a temperature change because they contend that true radiative equilibrium is never achieved in the atmosphere. Gebhardt does compute a change of equilibrium temperature of 1.2°C (increase) when CO<sub>2</sub> concentration is doubled. Ferland and Howell<sup>126</sup> have used a model involving radiative transfer and an energy balance equation which can be used to study effects of CO<sub>2</sub>, H<sub>2</sub>O, and particulate matter on the heat balance; doubling of CO2 to 600 ppmv in this model gave a warming of 1.89°C at the ground while halving it produced a cooling of

1.94°C. It seems likely that if the Manabe and Wetherald model (which in our opinion follows the best physical approach) were modified to include the near-infrared solar heating, the effect of doubling the CO<sub>2</sub> would be a warming of somewhat less than 2°C. It may be concluded, then, that the dependence of global mean sea-level temperature on CO<sub>2</sub> concentration is of the order of 6 X 10<sup>-3</sup> degree C/ppmv. Since the global increase since 1958 has only amounted to about 10 ppmy, the climatic effect can only have amounted to a global warming of 0.06°C, which would be undetectable in the noise level of climatological data. The above conclusions are, of course, reached under the assumption that no positive feedback loops are involved. We have already mentioned the possibility that a warming trend will drive more CO2 out of the sea, thus enhancing the heating, etc. Also, assuming that heating reduces the amount of ice cover, i.e.; that Budyko's climatic theory is correct, gives an additional positive feedback opportunity. On the other hand, if part of the warming due to CO<sub>2</sub> goes into evaporating additional water, then the resultant increase in mean cloudiness would reduce available solar energy. This would provide a negative feedback and so reduce the climatic effect of the CO<sub>2</sub>. Another possibility must be considered, namely, changes in the general circulation. If the Manabe and Wetherald model were applied, not to the global mean situation but to each latitude (i.e., a two-dimensional version) it is certain that the heating or cooling effects at the different pressure levels would be latitudedependent. This would change the baroclinicity (distribution of available potential energy for atmospheric motion) and give rise to changes in the jet stream and planetary wave configurations which could lead to significant climatic changes in marginal regions.

We may conclude in confidence that: (a) man's combustion of carbonaceous fossil fuels is raising the  $CO_2$  content of the atmosphere by about 0.2%/year; (b) that extrapolation of combustion rates plus consideration of the capacity of the sea to take up  $CO_2$  leads to an estimate of a  $CO_2$  concentration of 350 to 400 ppmv by the year 2000; (c) that the expected warming trend *due to the combustion CO\_2 alone* is of the order of  $0.06^{\circ}$ C/decade and hence will require a century or more to be detectable in climatological records; and (d) that monitoring of  $CO_2$  must be continued

for a similar length of time, and correlations with temperature records at first-quality climatological stations in all parts of the world must be studied to guard against the possibility of strong amplification of this weak climatic effect by positive feedback mechanisms. Modeling research must also be continued so that such positive feedback mechanisms may be anticipated before they become operative in the real world.

## DEPLETION OF ATMOSPHERIC OXYGEN

The same combustion which has added carbon dioxide to the atmosphere has removed a proportional amount of free oxygen. The question naturally arises whether continued combustion of fossil fuel at an ever-increasing rate could reduce the concentration of  $O_2$  to a level low enough to perturb the biosphere appreciably.

This question was raised at the Dallas Symposium in 1968, 128, 129 and again during SCEP. It was concluded that the direct effect of combustion would be negligible; SCEP referred to the oxygen situation as a "nonproblem." The reason for this conclusion is easy to arrive at. The estimated quantity of recoverable fossil carbon is about 3 × 10<sup>18</sup> g. Conversion of all of this to CO<sub>2</sub> consumes 8 X 10<sup>18</sup>g of O<sub>2</sub>. But the total atmospheric inventory of O<sub>2</sub> is 10<sup>21</sup> g; therefore, the burning of the entire world resources of fossil carbon would deplete the oxygen supply by only 0.8% (assuming no change in the balance between photosynthesis and oxidation processes other than the combustion), while increasing the CO<sub>2</sub> concentration by a factor of 6.8 to about 2170 ppmv if none goes into the sea, or to about 1100 ppmv at the time combustion stops if half goes consistently into the sea. Clearly, the effect of the CO2 increase is far more serious; a drop of 0.8 per cent in O<sub>2</sub> is equivalent to climbing from sea level to an altitude of only 75 m above sea level. The direct biological consequences of this would be quite negligible.

The 0.8% depletion tends to be somewhat of an underestimate because the fossil fuels contain a certain amount of hydrogen which also burns. This, however, is counterbalanced by the fact that some of the fossil fuel may not be recoverable.

Direct measurements of O<sub>2</sub> concentration in 1970 by Machta and Hughes<sup>130</sup> in clean air (mostly over the sea) between 50 and 60° N

latitude have a very consistent value of 20.946% by volume. There has thus been no detectable change in  $O_2$  concentration since 1910, in spite of the fact that something of the order of  $2 \times 10^{17} \mathrm{g}$  of carbon dioxide has been formed by combustion during that period.

Davitaya<sup>131</sup> arrived at an oxygen consumption of 2.46 × 10<sup>17</sup>g from 1920 to 1972, and estimated the total oxygen depletion at 2.73 × 10<sup>17</sup>g. The reduction in O<sub>2</sub> concentration due to this would be 0.004% by volume. She then made the pessimistic forecast that O<sub>2</sub> would drop below the life-support level in about 10<sup>5</sup> years, but that CO<sub>2</sub> would reach lethal levels within 100 to 700 years. She totally overlooked the fact that the fuel supply would be exhausted long before the O<sub>2</sub>. Also, her basis for arriving at such a short time as 100 years for a lethal level of CO<sub>2</sub> is not clear; most organisms can tolerate 1100 ppmv without great stress, and many plants grow much faster at such levels.

It is evident that combustion alone has done nothing measurable to deplete the  $O_2$  supply, and will not affect it materially before all fossil fuels have disappeared. A paper by Walker<sup>132</sup> suggests that there may be some stabilization mechanisms among natural sources (burial of reduced carbon in sediments, peat bogs, etc.) and sinks (weathering of reduced carbon in rocks). He suggests that the rate of supply of reduced carbon to ocean-bottom sediments may be dependent on the  $O_2$  concentration in the sea and atmosphere.

Although oxygen does appear to be a nonproblem insofar as combustion is concerned, this is not necessarily the case with respect to other human activities. Berkner and Marshall 133 in their paper on the evolution of the earth's atmosphere, expressed concern about a possible positive feedback runaway mechanism in which an initial drop in O2 lets a larger quantity of biocidal radiation (around 0.25  $\mu$ m in the ultraviolet) reach the ground and seas, reducing the plant population which brings photosynthetic production of O2 below oxidation losses, thus further depleting the O2, etc. The initial drop in O2, it is suggested by these authors, might be due to poisoning of plant life, mainly in the sea, by toxic effluents such as halogenated hydrocarbon, heavy metals, etc. Only a small part of the flora of the planet would have to be killed to bring photosynthesis below consumption; the total photosynthetic production is estimated<sup>128</sup> at 8 × 10<sup>16</sup> g/year, but the net excess over oxidation loss is only  $5 \times 10^{12}$  g/year; thus only 1/16000 of the photosynthetic plants on the planet would have to be killed in order to turn a surplus into a deficit.

Sisler<sup>129</sup> gives the opinion, however, that the outer integuments of most land plants and animals are impervious to ultraviolet and that the effect in the sea would simply be to move the photosynthetic zone a few centimeters deeper in the water. In any case, the problem is not an urgent one in terms of need for prompt action. The total supply of  $O_2$  in the atmosphere is  $10^{21}$  g; the present rate of oxidation must be very near to the photosynthetic production, 8 × 10<sup>16</sup> g/year. Assuming that the loss due to oxidation obeys first-order kinetics, i.e., is proportional only to the amount of O<sub>2</sub> in the air, the time required to reduce the O2 concentration to 60% of its present value (corresponding to an altitude of about 4 km at present) if all plants on the planet were to die suddenly and all photosynthesis stopped, is easily calculated to be 6385 years. Since the amount of matter available for oxidation would obviously decrease with time (less dead biomass to decay), the kinetics would probably be closer to secondorder; in that case the time to decrease the O<sub>2</sub> to a marginal level for man becomes 8333 years. In this worst-case hypothetical situation, then, it is obvious that all animals, including man, would have eaten each other and the last survivor would have starved to death long before breathing became a problem. We therefore concur with SMIC that repetition of measurements like those of Machta and Hughes should be done carefully about every ten years. We would add that careful monitoring of the sea biomass by oceanographers to detect any signs of substantial changes in flora due to toxic effluents should be carried on regularly.

# CLIMATIC EFFECTS OF NUCLEAR WEAPON POLLUTION

After the first nuclear bombs were used in World War II, and especially during the first period of thermonuclear weapons testing, a spate of publications predicting all manner of dire climatic consequences appeared, mainly in the news media and popular press. Most of these were produced by authors with little or no scientific background and a great deal of mysticism or emotional bias in their attitudes; these will not be considered in this

article. A few authors with some scientific standing did propose, or claim to have found, effects on weather. Martin 134 speculated on a number of such effects in a paper presented to the French Academy of Sciences; he suggested worldwide changes in the pH of rainwater, world rainfal' anomalies due to nucleating effects of bomb-raised dust, and pollution by oxides of nitrogen formed in the fireball. Of these, only the last has been found to merit concern; it will be discussed in connection with stratospheric pollution by aircraft. He later published a book with an alarmist title 135 and a preface by Albert Einstein in which he reiterated his potentially real but quantitatively highly exaggerated effects. Teichmann<sup>136</sup> and Weiller 137 suggested influences on the wind field. but since the kinetic energy given to the air by the bomb is radiated away rapidly in the form of gravity waves and dissipated by viscosity all over the globe, it is difficult to imagine anything but the most local and transient effects on the atmospheric circulation. Wickramasinghe 138 published a paper purporting to show that the resumption of nuclear testing by the U.S.S.R. in 1961-62 had influenced the general circulation of the atmosphere so as to bring about the very severe cold winter of 1962-63; our comments on this type of speculation without either a sound physical model or good statistical validation were given earlier in this paper. Arakawa<sup>139</sup> committed the same type of error; he noted that the cold summer of 1884 (after the Krakatoa eruption) and that of 1954 (after the first thermonuclear weapons tests) were about equally severe, and attributed the latter to stratospheric dust deposited by the bomb cloud. He did not consider the quantitative differences between the two events; the Krakatoa cloud has been estimated by H. H. Lamb (unpublished data) to have contained over 1010 tons (1016g) of solid matter, of which about 108 tons remained in the atmosphere for one year or more. The energy required to lift the persisting dust to the stratosphere against gravity is about 1.5 X 10<sup>23</sup> ergs. Taking the heat of explosion of TNT as 886 cal/g, it follows that the nuclear bomb equivalent is 4 megatons (the metric ton =  $10^6$  g has been used in this calculation). When one considers that only a small fraction of the released energy of a bomb goes into raising dust to the stratosphere, it is clear that the 1954 tests could not have introduced an amount of dust that was at all comparable to the Krakatoa

eruption. Furthermore, Arakawa did not show any increase in atmospheric turbidity to support his claim.

Most atmospheric scientists of the period recognized that the energetics of the global circulation are of a magnitude far greater than hundreds of megatons of TNT, so that any spectacular effects would be confined close to the explosion and for only a short time thereafter. Serious investigations after 1955 were directed toward two possible effects on weather: possible cloud nucleating effects of the dust and bomb debris, and influences of increased ionization by the radioactive dust and gases on the electrical parameters of the atmosphere.

No evidence has been found to suggest that the dust raised by bombs is in any way more effective as a cloud nucleating agent than natural aerosols. In fact, Kawano et al. 140 found that the concentration of radioactive material in the air in Japan in 1970 was positively correlated with the number of small positive ions in the atmosphere but was negatively correlated with the number of condensation nuclei available to clouds, and that the effect on global precipitation would have been too small to measure.

Some evidence for modification of the atmospheric electric parameters has been presented. The first such study by Israel<sup>141</sup> in 1958 gave negative results as far as electric parameters near the ground were concerned. Anderson and Servu<sup>142</sup> measured the atmospheric conductivity on flights through a 15-day-old bomb debris cloud and noted significant increases in conductivity at altitudes of 5000 and 17,000 feet above sea level. Stewart 143 analyzed the vertical potential gradient data near ground level for three British and two Portuguese locations and found systematic decreases since 1952 which (at the British stations) correlated with the measured beta-ray activity; he concluded that the decrease in field strength was due to increased ionization caused by the fallout deposited on the ground. Simon 144 conducted a similar study of potential gradient records at a number of stations distributed around the world, and also reached the conclusion that the increased ionization due to bomb debris was having a measurable effect on the electrical parameters of the atmosphere. Huzita<sup>145</sup> made simultaneous measurements of atmospheric conductivity and fallout radioactivity at Kyoto University and Osaka. He found that a U.S.S.R. bomb test on

30 October 1961 caused a temporary doubling of the conductivity. Tserfas<sup>146</sup> examined the atmospheric-electric data taken at Tashkent in central Asia from 1932 to 1967, and reported a correlation between observed increases in conductivity and decreases in field strength and the arrival of radioactive debris at the ground. Pierce<sup>147</sup> found the same type of correlation in a study of data from six stations in Britain, Japan, and Portugal for the period 1950 to 1964.

These observations show that nuclear weapons tests do produce measurable effects on the electrical parameters. These parameters are not primarily climatic elements since they are not directly perceptible to human senses, but there exists a slight possibility of a positive feedback mechanism which could affect the frequency or intensity of lightning in thunderstorms. It is well established that the vertical electric field strength, or potential gradient, between the ionosphere and the earth's surface is maintained by the charge separation of thunderstorms against the leakage due to conduction by atmospheric ions. Therefore, any decrease in the number and intensity of thunderstorms would reduce the fair-weather potential gradient over the globe. The mechanism by which large convective clouds separate electric charge is not well understood at present, but some theories, such as that of Sartor, 148 require a preexisting potential gradient in order to get the charge separation process started. A reduction of the global fair-weather field would therefore lead to slower buildup of thunderstorms, less charge separation, and so reduce the global field more, etc. If, in fact, the parameters of this system are such as to lead to runaway instability, an increase in ion-pair production by radioactivity, which in turn increases the conductivity and thereby reduces the field strength (by acting as a shunt across the generator) might lead to the elimination of lightning as a weather phenomenon. On the whole, this might be desirable, since lightning accounts for a considerable amount of loss and damage each year (mainly by starting forest fires). The negative aspects would be a slight reduction in nitrogen fixation, and an esthetic factor; there are doubtless many people who, in the words of W. S. Gilbert, have a "passion for a flight of thunderbolts."

It should be borne in mind, however, that it has not been established beyond doubt that a preexisting electric field is essential for charge separation in convective clouds. Many theories of cloud electrification do not require this field; if one of these is correct then the events suggested above will not take place.

The only other influence of nuclear testing on the atmosphere that is of possible significance arises from the nitrogen fixation which occurs when a nuclear device is fired in the atmosphere. The high initial temperature of the fireball causes oxidation of N<sub>2</sub> to NO or NO<sub>2</sub>, and the rapid cooling as the cloud rises preserves a substantial amount of these oxides, which are delivered in part to the stratosphere. Once there, they can affect the photochemical equilibria which govern the ozone concentration so as to reduce it. This, in turn, permits a higher flux of solar ultraviolet in the wavelength range around 0.3 µm to reach the surface, with possible biologically harmful results as described in the section on oxygen depletion. Some very slight and inconclusive evidence for this effect has been found; it will be discussed in a later section dealing with aircraft pollution of the stratosphere.

To the best of our knowledge, nobody has made a statistical study to see if, in fact, thunderstorm frequency or intensity (or both) showed any detectable decrease during periods of weapons testing. The effect is certainly not strong enough to be obvious, and is probably so weak as to be undetectable if it exists at all. It may therefore be concluded that the effects of nuclear energy release on climate are of trivial importance in comparison with the direct ecological effect of the radioactivity.

#### PARTICULATE MATTER: EFFECTS ON THE GLOBAL HEAT BALANCE

In contrast to the CO<sub>2</sub> problem, concern over possible global effects of man-made particulate matter did not arise until the nuclear weapons testing period starting in 1954. Earlier attention was directed mainly to the local effects in urban areas. The decade of the 1960s brought an increase in the study of aerosols, both natural and manmade, and their role in the planetary heat budget.

The reason for the lower level of past effort directed toward the aerosol problem as compared to  $CO_2$  is not hard to find.  $CO_2$  is a stable, homogeneous gaseous constituent of the atmosphere; outside the surface boundary layer it is a well mixed component. Particles, on the other

hand, are heterogeneous in chemical composition, size, shape, and optical properties. Furthermore, the sources of natural particles are much more variable then those of CO<sub>2</sub>. In addition, sampling and measuring of aerosols are more difficult than for CO2; particles are not well mixed and must usually be collected at high altitudes. The range of particle sizes is so great that no single collecting technique can cover the entire span. Because of the heterogeneity of aerosols, modeling of their effects on the radiation budget is inherently more difficult than for gases; scattering of radiation is at least equally important as absorption, especially at visible wavelengths. Therefore, studying the effects of even the natural aerosol is inherently more difficult in all respects than is the case for a gas like CO<sub>2</sub>, and detecting an anthropogenic component is even more so.

Natural particles in the atmosphere arise from seven sources: wind-raised soil mineral particles, evaporated sea spray, volcanoes, forest fires, meteorites, oxidation of gases such as SO<sub>2</sub>, and oxidation of organic vapors emitted by living and decaying vegetation. All of these sources are subject to considerable variation with time or meteorological conditions. The sink strength is also variable with time and altitude. The main mechanism for removal is precipitation; the particles may act as nuclei for cloud droplets or ice crystals or be scavenged by falling precipitation. As a result, the residence time of a particle in the lower atmosphere is of the order of one to two weeks, while in the stratosphere where sedimentation and slow Hadley-cell motions are the only removal mechanisms, the mean residence time is of the order of one to three years (SCEP, p. 13). It is therefore reasonable to treat these two regions of the atmosphere separately.

The natural aerosol in the troposphere is dominated by wind-raised dusts from desert areas, mainly in Africa, northwest India and Pakistan, and the Middle East. These dusts are found to reach up to as high as 9000 m above sea level, to be carried 5000 km or more by wind, and to involve particulate loadings (total overburden) of over 10<sup>4</sup> g/ha (ha = hectare = 10<sup>4</sup> m<sup>2</sup>). A second more widely distributed but weaker source is the blue haze formed by oxidation of terpenes from coniferous forests. Carbon and ash from forest fires is an intermittent source, sometimes strong enough to be observed 2000 km or more from the source. Sea salt particles are also numerous and found in the interiors of the continents.

Some man-made aerosols are indistinguishable from their natural counterparts, e.g., carbon, ash, sulfate particles; others may be readily distinguished by their chemical nature. Lead-bearing particles, for example, are inevitably of human origin, namely, the burning of automotive fuel; iron oxide is a product of the steel industry. Sampling at the ground and identification of chemical species is, therefore, a way of monitoring some of the man-made aerosol but does not provide data on the total amounts.

The total overburden or particulate loading is related to the atmospheric turbidity or optical thickness. The precise connection between them depends on the complex refractive index of the particles and their size distribution, but if these do not change too much, the turbidity is proportional to the particulate loading. Measurements of atmospheric attenuation of the direct solar beam over long periods thus provides information on trends of total aerosol.

Measurements of the electrical conductivity of the atmosphere also provide an approximate measure of particle loading when the loading is light. The conductivity results from the presence of molecular ions produced by radioactivity and cosmic rays. In the absence of particles, these light ions migrate rapidly in an electric field. When particles are present, the small ions attach themselves to the particles and are no longer so mobile; the conductivity is decreased. The precise relationship between conductivity and particle concentration depends on the size distribution and attachment coefficient; the latter depends in turn on the chemical species and state of the particle surface. Nevertheless, if the nature of the aerosol does not change but the amount does, the trend of conductivity with time is inversely related to that of particle number density.

Another remote sensing technique which is useful in studying the vertical distribution of particles is the lidar, or laser radar. <sup>150-153</sup> It has the same limitations as the use of turbidity as a measure of total loading because the backscattered light depends on refractive index and size distribution. Also, its long-term precision is poorer than a turbidity measuring system because variations in the solar constant are much less than those in laser output. Nevertheless, information on the relative amounts of aerosol as functions of height and time can contribute to an understanding of the transport of particles in the atmosphere.

All of the techniques described above have been

or are being used in studying the distribution and trends of atmospheric aerosol. Evidence for an upward trend in tropospheric particle loading has come from a variety of sources. An interesting correlation is shown in Figure 7. Bryson and Wendland<sup>149</sup> compared data on dustfall in the Caucasus mountains obtained by Davitaya with economic data of Powell on the capital input to the economy of the U.S.S.R. It suggests that particle production does seem to be in proportion to the sum total of human activity, but the fact that the dust production seems to lead the economy by one to three years is in need of explanation.

Turbidity measurements made in an urban area (Washington, D.C.) showed an increase of 57% in the period 1905 to 1964, and those in a rural mountain area (Davos, Switzerland) increased by 88% from 1920 to 1958. The Davitaya shows an analyzed turbidity data from 175 stations in the U.S.S.R. for the period 1954 through 1963 and found a mean decrease of 12% in mean annual insolation, which they interpret as a 150 to 300% increase in dust loading. Manes compared two sets of pyrheliometer (direct solar

beam intensity meter) data at Jerusalem, Israel; one series covered the period 1930 to 1934 and the second 1961 to 1968. He found an upward trend of 1% annually in the turbidity, a much more modest increase than in the Soviet Union.

Not all solar radiation stations, however, show an upward trend of turbidity. Data from Valentia in Ireland, 1955 to 1971, analyzed by McWilliams 158 show variations with season and kind of air mass, but no upward trend. The data at Mauna Loa at first seemed to indicate an upward trend, but this was found to be due to an artifact: the pyrheliometer calibration had drifted slowly. After Ellis and Pueschel<sup>159</sup> corrected the calibration by referencing all the clear-day data back to unit air mass, the trend disappeared, leaving only an annual oscillation and dips traceable to volcanic activity. Roosen et al.160 analyzed the data from 13 solar radiation stations of the Smithsonian Institution for the 50 years ending in 1972 and found no trend. Flowers and Viebrock<sup>161-163</sup> likewise found only turbidity increases in the Antarctic that were traceable to volcanic aerosol.

Atmospheric conductivity measurements have

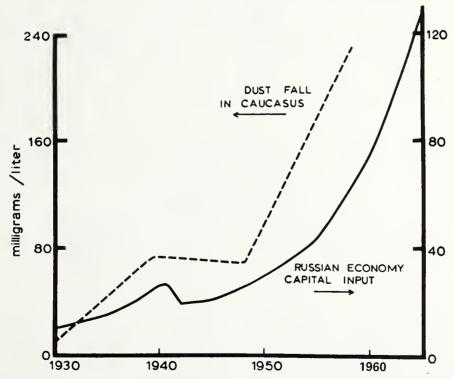


FIGURE 7. Relationship between dustrall in the High Caucasus and capital input to the economy of the USSR. (From Bryson, R. A. and Wendland, W. M., <sup>149</sup> Global Effects of Environmental Pollution, Springer-Verlag, New York, 1970, 130. With permission.)

been made on board oceanographic research vessels since 1907 with no essential change in technique. Gunn<sup>164</sup> made a set of such measurements across the North Atlantic in 1962 and noted that there had been a slight decrease on the average from the older data. The measurements were repeated in 1967 on a world-circling cruise of the NOAA research vessel "Oceanographer"; the results are shown in Figure 8, prepared by Cobb and Wells. 165 They compared their 1967 measurements in the North Atlantic and South Pacific with all the available earlier data, and found a downward trend in conductivity over the Atlantic, but none in the southern ocean. Misaki and Takeuti166 and Misaki and Ikegami167 made similar measurements in the North Pacific east of Japan and identified particle plumes there, but concluded that the levels were lower than over the North Atlantic. More recently, Cobb<sup>168</sup> has reviewed these and other data, as well as two sets of fair-weather conductivity data from Mauna Loa in 1960 and 1968. He concludes that most oceanic

areas except the North Atlantic east of the United States, the North Pacific east of Japan, and the North Indian Ocean are maintaining constant aerosol levels, and that the Indian Ocean increase is probably due to an increase in wind-raised dust because of drought conditions in Africa and Asia.

Some direct sampling of aerosols from ships in the North Atlantic in 1969 were reported by Parkin. 169 He found that in winter the particle concentration was roughly constant at 3 X 10<sup>-3</sup> μg/m<sup>3</sup> between Newfoundland and Ireland, but in summer it rose to 0.01 to 0.03 µg/m<sup>3</sup> near Newfoundland while remaining near the winter value near Ireland. The concentration rose steeply in the Bay of Maine and on occasion reached 4 μg/m<sup>3</sup> off Cape Cod. The main constituents of the samples were carbon and fly-ash spherules; the latter constituted 60% of the total catch near the North American coast, but only 5% in mid-ocean. He also estimated that the width of the pollution plume increased by a factor of 5 between Newfoundland and Ireland. In lower latitudes, he

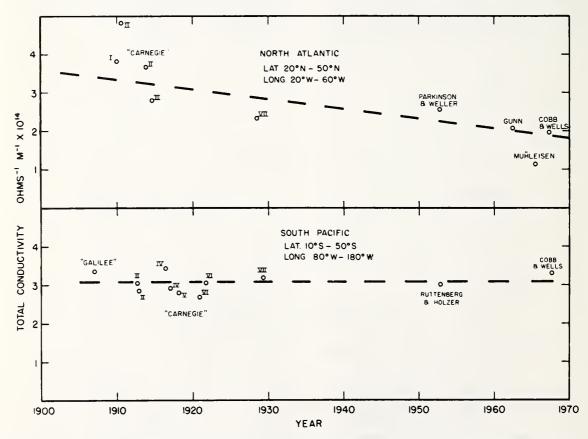


FIGURE 8. Downward trend in the electrical conductivity of the atmosphere over the North Atlantic, and absence of such trend in the South Pacific, as revealed by shipboard measurements from 1905 to 1967. (From Cobb, W. E. and Wells, H. J., 165 J. Atmos. Sci., 27, 814, 1970. With permission.)

found mainly the natural wind-raised African red dust, which reached concentrations of 10  $\mu g/m^3$  off Dakar.

The weight of the evidence presented above leads to the conclusion that man-made particulate matter is detectable in the troposphere, that its residence time is sufficiently long for it to exist in measureable amounts at distances of several thousand kilometers from the source regions, and that the turbidity of the atmosphere is increasing in and downwind of the source regions at a rate comparable to the expansion of industry and automobile usage in the source areas. On the other hand, regions of the globe in which air from the main pollution sources only arrives after many weeks or months of travel, such as Mauna Loa, the southern oceans, and Antarctica, show no upward trends of turbidity; the quantities of man-made particles reaching these locations are too small to have any climatic effect whatever.

The stratospheric aerosol loading has only been studied by direct sampling techniques for the relatively short time that aircraft capable of sustained flight at 20 km altitude have been available to atmospheric scientists, although some balloon sampling was done earlier. A series of balloon and aircraft observations by C. Junge and co-workers1 70-172 around 1960 demonstrated the existence of a persistent layer of aerosol with a broad maximum of concentration between 15 and 23 km height and covering at least all of the globe between 63°S and 72°N latitude. The particles collected had a mean radius of about 0.15  $\mu$ m, were very hygroscopic, and contained sulfur as a major constituent. Mossop 173 sampled the aerosol layer near 20 km altitude over Australia from a U-2 aircraft, catching the particles on electron microscope grids coated with nitrocellulose film. He also found that most of the particles were hygroscopic and water-soluble, and that the main constituent was ammonium sulfate. The small insoluble fraction contained mineral particles of volcanic origin and some which may have been meteoritic debris. Friend 174 found the particles to consist of (NH<sub>4</sub>)<sub>2</sub> SO<sub>4</sub> and (NH<sub>4</sub>)<sub>2</sub> S<sub>2</sub>O<sub>8</sub>, and observed that the particles may have been associated with some liquid. He noted an approximately log-normal size distribution over the range of 0.1 to 1.0 µm, and a concentration of the order of 0.05 particles/cm<sup>3</sup> at 18 km altitude, and observed that another population of smaller particles (Aitken nuclei) was present. Cadle and

co-workers at the National Center for Atmospheric Research (NCAR) in Boulder, Colorado, have analyzed a considerable number of filter samples taken on several aircraft including a WB-57F (Canberra) aircraft flown by the 58th Weather Reconnaissance Squadron of the U.S. Air Force for the Los Alamos Scientific Laboratory of the University of California. The results of their work, much of which was done in connection with the CIAP (study of potential effects of stratospheric pollution by aircraft), have appeared in part in a recent review, 175 and will appear shortly as part of a general review of the physical and chemical state of the stratosphere. 176 They found that sulfate was the primary anion present, but that most of this was in the form of small sulfuric acid droplets. They analyzed for various common anions and cations, and noted a tendency for the relative abundance of various species to vary with the kind of filter or impactor used for collection. Castleman<sup>177</sup> studied the isotope ratios in stratospheric sulfate and concluded that most of the sulfur was of volcanic origin.

Optical sensing techniques, both remote and in situ, have been used extensively to study the size and height distribution of the stratospheric aerosol layer. The properties of light scattered by the particles at twilight and dawn were used to estimate the aerosol loading at relatively early dates by Gruner, <sup>178</sup> Bigg, <sup>179</sup>, <sup>180</sup> Meinel and Meinel, <sup>181</sup> Rozenberg, <sup>182</sup> and Volz. <sup>183–187</sup> The measurements by the last author were the most systematic, and served to document the changes in the aerosol layer during the recent (1963 to 1970) period of volcanic activity. Turbidity measurements, from the ground at high elevations, and from aircraft or balloons, have also been used by Kondratyev<sup>188</sup> and Deirmendjian<sup>189</sup> during the periods of relatively heavy loading. Also the solar measurements at Mauna Loa and the South Pole fall into this category.

Vertical profiles using remote sensing from the ground (and in some cases from the air) were carried out using the backward scatter of incoherent radiation from searchlights by Elterman<sup>190-192</sup> and co-workers. The lidar technique, although more expensive in terms of hardware, is inherently more precise than the searchlight method, and is gradually supplanting the latter. Measurements of stratospheric aerosol with lidar have been made by Fiocco and Grams,<sup>150</sup>, <sup>153</sup> Collis and Ligda,<sup>151</sup> Clemesha and

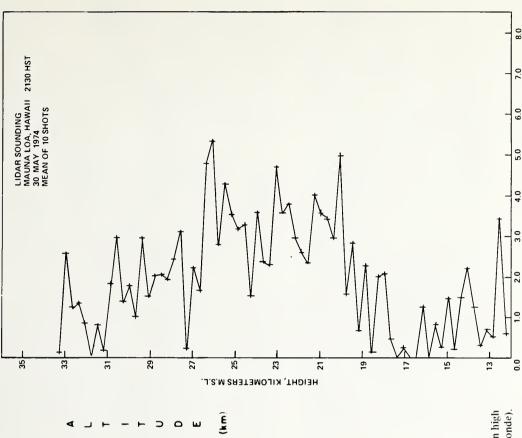
Rodrigues, <sup>193</sup> Schuster, <sup>194</sup> Fox et al. <sup>195</sup> (with an airborne lidar), and Russell et al. of the Stanford Research Institute. <sup>196</sup> A lidar with automatic data processing by mini-computer, designed and constructed by E. Barrett and coworkers of NOAA--APCL was placed in operation at Mauna Loa Observatory in June of 1974 and is being used on a regular schedule to monitor the stratospheric aerosol layer.

A balloon-borne nephelometer or "dustsonde" has been developed by Rosen at the University of Wyoming and flown to give vertical profiles of stratospheric particles of sizes greater than about 0.3  $\mu$ m. <sup>197-199</sup> These instruments are now being flown at ten stations distributed in latitude from Ice Island T-3 (variable, but near 85°N) to the South Pole, along with ozonesondes and conventional radiosondes.

The ensemble of data collected by all these methods shows: (a) the stratospheric aerosol layer is present as a persistent structure over the entire globe; (b) the maximum concentration by volume (e.g. particles/m<sup>3</sup> or  $\mu$ g/m<sup>3</sup>) lies near 10 to 12 km altitude in the polar region and rises through the mid-latitudes to 20 to 23 km in the tropics. The peak concentrations in the size range greater than 0.3 µm radius under "quiet" conditions (no recent volcanic augmentation) are of the order of 1 particle/cm<sup>3</sup>; (c) the major constituent of the layer is sulfate, mostly as free sulfuric acid in an unknown state of hydration, but partly neutralized by whatever cations are available (mostly ammonium); (d) smaller quantities of the common metals and anions found in natural land and oceanic aerosols occur, as well as small traces of extraterrestrial material; (e) the number density of particles increases strongly after large volcanic eruptions, to the point where the appearance of the twilight sky is so altered that no instrument other than the unaided eye is needed to observe it; (f) that a return to a base level takes place after an eruption with an e<sup>-1</sup> time constant of about 4 to 5 years; and (g) that the base concentration between eruptions is maintained by gas-to-particle conversions such as oxidation of H<sub>2</sub>S and SO<sub>2</sub> by atomic O or O<sub>3</sub> and hydration to H<sub>2</sub>SO<sub>4</sub>, and that much of the material added during an eruption is also due to oxidation of gaseous effluents from the volcano.

Figure 9 presents a typical pair of balloon dust soundings in high latitudes under conditions of no recent volcanic additions. Figure 10 gives a typical low latitude lidar sounding taken at Mauna Loa during final checkout of the lidar system in May 1974, also under conditions of no volcanic activity. The acrosol backscattering coefficient may be roughly related to the dustsonde particle concentration by the relationship: 1 particle/cm<sup>3</sup> =  $4 \times 10^{-9}$ /m/ steradian.

It seems most likely that any man-made additions to this layer would arise mostly from the oxidation of sulfur originating as SO<sub>2</sub> from combustion. Although a few carbon particles and other solids might be transported to that height by tall thunderstorms, volatile materials such as gases and vapors have much higher turbulent diffusivities unless the solid particles are very small. An estimate of the source strength of pollutant SO<sub>2</sub> in 1965 has been given by Robinson and Robbins<sup>201</sup> as 149 megatons/year, and that of H<sub>2</sub>S as a negligible 3 megatons/year. If totally converted to H<sub>2</sub>SO<sub>4</sub>, this would become a potential source of 237 megatons; they do not, however, include any volcanic emission of sulfur in their estimates. The pollutant production is thus over half the natural production (excluding volcanoes) at the earth's surface, and has been doubling each 25 years. If, then, the proportion of pollutant to natural sulfur were the same in the stratosphere as near the ground, a clear upward trend in stratospheric aerosol should be seen. Unfortunately, the available data do not show any such trend. Figure 11 shows the record of solar atmospheric transmittance (inversely related to turbidity) on cloudless days at Mauna Loa for the period 1958 to 1971. The period January 1958 to March 1963 was volcanically quiet and should therefore show any trend due to pollution. Except for a suggestion of an annual cycle and one or two irregular dips in transmittance, no signs of systematic change can be seen. The eruption of Agung in March of 1963 caused a prompt drop, followed by a slower decrease to an apparent minimum in 1964. This was followed by a generally upward recovery curve; punctuated by occasional drops related to other weaker volcanic activity. These data, and the similar record from the South Pole already cited, show that it has not been possible to detect any increase in stratospheric aerosol due to human activity which can compare in magnitude to the perturbations produced by volcanoes. If a trend is present, it will take many volcanically quiet years with data of all kinds from many monitoring stations to detect it. In principle,



<u>o</u>

8

ይ

--- T-3 (85 N)

Š

Œ

25

FIGURE 9. Vertical profiles of aerosol particle concentration (particle radius  $\ge 0.3~\mu m$  in high northern and southern latitudes as measured by a balloon-borne particle counter (dustsonde). (From Hofmann et al.<sup>2 o o</sup>)

AEROSOL CONCENTRATION (No./cm

FIGURE 10. Computer-produced plot of aerosol volume backscattering coefficient (proportional to particle concentration) versus height as observed with the lidar at Mauna Loa, Hawaii, 19.5° N Lat. (From Barrett, unpublished.)

AEROSOL VOLUME BACKSCATTERING FUNCTION, 1E-9/M/SR

8

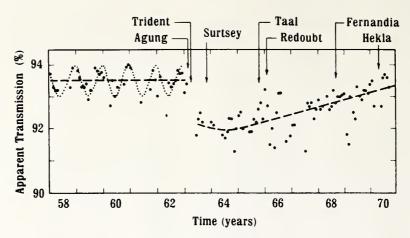
8

8

8

Ê

Œ



FIGURF 11. Time series of daily mean transmittances (referred to unit air mass or zero zenith angle) of solar energy in the band 0.3 to 2  $\mu$ m for cloudless days at Mauna Loa, Hawaii. Prior to March 1963, the variations reflect mainly an annual march (dotted sinusoidal curve) with a few dips. Times of known volcanic eruptions are indicated by names and arrows; the Agung eruption of March 1963 was the strongest of these. It produced a prompt decrease in transmittance followed by a slow and irregular recovery to pre-eruption levels by 1970. (From Ellis, H. T. and Pueschel, R. F., 159 Science, 172, 845, 1971. Copyright 1971 by the American Association for the Advancement of Science. With permission.)

chemical analysis of in situ samples should give at least a qualitative estimate of the fraction of surface generated pollutant which reaches the stratosphere. Cadle 175,176 has noted that the Br/Cl ratio in stratospheric aerosol samples is some 20 times greater than in sea water. Since a significant pollution source of bromide exists, namely, automobile exhaust, this does suggest that pollutants released in the lower atmosphere are in fact reaching the stratosphere. Another interpretation of this ratio can, however, be given. Barrett (unpublished results, 1954) conducted experiments at the University of Stockholm in which he passed ozone-rich air through samples of natural sea water from the west coast of Sweden, and then passed the air into a gas scrubber containing CCl4. The latter solvent acquired a yellow color within a few minutes. Spectrophotometric analysis showed that the bromide and iodide in the sea water had been converted to the molecular halogens almost quantitatively, but that no free chlorine (within the limits of detection) was formed. Experiments on pure NaCl solutions confirmed this. An examination of the oxidation-reduction potentials for the reactions show that iodide and bromide should be oxidized in aqueous solution by ozone, but that the potential for oxidation of chlorine is higher than that for the catalytic reduction of ozone to oxygen by water, so that chloride should be unaffected.

Since some ozone is present in sea level air, one may expect that in whitecaps on the sea such an oxidation of bromide and iodide ions to the free molecular species Br2 and I2 would take place at the air-sea interface. These gases, being much more mobile than chloride sea-spray particles, would reach the stratospheric "chemical kitchen" much more rapidly than the chloride, be converted back to the anions by some unspecified reduction reaction, and show up in exaggerated amounts relative to the seawater ratio. Since Barrett did not attempt to make quantitative measurements of the reaction rate, the actual production of Br<sub>2</sub>/cm<sup>2</sup> of sea surface cannot be computed at this time. This rate determination should be done in the laboratory and the theoretical source strength compared with that due to automobile production.

The presence of stable isotopes of lead should be a sure tracer for automobile pollution, because as of 1968 about 3.5 × 10<sup>5</sup> tons/year of lead<sup>202</sup> was being introduced into the atmosphere from this source; no natural source of volatile lead exists. The presence of fine lead aerosols in the ground-level atmosphere is well documented, but it has yet to be identified in stratospheric aerosol.

The human production of solid particles has been estimated at between 10 and 90 megatons/year, while the natural production is between 425 and 1100 megatons/year (SMIC, p. 189). The total particles converted from gaseous emissions of all

kinds is in the range 175 to 325 megatons/year for the human component, and 345 to 1100 megatons/year for the natural one, including volcanoes. The ratio of man-made particle production to total annual production is therefore in the range 16 to 19%; for the solid particles alone the man-made percentage is between 2 and 8, while for the converted gaseous emissions the human fraction is between 23 and 34%.

The volcanic contribution to the yearly source is given as 25 to 150 megatons/year while Mitchell<sup>203</sup> estimates the mean loading over the past 120 years as 4.2 megatons. The retainment factor, or mean residence time, is therefore, in the range 2 months to 10 days, indicating that most of the volcanic input falls out or is washed out of the troposphere in a relatively short time.

These figures show that the total of human aerosol production, both as ab initio particles and those converted from gases, is of the same order of magnitude as the average volcanic production, but that little or none of this gets into the longresidence-time region of the stratosphere. Virtually all the man-made particulate matter enters the troposphere, remains for a few days or weeks, and is returned to the surface by precipitation or fallout, as is the case with most natural aerosols which originate at the ground level. Another set of estimates by Weickmann and Pueschel<sup>204</sup> of the retainment factor for various species of aerosols gives a range of 1 year to  $10^{-5}$  year (5.25 hr), with a mean around  $10^{-3}$  year (8.75 days). They use a figure of 11.5%<sup>359</sup> for the anthropogenic share of the total aerosol (slightly less than the estimates given in SMIC), but point out that this is released over only 2.5% of the earth's surface. The short residence time and concentrated sources implies that any climatic effects of human aerosols is more likely to be felt on a regional rather than a global basis. These authors also estimate that, unless more stringent emission controls are imposed, the human component of particle production would equal the natural component in about 23 years.

We conclude that the weight of the evidence to date shows no evidence of a global increase in atmospheric aerosol due to human activities, but that regional increases of significant magnitude have occurred in and downwind of those nations which have had the largest industrial growth during the past half-century.

The effect of atmospheric aerosol on the planetary heat budget is even more difficult to model than that of CO<sub>2</sub>, because of the heterogeneous character of the aerosol. Ideally, one would have to know the size distribution and complex refractive index of each pure chemical species in the aerosol, or, failing in this, some effective mean values of these. The refractive index should be known throughout the solar and terrestrial wavelength bands from 0.3 to 30  $\mu$ m. Such complete data are rarely available even for a single chemical species. Given this information, the radiative-transfer equation, including Mie scattering by the particles, must be solved; the effects of CO<sub>2</sub>, H<sub>2</sub>O, O<sub>3</sub>, and clouds should also be incorporated in the model. Because neither the input data nor the model of radiative transfer can be completely accurate or exact, the effects predicted by the various models cover a considerable range. Given the same aerosol, some models predict warming and others cooling.

The most general statement one can make about the effect of a particle layer is that the earth atmosphere system as a whole must cool if the planetary albedo for solar radiation is increased by the aerosol, and this increase is not compensated for by an increase in the "greenhouse effect" by absorption and reemission of terrestrial long-wave radiation. From this, it follows that an aerosol which scatters but does not absorb at any wavelength must necessarily cause cooling; the scatter of solar radiation into the backward hemisphere represents a net loss to the planet. (Any realistic size distribution will scatter terrestrial radiation much more weakly than solar radiation.) When the aerosol absorbs in the solar band, the situation becomes more complicated. If the aerosol is at a high elevation, the absorbed energy will be delivered to the atmosphere and produce warming at the height of the particles; the sum of the absorbed and backscattered radiation will, however, be a deficit as far as the planetary surface is concerned. This may be partly compensated for by long-wave emission from the heated particles. The effect of an absorbing and scattering aerosol will therefore depend on the albedo of the underlying surface, the height of the aerosol above the surface, the relative heights of the aerosol and whatever clouds are present, etc.

Very few attempts were made to model the effect of aerosol prior to 1970. One of the earliest

is that of Sheppard,<sup>205</sup> who used some data taken in the urban atmosphere which showed that about 30% of the incoming solar energy was back-scattered and 25% absorbed under heavy pollution conditions; he calculated a net cooling of the bottom kilometer of the atmosphere of 2° to 3°C/day under these conditions. Charlson and Pilat<sup>206</sup> and Atwater<sup>207</sup> called attention to the difficulties discussed above.

The year 1970 brought the first really quantitative modeling attempts. Mitchell<sup>208,209</sup> introduced a zero-dimensional "budget" model which was very heavily parameterized insofar as the convective and radiative transfers were concerned. He at first concluded that under most circumstances a low-lying aerosol layer with typical ratio of absorption to scattering would produce a net warming at the ground unless the ground surface had a very low albedo. He later modified, the conclusions somewhat, so that cooling took place over surfaces with albedoes of the order of 10% or less, but warming took place over bright ground, snow, and ice. This model has the virtue of simplicity, but is very dependent on the parameterization scheme which is adopted to cope with exceedingly complex processes, and which is (in our opinion) difficult to defend.

Atwater<sup>210,211</sup> devised a one-dimensional model (11 to 15 levels in the vertical) incorporating CO2, water vapor, particles; and NO2. He made some reasonable assumptions about the complex refractive index and particle size distribution, and solved the initial-value problem when the aerosol is suddenly introduced at zero time. A weak point of his model was the use of a prespecified ground temperature. His prognosis gave a buildup with time of a temperature inversion with a maximum a short distance above the top of the aerosol layer. The over-all effect was a net cooling of the aerosol layer at night; the daytime effect could be made to go either way (relative to clean air) by choice of the ratio of solar energy absorption to scattering.

Barrett<sup>212</sup> developed what might be called a "1½-dimensional" model, in which the vertical structure of the atmosphere was specified in order to establish its optical properties, but was treated as fixed. The height and thickness of the aerosol layer, as well as the loading, were adjustable input data. The optical constants and size distribution

were also fixed so that previously published tables of Mie scattering could be used. The aerosol was treated as non-absorbing, and single scattering was the only radiative-transfer process considered. The Rayleigh scattering by the gases was modeled exactly but the Mie scattering by the aerosol was parameterized heavily in order to make the computations economically feasible. The effect of particle loading on daily totals of available solar energy at the ground were computed (by integration over the solar band 0.3 µm to 3 µm and from sunrise to sunset) for the solstices, the equinoxes, and some intermediate times of year, at 18 latitudes (each 5°) between equator and pole, and for 10 particulate loadings, distributed from 1 to 10<sup>4</sup> g/ha of aerosol as well as for a clean atmosphere. This model showed that the effect of the aerosol layer was strongly dependent on latitude and season; the percent depletion of solar energy by the aerosol was highest in winter at higher latitudes. The effect on global annual mean insolation was found to be nearly linear up to particulate loadings of 103 g/ha; this degree of loading gave a 13% drop in available solar energy. A loading of 10<sup>3</sup> g/ha corresponds to a total atmospheric burden of 51 megatons, or a little more than 10 times the estimated mean burden from volcanic sources. On the basis of simple radiative equilibrium calculations, this 13% depletion would cause a drop of 10°C in global mean temperature - more than enough to bring on a glacial period if sustained long enough.

The shortcomings of this model are (a) the neglect of the long-wave radiative transfer processes involving CO<sub>2</sub>, H<sub>2</sub>O, and aerosol absorption and emission; (b) neglect of absorption of solar radiation by the aerosol; (c) neglect of clouds; (d) inaccuracy due to parameterization of the aerosol scattering; (e) neglect of multiple scattering by the air and particles (not serious except for heavy loadings); and (f) neglect of backscattering from the ground to the aerosol and re-scattering to the ground (more serious). Its main virtue is that the output is in a form most useful for further study of climatic effects, as well as for engineers concerned with design of solar-powered equipment.

Kattawar and Plass<sup>213-215</sup> developed several models in which the effects of water vapor, CO<sub>2</sub>, clouds, and particles were combined. Their first model was concerned with the infrared absorption and emission. They dealt with the multiple-

scattering process by means of a Monte Carlo, or random walk technique. Their computations were done using fixed representative distributions of aerosol, water vapor, and clouds in the vertical. The calculations were made in the 6 µm region of the spectrum. They found that the aerosol contribution to the long-wave fluxes was negligible in comparison with that of water vapor unless the atmosphere was exceedingly dry. Their second model dealt with the effect of an aerosol layer on incoming solar flux at three wavelenths (0.4, 0.9, 1.67  $\mu$ m). The model and atmosphere were the same, but the total optical mass and the vertical distribution of the particles was varied. It was found that the vertical distribution of the aerosol had little effect on the insolation if the optical mass was held constant, but that the backscattered energy depended strongly on the number density of the particles. In the third paper, the Monte Carlo method of computation was replaced by a matrix-operator technique which was more economical of computer time, and calculations were made for a somewhat different aerosol size distribution and refractive index. The results were given in tabular form as functions of the aerosol optical thickness (non-dimensional) rather than particle loading (number of particles/cm<sup>2</sup> of earth's surface, or g/ha, etc). The albedo as seen from space varied from something very close to the assumed surface albedo for an optical thickness of order 10<sup>-3</sup> to nearly unity (0.998) for a very dense layer of optical thickness 4096.

Unfortunately, much more emphasis was placed in these papers on the accuracy with which the distribution of scattered light over the sky could be represented, and on the degree of agreement (very close) between the matrix and Monte Carlo method of computation, than on the ultimate effect on the heat budget. Also, the aerosols used in this study were assumed to be non-absorbing.

Rasool and Schneider<sup>216</sup> developed a model in which the effects of varying CO<sub>2</sub> or aerosols, or both, could be studied. It is similar in many respects to that of Manabe and Wetherald cited earlier in connection with the CO<sub>2</sub> problem, but allows for scattering and absorption by aerosols. They introduced their aerosol layer in the lowest kilometer of the atmosphere. They calculated the long-wave flux to space with a mean cloudiness of 50% (tops at 5.5 km) and CO<sub>2</sub> concentrations of 300 ppmv. A balance with received solar flux was obtained for a mean albedo of 30%; they achieved

this by assuming a cloud albedo of 32% and a surface albedo of 10%. They used a two-stream approximation to the radiative transfer equation which included effects of multiple scattering, and introduced aerosol absorption in both visible and infrared. The model was one-dimensional with 60 levels in the vertical.

Their calculations showed that an 8-fold increase in CO<sub>2</sub> would cause only a 2°C rise in global mean surface temperature (the large discrepancy between this result and that of Manabe and Wetherald is not explained), and that the rate of warming with addition of CO2 decreased with increasing CO<sub>2</sub> concentration. Therefore, no thermal runaway could occur within the framework of this model. Increases in their aerosol loading caused decreases in mean surface temperatures despite the permitted absorption of solar energy; quadrupling the aerosol loading resulted in a computed mean temperature decrease of 3.5°C. They therefore concluded that variations in atmospheric dust loading were more effective in inducing climate change than were variations in  $CO_2$ .

Ensor et al.<sup>217</sup> worked with a simple heavilyparameterized model in which the ratio of absorption to backscatter (integrated over the rear hemisphere) of the aerosol is compared with the ratio  $\frac{(1-A)}{A}$ , where A is the surface albedo in the absence of aerosol. Warming should occur if the former exceeds the latter, and cooling if the converse is true. By use of Mie scattering theory, they computed that if the real part of the refractive index of the aerosol were taken to be 1.5, then for a negative imaginary part of magnitude  $10^{-3}$  or smaller the aerosol would produce cooling over the entire earth, while if the magnitude of the imaginary part were 10<sup>-1</sup> or greater, warming would occur. For intermediate values, the effect depends on the local albedo; warming will occur over bright surfaces and cooling over dark ones. They also used the more elaborate but similar parameterized model of Mitchell<sup>208,209</sup> and arrived at similar conclusions about the imaginary part of the refractive index except that a bias toward warming appeared.

Twomey<sup>218</sup> has suggested a mechanism by which aerosol particles could exert an indirect influence on the heat budget through interaction with clouds. It requires, however, that the particles be active as condensation nuclei for cloud droplets. In the absence of enough nuclei, clouds

contain fewer and larger drops, while if a surplus of nuclei is available, the clouds will consist of a larger number of smaller drops. For a given total mass of water, the backscattering, and hence the cloud albedo, will be higher for the large number of small drops. This is because, although a large drop scatters more energy in proportion to its size than a small one, most of the energy is scattered in the forward direction. Small drops, on the other hand, scatter more symmetrically into the forward and backward hemispheres; this combination of greater number and greater symmetry of scattering causes a cloud of very small drops to have an albedo of as much as 90%, as against 50% for clouds consisting of larger drops. While this is not a complete model in itself, it is indicative of the kind of interactions that must be taken into account by any complete climate model. Twomey also<sup>219</sup> pointed out that, if a mixture of cloud drops and absorbing aerosol particles occupy the same volume, the particles are subjected to a diffuse illumination from the cloud drops in addition to the direct solar radiation, and hence will be warmed more than would be expected on the basis of sunlight alone.

Neumann and Cohen<sup>220</sup> studied the effects of introducing an aerosol layer below 2 km, one in the stratosphere, or both together, in a dry, cloudless atmosphere. They considered only the effect on solar radiation absorbed by the ground and atmosphere; long-wave exchanges were not considered. The thermal structure was that of the ICAO Standard Atmosphere, only the lowest 25 km was included in the study. Expressions for the heating rate involving the aerosol optical thickness for absorption and backscattering and the surface albedo were derived, and various combinations of these optical thicknesses were substituted therein. In the case of a single aerosol layer, the net effect on the entire earth atmosphere system was almost always a cooling, except when the extinction due to absorption was greater than that due to scattering. With two aerosol layers present, warming was possible for a larger number of combinations, but it was still necessary for the extinction due to absorption to exceed that due to scattering. This model is essentially a onedimensional version of the parameterized budget type similar to those of Mitchell, and Ensor et al., discussed above, but somewhat more sophisticated in that the vertical structure is taken into account.

A model which includes wavelength-averaged

radiative-transfer involving H2O and aerosols but no CO2, vertical turbulent exchange of heat and momentum, and horizontal wind was developed by Zdunkowski and McQuage<sup>221</sup>. They introduced their aerosol into the air at sunset and ran their model as an initial value problem. With an aerosol concentration of 400  $\mu$ g/m<sup>3</sup> near the ground, they computed about 2°C less cooling during the first night than for a particle-free atmosphere. However, when the model was run for several days, the result was always a strong net cooling compared to a clean atmosphere (because of depleted insolation) with their aerosol parameters. The cooling varied from 2° to 4° C/day. After three days, the maximum afternoon temperature was some 19°C lower than for a clean atmosphere.

Several other models have appeared in the recent literature; in general they represent attempts to refine the details of the types discussed up to this point. They will therefore be cited by number only.<sup>222-228,232,233</sup> Emphasis has shifted during the last two or three years to the use of the spherical-harmonics approximation to the radiative-transfer equations<sup>229,230</sup> rather than the computationally slower Monte Carlo methods. Application of this method by Stowe<sup>231</sup> to the effects of aerosols on the upward long-wave flux in the 6.3- and 15-µm bands (H<sub>2</sub>O and CO<sub>2</sub>) indicate that the aerosol influence on the flux is less than 1%.

Incorporation of a stratospheric dust cloud into a general circulation model was carried out by Batten.<sup>234</sup> The dust cloud was spread uniformly in the zone 25 to 75°N latitude, and consisted of particles less than 2 µm in diameter with a total volume of 0.04 km<sup>3</sup> (approximately the amount deposited in the stratosphére by the Krakatoa eruption of 1883). It was assumed that the dust perturbed the model by reducing solar input and by stimulating precipitation; the aerosol influences were thus heavily parameterized. The model was run for 60 days, with and without the aerosol. In the dust-covered latitude belt, the surface temperatures fell by 2° to 3°C and the temperature contrast between land and ocean increased. Precipitation decreased between 46° and 74°N, but increased in the zone 26 to 46°N. The overall effect on the general circulation was to weaken the mid-latitude Ferrel cell, decrease the baroclinicity at high latitudes, and increase it at low latitudes.

The diversity of conclusions about the sign and

magnitude of the effects of aerosols on the heat budget is greater than was the case for CO<sub>2</sub>. Generally speaking, those models which try to incorporate the maximum amount of detailed physics lead to the conclusion that the net effect of aerosol is a cooling for aerosols with a low ratio of absorption to scattering in the visible, such as H<sub>2</sub>SO<sub>4</sub> and many mineral dusts (quartz, etc.). Warming would be possible for a carbon aerosol over most of the globe. The heavily parameterized models, on the other hand, are more biased toward a prediction of warming when the aerosol absorption is relatively weak. It is our opinion that the more physically based models should receive the greater weight, and that the mixture of particles to be found in the present-day atmosphere do cause a cooling the magnitude of which is not yet precisely calculable. We concur, however, with the opinion of Schneider<sup>235</sup> that better data on the optical properties of atmospheric particles and better models are both needed.

Direct measurement of the climatic effect of atmospheric dust of human origin will require many decades of monitoring because it is buried in the noise level of natural aerosol fluctuations. One would think, then, that the climatic influence, on a short-term basis, of the large fluctuations in volcanic dust loading would be easier to detect. While this is undoubtedly correct, it turns out that the shortness of global climatological records (less than a century) and the inability to determine accurately the total dust loading after an eruption makes it impossible to establish a firm quantitative relationship between the two. Since 1855 there have been only four eruptions of the first magnitude, for which detection of influences should be easiest. There has also been a tendency for some weaker eruptions to be bunched together in time, sometimes close in time to one of the strong ones. There is no good data base for any first-magnitude eruption except possibly Agung in 1963; at the time of Krakatoa the synoptic weather networks were just recently organized, but only a few observatories were measuring atmospheric turbidity as such. Despite this, some attempts have been made to estimate the effects of earlier eruptions. McBirney, 236 in a semi-popular article on volcanology without references, mentions that the 1783 eruptions of Laki in Iceland and Asama in Japan caused "dry fogs" over most of Eurasia so dense that in France the sun could not be seen until it was 17° above the horizon, and that 1783

and the following 2 years were 3 of the coldest on record in the northern hemisphere. The 1815 outburst of Tamboro produced close to 100% extinction of solar energy for 3 days at distances of up to 500 km from the source; its long-lived stratospheric dust caused long, bright twilights for several years afterward. McBirney claims a fall of 1.1°C in "world temperature," and recalls that 1816 was the famous "year without a summer," but does not state how a representative global mean temperature could be calculated in 1816, and does not explain that the exceptionally cold summer of 1816 was felt mainly in the northeastern United States. His information on the aftermath of the Krakatoa eruption is more quantitative; he reports that solar radiation at the Montpellier Observatory in south central France dropped by 25% shortly after the eruption and remained depressed by 10% for about 3 years, and the global mean temperature dropped 0.45°C.

The 1963 eruption of Agung is the only one of high intensity which has occurred in a time when extensive surface and free-atmosphere climatological data were available; it appears, however, to have been much weaker than the earlier events cited by McBirney. The maximum reduction of solar radiation at Mauna Loa<sup>159</sup> was only about 2%, while at the South Pole it was somewhat greater — about 5 to 8%.<sup>161</sup> It thus appears that the Agung eruption and the group of weaker ones which followed it do not constitute a perturbation which is really large enough to provide a good case study for the effect of aerosol on global climate.

The earlier estimates of global temperature changes after eruptions cannot be taken too seriously because the baselines against which the changes were measured were not defined. It is not enough to calculate global mean temperatures for, say, two years after an eruption and two years before, and simply take the difference and attribute any cooling to the dust. It is also necessary to consider the trend of the temperature before and after the volcanic event. For example, computing a mean temperature for the two-year period after Agung (17 March 1963) and comparing this with 1960 to 1962 temperatures would be quite misleading because, as shown by Starr and Oort,<sup>237</sup> the northern hemisphere mean surface temperature fell 0.6°C between May 1958 and April 1963 in the pre-Agung period, and this decrease is, of course, part of the long-term trend which began in 1940. Also, the severe winter of 1962–63 preceded Agung; if the eruption had taken place a year earlier, it would doubtless have been blamed for the harsh winter. One may ascribe the cold winters of 1783–85 to volcanic dust, but if so, then the severe winter of 1788–89 in Europe must be accounted for. Thomas Jefferson (quoted by H. Riehl<sup>238</sup>) credited this winter's rigors with helping to bring on the French Revolution; he stated that "the Mercury was at times 50° below the freezing point of Fahrenheit," or -28°C, at Paris. Jefferson's temperatures may be considered trustworthy; he personally maintained a climatological station at his home in Virginia for many years.

Also, subjective estimates of the severity of a winter are likely to be more influenced by extremes than means; a winter with, say, a week with daily minimum temperatures of  $-30^{\circ}F$  at Chicago in January, but with a very warm February would certainly be remembered as a severe winter, while a winter without record-setting extremes but with a seasonal mean several degrees below the climatological mean might go unnoticed except for its effect on household fuel bills. Nevertheless, it is the seasonal mean which must be watched for signs of climatic change.

We can only conclude by stating that the visible indications of aerosol loading by the largest eruptions suggest an optical thickness great enough to have caused substantial depletion of received solar energy, and that there are suggestions that short-term cooling trends followed them, but that the precise effect of the volcanic dust on temperature cannot be isolated because it is of the same order as short-term trends in the absence of volcanic activity. Particles put into the atmosphere by man's activities constitute a loading which is less than the average amount of volcanic dust which, in turn, is several orders of magnitude less than the peak loading after major eruptions. Therefore, anthropogenic aerosols are only effective in regional and local weather and climate modification at the present-day production rate.

We note here that an effect of the Agung aerosol on the stratospheric temperature has been reported by Newell.<sup>253</sup> He analyzed radiosonde records at Port Hedland, Australia (20° S latitude) for the period 1958 to 1966, and noted a fairly sharp rise of about 5° to 6°C during the first few months after the eruption, followed by a downward trend through 1966. The most likely reason for the warming, which was strongest at the 60 to

80 mbar level, is direct solar heating of the aerosol. If this is the case, then the aerosol must have consisted of something other than, or in addition to, sulfuric acid droplets, since the latter do not absorb appreciably at solar wavelengths.

A very recent paper by Fegley and Ellis<sup>254</sup> reports on some observations of an aerosol layer at 18 to 20 km over Mauna Loa using the lidar system. The origin of the layer was not entirely clear, but it was probably from the eruption of Fuego volcano in Guatemala on 10 to 14 October 1974. The layer attained its second-highest optical density on 29 October; the peak density was found at 19.5 km. The 2300Z radiosonde ascent at Hilo. Hawaii (about 50 km from Mauna Loa) showed a marked rise in temperature, at precisely the same height, of about 8°C. This sounding was taken about 16 hours previous to the lidar observation. 2300Z corresponds to 1300 local time in Hilo; the temperature maximum is evidently due to absorption of solar radiation by the particles.

### THERMAL POLLUTION: GLOBAL EFFECTS

It is an unavoidable consequence of the laws of thermodynamics that all of the energy released by man, as well as the solar energy received at the ground, must eventually appear as heat which must be radiated to space (an exception is the small amount of chemical energy being stored in new fossil organic material, e.g., peat, each year, provided that this is not used for fuel later in history). This, in turn, requires that the global mean temperature adjust itself to the combined man-made and solar input. The long-range effects of energy release on the heat balance are therefore easy to estimate provided that no feedbacks exist by which human energy releases can alter the amount of net solar energy input to the planet. It is only necessary to make an inventory of total fuel use, multiply the amount of each fuel used per year by the heat of combustion of that fuel (or heat of reaction in the case of nuclear fuels), take the sum, add it to the annual solar input, and calculate the new equilbrium temperature on the basis of the Stefan-Boltzmann law or a more elaborate radiative-transfer model.

Such inventories have been taken and published in SCEP (p. 63 to 66) and SMIC (p. 55 to 60); we have no reason to modify the numbers given in those reports. An upper bound to the human

generation of heat in 1970 is given there as 8 × 10<sup>6</sup> megawatts, or 1.57 × 10<sup>-2</sup> watt/m<sup>2</sup> when spread uniformly over the globe. If it is regarded as being released only over the continents, it is 5.4 × 10<sup>-3</sup> W/m<sup>2</sup>; when it is treated as being released only in urban areas, it rises to 12 W/m<sup>2</sup>. The solar input, averaged over the globe and over the year, is about 100 W/m<sup>2</sup>. The human contribution to the budget is therefore 0.0157% of the solar; using the crude approximation of the Stefan-Boltzmann law gives an elevation of mean global temperature of only 0.01°C as a result of energy release by human activities as of 1970. This is undetectable against the background of natural fluctuations and trends.

The problem is therefore reduced to prediction of the future growth of energy release; this is, of course, less precise than calculation of past releases. SCEP (p. 64) gives a figure for the recent growth rate, based on a United Nations survey, of 5.7%/year for the world as a whole. If this figure were to remain constant, the human contribution would rise to 0.087% of the solar input by the year 2000 and the mean temperature (if no time lag existed) would be 0.06°C higher than if human production were zero. By 2050 the figures would be 1.5°% and 1.07°C, respectively, and would become significant. If this growth rate could be sustained until 2100, the human contribution would be 25.9% of the solar, and the corresponding temperature excess would be 17.1°C, a very serious state of affairs. However, this extreme condition could not possibly come about because: (a) the rate of fuel consumption would then be 1652 times the 1970 rate, and no such reserve of usable fossil fuel exists; and (b) the concentration of the release in urban areas would (on the basis of the ratio  $12/1.57 \times 10^{-2}$  given above) result in a concentration of energy in the cities of 198 times the solar input, and a local temperature of 808°C - somewhat warmer than the surface of Venus! This result is an exaggeration, of course, because the area of the globe covered by the energyreleasing activity would necessarily increase considerably during the 130 years and much of the heat would be dispersed by convection, but even allowing for any reasonable expansion of urbanindustrial regions over the land area of the planet, the centers of such activity would still be too hot for human comfort.

The exhaustion of fuel will, of course, preclude the possibility of such continued exponential growth. If we assume that the 5.7% annual growth

rate continues right up to the point when the estimated 3 X 106 megatons of carbon in fuel reserves is exhausted, assume that average coal is 70% carbon, and calculate with the estimated 1970 usage rate of 7.5 × 10<sup>3</sup> megatons/year, we find that the fuel supply would be exhausted after 62 years, i.e., in 2032. At that time the energy release would be 0.54% of the solar input, and the temperature excess would be 0.39°C averaged over the globe. A more realistic assumption is that the annual percentage increase in fuel usage will decrease with time as the remaining reserves become harder to mine, and then become negative so that the rate of fuel consumption eventually decreases to zero. Such a model leads to an integral equation which cannot be solved analytically; one can only conclude that there will be some time at which the waste heat will become a maximum and then start to decline, and that this maximum will be less than 0.54% of the solar input.

If, however, practical hydrogen-fusion reactors are developed so that there is virtually no limit on the annual energy production, and if the population growth continues exponentially, then there would no longer be any constraint on the growth of the thermal pollution; it would be difficult to predict whether the death of the planet's population would be due in the end to starvation or heatstroke.

The heat capacity of the sea would, of course, tend to buffer the atmosphere partially as is the case for CO<sub>2</sub>. But in this case also, only the upper mixed layer of the sea is in intimate contact with the air, and the heat transfer rate to this water layer is limited by the thermal diffusivities of the air and water near the interface. Only if the waste heat is piped to the deep sea water can the full buffering capacity of the sea be used; this would probably cause some severe disturbances to the marine ecology. We conclude that, unless a nearly unlimited energy source such as hydrogen fusion becomes available, thermal pollution will not pose a serious threat to the stability of global climate for at least 75 years, and that in any case the exhaustion of fossil fuels will occur before the global temperature rise from this cause becomes dangerous.

We also wish to point out an inconsistency between the 5.7% annual growth rate for energy release and the 4% annual growth rate for CO<sub>2</sub> released by combustion given in SCEP (p. 54).

Acceptance of both these figures implies that an ever-increasing share of the energy used by man is derived from sources other than carbonaceous fuel combustion. The relatively small share provided by nuclear power plants is not increasing fast enough to reconcile the two figures.

## POLLUTION OF THE STRATOSPHERE: SPECIAL PROBLEMS

The stratospheric layer between the temperature minimum at the tropopause (8 to 17 km altitude, depending on latitude and season) and the temperature maximum at the mesopeak (50 to 60 km altitude) is characterized by either constancy or increase of temperature with height. As a consequence of the laws of hydrostatics and thermodynamics, parcels of air in such an atmosphere are very stable against vertical displacements; a parcel that is impelled upward or downward will be acted upon by a restoring force so that it will oscillate about its original level until the motion is damped by viscous forces. This means that pollutants deposited in the layer can spread vertically only very slowly.

The stratosphere also has very low relative humidity except just at its bottom and under other very rare circumstances, hence clouds and precipitation do not form and no mechanism exists for the washout of pollutants.

Because of the reduced air density, and consequent small optical thickness of the overlying atmosphere, the downward flux of ultraviolet high energy photons from the sun is much greater than near the ground. Radiation quanta at these wavelengths have enough energy to raise atoms and molecules to energies above their ground states, resulting in dissociation or activation. The resulting single atoms, excited molecules, and free radicals are highly chemically reactive, and produce many chemical species as a result of their interactions.

Because of these three circumstances, pollutants introduced directly into the stratosphere may remain there for extended periods, and may affect both the physical state of the atmosphere and its chemical composition.

Most pollutants which enter the atmosphere near the ground are scavenged by clouds and precipitation; exceptions are gases which do not combine readily with water or undergo conversion to particles, such as CO<sub>2</sub> and halogenated hydro-

carbons. The percentage of most pollutants which reaches the stratosphere is therefore small.

Aircraft engines emit a variety of combustion products at rates as high as kilograms per second. These include CO<sub>2</sub>, water vapor, unburned hydrocarbons or free-radical fragments of these, SO<sub>2</sub>, oxides of nitrogen in various proportions (usually referred to as NO<sub>x</sub>) and carbon particles. Those rates of emission can be large compared to the reciprocal of the mean residence time of chemically inert matter in the stratosphere (one year or more) especially if large numbers of aircraft operate daily in the stratosphere.

Commercial transport aircraft currently in operation spend most of their flight time below the tropopause, except at high latitudes in winter. The supersonic transport aircraft (SST) which appeared on the drawing boards in the 1960s, however, can only fly efficiently at heights of 16 to 20 km, and hence must spend nearly all of their flight time in the stratosphere. By 1970 it became evident that the question of the severity of pollution by these aircraft could not be answered on the basis of available data. The Climatic Impact Assessment Program (CIAP) was set up (as described in the Introduction) to provide the data needed for the most accurate environmental impact statement which could possibly be prepared. The program involved extensive measurements of trace substances in the stratosphere by in situ and remote-sensing techniques, and development of models of all kinds, including chemical transport, radiation, and biological interactions which could be used to predict the fate of pollutants and the ultimate effects on the biosphere.

The results of more than two years of work by as many as a thousand researchers constitutes a huge mass of information. This information has appeared (and is continuing to appear) in publications issued by the CIAP office of the U.S. Department of Transportation. To date, three volumes of proceedings of conferences (unrefereed papers) and the official Report of Findings have been issued. In addition, detailed and refereed papers will appear shortly as a set of six large monographs. The total of these publications amounts to several thousand printed pages. It is patently impossible to give in this article a complete, detailed and documented review of such a gigantic mass of material. Furthermore, the monographs have not yet been released in final form, and many of the authors wish to publish

their results in the various scientific journals. Since we, as participants in CIAP, have privileged access to much of this material before it has been published, we would be acting unfairly toward our colleagues if we discussed this material here. For these reasons, we will limit discussion to material in the Report of Findings<sup>21</sup> and to previously published material referenced therein.

Basically, four questions were posed: (a) will the aerosols deposited by the aircraft, or formed by conversion of gaseous effluents to particles by chemical or photochemical processes (i.e., smog) be dense and persistent enough to affect the heat balance (as discussed in an earlier section of this article); (b) will the water vapor released into the stratosphere lead to persistent ice-particle clouds (contrails); (c) will the CO<sub>2</sub> output of the planes be large enough to raise the concentration in the stratosphere appreciably relative to the troposphere; and (d) will the pollutants enter into chemical reaction with the natural molecular species there so as to alter the concentration of the latter appreciably and so change the optical thickness of the atmosphere to the solar ultraviolet radiation. In brief, the answers found by the program are: (a) possibly; (b) only in very limited regions of the stratosphere; (c) no; and (d) yes, but the magnitude of the effects is rather uncertain.

Since the chemical effects are the most definite and potentially the most serious, they will be discussed first. The problem arises because of the high chemical reactivity of ozone (triatomic oxygen molecules,  $O_3$ ). This gas is produced photochemically; ultraviolet solar radiation of wavelengths shorter than about 0.24  $\mu$ m (designated  $h\nu_1$ ) splits  $O_2$  into single atoms; many of these recombine but some become attached to an undissociated  $O_2$  molecule by way of a three-body reaction. Ozone is also dissociated by solar ultraviolet of a slightly longer wavelength (0.28 to 0.33  $\mu$ m, designated  $h\nu_2$ ) to yield molecular and atomic oxygen. The set of reactions is

$$O_2 + h\nu_1 \rightarrow O + O$$
  
 $O_2 + O + M \rightarrow O_3 + M$   
 $O_3 + h\nu_2 \rightarrow O_2 + O$   
 $O + O_3 \rightarrow O_2 + O_2$ 

where M is any available molecule.

This scheme, first proposed by Chapman<sup>239</sup> would be valid for an atmosphere containing only oxygen and chemically inert molecules combined

in a quartz flask and irradiated with ultraviolet. In this case, the equilibrium proportions of  $0, 0_2, 0_3$ would be predicted exactly if the intensity and wavelength distribution of the radiation were prescribed. Unfortunately, the real atmosphere is not so simple. The intensity of the two bands of radiation at any level in the atmosphere depends on how much O2 and O3 lie above that level, since the first and third reactions represent absorption of the radiation. The rate of the second reaction is dependent on the density of third bodies M, and therefore on the atmospheric density at each level. Furthermore, the atmosphere is in motion; ozone formed at one location may be moved by wind to another. The result, in an oxygen-nitrogen atmosphere, is a three-dimensional distribution of O<sub>3</sub> which is unsteady and not predictable by the simple reaction set and laboratory rate data.

The importance of ozone to the biosphere is contained in the third reaction of the set. The radiation in the 0.28 to 0.33  $\mu$ m band (h $\nu_2$ ) is quite active biologically; it is responsible for sunburn, for example. The amount of ozone in the stratosphere is sufficient to attenuate this band substantially, so that radiation shorter than 0.29 µm is virtually unmeasurable at the ground. Complete removal of the ozone would permit transmission of this band with only scattering attenuation; the increased intensity would have various effects on the biosphere, many of which are detrimental. Increased severity of sunburn is an obvious consequence, but greater frequency of skin cancer among the paler strains of the white race, disturbances to land and water flora and fauna, and more rapid deterioration of materials (plastics, cloth, paints, etc.) are also likely consequences.

The four reactions given above, plus the effects of transport by the general circulation and diffusion process, give rise to an ozone layer in which the mixing ratio by volume of  $O_3$  (in the time mean) as a function of height is a bell-shaped curve with the maximum mixing ratio found near 20 km; it decreases to a low value at 60 km and also near the ground. The absorption of the  $h\nu_2$  radiation is, however, most effective in heating the stratosphere in the upper part of the layer; this is the reason for the temperature maximum there. The removal of all ozone would eliminate this heating, totally altering the atmospheric general circulation in the stratosphere and possibly influencing that in the troposphere to some extent.

The mean lifetime of  $O_3$  molecules against decomposition by the third reaction is also strongly altitude dependent. Above the ozone maximum it is very short, decreasing to a few minutes at 60 km, while below the peak the lifetime is months or even years.

The presence of other chemical species besides oxygen and inert gases complicates the picture tremendously. Once hydrogen compounds (such as water), SO<sub>2</sub>, NO<sub>x</sub>, halogens, methane, etc., are allowed to enter the stratosphere, the number of reactions which must be considered in attempting to compute the O<sub>3</sub> distribution by a model increases from 4 to something of the order of 150 or more. Obviously, some reactions are more critical than others, so the usual tradeoffs of completeness against tractability (computer time and memory limitations) are required. Some models have used as few as 10 reactions, others as many as 40.

While it is true that the species listed above can be considered as trace materials, their effects on the chemistry of ozone (itself a trace material with volume mixing ratio of a few parts per million) are not negligible. This is because of the highly reactive character of the O<sub>3</sub> molecule, and because some of the reactions are catalytic. A particular species may react with an ozone molecule, decomposing it and being itself changed only to be regenerated in another reaction. It is such reactions which require the closest attention. One of the earliest to be considered<sup>240</sup> involved the free hydroxyl radical, HO, produced by the reaction between water and excited atomic oxygen

$$O(^{1}D) + H_{2}O \rightarrow 2HO$$

and subsequent reactions of the hydroxyl as follows

$$HO + O_3 \rightarrow HO_2 + O_2$$
  
 $HO_2 + O_3 \rightarrow HO + 2O_2$ 

with the net effect of eliminating two molecules of ozone and leaving the HO radical still available to repeat the cycle. In 1973<sup>24</sup> 1-2<sup>43</sup> it was found that the rates of these reactions, especially the last, are rather slow, but the mechanism should account for some destruction of the "sheltered" ozone in the lower stratosphere and upper troposphere. On the other hand, the relatively small amount of

water vapor mass contributed by the SST fleet relative to the total water present in the stratosphere should not accelerate the process significantly. Some other reactions involving ozone, hydroxyl, and perhydroxyl (HO<sub>2</sub>) radicals may be important above 40 km, but these need not concern us here.

Another and more important reaction pair, first discussed by Johnston<sup>244,245</sup> is

$$NO + O_3 \rightarrow NO_2 + O_2$$
  
 $NO_2 + O \rightarrow NO + O_2$ 

with the net result of removing one O<sub>3</sub> molecule and one O atom, and regenerating the NO for recycling. The second reaction is the rate-determining step; the actual rate, of course, depends on the product of the concentrations of NO<sub>2</sub> and O. Since the concentration of O atoms increases with altitude, it follows that the ozone destruction by small amounts of NO<sub>2</sub> will be greater in the upper part of the ozonosphere. At lower altitudes, Johnston has suggested the set

$$NO_2 + O_3 \rightarrow NO_3 + O_2$$
  
 $NO_3 + h\nu \text{ (red light)} \rightarrow NO + O_2$   
 $NO + O_3 \rightarrow NO_2 + O_3$ 

in which NO<sub>2</sub> is the catalyst and the energy source is visible light from the sun (which is available at about equal strength at all heights).

In order to calculate the change in O<sub>3</sub> concentration resulting from pollution with NO, it is necessary to know the rate constants of the reactions, plus the concentrations of all other reactants at the time of injection. Two difficulties arise: (a) natural abundances of NO<sub>x</sub> had not been measured with acceptable accuracy before CIAP; and (b) the reactions involving NO<sub>x</sub> are coupled (through atomic oxygen) to the Chapman set and most of the other 130-odd reactions involving neutral species, so that one would have to invert a 130-row square matrix in order to solve for the concentrations of all species. For example, the hydroxyl radical acts as described to reduce ozone, but it also participates in the conversion of NO, to HNO<sub>3</sub>, thus eliminating one pair of catalytic reducers and slowing down the ozone destruction. It is therefore not at all surprising that 13 models, most of them developed with CIAP support, gave ozone reduction percentages ranging over 3 orders

of magnitude. (See Reference 21, p. 27.) These included one- two- and three-dimensional models including varying numbers of the chemical reactions plus radiation and atmospheric transport. The relationship between ozone reduction and NO<sub>x</sub> emission adopted by CIAP was based on the results of the 1974 two- and three-dimensional models by Chang (not yet published) and Hunten (not yet published). The mean of these 2 models gives a somewhat non-linear relation; when this is combined with estimates of NO, emissions (Reference 21, p. 23), one obtains a prediction of 0.8% ozone reduction by 1985, 8% by 1995, and 10.6% by 2005. On the basis of some statistical studies sponsored by CIAP, these figures go over almost identically into the percentage increase of skin cancer incidence. If the NO<sub>v</sub> is considered to be retained in one hemisphere, the cancer rates are doubled (Reference 21, p. 37). A time lag of 30 to 50 years is involved in the relationship. Other effects on the biosphere are being studied, but no conclusive results are yet available.

In considering this conclusion, and others to follow, the reader is warned to keep in mind that the models which give rise to the conclusions are necessarily parameterized, incomplete, and involve estimates of quantities such as turbulent diffusion coefficients, etc., which vary by orders of magnitude from one model to another. Work is in progress, partly sponsored by CIAP, to obtain better data on the stratospheric NO<sub>x</sub> loading with new and more sophisticated airborne instrumentation. As better data become available, the model outputs will change accordingly; the figures given here are very tentative.

A set of reactions<sup>246</sup> involving chlorine has also been studied; the principal catalytic cycle in this case is

$$Cl_2 + h\nu \rightarrow Cl + Cl$$
  
 $Cl + O_3 \rightarrow ClO + O_2$   
 $ClO + O \rightarrow Cl + O_2$ 

but 26 other reactions can be written which connect the chlorine with HCl and ClO<sub>2</sub>, etc., and must be considered to be coupled to the above. Free chlorine or HCl would not be abundant in the stratosphere except possibly after volcanic eruptions. The concern about chlorine chemistry by CIAP stemmed from the fact that some rocket propellants proposed for space shuttles contain chlorine compounds. Since the problem was not

referred to in the main text of the Report of Findings, we conclude that it must have been considered much less important than that of NO<sub>v</sub>. Recently, however, a potential chlorine source due to human activities has been suggested by several authors247-250 in the form of the chlorofluoromethanes CF<sub>3</sub>Cl and CF<sub>2</sub>Cl<sub>2</sub>, better known as Freons. These compounds are used extensively as working fluids in refrigerators and as propellants in spray cans for cosmetics, insecticides, etc. The latter use involves an obvious intentional discharge to the atmosphere. They are very inert chemically and hence will remain in the atmosphere indefinitely and diffuse throughout its depth. The only recognizable sink is in the stratosphere above 30 km or so, where it is photo-dissociated by ultraviolet radiation of wavelength less than 0.23 µm, so that the set of reactions written above for chlorine is still applicable if we replace the first by

$$CF_xCl_v + h\nu \rightarrow CF_xCl_{v-1} + Cl$$

The authors cited contend that this reaction set may well constitute a stronger ozone sink than the NO<sub>x</sub> cycle, because the rate constant for the regeneration of Cl atoms in the third reaction of the chlorine set is much larger than the corresponding reactions for NO and NO2 regeneration. The ultimate sink for the chlorine is HCl, but only after many cycles as a catalyst. The fluorine, on the other hand (after further photolysis of the free radicals) goes directly to HF and has no effect on the ozone. The consensus of the authors cited is that depletions of the ozone layer of the order of 5 to 10% will result from present levels of Freon release, and that, because of the time needed for diffusion, the effects will lag the release by as much as 80 years. If the use of Freons should be growing exponentially, then the effects would, of course, be even larger. The combined effects of SST and chlorine pollution could result in an ozone depletion of up to 20% by the end of the century if the models are quantitatively sound.

The stratospheric ozone overburden, as measured at any one station, is quite variable. An annual cycle is a regular feature. In addition, stations outside the tropics show wide fluctuations associated with the movement of troughs and ridges of the planetary waves in the general circulation of the atmosphere. Fortunately, a worldwide network of monitoring stations has been measuring total overhead ozone since the IGY.

While not all stations maintain the highest standards of calibration, enough of them do so that a fairly good data base for detection of long-term trends is available. A statistical study was carried out by the Inadvertent Modification Program personnel<sup>251</sup> of NOAA — APCL at the suggestion of H. Weickmann, who pointed out that present day commercial aircraft were spending part of their time in the stratosphere in high latitudes, that supersonic military aircraft were already operating at SST cruise altitudes, and that if the pollution effect were large, it might already be detectable. When the data from 11 North American stations for the decade 1961 to 1970

were analyzed for a linear trend, it was found that all stations showed an upward tendency. When data from other quadrants of the globe were analyzed, an upward trend was found at almost all stations, thereby eliminating the possibility that the North American trend was regional. The data (after removing the mean annual cycle by numerical filtering) from the stations over the globe for which the statistical significance of the trend was greatest is shown in Figure 12. The increases per decade varied from  $2.4 \pm 0.6\%$  at Mauna Loa to  $10.0 \pm 0.4\%$  at Kodaikanal, India. Since 1970, however, the trend has reversed and the ozone has been decreasing on a global scale, as

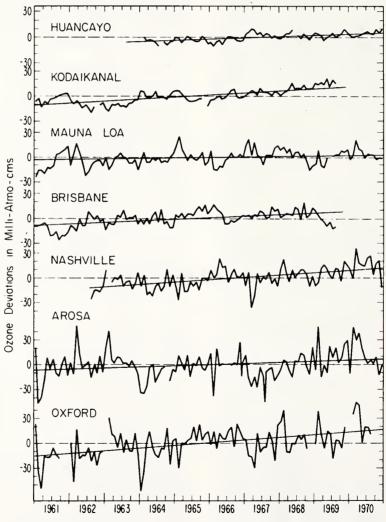


FIGURE 12. Time series of deviations of monthly mean values (from the period means) of total ozone mass in a vertical column at several stations distributed over the globe. All stations show upward trends with time. (From Komhyr, W. D., Barrett, E. W., Slocum, G., and Weickmann, H. K., <sup>251</sup> Nature, 232, 390, 1971. With permission.)

shown in Figure  $13.^{252}$  These data show that long-term variations in global ozone of the same magnitude as the suggested effects of pollution do occur naturally. The causes of such variations are not clear, but they may reflect changes in the vertical and meridional transports of  $O_3$  by the general circulation of the atmosphere so as to bring more or less of the gas into the protected region of the lower stratosphere under different flow regimes. Unambiguous determinations of the

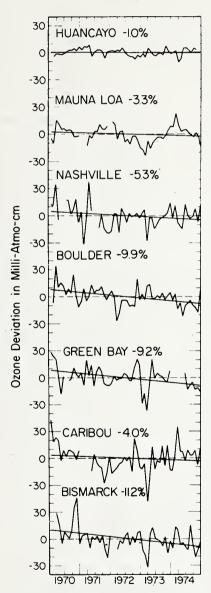


FIGURE 13. Time series of deviations of monthly means (from the period mean) of total ozone mass in a vertical column for several stations, showing general downward trend since 1970. (From Grass and Komhyr.<sup>252</sup>)

magnitude of the pollution effect will not be possible until several more decades of global ozone data are available; it is premature to claim (as some newspaper articles have done) that the recent downward trend is a verification of the pollution-effect predictions.

The question of persistent ice cloud formation from water vapor emitted by the SST was examined in a CIAP study using different models derived by Appleman and Barrett (Reference 21, p. E124-E126). It was found that, because of the generally low relative humidity in the stratosphere, the risk of persistent condensation-trail clouds is negligible except near the tropical tropopause (16 to 18 km elevation between 15°S and 15°N latitude) and in the winter polar night regions above 70° latitude, with the former being the most serious because conditions for cloud formation are favorable there all year round.

The effect on the radiation balance of the direct particle emissions and the chemical conversion of exhaust gases to particles was also examined in a CIAP study (Reference 21, p. 100, p. E134-147) by Herman et al. Under the assumption that the SO<sub>2</sub> emissions are converted to 75% H<sub>2</sub>SO<sub>4</sub> solution droplets, and the use of Mie scattering theory, it was found that a fleet of from 1,100 to 2,070 Concorde-type SSTs would cause the optical thickness of the stratosphere to increase by  $2 \times 10^{-3}$ , or by about 10% of the unpolluted value. The large spread in number of aircraft is due to different assumptions about cruising altitude. This increase in optical thickness translates into a mean global temperature decrease of 0.07°C, but the effect on countries in higher latitudes such as Canada and the U.S.S.R. could be as large as 0.3°C.

For purposes of comparison, it may be noted that the greatest change in optical thickness at Mauna Loa produced by aerosol from the Agung eruption was 0.02, or about 10 times as much as the projected SST contribution.

It thus appears that the potentially most severe effect of human pollution of the stratosphere is not a direct impact on the ordinary climatic parameters, but is the alteration of the solar-energy spectrum at the ground by ozone depletion so that more of the photochemically active wavelengths reach the ground. The particle production by aircraft would eventually lead to a

slight cooling, provided, as always, that it was not compensated by decreased cloudiness. The reduction of ozone would lead to a markedly cooler stratosphere, this might induce some changes in the general circulation. This last could be investigated with three-dimensional models.

Because of the degree of uncertainty in some of the parameters of the chemical-plus-transport models, and because it is not possible to be certain that all possible reactions have been identified, the quantitative estimates of ozone depletion must be regarded as highly tentative. It is clear that ozone monitoring, plus monitoring of solar radiation in the 0.29 to 0.33  $\mu$ m band received at the ground, must be continued with scrupulous attention to calibration of the instruments for many decades to come. It would also be highly desirable to develop techniques for detection of chlorine (either in situ or by remote sensing) in the stratosphere at volume mixing ratios of less than  $10^{-10}$ , in order to settle the question of whether or not this pollutant is actually reaching the stratosphere.

In an earlier section, the nuclear weapon was identified as a polluter of the stratosphere with nitrogen oxides. One would expect, then, that ozone reductions should have been noticeable during or after periods of heavy weapons testing in the atmosphere. Examination of the ozone data of Komhyr et al. and Newell (Reference 21, p. 26) shows no evidence for a global decrease during or after the 1961-62 test series; more stations showed an increase than the contrary. It appears evident that either the atmospheric models are leaving something out, or the estimates of NO<sub>x</sub> production by nuclear weapons were much too high. In addition to sustained monitoring efforts, continued work to improve atmospheric models involving chemistry is needed. In particular the modelers should take care not to let their commendable concern over detrimental effects have a biasing influence on their models toward greater severity of prediction, and should state the fact clearly when they are intentionally making a "worst case" prediction.

Subsequent to the writing of the first draft of this article, a review of the CIAP findings by an independent Climatic Impact Committee set up by the National Academy of Sciences of the U.S. 362 was released. The conclusions presented in this new report do not differ markedly from those given in Reference 21 although the new report lays more stress on the potential biological damage resulting from ozone depletion.

# LOCAL AND REGIONAL EFFECTS OF POLLUTANTS: THE URBAN HEAT ISLAND

With few exceptions, the primary sources of pollutants, including waste heat, are large metropolitan areas with concentrations of heavy industry. The local perturbation of CO<sub>2</sub> concentration by the Buffalo, New York area is shown in the horizontal (at 300 m above mean terrain height) in Figure 14 while two vertical profiles taken on the same flight are shown in Figure 15. The flask samples were taken and analyzed by Mr. T. Harris, formerly of NOAA-APCL and currently NOAA-ARL. Excesses of 55 ppmv, or 17% of the normal background of 320 ppmv, were observed, and the excess persisted to a height of 1200 m above the city; mixing was rapid above this level. Similar concentrations of excess aerosol (as measured with the Aitken particle counter by Mr. P. Allee of NOAA-ACPL) are given in Figures 16 and 17. The particle number density is greater by a factor of more than three than in the cleaner air to the northwest. The particle count falls off more slowly with elevation than does the CO<sub>2</sub>.

Differences between urban and rural climates had been recognized long before the establishment of climatological networks. Unfortunately, these differences have also been responsible for difficulties in obtaining representative climatological data. For reasons of convenience, many stations of national meteorological networks were formerly located in or near the centers of cities; the long-term trends of data from these stations reflect nothing more than the urban growth. Relocations of the stations to municipal airports brought about some improvement, but as the cities have grown and urban sprawl has reached almost to the ends of the runways, the airport data have become unrepresentative, at least for large cities. This situation account: partially for the difficulty of finding true global climatic trends. It is essential that climatological benchmark stations whose data are to be relied upon be established only in wilderness areas which are guaranteed by law (or undesirability as places for human habitation) to remain so for decades or even centuries.

The effect on temperature and its vertical distribution of the concentration of energy release in a city is the first climatic perturbation to be measured quantitatively (smoke being the earliest to be noted for its nuisance value). A bibliography

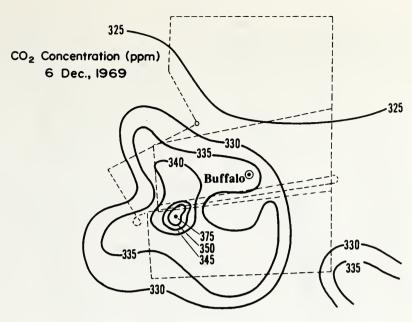


FIGURE 14. Distribution of volume mixing ratio (ppmv) of carbon dioxide at approximately 300 m above mean terrain level around Buffalo, New York, on 6 December 1969. (From Barrett et al.<sup>360</sup>)

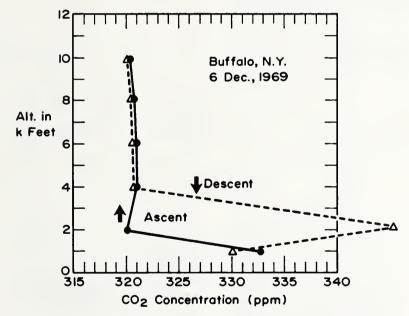


FIGURE 15. Vertical profiles of volume mixing ratio (ppmv) of carbon dioxide on aircraft ascent and descent over Buffalo, New York, on 6 December 1969. (From.Barrett et al.<sup>360</sup>)

of early publications (1833 to 1951) on the subject of urban climates has been published.<sup>255</sup> Most of the early data dealt with differences between daily maxima, minima, and marches of temperature in the city and the adjacent rural areas. Some experiments were carried out with

rapid response temperature sensors mounted on motor vehicles to obtain one- or two-dimensional distribution of temperatures near the ground at different times of the day or night.<sup>256,257</sup> The most striking differences appeared between the nocturnal temperatures in the city center and in

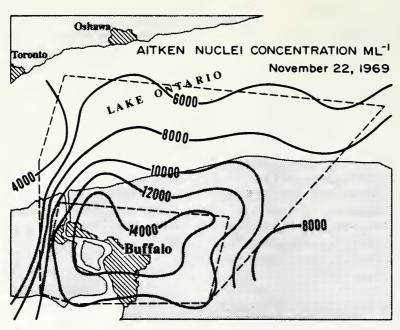


FIGURE 16. Distribution of Aitken nuclei (total small aerosol particles) at approximately 300 m above mean terrain level around Buffalo, New York, on 22 November 1969. (From Barrett et al. 360)

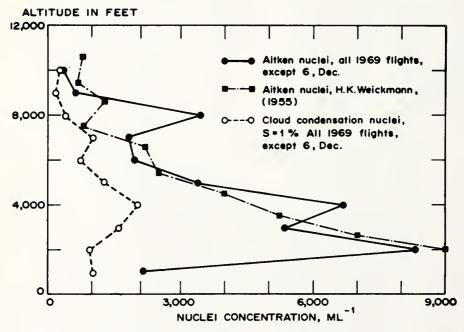


FIGURE 17. Vertical distributions (mean of several aircraft soundings) of Aitken nuclei (solid circles) and cloud condensation nuclei effective at 1% supersaturation (open circles) near Buffalo, New York in the autumn of 1969. Similar Aitken nucleus data from New Jersey in 1955 (solid squares) are also shown. (From Barrett et al.<sup>360</sup>)

rural basin areas; these differences amount to as much as 20°C on calm, clear winter nights.

Vertical distributions of temperature in cities are more difficult to obtain, but some data of this kind have been obtained by mounting recording thermometers on radio or television broadcasting antenna towers.258 As one might anticipate, the heat released in the city prevents the formation of the nocturnal ground-based temperature inversion which is regularly observed over open country under conditions of light wind. Instead, an isothermal layer, or even one with a marked lapse of temperature with height, is found over the city; this may be topped by an inversion aloft when the air outside the city is stably stratified. Some three-dimensional studies of the urban "heat island" have been carried out259-261,269 using ground vehicles, fixed-wing aircraft, and helicopters, together with pilot balloons and chemical tracers to map the field of motion. These studies reveal the destabilization of the thermal stratification as the air is heated and stirred by moving over the rough surface caused by the buildings, and the upward and downwind spread of the thermal plume thus generated.

The destabilization produced by heating and mechanical mixing takes place in the daytime as well. If the synoptic situation is otherwise favorable for convective cloud formation (conditional instability), these clouds are observed to form earlier over the city.261-265 A number of models (in two or three dimensions) have been developed to study the fields of temperature and motion produced when air moves over a warm and rough urban region.<sup>266-268</sup> They predict (with greater symmetry than exists in the real world) a toroidal convective rise which, in the presence of a mean wind, is modified into a two-cell roll circulation extending downwind and giving some downwash of pollutants to left and right of the downwind direction. The direct influence of the heat island extends 20 km or more downwind from a large city.<sup>270</sup> The type of circulation predicted by the models has been verified in a tracer experiment by Hilst and Bowne. 269

The heat islands of large cities are readily sensed by the infrared radiometers of meteorological satellites;<sup>271</sup> "signatures" 3° to 4°C warmer than the surroundings have been noted for large cities on the east coast of the United States.

Some calculations have been made of the heat budgets of metropolitan areas in order to evaluate the ratio of man-released to solar heating. In the case of Budapest, Hungary, <sup>2</sup> <sup>72</sup> with a continental climate, the mean solar input is 87.0 kcal/cm²/year and the mean non-solar is 11.7 of the same units, or 13.4% of the solar. In December, however, the artificial heat exceeds the solar input. In the more maritime (but also cloudier) climate of Sheffield, England, <sup>2</sup> <sup>73</sup> the artificial heat (for the year 1952) was about one third of the total insolation. The fact that these percentages are already so large is the basis for the concern over long-term climatic effects of thermal pollution if present exponential growth rates of energy use continue.

# LOCAL AND REGIONAL EFFECTS OF OTHER URBAN POLLUTANTS: WATER VAPOR AND AEROSOLS

The large ratios of artificial to solar energy cited in the preceding sections are due, in part at least, to the diminution of available solar energy by increased cloudiness and by increased turbidity due to aerosols; a partial compensation for the excess waste heat is thereby achieved. In addition to the studies already cited in the section on global effects of aerosols, several other studies of turbidity over cities should be mentioned. Fedorov<sup>2</sup> 74 studied the variations in turbidity at Zaporozhe during the period 1950 to 1953 and found a mean depletion of total insolation (sun plus diffused sky light) of 13% with a minimum of 4 to 6% in May and maximum of 21% in December. Volz<sup>275</sup> has examined turbidity data collected by two extensive urban networks in North America and Europe by means of an economical two-wavelength sun photometer designed by him; his analyses are expressed in terms of the optical thickness (natural logarithm of reciprocal of transmittance) of the atmosphere along a vertical path. Unfortunately, his paper deals only with short-term trends in relation to synoptic events such as frontal passages, etc., rather than with longer trends (the networks were probably too young to yield significant data at the time). He describes a case (March 1953) in which the optical thickness in various cities from Brussels in the west to Potsdam in the east ranged from about 0.07 before a stagnation period (weak general circulation) to 1.15 (in Brussels) at the peak of the episode. (Optical thickness is referred to a wavelength of  $0.5 \mu m$ ). The significance of this is that in a region

as heavily industrialized as Belgium and Germany, the individual aerosol plumes overlap sufficiently to produce a regional loss of solar energy over thousands of square kilometers.

Cities without heavy industry show smaller but nevertheless noticeable increases to turbidity. Goldberg and Klein<sup>2,76</sup> reported a 6% decrease in total insolation in the 50 years between 1919 and 1969 at Washington, D. C. The extinction of the direct solar beam was 15%, but scattering by the aerosols made up for the 9%. While some of the turbidity was undoubtedly due to automobile pollution, it is likely that plumes from the heavily industrialized regions of Delaware and New Jersey to the northeast were the major sources of the aerosol.

Cities located under persistent temperature inversions with poor ventilation suffer the strongest local effects of pollution. Los Angeles is the best example of a city which has aerosol pollution problems quite out of proportion to the amount of heavy industry in and around the city. Total insolation depletions of as much as 30% are not uncommon there under severe smog situations (F. Hall, private communication).

While the greenhouse effect of suspended particles appears to be negligible on a global scale, this is not necessarily the case with the dense urban aerosol blankets. Yamamoto<sup>277</sup> and Idso<sup>278</sup> have found that nighttime minimum temperatures are correlated positively with aerosol turbidity over cities; the latter author found increases of 4% or more in the downward flux of long-wave radiation from the night sky when the air was very dirty. Unless, therefore, the urban aerosols are strong absorbers in the visible spectrum, the particles act to reduce the amplitude of the diurnal march of temperature in cities.

In the section on global effects of aerosols it was pointed out that the pollution plumes from heavily industrialized regions can be detected well out over the downwind oceans, both by direct sampling and by the decrease in atmospheric electrical conductivity they cause. As cloud physicists became more aware of the importance of condensation and ice nuclei in the life cycles of clouds and the formation of precipitation, the question of the extent to which clouds were being modified by urban pollutants began to be raised.

A number of studies have been made of the aerosol distribution near the ground around large cities using various forms of the Aitken nucleus counter. Schmidt<sup>279</sup> found that Aitken counts were increased by a factor of 10 when air moved across the city of Vienna. Wuerfel<sup>280</sup> found a similar but weaker increase in Aitken counts for air moving across Berlin. Figures 15 and 16 of this paper give an example of the three-dimensional distribution of Aitken particles. These measurements, useful as they are in obtaining a measure of the total number of particles in a unit volume of air, do not give any information on their nucleating power because the Aitken counter exposes the particles to very high supersaturations whereas cloud condensation nuclei must be effective at about 1% supersaturation. In recent years, therefore, instruments for counting particles which form drops at such low supersaturations, and also for counting nuclei which cause supercooled drops to freeze at specified temperatures have been developed and used to study the spatial and temporal distributions of these nuclei.

The role of urban smokes as fog condensation nuclei was recognized quite early, and gave rise to the term "smog." The city of London was for over 200 years a prime example of an urban cloud condensation nucleus (CCN) generator on a large scale.<sup>281,282</sup> The smog disaster of 1952, in which deaths from respiratory ailments and their complications rose to alarming levels, ultimately brought about the Clean Air Act of 1956. This act invoked strong smoke-abatement procedures for the London metropolitan area and other industrial cities throughout the United Kingdom. Within a very few years, dramatic reductions in the density and frequency of fogs took place. Kew Observatory (in the London metropolitan area), 283, 284, 286 experienced an increase of 50% in hours of sunshine in the November to January season for the period 1958 to 1967 over the mean for the climatological epoch 1931 to 1960. Suburban areas and the Heathrow Airport 285 showed similar improvement as did Glasgow Airport<sup>287</sup> after Scotland began to enforce its own Clean Air Orders sometime between 1962 and 1968.

The reason for such marked change is to be found in the hygroscopic character of some of the constituents of urban aerosol; these particles become active as CCN at considerable undersaturation. Junge<sup>288</sup> considered the H<sub>2</sub>SO<sub>4</sub> formed by oxidation of combustion SO<sub>2</sub> to be the primary hygroscopic CCN. On the other hand, Neiburger and Wurtele<sup>289</sup> noted that Los Angeles fog and low stratus clouds were often stable at relative

humidities as low as 90%, while at Santa Maria (an unpolluted town near the coast some 150 km to the north) the fogs under the same meteorological conditions existed at water saturation (100% relative humidity). These authors were at a loss to identify the particular pollutant responsible for this; they ruled out both  $\rm H_2SO_4$  and sea salt because equilibrium at 90% humidity would require a 23%  $\rm H_2SO_4$  solution, or a 17% NaCl solution, in the cloud droplets.

While the fact that cities produced copious supplies of CCN and thereby increased the persistence and density of fog and low clouds was thus well established at a fairly early point in time, the magnitude (or sign) of an influence on precipitation was not. Ashworth<sup>290</sup> suggested as early as 1929 that precipitation at Rochdale (England) was augmented by the urban particulate matter. Neuwirth<sup>291</sup> argued in favor of a global effect of industrial aerosols on the hydrologic cycle, but did not produce any quantitative data or model to support the argument.

A problem in prediction of the influence of aerosols on precipitation is that two mechanisms, acting either separately or together, are involved in bringing together the large number of small cloud droplets required to make one raindrop. If a cloud forms under conditions of CCN shortage, it will contain a smaller number of droplets, but a broader spectrum of sizes; this increases the probability of drop growth by collision and coalescence (growth by diffusion alone to raindrop size is much too slow to be of any importance). On the other hand, if a surplus of CCN is available, the cloud will consist of a large number of very small drops, all of which will be nearly the same size; such a cloud has high colloidal stability with respect to the coalescence process of raindrop formation. If this mechanism were the only one available, then the urban industrial CCN should cause a drop in precipitation due to overseeding. In the case of clouds whose tops extend well above the O°C isotherm there is another mechanism leading to quick production of larger cloud particles. It is an important fact of nature that water droplets away from contact with solid bodies cannot freeze at O°C; this temperature is the melting point of atmospheric water but never the freezing point. Freezing will occur at sub-zero temperatures when water drops come into contact with solid particles, but the effectiveness of these particles depends on their size, chemical nature, crystal structure, and condition of their surfaces. If no particles at all are present, spontaneous freezing can take place, but the mean lifetime of a drop against this event is longer than the mean lifetime of a cloud until the temperature nears -40°C. In the absence of particles, then, cloud droplets would remain supercooled at temperatures warmer than this. Particles which induce freezing at temperatures warmer than this are termed ice nuclei (IN). Any wettable particle will act as an ice nucleus at the cold end of the temperature range -40°C to 0°C, but the choice narrows down as the temperature rises. At -20°C many natural minerals are still effective, but at -10°C very few natural IN can be found.

Once some cloud droplets have frozen at temperatures below 0°C, they undergo rapid growth by diffusion because they are in an environment which is strongly supersaturated with respect to ice. These large ice crystals can then settle through the cloud relative to the small drops, sweep up some of the latter and grow by this accretion. If the melting level is far enough above ground, they will melt and fall as raindrops.

This ice-crystal process of rain (or snow) production is the most efficient one in continental clouds of middle and high latitudes (and, in general, for any cloud which grows well above the 0°C isotherm), while the coalescense process is most important in low latitude maritime clouds.

The effect of introducing aerosol particles into a cloud is seen to be dependent on the relative amounts of CCN and IN in the aerosol and on the type of cloud. If the CCN count is high and the IN count is low, precipitation will be inhibited very strongly in warm, shallow clouds, and still inhibited, but less strongly, in taller or colder clouds. If the CCN count is low and the IN count is high, there will be little effect on warm clouds over land (because the natural CCN supply is usually adequate) but tall or cold clouds should be stimulated to produce precipitation more rapidly. This is especially true if the pollution aerosol contains IN which are active at warmer temperatures than the natural IN (which are often in short supply or active only at low temperatures; this is the whole rationale behind the intentional modification of clouds by seeding with artificial IN, such as silver iodide, that are active at temperatures as high as  $-4^{\circ}$ C).

In the extreme case where the pollution aerosol is very rich in both CCN and IN, the clouds will

consist of very small droplets in the warmer part, and very small ice crystals in the colder part (because the crystals will be competing for the available water supply and therefore cannot grow rapidly by diffusion). Such a completely overseeded cloud will produce little or no precipitation.

It follows from the foregoing that the effect of pollution aerosol may be either to decrease or increase precipitation, depending on the circumstances, particularly on the concentration of IN in the aerosol.

Schaefer<sup>292,293</sup> and Morgan and Allee<sup>44</sup> have pointed out that lead from automobile exhausts is a potential source of pollution IN. When exposed to iodine vapor, the resultant PbI aerosol is nearly as effective as AgI as a freezing nucleus. The question is whether enough free I<sub>2</sub> is available in the atmosphere, either naturally or as a pollutant, to make automotive exhaust a significant source of IN. It was pointed out in an earler section that free 1<sub>2</sub> is formed by reaction of ozone with sea water, but the strength of this source in nature is unknown. Langer<sup>294</sup> has shown that the aerosol emitted by steel mills contains significant amounts of IN. Reynolds<sup>295</sup> made aircraft probings in plumes from copper smelters south of Salt Lake City, Utah, and found ice-nucleus counts as high as 6,000 per liter. On 15 of the 21 flights, counts greater than 1000/1 were obtained. (Natural background counts are generally of the order of one nucleus per liter.) Telford<sup>296</sup> measured IN counts of over 50 times the clean air background in effluents from steel mills in Australia. Squires<sup>299</sup> measured CCN in the air over Denver, Colorado, and divided this by the estimated fuel combustion to obtain an emission index; from this he estimated that, for the northern hemisphere as a whole, the CCN production averaged about 9 particles/cm<sup>2</sup>/sec, or about 5% of the natural production, but that near cities the concentration was equal to or greater than the natural background. On the basis of preliminary data from the NOAA ice nucleus network, Allee<sup>336</sup> has estimated the current production rate of IN in the western U.S. to be of the order of 2 IN/m<sup>2</sup>/min.

These observers, and some other writers on the subject of urban climatology 300-306,315 suggested that these pollutant nuclei should have a measurable effect on precipitation but, in most cases, did not have adequate data to establish any correlations. In 1968, Changnon<sup>297</sup> analyzed the

data from a cooperative (volunteer) climatological station at La Porte, Indiana, a village located about 50 km east of the southern end of the Chicago metropolitan area where the steel-making industry is concentrated. He documented some very large but very localized effects; during the years 1961 to 1965, La Porte had 31% more precipitation, 38% more thunderstorms, and 246% more hail days than other stations some 30 km distant. The precipitation excess was found to be greatest in the warmer half of the year. Also, the curve of warm season precipitation from 1925 through 1965 was highly correlated with the annual steel production by the mills to the west and with the curve of smoke/haze days at Chicago. Changnon was surprised at the magnitude of these effects, and gave consideration to the possibilities of observer bias, change in rain gauge exposure, etc. He concluded that none of these was sufficient to account for what was henceforth called the La Porte anomaly, and that the anomaly was real. This conclusion was challenged by Holzman and Thom, 298 who attributed the anomaly to observer bias in reading the stick-type rain gauge and to other vaguely specified observer faults. This contention was refuted by Changnon<sup>298</sup> in his reply, in which he argued that only deliberate falsification of reports could account for the anomaly if it was not real, and that if such were the case, no confidence could be placed in any cooperative observer data. He rejected this explanation and expressed the conviction that the anomaly was real. He also published results of another study<sup>3 0 3</sup> of rainfall data from networks in Chicago and Urbana, Illinois, and St. Louis, Missouri. Some indications of higher rainfall totals within and downwind of the city centers were found, but they were by no means as strong as at La Porte.

Evidence in support of the reality of the La Porte anomaly has been offered by Harman and Elton. They noted that an abrupt change in forest type (from beech and maple to oak) coincides with the western margin of the area of high precipitation. Study of tree rings in living trees near La Porte showed a pattern which would be expected if the anomaly is real. While the tree-ring analysis may be good supporting evidence, it would seem that the change in forest type must certainly be a feature which antedates the establishment of the steel industry and therefore implies a natural effect of topography, the lake, or soil differences.

Better supporting evidence comes from an analysis of the flow of the upper Kankakee River by Hidore.<sup>308</sup> This river carries the runoff from the La Porte region. The temporal variations of the runoff agreed with what would be expected on the basis of the rain gauge record at La Porte.

The question naturally arises as to why the downwind effect at La Porte should be more marked than at other cities. We suspect that a fortuitous combination of geographic and meteorological factors is involved. First, the pollution source region is highly concentrated, so that the particle concentration in the plume is enormous. Second, the air over Lake Michigan in summer with westerly winds is markedly cooler than the air over the land. This cold dome of air acts like a physical barrier to air flow and channels the flow around the south end of the lake, thereby creating convergence and lifting of the warm, humid air and the development of convective clouds and thunderstorms. The clouds and the seeding agent are thus channeled into the right place at the right time.

It is interesting to note that the exact opposite effect of steel mills on downwind rainfall has been reported in India. Ramana Rao and Ramana Murty<sup>309</sup> examined the monthly rainfall data for February (dry northeast monsoon season) and August (wet southwest monsoon) at a number of stations 100 to 200 km downwind from the Jamshedpur-Burnpur steel mill complex, for the period since 1872. They found decreases in precipitation as great as 63% in February and 27% in August at some stations (relative to upwind control stations) since establishment of the steel industry. The reasons for the different effects in India and North America are not at all obvious. It is conceivable that the nucleus populations generated by the mills are not the same because of differences in the composition of the iron ore and coal. Another possibility is that the Indian rain gauge stations were too far downwind (twice to four times the Gary to La Porte distance) to detect a local region of enhanced precipitation. Another and more likely possibility is that most of the February precipitation in India may come from warm clouds. In this case, the mill effluents would overseed the clouds with CCN and thereby reduce precipitation. In Indiana, on the other hand, nearly all of the precipitation, summer or winter, comes from cold-top clouds in which the ice crystal process is dominant; the IN output from the mills is then the most important factor.

The doubts and uncertainties surrounding the La Porte anomaly served a useful purpose in stimulating interest in the study of downwind regional influences of cities on precipitation. Some of these studies took the form of analyses of past data, such as the investigation of the influence of the large industrial pollution output of the New York-eastern New Jersey region by Shulman and Greenway. The results of this analysis were not clear-cut; there was some evidence that precipitation increased downwind when the winds were deep northeasterly or southwesterly, but in typical warm front precipitation regimes, with northeast winds at lower levels and southerly winds aloft, the precipitation pattern was more complicated.

A more important consequence of the La Porte controversy was the stimulus it provided for an organized field program designed to measure the urban weather influences directly and currently rather than trying to extract them by statistical means from past data. The St. Louis metropolitan area was selected for the program because of its central location and relative freedom from complicating orographic factors or land-and-sea breeze circulations. The program evolved as a cooperative effort between several independently funded organizations; coordination was handled by annual election of a program coordinator from among the principal investigators. This program, called METROMEX (for Metropolitan Meteorological Experiment)18 began field operations in June of 1971 and is expected to terminate after the summer of 1975. The field instrumentation included a surface rain gauge/hail pad network (228 stations), 13 pilot balloon tracking stations, a number of special recording instruments (sky cameras, atmospheric electricity, etc.), radar, lidar, and as many as 7 aircraft equipped for various kinds of measurement and sampling from near the ground to the stratosphere.

Measurements made included: rainfall and hail distributions; deformation of the wind field by the city; the heat island (three-dimensional thermal distribution), its diurnal variation and its effect on the three-dimensional flow field and convection; the three-dimensional distribution of total aerosol, CCN, and IN; tracer experiments to verify the entrainment of air from the urban boundary layer into the clouds and precipitation; and studies of drop-size distributions in upwind and downwind clouds. Results reported to date<sup>261</sup> show that total rainfall, lightning, and hail are maximum at 15 to 25 km downwind of the urban area. It was

also shown that air which has been modified and polluted in the urban boundary layer rises in plumes (because of the urban heating) and enters the cloud bases. Direct evidence of large downwind increases of CCN (50 to 90%) was obtained.<sup>311-313</sup> These were observed to enter the clouds; the drop-size spectra of the modified clouds differed from those of upwind clouds in just the way predicted by a cloud model.

The experiment has thus demonstrated, both statistically and physically, that the thermal and particulate emissions from an industrialized metropolitan area do cause measurable increases in downwind precipitation and thunderstorm activity. By the time of its termination, it is to be hoped that the statistics of the magnitude of the effect will be significant enough to permit estimates of the overall contribution of precipitation increase to the regional and global hydrologic cycle.

A direct connection between industrial pollution plumes, ice nuclei, and winter snowfall has been measured and observed by NOAA—APCL personnel.<sup>314</sup> In Figure 18 the two-dimensional distribution of IN (number per liter) is plotted at

various points along the flight track of the aircraft. Measured winds are also shown at a number of points. The locations of snow showers reported on the ground are given by the conventional symbol; radar echoes indicating precipitation-size snow-flakes are shown heavily shaded. It can be seen that all of the precipitation areas lie on or very near to three plumes of high IN concentration extending downwind from Buffalo, Toronto, and Oshawa, and that no snow is falling elsewhere. It is apparent that the snow which fell at this time was due entirely to inadvertent seeding by industrial pollutants.

A very thorough review of urban climatic influences is given in a recent article by Landsberg. 363

#### NON-URBAN AEROSOLS AS NUCLEI

Although cities and industries in and around them are the principal sources of anthropogenic pollutants, some agricultural activities involving extensive burning of vegetable matter generate enough nuclei to have at least a local effect on clouds and precipitation. Warner<sup>316</sup> examined 60

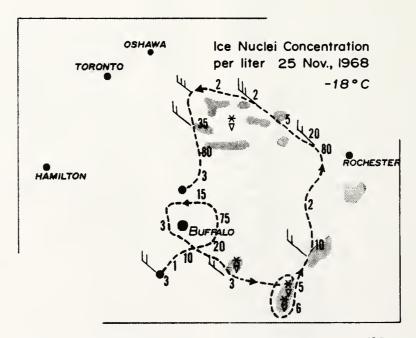


FIGURE 18. Distribution of concentration of ice nuclei (active at - 18°C) and winds along a flight track near Buffalo, western New York State, and southern Lake Ontario, 25 November 1968. Note plumes of elevated IN concentration downwind of the industrial centers of Buffalo, Toronto, and Oshawa, and the occurrence of snow showers only in or near those plumes. (From Weickmann, H., 314 Weatherwise, 25, 260, 1972. With permission.)

years of data for rain gauges located both upwind and downwind of sugar cane fields in Australia, and found that rainfall at the downwind stations was less, on the average, relative to the upwind station during the cane harvesting season (September to November) than during March. Cane is prepared for harvesting by setting entire plantations afire to remove the leaves; much smoke is generated by this combustion. Because the shower-type precipitation in this region (around 20°S latitude) is mainly from warm maritime-type clouds, Warner concluded that CCN (which he had previously measured in cane-fire smoke) from this combustion were stabilizing the clouds and inhibiting rainfall.

High CCN counts in smoke from combustion of natural ground-cover plants in Florida have been measured in the laboratory<sup>317</sup> (as many as 10<sup>10</sup> nuclei per gram of plants burned). It is therefore probable that the production of CCN by natural fires<sup>320,321</sup> and fires unintentionally started by man far exceeds the production by agricultural burning.

It has been suggested by Komabayasi<sup>318,319</sup> that volcanic dust inhibits thunderstorms. He noted that thunderstorms were only about half as frequent near Asama volcano during summers when it is active than when it is quiet. It seems very likely, however, that the reduction is due mainly to the increased turbidity of the atmosphere which reduces the solar heating and therefore the energy available to produce convective clouds, rather than to any nucleating effect of the dust. Price and Pales<sup>322</sup> made twice-daily ice nucleus counts at Mauna Loa while the air was polluted by the Kilauea-Iki and Puna eruptions of 1959 to 1960 and found no noticeable increase over the counts in clean air.

Recently, NOAA has established an ice nucleus monitoring network in the 17 westernmost contiguous United States<sup>3 3 6</sup> under the supervision of P. Allee of APCL. Samples of aerosol are collected daily on membrane filters and activated in a test chamber at -15°C and -20°C on alternate days. The data permit synoptic analyses of IN distributions, and, over the long term, will provide information on regional trends, if any exist.

# WATER VAPOR AS A CONTRIBUTOR TO WEATHER MODIFICATION

The quantity of water vapor added to the

atmosphere by man is trivially small in comparison to the total mass of water in the entire earth atmosphere system, so that no question of effects like those of  $CO_2$  arises. The only way in which addition of water by man might contribute significantly to inadvertent modification would be by altering the mean cloudiness. This would happen if the water is introduced consistently at a place where the relative humidity is close to saturation with respect to water.

In the section dealing with stratospheric pollution, it was demonstrated that the risk of generating such clouds in the stratosphere was low except in those circumstances where the stratosphere was extremely cold and close to saturation, e.g., the tropical tropopause and the polar night zone. When the atmosphere as a whole is considered, the tropopause at any latitude, and occasionally other layers of the upper troposphere, are sufficiently humid for condensation-trail formation. Thus, the subsonic transports currently in operation are very likely to contribute to the contrail-cloud amount.

It is a familiar fact that on many days the contrails laid down by aircraft persist for only a few minutes, while on other days they persist for hours and spread extensively. Georgi<sup>3 2 3</sup> described one such situation where a contrail crossed the entire sky. Fall streaks hung down from this and formed a narrow cirrostratus nebulosus band. After a half hour, this cloud attained an angular width (transverse to its length) of 20° of arc. Knollenberg<sup>3 2 4</sup> measured the size distribution and quantity of ice crystals in a persistent contrail during its life history, and found that the total mass of ice was of the order of 10<sup>4</sup> times as much as the mass of water vapor in the engine exhaust.

The foregoing observations lead to the conclusion that persistent contrail clouds form when the water vapor is introduced into air that is slightly undersaturated with respect to water but supersaturated with respect to ice. Unless the temperature is exceedingly cold (-90°C or colder) direct condensation from vapor to ice does not occur in the atmosphere; true sublimation nuclei are rare or possibly nonexistent. When the aircraft exhaust raises the humidity to water saturation, a water cloud forms quickly and, if the temperature is fairly cold (-40°C) will quickly freeze. The particles then grow by diffusion until they have used up not only the exhaust water but the reservoir which existed because of the supersaturation. The resulting artificial cirrus cloud will persist until the particles fall out into a drier layer below or the air is warmed by subsidence. Murcray<sup>3 2 5</sup> and others have noted that, if the fallout from these clouds survives evaporation and enters a lower cloud deck, the latter will be seeded and possibly produce more precipitation than it would have otherwise.

Machta and Carpenter<sup>3 2 6</sup> studied cloudiness data at a number of stations where relative absence of lower clouds made it possible to acquire a good statistical sample. They found slight increases in reported high cloud cover at Salt Lake City, Utah, and Denver, Colorado, since commercial jet aircraft began operation in 1958, but concluded that the correlation was not significant; the increase could have been due to changes in the general circulation or to changes in observing and reporting procedures at the stations.

Kuhn<sup>327,328</sup> has modeled the effect of contrail cirrus on the heat budget, based on measurements of the short-wave scattering and long-wave emissivity of such clouds. He found that a typical contrail 500 m thick increases the downward long wave flux by 21% but reduces the solar input to the ground by 15%. A complete overcast would therefore reduce ground temperature by 5.3°C. If a 5% sky coverage by such clouds is assumed, the reduction in ground temperature is 0.15°C. On a global basis, the sky cover from persistent contrails is certainly less than 5%; it may therefore be concluded that the effects of contrails will be sporadic and local or regional and will be manifest as a slight cooling, a reduction in convective clouds and thunderstorms in summer, and a possible slight increase in winter precipitation.

Another local or regional effect which is only a minor nuisance at the present time is the evaporation of water from cooling towers or ponds used to get rid of the waste heat from electrical power generating plants. Carson<sup>329</sup> and Huff,<sup>330</sup> among others, have considered possible effects of this addition of heat and moisture to the atmosphere. The principal effect, quite noticeable at present, is the generation of local ground fog under conditions of high stability (temperature inversion) and low wind. The possibility of increased convective cloudiness on warm, humid summer days exists, but a significant effect is yet to be demonstrated. The effects are not serious as yet, but if energy demands continue to grow, they could become very significant as a part of the consequence of the waste heat disposal problem.

# CLIMATE MODIFICATION BY LAND-USE CHANGES

Changes in the character of the earth's surface by man in the course of his agricultural or industrial activities, if carried out over a wide enough area, have the potential for modifying climate on a scale comparable to the area involved in the change. The possible effects include: (a) change in the evaporation from the surface; (b) change in albedo; (c) change in roughness, thereby affecting winds; (d) change in amount of wind-raised particles, thereby affecting the radiation budget and the supply of CCN and IN; and (e) change in the water retention and thus of the runoff rate. The net effect for any particular change and region will be due to a combination of these.

Several examples of regional climatic alterations associated with land-use changes have been reported. Durdik<sup>3 3 1</sup> compared rainfall records in Bohemia for the 2 25-year epochs 1876 to 1900 and 1901 to 1925 and found that the dry regions became drier and the wet regions wetter; he attributed this to deforestation and changes in drainage which occurred at the beginning of the century. Two opposite effects have been claimed for different parts of Argentina. Schwerdtfeger<sup>3 3 2</sup> attributes a 20% increase in precipitation at Rosario to a tripling of the cultivated land area, thereby decreasing runoff and raising the humidity. Farther south, however, Galmarini et al.333 claim that overgrazing by sheep in Patagonia has led to warming and a decrease in precipitation and a reduction in useful pasturage. Fenninger<sup>3 3 4</sup> attributes a decreasing rainfall in the Amazon Basin over the past 15 years to deforestation; he suggests a double effect of decreased evapotranspiration and increased wind-raised CCN. Newell<sup>335</sup> is of the opinion that the change in evapotranspiration which would ensue if a major part of the Amazon Basin were deforested would be large enough to influence the general circulation. It should be noted that, because of the high ratio of leaf area to ground area for many types of vegetation, the evapotranspiration from a vegetated area can exceed that from a free water surface; plants are sometimes "wetter than water."

The problem of verification of climatic effects of land use changes is a difficult one because there is rarely an opportunity to make comparisons with an identical control area to insure that the

observed climatic trend would not have happened anyway. There is no doubt that the local climate will be influenced if any of the parameters enumerated above is altered greatly. The extent to which global climate is affected will be more or less proportional to the area of land involved. The question of positive feedbacks arises, because the alteration of the surface properties may produce local effects on climate which lead to the same kind of alteration of adjacent areas; the spreading of deserts due to overgrazing of marginal lands is often cited as an example. One may question, however, whether the atmospheric properties change, or whether the atmosphere acts as a passive agent in extending the area of altered surface. For example, the conversion of tremendous areas of grass-covered or even artemisia steppe in the high plains of North America from cattle grazing to wheat culture early in this century might be said to have contributed to the drought which created the "dust bowl" of the 1930s by increasing the wind-raised CCN count and thereby decreasing precipitation. On the other hand, it can also be argued that removal of the native grass cover and exposing the bare earth for several months of the year simply permitted the natural wind and runoff to remove the humus and render the land less fertile, and that the drought was due to a secular perturbation in the general circulation which would have occurred in any case. The expansion of desert areas by overgrazing may be considered in the same way. In any case, the local microclimate is altered by any marked change in the surface properties, and it is this local microclimate which controls plant growth, so that great consideration should be given to climatological data before any extensive land-use change is implemented. If the western high plains of North America had never felt the plow, the price of beef might be somewhat lower today and the population of California might be somewhat less because the westward migration of impoverished highplains farmers would not have occurred. On the other hand, it is not possible to attribute any climatic change in North America as a whole to the attempt to cultivate these marginal lands; the effect on a large scale, if any, is lost in the noise.

# PROGRESS IN PROGNOSTIC MODELS OF CLIMATE

An essential goal which must be achieved if

reliable advance warning of climatic change (natural or man-induced) is to be possible is the construction of mathematical models incorporating in as much detail as possible the mechanics, physics, and chemistry of the atmosphere-ocean-land surface system in three dimensions and time. These models must be capable of running at ratios of model time to real time of several thousand to one. This ideal has not been even remotely approached as yet, but the last decade has seen some advance.

Some models, such as those already discussed in connection with the CO<sub>2</sub> and aerosol problems, treat one or two aspects of the total problem in order to get an idea of the magnitude of the effect of varying one or two factors. Sometimes the isolation is geographical, as in Fletcher's 337 treatment of the heat budget of the Arctic basin and its relation to the hemispheric general circulation which was designed to be the basis for further numerical experiments by the Rand Corporation on climatic change, or Joseph's 338 radiativetransfer model involving CO2, water vapor, and clouds which was designed to be embedded in a general circulation model. This model, by itself, required 90 msec of 1966-style computer time to compute a temperature sounding at one geographic point. Manabe and co-workers 339 designed a general circulation model incorporating some radiative-transfer features plus a hydrologic cycle of evaporation and precipitation. After 150 to 180 days of model time, the mean annual precipitation, the radiative fluxes, and the Bowen ratio agreed well with observations, but the model predicted a flux of water vapor from the dry subtropics to the wet tropics as a result of an excessively strong meridional Hadley circulation. A later version<sup>340</sup> resulted in better predictions in lower latitudes.

Mintz et al.<sup>341,342</sup> have developed general circulation models using the so-called primitive equations of atmospheric mechanics which are smoothed so as to allow long-term prognosis. The models allow experiments to be made in which the forcing is altered, e.g., changes in the Arctic ice pack. One shortcoming of these models is that they treated only two levels in the vertical; this was recognized by the developers, who commented that computers having one order of magnitude greater memory and two or three orders of magnitude increase in speed over the 1966 capabilities would be needed to handle a

reasonably complete model. Later workers at the Rand Corporation<sup>343,344</sup> continued to refine these basic models as computer capabilities improved.

Some modelers, such as Saltzman<sup>3 4 5</sup> have attempted to cope with the computer-imposed limitations by using zonally averaged two-dimensional models. Since such models cannot possibly incorporate the variation of the properties of the planetary surface with longitude, they can only be useful as prototypes for future development.

Sellers<sup>346</sup> has experimented with a model which, while three-dimensional, is heavily parameterized and makes use of only one physical equation, namely the first law of thermodynamics averaged over time (one month). The vertical profiles of temperature, wind speed, and water vapor are parameterized as functions of their respective surface values, the pressure, and the poleward temperature gradient. Mean values of quantities such as incoming solar radiation, albedo of land and water surfaces, ratio of land area to water area, etc., are specified for each 10° latitude belt. The main advantage of the model is the high ratio of model to real time; 1 model year uses 18 seconds of time on a CDC-6400 computer. Radiative effects of CO<sub>2</sub>, O<sub>3</sub>, and H<sub>2</sub>O are included in the model, as well as variable aerosol turbidity.

Variations of CO<sub>2</sub> concentration in the model gave rise to smaller surface temperature changes than those forecast by the models discussed in the section of CO<sub>2</sub>; this is probably due to the gray body approximation made in the model. The sensitivity to turbidity changes was more marked; a change in optical thickness from 0.3 to 0.415 reduced the global mean surface temperature from 14.2° to 1.7°C in February and moved the latitudes of 50% snow cover from 52 to 36°N and 62 to 47°S. In August the temperature was dropped from 16.3° to 2.5°C, and the latitude of 50% snow cover was lowered from 70 to 43°N, and 55 to 41°S. A strong dependence of global mean surface temperature on solar constant was also obtained; a 1% decrease lowered the temperature to 8.5°C, while an increase of the same amount raised it to about 18°C. A bistable solution for the mean global temperature at the present value of the solar constant was obtained, depending on whether the solar constant was rising or falling previously; Sellers suggested that the

Pleistocene oscillations might be accounted for by this hysteresis if some perturbation such as increased turbidity due to volcanic dust had taken place.

This model, while heavily parameterized, does incorporate at least one positive feedback loop, namely, the negative correlation between surface temperature and surface albedo over land (due to dependence of snow cover on temperature).

The parameterized quantities in Sellers' model are time-independent. This constraint was removed by Schneider and Gal-Chen<sup>347</sup> in order to determine if fluctuations in time without changes in forcing might be as large as those induced by changing the turbidity or solar constant. They obtained results close to Sellers for changes in the external forcing; when initial conditions of temperature were perturbed without changes in forcing, the model was found to be monostable (i.e., only one stable state) for increases in initial temperature, weakly bistable (two solutions differing by about 0.2°C) for decreases of less than 18°C, and strongly bistable for decreases greater than 18.3°C. With changed parameterization of the temperature-albedo relationship, however, the bistable conditions arose for decreases of only a few tenths of a degree; this illustrates clearly the problems inherent in heavily parameterized models.

Manabe and Holloway<sup>348</sup> coupled the 9-level model with hydrology and radiative transfer with a 5-level ocean model in order to include the heat storage and transport by the sea and the driving force of the wind on the sea. A very smoothed distribution of land and sea was used. Since the time scale of events in the sea is slower than in the atmosphere, the interaction between them was not continuous but intermittent. Even with these simplifications the model was very costly in computer time; I model year for the atmosphere (or 100 model years for the ocean) corresponded to 1200 hours computation time on a Univac 1108.

Effects of the ocean were examined by comparing results of runs with the atmospheric model alone and the combined model. A reduction of sea temperature near the equator reduced the tropical precipitation, while rainfall along the east coasts of continents was increased by the warm currents (model equivalents of the Gulf Stream and Kuroshio).

Washington<sup>349,350</sup> has experimented with

thermal perturbation of a general-circulation model developed at the National Center for Atmospheric Research, to simulate the effects of thermal pollution. When 50 langleys/day were added to the heating function (corresponding to about 100 times the present thermal pollution), little change was found in tropical temperatures, but polar region temperature rose by about 8°C. On the other hand, artificial perturbation of other parameters, such as the wind field, while holding the heat input constant gave rise to perturbations of the same order of magnitude. Prognostic times involved were of the order of 90 days.

Models which include chemical interactions between molecular species, i.e., in which the continuity equations for different species are coupled to each other via reaction rate constants, which in turn are pressure- and temperaturedependent and so are sensitive to transport by the wind field, are an order of magnitude more difficult and demanding of computer time. Until the CIAP demonstrated an urgent need for them, very little attention had been directed toward such modeling, and most of that was one-dimensional (mean vertical profiles of temperature and composition). In these models, a subset of the 130-odd chemical reactions which the modeler believed to be the most significant were combined with parameterizations of atmospheric transport to give a set of first-order differential equations in the time; these were integrated forward to equilibrium (or solved algebraically under the assumption of steady state). Examples of this type have been given by, among others, Chang<sup>351</sup> and Crutzen.<sup>352</sup> Two-dimensional models involving chemistry were developed during CIAP by Hesstvedt, 353 Prinn et al., Rao-Vupputuri, 355 and Widhopf.<sup>3 5 6</sup> One three-dimensional model, or rather, experiment, involving no chemistry as such, but tracing the time history of an inert pollutant released as a point source in the stratosphere, was developed by Mahlman. 357

The ultimate in climatic models would necessarily have to include transport, radiative transfer, chemistry, air-sea interactions, topography and albedo of land surfaces, the hydrologic cycle and clouds, and aerosols as turbidity and as nuclei. It would permit perturbing any of the input parameters, either by transient or permanent changes, and would be capable of prognostic use for hundreds or thousands of model years in a few hours of computer time. Only then

can the effects of human perturbation be compared with the statistical range of natural variability of climate, and the questions raised by Lorenz<sup>3 5 8</sup> about the transitivity or intransitivity. or in the terms of this article, the mono- or multi-stability of the earth-atmosphere system be answered. It is as yet too early to say how closely this ideal can be approached in practice. It would seem that the limits imposed by signal propagation speeds through computers might be the limiting factor in an approach to the ideal. On the other hand, it may turn out that some seemingly crude parameterizations may be accurate enough to permit simplification and great economy of computer time. Much remains to be done before the ultimate limits of climatic modeling will be established.

## DISCUSSION AND SUMMARY

The many investigations which have been discussed or referred to in this article, especially those of the last decade, have reduced considerably the range of uncertainty in the estimates of what man has already done, and can do in the future, to cause climatic changes. The qualitative nature of the various effects and influences are reasonably well understood, and the extreme and sometimes irrational fears of imminent disaster which were expressed in the popular press and news media a few years ago have been shown to be quite unfounded. The gradual increase of carbon dioxide in the atmosphere at a rate of the order of a quarter percent per year has been well established, but no parallel climatic trend, such as a temperature increase, is detectable in the data at any appreciable level of statistical significance. The irreversible removal of oxygen from the atmosphere by combustion has been found to be insignificantly small unless the supply of fossil fuels is vastly larger than presently known reserves.

Man-made aerosols are as yet undetectable on a global basis against the fluctuating natural background due to volcanoes and wind-raised dusts, but are measurable on a regional scale when sensitive techniques are used. These aerosols do cause measurable local losses of solar energy by day, and increased long-wave energy from the sky at night; the result is a reduction in the amplitude of the diurnal march of temperature. The net effect on mean temperature depends on the

optical properties of the particles and the underlying surface. Many of the particles in combustion and industrial aerosols are effective cloud condensation nuclei and ice nuclei, and play a role in modification of clouds on a relatively local scale. The modification induced depends on the prevalent cloud type; precipitation in maritime tropical clouds tends to be reduced by overseeding with cloud condensation nuclei, while continental clouds in middle latitudes are stimulated by more nearly optimal seeding with the ice nuclei of the pollution aerosol. These responses are confined to a circle of diameter of order 200 km or so around a source region, with maximum effects at 20 to 30 km downwind.

Hygroscopic nuclei, such as sulfuric acid droplets, are active as CCN at less than water saturation. The duration and severity of fog in humid cities with heavy aerosol pollution are therefore greater than in clean air.

All of the energy used by man ultimately ends up as heat, to be radiated to interplanetary space. This radiation is in addition to the solar energy absorbed by the earth and atmosphere, which also is returned to space. At present, the sum total of nonsolar (i.e., combustion, geothermal, and nuclear) power is only about one part in 5000 of the mean solar flux absorbed by the planet, and causes an elevation of only about 0.01°C in global mean temperature. Most of the energy release, however, occurs in metropolitan areas, causing "heat islands" with mean temperatures several degrees Celsius above the rural upwind districts. These heat islands enhance convection and vertical mixing of pollutants by day, thereby increasing the frequency and duration of convective showers and thunderstorms in middle latitudes.

Aircraft combustion products differ from most other man-made pollutants in that they are introduced into the atmosphere at various levels well above the atmospheric boundary layer and can therefore appear in locally high concentrations at great heights. Exhaust water vapor frequently produces local supersaturations leading to condensation trails; under certain conditions of relative humidity (supersaturation with respect to ice and nearly saturated with respect to water) these trails will bring about the condensations of much more atmospheric water vapor in artificial cirrus clouds. This occurs most frequently at or slightly below the tropopause. Some slight evidence exists in support of increased cirrus sky cover since 1958, but the increase is not enough to cause an

appreciable loss of solar energy at present. The effect might be of the same order of magnitude as the waste heat influence but of opposite sign. Occasional seeding of lower cloud decks by crystals falling from the clouds may cause small local increases of precipitation.

Exhaust products emitted into the stratosphere by supersonic transports constitute a potential special problem because: (a) there are no washout mechanisms such as cloud and precipitation scavenging operative there, and vertical mixing is slow, hence residence times are long (one year or more); and (b) the presence of a strong flux of solar ultraviolet radiation permits the photochemical formation of exotic and excited molecular species and therefore chemical transformations which do not occur in the lower atmosphere. Ozone produced in this way is an effective shield against a band of solar radiation of about 0.3 µm wavelength which is capable of disrupting the protein molecules of living organisms including man. Oxides of nitrogen formed by combustion have been shown to be effective in catalyzing the reduction of ozone to ordinary oxygen; a relatively small mass of NO, added to the stratosphere could theoretically reduce the ozone layer by 10% or more. On the other hand, considerable quantities of NO, introduced into the stratosphere by nuclear weapons testing produced no statistically significant disturbance of the ozone layer.

Recently it has been shown in the laboratory that certain carbon halides (CF<sub>3</sub>Cl, CF<sub>2</sub>Cl<sub>2</sub>) are dissociated by solar ultraviolet so as to yield atomic chlorine, which can also catalyze the reduction of ozone even more effectively than NO<sub>v</sub>. These compounds (Freons) are the propellants used in spray cans, and are therefore being introduced daily into the lower atmosphere; this discharge has been going on for the past 20 years or so at an ever-increasing rate. It has been suggested that, because of the lag in diffusion of this material to the appropriate altitude (30 km or so), the effects have not been noticed before, but will be more evident in the near future. The ozone records of the past 15 years or so show both upward and downward changes of the same order of magnitude (10%) as that to be expected from present levels of Freon release, so at the present time we can only render the Scotch legal verdict "not proven," which allows a re-examination if new evidence becomes available.

The effects of nuclear weapons testing on

climate and weather are confined almost totally to the local area of firing and a short distance downwind. The aerosols raised by the tests are no more effective as nuclei than natural or other man-made aerosols and the mass of such aerosol is insignificant compared to other sources. The increased ionization of the atmosphere by radioactive aerosol has been observed to increase the conductivity and reduce the strength of the electric field in the atmosphere; if certain theories of the mechanism of thundercloud charging are correct, this could lead to a decrease of lightning frequency, perhaps to zero. The theories involved, however, have never been proved, and have equally viable competitors which would, if correct, preclude the great reduction in lightning unless the radioactivity was well above lethal levels.

If then, we pose the question, "What have we done to our climate?" the answer is, nothing that the great majority of the human race can notice or detect. The global influences of all the pollutant effects enumerated above are lost in the background of unexplained natural fluctuations up to the present time. Only the inhabitants of large metropolitan regions in the highly industrialized countries have the dubious privilege of feeling the climatic effects of pollution in the form of higher temperature, precipitation, and (in some cases) fog frequency than their country cousins experience.

We sincerely hope that any reader who has reached this point and who is in any way influential in setting priorities for government funding of climatic change monitoring and research programs will not stop and leap to the conclusion that these programs have done their jobs and that no further effort is needed. Nothing could be farther from the truth. The most important question remains, "What will we do to the climate in the future?"

It has been pointed out many times in the body of this paper that the time series for many climatic parameters and measures of pollution are far too short to permit the detection and quantitative determination of anthropogenic trends. A much denser network of professionally managed climatological benchmark stations must be established, and several decades of good data acquired, before statistically significant statements can be made about weak trends; strong ones will, of course, be picked up sooner by the existing stations. A sizeable investment in monitoring is therefore mandatory.

Adequate support of modeling research is also essential. We have repeatedly referred to interactions and feedbacks which might either accelerate and amplify or retard and damp out a trend in one or more climatic elements. Speculation about such couplings is an exercise in futility unless it leads eventually to some computer software. The old descriptive climatology, concerned mainly with statistics and verbal interpretation of them, is evolving into a new mathematical, or dynamic, climatology with predictive capability based on physical-mathematical processes rather than extrapolation of statistical measure. None of the models referred to in this article can be considered final and definitive; all are incomplete and more or less primitive. It is to the modelers that we must ultimately turn to get a good early warning system against undesirable climatic trends while there is still time to take some remedial action. The monitoring networks alone are the analog of the canaries that miners took into shafts to warn of rising levels of dangerous pollutant gases; the information may sometimes be too late. On the other hand, the data from the monitoring networks are essential to the refinement of models in a variety of ways; the two activities complement each other.

It is really premature to try to give any authoritative answer to the last question posed. Even if completely trustworthy prognostic models existed, good forecasts could not be made without a set of essential input data, namely, future emission levels of all the pertinent pollutants. These can only be based on extrapolation of current trends.

With the exception of the chlorine-ozone interaction and land-use changes all of the climatic modifications are linked to combustion pollutants. The key to any successful forecast of human impact on global climate is, then, a good forecast of future combustion rates, or, more generally, future energy use.

It was stated in the section on thermal pollution that the annual growth rate of energy use as of 1970 was 5.7%, and that if this rate of growth continued until all of the estimated fossil fuel reserves were consumed, this event would occur in the year 2032. This worst-case situation can be used to set some exceedingly crude estimates of upper and lower bounds on some climatic effects if it is assumed that no feedbacks are involved. Burning of the estimated 3 × 10<sup>6</sup> megatons of carbon reserves would generate 11 × 10<sup>6</sup> mega-

tons of CO<sub>2</sub>. Assuming that the sea and biosphere continue to take up half the combustion product, the atmosphere would contain 5.5 × 10<sup>6</sup> megatons more CO<sub>2</sub> than in 1970, giving a volume mixing ratio in the year 2032 of 1027 ppmv, or a little more than 3 times the current concentration. The biosphere, including man, could probably live with this level of CO<sub>2</sub>. The enhanced greenhouse effect would cause a temperature rise of 3 to 4°C. The waste heat, averaged over the globe, would amount to 0.54% of mean solar energy at the ground. Assuming arbitrarily that half of this is stored in the sea, then the temperature increase from the waste heat would be 0.2°C; this gives a lower bound to the increase of global mean temperature of 3.2°C (it would be greater because the greenhouse effect of the CO2 would act on the waste-heat radiation).

If we assume that all the fuel is burned efficiently so that no carbon aerosol (soot) is released to the atmosphere, the particulate matter would consist of fly ash and sulfate aerosol from gas-to-particle conversions. Such particles would absorb little solar radiation, and so would have a cooling effect. Assuming Mitchell's estimate of 2 megatons of anthropogenic aerosol in 1970 to be correct, and assuming that the aerosol production has the same annual growth rate as the energy use (a conservative assumption because much of the fuel would be high sulfur coal), the particulate load in 2032 would be about 67 megatons, or 1314 g/ha averaged over the globe. The resultant cooling, using the simple Barrett model described earlier, is 13°C; this would be slightly offset by an enhanced greenhouse effect of the aerosol.

It thus appears that, at some point in the relatively near future, the thermal effect of the aerosol should begin to overcompensate for the effects of waste heat and CO<sub>2</sub>. This conclusion, however, rests on the accuracy of Goldberg's estimate of 20 megatons/year for the aerosol production rate and Mitchell's estimate of 2 megatons as the current burden, both in 1970. The resultant mean residence time of 0.1 year for the aerosol is a sensitive parameter in the foregoing calculation.

It is of some comfort then to note that even at this extremely unrealistic rate of use of fossil fuel, the influence on global climate would be relatively small; it is conceivable that the opposite effects of  $CO_2$  and waste heat and of particulate pollution might come close to canceling each other.

Perhaps the most important conclusion to be

drawn from the foregoing analysis is a nonclimatological one; namely, that if the estimate of fuel reserves equivalent to 3 × 10<sup>6</sup> megatons of carbon is even roughly correct, then the current growth rate in energy use of 5.7% annually must cease within a very few years. Even if the growth rate dropped to 1% annually after 1970, the fuel would be exhausted in 190 years; if all growth had stopped in 1970 the time would be extended to 571 years. If the current growth rate is not checked, the time frame will be too short for the climatic effects to become important at all in comparison with the energy crisis.

The importance of improvements in modeling is also brought out by the foregoing analysis. The assumption that half the combustion CO<sub>2</sub> enters the sea regardless of the combustion rate is certainly incorrect, so that the CO<sub>2</sub> concentration and warming would probably be greater than given above.

If the rate of growth of energy use can be checked, then the need for monitoring and better modeling becomes more critical because the time for inadvertent modification to produce climatic change is lengthened. It will be very important to know whether net warming or cooling is the direct result of combustion pollutants. The feedbacks involving cloud modification and circulation changes must be coupled in, since they may turn out to be overriding in importance.

In the event that a "clean" noncombustion energy source such as hydrogen fusion or even total conversion of matter to usable energy is developed, then as was shown in an earlier section, inadvertent climate modification by waste heat will be the factor which will set the ultimate limits to annual energy use. This qualitative statement is a consequence of the law of radiative heat transfer and is beyond question; there exists a Malthusian limit to the product of energy use per capita times population which cannot be circumvented by any human ingenuity. The magnitude of this maximum energy use will be determined by how great a rise in global mean temperature can be tolerated without unacceptable ecological and socialpolitical consequences. Although concern over possible new ice ages would disappear, the loss of much low-lying land containing some of the largest and most important cities by a rise of 100 m or more in sea level would create severe social and economic stresses even though the melting of the ice would take place slowly and allow time for relocation.

If we assume that the estimated mean midlatitude temperature of about 21°C which prevailed at the climatic optimum of the Eocene, some 50 million years ago, represents an upper bound to what is ecologically acceptable, as compared to 10°C at present, then the corresponding rise of about 6°C in global mean temperature (keeping the tropical belt at the same temperature as at present) will be achieved when human energy use rises to about 8.6 W/m<sup>2</sup> averaged over the earth, or about 500 times the current demand. This rough estimate might have to be revised upward or downward; the upper bound to temperature would be determined by the tolerances of staple food plants and animals.

This, of course, brings up the question: What is the optimum global climatic regime? Half of man's period of existence as a species has been spent in an ice age which is still continuing, and the entire period during which man has been able to communicate in any meaningful way across time to his descendants has elapsed during a warm peak (one of ten or so) of this ice age. There is no good reason to believe that the cycles of more and less ice cover will not recur. A disinterested visitor from another planet would almost certainly conclude that, if energy were available for intentional modification of global climate, the shift should be away from these unexplainable but recurrent climatic oscillations and to a stable regime in which the race could be comfortable and settled for millions of years. On the other hand, civilized man has adapted to conditions as they are, and might therefore be understandably reluctant to initiate global changes whose ultimate ecological consequences cannot be forecast.

The 8.6 W/m<sup>2</sup> which was given above as an estimate of the tolerable upper bound to energy use is only about 8.6% of the solar radiation absorbed by the planet. It might seem that both the fuel exhaustion problem and the waste heat problem could be solved if a few percent of the solar power could be channeled into forms usable by man. This is feasible to a certain extent, but the amount of energy obtainable in this way is limited by practical restrictions and by a risk of inadvertent climate modification as well. It is often overlooked by proponents of solar energy utilization that a sizeable fraction of that energy is already doing things; namely, providing the driving power for photosynthesis and hence all animal body energy, and also the much heavier job of

driving the circulations of the atmosphere and oceans. The only practical means so far of diverting solar power for human use on a large scale is by the use of thin glasshouses with very low inside albedo and a grid of tubes through which a heat storage fluid, usually water, can circulate to transfer the heat to a reservoir. Collection of large amounts of power in this way requires covering a large land area with such glasshouses. Every square meter thus covered is withdrawn from photosynthetic production, so the power is collected at the expense of some food and fiber unless the collectors are placed only on barren land. The area of the earth available for collectors on a large scale is then practically restricted to the large subtropical desert areas of the continents; something over 90% of the total solar power is therefore unavailable for diversion.

The energy obtained by these collectors is very low grade; the maximum temperature is the boiling point of water. Most needs of industry and transportation require energy at a much higher potential. Photovoltaic cells can convert solar to (dc) electric power, but at rather low efficiency. Solar powered Carnot-cycle engines can be built, but the gigantic arrays of steerable mirrors that are required pose some severe engineering problems. Storage of megajoules of energy in any form for use when the sun is below the horizon also requires much space (though this could be underground) and considerable ingenuity to prevent radiative and convective losses.

Covering of thousands of square kilometers with highly efficient solar power collectors and transferring the energy for final release elsewhere would necessarily cause climatic change. The heat flux which would normally take place from the heated sand of the subtropical deserts to the atmosphere by convection would not take place, and this heat would finally be delivered to the atmosphere in the middle latitudes. A weakening of the lower latitude side of the westerly wind belt would follow; the subtropical jet stream would become less intense while the polar jet would strengthen. Marked alterations in storm tracks and precipitation patterns would surely ensue.

None of the foregoing should be interpreted as opposition to the use of solar power for the things that it can do. It seems eminently feasible that the roofs of buildings, which are waste space otherwise, should be covered with solar power collectors to provide as much of the buildings' interior

temperature regulation (both heating and cooling) as possible. But it is unlikely that any major fraction of man's energy needs for industry and transportation can be met by solar power.

The only possible major pollutant not derived from combustion, at least so far, is the chlorine which may be generated by chlorofluoromethane photolysis. Its effect on the ozone layer, while not proved by direct evidence, is demonstrable theoretically. The key question here is, how important really is the shielding effect of the ozone layer to the biosphere? As far as direct impact on man is concerned, the overall effect would be small. The skin cancer increase would affect only the white race, which is a planetary minority, and would be borne most heavily by a sub-group of that race; namely, the nontanning, light-skinned, red- or sandy-haired Celts or Scandinavians. Prophylactic measures for sensitive people are available in the form of suntan lotions, so that with a little inconvenience the skin cancer hazard need not materialize. Widespread damage to the plant kingdom is a much more serious possibility; research on this matter is, and should continue to be, of very high priority. Until CIAP sponsored biological studies were initiated, virtually nothing was known about ultraviolet tolerance of the earth's flora; not enough time has vet passed to bring these studies to statistically significant conclusions. It should be noted that potentially beneficial effects of increased UV flux are just as valid a subject for speculation as detrimental ones; the former include enhanced vitamin D production and destruction of airborne pathogenic bacteria and viruses. Although the

consensus of those members of the life sciences community concerned with CIAP is that the net effect of an ozone decrease would be detrimental (Reference 21, Appendix G), this conclusion rests more on speculation than on a solid data base, and may be subject to future revision.

Until the true hazards are known, a close watch must be kept on the ozone layer. Also, accurate measurements of atomic chlorine and chlorine oxides in the stratosphere must be made, and research into possible sinks, either physical, chemical or biological, of these carbon halides at the ground must be extended.

We conclude by saying that, while man has not made any noticeable impact on climate except in and near his metropolitan areas, the potentials do exist when existing rates of growth are extrapolated for relatively short periods into the future. Monitoring programs and modeling research in climatic change should be expanded; they should be regarded as an important aspect of national defense, or, more accurately, of defense of the entire planet against a common threat. Even if human impacts are found to be small, the knowledge gained may be very significant. Until the reasons for those enigmatic oscillations in glaciation during the last million years are firmly and quantitatively established, physical climatology has a large piece of unfinished business on hand. If a dependable monitoring network is functioning when and if the next downward oscillation starts, the mechanism may become clear in time to permit countermeasures, in the form of intentional climate modification efforts, to be taken.

#### ARTICLES REVIEWED

Bolin, B., Carbon cycle, Sci. Am., 223, 124, 1970.

Brooks, C. E. P., Geological and historical aspects of climatic change, in *Compendium of Meteorology*, Malone, T. F., Ed., American Meteorological Society, Boston, 1951, p. 1004.

Bryson, R. A., Perspective on climatic change, Science, 184, 753, 1974.

Bundy, McG., Charting the complexities, Sat. Rev., 53, 56, 1970.

Flohn, H., Globale Energiebilanz und Klimaschwankungen, Bonner Meteorol. Abhdlg., 19 (Sonderheft), 76, 1973.

Flohn, H., Naturliche und anthropogene Klimamodification, Ann. Meteorol., 6, 59, 1973.

Federov, E. K., Interaction of man and the environment, Bull. At. Sci., 28, 5, 1972.

Frisken, W. R., 1971, Extended industrial revolution and climate change, Eos, 52, 500, 1971.

Frisken, W. R., Atmospheric Environment, Johns Hopkins University Press, Baltimore, 1974.

Gates, D., Weather modification in the service of mankind; promise or peril?, in Environmental Crisis: Man's Struggle to Live with Himself, Helfrich, H. W., Jr., Ed., Yale University Press, New Haven, Conn., 1970, p. 33.

Joint Organizing Committee, Global Atmospheric Research Programme, The Physical Basis of Climate and Climate Modelling, GARP Publications Series No. 16, World Meteorological Organization, Geneva, 1975.

Kondratyev, K. YA., Vasiliev, O. V., Ivlev, L. S. Nikolskii, G. A., and Smokty, O. I., Vlienye Aerosolya na Perenos Islyudienya vosmochenye Klimaticheski Poslecdstviya (Influence of Aerosol on Radiation Transfer: Possible Climatic Consequences), Leningrad University Press, Leningrad, 1973.

Landsberg, H. E., Climate, man, and some world problems, Scientia, 102, 1, 1967.

Landsberg, H. E., Man-made climatic changes, Science, 170, 1265, 1970.

Landsberg, H. E., Man-made climatic changes, Pt. 1, The Environment This Month, 1, 54, 1972.

Landsberg, H., Inadvertent atmospheric modification through urbanization, in Weather and Climate Modification, Hess, W. N., Ed., John Wiley & Sons, New York, 1974, p. 726.

Lodge, J. P., Jr., An atmospheric scientist views environmental pollution, Bull. Am. Meterol. Soc., 50, 530, 1969.

MacDonald, G. J. F., Pollution, weather, and climate, in *Environment: Resources, Pollution, and Society*, Murdoch, W. S., Ed., Sinauer Associates, Stamford, Conn., 1971, p. 326.

MacDonald, G. J. F., Modification of Planet Earth by Man, Technol. Rev., 71, 26, 1969.

Machta, L. and Telegadas, K., Inadvertent large-scale weather modification, in Weather and Climate Modification, Hess, W. N., Ed., John Wiley & Sons, New York, 1974.

Matthews, W. H., Kellogg, W. W., and Robinson, G. D., Eds., Man's Impact on the Climate, MIT Press, Cambridge, Mass., 1971.

Mitchell, J. M., Jr., 1s man's industry upsetting world weather? ESSA World, 3, 4, 1968.

National Research Council, Committee on Atmospheric Sciences, Weather and Climate Modification, National Academy of Sciences, Washington, D.C., 1973.

Newell, R. E., Global circulation of atmospheric pollutants, Sci. Am., 224, 32, 1971.

Roberts, W. O., Inadvertent weather modification, in A Century of Weather Progress, Caskey, J. E., Ed., American Meteorological Society, Boston, 1970, p. 165.

Sawyer, J. S., Possible effects of human activity on world climate, Weather, 26, 251, 1971.

Schaefer, V. J., Inadvertent modification of the atmosphere by air pollution, Bull. Am. Meteorol. Soc., 50, 199, 1969.

Sewell, W. R. D., Ed., Modifying the Weather: A Social Assessment, University of Victoria, Victoria, B.C., 1973.

Shapley, H., Climatic Change, Harvard University Press, Cambridge, Mass., 1953.

Singer, S. F., Global Effects of Environmental Pollution, Springer-Verlag, New York, 1970.

Smagorinsky, J., Global atmospheric modeling and the numerical simulation of climate, in Weather and Climate Modification, Hess, W. N., Ed., John Wiley & Sons, New York, 1974, p. 633.

Voeikov, A. I., Vozdeistvie Cheloveka na Prirodu (The Influence of Man on Nature,) Gos. 1zdat., Moscow, 1949.

Wilson, C. L., Ed., Man's Impact on the Global Environment, Study of Critical Environmental Problems, MIT Press, Cambridge, Mass., 1970.

Wilson, C. L., Ed., Report of the Study of Man's Impact on the Climate: Inadvertent Climate Modification, MIT Press, Cambridge, Mass., 1971.

# REFERENCES

- 1. Fox, R. L., New Mauna Loa Observatory unit, Nature, 178, 1272, 1956.
- 2. Fox, R. L., Mauna Loa Observatory, Weatherwise, 9, 147, 1956.
- 3. Fox, R. L., Mauna Loa Observatory, J. Wash. Acad. Sci., 46, 310, 1956.
- 4. Fox, R. L., Mauna Loa Observatory, Bull. Am. Meteorol. Soc., 37, 487, 1956.
- 5. Singer, S. F., Global Effects of Environmental Pollution, Springer-Verlag, New York, 1970.
- 6. Wilson, C. L., Ed., Man's Impact on the Global Environment, Study of Critical Environmental Problems (SCEP), MIT Press, Cambridge, Mass., 1970.
- 7. Wilson, C. L., Ed., Study of Man's Impact on Climate (SMIC), Inadvertent Climate Modification, MIT Press, Cambridge, Mass., 1971.
- 8. Anon., Brief Survey of the Activities of the World Meteorological Organization Relating to Human Environment, World Meteorological Organization, Geneva, 1970.
- 9. Roberts, W. O., Benchmark stations for the measurement of presently-missing parameters, *Meteorol. Monogr.*, 11, 412, 1970.

- 10. Robinson, G. D., Global environment monitoring, Technol. Rev., 73, 18, 1971.
- Anon., Global Environmental Monitoring, International Council of Scientific Unions, Commission on Monitoring, Stockholm, 1972.
- U.S. President's Council on Environmental Quality, Man's inadvertent modification of weather and climate, Bull. Am. Meteorol. Soc., 51, 1043, 1970.
- 13. Price, S. and Pales, J. C., The Mauna Loa High-Altitude Observatory, Mon. Weather Rev., 87, 1, 1959.
- 14. Machta, L., Mauna Loa and global trends in air quality, Bull. Am. Meteorol. Soc., 53, 402, 1972.
- 15. Purrett, L. A., Analyzing the atmosphere, Sci. News, 102, 60, 1972.
- 16. Pack, D. A., personal communication, 1975.
- 17. Komhyr, W. D., personal communication, 1975.
- 18. Changnon, S. A., Huff, F. A., and Semonin, R. G., METROMEX, an investigation of inadvertent weather modification, Bull. Am. Meteorol. Soc., 52, 958, 1971.
- 19. U.S. Office of Supersonic Transport Development, Supersonic transport development: environmental impact statement, United States Department of Transportation, Washington, D.C. (available from National Technical Information Service, Springfield, Virginia 22151), 1970.
- 20. Cannon, R. H., Jr., Planning a program for assessing the possibility that SST aircraft might modify climate, Bull. Am. Meteorol. Soc., 52, 836, 1971.
- 21. Grobecker, A. J., Coroniti, S. C., and Cannon, R. H., Jr., Report of findings: the effects of stratospheric pollution by aircraft, U.S. Department of Transportation, CIAP, Office of the Secretary of Transportation, Washington, D. C. 20590 (available from NTIS, Springfield, Virginia 22151), 1974.
- 22. Simpson, G. C., Past climates, Mem. Manchester Lit. Phil. Soc., 74, 1, 1929.
- 23. Oepik, E. J., Climatic change in cosmic perspective, Icarus, 4, 289, 1965.
- 24. Hoyle, F. and Littleton, R. A., The effect of interstellar matter on climatic variation, *Proc. Cambridge Phil. Soc.*, 35, 405, 1939.
- 25. Milankovich, M., Mathematische Klimalehre und astronomische Theorie der Klimaschwankungen, in Handbuch der Klimatologie, 1, Part A, Koeppen, W. and Geiger, R., Eds., Gebr. Borntraeger, Berlin, 1930, p. 1.
- 26. Arrhenius, S., On the influence of carbonic acid in the air upon the temperature of the ground, London, Edinburgh, and Dublin Phil. Mag., 5th Series, 41, 237, 1896.
- 27. Arrhenius, S., Ueber die Waermeabsorption durch Kohlensaeure und ihren Einfluss auf die Temperatur der Erdoberflaeche, Svenska Vetenskapsakad. Förhandlingar, 58, 25, 1901.
- 28. Chamberlin, T. C., A group of hypotheses bearing on climatic changes, J. Geol., 5, 653, 1897.
- 29. Chamberlin, T. C., The influence of great epochs of limestone formation upon the composition of the atmosphere, J. Geol., 6, 609, 1898.
- 30. Chamberlin, T. C., An attempt to frame a working hypothesis of the cause of glacial periods on an atmospheric basis, J. Geol., 7, 545, 1899.
- 31. Humphreys, W. J., Volcanic Dust and other factors in the production of climatic changes, and their possible relation to ice ages, Bull. Mt. Weather Obs., 6, 1, 1913.
- 32. Wexler, H., On the effects of volcanic dust on insolation and weather (I), Bull. Am. Meteorol. Soc., 32, 10, 1951.
- 33. Anon. (Rhode Island University), Volcanic eruptions; stronger than nuclear blasts? Can they change our climate? *Maritimes*, 18, 1, 1974.
- 34. Brooks, C. E. P., Geological and historical aspects of climatic change, in *Compendium of Meteorology*, Malone, T. F., Ed., American Meteorological Society, Boston, 1951, p. 1004.
- 35. Budyko, M. I., O termicheskoi zonal'nosti Zemli (Thermal zonality of the Earth), Meteorol. Gidrol., 11, 7, 1961.
- Budyko, M. I., Future climate, Eos, 53, 868, 1972.
- 37. Budy ko, M. I., Stability of the climate of our age, *Idôjárás*, 76, 9, 1972.
- 38. Ewing, M. and Donn, W. L., A theory of ice ages, Science, 123, 1061, 1956.
- 39. Ewing, M. and Donn, W. L., A theory of ice ages. Pt. 2, Science, 127, 1159, 1958.
- 40. Donn, W. L. and Ewing, M., Theory of ice ages. Pt. 3, Science, 152, 1706, 1966.
- Wilson, A. T., Variation in solar insolation to the south polar region as a trigger which induces instability in the Antarctic ice sheet, Nature, 210, 477, 1966.
- 42. Mitchell, J. M., Jr., Changes of mean temperature since 1870, Ann. N.Y. Acad. Sci., 95, 235, 1961.
- 43. Budyko, M. I., Climate and Life, International Geophysics Series, Vol. 18, Academic Press, New York, 1974, p. 294.
- Morgan, G. M., and Allee, P. A., The production of potential ice nuclei by gasoline engines, J. Appl. Meteorol., 7, 241, 1968.
- 45. Anon., Bibliography on carbon dioxide in the atmosphere, 1764-1951, Meteorol. Abstr. and Bibl., 3, 138, 1952.
- 46. Trabert, W., Absorption und diffuse Reflexion der Atmosphaere, Meteorol. Z., 11, 236, 1894.
- 47. Callendar, G. S., The artificial production of carbon dioxide and its influence on temperature, Q. J. R. Meteorol. Soc., 64, 223, 1938.
- 48. Callendar, G. S., Variation of the amount of CO<sub>2</sub> in various air currents, Q. J. R. Meteorol. Soc., 66, 395, 1940.
- 49. Callendar, G. S., The composition of the atmosphere through the ages, Meteorol. Mag., 74, 33, 1939.
- 50. Buch, K., Beobachtungen ucber das Kohlensaeuregleichgewicht und ueber den Kohlensaeureaustausch zwischen Atmosphaere und Meer im Nordatlantischen Ozean, Abo Akademi, Acta Math. Phys., 11, 1, 1939.

80

- 51. Buch, K., Kolsyra och klimat, Tek. Tidskr., 81, 17, 1951.
- 52. Fonselius, S., Koroleff, F., and Warme, K-E., Carbon dioxide in the atmosphere, Tellus, 8, 176, 1956.
- 53. Eriksson, E. and Welander, P., On a mathematical model of the carbon cycle in nature, Tellus, 8, 155, 1956.
- 54. Plass, G. N., The carbon dioxide theory of climatic change, Tellus, 8, 140, 1956.
- 55. Plass, G. N., Effect of carbon dioxide variations on climate, Am. J. Phys., 24, 376, 1956.
- 56. Suess, H. E., Radiocarbon concentration in modern wood, Science, 122, 416, 1955.
- 57. Callendar, G. S., On the amount of carbon dioxide in the atmosphere, Tellus, 10, 243, 1958.
- 58. Schloesing, J. J. T., Sur la constance de la proportion d'acide carbonique dans l'air, C.R. Acad. Sci., 90, 1410, 1880.
- 59. Harden, H., Atmospheric and oceanic carbon dioxide, Nature, 71, 283, 1905.
- 60. **Krogh, A.,** On the tension of carbonic acid in natural waters, and especially in the sea, Kommissionen for Ledelsen af de geologiske og geographiske Undersφgelser in Grφnland, Meddelelser om Grφnland, 26, 333, 1904.
- 61. Hann, J., Der Ozean als Regulator des Kohlensaeuregehaltes der Atmosphaere, Meteorol. Z., 22, 89, 1905.
- 62. Brodie, J. W. and Burling, R. W., Age determinations of southern ocean waters, Nature, 181, 107, 1958.
- 63. Bien, G. S., Rakestraw, N. W., and Suess, H. E., Radiocarbon dating in the Pacific and Indian Oceans and its relation to deep water movements, *Limnol. Oceanogr.*, 10 (supplement), R25, 1965.
- 64. Craig, H., The natural distribution of radiocarbon and the exchange time of carbon dioxide between atmosphere and sea, Tellus, 9, 1, 1957.
- 65. Rafter, T. A. and Fergusson, G. J., Recent increase in the C<sup>14</sup> content of the atmosphere, biosphere, and surface waters of the oceans, N. Z. J. Sci. Technol., Sect. B, 38, 871, 1957.
- 66. Haxel, O., Der Kohlenstoff-14 in der Natur, Naturwiss. Rundsch., 15, 133, 1962.
- 67. Koczy, F. and Szabo, B., Renewal time of bottom water in the Pacific and Indian oceans, J. Oceanogr. Soc. Japan, 20th anniversary volume, 590, 1962.
- 68. Revelle, R. and Suess, H. E., Carbon dioxide exchange between atmosphere and oceans and the question of an increase in atmospheric CO, during the past decades, *Tellus*, 9, 18, 1957.
- Suess, H. E., Residence time of CO<sub>2</sub> in the atmosphere from C<sup>14</sup> measurements, in Proceedings of the Conference on Recent Research in Climatology, University of California, Scripps Institute of Oceanography, La Jolla, California, 1957, p. 50.
- 70. Suess, H. E., 1961, Fuel residuals and climate, Bull. At. Sci., 17, 374, 1961.
- 71. Keeling, C. D., Rakestraw, N. W., and Waterman, L. S., Carbon dioxide in surface waters of the Pacific Ocean, Pt. 1, Measurements of the distribution, J. Geophys. Res., 70, 6087, 1965.
- 72. Waterman, L. S., Carbon dioxide in the surface waters, Nature, 205, 1099, 1965.
- 73. Kelley, J. J., Jr., Carbon dioxide in the surface waters of the North Atlantic Ocean and the Barents and Kara Seas, Limnol. Oceanogr., 15, 80, 1970.
- 74. Kelley, J. J., Jr. and Hood, D. W., Carbon dioxide in the Pacific Ocean and Bering Sea; upwelling and mixing, J. Geophys. Res., 76, 745, 1971.
- 75. Kelley, J. J., Jr. and Hood, D. W., Carbon dioxide in the surface water of the ice-covered Bering Sea, *Nature*, 229, 37, 1971.
- 76. Liakhin, lu. I., Obmen CO<sub>2</sub> mezhdu okeanom i atmosferoi v iugo-vostochnoi Atlantike (CO<sub>2</sub> exchange between ocean and atmosphere in the southeast Atlantic), Okeanologiia, 11, 48, 1971.
- 77. Kanwisher, J., Effect of wind on CO<sub>2</sub> exchange across the sea surface, J. Geophys. Res., 68, 3921, 1963.
- 78. Sugiura, Y., Ibert, E. R., and Hood, D. W., Mass transfer of carbon dioxide across sea surfaces, J. Mar. Res., 21, 11, 1963.
- 79. Keeling, C. D., Carbon dioxide in surface waters in the Pacific Ocean, Pt. 2, Calculation of the exchange with the atmosphere, J. Geophys. Res., 70, 6099, 1965.
- 80. Dingle, A. N., The carbon dioxide exchange between the North Atlantic Ocean and the atmosphere. *Tellus*, 6, 343, 1954.
- 81. Alekin, O. A. and Moricheva, N. P., K vorposu o roli organizmov privydelenii karbonatov iz prirodnykh vod (The role of organisms in the isolations of carbonates from natural waters), Gidrokhim. Materi., 34, 95, 1961.
- 82. Eriksson, E., Possible fluctuations in atmospheric carbon dioxide due to changes in the properties of the sea, J. Geophys. Res., 68, 3871, 1963.
- 83. Berger, R. and Libby, W. F., Equilibration of atmospheric carbon dioxide with sea water: possible enzymatic control of the rate, Science, 164, 1395, 1969.
- 84. Bolin, B. and Eriksson, E., Changes in the carbon dioxide content of the atmosphere and sea due to fossil fuel combustion, in *The Atmosphere and the Sea in Motion*, Bolin, B., Ed., Rockefeller Institute Press, New York, 1959, p. 130.
- Brannon, H. R., Jr., Daugherty, A. C., Perry, D., Whitaker, W. W., and Williams, M., Radiocarbon evidence on the dilution of atmospheric and oceanic carbon by carbon from fossil fuels, Trans. Am. Geophys. Union, 38, 643, 1957.
- 86. Callendar, G. S., Effect of fuel combustion on the amount of carbon dioxide in the atmosphere. *Tellus*, 9, 421, 1957.
- 87. Bolin, B., On the exchange of carbon dioxide between the atmosphere and the sea, Tellus, 12, 274, 1960.
- 88. Smith, V. N., A recording infrared analyser, Instruments, 26, 225, 1953.
- 89. Bischof, W., Periodical variations of the atmospheric CO<sub>2</sub> content in Scandinavia, Tellus, 12, 216, 1960.

- 90. Keeling, C. D., The concentration and isotopic abundance of carbon dioxide in the atmosphere, *Tellus*, 12, 200, 1960.
- Kelley, J. J., Jr., Analysis of carbon dioxide in the Arctic atmosphere at Point Barrow, Alaska, 1961-1963, Tech. Rep., Contract Nonr 477(25) NR307-252, Dept. of Meteorology and Climatology, University of Washington, Scattle, 1964, p.1.
- Kelley, J. J., Jr., Analysis of carbon dioxide in the atmosphere at Barrow, Alaska during 1961-1962-1963, Tech. Rep. Contract Nonr 477(24) NR307-252, No. 2, University of Washington, Seattle, 1966, p. 1.
- 93. Bischof, W., Variations in concentration of carbon dioxide in the free atmosphere, Tellus, 14, 87, 1962.
- 94. Bischof, W. and Bolin, B., Space and time variations of the CO<sub>2</sub> content of the troposphere and lower stratosphere, *Tellus*, 18, 155, 1966.
- 95. Bischof, W., Carbon dioxide measurements from aircraft, Tellus, 22, 545, 1970.
- 96. Bolin, B. and Bischof, W., Variations of the carbon dioxide content of the atmosphere in the northern hemisphere. *Tellus*, 22, 431, 1970.
- 97. De Maio, A., Moretti, M., and Sansorre, E., Considerazioni e resultati delle misure di CO<sub>2</sub> atmosferico eseguite in alcune località Italiane negli anni 1954, 1965, e 1966, in *Scientific Report*, Il ASR 31, Istituto di Fisica dell'Atmosfera, Rome, 1970, p. 1.
- 98. Keeling, C. D., The concentration and isotopic abundances of atmospheric carbon dioxide in rural areas, Geochim. Cosmocliim. Acta, 13, 322, 1958.
- 99. Fonselius, S. and Warme, K.-E., A method to make standard CO<sub>2</sub> samples for infrared gas analysis and the operation of an IRGA analyzer for air samples from the Scandinavian network, *Tellus*, 12, 227, 1960.
- 100. Callendar, G. S., Can carbon dioxide influence climate? Weather, 4, 310, 1949.
- 101. Kramer, C., Nogmaals; het koolzuurgas in de atmosfeer en het klimaat, Hemel en Dampkring, 48, 189, 1950.
- 102. Slocum, G., Has the amount of carbon dioxide in the atmosphere changed significantly since the beginning of the twentieth century? Mon. Weather Rev., 83, 225, 1955.
- 103. Bray, J. R., An analysis of the possible recent change in atmospheric carbon dioxide concentration, Tellus, 11, 220, 1959.
- 104. Brown, C. W. and Keeling, C. D., Concentration of atmospheric carbon dioxide in Antarctica, J. Geophys. Res., 70, 6077, 1965.
- 105. Kelley, J. J., Jr., An analysis of carbon dioxide in the arctic atmosphere near Barrow, Alaska, 1961-1967, Report No. NR307-252, Department of Meteorology and Climatology, University of Washington, Seattle, 1969, p. 1.
- 106. Bischof, W., Carbon dioxide concentration in the upper troposphere and lower stratosphere, 111, Tellus, 25, 305, 1973.
- 107. Kanwisher, J., pCO<sub>2</sub> in seawater and its effect on the movement of CO<sub>2</sub> in nature, Tellus, 12, 209, 1960.
- 108. Tyndall, J., On radiation through the Earth's atmosphere, Phil. Mag., Ser. 4, 25, 1863.
- 109. Revelle, R., Probable future increase in atmospheric carbon dioxide: kinds of monitoring for prediction, in *Man's Impact on the Climate*, Matthews, W. H., Kellogg, W. W., and Robinson, G. D., Eds., MIT Press, Cambridge, Mass., 1971, p. 281.
- 110. Machta, L., The role of the ocean and the biosphere in the carbon dioxide cycle, paper presented at the Nobel Symposium No. 20, Gothenburg, Sweden, 16-20 August, 1971.
- 111. Telegadas, K., The seasonal atmospheric distribution and inventories of excess C<sup>1,4</sup> from March 1955 to July 1969, in *Report HASL--243*, U.S. Atomic Energy Commission, Washington, D.C., 1971, p. 1.
- 112. Cramer, J. and Myers, A. L., Rate of increase of atmospheric carbon dioxide, Atmos. Environ., 6, 563, 1972.
- 113. Keeling, C. D., Carbon dioxide cycle: reservoir models to depict the exchange of atmospheric carbon dioxide with the oceans and land plants, in *Chemistry of the Lower Atmosphere*, Rasool, S. 1., Ed., Plenum Press, New York, 1973, p. 251.
- 114. Bolin, B. and Keeling, C. D., Large-scale atmospheric mixing as deduced from the seasonal and meridional variations of carbon dioxide, J. Geophys. Res., 68, 3899, 1963.
- 115. Lieth, H., Role of vegetation in the carbon dioxide content of the atmosphere, J. Geophys. Res., 68, 3887, 1963.
- 116. Pearman, G. I. and Garratt, J. R., Global aspects of carbon dioxide, Search, 3, 67, 1972.
- 117. Kaplan, L. D., The influence of carbon dioxide variations on the atmospheric heat balance, Tellus, 12, 204, 1960.
- 118. Plass, G. N., (comment on) Lewis D. Kaplan: Influence of carbon dioxide on the atmospheric heat balance, and (reply by) Kaplan, *Tellus*, 13, 296, 1961.
- 119. Moller, F., On the influence of changes in the CO<sub>2</sub> concentration in air on the radiation balance of the Earth's surface and on the climate, J. Geophys. Res., 68, 3877, 1963.
- 120. Elsasser, W. M. and Culbertson, M. F., Atmospheric radiation tables, Meteorol. Monogr., 4, 1, 1960.
- 121. Plass, G. N., (comments on) Fritz Möller: On the influence of changes in the CO<sub>2</sub> concentration in air on the radiation balance of the Earth's surface and on the climate and (reply by) Möller, J. Geophys. Res., 69, 1663, 1964.
- 122. Manabe, S. and Wetherald, R. T., Thermal equilibrium of the atmosphere with a given distribution of relative humidity, J. Atmos. Sci., 24, 241, 1967.
- 123. Newell, R. E. and Dopplick, T. G., Effect of changing CO<sub>2</sub> concentration on radiative heating rates, J. Appl. Meteorol., 9, 958, 1970.
- 124. Newell, R. E., Herman, G. F., Dopplick, T. G., and Boer, G. J., Effect of changing CO<sub>2</sub> concentration on radiative heating rates: turther comments, J. Appl. Meteorol., 11, 864, 1972.

- 125. Gebhardt, R., On the significance of the shortwave CO<sub>2</sub> absorption in investigations concerning the CO<sub>2</sub> theory of climatic change, Arch. Meteorol. Geophys. Bioklimatol. Ser. B, 15, 52, 1967.
- Ferland, R. E. and Howell, J. R., Water vapor, CO<sub>2</sub>, and particulate effects on the atmospheric temperature profile, in, *Proc. Heat Transfer and Fluid Mechanics Inst.*, San Fernando Valley State College, June 14-16, 1972, Landis, R. B. and Hordemann, L. J., Eds., Stanford University Press, Stanford, Ca, 1972, p. 146.
- 127. Pales, J. C. and Keeling, C. D., Concentration of atmospheric carbon dioxide in Hawaii, J. Geophys. Res., 70, 6053, 1965.
- 128. Johnson, F. S., Oxygen and carbon dioxide balance in the Earth's atmosphere, in Global Effects of Environmental Pollution, Singer, S. F., Ed., Springer-Verlag, New York, 1970, p. 4.
- 129. Sisler, F. D., Impact of land and sea pollution on the chemical stability of the atmosphere, in Global Effects of Environmental Pollution, Singer, S. F., Ed., Springer-Verlag, New York, 1970, p. 12.
- 130. Machta, L. and Hughes, E., 1970, Atmospheric oxygen in 1967 to 1970, Science, 168, 1582, 1970.
- 131. Davitaya, .F. F., Izmeneniye gazovogo sostava atmosfery i problemy biosfery (changing gas composition of the atmosphere and problems of the biosphere), Akad. Nauk SSSR, Moscow, Izvestiya, Ser. Geogr., 3, 22, 1972.
- 132. Walker, J. C. G., Stability of atmospheric oxygen, Am. J. Sci., 274, 193, 1974.
- 133. Berkner, L. V. and Marshall, L. C., On the origin and rise of oxygen concentration in the earth's atmosphere, J. Atmos. Sci., 22, 225, 1965.
- 134. Martin, C. N., Sur les effects accumulatifs provoqués par les explosions thermonucléaires à la surface du globe, C. R. Acad. Sci., 239, 1287, 1954.
- 135. Martin, C. N., L'Heure H, a-t-elle Sonné pour le Monde? Effets Accumulatifs des Explosions Nucléaires, Bernard Grasset, Paris, 1955.
- 136. Teichmann, H., Wettereinfluss von Atomexplosionen als Stoerung periodischer Stroemungen in der Stratosphaere, *Naturwissenschaften*, 41, 498, 1954.
- 137. Weiller, A. R., Les tempetes artificielles sont-elles pour demain? La Météorologie, Ser. 4, 34, 127, 1954.
- 138. Wickramasinghe, G. M. N., Influence of nuclear explosions on the weather pattern of Europe and northern Asia, *Indian J. Meteorol. Geophys.*, 20, 333, 1969.
- 139. Arakawa, H., Possible atmospheric disturbances and damages to rice-crops in northern Japan that may be caused by experimentation with nuclear weapons, *Geophys. Mag.* (Tokyo), 26, 125, 1955.
- 140. Kawano, M. et al., The interaction between radioactive ions and condensation nuclei, J. Meteorol. Soc. Japan, 48, 69, 1970.
- 141. Israel, H., Luftelektrische Wirkung der kuenstlichen Radioaktivitaet, Z. Phys., 151, 35, 1958.
- 142. Anderson, R. V. and Servu, G. P., Airborne measurement of atmospheric conductivity in fifteen-day-old thermonuclear debris, J. Geophys. Res., 65, 223, 1960.
- 143. Stewart, K. H., Some recent changes in atmospheric electricity and their cause, Q. J. R. Meteorol. Soc., 86, 399, 1960.
- 144. Simon, A., A nukléaris robbantások hatása a légkör elektromos állapotára (Effects of nuclear explosions on atmospheric electricity), *Idöjárás*, 66, 146, 1962.
- 145. Huzita, A., Effect of radioactive fallout upon the electrical conductivity of the lower atmosphere, J. Geomagn. and Geoelectr., (Kyoto), 18, 363, 1966.
- 146. Tserfas, K. E., O vliiani isskusstvennykh radioaktivnykh vypadenii na sostoianie atmosfernogo elektrichestva (Effect of artificial radioactive fallout on the atmospheric-electric state), *Meteorol. Gidrol.*, 6, 55, 1968.
- 147. Pierce, E. T., Radioactive fallout and secular effects in atmospheric electricity, J. Geophys. Res., 77, 482, 1972.
- 148. Sartor, J. D., On the role of the atmosphere's fair-weather electric field in the development of thunderstorm electricity, in Fourth International Conference on the Universal Aspects of Atmospheric Electricity, Tokyo, 1968, Planetary Dynamics, Vol. 2, Gordon & Breach, New York, 1969, p. 161.
- 149. Bryson, R. A. and Wendland, W. M., Climatic effects of atmospheric pollution, in *Global Effects of Environmental Pollution*, Singer, S. F., Ed., Springer-Verlag, New York, 1970, p. 130.
- 150. Fiocco, G. and Grams, G., Observations of the aerosol layer at 20 km by optical radar, J. Atmos. Sci., 21, 323, 1964.
- 151. Collis, R. T. H. and Ligda, M. G. H., Note on lidar observations of particulate matter in the stratosphere, J. Atmos. Sci., 23, 255, 1966.
- 152. Barrett, E. W. and Ben-Dov, O., Application of the lidar to air pollution measurements, J. Appl. Meteorol., 6, 500, 1967.
- 153. Grams, G. and Fiocco, G., Stratospheric aerosol layer during 1964 and 1965, J. Geophys. Res., 72, 3523, 1967.
- 154. McCormick, R. A. and Ludwig, J. H., Climate modification by atmospheric aerosols, Science, 156, 1358, 1967.
- 155. Davitaya, F. F., Zagriazenie zemnoi atmosfery i izmenenie ee gazovogo sostava (Pollution of Earth's atmosphere and the change of its gas composition), Akad. Nauk SSSR, Moscow, Izvestiya, Ser. Geogr., 4, 5, 1971.
- 156. Pivovarova, Z. I., Study of the regime of atmospheric transparency, W. M. O. Tech. Note, 104, 181, 1970.
- 157. Manes, A., Atmospheric turbidity over Jerusalem, Meteorol. Service of Israel, Meteorol. Notes, Ser. A, 26, 1, 1972.
- 158. McWilliams, S., Atmospheric turbidity at Valentia Observatory, Meteorol. Service of Ireland, Tech. Notes., 36, 1, 1973.
- 159. Ellis, H. T. and Pueschel, R. F., Solar radiation: absence of air pollution trends at Mauna Loa, Science, 172, 845, 1971.

- Roosen, R. G., Angione, R. J., and Klemcke, C. H., Worldwide variations in atmospheric transmission: Pt. 1, Baseline results from Smithsonian observations, Bull. Am. Meteorol. Soc., 54, 307, 1973.
- Flowers, E. C. and Viebrock, H. J., Solar radiation: an anomalous decrease of direct solar radiation, Science, 148, 493, 1965.
- 162. Flowers, E. C. and Viebrock, H. J., Recent decrease in solar radiation at the South Pole, W. M. O. Tech. Note, 87, 116, 1967.
- 163. Viebrock, H. J. and Flowers, E. C., Comments on the recent decrease in solar radiation at the South Pole, Tellus, 20, 400, 1968.
- 164. Gunn, R., Electrical conductivity and electric field intensity over the North Atlantic and its bearing on changes in the world-wide pollution of the free atmosphere, in *Final Report, Contract NSF C 183*, American University, Washington, D. C., 1963, p. 1.
- 165. Cobb, W. E. and Wells, H. J., The electrical conductivity of oceanic air and its correlation to global atmospheric pollution, J. Atmos. Sci., 27, 814, 1970.
- 166. Misaki, M. and Takeuti, T., Extension of air pollution from land over ocean as revealed in the variation of atmospheric electric conductivity, J. Meteorol. Soc. Japan, 48, 263, 1970.
- Misaki, M., Ikegami, M., and Kanazawa, I., Atmospheric-electrical conductivity measurement in the Pacific Ocean, exploring the background level of global pollution, J. Meteorol. Soc. Japan, 50, 497, 1972.
- 168. Cobb, W. E., Oceanic aerosol levels deduced from measurements of the electrical conductivity of the atmosphere, J. Atmos. Sci., 30, 101, 1973.
- 169. Parkin, D. W., Airborne dust collections over the North Atlantic, J. Geophys. Res., 75, 1782, 1970.
- 170. Chagnon, C. W. and Junge, C. E., The vertical distribution of submicron particles in the atmosphere, J. Meteorol., 18, 746, 1961.
- 171. Junge, C. E., Chagnon, C. W., and Manson, J. E., Stratospheric aerosols, J. Meteorol., 18, 81, 1961.
- 172. Manson, J. E., Junge, C. E., and Chagnon, C. W., The possible role of gas reactions in the formation of the stratospheric aerosol layer, in *Proceedings, International Symposium on Chemical Reactions in the Lower and Upper Atmosphere*, Interscience Publications, New York, 1961, p. 139.
- 173. Mossop, S. C., Stratospheric particles at 20 km, Nature, 199, 325, 1963.
- 174. Friend, J. P., Properties of the stratospheric aerosol, Tellus, 18, 465, 1966.
- 175. Cadle, R. D., Particulate matter in the lower atmosphere, in *Chemistry of the Lower Atmosphere*, Rasool, S. I., Ed., Plenum Press, New York, 1973, p. 117.
- 176. Cadle, R., Lazrus, A., Penndorf, R., and Rosen, J. M., Aerosol particles, composition of the stratosphere, in CIAP Monograph I, U.S. Dept. of Transportation, Washington, D. C. 20590, in press.
- 177. Castleman, A. W., Jr., Munkelwitz, H. R., and Manowitz, B., Contribution of volcanic sulphur compounds to the stratospheric aerosol layer, *Nature*, 244, 345, 1973.
- 178. Gruner, P., Daemmerungserscheinungen, Hand. Geophys., 8, 432, 1942.
- 179. Bigg, E. K., The detection of atmospheric dust and temperature inversions by twilight scattering, J. Meteorol., 18, 262, 1956.
- 180. Bigg, E. K., Atmospheric stratification revealed by twilight scattering, Tellus, 18, 76, 1964.
- 181. Meinel, M. P. and Meinel, A. B., Late twilight glow of the ash stratum from the eruption of Agung volcano, *Science*, 142, 582, 1963.
- 182. Rozenberg, G. V., Twilight, Plenum Press, New York, 1966.
- 183. Volz, F. E. and Goody, R. M., Intensity of the twilight and upper atmospheric dust, J. Atmos. Sci., 19, 385, 1962.
- 184. Volz, F. E., Twilight phenomena caused by the eruption of Mt. Agung volcano, Science, 144, 1121, 1964.
- 185. Volz, F. E., Note on the global variation of stratospheric turbidity since the eruption of Agung volcano, *Tellus*, 17, 513, 1965.
- 186. Volz, F. E., On the dust in the tropical and mid-latitude stratosphere from recent twilight measurements, J. Geophys. Res., 75, 1641, 1970.
- 187. Volz, F. E., Atmospheric turbidity after the Agung eruption of 1963 and size distribution of the volcanic aerosol, J. Gcophys. Res., 75, 5185, 1970.
- 188. Kondratiev, K. Ya., et al., Direct solar radiation up to 30 km and stratification of attenuation in the stratosphere, Appl. Opt., 6, 197, 1967.
- 189. Deirmendjian, D., Global turbidity studies, Pt. 1, volcanic dust effects: a critical survey, in Report R-886-ARPA, Rand Corporation, Santa Monica, California, 1971, p. 1.
- 190. Elterman, L., UV, visible, and IR attenuation for altitudes to 50 km, 1968, in *Environmental Research Papers*, No, 285, Air Force Cambridge Research Labs., Bedford, Mass., 1968, p. 1.
- 191. Elterman, L., Wexler, R., and Chang, D. T., Features of tropospheric and stratospheric dust, Appl. Opt., 8, 893, 1969.
- 192. Elterman, L., Toolin, R. B., and Essex, J. D., Stratospheric aerosol measurements with implications for global climate, Appl. Opt., 12, 330, 1973.
- 193. Clemesha, B. R. and Rodrigues, S. N., The stratospheric scattering profile at 23° South, J. Atmos. Terr. Phys., 33, 1119, 1971.
- 194. Schuster, B. G., Detection of tropospheric and stratospheric aerosol layers by optical radar (lidar), J. Geophys. Res., 75, 3123, 1970.

- 195. Fox, R. J., Grams, G. W., Schuster, B. G., and Weinman, J. A., Measurements of stratospheric aerosols by airborne laser radar, J. Geophys. Res., 78, 7789, 1973.
- 196. Russell, P. B., Viezee, W., and Hake, R. D., Lidar Measurements of the Variability of Stratospheric Particulates, Stanford Reserach Institute, Menlo Park, California, 1973, p. 1.
- 197. Rosen, J. M., The vertical distribution of dust to 30 kilometers, J. Geophys. Res., 69, 4673, 1964.
- 198. Rosen, J. M., Simultaneous dust and ozone soundings over North and Central America, J. Geophys. Res., 73, 479, 1968.
- 199. Rosen, J. M., Stratospheric dust and its relationship to the meteoric influx, Space Sci. Rev., 9, 58, 1969.
- 200. Hofmann, D. J., Rosen, J. M., Pepin, J. T., and Kroening, J. L., Global measurements of stratospheric aerosol, ozone, and water vapor by balloon-borne sensors, in *Proceedings of the Second Conference on the Climatic Impact Assessment Program*, Broderick, A. J., Ed., U.S. Dept. of Transportation, (available through NTIS, Springfield, Virginia 22151), 1973, p. 23.
- 201. Robinson, E. and Robbins, R. C., Gaseous atmospheric pollutants from urban and natural sources, in *Global Effects of Environmental Pollution*, Singer, S. F., Ed., Springer-Verlag, New York, 1970, p. 50.
- 202. Goldberg, E. D., The chemical invasion of the oceans by man, in Global Effects of Environmental Pollution, Singer, S. F., Ed., Springer-Verlag, New York, 1968, p. 178.
- 203. Mitchell, J. M., Jr., Pollution as a cause of the global temperature fluctuation, in *Global Effects of Environmental Pollution*, Singer, S. F., Ed., Springer-Verlag, New York, 1970, p. 139.
- 204. Weickmann, H. K. and Pueschel, R. F., Atmospheric aerosols: residence times, retainment factor, and climatic effects, Contrib. Atmos. Phys., 46, 112, 1973.
- 205. Sheppard, P. A., The effect of pollution on radiation in the atmosphere, Int. J. Air Pollut., 1, 31, 1958.
- 206. Charlson, R. J. and Pilat, M. J., Climate: the influence of aerosols, J. Appl. Meteorol., 8, 1001, 1969.
- 207. Atwater, M. A., Planetary albedo changes due to aerosols, Science, 179, 64, 1970.
- 208. Mitchell, J. M., Jr., Effect of Atmospheric Aerosol on Climate with Special Reference to Surface Temperature, NOAA TM EDS 18, Environmental Data Service, National Oceanic and Atmospheric Administration, Silver Spring, Md. 20910, 1970, p. 1.
- Mitchell, J. M., Jr., Effect of atmospheric aerosols on climate with special reference to temperature near the Earth's surface, J. Appl. Meteorol., 10, 703, 1971.
- 210. Atwater, M. A., Thermal effects of pollutants evaluated by a numerical model, in *Preprints of Papers*. Conference on Air Pollution Meteorology, April 5-9, 1971, Raleigh, North Carolina, American Meteorological Society, Boston, Mass., 1971, p. 108.
- 211. Atwater, M. A., Radiation budget for polluted layers of the urban environment, J. Appl. Meteorol., 10, 205, 1971.
- 212. Barrett, E. W., Depletion of short-wave irradiance at the ground by particles suspended in the atmosphere, Sol. Energy, 13, 323, 1971.
- 213. Kattawar, G. W. and Plass, G. N., Influence of aerosols, clouds, and molecular absorption on atmospheric emission, J. Geophys. Res., 76, 3437, 1971.
- 214. Plass, G. N. and Kattawar, G. W., Effect of aerosol variation on radiance in the earth's atmosphere-ocean system, Appl. Opt., 11, 1598, 1972.
- 215. Kattawar, G. W. and Plass, G. N., Matrix operator theory of radiative transfer, Pt. 2, Scattering from maritime haze, Appl. Opt., 12, 1071, 1973.
- 216. Rasool, S. I. and Schneider, S. H., Atmospheric carbon dioxide and aerosols: effects of large increases on global climate, *Science*, 173, 138, 1971.
- Ensor, D. S., Porch, W. M., Pilat, M. J., and Charlson, R. J., Influence of the atmospheric aerosol on albedo, J. Appl. Meteorol., 10, 1303, 1971.
- 218. Twomey, S., Influence of atmospheric particulates on cloud and planetary albedo, in *Proceedings, International Conference on Weather Modification, Canberra, Australia, Sept. 6-11, 1971*, American Meteorological Society, Boston, Mass., 1971, p. 265.
- 219. Twomey, S., Effect of cloud scattering on the absorption of solar radiation by atmospheric dust, J. Atmos. Sci., 29, 1156, 1972.
- 220. Neumann, J. and Cohen, A., Climatic effects of aerosol layers in relation to solar radiation, J. Appl. Meteorol., 11, 651, 1972.
- 221. Zdunkowski, W. G. and McQuage, N. D., Short-term effects of aerosol on the layer near the ground in a cloudless atmosphere, *Tellus*, 24, 237, 1972.
- 222. Unsworth, M. H. and McCartney, H. A., Effects of atmospheric aerosols on solar radiation, *Atmos. Environ.*, 7, 1173, 1973.
- 223. Eschelbach, G., Der Einfluss des Dunstes auf den Strahlungehalt der Atmosphaere in solaren Spektralbereich, Ann. Meteorol., 6, 327, 1973.
- 224. Kondraťyev, K. Ya. and Smoktiy, D. I., O vliyanii aerozolya na spektraľnoye aľbedo sistemy atmosfery: podstilayúshchaya poverkhnost (Influence of aerosol on the spectral albedo of the atmospheric system: Underlying surface), Akad. Nauk SSSR, Moscow, Izvestiya, Fizika Atmosfery i Okeana, 9, 1269, 1973.
- 225. Grassl, H., Aerosol influence on radiative cooling, Tellus, 25, 386, 1973.

- 226. Braslau, N. and Dave, J. V., Effect of aerosols on the transfer of solar energy through realistic model atmospheres, Pt. 1, Non-absorbing aerosols, J. Appl. Meteorol., 12, 601, 1973; Pt. 2, Partly-absorbing aerosols, 616, 1973.
- 227. Bergstrom, R. W., Jr. and Viskanta, R., Modeling of the effects of gaseous and particulate pollutants in the urban atmosphere, Pt. 1, J. Appl. Meteorol., 12, 901, 1973; Pt. 2, 913, 1973.
- 228. Bergstrom, R. W. Jr. and Viskanta, R., Prediction of the solar radiant flux and heating rates in a polluted atmosphere, *Tellus*, 25, 486, 1973.
- 229. Sekera, Z. and Stowe, L. L., Jr., Effects of particulate matter on the radiance of terrestrial radiation: theory, Contrib. Atmos. Phys., 46, 101, 1973.
- 230. Dave, J. V., A direct solution of the spherical-harmonics approximation to the transfer equation for the plane-parallel, non-homogeneous atmosphere, in Report under Contract No. w-7405-Eng-48 to U.S. Atomic Energy Commission, Lawrence Livermore Laboratory, University of California, Livermore, California (available from NTIS, Springfield, Virginia 22151), 1974, p. 1.
- 231. Stowe, L. L., Jr., Effects of particulate matter on the radiance of terrestrial infrared radiation: results, J. Atmos. Sci., 31, 755, 1974.
- 232. Chylek, P. and Coakley, J. A., Jr., Aerosols and climate, Science, 183, 75, 1974.
- 233. Atwater, M. A. and Brown, P. S., Jr., Numerical computations of the latitudinal variation of solar radiation for an atmosphere of varying opacity, J. Appl. Meteorol., 13, 289, 1974.
- 234. Batten, E. S., Atmospheric response to a stratospheric dust cloud as similated by a general circulation model, in Report R-1324-ARPA, Rand Corporation, Santa Monica, California, 1974, p. 1.
- 235. Schneider, S. H., Atmospheric particles and climate: the impact of man's activities, in *New Concepts in Air Pollution Research*. Williams, J.-O., Ed., John Wiley & Sons, New York, 1974, p. 17.
- 236. McBirney, A., Volcanoes dimly understood danger, Ind. Res., 16, 20, 1974.
- 237. Starr, V. P. and Oort, A. H., Five-year climatic trend for the Northern Hemisphere, Nature, 242, 310, 1973.
- 238. Riehl, H., Introduction to the Atmosphere, McGraw-Hill, New York, 1965.
- 239. Chapman, S., A theory of upper-atmospheric ozone, Mem. R. Meteorol. Soc., 3, 103, 1930.
- 240. McGrath, W. D. and Norrish, R. G. W., Studies of the reactions of excited oxygen atoms and molecules produced in the flash photolysis of ozone, *Proc. R. Soc. London, Ser. A*, 254, 317, 1960.
- 241. DeMore, W. B., Rate constants for the reactions of OH and HO<sub>2</sub> radicals with ozone, Science, 180, 735, 1973.
- 242. Anderson, J. G. and Kaufman, F., Kinetics of the reaction OH(v = O) + O<sub>3</sub> = HO<sub>2</sub> + O<sub>2</sub>, Chem. Phys. Lett., 19, 483, 1973.
- 243. Simonaitis, R. and Heicklen, J., The reaction of HO<sub>2</sub> with O<sub>3</sub>, J. Phys. Chem., 77, 1932, 1973.
- 244. Johnston, H. S., Catalytic reduction of stratospheric ozone by nitrogen oxides, in *Report UCRL-20568*, Lawrence Radiation Lab., University of California, Berkeley, California, 1971, p. 1.
- Johnston, H. S., Reduction of stratospheric ozone by nitrogen oxide catalysts from SST exhausts, Science, 173, 517, 1971.
- 246. Johnston, H. S., Davis, D. D., and Crutzen, P. J., Summary of reactions that need to be considered in the modeling of the stratosphere, in *The Natural Stratosphere of 1974, CIAP Monograph 1*, U.S. Department of Transportation, Washington, D. C., 1975, in press.
- 247. Molina, M. J. and Rowland, F. S., Stratospheric sink for Chlorofluoromethanes chlorine atom catalyzed destruction of ozone, *Nature*, 249, 810, 1974.
- 248. Crutzen, P., Estimates of possible future ozone reductions from continued use of fluorochloromethanes (CF<sub>2</sub>Cl<sub>2</sub>, CI-Cl<sub>3</sub>), Geophys. Res. Lett., 1, 205, 1974.
- 249. Rowland, F. S. and Molina, M. J., Chlorofluoromethanes in the environment, Rev. Geophys. Space Phys., 13, 1, 1975.
- 250. Cicerone, R. J., Stolarski, R. S., and Walters, S., Stratospheric ozone destruction by man-made chlorofluoro-methanes, Science, 185, 1165, 1974.
- 251. Komhyr, W. D., Barrett, E. W., Slocum, G., and Weickmann, H. K., Atmospheric total ozone increase during the 1960's, *Nature*, 232, 390, 1971.
- 252. Grass, R. and Komhyr, W. D., personal communication.
- 253. Newell, R. E., Stratospheric temperature change from the Mt. Agung volcanic eruption of 1963, J. Atmos. Sci., 27, 977, 1970.
- 254. Fegley, R. W. and Ellis, H. T., Lidar observations of a stratospheric dust cloud layer in the tropics, Geophys. Res. Let., 2, 139, 1975.
- 255. Brooks, C. E. P., Selective annotated bibliography on urban climates, Meteorol. Abstr. Bibliogr., 3, 736, 1952.
- 256. Floor, C., Onderzoek Utrechts stadsklimaat met weerbus, Hemel en Dampkring, 5, 107, 1970.
- 257. Middleton, W. E. K. and Spilhaus, A. F., Meteorological Instruments, 3rd Edition, University of Toronto Press, Toronto, 1953, p. 61.
- 258. DeMarrais, G. A., Vertical temperature difference observed over an urban area, Bull. Am. Meteorol. Soc., 42, 548, 1961.
- 259. Clarke, J. F., Nocturnal urban layer over Cincinnati, Ohio, Mon. Weather Rev., 97, 582, 1969.
- 260. Dirks, R. A., Urban atmosphere: warm, dry envelope over St. Louis, J. Geophys. Res., 79, 3473, 1974.
- 261. Huff, F. A., Ed., Summary Report of METROMEX Studies, 1971-1972, Report of Investigations, No. 74, Illinois State Water Survey, Urbana, Illinois, 1973.

- 262. Stranz, D., Ausloesung von Schneefall ueber einer Grosstadt, Z. Meteorol., 3, 359, 1949.
- 263. Parry, M., An "urban rainstorm" in the Reading area, Weather, 11, 41, 1956.
- 264. Jefferson, G. J., Man-made cumulus, Meteorol. Mag., 89, 16, 1960.
- 265. Atkinson, B. W., Reality of the urban effect on precipitation: a case-study approach, W. M. O. Tech. Notes, 108, 342, 1970.
- 266. Vukovich, F. M., Theoretical analysis of the effect of mean wind and stability on a heat island circulation characteristic of an urban complex, Mon. Weather Rev., 99, 919, 1971.
- 267. Olfe, D. B. and Lee, R. L., Linearized calculations of urban heat island convection effects, J. Atmos. Sci., 28, 1374, 1971.
- 268. Leakey, D. M. and Friend, J. P., Model for predicting the depth of the mixing layer over an urban heat island with applications to New York City, J. Appl. Meteorol., 10, 1162, 1971.
- 269. Hilst, G. R. and Bowne, N. E., Diffusion of aerosols released upwind of an urban complex, Environ. Sci. Technol., 5, 327, 1971.
- 270. Hanna, S. R. and Swisher, S. D., Meteorological effects of the heat and moisture produced by man, Nucl. Saf., 12, 114, 1971.
- 271. Krishna Rao, P., Remote sensing of urban "heat islands" from an environmental satellite, Bull. Am. Meteorol. Soc., 53, 647, 1972.
- 272. Probald, F., Városi energiaforrások jelentősége Budapest éghajlatában (Importance of urban sources of energy in the climate of Budapest), *Idöjárás*, 67, 162, 1965.
- 273. Garnett, A. and Bach, W., Estimation of the ratio of artificial heat generation to natural radiation heat in Sheffield. Mon. Weather Rev., 93, 383, 1965.
- 274. Fedorov, M. M., Vliianie zadymlennosti na svetovoi rezhim goroda (The effect of smoke on the regime of light in a city), Gig. Sanit., 23, 14, 1958.
- 275. Volz, F. E., Some results of turbidity networks, Tellus, 21, 625, 1969.
- 276. Goldberg, B. and Klein, W. H., Comparison of normal-incident solar energy measurements at Washington, D. C., Sol. Energy, 13, 311, 1971.
- 277. Yamamoto, T., The secular change of the climate in Japan, Geophys. Mag. (Tokyo), 21, 249, 1950.
- 278. Idso, S. B., Thermal radiation from a tropospheric dust suspension, Nature, 241, 448, 1973.
- 279. Schmidt, W., Messungen des Staubkerngehalts der Luft am Rande einer Grosstadt. Meteorol. Z., 35, 281, 1918.
- 280. Wuerfel, H., Ergebnisse einjaehriger Messungen des Kerngehalts der Luft am Rande der Grosstadt Berlin. Angew. Meteorol., 1, 333, 1953.
- 281. Pilpel, N., Contaminated fogs, Research, 6, 481, 1953.
- 282. Scorer, R. S., Smog, Sci. Prog., 42, 396, 1954.
- 283. Jenkins, I., Increase in averages of sunshine in greater London, Weather, 24, 52, 1969.
- 284. Brazell, J. H., Meteorology and the Clean Air Act, Nature, 226, 694, 1970.
- 285. Kelly, T., Thick and dense fog at London/Heathrow Airport and Kingsway/Holborn during the two decades 1950-59 and 1960-69, Meteorol. Mag., 100, 257, 1971.
- 286. Jenkins, I., Decrease in the frequency of fog in Central London, Meteorol. Mag., 100, 317, 1971.
- 287. McKellar, H. A., Success of clean air as seen by a meteorologist, Smokeless Air, 40, 26, 1969.
- 288. Junge, C. E., Das Wachstum der Kondensationskerne mit der relativen Feuchtigkeit. Ann. Meteorol., 3, 129, 1950.
- 289. Neiburger, M. and Wurtele, M. G., On the nature and size of particles in haze, fog, and stratus of the Los Angeles region, Chem. Rev., 44, 321, 1949.
- 290. Ashworth, J. R., The influence of smoke and hot gases from factory chimneys on rainfall, Q. J. R. Meteorol. Soc., 55, 341, 1929.
- 291. Neuwirth, R., "Kerne" in der Luft, eine Voraussetzung fuer Niederschlaege. Umschau, 56, 212, 1956.
- 292. Schaefer, V. J., Ice nuclei from automobile exhausts and iodine vapor, Science, 154, 1555, 1966.
- 293. Schaefer, V. J., Ice nuclei from auto exhaust and organic vapors, J. Appl. Meteorol., 7, 148, 1968.
- 294. Langer, G., Ice nuclei generated by steel mill activity, in *Proceedings, First National Conference on Weather Modification*, American Meteorological Society, Boston, 1968, p. 220.
- 295. Reynolds, G. W., Cloud seeding potential of Salt Lake Valley air pollution: cold season, in *Collection of Preprints*, Conference on Cloud Physics, August 24-27. 1970, Colorado State University, Fort Collins. Colorado, American Meteorological Society, Boston, 1970, p. 29.
- 296. Telford, J. W., Freezing nuclei from industrial processes, J. Meteorol., 17, 676, 1960.
- 297. Changnon, S. A., Jr., La Porte weather anomaly, fact or fiction? Bull. Am. Meteorol. Soc., 49, 4, 1968.
- 298. Holzman, B. G. and Thom, H. C. S., (comments on) Stanley A. Changnon, Jr., La Porte weather anomaly, fact or fiction? and (reply by) Changnon, Bull. Am. Meteorol. Soc., 51, 335, 1970.
- 299. Squires, P., An estimation of the anthropogenic production of cloud nuclei, J. Rech. Atmos., 2, 297, 1966.
- 300. Landsberg, H. E., The climate of towns, in *Man's Role in Changing the Face of the Earth*, University of Chicago Press, Chicago, 1956, p. 584.
- 301. Kratzer, A., Vieweg, F., and Braunschweig, S., *The Climate of Cities*, English translation by American Meteorological Society, Boston. 1956.

- 302. Atkinson, B. W., A preliminary examination of the possible effect of London's urban area on the distribution of thunder rainfall 1951-1960, Trans. Papers, Inst. Br. Geographers, 44, 97, 1968.
- 303. Changnon, S. A., Jr., Recent studies of urban effects on precipitation, in the United States, Bull. Am. Meteorol, Soc., 50, 411, 1969.
- 304. Alkezweeny, A. J. and Green, W. D., Effect of air pollution on the concentration of ice and condensation nuclei. J. Rech. Atmos., 1, 31, 1970.
- Smith, T. B., Pollutants and cloud condensation processes, in Man's Impact on the Climate, Matthews, W. H., Kellogg, W. W., and Robinson, G. D., Eds., MIT Press, Cambridge, Mass., 1971, p. 400.
- 306. Hidy, G. M., and Alkezweeny, A., Inadvertent weather modification and Los Angeles smog. in Aerosols and Atmospheric Chemistry, Hidy, G. M., Ed., Academic Press, New York, 1972, p. 339.
- Harman, J. R. and Elton, W. M., La Porte, Indiana, precipitation anomaly, Ann. Assoc. Am. Geographers, 61, 468, 1971.
- 308. Hidore, J. J., Effects of accidental weather modification on the flow of the Kankakee River. Bull. Am. Meteorol. Soc., 52, 99, 1971.
- 309. Ramana Rao, T. and Ramana Murty, Bh. V., Effect of steel mills on rainfall at distantly located stations, *Indian J. Meteorol. Geophys.*, 24, 15, 1973.
- 310. Shulman, M. D. and Greenway, A. R., Investigation of the effects of urbanization on precipitation type, frequency, areal, and temporal variation, in *Final Report, Contract 14-37-0001-3530*, New Jersey Water Resources Research Institute, Rutgers University, New Brunswick, 1971, p. 1.
- 311. Fitzgerald, J. W. and Speyers-Duran, P. A., Changes in cloud nucleus concentration and cloud droplet size distribution associated with pollution from St. Louis, J. Appl. Meteorol., 12, 511, 1973.
- 312. Braham, R. R., Jr., Project METROMEX-I, Cloud Physics Laboratory Technical Note No. 45, Department of the Geophysical Sciences, University of Chicago, 1972.
- 313. Braham, R. R., Jr., Cloud Physics Approach to Urban Weather Modification, Cloud Physics Laboratory Technical Note No. 46, Department of the Geophysical Sciences, University of Chicago, 1973.
- 314. Weickmann, H., Man-made weather patterns in the Great Lakes Basin, Weatherwise, 25, 260, 1972.
- 315. Kocmond, W. C. and Mack, E. J., Vertical distribution of cloud and Aitken nuclei downwind of urban pollution sources, J. Appl. Meteorol., 11, 141, 1972.
- 316. Warner, J., Reduction in rainfall associated with smoke from sugar-cane fires, J. Appl. Meteorol., 7, 247, 1968.
- 317. Holle, R. L., Effects of cloud condensation nuclei due to fires and surface sources during south Florida drought, J. Appl. Meteorol., 10, 62, 1971.
- 318. Komabayasi, M., The suppression of thunder cloud occurrence by frequent volcanic eruptions, J. Meterorol. Soc. Japan, 75th anniversary volume, 25, 1957.
- 319. Komabayasi, M., The suppression of thunder cloud occurrence by frequent volcanic eruptions, Pt. 2, J. Meteorol. Soc. Japan, Ser. 2, 37, 79, 1959.
- 320. Johnson, O., The development of a cumulus cloud over a prairie grass fire, Weather, 14, 212, 1959.
- 321. Dessens, H., Orages sur un foyer convectif artificiel, Puy de Dôme Observatoire Bull., 1, 27, 1960.
- 322. Price, S. and Pales, J. C., Local volcanic activity and ice nuclei concentrations on Hawaii, Arch. Meteorol. Geophys. Bioklimatol. Ser. A, 13, 398, 1963.
- 323. Georgi, J., Flugzeug-Kondensfahne erzeugt ausgedehntes Wolkenfeld, Z. Meteorol., 14, 102, 1960.
- 324. Knollenberg, R. G., Measurements on the growth of the ice budget in a persisting contrail, J. Atmos. Sci., 29, 1367, 1972.
- 325. Murcray, W. B., On the possibility of weather modification by aircraft contrails, Mon. Weather Rev., 98, 745, 1970.
- 326. Machta, L. and Carpenter, T., Trends in high cloudiness at Denver and Salt Lake City, in *Man's Impact on the Climate*, Matthews, W. H., Kellogg, W. W., and Robinson, G. D., Eds., MIT Press, Cambridge, Mass., 1971, p. 410.
- 327. Kuhn, P. M., Applications of thermal radiation measurements in atmospheric science, Adv. Geophys., 14, 331, 1970.
- 328. Kuhn, P. M., Airborne observations of contrail effects on the thermal radiation budget, J. Atmos. Sci., 27, 937, 1970.
- 329. Carson, J. E., Atmospheric effects of thermal discharges into a large lake, J. Air Pollut. Control Assoc., 22, 523, 1972.
- 330. Huff, F. A., Potential augmentation of precipitation from cooling tower effluents, Bull. Am. Meteorol. Soc., 53, 639, 1972.
- 331. Durdik, M., Vliv člověka na podnebí v Čechách v letech 1876 až 1925, Meteorol. Zpr., 6, 65, 1953.
- 332. Schwerdtfeger, W., Betrachtungen ueber eine Klima-aenderung in Argentinien, Meteorol. Rundsch., 8, 7, 1955.
- 333. Galmarini, A. G., Raffo del Campo, J. M., and Amigo, A., Investigation of possible changes in the climate of Patagonia; overgrazing in the Patagonia region: its causes and proposed solutions, in *Water for Peace*, Vol. 2, U. S. Govt. Printing Office, Washington, D. C., 1968, p. 721.
- 334. Feininger, T., Less rain in Latin America, Science, 160, 13, 1968.
- 335. Newell, R. E., Amazon forest and atmospheric general circulation, in *Man's Impact on the Climate*, Matthews, W. H., Kellogg, W. W., and Robinson, G. D., Eds., MIT Press, Cambridge, Mass., 1971, p. 457.

- 336. Allee, P. A., Ice nuclei concentration measured by a benchmark network, in *Preprint Volume, 4th Conference on Weather Modification, Ft. Lauderdale, Florida, Nov. 18-21, 1974*, American Meteorological Society, Boston, 1974, p. 242.
- 337. Fletcher, J. O., Heat budget of the Arctic Basin and its relation to climate, in *Report R-444-PR*, Rand Corporation, Santa Monica, California, 1965, p. 1.
- 338. Joseph, J. H., Calculation of radiative heating in numerical general circulation models, in *Technical Report No. 1*, Numerical Simulation of Weather and Climate, Dept. of Meteorology, University of California, Los Angeles, 1966, p. 1.
- 339. Manabe, S., Smagorinsky, J., and Strickler, R. F., Simulated climatology of a general circulation model with a hydrologic cycle, Mon. Weather Rev., 93, 769, 1965.
- 340. Manabe, S. and Smagorinsky, J., Simulated climatology of a general circulation model with a hydrologic cycle, Pt. 2, Analysis of the tropical atmosphere, Mon. Weather Rev., 95, 155, 1967.
- 341. Mintz, Y., Very long-term global integration of the primitive equations of atmospheric motion, W. M. O. Tech. Notes, 66, 141, 1965.
- 342. Mintz, Y. et al., Report of working group on development of atmospheric circulation models, in *Research Memorandum RM-5233-NSF*, Rand Corporation, Santa Monica, California, 1966, p. 468.
- 343. Rapp, R. R., Climate modification and national security, U. S. Air Weather Serv. Tech. Rep., 242, 307, 1971.
- 344. Gates, W. L., Understanding climatic change, in *Paper P-5114*, Rand Corporation, Santa Monica, California, 1973, p. 1.
- 345. Saltzman, B., Steady-state solutions for axially-symmetric climatic variables, in *Research on the Theory of Climate*, Saltzman, B., Ed., Travelers Research Center, Inc., Hartford, Conn., 1967, p. 1.
- 346. Sellers, W. D., New global climatic model, J. Appl. Meteorol., 12, 241, 1973.
- 347. Schneider, S. H. and Gal-Chen, T., Numerical experiments in climate stability, J. Geophys. Res., 78, 6182, 1973.
- 348. Manabe, S. and Holloway, J. L., Jr., Climate Modification and a Mathematical Model of Atmospheric Circulation, Geophysical Fluid Dynamics Laboratory/ESSA, Princeton University, Princeton, New Jersey, 1970.
- Washington, W. M., Numerical climatic-change experiments: the effect of man's production of thermal energy, J. Appl. Meteorol., 11, 768, 1972.
- 350. Washington, W. M., On the possible uses of global atmospheric models for the study of air pollution, in Air and Water Pollution: Proceedings, Colorado Associated University Press, Boulder, Colorado, 1972, p. 599.
- 351. Chang, J. S., Global transport and kinetics model, in First Annual Report, DOT-CIAP, Report UCRL-51336, Lawrence Livermore Laboratory, University of California, Livermore, California, 1973.
- 352. Crutzen, P. J., Ozone production rates in an oxygen-hydrogen-nitrogen oxide atmosphere, J. Geophys. Res., 76, 7311, 1971.
- 353. Hesstvedt, E., A simplified time-dependent two-dimensional photochemical model of the stratosphere, paper presented at International Conference on Structure, Composition, and General Circulation of the Upper and Lower Atmospheres and Possible Anthropogenic Perturbations, Melbourne, Australia, January 14-25, 1974.
- 354. Prinn, R. G., Alyea, F., Katz, A., and Cunnold, D., The distribution of odd nitrogen and carbon compounds in the natural and perturbed stratosphere, paper presented at AlAA Second International Conference on the Environmental Impact of Aerospace Operations in the High Atmosphere, San Diego, California, July 8-10, 1974.
- 355. Rao-Vupputuri, R. K., A zonally-averaged circulation model of the stratosphere incorporating radiative heating and ozone photochemistry in an oxygen-hydrogen-nitrogen atmosphere, in *Proceedings, Third Conference on the Climatic Impact Assessment Program*, Broderick, A. J., and Hard, T. M., Eds., U.S. Department of Transportation, Washington, D.C., 1974, p. 390.
- 356. Widhopf, G. F., Distribution of trace species in the stratosphere and the effects of SST pollutants, paper presented at the Fall Annual Meeting, American Geophysical Union, 12 December 1974, San Francisco, California.
- 357. Mahlman, J. D., A three-dimensional stratospheric point-source experiment, and its implications for dispersion of effluent from a fleet of supersonic aircraft, AlAA Paper 73-528, presented at the American Institute of Aeronautics and Astronautics/American Meteorological Society Conference on the Environmental Impact of Aerospace Operations in the High Atmosphere, Denver, Colorado, June 1973.
- 358. Lorenz, E. N., Climatic change as a mathematical problem, J. Appl. Meteorol., 9, 325, 1970.
- 359. Robinson, E. and Robbins, R. C., Emissions, concentrations, and fate of particulate atmospheric pollutants, in *Final Report*, SRI Project SCC-8507, Stanford Research Institute, Menlo Park, California, 1971, p. 1.
- 360. Barrett, E. W., Pueschel, R. F., Weickmann, H. K., and Kuhn, P. M., Inadvertent Modification of Weather and Climate by Atmospheric Pollutants, U.S. Department of Commerce, Environmental Science Services Administration, Research Laboratories, Boulder, Colorado, 1970.
- 361. Smagorinsky, J., Global atmospheric modeling and the numerical simulation of climate, in Weather and Climate Modification, Hess, W. N., Ed., John Wiley & Sons, New York, 1974, p. 633.
- 362. Climatic Impact Committee, Environmental Impact of Stratospheric Flight, National Academy of Sciences, Washington, D.C., 1975.
- 363. Landsberg, H., Inadvertent atmospheric modification through urbanization, in *Weather and Climate Modification*, Hess, W. N., Ed., John Wiley & Sons, New York, 1974, p. 726.

# Source of Seasonal Variations in Solar Radiation at Mauna Loa

B. A. Bodhaine<sup>1</sup> and R. F. Pueschel

Atmospheric Physics and Chemistry Lab., NOAA, Boulder, Colo. 80302

9 April 1973 and 29 October 1973

#### ABSTRACT

Solar radiation transmission data taken at Mauna Loa exhibit a seasonal variation with the minimum in summer. On the basis of Barrett's model for the depletion of solar radiation by aerosols, it is suggested that these variations are due to the seasonal generation of organic aerosols by the biosphere. It is suggested that the naturally produced atmospheric background aerosol of organic origin causes the typical seasonal turbidity variations. Furthermore, changes in the amplitude or phase of transmission data could be used to indicate whether aerosols from anthropogenic sources would influence the earth's albedo.

Precipitable water calculations suggest that humidity data above Mauna Loa are not accurate enough to make a quantitative estimate of the effect of atmospheric water vapor on Mauna Loa radiation data. However, water vapor apparently cannot account for these variations on the basis of phase angle considerations.

### 1. Introduction

The effect of the atmospheric aerosol load on the earth's climate has been of great concern during the past decade. McCormick and Ludwig (1967), Bryson (1968) and Mitchell (1970) suggested that an increase of particulate loading would lead to a decrease in incoming solar radiation that would, in turn, lead to a general cooling of the earth's temperature as observed during the past 30 years. Subsequently, other investigators (Charlson and Pilat, 1969; Mitchell, 1971) have suggested that the inclusion of the absorption effects of tropospheric aerosols could very well lead to a warming at the earth's surface. It is generally agreed that stratospheric aerosols would lead to surface cooling, whereas uncertainty prevails about the consequences of an increase in tropospheric particulate loading.

The effects of atmospheric water vapor on incoming solar radiation are understood, and the dominant intense absorption spectrum in the near infrared is well known. The classical work of Fowle (1915) gave basic data for determining absorption of solar radiation by atmospheric water vapor. Other workers (e.g., MacDonald, 1960; Möller, 1963; Gates, 1960; Eldridge, 1967) have treated the subject further, but all refer to the basic data of Fowle.

Solar radiation has been monitored at Mauna Loa Observatory, Hawaii (3.4 km MSL, 20N, 155W) since 1957. Since then there has been no significant change at Mauna Loa attributable to anthropogenic sources (Ellis and Pueschel, 1971). In addition, the data from

Mauna Loa exhibit three important effects: 1) an abrupt increase in turbidity in 1963, attributable to volcanic acrosols ejected into the stratosphere by the cruption of Mount Agung, Bali; 2) a seasonal variation in the amount of normal incident solar radiation; and 3) a phase angle that gives a summer maximum in attenuation (Pueschel et al., 1972).

Seasonal variations in atmospheric transmission have been observed elsewhere as early as 1908 (Roosen, 1972), but until now there has been no serious attempt to explain these variations. In all cases, including the Southern Hemisphere, atmospheric transmission shows a summer minimum (Flowers et al., 1969). Although other investigators agree that seasonal variations exist, controversy persists about whether these changes are caused by tropospheric or stratospheric constituents (Dyer and Hicks, 1968; Elsaesser et al., 1972), and which constituents play the major role. An answer to this question is important because of possible climatic implications of an increased atmospheric aerosol load. Furthermore, if the seasonal turbidity variations are typical for the atmospheric background aerosol, the parameters (amplitude and phase) of this periodic function could be used as criteria that are sensitive to changes of aerosols from anthropogenic sources.

Implications are that the seasonal turbidity variations at Mauna Loa most likely originate in the upper troposphere, since it is well known that the residence times of stratospheric, upper tropospheric and lower tropospheric constituents are of the order of years, months and days, respectively. The long residence time of stratospheric aerosols is well illustrated by the slow recovery of the Mauna Loa radiation data after the Agung eruption in 1963.

<sup>&</sup>lt;sup>1</sup> Present affiliation: Mauna Loa Observatory, Hilo, Hawaii 96720.

This paper presents a quantitative explanation of the Mauna Loa data in terms of atmospheric water vapor and aerosol particles.

# 2. Precipitable water above Mauna Loa

To estimate the water vapor content of the atmosphere over Mauna Loa, 13 years of Hilo, Hawaii, radiosonde data were analyzed and precipitable water was calculated according to the method of Solot (1939). Harrison (1970) gives an exhaustive discussion of the theory of precipitable water calculations, but we feel that radiosonde humidity values above Mauna Loa do not merit such an exact treatment. The years 1958 through 1970 were used because these are the years of radiation data presented by Ellis and Pueschel (1971). All precipitable water calculations began at the 700mb level, since this is the approximate level of Mauna Loa Observatory and because this is a standard level given in the National Climatological Summary (Environmental Data Service). Two sets of data were used: 1) monthly data from the Climatological Summary were used to determine the general seasonal moisture climatology over Mauna Loa; and 2) individual daily ascent data were used for all control days as defined by Ellis and Pueschel (1971) for 1958 to 1970 in order to determine moisture trends directly related to control day solar radiation measurements.

It is not possible to deduce precipitable water from surface humidity data, as shown by Reber and Swope (1972) for three locations in California. It appears even less likely at Mauna Loa, being an isolated peak above a marine environment.

To facilitate computations with a desk-top programmable calculator, values of saturation vapor pressure from 10 to -50C taken from List (1966) were approximated by a second-degree logarithmic least-squares fit:

$$\ln e_s = 1.81638 + 0.071676T - 0.00038948T^2, \quad (1)$$

where  $e_s$  is the saturation vapor pressure (mb), and T the temperature (°C). The standard deviation was  $\sigma = 0.000959$  and the fit provided better than 1% accuracy all along the curve.

The mixing ratio at any given level was then calculated from

$$w = \frac{6.22e_s R}{P - 0.378e_s},\tag{2}$$

where w is the mixing ratio (gm kg<sup>-1</sup>), R the relative humidity (percent), and P the pressure (mb).

Finally, values of precipitable water were calculated ipward from 700 mb by the standard formula:

$$W = \frac{1}{980} \sum w \Delta P,\tag{3}$$

where W is the precipitable water (cm) and  $\Delta P$  the layer thickness (mb) between significant levels.

Data were read from a microfilm reader and entered directly into the calculator, level by level, with a running total of precipitable water being kept automatically by the machine.

Several points must be kept in mind when calculating precipitable water from radiosonde humidity data. For a lithium chloride sensor, the data are reliable until the signal at the receiver begins to "motorboat," indicating that the sensor has reached its lower limit, usually at relative humidities near 15%. In these instances, a statistical value of relative humidity is assigned; however, when a carbon element is used, statistical values are not assigned. To be assured that only reliable humidity data were used, we considered only non-motorboating data. The changeover from lithium chloride sensors to carbon sensors took place in the early 1960's but, unfortunately, was made gradually so that no single date can be given for all stations (Whiting, 1971). Finally, diurnal variations in humidity data due to solar heating of the carbon elements were discussed by Morrissey and Brousaides (1970), Salemela and Sissenwine (1970) and Whiting (1971). The problem was defined and solved (Teweles, 1970; Friedman, 1972) by a new design for the radiosonde case.

A glance at the Hilo, Hawaii, radiosonde data reveals that the change to the carbon element must have been accomplished in January 1965, since relative humidity values are given at consistently high altitudes after that time. Therefore, Hilo radiosonde data on individual control days were analyzed for monthly averages for 1958-64 and 1965-70. These calculations were performed using the 0130 HST ascents and repeated using an average of the 0130 and 1330 HST ascents. This was done because all radiation data used for control day values were taken during the early morning. However, we feel that the nighttime values alone are more representative of water vapor above Mauna Loa because the 1330 HST ascent is well after the thermally induced upslope windflow is established. In addition, we feel that precipitable water calculations above Mauna Loa are more reliable for 1965 and after.

Monthly averages of the radiation data have been considered for the same periods: 1958-64 and 1965-70. Fortunately, 1958-64 also spans the pre-Agung period of radiation data acquisition at Mauna Loa.

Fig. 1 shows monthly average precipitable water and radiation data for 1958-64 and 1965-70. These data were subjected to a 12-point harmonic analysis to show annual and semi-annual trends, and the results are shown in Table 1 and Fig 1. Note that during 1958-64, radiation data show a seasonal variation with a minimum in June amounting to a peak-to-peak variation of approximately 0.9% about the mean of 0.932. The water vapor data show fairly erratic behavior with a possible peak-to-peak variation of as much as 0.1 cm,

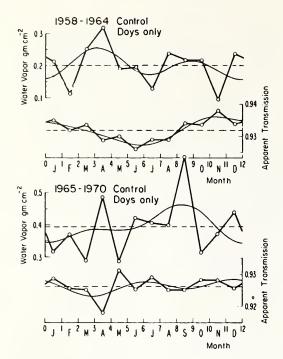
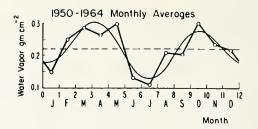


Fig. 1. Precipitable water above 700 mb calculated from Hilo, Hawaii, radiosonde data for control day monthly averages. Only the nighttime ascents were used. Upper curves give water vapor and apparent transmission for 1958-64, lower curves for 1956-70. Smooth curves show harmonic fits, dashed lines averages.

but this is apparently not in phase with the radiation data. A correlation coefficient of -0.23 for transmission and water vapor data showed a predominantly semi-annual trend. This suggests either that precipitable water calculations may not be reliable above the level of Mauna Loa or that changes in transmission are caused by variations in atmospheric constituents other than water vapor. Of the two time periods considered, 1965-70 shows the most erratic behavior of radiation data, most certainly because of the Agung eruption and the increase of the stratospheric dust which would mask the background variations of the pre-Agung period. The average transmission is significantly lower during the post-Agung period, although the full impact

Table 1. Twelve-point harmonic analysis of water vapor and radiation data for monthly averages of 1958-64 and 1965-70: W, precipitable water (gm cm<sup>-2</sup>); T, atmospheric transmission as defined by Ellis and Pueschel (1971); m, month with m=0 at 0000 HST 1 January. Water vapor data are for the nighttime ascents on control days only.

Years	Precipitable Water	Atmospheric Transmission			
	$W = 0.2021 + 0.0213 \cos \frac{\pi}{6} (m - 3.7)$	$1 = 0.9319 + 0.0040 \cos \frac{\pi}{6} \text{ (m} - 11.3)$			
1958 - 1964	+ 0 0340 cos $\frac{\pi}{3}$ (m 0 1)	+ 0 0010 cos $\frac{\pi}{3}$ (m 0 9)			
	•	-			
1965 1970	# = 0 3965 + 0 0445 cos 6 (+ - 1 7)	$1 = 0.9262 + 0.0013 \cos \frac{\pi}{6} \text{ (m} - 9.3)$			
1905 1970	+ 0 0266 cos $\frac{\pi}{3}$ ( $\tau$ 5 2)	+ 0 0010 $\cos \frac{\pi}{3} (\pi - 5.4)$			



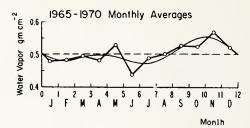


Fig. 2. Precipitable water above 700 mb calculated from National Climatological Summary monthly averages for Hilo, Hawaii. Upper curve is for 1950-1964, lower curve for 1965-70. Smooth curves show harmonic fits, dashed lines averages.

of the eruption is masked by the long-term average. Water vapor data are again erratic but appear to be more in phase with transmission and show a correlation coefficient of -0.64.

It is interesting at this point to consider precipitable water above Mauna Loa calculated from the monthly data in the *National Climatological Summary*. Fig. 2 shows monthly averages of precipitable water for 1950-64 and 1965-70. The semi-annual trend is very evident in 1950-64 but to a lesser extent in 1965-70. The data of 1950-64 have a much lower average value because of the use of the lithium chloride element through 1964. The results of a harmonic analysis are shown in Table 2.

The effects of variations of water vapor on solar radiation may be studied by referring to the works of Fowle (1915), MacDonald (1960) and Kondratyev (1969). All three agree that with about 0.5 gm cm<sup>-2</sup> of water vapor in the ray path, radiation depletion would amount to about 10% per gm cm<sup>-2</sup>. Note that typical fluctuations in water vapor have peak-to-peak variations of about 0.1 gm cm<sup>-2</sup>, which corresponds to a 1%

Table 2. Twelve-point harmonic analysis of precipitable water calculated from the *National Climatological Summary* for 1950-64 and 1965-70.

Years	Precipitable Water			
1950 - 1964	$W = 0.2217 + 0.0288 \cos \frac{\pi}{6} \text{ (m - 1.2)} + 0.0704 \cos \frac{\pi}{3} \text{ (m - 0.7)}$			
1965 - 1970	$w = 0.5048 + 0.0281 \cos \frac{\pi}{6} (m - 10.1) + 0.0227 \cos \frac{\pi}{3} (m - 1.6)$			

variation in solar radiation. Unfortunately, the phase angle of the water variations does not occur such that maximum water vapor coincides with minimum solar radiation. It appears, therefore, that on the basis of precipitable water calculations from radiosonde ascents, we must look to other causes for seasonal variations in solar radiation at Mauna Loa.

#### 3. Aerosols above Mauna Loa

In general, the atmosphere above Mauna Loa is extremely clean and fairly representative of a background tropospheric aerosol of continental origin (Simpson, 1972). Typical values for the total background aerosol mass at Mauna Loa Observatory are about 1 μg m<sup>-3</sup>. This is complicated further by a diurnal mountain wind system (Mendonca, 1969) that induces an upslope component during daytime and a downslope component at night. Consequently, a well-developed upslope windflow may penetrate the tradewind inversion (Mendonca and Iwaoka, 1969) bringing maritime and island aerosol components to Mauna Loa (Pueschel and Mendonca, 1972; Bodhaine and Pueschel, 1972). The cleanest time of the day, therefore, is in the early morning before upslope flow develops.

To predict the depletion of solar irradiance due to aerosols above Mauna Loa, it is particularly convenient to use Barrett's (1971) model, although it neglects absorption and longwave effects. This model includes both direct and diffuse radiation over the entire hemisphere, whereas the Mauna Loa data are taken in a 7° arc centered on the solar beam. However, at least 80% of the solar energy at Mauna Loa is contained in the solar beam (Barrett, personal communication; Kondratyev, 1969) and, in addition, in the following discussion we are concerned primarily with relative changes rather than absolute values of radiation. From Barrett (1971), for low particulate loads (<1000 gm per hectare), the percent depletion is a linear function of aerosol mass and may be represented by  $D=0.0\beta M$  at latitude 20N, where D is the percent depletion and M the global aerosol load (gm ha-1). In this linear region, any changes in aerosol will be reflected by  $\Delta D = 0.013 \ \Delta M$ .

If we first direct our attention to the major decrease in transmission occurring in 1963 after the Agung eruption, we find a decrease in average transmission of about 2% from the Mauna Loa data. According to Barrett's model, this corresponds to an addition of about 150 gm ha<sup>-1</sup>, or a total averaged over the globe of about 8×10<sup>6</sup> metric tons. Mitchell (1970) estimates independently that the eruption ejected approximately 15×10<sup>5</sup> tons of aerosol into the stratosphere. The agreement is excellent and strongly suggests that the Barrett model is applicable to explain the additional features of the Mauna Loa data.

A rather obvious tropospheric summer aerosol source, which is receiving more attention (Rasmussen and Went, 1965; Fish, 1972; Rasmussen, 1972) is that of

organic nature. Junge (1963) and Went (1966) estimate that the biosphere adds approximately (20-40) ×10<sup>5</sup> metric tons of aerosol of organic nature to the troposphere each summer. Atmospheric aerosol models (Valley, 1965) suggest that one-tenth of the tropospheric aerosol load may be located above the level of Mauna Loa, and it is reasonable to expect lateral transport of this continentally produced aerosol throughout the troposphere in a matter of weeks or months. This would amount to about 40 to 80 gm ha<sup>-1</sup> over Mauna Loa and would correspond to a seasonal variation in solar radiation of about 1% according to Barrett's model. Hence we see that a summer aerosol source of organic nature accounts very well for the seasonal trend in radiation observed at Mauna Loa.

# 4. Other atmospheric constituents above Mauna Loa

Other atmospheric variables, notably carbon dioxide and ozone, exhibit seasonal effects that may contribute to seasonal variations in solar radiation. However, these contributions will now be shown to be small. Absorption of solar radiation by carbon dioxide is very weak (Kondratyev, 1969; Möller, 1963), so that the 2% variation of carbon dioxide concentration with season, as measured at Mauna Loa (Machta, 1972), gives a negligible effect on solar radiation. Ozone measurements at Mauna Loa (Komhyr et al., 1971) show some scatter with deviations up to 5% but essentially no seasonal variation. Since total absorption of solar radiation by ozone amounts to only 2% (Kondratyev, 1969), any variations caused by ozone must be negligible. The choice of "control days" by Ellis and Pueschel (1971) was designed to eliminate any effects of clouds.

# 5. Discussion

Radiosonde humidity data taken at Hilo appear to be substantially more reliable after 1965, but are probably not reliable enough on the exceptionally clear days (defined as control days) to calculate sufficiently accurate values of precipitable water to rigorously explain variations in solar radiation. However, the data in Fig. 1 show that we may expect variations in water vapor of the order of 0.1 cm which would cause variations in solar radiation of about 1%. On the other hand, precipitable water calculated from the National Climatological Summary monthly average humidity data (Fig. 2) shows a very clear semi-annual cycle, which reflects storms and large-scale systems near Hawaii. Controlday data and the Climatological Summary data strongly resemble each other in amplitude and phase but not in overall average value. This suggests that the choice of "control days" has not eliminated the water vapor variable, as was intended by Ellis and Pueschel (1971), and that the water vapor content above Mauna Loa on a day-to-day basis could indeed be responsible for a

portion of the variations in solar radiation observed at Mauna Loa.

This was suggested by Pueschel et al. (1974) on the basis of correlations between solar radiation, infrared hygrometer precipitable water, radiosonde precipitable water, and solar aureole measurements taken on control days over the period from August 1971 to May 1972. Correlation between infrared hygrometer data and radiation data was considerably higher than that between radiosonde precipitable water and radiation data. The not unexpected conclusion is that radiosonde precipitable water calculations above Mauna Loa, although sufficient to give a rough estimate, are not accurate enough to apply as a direct correction, on a day-to-day basis, to Mauna Loa radiation data. The radiosonde humidity element is simply not sensitive enough to give reliable readings at the low values of temperature and humidity encountered above Mauna Loa. Although it is difficult to estimate the amplitude of variations in radiation due to water vapor, the phase relationship between water vapor and radiation is such that there must be an additional, stronger contribution from some other source.

Atmospheric aerosols have been suggested as sources contributing to the variations in solar radiation, and a springtime tropospheric source of natural aerosols of only  $(20\text{--}40)\times10^6$  metric tons of organic nature is likely to induce the observed variations and would provide the correct phase angle relationship. The presence of 50 gm ha<sup>-1</sup> over Mauna Loa amounts to only about 0.5  $\mu g$  m<sup>-3</sup>, less than that measured at Mauna Loa Observatory.

Although the above speculations await more precise measurements of water vapor and aerosols above Mauna Loa, seasonal variations in turbidity observed at Mauna Loa probably reflect variations in the naturally produced tropospheric background aerosol. Any changes in the amplitude or phase of this periodic function may indicate an increased anthropogenic aerosol load.

Acknowledgments. We thank Ed Flowers and Don Pack for their helpful comments, Howard Ellis for providing control day radiation data, and Fred Rangel and Mary Jane Foley, University of Colorado students, for performing many of the calculations. Dr. Bodhaine has been supported under a National Research Council Resident Research Associateship.

### REFERENCES

- Barrett, E. W., 1971: Depletion of short-wave irradiance at the ground by particles suspended in the atmosphere. *Solar Energy*, 13, 323-337.
- Bodhaine, B. A., and R. F. Pueschel, 1972: Flame photometric analysis of the transport of sea salt particles. J. Geophys. Res., 77, 5106-5115.
- Bryson, R. A., 1968: "All other factors being constant . . .". Weatherwise, 21, 56-61.
- Charlson, R. J., and M. J. Pilat, 1969: Climate: The influence of aerosols. J. Appl. Meteor., 8, 1001-1002.

- Dyer, A. J., and B. B. Hicks, 1968: Global spread of volcanic dust from the Bali eruption of 1963. Quart. J. Roy. Meteor. Soc., 94, 545-554.
- Eldridge, R. G., 1967: Water vapor absorption of visible and near infrared radiation. *Appl. Opt.*, **6**, 709–713.
- Ellis, H. T., and R. F. Pueschel, 1971: Solar Radiation: Absence of air pollution trends at Mauna Loa. Science, 172, 845-846.
- Elsaesser, H. W., R. F. Pueschel and H. T. Ellis, 1972: Turbidity of the atmosphere: Source of its background variation with season. *Science*, 176, 814-815.
- Fish, B. R., 1972: Electrical generation of natural aerosols from vegetation. *Science*, 175, 1239-1240.
- Flowers, E. C., R. A. McCormick and K. R. Kurfis, 1969: Atmo spheric turbidity over the United States, 1961–1966. J. Appl Meteor., 8, 955–962.
- Fowle, F. E., 1915: The transparency of aqueous vapor. Astrophys. J., 42, 394–411.
- Friedman, M., 1972: A new radiosonde case: The problem and the solution. Bull. Amer. Meteor. Soc., 53, 884-887.
- Gates, D. M., 1960: Near infrared atmospheric transmission to solar radiation. J. Opt. Soc. Amer., 50, 1299-1305.
- Harrison, L. P., 1970: Calculation of precipitable water. ESSA Tech. Memo. WBTM TDL 33.
- Junge, C. E., 1963: Air Chemistry and Radioactivity. New York, Academic Press, 382 pp.
- Komhyr, W. D., E. W. Barrett, G. Slocum and H. K. Weickmann, 1971: Atmospheric total ozone increase during the 1960's. Nature, 232, 390-391.
- Kondratyev, K. Y., 1969: Radiation in the Atmosphere. New York, Academic Press, 912 pp.
- List, R. J., 1966: Smithsonian Meteorological Tables. Smithsonian Institution Press, Washington, D. C.
- Machta, L., 1972: Mauna Loa and global trends in air quality. Bull. Amer. Meteor. Soc., 53, 402-420.
- McCormick, R. A., and J. H. Ludwig, 1967: Climate modification by atmospheric aerosols. Science, 156, 1358-1359.
- MacDonald, J. E., 1960: Direct absorption of solar radiation by atmospheric water vapor. J. Meleor., 17, 319-328.
- Mendonca, B. G., 1969: Local wind circulation on the slopes of Mauna Loa. J. Appl. Meteor., 8, 533-541.
- —, and W. T. Iwaoka, 1969: The trade wind inversion at the slopes of Mauna Loa, Hawaii. J. Appl. Meteor., 8, 213-219.
- Mitchell, J. M., Jr., 1970: A preliminary evaluation of atmospheric pollution as a cause of the global temperature fluctuation of the past century. *Global Effects of Environmental Pollution*, S. F. Singer, Ed., New York, Springer-Verlag, 218 pp.
- —, 1971: The effect of atmospheric aerosols on climate with special reference to temperature near the earth's surface. J. Appl. Meteor., 10, 703-714.
- Möller, F., 1963: On the influence of changes in the CO<sub>2</sub> concentration in air on the radiation balance of the earth's surface and on the climate. *J. Geophys. Res.*, **68**, 3877–3886.
- Morrissey, J. F., and F. J. Brousaides, 1970: Temperature induced errors in the ML-476 humidity data. J. Appl. Meteor., 9, 805-808.
- Pueschel, R. F., and B. G. Mendonca, 1972: Sources of atmospheric particulate matter on Hawaii. *Tellus*, 24, 139–149.
- ---, H. T. Ellis, G. F. Cotton, E. C. Flowers and J. T. Peterson, 1972: Normal incidence solar radiation trends on Mauna Loa, Hawaii. Nature 240, 545-547.
- --, C. J. Garcia and R. T. Hansen, 1974: Solar radiation: Effects of atmospheric water vapor and volcanic aerosols. J. Appl. Meteor., 13 (in press).
- Rasmussen, R. A., 1972: What do the hydrocarbons from trees contribute to air pollution? J. Air Pollut. Control Assoc., 22, 537-543.
  - -, and F. W. Went, 1965: Volatile organic material of plane origin in the atmosphere. *Proc. Nat. Acad. Sci.*, 53, 215-220.

- Reber, E. E., and J. R. Swope, 1972: On the correlation of the total precipitable water in a vertical column and absolute humidity at the surface. Rept. TR-0172 (2230 20)-13, The Aerospace Corporation, Los Angeles..
- Roosen, R. G., 1972: Unpublished data presented at ASTRA Symposium, University of Washington, April 1972.
- Salmela, H. A., and N. Sissenwine, 1970: A note on errors in upper air humidity climatology. J. Appl. Meteor., 9, 954-955.
- Simpson, H. J., 1972: Aerosol cations at Mauna Loa Observatory. J. Geophys. Res., 77, 5266-5277.
- Solot, S. B., 1939: Computation for depth of precipitable water in a column of air. Mon. Wea. Rev., 67, 100-103.
- Teweles, S., 1970: A spurious diurnal variation in radiosonde
- humidity records. Bull. Amer. Meteor. Soc., 51, 836-840. Valley, S. L., 1965: Handbook of Geophysics and Space Environments. Air Force Cambridge Research Laboratories.
- Went, F. W., 1966: On the nature of Aitken condensation nuclei. Tellus, 18, 549-556.
- Whiting, D. M., 1971: Errors in upper air humidity climatology. J. .1 ppl. Meteor., 10, 833-834.

#### PHYSICAL BASIS FOR SEEDING COLD OROGRAPHIC CLOUDS

# Charles F. Chappell

Atmospheric Physics and Chemistry Laboratory NOAA, Boulder, Colorado 80302

#### INTRODUCTION

A physical basis for seeding cold orographic clouds was presented by Bergeron (1949). He suggested an efficient precipitation release might depend upon temperature, size and concentration of cloud droplets, and the ratio of droplet concentration to effective ice nuclei concentration. He concluded that a substantial potential for precipitation augmentation would exist in supercooled orographic clouds with temperatures warmer than -10°C.

Ludlam (1955) presented a more detailed treatment on the physics of seeding cold orographic clouds. Cloud efficiency was considered by comparing the growth rate of ice by deposition to the growth rate of liquid water in the cloud system. He emphasized that increases in precipitation efficiency would depend not only upon increased cloud efficiency, but also upon crystal settling speeds and the speed of the wind flow over the mountain barrier.

The Climax Experiment (Grant and Mielke, 1967) was, to a large extent, designed to test the cloud seeding concepts presented by Ludlam. These basic concepts can be demonstrated graphically by using a rather simple lagrangian cloud model. It is the purpose of this paper to illustrate these fundamental physical concepts.

#### 2. DEFINITION OF CLOUD EFFICIENCY

Any definition of cloud efficiency (CE) is somewhat arbitrary. We define CE as the snow content of a cloud parcel compared to the available snow potential (ASP) of that cloud parcel, where snow refers to all forms of ice. ASP can be, in turn, partitioned into the sum of three components; the liquid water in the parcel at the origin of its trajectory over the orographic barrier, the increment of liquid water that is produced by condensation as the parcel is lifted from the origin of its trajectory to the crest (assuming water saturation), and the increment of vapor representing the difference between water and ice saturation at the crest temperature. In other words, the maximum accumulation of snow in the cloud parcel is realized when the initial liquid water is converted to ice and the parcel reaches the crest saturated with respect to ice. This maximum obtainable snow content is defined as the ASP and is given by

$$ASP = q_{\ell} + [q_{W}(T_{b}) - q_{W}(T_{c})] + [q_{W}(T_{c}) - q_{i}(T_{c})],$$
[1]

and CE is then

$$CE = \frac{(q_S)}{[q_Q + q_W(T_b) - q_i(T_C)]},$$
 [2]

where symbols are defined in an appendix.

#### 3. CLOUD MODEL

2 0

10

20

Temporal changes in supersaturation with respect to ice of a mixed phase cloud parcel are given by

$$\dot{S}_{i} = \phi_{1} w - \phi_{2} N_{d} \dot{M}_{d} - \phi_{3} N_{c} \dot{M}_{c} - (1 + S_{i}) (1 - \phi_{4} N_{d} M_{d} - \phi_{5} N_{c} M_{c}) (\frac{\rho}{\rho}) .$$
 [3]

Eq. 3 gives the cloud supersaturation as a function of the interplay among the updraft speed, crystal concentration and growth rate, and droplet concentration and growth rate. This equation is integrated along the trajectory depicted in Figure 1 to obtain the trend of cloud supersaturation over the orographic barrier. The height of the trajectory is given by  $z=-2.449(10^{-5})d^3\neq 1.51(10^{-3})d^2\neq 3.2$ , and the vertical velocity along it by  $w=-7.346(10^{-5})d^2u\neq 3.02(10^{-3})du$ . Crystal settling speeds are computed from the empirical relation determined by Brown (1970), or  $V_{\rm C}=620^{0.217}$ .

An upwind site is specified in Figure 1 about 20 km downwind from the trajectory origin where the updraft has a maximum value. This upwind site will be referred to again when discussing the results of the various integrations of [3].

Initial conditions specified for the cloud parcel at the trajectory origin include: pressure, 680 mb; temperature, -2.5°C; droplet concentration, 300 per cm<sup>3</sup>; liquid water content, 1 gm/m<sup>3</sup>; and water vapor content, 4.07 gm/m<sup>3</sup>. Saturation with respect to water was assumed for the cloud parcel at the origin. Results of eight integration runs are shown in Figures 2-9 and in Table 1.

TABLE 1. Conditions at selected points along the trajectory.

			UPWIN	D SITE	CRES	T	PT. OF	MAX.	SNOW ACCU	
	u	N <sub>C</sub>	CE	٧ <sub>c</sub>	CE	٧ <sub>c</sub>	CE	٧ <sub>c</sub>	Dista from o	
	m/sec	/liter	%	cm/sec	% сп	/sec	% c	m/sec	kr	
Run	1 10	1	0.7	44	5.0	54	13.1	60	26	DW
Run	2 10	10	6.8	43	49.0	54	88.1	57	11	DW
	3 10	200	74.1	41	100.0	42	100.0	42	0	
Run		2000	75.5	32	100.0	33	100.0	33	0	
	5 30	1	0.1	34	0.5	42	1.5	47	26	DW
	6 30	10	0.7	34	5.1	42	14.4	47	25	DW
Run		200	14.0	34	95.8	42	99.9	42	1	DW
Run	8 30	2000	73.3	30	100.0	33	100.0	33	0	
5		·								
3	ORIG	GIN		SITE		CREST (w = 0)				

HORIZONTAL DISTANCE - d (km)
FIGURE 1. Cloud Parcel Trajectory Used for Computations.

40

50

60

70

30

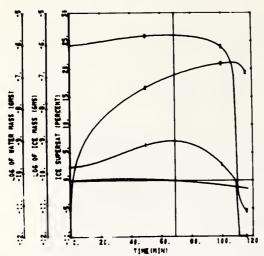


Fig. 2. Trend of supersaturation (curve 1), cloud ice (curve 2), cloud water (curve 3), and vertical velocity (not numbered and plotted in mps on the supersaturation scale) for Run 1.

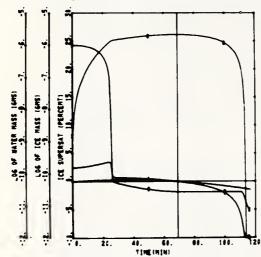


Fig. 4. As in Fig. 2 except for Run 3.

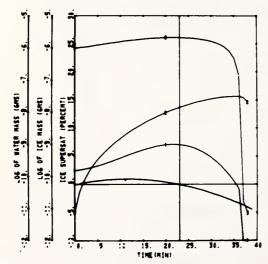


Fig. 6. As in Fig. 2 except for Run 5.

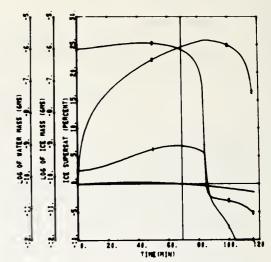


Fig. 3. As in Fig. 2 except for Run 2.

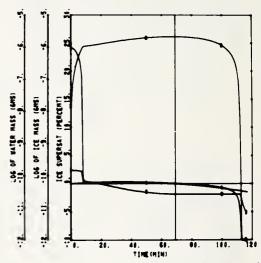


Fig. 5. As in Fig. 2 except for Run 4.

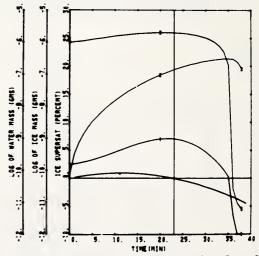


Fig. 7. As in Fig. 2 except for Run 6.

#### 4. RESULTS

The results of Run 1 are shown in Figure 2. Note that with the nucleation of one crystal per liter, the cloud remains considerably above ice saturation to the lee of the crest, and snow continues to grow in the cloud up to 26 km downwind of the summit. The cloud also contains more liquid water than ice for up to 23 km downwind of the crest. From Table 1 it is seen that CE is very low for Run 1. Only 0.7% of the ASP is realized at the upwind site, increasing to 5% at the crest, and reaching a maximum of 13.1% at a distance of 26 km downwind of the summit.

The same initial conditions apply for Run 2 (Figure 3) except that 10 crystals per liter are nucleated. Note that the cloud remains above ice saturation until sudden glaciation occurs about 11 km downwind of the summit. Again, snow continues to grow in the cloud up to 11 km downwind of the summit. Equal parts of cloud ice and liquid cloud water now appear at the summit. CE (Table 1) is much improved but snow accumulation

remains below the ASP everywhere along the trajectory.

Initial conditions for Run 3 (Figure 4) remain the same except that 200 crystals per liter are now nucleated. Rapid glaciation on the upwind side of the crest now occurs. Simultaneously, cloud supersaturation falls abruptly to just slightly above ice saturation, remains there until the crest and then drops below ice saturation to the lee of the crest. Essentially, an ice cloud is present now extending from the upwind site over the crest to several km leeward of the summit. Note in Table 1 that all the ASP (100% CE) is now realized at the crest, while 74.1% is obtained at the upwind site. This is nearly the maximum obtainable (actually 75.5% is possible) at the upwind site, since there is less total lifting realized there as compared to the crest. Note that the settling speed of crystals at the crest has decreased 12 cm/sec compared to Run 2.

Run 4 (Figure 5) yields results for a crystal concentration of 2000 per liter. Extremely rapid glaciation of the cloud occurs and CE is maximized over much of the upwind trajectory. A slight supersaturation with respect to ice continues to promote snow growth up to the crest. A decrease in crystal settling speed of 9 cm/sec over most of the trajectory is noted compared to Run 3. This suggests that snowfall redistribution is likely with these crystal concentrations, and that the threshold of overseeding may

be near.

Figures 6-9 show results for similar initial conditions, except the horizontal speed along the trajectory is increased to 30 meters per second. While greater vertical velocities also accompany these stronger horizontal wind speeds, the shorter residence times for microphysical processes to transpire tends to produce even loss CF for a given exectal consentration

pire tends to produce even less CE for a given crystal concentration.

Note the results of Run 5 (Table 1) that show less than 2% of the ASP is realized anywhere along the trajectory. It is evident from Figure 6 that the cloud remains considerably above ice saturation to the lee of the crest, and again snow continues to grow in the cloud up to 26 km downwind of the summit. Mainly a water cloud extends from upwind on over the crest to a considerable distance downwind.

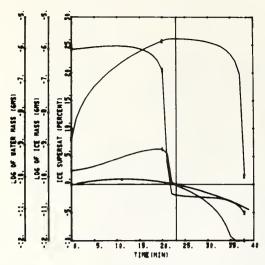


Fig. 8. As in Fig. 2 except for Run 7.

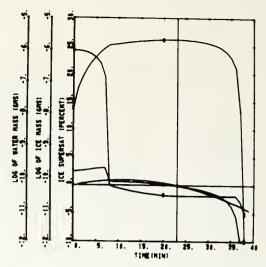


Fig. 9. As in Fig. 2 except for Run 8.

A major difference is seen in the results of Run 6 (Figure 7 and Table 1) when compared to Run 2, even though these runs have identical initial conditions except for the difference in horizontal wind speed. Note that in spite of the presence of 10 crystals per liter, less than 1% of the ASP is realized at the upwind site, and only 5.1% is obtained at the summit. This represents nearly an order of magnitude less snow production than obtained under the lighter wind condition. Snow growth and the liquid water cloud persist 25 km downwind of the crest, even though the crystal concentration is 10 per liter.

Note for Run 7 (Figure 8 and Table 1), that in spite of a concentration of 200 crystals per liter, only 14% of the ASP is realized at the upwind site, and 100% CE is not quite achieved anywhere along the trajectory. For this case snow growth persists only slightly leeward of the crest.

The results of Run 8 (Figure 9 and Table 1) show that for a concentration of 2000 crystals per liter only 40.7% of the ASP is realized at the upwind site. This is about half that obtained under the lighter wind conditon. Full CE is realized at the crest, and again, crystal settling speeds suggest that snowfall redistribution is likely and that the threshold of overseeding may be near.

#### 5. CONCLUSIONS

This relatively simple microphysical model enables one to define the physical processes that control efficiency of cold orographic clouds and the potential for snow augmentation. This potential and CE are largely dependent upon crystal concentrations in the cloud. Since these concentrations are observed to generally decrease with warmer cloud top temperatures and ASP increases with cloud temperature for a given trajectory and initial conditions, one would expect seeding effectiveness to increase with cloud temperature. This dependence of seeding effectiveness upon cloud temperature was an important finding of the Climax Experiment.

It is evident from the results presented that the objectives and constraints of a modification program must be clearly defined before seeding delivery systems, seeding rates, and opportunity recognition criteria are selected. Whether snow is to be maximized on the upwind side, at the crest, on the lee side, or optimized

on the barrier will affect overall seeding strategy.

Redistribution and targeting of snowfall are affected by changes in ing growth, crystal habit, crystal size, as well as agglomeration. Since these processes are influenced by cloud supersaturation and cloud liquid water, which in turn respond to changing crystal concentrations, it should be possible to redistribute and target snowfall through seeding.

It may be expecially difficult to concentrate snowfall on the upwind side during strong wind conditions. The reason is that the larger crystal concentrations needed for timely upwind glaciation lead to smaller crystals, which may consequently experience even more difficulty in settling to the upwind surface. Under these conditions the increased CE on the upwind side may not necessarily be realized at the ground as increased precipitation.

Acknowledgments. The author is indebted to Mr. David R. Smith for programming assistance and several helpful discussions.

#### APPENDIX List of Symbols

horizontal distance downwind from trajectory origin d D crystal diàmeter mass of ice crystals and of cloud droplets concentration of ice crystals and of cloud droplets mixing ratio of liquid water and of cloud ice saturation vapor mixing ratio with respect to water and ice ٩i supersaturation with respect to plane ice temperature at the trajectory origin temperature at the crest of the trajectory horizontal wind speed along the trajectory crystal settling speed updraft speed along the trajectory height of the trajectory above mean sea level thermodynamic functions  $\phi_2, \phi_3, \phi_4, \phi_5$ air density dots indicate total differentiation with respect to time

#### REFERENCES

Bergeron, T., 1949: The problem of an artificial control of rainfall on the globe; I. General effects of ice-nuclei in clouds. <u>Tellus</u>, 1, 32-50.

Brown, S.R., 1970: Terminal velocities of ice crystals. <u>Atmos. Sci. Paper</u> 170, Dept. of Atmos. Sci., Colorado State U., Fort Collins, 52 pp.

Grant, L.O., and P.W. Mielke, Jr., 1967: A randomized cloud seeding experiment at Climax, Colorado, 1960-65. Proc. of the Fifth Berkeley Symposium on Math. Statis. and Prob., 5, 115-131.

Ludlam, F.H., 1955: Artificial snowfall from mountain clouds. <u>Tellus</u>, 7, 277-290.

### Potential for Snow Augmentation in Cold Orographic Clouds

CHARLES F. CHAPPELL

Atmospheric Physics and Chemistry Laboratory, NOAA, Boulder, Colo. 80302

FLOYD L. JOHNSON

Woodward-Envicon, Inc., Scottsdale, Ariz.

(Manuscript received 14 August 1973, in revised form 28 January 1974)

#### ABSTRACT

A simple numerical model is formulated for a mixed-phase cold cloud which simulates the interaction among the updraft, crystal growth, droplet growth or evaporation, and ice crystal concentration. The model accounts for temperature and pressure changes due to vertical displacements, and crystal concentrations are specified as a function of cloud-top temperature. Cloud temperature and updraft speed were varied in the model and equations integrated for a time period of up to 1 hr. Results indicate that a cloud-top temperature of about  $-25 \mathrm{C}$  will demarcate cold orographic cloud systems with respect to a potential for snowfall augmentation. There is also a suggestion that the concentrations of artificial ice nuclei, one would add to maximize snowfall, probably need not be considered single-valued. Rather, it appears that crystal concentrations may exceed a critical concentration by an order of magnitude without noticcable adverse effects on precipitation efficiency, even in the absence of agglomeration mechanisms.

#### 1. Introduction

It was suggested early (Wegner, 1911) that ice crystals would grow rapidly within supercooled water clouds. However, it was not until Schaefer (1946) demonstrated the conversion of a supercooled water cloud to ice, and Vonnegut (1947) reported a method for nucleating ice formation on a large scale in the atmosphere, that attempts at precipitation augmentation began in earnest.

A physical basis for seeding cold orographic clouds was presented by Bergeron (1949). He suggested that a natural ice nuclei precipitation release might have an optimum response that depended upon 1) temperature, 2) size and concentration of cloud droplets, and 3) the ratio of droplet concentration to effective ice nuclei concentration. Moreover, Bergeron predicted that a substantial potential for precipitation augmentation would exist in orographic clouds containing sufficiently strong updrafts, which surpass the 0C isotherm, but not the -10C isotherm.

Ludlam (1955) developed further the ideas expressed by Bergeron. He considered orographic cloud efficiency through comparison of the growth rate of ice by vapor deposition to the growth rate of liquid water in the cloud system. Ludlam also pointed out that artificially induced increases in precipitation efficiency would depend not only upon increased cloud efficiency, but also upon crystal settling speed and the velocity of the wind flow over the mountain barrier.

Precipitation inefficiency associated with cold orographic clouds is manifested in two distinct ways. If a mixed-phase cold cloud is slightly supersaturated with respect to water and crystal concentrations are very small, cloud droplets grow and liquid water accumulates in the updraft only to evaporate in the subsiding air to the lee of the mountain barrier. This liquid water is therefore not realized as precipitation on the mountain. On the other hand, if crystal concentrations are too large, a rapid glaciation may be produced. Under these conditions the cloud quickly approaches ice saturation, and the slow crystal growth that results may not lead to the timely production of precipitation size particles. Crystals may then be carried over the barrier to evaporate in the subsiding air in the lee of the mountain barrier, or in the subcloud layer.

One can envisage that somewhere between the two situations described above there exists a critical crystal concentration, or perhaps a range of crystal concentrations, that will convert the cloud liquid water to ice growth within the transit time available, and in a form to bring precipitation to the mountain surface. One can further envisage that a goal of cloud seeding should be to minimize, or climinate, this evaporative loss of liquid water, by adding effective artificial ice nuclei to the cloud when needed, and in sufficient numbers to produce at least the critical crystal concentration. As demonstrated by Jiusto (1971), one can affect the historical trend of cloud supersaturation, and control the elapsed time required for glaciation, by varying

the crystal concentration in the cloud. The problem to be addressed here is how to recognize which clouds are naturally inefficient and present seeding opportunities.

The requirement of a critical ice concentration to bring about complete cloud glaciation was presented in terms of fixed values of liquid water content by Twomey (1958) and Todd (1964). Jiusto (1968) reported a general expression for critical ice crystal concentrations that accounted for the variable generation rate of water vapor in a cloud, and the rate of extraction of vapor onto ice crystals of given type and size. Grant *et al.* (1968) and Chappell (1970b) demonstrated the dependence of the critical ice crystal concentration upon cloud temperature.

A time-dependent equation for the supersaturation of a mixed-phase cold cloud was presented by Jiusto and Schmitt (1970) and Jiusto (1971), which provided the basis for formulating a cold cloud microphysical model. Realistic numerical modeling of such clouds is complicated by variations in crystal types, vapor diffusion fields, crystal settling speeds, uncertainties in crystal-droplet and crystal-crystal interactions, and possible existence of crystal enhancement processes. Nevertheless, this unsophisticated one-dimensional model simulated many features observed during Great Lakes snowfall episodes.

In the following work, we present a slightly more rigorous form of the supersaturation equation. Then, similar to Jiusto's (1971) approach, this equation is used to formulate a simple microphysical model for application to supercooled orographic clouds.

The present model differs from the one presented by Jiusto (1971) in that it accounts for temperature and pressure changes due to vertical displacement, and crystal concentrations are not specified arbitrarily, but as a function of cloud-top temperature. Time changes in cloud supersaturation are determined as a function of ice nuclei concentration (or essentially cloud-top temperature) and the interaction among the updraft, crystal growth, and droplet growth or evaporation. These results are then applied to the problem of demarcating conditions associated with an opportunity to increase snowfall by seeding cold orographic clouds.

#### 2. Model equations

#### a. Cloud supersaturation

Temporal changes in the supersaturation of a mixedphase cold cloud are given by

$$(dS_i/dt) = \phi_1 U - \phi_2 V_d (dm/dt)_d - \phi_3 V_c (dm/dt)_c, \quad (1)$$

where  $(dm/dt)_c$  and  $(dm/dt)_d$  are mass growths by vapor diffusion of an ice crystal and a cloud droplet, respectively. Other symbols are defined in the Appendix.

The thermodynamic functions appearing in (1) are evaluated by

$$\phi_1 = \frac{cgeL_s}{c_iR_dT^2C_p} - \frac{cg}{e_iR_dT},\tag{2}$$

$$\phi_2 = \frac{e\epsilon L_c L_s}{e_i C_n PT} + \frac{R_d T}{e_i \epsilon},\tag{3}$$

$$\phi_3 = \frac{c\epsilon L_s^2}{e_i C_p P T} + \frac{R_d T}{e_i \epsilon}.$$
 (4)

Expressions similar to (1)-(4) were presented by Jiusto (1971). However, he assumed that  $e/e_i \approx 1$  and dropped this ratio from the equations. Furthermore, the diffusional ice growth term was added to (1) while maintaining thermodynamic functions  $\phi_1$  and  $\phi_2$  in a form applicable strictly for warm clouds. Differences in results stemming from these two forms of the supersaturation equation appear minor.

#### b. Droplet growth

The equation for the growth of water droplets by vapor diffusion is given by Fletcher (1962) as

$$(dm/dt)_d = 4\pi r_d \rho_w G \left( S_w - \frac{a}{r_d} + \frac{b}{r_d^3} \right). \tag{5}$$

The Kelvin curvature term is evaluated by  $a=3.3 \times 10^{-5}/T$ , and the nucleus solubility term, given by Mason (1971), is computed by  $b=8.6m/M_s$  for a dilute sodium-chloride nuclei. Condensation nuclei are assumed to be sodium chloride with radii equal to  $0.1 \, \mu \text{m}$ . The thermodynamic function is evaluated from

$$G = \left(\frac{L_c^2}{R_c T^2 K} + \frac{R_v T}{e_{cD}}\right)^{-1}.$$
 (6)

The mass of each water droplet is related to its radius by

$$m = 4\pi r_d^3 \rho_w / 3,\tag{7}$$

where  $\rho_w = 1$  gm cm<sup>-3</sup>.

#### c. Crystal growth

The equation for the growth of ice crystals by vapor diffusion is given by Fletcher (1962) as

$$(dm/dt)_c = 4\pi C S_i G' \rho_i, \tag{8}$$

where G' is a thermodynamic function defined by

$$G' = \left(\frac{L_s^2}{R_v T^2 K} + \frac{R_v T}{e_i D}\right)^{-1}.$$
 (9)

Ice crystals are assumed to be planar disks with  $C = 2r_c/\pi$ , and the empirical relationship derived by Nakaya and Terada (1934) is used for converting crystal mass to crystal radius. This relationship is  $r_c = (m_c/0.00152)^{\frac{1}{2}}$  for a planar disk.

#### d. Crystal concentration

Ice crystal concentrations are assumed to be homogeneous in the cloud, and specified by the number of ice

TABLE 1. Initial conditions of cloud supersaturation (ice), cloud-top temperature, and effective ice nuclei concentrations specified as a function of cloud-base temperature for a model cloud with base and top at 750 and 500 mb, respectively. A pseudo-adiabatic lapse rate is assumed for the cloud layer to define cloud-tor temperature and initialize ice nuclei concentration.

Cloud-base temperature (°C)	Ice supersaturation ((,0)	Cloud-top temperature (°C)	Number of ice nuclei (liter <sup>-1</sup> )
0.0	0.0	-21.5	4
-2.5	2.5	-24.9	30
-5.0	5.0	-28.2	223
-7.5	7.6	-31.4	1521

nuclei effective at cloud-top temperature and warmer. The average temperature activation spectrum of ice nuclei given by Fletcher (1962) is employed to define the crystal concentrations. Natural crystal concentrations are therefore given by

$$N_c = 10^{-5} \exp(-0.6T_c),$$
 (10)

where  $T_c$  is the cloud-top temperature (°C), and a one-to-one correspondence between ice nuclei concentrations effective at cloud-top temperature and ice crystal concentrations is assumed.

#### e. Vertical changes

Changes in parcel temperature due to vertical displacements and the release of latent heat are solved from the relation  $dT = (L_c dW + L_s dI - g dZ)/C_p$ . This relationship stems from the atmospheric energy equation for a cold cloud parcel after 1) assuming a steady-state pressure field and frictionless flow, and 2) neglecting other non-adiabatic heating effects and the small contribution of the kinetic energy term.

Changes in pressure resulting from vertical displacement are given by the hydrostatic equation.

#### f. Initial conditions

The computer program requires the specification of initial conditions for temperature, pressure, droplet

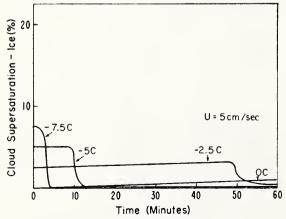


Fig. 1. Trend of cloud supersaturation (ice) with time for various cloud-base temperatures and an updraft of 5 cm sec<sup>-1</sup>.

radius and concentration, ice crystal radius and concentration, supersaturation with respect to ice, and updraft speed. An orographic cloud with base at 750 mb and top at 500 mb is taken as representative of winter cloud systems over the western United States. Cloud base temperature, therefore, becomes the initial temperature of the cloud parcel. A pseudo-adiabatic lapse rate is then assumed for the cloud layer to determine cloud-top temperature and specify the crystal concentration for the parcel.

Fixed initial conditions of model parameters include:

$$N_d = 300 \text{ cm}^{-3};$$
  $r_c = 0.1 \mu\text{m}$   
 $r_d = 7 \mu\text{m};$   $P = 750 \text{ mb}$ 

The cloud model was run for updraft speeds of 5 cm sec<sup>-1</sup>, 20 cm sec<sup>-1</sup>, and 1 m sec<sup>-1</sup> for each set of initial conditions. In turn, for each updraft speed cloud base temperatures of 0, -2.5, -5 and -7.5C were employed.

Cloud supersaturation was initialized for each cloud base temperature by using the relation  $S_i = (e_w/e_i) - 1$ , with the assumption that the cloud was initially at water saturation. See Table 1 for initial values of cloud supersaturation.

#### g. Computer program

A fourth-order Runge-Kutta method was used to numerically solve the above set of equations. Time steps employed in the numerical integration were 0.01 sec initially, 0.1 sec after crystal mass exceeds  $5\times10^{-8}$  gm, and 1.0 sec after crystal mass exceeds  $5\times10^{-7}$  gm.

#### 3. Results

Time histories of cloud supersaturation are shown in Figs. 1–3 as a function of updraft speed and cloud temperature. Updraft speeds of 5 cm sec<sup>-1</sup>, 20 cm sec<sup>-1</sup>, and 1 m sec<sup>-1</sup> are depicted, along with cloud-base temperatures of 0, -2.5, -5.0 and -7.5C. Cloud-base temperatures warmer than 0C are not displayed because

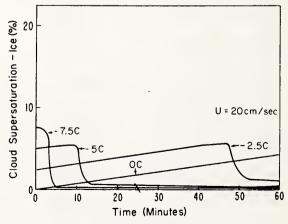


Fig. 2. As in Fig. 1 except for an updraft of 20 cm sec<sup>-1</sup>.

glaciation was not attained within an hour of elapsed time. For cloud-base temperatures of -10C and colder, concentrations of effective ice nuclei are of such magnitude as to produce glaciation within an elapsed time of  $1\frac{1}{2}$  min for all updraft speeds. These runs are therefore not displayed.

Note from Figs. 1-3 that four ice nuclei per liter (OC cloud-base temperature) of air are not sufficient to glaciate the model cloud within 1 hr even in a weak updraft of 5 cm sec<sup>-1</sup>. However, crystal concentrations of about 30 liter<sup>-1</sup> (cloud-base temperature colder than -2.5C) will glaciate the model cloud within 1 hr even for relatively strong updrafts of 1 m sec<sup>-1</sup>. These results are consistent with those presented by Jiusto (1968, 1971), Grant et al. (1968) and Chappell (1970b).

Note also in these figures that for a given cloud temperature, the greater the value of cloud supersaturation attained prior to glaciation, the more abruptly cloud supersaturation falls during the glaciation process and the larger the value assumed after the glaciation episode.

Time histories of ice crystal growth are depicted in Figs. 4–6. Note that initial crystal growth is rapid and crystals with appreciable fallspeeds are realized within 10 min. An exception is the warmest cloud system, which combines with weak updrafts to produce unusually slow crystal growth. The rate of crystal growth is also seen to slow markedly after glaciation in response to low values of cloud supersaturation.

Time histories of droplet growth are shown in Figs. 7-9. Note that evaporation of supercooled water droplets reaches a maximum during glaciation as would be expected. Nearly all liquid water is converted to ice during glaciation, although droplet radii tend to stabilize around  $1 \mu m$  or less after the main glaciation episode. This stabilization is apparently due to the interplay between cloud supersaturation, the Kelvin curvature term, and the nucleus solubility term in (5), which

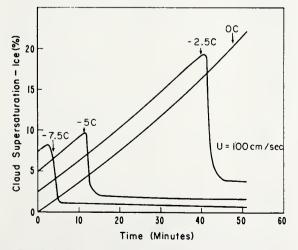


Fig. 3. As in Fig. 1 except for an updraft of 100 cm sec-1.

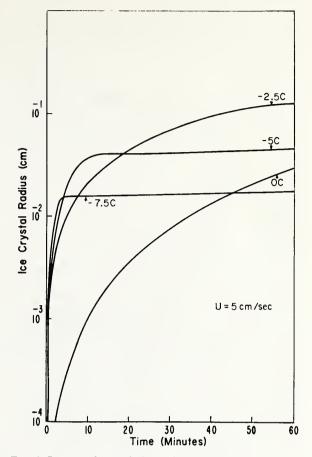


Fig. 4. Ice crystal growth for various cloud-base temperatures and an updraft of 5 cm sec<sup>-1</sup>.

reduces the evaporation rate of the droplets to near zero before total evaporation is complete.

For purposes of targeting snowfall, a one-dimensional model is obviously not satisfactory. However, by selecting an interval of time for a cloud parcel to traverse an orographic updraft, inferences regarding the presence of a potential for snowfall enhancement can be made. Assume 50 min as a representative interval of time for a cloud parcel to traverse an orographic updraft in the western United States. To optimize snowfall, it would be desirable to have glaciation occur and grow the maximum snow content in the cloud parcel before it leaves the orographic updraft. In addition, individual crystals must grow sufficiently large for snow to eventually settle to the mountain surface.

Fig. 10 depicts cloud supersaturation, snow crystal radius, and snow content after an elapsed time of 50 min as a function of cloud-top temperature. Results for three different updraft speeds are included. Note for a cloud-top temperature around -25C that 1) glaciation has occurred for all updraft speeds, 2) total snow content of the cloud parcel has stabilized near a maximum value, and 3) snow crystal size has attained or remains

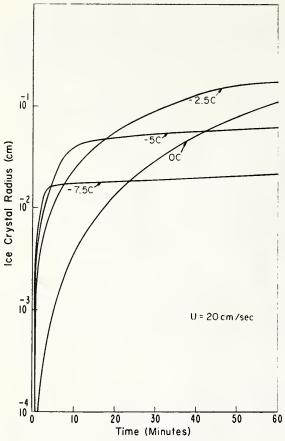


Fig. 5. As in Fig. 4 except for an updraft of 20 cm sec<sup>-1</sup>.

near a peak value. All criteria for optimizing snowfall have therefore been fulfilled. A potential for increasing snowfall will exist then, only for cloud systems warmer than the above critical temperature. Cloud systems colder than the above temperature will have no potential for increased snowfall. Note also for temperatures lying immediately below -25C, that snow content is relatively constant while crystal size decreases rapidly, although individual crystal sizes remain sufficiently large for crystals to settle to the mountain surface. Hence, there is probably little loss in precipitation efficiency in this temperature range. For cloud-top temperatures of -30C and colder, however, natural crystals are of such size that further increases in crystal concentrations from cloud seeding might appreciably reduce crystal settling speeds and bring about an adverse affect on crystal trajectories to produce overseeded conditions. The maintenance of natural snowfall efficiency indicated between cloud-top temperatures of -29 and -25C suggests that the concentrations of artificial ice nuclei that one would add to maximize snowfall, probably need not be considered single-valued. Rather, it appears that crystal concentrations may exceed a critical value by an order of magnitude without noticeable adverse effects on precipitation efficiency,

even in the absence of agglomeration mechanisms. This is consistent with estimates of Ludlam (1955), who suggested that ice nuclei could be in excess of a critical concentration by a factor of 10 before effects of overseeding come into play.

The demarcation of modification potential near a cloud-top temperature of -25C is in good agreement with many results reported from cold orographic cloud seeding experiments. These include Climax I, Climax II, Monarch and Wolf Creek experiments in southern and central Colorado (Grant et al., 1971), the Park Range experiment in northern Colorado (Rhea and Davis, 1970), the Wasatch mountain experiment in Utah (Chappell, 1972), and the Jemez Mountain experiment in New Mexico (Keyes et al., 1973).

#### 4. Model versus reality

The simplified universe of this model departs somewhat from conditions found in real cold orographic clouds. Simplifications include 1) neglect of the variation of crystal habit with temperature, 2) neglect of crystal growth by accretion, 3) specification of crystal concentration by cloud-top temperature with neglect of possible crystal enhancement processes, 4) the

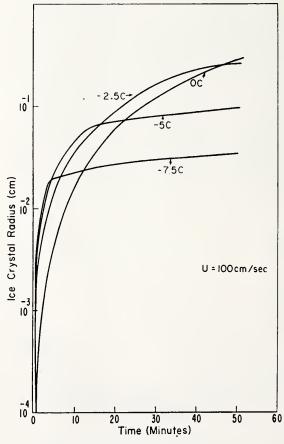


Fig. 6. As in Fig. 4 except for an updraft of 100 cm sec-1.

assumption that crystal concentrations are homogeneous throughout the cloud, and 5) specification of certain initial conditions.

Large spatial and temporal variations of ice nuclei concentrations in the atmosphere may cause concentrations observed at a given time and place to differ substantially from those given by (10). This problem can be lessened by monitoring temperature activation spectra of ice nuclei at a given location, and replacing (10) by relationships determined on a real-time basis.

The venturesome method of estimating ice crystal concentrations from cloud-top temperature, through application of ice nuclei temperature activation spectra, is of some concern. In view of the well-known uncertainties concerning ice nuclei measurements and crystal enhancement processes, it is possible that crystal concentrations in clouds may not correspond to ice nuclei concentrations specified from measured temperature activation spectra.

It is outside the scope of this paper to fully discuss possible crystal enhancement processes, but present evidence suggests that prolific crystal multiplication may be confined mainly to cumulus clouds (Mossop, 1970). Grant (1968) found the correspondence of crystal concentration to ice nuclei concentration effective at cloud-top temperature to be within a factor of 10 for continental orographic clouds in central Colorado. However, Auer et al. (1969) found a larger disparity between these concentrations for an isolated cap cloud in southern Wyoming. Hobbs (1969) noted that observations of the ratio of ice crystal concentration to ice nuclei concentration effective at cloud-top temperature, reported by several investigators for various cloud systems (maritime and continental characteristics as well as cumulus and orographic types), crudely indicated an exponential increase of this ratio with summit temperatures above about -25C. This

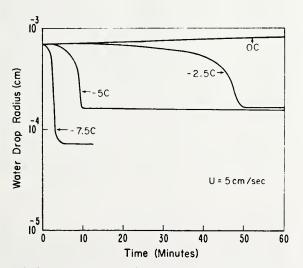


Fig. 7. Cloud droplet growth (evaporation) for various cloud-base temperatures and an updraft of 5 cm sec<sup>-1</sup>.

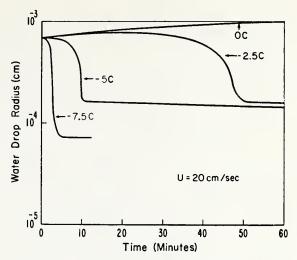


Fig. 8. As in Fig. 7 except for an updraft of 20 cm sec<sup>-1</sup>.

ratio, however, was near unity for cloud-top temperatures around -25C and colder.

The obvious question at this point is whether crystal enhancement processes in cold orographic clouds are sufficient, at the appropriate temperatures, to displace the demarcation of seeding potential toward warmer cloud-top temperatures, or possibly even obliterate such potential. Unfortunately, this question cannot be answered conclusively at this time, but results from the several cold orographic cloud seeding experiments mentioned above suggest a limiting, rather than an eliminating, of seeding potential. Moreover, only minor

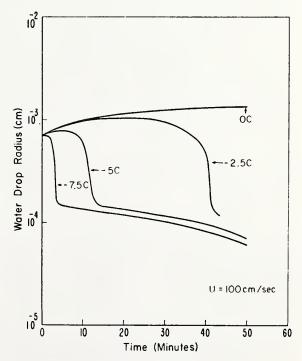


Fig. 9. As in Fig. 7 except for an updraft of 100 cm sec-1.

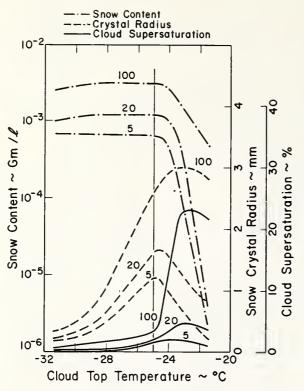


Fig. 10. Cloud supersaturation (ice), crystal radius, and snow content after 50 min as a function of cloud-top temperature for various updraft speeds.

displacements of the summit temperature that demarcates seeding potential are indicated by these same experimental results.

The assumption that crystal concentrations are homogeneous throughout the cloud is also at some variance with conditions found in real clouds. However, for orographic clouds with no convective elements and containing updraft speeds less than crystal fall velocities, this assumption may be tolerable. In this case, the great majority of ice crystals will nucleate in the coldest upper region of the cloud, and settle through the cloud in rather homogeneous concentrations. Orographic clouds containing strong convective elements, substantial ice crystal enhancement processes, or large updraft speeds would likely contain more heterogeneous crystal concentrations.

It is difficult to realistically specify initial conditions for ice crystal size. It follows, from assuming crystals nucleate near cloud top and settle through the cloud, that crystal sizes in the cloud increase downward to cloud base. This conflicts, however, with initial conditions which assign a  $0.1\,\mu\mathrm{m}$  radius to ice crystals at cloud base, and allows crystal growth to occur within a parcel as it ascends in the updraft. The historical trend of total ice growth in the parcel is thus affected by the choice of initial conditions, and the choice made here leads to underestimates by the model of initial

growth rates. The choice of disk-shaped crystals to represent growth habits for all temperatures was made for purposes of simplification. It is well established, however, that crystal growth habits are a function of environmental habitat, especially of temperature and to some extent of supersaturation. Very complex crystal forms are observed in nature and reflect the varying habitats in which many crystals grow. The simplification made here seems appropriate for a first attempt to delimit seeding potential, as the error introduced in computing total ice growth is probably considerably less than the uncertainty interposed by the method of specifying crystal concentration.

Finally, the consequences of neglecting crystal growth by accretion of supercooled cloud droplets needs some discussion. An efficient precipitation process for cold orographic clouds requires that total ice growth consume the vapor supplied by the updraft and produce timely glaciation of the cloud parcel. Moreover, total ice growth may be composed of both depositional and accretional growth processes, and while these two processes are additive, they do not operate independently. Heavy riming requires the presence of significant quantities of cloud water. However, the growth of large quantities of cloud water is discouraged by the presence within the cloud of strong diffusional ice growth which tends to effectively convert the cloud water to ice. The probability that substantial numbers of cloud droplets will attain the sizes required to support an efficient accretional growth process is thus reduced for these conditions. Observations of crystal riming at Climax, Colo. (Chappell, 1970a), indicate quite markedly how the onset of heavy riming is related to the increasing inefficiency of ice growth by the diffusional process.

Jiusto (1971) demonstrated with a mixed-phase cloud model that the onset time of heavy riming varies considerably with updraft speed and crystal concentration. For updraft speeds characteristic of orographic clouds (≤ 100 cm sec⁻¹), heavy riming generally developed in the model only when crystal concentrations were insufficient to produce timely glaciation. Thus, it appears from the above evidence that the neglect of crystal growth by riming in the present model probably introduced only a minor error in delimiting conditions under which modification potential exists. However, since the magnitude of riming growth is additive to the amount of ice growth by the diffusional process, the magnitude of seeding potential would be exaggerated by the present model.

#### 5. Discussion and summary

This relatively simple microphysical model enables one to crudely differentiate meteorological conditions associated with a potential for snowfall augmentation in cold orographic clouds, and to study the sensitivity of this potential to various model parameters. Certain general conclusions are suggested.

Crystal concentrations in the cloud largely control whether a potential for snowfall enhancement exists. Knowledge of the temperature activation spectrum of ice nuclei and cloud-top temperature is therefore important to the specification of such potential. Since crystal multiplication processes may contribute to the enhancement of crystal concentrations in the cloud, an understanding of this phenomenon is vital to the development of more realistic models.

The strength of the updraft in an orographic cloud is a secondary factor in determining whether a potential for snowfall enhancement exists. Given that this potential exists, however, the updraft speed largely determines its magnitude.

Crystal concentrations ≤ 5 liter<sup>-1</sup> are probably not adequate for timely glaciation of the cold orographic clouds found in the western United States. Crystal concentrations of 30 liter<sup>-1</sup> are probably sufficient in most instances for timely glaciation, and it appears that concentrations of 30 to 200 liter<sup>-1</sup> will accomplish this same purpose without serious overseeding effects. While crystals associated with this latter case would still have sufficient size and settling speeds to reach the mountain surface, one might expect some variation in their trajectories. This redistribution of precipitation could result from affecting changes in riming growth, crystal habit and size, or in the agglomeration mechanism.

It should be pointed out that most of the uncertainties involved in modeling the microphysics of cold orographic clouds are found in the warmer supercooled cloud systems (summit temperatures warmer than -25C). The presence of increased riming and coalescence growth, more fragile crystal habits, and crystal multiplication processes, all apparently tend to partially compensate for the increasing inefficiency of the total diffusional ice growth process in these warmer clouds. Considerable research is needed to identify these various processes, specify their magnitude, and describe their behavior with varying meteorological conditions, before realistic models can be developed. Until these uncertainties and those related to measuring ice nuclei are resolved, models such as this one must remain theoretical and applied to real cloud systems with great prudence.

In view of the uncertainties and simplifications inherent in the model, there may be some error in the cloud-top temperature that demarcates seeding potential. If crystal concentration is varied by a factor of 10 in the model, the demarcation temperature is shifted about 4–5C. Thus, one can envisage that the demarcation temperature could be in error by several degrees. It is therefore noteworthy that several cold orographic cloud experiments (mentioned above) give integrated results that are in good agreement with the model.

Acknowledgments. Most of this work was accomplished by the authors at the Utah Water Research Laboratory, Utah State University, and sponsored by Contract 14-06-D-7184 of the Division of Atmospheric Water Resources Management of the Bureau of Reclamation. Ronald H. Campbell contributed substantially to the computer programming.

#### APPENDIX

#### List of Symbols

	droplet curvature term $\lceil = 3.3 \times 10^{-5} / T \rceil$
(l L	droplet curvature term $[=3.5 \times 10^{-7} I]$ droplet solubility term $[=8.6m/M_s]$
b C	
$C_p$	crystal shape (capacitance) factor (°C) specific heat of air at constant pressure
D	diffusivity of water vapor
e	vapor pressure of the environment
_	saturation vapor pressure of the environment
$e_i, e_w$	(over a plane ice surface, over a plane water surface)
$\overset{g}{G}$	gravitational acceleration
G	thermodynamic function in droplet growth equation [defined by Eq. (6)]
G'	thermodynamic function in ice crystal growth equation [defined by Eq. (9)]
I	grams of ice per unit volume of air
K	thermal conductivity of air
$L_c, L_s$	latent heat of condensation and of sublima-
	tion
m	mass
$M_s$	molecular weight of the soluble condensation nucleus
$N_c, N_d$	concentration of ice crystals and of water droplets per unit volume of air
P	atmospheric pressure
$r_c, r_d$	radius of ice crystal and water droplet
$R_d$ , $R_v$	specific gas constant for dry air, and for water vapor
$S_i S_w$	supersaturation with respect to ice and water
t	time
T	temperature
$T_c$	cloud-top temperature (°C)
l.	updraft velocity
IV	grams of liquid water per unit volume of air
Z	height
E	the ratio of the molecular weight of water vapor to that of air (0.622)
$\rho, \rho_w, \rho_i$	density of air, water and of ice
$\phi_1, \phi_2, \phi_3$	thermodynamic functions in supersaturation equation [defined by Eqs. (2), (3) and (4),

#### REFERENCES

respectively]

Auci, A. H., D. L. Veal and J. D. Marwitz, 1969: Observations of ice crystal and ice nuclei concentrations in stable cap cloud. J. Atmos. Sci., 26, 1342-1343.

- Bergeron, T., 1949: The problem of an artificial control of rainfall on the globe: I. General effects of ice-nuclei in clouds. *Tellus*, 1, 32-50.
- Chappell, C. F., 1970a: Snow crystal riming related to cloud system characteristics. Preprints Conf. Cloud Physics, Ft. Collins, Amer. Meteor. Soc., 49-50.
- —, 1970b: Modification of cold orographic clouds. Atmos. Sci. Paper 173, Colorado State University, Fort Collins, 196 pp.
- —, 1972: Airborne seeding of wintertime Wasatch mountain clouds during Project Snowman. *Preprints Third Nat. Conf. Weather Modification*, Rapid City, Amer. Meteor. Soc., 129-132.
- Fletcher, N. H., 1962: The Physics of Rain Clouds. New York, Cambridge University Press, 309 pp.
- Grant, L. O., 1968: The role of ice nuclei in the formation of precipitation. Proc. Intern. Conf. Cloud Physics, Toronto, 305-310.
- —, C. F. Chappell and P. W. Mielke, Jr., 1968: The recognition of cloud seeding opportunity. *Preprints First Nat. Conf. Weather Modification*, Albany, Amer. Meteor. Soc., 372-385.
- —, —, and —, 1971: The Climax experiment for seeding cold orographic clouds. *Preprints Intern. Conf. Weather Modification*, Canberra, Amer. Meteor. Soc., 78-84.
- Hobbs, P. V., 1969: Ice multiplication in clouds. J. Atmos. Sci., 26, 315-318.
- Jiusto, J. E., 1968: Snow crystal development in supercooled clouds. Preprints First Nat. Conf. Weather Modification, Albany, Amer. Meteor. Soc., 287-295.
- —, 1971: Crystal development and glaciation of a supercooled cloud. J. Rech. Atmos., 5, 69-85.

- ----, and R. K. Schmitt, 1970: A model of supercooled cloud microphysics. *Preprints Second Nat. Conf. Weather Modification*, Santa Barbara, Amer. Meteor. Soc., 41-44.
- Keyes, C. G., F. D. Stover, R. D. Wilkins and M. Lentner, 1973: Tentative results of four years of randomized seeding in the Jemez mountains. Tech. Rept. No. 79, Enginering Experiment Station, New Mexico State University, Las Cruces, 33 pp.
- Ludlam, F. H., 1955: Artificial snowfall from mountain clouds. Tellus, 7, 277-290.
- Mason, B. J., 1971: The Physics of Clouds. Belfast, Oxford University Press, 671 pp.
- Mossop, S. C., 1970: Concentrations of ice crystals in clouds. Bull. Amer. Meteor. Soc., 51, 474-479.
- Nakaya, U., and T. Terada, 1934: Simultaneous observations of the mass, falling velocity, and form of individual snow crystals. J. Fac. Sci. Hokkaido Univ. Ser. II, 1, No. 7.
- Rhea, J. O., and L. G. Davis, 1970: Statistical results of the Park Range winter orographic cloud seeding experiment. Preprints Third Nat. Conf. Weather Modification, Santa Barbara, Amer. Meteor. Soc., 70-75.
- Schaefer, V. J., 1946: The production of ice crystals in a cloud of supercooled water droplets. *Science*, 104, 457.
- Todd, C. J., 1964: A system for computing ice-phase hydrometer development. Rept. ARG 64 Pa-121, Meteorology Research Inc., 30 pp.
- Twomey, S., 1958: Quantitative aspects of seeding rates for use in supercooled clouds. Bull Obs. Puv de Dôme, 2, 33-42.
- Vonnegut, B., 1947: The nucleation of ice formation by silver iodide. J. Appl. Phys., 18, 593.
- Wegner, A., 1911: Thermodynamik der Atmosphäre. Leipzig.

## On the Computation of Isobaric Wet-Bulb Temperature and Saturation Temperature over Ice

CHARLES F. CHAPPELL, E. L. MAGAZINER AND J. MICHAEL FRITSCH

Atmospheric Physics and Chemistry Laboratory, NOAA, Boulder, Colo. 80302

12 December 1973 and 19 June 1974

#### ABSTRACT

Non-iterative methods for computing isobaric wet-bulb temperature and the temperature at the lifted sublimation level are presented. These quantities are then computed by these direct techniques and compared to values derived through iterative methods. In the case of the isobaric wet-bulb temperature, differences in the two methods are less than 1C, over normal ranges of atmospheric temperature and pressure for dewpoint depressions <30C. Differences in the two methods are less than 0.03C for the temperature at the lifted sublimation level over the same range of dewpoint depression.

#### 1. Introduction

Realistic simulation of cloud and precipitation processes must include effects of evaporation and icephase processes. In modeling these effects, one frequently needs to evaluate the isobaric wet-bulb temperature and the saturation temperature with respect to ice. Computation of the isobaric wet-bulb temperature  $T_w$  (List, 1971) generally requires an iterative procedure (McDonald, 1963; Stackpole, 1967), since the saturation vapor mixing ratio corresponding to  $T_w$ is also unknown. Similarly, computation of saturation temperature  $T_{lsl}$  also requires an iteration procedure since the corresponding pressure is unknown. In this note we present straightforward methods for computing  $T_w$  and  $T_{lsl}$  having sufficient accuracy for many atmospheric applications. If greater accuracy is required, the methods presented here can provide accurate first estimates to be used in iterative techniques.

#### 2. Isobaric wet-bulb temperature

Let a parcel of moist air be in the state (T, p, W), where T is air temperature, p pressure, and W vapor mixing ratio. All symbols are defined in the Appendix. Suppose that some water is evaporated into the parcel at constant pressure. In this case dW is positive, and the air provides the latent heat of vaporization L by cooling. If  $(dT)_p$  is the resulting isobaric change in temperature of the air, the final state of the air is  $[T+(dT)_p, p, W+dW]$ . If we assume only dry air is cooled, we obtain

$$-LdW = C_{p}(dT)_{p}, \tag{1}$$

where  $C_p$  is the specific heat of dry air at constant pressure.

If we substitute for L and  $C_p$ , and solve for  $(dT)_p$ , the result is

$$(dT)_{p} = -cdW, \tag{2}$$

where W is expressed in grams of vapor per gram of dry air, and c = [597.3 - 0.566(T - 273.16)]/0.24.

Consider now the process where a parcel of moist air is 'dried out by an isobaric process which is also adiabatic. In this fictitious case, the water vapor is condensed out of the parcel with the latent heat released being used to heat the air itself. The resulting temperature is called the isobaric equivalent temperature  $T_{\epsilon}$ . An expression for this temperature is formulated using (2) and is written

$$T_e = T + cW. (3)$$

If water vapor is evaporated into the initial parcel isobarically, while obtaining the necessary latent heat by cooling, the temperature of the parcel will fall from its initial value T, while the mixing ratio rises from its initial value W. The temperature where the air becomes saturated is the isobaric wet-bulb temperature  $T_w$ . The corresponding saturation vapor mixing ratio is denoted by  $W_w$ . Something akin to this process may occur when precipitation falls through a layer of unsaturated air. If (2) is integrated between initial and saturated states, we obtain an expression for  $T_w$ :

$$T_w - T = -c(W_w - W). \tag{4}$$

Consider now the proportionality formed by the difference between the equivalent temperature  $T_{\bullet}$  and

the equivalent temperature corresponding to saturation at the ambient temperature,  $T_{el}$ , divided by the spread between equivalent temperatures corresponding to saturation at ambient and dewpoint temperatures,  $T_{el} - T_{ed}$ , i.e.,

$$K = (T_{et} - T_e)/(T_{et} - T_{ed}).$$

An expression for the isobaric wet-bulb temperature can then be written in terms of k and other known quantities, i.e.,

$$T_{\mathbf{w}} = T - k(T - T_d). \tag{5}$$

The two equivalent temperatures  $T_{et}$  [=  $T+cW_t$ ] and  $T_{ed}$  [=  $T_d+cW$ ] can readily be computed, since for temperatures T and  $T_d$  on the initial isobar, one can solve for corresponding saturation mixing ratios,  $W_t$  and W, respectively.

If the air is saturated,  $T_d = T_w = T$ , and no computation of  $T_w$  by (5) is required. For unsaturated conditions,  $T_d < T_w < T$ , and note that (5) always yields a value of  $T_w$  less than T.

If (3) and expressions for  $T_{et}$  and  $T_{ed}$  are substituted into (5), we obtain the convenient expression

$$T_{\mathbf{w}} = T - [abc/(a+bc)], \tag{6}$$

where a is the dewpoint depression  $[=T-T_a]$ , and b the depression of vapor mixing ratio below that for water saturation  $[=W_t-W]$ . Thus,  $T_w$  can be computed directly by (6) if temperature and the moisture content of the air at a given pressure are known.

The isobaric wet-bulb temperature was computed using (6) and by iteration employing (4) over a wide range of the independent variables. Results are shown in Figs. 1 and 2 for pressures of 1000 and 400 mb, respectively. Note the difference in the two methods is less than 1C over normal ranges of atmospheric temperature and pressure if dewpoint depressions are less than 30C. The accuracy obtained employing (6) is satisfactory for many atmospheric applications. When more accuracy is required, (6) can provide a much improved first estimate for the usual iterative solution resulting in fewer iterations.

#### 3. Saturation temperature with respect to ice

Several approximate techniques for directly calculating the lifted condensation level temperature for water saturation processes are now available (Barnes, 1968; Inman, 1969). To avoid time-consuming iterative procedures for ice saturation processes as well, the following explicit empirical expression was derived for approximating the ice saturation temperature:

$$T_{lsl} = T_d - (0.182 + 0.00113T_d - 0.000358T)$$

$$\times (T-T_d), \quad (7)$$

where temperatures are expressed in degrees Celcius. Inman's corresponding equation for the saturation temperature with respect to water is listed below for

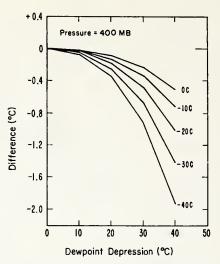


Fig. 2. As in Fig. 1 except for a pressure of 400 mb.

easy reference:

$$T_{lel} = T_d - (0.212 + 0.001571T_d - 0.000436T) \times (T - T_d).$$
 (8

Eq. (7) was derived by applying a least-square fit to a set of iteratively generated saturation temperatures. The iteration scheme (Stackpole, 1967) consisted of successive calculations using the Poisson equation, Teton's equation with ice coefficients, and the relation

$$W_i = \frac{0.622e_i}{b - e_i},\tag{9}$$

where  $W_i$  is the saturation vapor mixing ratio with

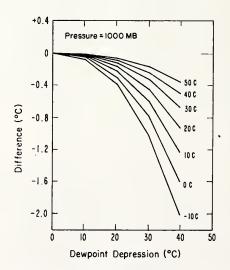


Fig. 1. Differences between the empirical and iterative solutions for the isobaric wet-bulb temperature. Differences are shown as a function of temperature and dewpoint depression for a pressure of 1000 mb.

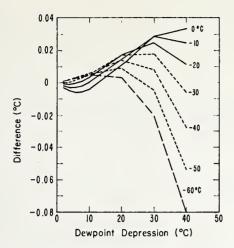


Fig. 3. Differences between the empirical and iterative solutions for the saturation temperature with respect to ice. Differences are shown as a function of temperature and dewpoint depression.

respect to ice and  $e_i$  the saturation vapor pressure over a plane ice surface.

Fig. 3 shows the difference between the evaluation from (7) and the iterative solution as a function of temperature and dewpoint depression. Note that over the normal range of atmospheric temperatures and dewpoint depressions, the approximated temperature agrees with the iteratively generated temperature within  $\pm 0.1$ C. Furthermore, the differences are less than 0.03C for depressions  $\leq$  30C. Although this type of accuracy is not realistic in many practical applications, it may be important for modeling microphysical and other relatively small-scale processes where exact values are desirable.

#### APPENDIX

#### List of Symbols

a dewpoint depression  $[=T-T_d]$ 

the vapor mixing ratio depression below water saturation  $= W_t - W$ 

a function of temperature  $\{=[597.3-0.566(T-273.16)]/0.24\}$ 

C<sub>p</sub> specific heat of dry air at constant pressure

 $e_i$  saturation vapor pressure over a plane ice surface

L latent heat of vaporization

p air pressure

T air temperature

T<sub>d</sub> dewpoint temperature

T<sub>e</sub> isobaric equivalent temperature

 $T_w$  isobaric wet-bulb temperature

 $T_{et}$  isobaric equivalent temperature if air was saturated at its temperature T

 $T_{ed}$  isobaric equivalent temperature if air was saturated at its dewpoint temperature  $T_d$ 

 $T_{lel}$  temperature at the lifted condensation level or saturation temperature with respect to water

 $T_{lsl}$  temperature at the lifted sublimation level or saturation temperature with respect to ice

W vapor mixing ratio of air or saturation vapor mixing ratio at the dewpoint temperature

W<sub>i</sub> saturation vapor mixing ratio with respect to ice

 $W_t$  saturation vapor mixing ratio at the air temperature

 $W_w$  saturation vapor mixing ratio at the wet-bulb temperature

#### REFERENCES

Barnes, S. L., 1968: An empirical shortcut to the calculation of temperature and pressure at the lifted condensation level. J. Appl. Meteor., 7, 511.

Inman, R. L., 1969: Computation of temperature at the lifted condensation level. J. Appl. Meteor., 8, 155-158.

List, R. J., 1971: Smithsonian Meteorological Tables, 6th rev. ed. Smithsonian Institution, Washington, D. C., p. 318.

McDonald, J. E., 1963: The saturation adjustment in numerical modeling of fog. J. Atmos. Sci., 20, 476-478.

Stackpole, J. D., 1967: Numerical analysis of atmospheric soundings. J. Appl. Meteor., 6, 464-467.

## Generation of Available Buoyant Energy by Cloud Glaciation

By Charles F. Chappell<sup>1</sup>) and David R. Smith<sup>1</sup>)

#### Abstract

The available buoyant energy (ABE, energy from the environment which becomes available to a parcel for buoyant accelerations) arising from glaciation is computed by integrating upward the differences in temperature between a parcel that undergoes instantaneous and isenthalpic freezing followed by an ice-saturation ascent, and one that experiences only a water-saturation ascent from the same initial cloud base conditions. This quantity is computed for three initial cloud base conditions representative of tropical, High Plains summertime, and Great Lakes wintertime cumuli. Substantial increases in parcel updraft speed are realized for all clouds if the ABE arising from glaciation is completely converted to parcel kinetic energy. Variations of the three components of parcel heating involved in the glaciation process (i.e., (1) release of latent heat of fusion from freezing of liquid water, (2) cooling or warming from sublimation or deposition as vapor pressure adjusts from water saturation to ice saturation at the post glaciation temperature, and (3) the additional warming or cooling relative to the initial water-saturation adiabat as the parcel follows an icesaturation ascent to a specified upper reference level) are also determined as functions of glaciation temperature. It is found that sublimation substantially counteracts the parcel warming arising from the freezing of liquid water in the case of warm moist cumuli. In addition, it is found that in some instances ice-saturation ascent following glaciation can produce cooling relative to the initial departure from the water saturation adiabat. This was indicated for Great Lakes wintertime cumuli and also for warm moist cumuli with glaciations at very cold temperatures. The effect upon the buoyancy force, of the change in the mass of condensate during glaciation, is small and can usually be neglected.

#### 1. Introduction

The importance of heat released by cloud seeding was first discussed by Kraus and Squires (1947). In the same year, Langmuir et al. (1947) pointed to the availability of another heat source during cloud seeding besides the latent heat of fusion. Langmuir said, 'when supercooled liquid water droplets are made to evaporate and condense on ice nuclei, the amount of ice formed is considerably greater than the amount of water which evaporates because the vapor pressure is lower than the water so that there is a lowering of the water vapor content in the cloud. There are thus, two sources of heat which tend to raise the temperature of the cloud, viz., the heat of fusion and the heat of sublimation of the extra amount of water which is converted from vapor to ice.' However, Macready and Skutt (1967) demonstrated that this latter effect discussed by Langmuir could act to either increase or decrease the parcel temperature,

<sup>&</sup>lt;sup>1</sup>) Atmospheric Physics and Chemistry Laboratory, National Oceanic and Atmospheric Administration, Boulder, Colorado 80302, USA.

since both cooling from sublimation or heating by deposition was possible. In addition, they presented a graphical technique for estimating the increase in cloud buoyancy from seeding. Fukuta (1972) and Orville and Hubbard (1973) also noted that cooling from sublimation may in reality counteract the warming realized from freezing liquid water and reduce cloud buoyancy.

SAUNDERS (1957) provided a basis for considering the dynamic effects of introducing ice in cloud parcels. He presented equations that describe both reversible and pseudoadiabatic expansions of air saturated with respect to plane surfaces of water and ice. He also presented an expression for evaluating the temperature change of an instantaneous and isobaric freezing process. Since this freezing technique can also be applied to freezing over a temperature interval, it may be conveniently used in cloud models.

ORVILLE and HUBBARD (1973) emphasized the importance of treating the freezing process accurately in cloud models, particularly when simulating the effects of 'dynamic' seeding (WOODLEY, 1970; SIMPSON and WIGGERT, 1971). Furthermore, they found that the imprecise manner in which the freezing process was incorporated into some cumulus models led to a bias against the natural cloud and overestimates of their seedability.

The process of glaciation produces a total parcel heating that is composed of three components (ORVILLE and HUBBARD, 1973). The first two occur at the time of freezing and are due to the release of latent heat of fusion as the supercooled liquid water freezes, accompanied by either cooling from sublimation or heating from deposition as the vapor mixing ratio adjusts to ice-saturation at the new post-freezing temperature. The third component is realized when the parcel ascends to higher levels in the atmosphere and cools at a rate specified by an ice-saturation expansion.

The purpose of this paper is to explore the effects of cloud glaciation on the available buoyant energy (ABE, energy from the environment which becomes available to a parcel for buoyant accelerations). Variations of the three thermal components with glaciation temperature are also investigated for three different initial conditions. These initial conditions are chosen to represent typical cloud bases for tropical cumuli, High Plains summertime cumuli, and Great Lakes wintertime cumuli. Effects of the thermal components, which arise from glaciation and subsequent ice-saturation ascent, are integrated upward to an upper reference level to estimate their contribution to the production of ABE. Finally, the depositional growth or sublimation that accompanies the adjustment of saturation vapor pressure during glaciation is investigated, and its importance relative to thermal effects is defined.

#### 2. Equations and computational methods

#### (a) Computation of ABE

We wish to compute the amount of ABE below some upper reference level that arises from the glaciation process, and determine quantitatively how changes in the glaciation

level affect this quantity. This is accomplished by assuming that a cloud parcel follows a water-saturation (reversible adiabatic or pseudoadiabatic) ascent from an arbitrarily specified cloud base up to the reference level. Temperatures along this thermodynamic path are designated  $T_1$ . We now consider that a cloud parcel with identical cloud base characteristics experiences isobaric and instantaneous freezing at some arbitrarily specified pressure level, after which it follows an ice-saturation ascent to the reference level. Temperatures describing this second thermodynamic path are identified  $T_2$ . These two thermodynamic processes are illustrated in Fig. 1.

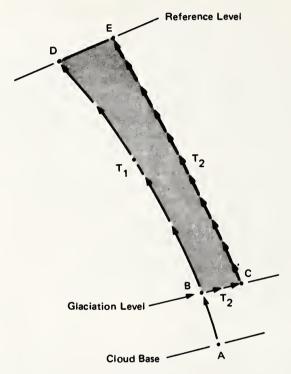


Figure 1

Diagram of relevant thermodynamic processes. ABD represents a water-saturation expansion (pseudoadiabatic or reversible). BC depicts instantaneous and isobaric freezing. CE represents an ice-saturation expansion (pseudoadiabatic or reversible).

If the temperature difference between these two thermodynamic paths is integrated from the glaciation level to the reference level, the amount of ABE below the reference level, arising from glaciation and ice-saturation ascent, is given by

ABE = 
$$R_d \int_{p_a}^{p_r} (T_2 - T_1) d(\ln p),$$
 (1)

where symbols are given in the appendix.

An upper reference level at 200 mb is used to integrate (1) for the tropical and High Plains summertime cumuli, while 400 mb is employed for the Great Lakes wintertime cumulus.

Solutions to (1) require that water-saturation and ice-saturation equations (reversible adiabatic and pseudoadiabatic) be computed, as well as the equation that describes instantaneous and isobaric freezing.

#### (b) Parcel warming during glaciation

In an isenthalpic freezing process total enthalpy of the system is conserved and the temperature T', resulting from the freezing of a supercooled cloud of droplets initially at a temperature T, is given by

$$[C_{vd} + C_{vv}q_i(T') + C_iq_{ci}](T' - T) = q_{cw}L_f + [q_w(T) - q_i(T')]L_s.$$
 (2)

Equation 2 can be written in terms of the total mixing ratio of water substance, q, (SAUNDERS, 1957) by noting that  $q = q_i(T') + q_{ci}$  and  $C_{pv} \approx C_i$ . The latter relationship is exact at about -34C using the expressions for  $C_{pv}$  and  $C_i$  defined here. If we take  $C_{pv} \approx C_i$  for all temperatures of interest, (2) takes the form

$$(C_{vd} + C_{vv}q)(T' - T) = q_{cw}L_f + [q_w(T) - q_i(T')]L_s.$$
(3)

This form of the freezing equation is amenable to physical interpretation but is not convenient computationally, since it requires an iterative process for solution. A more computationally convenient form of (3) can be formulated by assuming that (T'-T) is small enough to be treated as a differential, and then equating  $e_i(T')$  to a Taylor series expansion in  $e_i(T)$ . By employing the first two terms of this expansion, the Clausius-Clapeyron relation, and the assumption that  $p - e_i(T) \approx p - e_i(T')$ , the temperature change due to freezing can be expressed in terms of the temperature prior to freezing and (3) becomes

$$(T'-T) = \frac{q_{cw}L_f + \frac{\varepsilon L_s e_w(T)}{p - e_w(T)} - \frac{\varepsilon L_s e_i(T)}{p - e_i(T)}}{C_{pd} + qC_{pv} + \frac{\varepsilon^2 L_s^2 e_i(T)}{[p - e_i(T)]R_d T^2}}.$$

$$(4)$$

The procedure adopted here is to calculate T' using (4), and then to insert T' into (3) to compute temperature changes associated with the terms on the right hand side of the equation. Thus, the physically meaningful thermal components,  $\Delta T_f = q_{cw} L_f/(C_{pd} + qC_{pv})$  (temperature change due to freezing of liquid water) and  $\Delta T_d = [q_w(T) - q_i(T')]L_s/(C_{pd} + qC_{pv})$  (temperature change due to deposition or sublimation) are evaluated directly.

The third thermal component,  $\Delta T_i$ , which is realized when the parcel is lifted from the glaciation level, is computed at the upper reference level for a given set of initial conditions by  $\Delta T_i = (T_2 - T_1) - (\Delta T_f + \Delta T_d)$ , where  $(T_2 - T_1)$  is evaluated at the upper reference level, and  $(\Delta T_f + \Delta T_d)$  is the net change in parcel temperature realized at the glaciation level.

#### (c) Condensate effects

During the glaciation processs depositional growth or sublimation will generally accompany the adjustment of vapor pressure from saturation over a plane water surface to saturation over a plane ice surface at the new post-freezing temperature. This adjustment may produce either an increase or a decrease in the mass of condensate within the updraft parcel. The downward force corresponding to this change in the mass of condensate is then given by  $-g[q_w(T) - q_i(T')]$ . If this quantity is equated to the buoyancy force,  $g\Delta T/T$ , the change in the mass of condensate can be transformed to an equivalent temperature difference at the glaciation level, or  $\Delta T = T[q_w(T) - q_i(T')]$ . This equivalent temperature difference can then be divided by the parcel warming realized during glaciation ( $\Delta T_f + \Delta T_d$ ) to define its relative importance to buoyancy production at the glaciation level.

#### (d) Reversible adiabatic processes

Changes in temperature of a cloud parcel as a function of pressure during a reversible water-saturation adiabatic ascent are given by

$$\frac{dT}{dp}\Big)_{w} = \frac{\left(\frac{R_{d}T}{C_{pd}p}\right)\left(1 + \frac{q_{w}}{\varepsilon}\right)\left(1 + \frac{q_{w}L_{c}}{R_{d}T}\right)}{\left[1 + \frac{C_{w}q_{cw}}{C_{pd}} + \frac{C_{pv}q_{w}}{C_{pd}} + \frac{L_{c}^{2}q_{w}(q_{w} + \varepsilon)}{C_{pd}R_{d}T^{2}}\right]}$$
(5)

A similar expression for the reversible ice-saturation adiabatic ascent is given by

$$\frac{dT}{dP}\Big|_{t} = \frac{\left(\frac{R_{d}T}{C_{pd}p}\right)\left(1 + \frac{q_{i}}{\varepsilon}\right)\left(1 + \frac{q_{i}L_{s}}{R_{d}T}\right)}{\left[1 + \frac{C_{i}q_{ci}}{C_{pd}} + \frac{C_{pv}q_{i}}{C_{pd}} + \frac{L_{s}^{2}q_{i}(q_{i} + \varepsilon)}{C_{pd}R_{d}T^{2}}\right]}$$
(6)

#### (e) Pseudoadiabatic processes

Changes in temperature of a cloud parcel as a function of pressure during a pseudoadiabatic water-saturation ascent are calculated by

$$\frac{dT}{dp}\Big|_{w} = \frac{\left(\frac{R_{d}T}{C_{pd}p}\right)\left(1 + \frac{q_{w}}{\varepsilon}\right)\left(1 + \frac{q_{w}L_{c}}{R_{d}T}\right)}{\left[1 + \frac{q_{w}}{C_{pd}}\left(C_{pv} - C_{w} + \frac{L_{c}}{T}\right) + \frac{L_{c}^{2}q_{w}(q_{w} + \varepsilon)}{C_{pd}R_{d}T^{2}}\right]}$$
(7)

The corresponding expression for a pseudoadiabatic ice-saturation ascent is given by

$$\frac{dT}{dp}\Big)_{i} = \frac{\left(\frac{R_{d}T}{C_{pd}p}\right)\left(1 + \frac{q_{i}}{\varepsilon}\right)\left(1 + \frac{q_{i}L_{s}}{R_{d}T}\right)}{\left[1 + \frac{q_{i}L_{s}}{C_{pd}T} + \frac{L_{s}^{2}q_{i}(q_{i} + \varepsilon)}{C_{pd}R_{d}T^{2}}\right]}$$
(8)

In (7), terms that arise from including the variation of  $L_c$  with temperature have been retained while in (8) the very small variation of  $L_s$  with temperature has been neglected.

The assumption that total pressure is equal to the partial pressure of dry air is not made in (7) or (8).

#### (f) Other computational procedures

Values of the latent heats of condensation and fusion in cal gm<sup>-1</sup> are given by

$$L_c = 597.3 - 0.566(T - 273.16)$$

and

$$L_t = 80.2 + 0.566(T - 273.16).$$

The specific heat of ice in cal gm<sup>-1</sup> K<sup>-1</sup> is calculated by

$$C_i = 0.503 + 0.0018(T - 273.16),$$

while values of the specific heat of water in cal gm<sup>-1</sup> K<sup>-1</sup> are given by

$$C_w = 1.00 \text{ for } T \ge 288.16 \text{K},$$

and

$$C_w = 9.2709297 - 0.06051832T + 0.00011052521T^2$$
 for  $T < 288.16K$ .

Saturation vapor pressure (in mbs) over plane water and ice surfaces are computed with TETENS' (1930) expression or

$$\ln e_s = \ln 6.1078 + [a(T - 273.16)/(T - 273.16 + b)] \ln 10,$$

where a = 7.5 and b = 237.3 for saturation over a plane water surface, and a = 9.5 and b = 265.5 for saturation over a plane ice surface.

The amount of liquid condensate,  $q_{cw}$ , is taken to be the adiabatic water content (reversible or pseudo) which develops in the parcel as it rises from cloud base to the glaciation level following a water-saturation expansion, or

$$q_{cw} = q_w(T_{cb}) - q_w(T_1).$$

The amount of ice condensate,  $q_{ci}$ , above the glaciation level, is given by a similar expression, or

$$q_{ci} = q_w(T_{cb}) - q_i(T_2).$$

#### 3. Results

The three thermal components that make up the total parcel heating are depicted in Fig. 2 as a function of glaciation temperature for initial conditions representative of a tropical cumulus cloud base. The large amount of liquid water generated under these conditions leads to large positive values of  $\Delta T_f$  due to release of latent heat of fusion. However, this warming is not fully realized by the parcel during glaciation

since cooling by sublimation ( $\Delta T_a < 0$ ) substantially reduces the net warming. Note this cooling by sublimation exists at all glaciation temperatures for these initial conditions. It is interesting to note that warming by release of heat of fusion is relatively constant with glaciation temperature, reaching a slight maximum for temperatures around -20C to -25C. The slight drop off at colder glaciation temperatures is due to the decrease in the latent heat of fusion,  $L_f$ , while little additional liquid condensate becomes available to the cloud parcel at these colder temperatures.

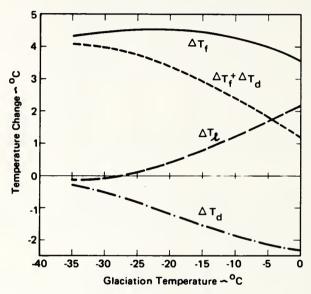


Figure 2

Individual temperature changes associated with cloud glaciation as a function of glaciation temperature for a tropical-cumulus cloud base (p = 900 mb and T = 22C).  $\Delta T_t$  is the temperature change due to freezing of liquid water.  $\Delta T_d$  is the temperature change due to sublimation or deposition as vapor pressure adjusts from saturation over a plane water surface to saturation over a plane ice surface at the new post-glaciation temperature.  $\Delta T_t$  is an additional departure of temperature from the initial water-saturation adiabat that is realized as the cloud parcel ascends from the glaciation level following an ice-saturation adiabat to an upper reference level of 200 mb.

Note also in Fig. 2 that lifting from the glaciation level along a reversible ice-saturation adiabat results in a parcel temperature at 200 mb that may be warmer or cooler relative to its initial departure from the reversible water-saturation adiabat. At warmer glaciation temperatures, however, additional relative warming is realized through lifting.

Variations of the three thermal components with glaciation temperature for initial conditions representative of a High Plains cumulus cloud base are shown in Fig. 3. These curves are similar to those for the tropical cumulus case except that the magnitudes of the temperature changes are generally reduced for all thermal components.

In the case of initial conditions representative of Great Lakes wintertime cumulus clouds, the variations of the three thermal components with glaciation temperature show some important differences. Note in Fig. 4 that warming due to deposition now exists for all glaciation temperatures, and is comparable to the warming associated with the release of heat of fusion, especially at warmer glaciation temperatures. Lifting of the cloud parcel along a reversible ice saturation adiabat now results in a relative cooling (again relative to the initial reversible water-saturation adiabat) at 400 mb for most glaciation temperatures.

It is apparent in Figs. 2-4 that the thermal components associated with the sublimation and lifting processes are nearly equal, but opposite in sense, over a large range

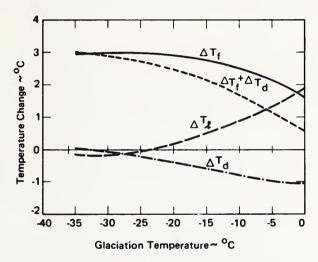


Figure 3 Same as Fig. 2 except for a high plains cumulus cloud base (p = 650 and T = 11C).

of glaciation temperatures for all clouds. Moreover, if the  $\Delta T_l$  curve is added to the  $\Delta T_f + \Delta T_d$  curve in Figs. 2-4, the parcel warming realized at the upper reference level,  $\Delta T_f + \Delta T_d + \Delta T_l$ , is nearly constant with glaciation temperature. Thus, as pointed out by SAUNDERS (1957), and discussed further by ORVILLE and HUBBARD (1973), the final parcel temperature obtained is largely independent of the temperature at which glaciation occurs.

The effects of glaciation temperature upon the ABE and the resultant theoretical updraft speed at the upper reference level are depicted in Fig. 5. Data are displayed for both pseudoadiabatic and reversible adiabatic processes, and for initial conditions representative of tropical, High Plains, and Great Lakes wintertime cumulus cloud bases. Glaciation produces greater amounts of ABE and larger updraft speeds in the tropical cumuli. For these cloud conditions glaciation at -5C or warmer produces theoretical increases in updraft speed of over 40 mps for both pseudoadiabatic and

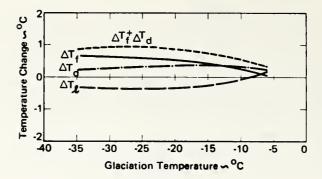


Figure 4
Same as Fig. 2 except for a Great Lakes wintertime cumulus cloud base (p = 900 and T = -5C) and an upper reference level of 400 mb.

reversible adiabatic processes. These values decrease to around 20 mps for glaciation at -35C. The ABE and updraft speed at 200 mb generated in the High Plains cumulus is less than for the tropical cumulus for all glaciation temperatures. Values of updraft speed generated at 200 mb vary from about 35 mps for glaciation at -5C to near 18 mps for glaciation at -35C.

In the case of the Great Lakes wintertime cumulus, the ABE and the resultant theoretical updraft speeds generated at 400 mb are considerably smaller, and exhibit only a slight increase with glaciation temperature. This reflects the small amount of liquid condensate available in these relatively cold clouds, and also the fact that the integration is terminated at 400 mb.

Note in Fig. 5 that values of ABE and theoretical updraft speeds at the upper reference level are greater when computed using the pseudoadiabatic equation. This reflects the greater warming of the cloud parcel by latent heat release, since none of the latent heat is expended to warm condensate in the pseudoadiabatic system.

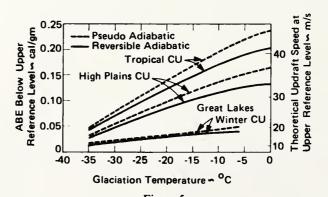


Figure 5

ABE and theoretical updraft speeds realized at the upper reference level due to glaciation as a function of glaciation temperature.

The effect of deposition or sublimation, when saturation vapor pressure adjusts during the glaciation process, has not been included in the results presented so far. However, the change in the mass of condensate arising from this adjustment will have some effect on cloud buoyancy, and therefore on the generation of updraft speed. The relative importance of this effect at the glaciation level is depicted in Fig. 6. Note that the effect on the buoyancy force at the glaciation level, of changing the mass of condensate by deposition or sublimation during glaciation, amounts to less than 5 percent of the buoyancy force produced by parcel warming for all glaciation temperatures

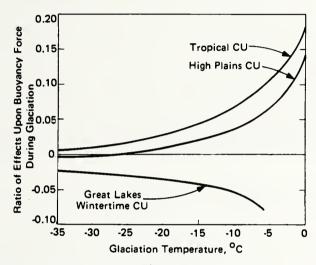


Figure 6

Ratio of the effects upon buoyancy force of condensate change and parcel warming realized during glaciation. The change in condensate during glaciation, due to deposition or sublimation as the vapor pressure adjusts from water saturation to ice saturation at the new glaciation temperature, is converted to an equivalent temperature difference, or  $\Delta T = T[q_w(T) - q_i(T')]$ . This quantity is then divided by the parcel warming realized during glaciation or  $(\Delta T_f + \Delta T_d)$ .

colder than -14C. This effect reaches 10 percent to 18 percent at glaciation temperatures warmer than -6C for tropical cumuli. Note that the effect on the buoyancy force is mainly positive (i.e. sublimation reduces the mass of ice condensate) for tropical and High Plains cumuli, but is negative for Great Lakes wintertime cumuli.

#### 4. Summary and conclusions

The variations of the three thermal components with glaciation temperature are interesting. While the parcel warming due to release of fusion heat is always positive, the decrease in the latent heat of fusion with temperature more than compensates for smaller increases in liquid water to produce a maximum warming for glaciation

temperatures between -20C to -30C for warm moist cumuli. The adjustment of vapor pressure, from saturation over a plane water surface to saturation over a plane ice surface at the new post-glaciation temperature, may produce warming or cooling of the parcel. This effect generally acts to increase the buoyancy of wintertime cumulus clouds and to decrease the buoyancy of warm moist cumuli. Lifting following glaciation does not always result in further relative warming of the cloud parcel.

Relative warming is mainly realized with warm moist cumuli and with glaciations that occur at relatively warm temperatures. The total parcel warming realized from glaciation and subsequent ice-saturation ascent, compared with a water-saturation ascent, amounts to 3C to 4C at 200 mb for warm moist cumuli.

As one might anticipate, in spite of eccentric variations of two thermal components, total parcel heating integrated with height yields an increase in ABE and theoretical updraft speeds at the reference level that increase rather smoothly with glaciation temperature. Also, the warmer the temperature at which glaciation occurs, the greater the ABE and theoretical updraft speed attained at the reference level for all cloud systems. The change in ABE with glaciation temperature decreases above -10C, for warm moist cumuli, so that small differences in results are indicated between glaciations at 0C and -5C. This flattening effect is most pronounced for the reversible adiabatic system.

This study emphasizes the important role that glaciation plays in the dynamics of cumulus clouds. In addition, it demonstrates that substantial amounts of energy are available to be tapped by controlling glaciation temperature through cloud seeding. While we have shown theoretical increases in updraft speed arising from glaciation processes, in reality much of this ABE is likely to be dissipated in entrainment and turbulent processes. Actual updraft speeds attained by cloud parcels are therefore likely to be considerably less than these theoretical values.

# Appendix List of Symbols

$C_i$	specific heat of ice
$C_{pd}$	specific heat at constant pressure for dry air [= 0.240 cal gm <sup>-1</sup> K <sup>-1</sup> ]
$C_{pv}$	specific heat at constant pressure for water vapor [=0.441 cal gm <sup>-1</sup> K <sup>-1</sup> ]
$C_w$	specific heat of water
$e_i$	saturation vapor pressure over a plane ice surface
$e_w$	saturation vapor pressure over a plane water surface
g	acceleration due to gravity
$L_c$	latent heat of condensation
$L_f$	latent heat of fusion
$L_{\mathtt{s}}$	latent heat of sublimation [= 677.5 cal gm <sup>-1</sup> ]
p	atmospheric pressure
$p_g$	pressure at the glaciation level
n	pressure at the upper reference level

- $R_d$  specific gas constant for dry air  $[= 0.06852 \text{ cal gm}^{-1} \text{ K}^{-1}]$
- q mixing ratio of total water substance
- $q_i$  saturation vapor mixing ratio over a plane ice surface
- $q_w$  saturation vapor mixing ratio over a plane water surface
- $q_{ci}$  mixing ratio of ice condensate
- $q_{cw}$  mixing ratio of liquid water condensate
- T temperature
- T' temperature of a cloud parcel after isobaric freezing
- T<sub>1</sub> locus of cloud parcel temperatures described by a water saturation ascent from cloud base to an upper reference level
- Iocus of cloud parcel temperatures described by a water-saturation ascent from cloud base to an arbitrarily specified glaciation level, followed by isobaric freezing and subsequent ice-saturation ascent to an upper reference level
- $\Delta T_d$  temperature change during glaciation due to sublimation or deposition as vapor pressure adjusts from saturation over a plane water surface to saturation over a plane ice surface at the new post-glaciation temperature
- $\Delta T_t$  temperature change during glaciation due to freezing of liquid water
- $\Delta T_l$  additional departure of temperature from the initial water-saturation adiabat that is realized as the cloud parcel ascends after glaciation following an ice-saturation adiabat
- the ratio of the molecular weights of water vapor to dry air

#### REFERENCES

- N. Fukuta (1972), Thermodynamics of cloud glaciation, Preprints, Third Conference on Weather Modification, Rapid City, S.D., Amer. Meteor. Soc., 192-194.
- E. B. Kraus and P. Squires (1947), Experiments on the stimulation of clouds to produce rain, Nature 159, 489-494.
- I. LANGMUIR, V. J. SCHAEFER, B. VONNEGUT, R. E. FALCONER, K. MAYNARD, and R. SMITH-JOHNSON (1947), General Electric Research Laboratory, First Quarterly Progress Report, Meteorological Research, Schenectady, N.Y. [The portion of this report written by Langmuir was reprinted in 1962 in *The Collected Works of Irving Langmuir*, Vol. 11, Cloud Nucleation. General Editor, C. Guy Suits, Executive Editor, Harold E. Way. Printed in Poland to the order of PWN-Polish Scientific Publishers by the Scientific-Technical Printing House (DRP), Warsaw. Publisher is Pergamon Press, N.Y., Oxford, London, Paris, 597 pp., Library of Congress Card No. 60-7068].
- P. F. Macready, Jr. and R. F. Scutt (1967), Cloud buoyancy increase due to seeding, J. Appl. Meteor. 6, 207-210.
- H. D. ORVILLE and K. HUBBARD (1973), On the freezing of liquid water in a cloud, J. Appl. Meteor. 12, 671-676.
- P. M. SAUNDERS (1957), The thermodynamics of saturated air: A contribution to the classical theory, Q. J. R. met. Soc. 83, 342-350.
- J. SIMPSON and V. WIGGERT (1971), Florida cumulus seeding experiment: numerical model results, Mon. Wea. Rev. 99, 87-118.
- O. TETENS (1930), Über einige meteorologische Begriffe, Z. Geophys. 6, 297-309.
- W. L. WOODLEY (1970), Rainfall enhancement by dynamic cloud modification, Science 170, 127-131.

(Received 2nd April 1975)

## WORLD METEGROLOGICAL ORGANIZATION

# SPECIAL ENVIRONMENTAL REPORT No. 3

# Observation and measurement of aimospheric polintion

Proceedings of a Technical Conference on the Observation and Measurement of Atmospheric Pollution (TECOMAP) jointly organized by the World Meteorological Organization and the World Health Organization

Helsinki, 30 July -4 August 1973



WMO - No. 368

Secretariat of the World Meteorological Organization - Geneva - Switzerland

## Atmospheric Electrical Conductivity and the Detection of Global Aerosol Pollution

#### William E. Cobb

## 1. Introduction

The possible climatic consequences resulting from secular changes in the atmospheric burden of suspended particulates has made it important to document the concentration, size distribution and nature of the atmospheric aerosol as accurately as possible. It is worthwhile to consider the electrical conductivity of the atmosphere as a useful tool in aerosol research, particularly with respect to global air pollution.

## 2. Atmospheric conductivity - correlation to suspended particulates

The fact that the atmosphere is slightly conducting is easily demonstrated by observing that an electrically charged and highly insulated conductor placed in the atmosphere, will systematically lose its charge to the surrounding air. Such conductivity as does exist, is due to the presence of highly mobile ions produced in the atmosphere by cosmic rays and local radioactive sources. The relationship between conductivity and ion concentration is expressed as follows:

$$\lambda = n e k$$
, (1)

where  $\lambda$  is the conductivity; n, the small ion density; k, the small ion mobility and e, the elementary charge per ion.

A balanced small ion concentration is maintained at any particular location in the atmosphere since ions are being removed at the same rate that they are being produced. They are removed by recombination with oppositely charged small ions, thus neutralizing the charge, and by attachment to much larger aerosols, both charged and uncharged.

The following well known equation describes the change of small ion density with time in terms of the production and disappearance of the small ions in the atmosphere. Thus, considering positive small ions.

$$\frac{dn}{dt} = q - \alpha n_1 n_2 - \eta_{12} n_1 N_2 - \eta_{10} n_1 N_0, \qquad (2)$$

where  $n_1$ ,  $N_1$  and  $n_2$ ,  $N_2$  are the small and large positive and negative ion densities respectively;  $N_0$  is the concentration of uncharged nuclei; q is the ion pair production rate;  $\alpha$ ,  $\eta_{12}$  and  $\eta_{10}$  are the respective coefficients of recombination between oppositely charged small ions and negative large ions, and between positive small ions and uncharged nuclei. An equivalent expression exists for small negative ions. It should be noted that positive and negative large ions are nothing more than particles which have acquired a net charge, probably due to collisions with small ions, and that the atmospheric fine-particle pollution is largely composed of the total mass of charged and uncharged particles. These particles are usually called condensation or Aitken nuclei and their concentration is given by,

$$Z = N_1 + N_2 + N_0 (3)$$

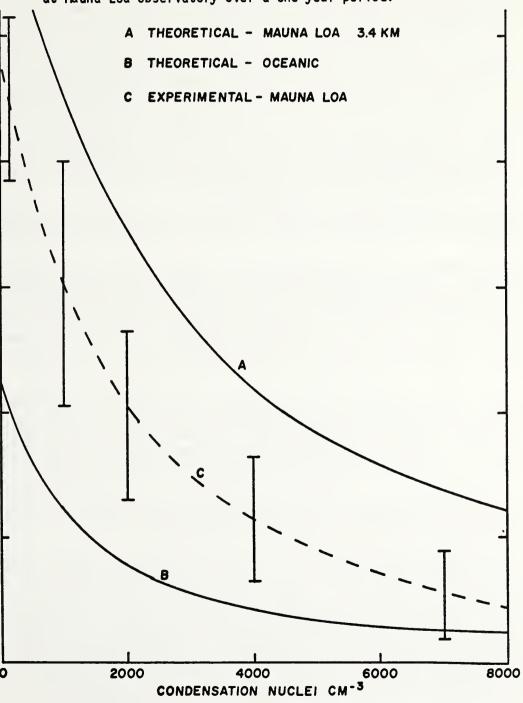
It is apparent from equation (2) that the last three "recombination" terms are factors which tend to reduce the small ion concentration and thus the conductivity. The relative importance of the recombination terms depends largely on the nuclei content of the air. In exceptionally clean air the last two terms become insignificant; in highly polluted air they become predominant.

The relationship, conductivity vs condensation nuclei density, is shown graphically in Fig. 1, where (a) and (c) are mathematically derived for 3400 m and at sea level over the mid-North Pacific, and (b) is based on measurements of the conductivity and the Aitken nuclei at the Mauna Loa high altitude observatory in Hawaii. The sensitivity of the conductivity to changes in the nuclei density is clearly evident and also the fact that this sensitivity increases as the air becomes cleaner.

Particulates which have appreciable atmospheric suspension times are largely sub-micron sized, however, they are much larger than the molecular sized small ions. Their role with respect to the conductivity is mainly a passive one, that of providing relatively immobile surfaces for the diffusional attachment of small ions thus reducing the electrical conductivity.

Aerosol pollution might well be defined as being the total volume which particulates occupy in a given space. It is this parameter which largely controls the conductivity. Thus in an atmospheric sample containing both small ions and Aitken type nuclei, the extent to which the conductivity is reduced will depend both on the size and the concentration of the suspended nuclei.

 Condensation nuclei vs electrical conductivity. Curves A and B are derivations for oceanic air at 3.4 km and at the surface. The dashed curve is based on observations made at Mauna Loa Observatory over a one year period.



## 3. <u>Instrumentation - the Gerdien system</u>

The conductivity measurement method devised by Gerdien (1905) and substantiated by Swann (1914) has been used for many years. While the hand-turned fan and quadrant electrometer have been replaced, the basic sensor remains essentially unchanged and makes the comparison of data through the years more reliable than would otherwise be the case.

The Gerdien method has been described by Chalmers (1957). In brief the sensor consists of a cylindrical condenser with an inner charged and highly insulated electrode. As air is drawn through the condenser, the electrode will attract oppositely charged ions and the collected ionic current can be continuously measured and recorded. It is necessary that sufficient air flow through the condenser be maintained so that Ohm's law conditions exist. The conductivity is easily calculated after knowing the electrode collecting potential and the capacity of the cylindrical condenser.

## 4. Observational procedures - "fair-weather" data and the "benchmark" concept

The conductivity, used to establish an index related to suspended particulates, is usually monitored at sites remote from sources of aerosol pollution. Measurements are thus made from mountain tops, polar regions and ocean vessels, where the objective is to obtain a reproducible data set which represents a reference standard, i.e., an "atmospheric benchmark" at a site where measurements are representative of the regional environment.

Each of the sites mentioned above have advantages other than their remoteness. At the South Pole, for example, effects associated with diurnal changes are absent during the long polar periods of sunlight and darkness. The Mauna Loa Observatory in Hawaii (Cobb, 1968, 1973) is located at 3400 m, well above the Austausch and the trade wind inversion which inhibits the vertical transport of low-level particulates. Ocean vessel measurements are particularly important because new data may be compared to the well known measurements of the sailing vessel "Carnegie", made during the period 1911-1929.

When attempting to establish benchmarks of the atmospheric electric climate it is customary to consider only the data gathered on "fairweather" days. Days with rain, fog, thunderstorms, blowing snow, etc., are associated with electrical effects considered typical of the local environment while it is desirable to have the conductivity air sample representative of the largest possible area. Fair-weather days are usually selected from meteorological observations although the fluctuations in the continuously recorded conductivity associated with disturbed weather are easily identified by the trained observer.

## 5. Historical data - importance of the "Carnegie" measurements

Much credit must go to the Carnegie Institution of Washington, whose scientists had the foresight 70 years ago to recognize the importance of monitoring the electrical properties of oceanic air. Their classic measurements made aboard the sailing vessel "Carnegie" and its predecessor "Galilee" have established an invaluable atmospheric benchmark of an era preceding much of the increase in anthropogenic pollution sources.

The scientific cruises of the "Carnegie" ended at the island of Samoa in 1929 when a tragic fire and explosion resulted in the sinking of the ship and the death of her captain. One need only read the accounts of the "Carnegie" cruises to appreciate the remarkable achievements of these dedicated sailor-scientists. Their meticulous care in making atmospheric observations has set an example seldom equaled.

Fortunately, the basic conductivity sensor has remained essentially unchanged. The "Carnegie" measurements have, for the most part, withstood advances in the state of the art. Thus new measurements may be compared to the "Carnegie" data in order to detect secular changes in the conductivity of oceanic air.

## 6. Recent conductivity measurements

Conductivity measurements in recent years have been made from oceanic regions (Cobb and Wells, 1970; Cobb, 1973; Morita, 1971; Gunn, 1964; Misaki and Takeuti, 1970; Anderson and Trent, 1962; Muhleisen, 1968) and polar regions (Ruhnke, 1962; Kondo, 1971). None of these investigations have approached the scope of the "Carnegie" measurements.

It is not the purpose of this report to present data, thus it is sufficient to say that several of the investigators above have reported oceanic regions where the conductivity has shown a downward trend and other regions where no secular trend was detectable. As might be expected, oceanic regions where conductivity measurements indicate an increased aerosol concentration, have been identified as windward extensions of pollution from populated land areas. Such regions represent areas within the global atmosphere the natural processes of aerosol removal have not kept pace with the increased anthropogenic production of particulates. The conductivity measurement can be a useful tool in the investigation of these regions of increased particulate concentration.

## 7. Stratospheric aerosol measurements

It is important that we document aerosol conditions in the stratosphere as well as near the earth's surface. Particulates are transported to above the tropopause by volcanic eruptions, forest fires, thunderstorms, etc., or formed from gas transformation directly in the stratosphere. It is also necessary to consider pollutants from stratospheric aircraft. The average residence time of suspended particulates is much greater in the stratosphere than for the troposphere. Volcanic ash has been known to circle the earth for several years. Relatively low concentrations of stratospheric particulates will influence the absorption and radiation of solar energy.

Balloon borne radiosondes, modified to measure atmospheric electric parameters, were successfully used at the Amundsen-Scott South Pole station recently, and during 1974 weekly soundings will be made in order to establish a benchmark of the atmospheric electric climate to 30 km. An example is shown (Fig. 2) of an air-earth current record, a parameter also sensitive to aerosol conditions. The sounding does not reveal layers of particulate concentrations in this single example.

## 8. <u>Summary and conclusions</u>

It has become important to the well-being of mankind on this planet to assess the consequences of the particulate material which is produced and injected into the atmosphere through the activities of an expanding human population. The distribution of particulate matter in the atmosphere results from the dynamic balance of processes which continuously cleanse and replenish the air with nuclei. The atmospheric processes of particle injection, transport, and eventual deposition have maintained a balanced aerosol level presumably for centuries, with the exception of periods of up to a few years following great volcanic eruptions. Within this century particulates produced by human activities have become a factor to be considered.

The relative abundance or scarcity of condensation nuclei can be of great importance to the physics of precipitation since nearly each cloud droplet requires a grain of particulate matter at its birth. Of equal or greater importance is the effect of the total particulate suspension on the global radiation budget and the resulting temperature at the earth's surface.

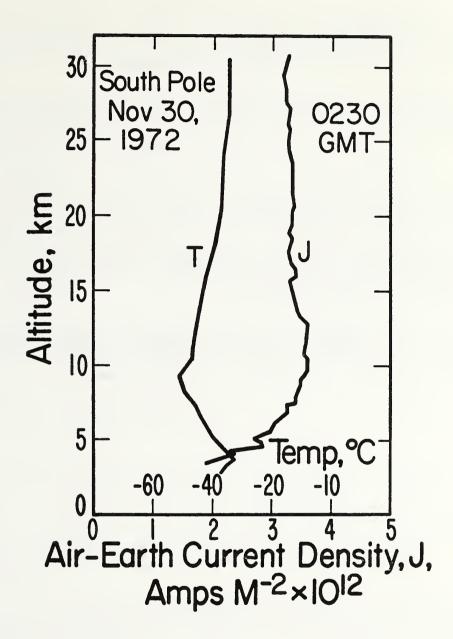


Fig. 2. Example of an atmospheric electric radiosonde flight made at the South Pole. An accumulation of such soundings will be made to establish an environmental benchmark for future reference with respect to global aerosol conditions.

The implications of possible climatic changes in global cloudiness, precipitation and temperature, associated with increased aerosol pollution, make it imperative that we observe and record atmospheric aerosol conditions as accurately as possible.

The application of atmospheric electric methods, as discussed in this report, provides a somewhat unique and sensitive way of documenting aerosol conditions particularly with respect to long term trends in the level of suspended particulates.

Aerosol research is a science which requires knowledge from several disciplines-chemistry, to determine aerosol composition, possible sources, gas to particle conversion processes, etc; physics, to determine size, concentration, electrical effects; meteorology, to investigate atmospheric sources and sinks, aerosol transport, residence times, removal processes, etc; and engineering, for instrumentation and new techniques such as air pollution surveillance from earth orbiting satellites.

An important aspect of this international forum (Technical Conference on the Observation and Measurement of Atmospheric Pollution) is the opportunity to become familiar with air pollution research by those outside our frequently specialized areas.

#### REFERENCES

- Anderson, R. V., and E. M. Trent, 1962: Atmospheric electricity measurements in the North Atlantic during FALLEX-60. U. S. Naval Research Laboratory, NRL Rept. 5833.
- Chalmers, J. A., 1957: Atmospheric Electricity. New York, Pergamon Press, pp 128, 129.
- Cobb, W. E., 1968: The atmospheric electric climate at Mauna Loa Observatory, Hawaii. J. Atmos. Sci., 25, 470-480.
- of oceanic air and its correlation to global atmospheric pollution. J. Atmos. Sci., 27, 814-819.
- , 1973: Oceanic aerosol levels deduced from measurements of the electrical conductivity of the atmosphere. J. Atmos. Sci., 30, 101-106.
- Gerdien, H., 1905: Demonstration eines Apparates zur absoluten Messung der electrischen Leitfähigkeit der Luft. Phys. Z, 6, 800-801.
- Kondo, G., 1971: Data of atmospheric electricity at Syowa Station in 1969-1970. Polar Research Center, Tokyo. Report No. 11, Japanese Antarctic Research Expedition.
- Misaki, M., and T. Takeuti, 1970: The extension of air pollution from land over the ocean revealed in the variation of atmospheric electrical conductivity. J. Meteor. Soc. Japan, 48, 263-270.
- "M. Ikegami and J. Kanazawa, 1972: Atmospheric electrical conductivity measurement in the Pacific Ocean, exploring the background level of global pollution. J. Meteor. Soc. Japan, 50, 497-500.
- Morita, Y., 1971: The diurnal and latitudinal variation of electric fie'd and electric conductivity over the Pacific Ocean. J. Meteor. Soc. Japan, 49, 56-58.
- Ruhnke, L. H., 1962: Electrical conductivity of air on the Greenland ice cap. J. Geophys. Res., 67, 2767-2772.
- Swann, W. F. G., 1914: The theory of electrical dispersion into the atmosphere, with a discussion of the Gerdien conductivity apparatus. Terr. Magn. Atmos. Elec., 19, pp. 88, 219, 242.

WIND TUNNEL TESTS OF AN AIRBORNE
ISO-KINETIC ICE CRYSTAL DECELERATOR

David Eyre

Atmospheric Physics and Chemistry Laboratory Boulder, Colorado September 1974

UNITED STATES
DEPARTMENT OF COMMERCE
Frederich B. Dent, Secretary

NATIONAL OCEANIC AND ATMOSPHERIC ADMINISTRATION Robert M. White, Administrator Environmental Research Laboratories Wilmot N. Hess, Director



#### Abstract

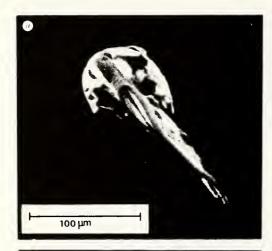
The design and wind tunnel tests of an aircraft mounted ice crystal decelerator and collector are described. The device incorporates a method to control and calibrate air flow volume samples. The system can be made to function iso-kinetically to reduce destruction of the crystals as they are intercepted in flight. Iso-kinetic sampling can also be accomplished by vacuum pumping in the decelerator receiver after the particles have been decelerated. The crystals are readily available for examination within the aircraft.

The decelerator is designed to operate at flight speeds of 90 m sec<sup>-1</sup> in pressurized multi-engine aircraft with air velocities at the collection station of 1.7 to 12.9 m sec<sup>-1</sup>. Ice crystals 800 microns in size have been collected in this manner without damage on impact.

#### Aerosol particles on tobacco trichomes

MARTELL¹ has described a plausible chain of events by which atmospheric radioactivity is incorporated into insoluble particles that are deposited in the lungs of tobacco smokers. The subsequent long exposure of the lungs to alpha activity is a strong candidate for the cause of bronchial cancer. Here we provide evidence for one of the steps in the sequence.

The accepted major sources of  $\alpha$  radioactivity in the atmosphere are radon and its decay products, which condense by attaching themselves to sub-micron atmospheric particles. According to Martell, many such aerosols contact and are incorporated into the sticky tips of tobacco trichomes (spine-like protuberances on the leaves). To contact the trichome tips directly the smaller particles that carry most of the radioactivity



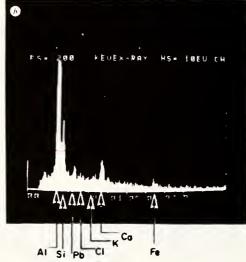


Fig. 1 a, Scanning electron micrograph of a cured tobacco trichome and b, X-ray spectrum of a trichome tip. Si, Fe, Pb, and Cl are elements commonly found in acrosols; K and Ca are components of the tobacco itself; and Al is a background signal from the sample holder.

must diffuse to the sticky, exudate-coated tips of the trichomes. Later, during tobacco curing, the sticky exudate polymerises to encapsulate the aerosols in highly insoluble particles. Thus, when inhaled as part of tobacco smoke, the radioactive aerosols have long residence times in the deep lung.

Martell has shown that trichomes of cured tobacco are radioactive and that the most insoluble, filterable portion of tobacco smoke is the most radioactive. In support of Martell's inference that the radioactivity observed on trichomes comes from atmospheric aerosols, we present evidence that aerosols are on and inside trichome tips.

Trichomes from North Carolina flue-cured and Turkish air-cured tobacco leaves were examined in a Cwikscan-100 equipped with a Kevex X-ray energy spectrometer. This instrument allows visual observation at high magnification and detection of elements heavier than neon in particles down to 250 Å in diameter. Silicon, sodium, chlorine, calcium and potassium were seen frequently (Fig. 1), iron and lead occasionally. Only potassium and calcium were seen regularly in all tips and stems equally. These known components of tobacco<sup>2</sup> mask attempts to observe them in sub-micron silicate aerosols.

Aerosols of  $> 0.5~\mu m$  diameter can be analysed individually on the surface of trichomes. These larger particles could be seen attached to most of the trichome tips of the North Carolina tobacco and half of those on Turkish tobacco. Of five individual particles analysed on North Carolina trichomes, four gave clear signals from silicon; one was doubtful. Iron was detected in several particles. One 0.5  $\mu$ m particle on Turkish tobacco contained chlorine. These compositions imply that the particles were silicate minerals and salt, respectively.

Trichome tips at positions where no exterior particles were visible showed silicon in half of the North Carolina samples. Portions other than the tips showed none. For Turkish tobacco sodium and chlorine were found on tips, and stems. Silicon and lead were present in about half of the tips. Some of the silicon was associated with visible sub-micron particles.

In short, tips, like the particles on them, contain elements commonly associated with both continental and marine aerosols. The direct inference is that where individual particles are not seen, the signal comes from many tiny aerosols trapped within the exudate on the tips. This observation provides an experimental link in Martell's reasoning that radon daughter radioactivity precipitates on aerosols which diffuse to trichome tips and later become insoluble residues in tobacco smoke. Martell proved that the radon daughter radioactivity is present in trichomes; we have shown that the aerosols which normally carry this radioactivity are present in the tips.

We thank E. A. Martell and S. E. Poet for discussions and for the tobacco samples.

R. L. FLEISCHER

Atmospheric Physics and Chemistry Laboratory, National Oceanic and Atmospheric Administration and National Center for Atmospheric Research, Boulder, Colorado 80303 and General Electric Research and Development Center, Schenectady, New York 12301

F. P. Parungo

Received March 18, 1974.

<sup>1</sup> Martell, E. A., Nature, 249, 215 (1974).

Atmospheric Physics and Chemistry Laboratory

<sup>2</sup> Schmeltz, I. (ed.), The chemistry of tobacco and tobacco smoke, 30, 54 (Plenum, New York, 1972).

#### SYNOPTIC-MESO SCALE BUDGET RELATIONSHIPS

#### FOR A TORNADO PRODUCING SQUALL LINE

#### J. Michael Fritsch

National Oceanic and Atmospheric Administration Atmospheric Physics and Chemistry Laboratory Boulder, Colorado 80302

#### 1. INTRODUCTION

Incorporation of the effects of moist convection on the synoptic scale requires either the simultaneous resolution of both the convective and synoptic scales (directly or by nesting grids), or knowledge of relationships between the synoptic forcing and the convective response (parameterization). Several parameterization techniques have been developed which relate the amount of convection to mass, moisture, or energy budgets of • the larger scale. For example, Arakawa and Schubert (1974) relate the amount of convection to the rate of destabilization by the large scale. Fraedrich (1974) uses total energy and potential vorticity as controls, while Ceselski (1974) regulates the convection by using large scale low-level convergence as the mass flux into cloud base. These types of techniques clearly allow for interaction of the convection with the synoptic scale, however strong mesoscale organization and development are not accounted for. Mesoscale organization and intensification may sometimes cause a significantly larger amount of mass and moisture to be "processed" through deep convective clouds than that indicated by synoptic scale budgets.

In order to obtain estimates for the mass and moisture budget relationships between a developing mesoscale convective system and associated synoptic scale wave, synoptic scale budgets were objectively calculated for a case which produced a well defined squall line with attendant severe weather. The meso- $\beta$  scale mass and moisture budgets for this case were previously calculated by Newton (1966). The following sections describe the synoptic and meso-scale situation and the mass and moisture budgets for both these scales. The results are discussed in light of convective parameterization requirements.

#### SYNOPTIC AND MESOSCALE SITUATION

#### 2.1 Surface Development

During the late afternoon of 21 May, 1961, a well-defined squall line developed from southeastern Kansas to south central Oklahoma. Figures 1 through 5 show the relevant surface maps for the period 12Z May 21 to 12Z May 22. Figures 6 through 14 show the corresponding radar analyses for the same period. All symbols are in the conventional notation used on National Weather Service facsimile charts. In general, the situation did not exhibit exceptionally strong dynamics or thermodynamics, but was rather typical of the average mesoscale development which occasionally produces severe weather. In this instance, hail,

up to three inches in diameter, was reported at several locations from Wichita Falls, Texas to points northwest of Muskogee, Oklahoma. Tornadoes were reported 40 miles southwest and 40 miles northeast of Oklahoma City.

Radar indicated initial stages of line development as early as 18Z with a fairly long line by 21Z. Newton (1966) observed that when the squall front passed through the 96 by 154 km National Severe Storms Project (NSSP) network around 00Z, it was essentially unbroken. At 06Z on the 22nd, the squall line had reached maturity and began to decay rapidly; by 12Z, the line disappeared from the radar analysis.

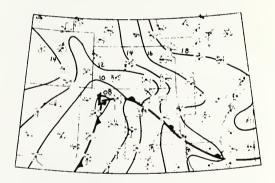


Figure 1. Surface analysis for 122 May 21, 1961.

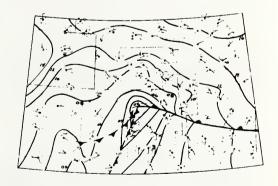


Figure 2. Surface analysis for 002 May 22, 1961.

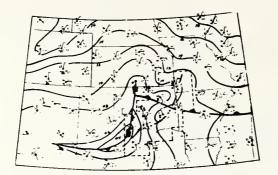


Figure 3. Surface analysis for 03Z May 22, 1961



Figure 4. Surface analysis for 06Z May 22, 1961



Figure 5. Surface analysis for 12Z May 22, 1961

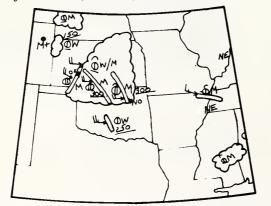


Figure 6. Radar depiction for 122 May 21, 1961

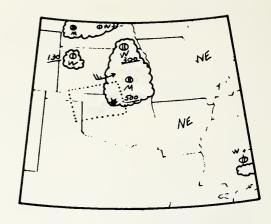


Figure 7. Radar depiction for 152 May 21, 1961

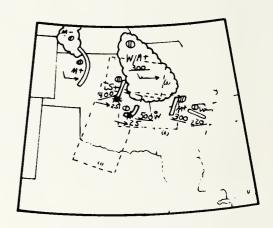


Figure 8. Radar depiction for 18Z May 21, 1961

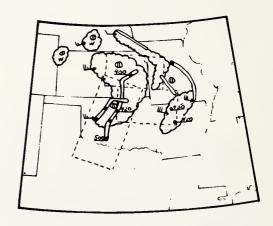


Figure 9. Radar depiction for 21Z May 21, 1961

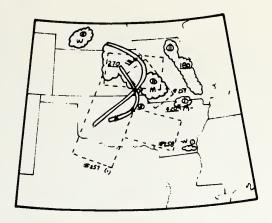


Figure 10. Radar depiction for 002 May 22, 1961

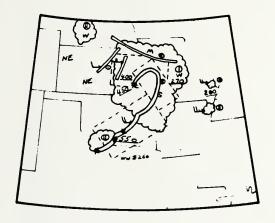


Figure 11. Radar depiction for 032 May 22, 1961



Figure 12. Radar depiction for 06Z May 22, 1961

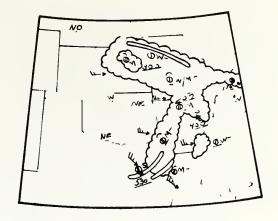


Figure 13. Radar depiction for 092 May 22, 1961

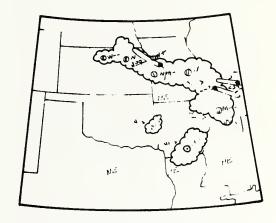


Figure 14. Radar depiction for 122 May 22, 1961

#### 2.2 Upper Air Features

The surface wave shown above was associated with an upper level cold trough that moved east out of the Rocky Mountains onto the Central Plains. Figures 15 through 17 show the 500 mb analyses for the three sounding times centered on 00Z May 22, 1961. The upper-level cold pool moved rapidly eastward on the 21st and developed a rather strong vertical motion field at 500 mb by OOZ on the 22nd (see Figure 18). Horizontal convergence at 700 mb was also quite strong as was the moisture convergence at 850 mb (See Figures 19 and 20). Note the focusing of vertical motion, and mass and moisture convergence in north central and northeastern Oklahoma. This area was also the scene of initial convective activity and line development (see the 15Z and 18Z radar depictions).

All of the upper air analyses were determined from the standard synoptic scale upper-air network using an objective analysis technique adapted from Fritsch (1971). Radiosonde stations used in the objective analysis are shown in the 500 mb analyses.

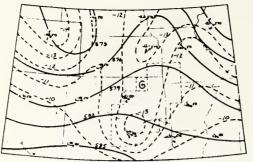


Figure 15. 500 mb analysis for 122 May 21, 1961. Solid lines are height contours and heavy dashed lines are isotherms.

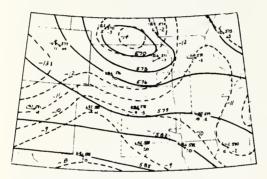


Figure 16. 500 mb analysis for 002 May 22, 1961. Solid lines are height contours and heavy dashed lines are isotherms.

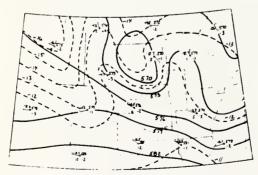


Figure 17. 500 mb analysis for 122 May 22, 1961. Solid lines are height contours and heavy dashed lines are isotherms.

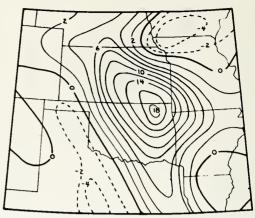


Figure 18. Vertical motion at 500 mb. Solid lines indicate rising motion and dashed lines show sinking air. Units are cm/sec.002, May 22, 1961

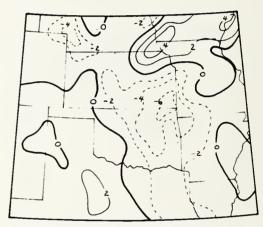


Figure 19. Horizontal divergence at 700 mb. Solid lines indicate divergence and dashed lines show convergence. Units are 10-5 sec-1. 002, May 22, 1961.

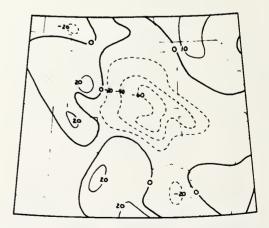


Figure 20. Horizontal moisture divergence at 850 mb. Solid lines indicate divergence and dashed lines show convergence. Units are  $10^{-11}$  gm sec<sup>-1</sup> cm<sup>-3</sup>. 00Z, May 22, 1961.

#### 3.1 Synoptic Scale

The development of the moisture budget equations for a volume has been treated in detail in several other studies (see, for example, Bradbury, 1957 and Fankhauser, 1965) and will not be repeated here. In this study, evaporation and transport of liquid and solid water are neglected and only precipitation and water vapor are considered. The following conservation equation may then be used to describe the change in water vapor in a volume, V:

$$\int_{V} \frac{\partial \rho \mathbf{r}}{\partial t} dV = - \int_{V} (\nabla_2 \cdot \rho \mathbf{r} \mathbf{V}_2 + \frac{\partial \rho \mathbf{r} \mathbf{w}}{\partial Z} + P) dV \quad (1)$$

where  $\rho$  = density of air

r = water vapor mixing ratio

∀2 = horizontal wind w = vertical wind

p = precipitation rate

The mass budget may be calculated using the continuity equation in the form:

$$\int_{\mathbf{V}} \frac{\partial \rho}{\partial \mathbf{t}} d\mathbf{V} = -\int_{\mathbf{V}} (\nabla_2 \cdot \rho \mathbf{V}_2 + \frac{\mathbf{v} \cdot \rho \mathbf{w}}{\partial \mathbf{Z}}) d\mathbf{V}$$
 (2)

Equations (1) and (2) were integrated over, a volume having a depth that extends from the surface to 50 mb and an area indicated by the thin dashed lines in the surface and 500 mb analyses. This area is  $2.32 \times 10^5 \ \mathrm{km^2}$  and grid points within the area were spaced at each degree of a latitude-longitude grid mesh. The volume was selected to encompass the synoptic scale area supplying mass and moisture to the squall line. Except for the surface layer, which was integrated by hand, the remainder of the integration was carried out by computer using 50 mb increments from 950 to 50 mb.

#### 3.2 Mesoscale

The mesoscale mass and moisture budgets were obtained by extending the calculations of Newton (1966) over a longer portion of the squall line. Newton found that the portion of the squall front passing through the NSSP network was essentially unbroken and, that on the average, radar showed one convective cell per 20 km Using the observed mass and moisture convergence on the mesoscale, Newton then calculated the mass and moisture budget for a "mean" convective cell. Assuming that the portion of the line in the budget volume of this study was unbroken, and using the same cell density as Newton, there were approximately 32 "mean" cells in the line within the budget volume. Assuming further that the "mean" cell budget quantities, observed by Newton for the length of the line in the NSSP network, are approximately the same for cells in the remainder of the line in the budget volume, a mesoscale budget for the budget volume can be estimated.

#### 4. RESULTS

Figures 21 and 22 show the vertical distribution of the synoptic scale mass and moisture divergence for the budget volume. Note the strong horizontal convergence of mass and moisture up to 600 mb. The large scale vertical flux of moisture out of the boundary layer was about half of the horizontal moisture convergence indicating a net moistening of the budget volume.

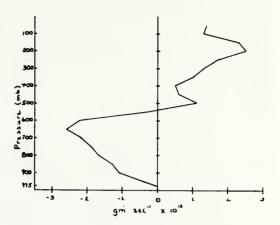


Figure 21. Vertical distribution of synoptic scale mass divergence for the budget volume. 002, May 22, 1961.

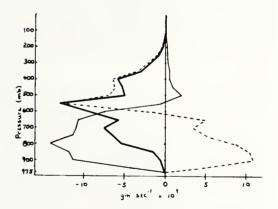


Figure 22. Vertical distribution of synoptic scale moisture divergence for the budget volume. Thin solid line is the horizontal moisture divergence; dashed line is vertical moisture divergence and heavy solid line is the total moisture divergence. 002, May 22, 1961.

Column 2 of Table 1 shows the vertically integrated mass and moisture divergence calculated from synoptic scale data. The mass divergence integrated over the total depth is zero since the vertical motion was adjusted (Smith, 1971) to zero at both the surface and 50 mb, and the divergence was brought into agreement with this adjusted vertical motion. Column 1 of Table 1 is the

Meso scale consumption	Mass	Maisture	Synoptic Scale Supply		Moisture		10
(flow into storms)	8m X 10 <sup>1 2</sup>		(Horiz. convergence)	sec_102	<u>gm</u> wec x 100	Mass	Moisture
			Surface to 850 mb	2.8	2.7	. 14	.11
Surface to 700 mb	20.3	1 25.5	Surface to 700 mb	8.6	6.4	. 42	. 25
Surface to 360 mb	32.8	27.6	Surface to 550 mb	13.7	7.8	.42	.28

Table 1. Synoptic and meso-scale vertically integrated mass and moisture bullets. See text for additional explanation of Tables.

mesoscale consumption, and column 3 is the ratio of synoptic scale rate of supply to the mesoscale consumption. Table 3 shows the percent of the observed mesoscale precipitation rate accounted for by synoptic scale moisture convergence. In general, the synoptic scale horizontal mass and moisture convergence in the subcloud layer (surface to 850 mb) accounted for about 10% to 15% of the computed mesoscale consumption rate and 20% of the observed precipitation rate. However, Newton found that the flux of mass and water vapor into the forward side of the squall line was deeper than the subcloud layer and was primarily in the layer from the surface to about 700 mb. Integrating synoptic scale convergence up to 700 mb accounts for about a fourth to a half of the mesoscale consumption rate, while integrating to the level of non-divergence (  $\approx$  550 mb) gives a maximum synoptic moisture supply rate of about 60% of the rate of mesoscale consumption.

Bear in mind that the above results are for the relatively large area which is supplying the squall line over a period of time. It is interesting to compare the synoptic and mesoscale mass and moisture budgets for an individual grid element which contains a portion of the squall line. The grid element which exhibited the maximum synoptic scale moisture convergence at 850 mb was selected (labeled G in Figure 15). This type of comparison is more relevant to numerical modeling since it is an indication of the rate at which convection would be forced in some parameterization techniques relative to the rate at which convection is actually proceeding on the mesoscale. Figures 23 and 24 show the vertical distribution of the synoptic scale mass and moisture divergence for the grid element, G. The vertical distribution of mass and moisture convergence in the element, G, are very similar to the area integrated distributions except that more of the convergence is concentrated at lower levels. Tables 2 and 4 are structured the same as Tables 1 and 3 except they apply for the grid element instead of the entire budget volume. Column 3 of Table 2 indicates that both the synoptic scale mass and moisture convergence in the subcloud layer are about one tenth of the mesoscale consumption rate. When compared to the observed precipitation rate, the large scale horizontal moisture convergence in the subcloud layer accounted for approximately 20% of the rainfall (Table 4).

			Synoptic scale supply		Moisture		
(flow into storms)	gm x 10 <sup>2</sup> sec	sec x 100	(horiz. convergence)	$\frac{gm}{sec} \times 10^2$	<u>gm</u> x 10 <sup>()</sup> sec	Mass	Moisture
	2 ( 2		Surface to 850 mb	0.41	0.47	.11	.10
Surface to 700 mb	3.68 4.62	I 4.6/ i	Surface to 700 mb	0.91	0.88	. 25	.19
Surface to 360 mb	5.93	4.99	Surface to 550 mb	1.29	1.02	.22	.20

Table 2. Synoptic and meso-scale vertically integrated mass and moisture budgets of element G.

		Synoptic Scale horiz. convergence	% of Meso
i	sfc. to 850 mb	2.7 X 10 gm sec -1	20
-	sfc. to 700 mb	6.4 X 10 gm sec -1	47
	sfc to 550 mb	8.2 X 10 gm sec -1	60
Ì	sfc. to 50 mb	7.8 X 10 gm sec -1	57

Table 3. Percent of observed meso-scale precipitation rate accounted for by synoptic scale moisture convergence.

Atmospheric layer	Synoptic scale Horiz.Convergence	% of meso
sfc. to 850_mb	4.7 X 10 <sup>9</sup> gm sec <sup>-1</sup>	19
	9.9 X 10 gm sec 1	40
	10.2 X 10gm sec -1	41
sfc. to 50 mb	9.9 X 10 <sup>9</sup> gm sec <sup>-1</sup>	40

Table 4. Percent of alsorved reso-scale precipitation rate accounted for by synoptic scale moisture convergence in element G.

#### DISCUSSION

The results of the budget study confirm that mesoscale organization and development can generate much stronger low-level mass forcing, and provide a substantially larger rate of moisture convergence than that indicated by the synoptic scale. Since there were additional line segments and scattered areas of active convection in the budget volume, other than the primary squall line, and since the extension of the volume northward from the NSSP network included an area of stronger large scale convergence, these estimates of the relationship between mesoscale consumption rate and synoptic scale supply rate are

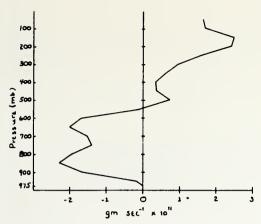


Figure 23. Vertical distribution of synoptic scale mass divergence for the grid element, G. 002, May 21, 1961

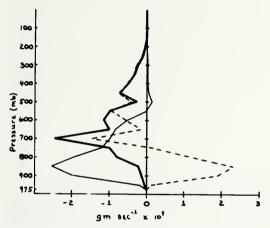


Figure 24. Vertical distribution of synoptic scale moisture divergence for the grid element, G. Thin solid line is horizontal moisture divergence; dashed line is vertical moisture divergence and heavy solid line is the total moisture divergence. 002, May 22, 1961.

probably conservative (i.e., synoptic scale accounts for even less than what is indicated).

Consider now the moisture budget studies for individual cumumlonimbi embedded in moderate to strong shear. Summaries of these studies (Marwitz, 1972; Foote and Fankhauser, 1973) indicate that storms in moderate to strong shear are inefficient relative to storms in little or weak shear (efficiency is defined to be the ratio of precipitation to vertical moisture flux into the updraft). In addition, Wills (1969) and Novlan and Gray (1974) have shown that most severe weather producing convective systems are embedded in moderate to strong vertical shear and the case study here is no exception. If then, in a large scale numerical model, the amount of convection for a case with moderate or strong shear is regulated by synoptic scale low level moisture convergence, and a convective cloud model is employed which realistically simulates

the inefficiency of individual thunderstorms, the total amount of precipitation from these storms should be small. However, if mesoscale organization occurs, then a significantly larger amount of mass and moisture is processed through the storms which compensates for the inefficiency of the individual clouds. Thus, the increased precipitation may appear to closely match the synoptic scale time integrated moisture convergence, even though the use of the synoptic scale convergence as a control in parameterization would greatly underestimate the amount of mass processed through convective overturning.

There are several potential errors which may enter into numerical models if mesoscale development, and the inefficiency of thunderstorms in shear, are not properly accounted for. Consider for example, the "tuning" of numerical cloud models using synoptic scale forcing and observed precipitation. If the amount of mass entering cloud base is determined from the low level synoptic forcing, and cloud dimensions or microphysics are then adjusted so that the model precipitation agrees with the observed, clearly the resulting cloud model characteristics will be in error (this same argument applies for cloud ensembles). More importantly, if then the cloud model is used in parameterizing the effects of the convection on the large scale, the magnitude and vertical distribution of the thermodynamic adjustment may be substantially different from the actual effects of the convection. The fact that the mesoscale vertical mass transfer rate can be several times larger than the synoptic scale rate indicates that a substantial amount of "local" vertical circulation is present. Since this local circulation occurs for the most part via "inefficient" moist convection, vertical stabilization is significantly larger for situations with mesoscale development. The additional stabilization associated with the local circulations that arise must therefore be accounted for in parameterization of mid-latitude convection.

#### REFERENCES

Arakawa, A. and W.H. Schubert, 1974: Interaction of a cumulus cloud ensemble with the large-scale environment, Part I. J. Atmos. Sci., 31, 674-701.

Bradbury, D.L., 1957: Moisture analysis and water budget in three different types of storms. J. of Meteor., 14, 559-565.

Ceselski, B.F., 1974: Cumulus convection in weak and strong tropical disturbances. J. Atmos. Sci., 31, 1241-1255.

Fankhauser, J.C., 1965: A comparison of kinematically computed precipitation with observed convective rainfall. Tech. Note 4-NSSL-25.

Foote, G.B., and J.C. Fankhauser, 1973: Airflow and moisture budget beneath a northeast Colorado hailstorm, J. Applied Meteor., 12, 1330-1353.

Fraedrich, K., 1974: Dynamic and thermodynamic aspects of the parameterization of cumulus convection: Part II. J. Atmos. Sci., 31, 1838-1849.

Fritsch, J.M., 1971: Objective analysis of a two dimensional data field by the cubic spline technique. Mon. Wea. Rev., 99, 379-386.

Marwitz, J.D., 1972: Precipitation efficiency of thunderstorms. Proc. Third Conf. on Wea. Mod., Rapid City, S.D., June 26-29, 1972, 245-247.

Newton, C.W., 1966: Circulations in large sheared cumulonimbus. Tellus, 18, 699-712.

Novlan, D.J. and W.M. Gray, 1974: Hurricane spawned tornadoes. Mon. Wea. Rev., 102, 476-488.

Smith, P.J., 1971: An analysis of kinematic vertical motions. Mon. Wea. Rev., 99, 715-724.

Wills, T., 1969: Characteristics of the tornado environment as deduced from proximity soundings. Sixth Conf. on Severe Local Storms, Amer. Meteor. Soc.

## Cumulus Dynamics: Local Compensating Subsidence and its Implications for Cumulus Parameterization

By J. MICHAEL FRITSCH<sup>1</sup>)

#### Abstract

Observations of air flow in and around convective clouds are summarized and discussed in light of the requirements for parameterization of midlatitude convection. Both theory and observation indicate that a substantial portion of the compensating subsidence occurs as dry downdrafts in the immediate vicinity of convective clouds, which suggests that an additional physical mechanism is necessary in linking convection to the large scale. A conceptual three-dimensional model of midlatitude organized convection along with its implications for parameterization, particularly in mesoscale modeling, is presented. The effects of moist downdrafts are also considered and some differences between midlatitude and tropical convection are discussed.

#### 1. Introduction

For different large scale conditions, the atmosphere exhibits different forms of convection. Ludlam (1966) described four principal kinds of convection which he classified according to scale: 1) small scale convection such as cumulus convection, 2) intermediate-scale convection such as mountain or sea-breeze circulations, 3) cumulonimbus convection such as observed in squall lines, cloud clusters, easterly waves, hurricanes, etc. Moncrieff (1974) extended Ludlam's classification by relating several distinct types of cumulonimbus convection to specific ranges of Richardson number (Ri). Using a Richardson number defined by the ratio of available buoyant energy to available kinetic energy, Moncrieff's studies indicated that for -Ri > 1 cumulonimbus convection would be characterized by 'air mass' type thunderstorms, tropical type cumulonimbus would be expected for -Ri > 2, and for  $-\frac{1}{4} \le -Ri \le 1$  midlatitude organized convection would be likely.

Each of these convective types exhibits important differences in thermodynamic and dynamic structure and therefore in the mode in which they interact with their environment. Thus, it seems reasonable that cumulus parameterization techniques should account for these differences. Betts (1974), Berkofsky (1974), Ogura (1972), Bates (1972), and Yanai (1972) have discussed the existing parameterization theories so a

<sup>&</sup>lt;sup>1</sup>) Atmospheric Physics and Chemistry Laboratory, National Oceanic and Atmospheric Administration, Boulder, Colorado, 80302, USA.

review of current techniques will not be included in this paper. Rather, certain aspects of the circulation of cumulus and cumulonimbus will be considered and some specific characteristics of midlatitude convection and their implications for parameterization will be discussed.

#### 2. Observations of convective circulations

As early as 1952, observations of circulations in cumulus clouds were being taken by specially instrumented aircraft. These observations, initiated by MALKUS (1954), revealed the vertical motion, temperature, and moisture structure within and immediately adjacent to two trade cumuli. Since that time, many such observations have been taken by other investigators for other types of cumulus clouds and clouds in general. For the most part, efforts have been concentrated within the visible limits of the clouds, with only superficial treatment given to the areas immediately adjacent to the clouds. As a result, our knowledge of 'in-cloud' circulations has increased substantially (see for example, BATTAN and THIESS 1966, 1970; KROPFLI and MILLER 1975), while our understanding of processes in the immediate environment of the clouds is still relatively unexplored. Fortunately, there have been some cloud investigation programs where observations were taken over short distances prior to entering and subsequent to exiting the visible cloud boundaries. These observations cover a wide variety of convective cloud types and locations. However, certain general characteristics of convective cloud circulations are evident from the observations and some of these are discussed below.

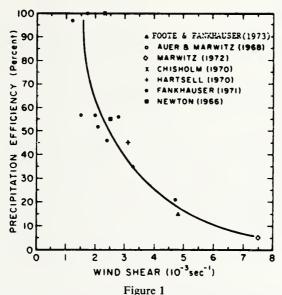
#### 2.1. Moist downdrafts and vertical wind shear

Precipitating midlatitude convective clouds (particularly multi-celled systems and organized lines) frequently exhibit a substantial moist downdraft. The mechanisms which produce the downdraft, notably droplet drag and cooling from evaporation of cloud water and rain into drier environmental air, have been very well documented (see for example BYERS and BRAHAM, 1949; FUJITA, 1959; HOOKINGS, 1965, TAKEDA, 1966; and NEWTON, 1966). In midlatitude convection, where cloud bases are frequently higher than in the tropics, and middle level dry air intrudes into the rear of the storm, moist downdrafts may cool the surface temperature by as much as 5°C to 15°C. KAMBUROVA and LUDLAM (1966), in a model simulation of rainfall evaporation in thunderstorm downdrafts, found that a strong downdraft descending from 500 mb to 800 mb with intense rain produced a cooling of about 10°C at 800 mb. Even in tropical cumulus clouds, with lower cloud bases and a more moist environment, there are strong indications of downdraft effects in the lowest 200 mb (Dugan, 1973; Betts, 1973).

In addition to the cooling, a local circulation<sup>2</sup>) and more low level convergence are

<sup>&</sup>lt;sup>2</sup>) The term 'local circulation' is considered here to mean a vertical mass circulation which is not reflected in the synoptic scale vertical motion.

other important by-products of moist downdrafts (GRAY, 1972). TAKEDA (1965) and MARWITZ (1972a) have pointed out that the updrafts which form in response to the moist downdrafts are stronger and more organized in situations with vertical wind shear. This implies a definite dynamic distinction between midlatitude convection where vertical wind shear is virtually always present and tropical convection where vertical wind shear is generally very weak. Moncrieff's studies (1974) further support this distinction. Another feature which suggests a distinction between midlatitude and tropical convection is the effect of vertical wind shear on precipitation efficiency. Marwitz (1972b) in a study of thunderstorm precipitation efficiency vs. vertical wind



Precipitation efficiency (ratio of rainout to water vapor inflow) as a function of vertical wind shear in layer from cloud base to cloud top (adapted from Foote and Fankhauser, 1973; originally produced by Marwitz, 1972b; reproduced with permission of authors).

shear, found that the precipitation efficiency diminished substantially as wind shear increased. Foote and Fankhauser (1973) extended Marwitz's study and found an even stronger correlation between wind shear and precipitation efficiency (see Fig. 1). One must be carfeul to interpret Fig. 1 correctly since a reduction in efficiency does not necessarily mean that less precipitation falls from storms in shear. On the contrary, even though the cloud's 'efficiency' may be reduced, the total amount of moisture processed may be greatly increased by the storm's organization and this may more than compensate for the reduction in cloud efficiency.

If a substantial portion of the evaporation occurs through precipitation evaporation in the moist downdraft, then the convective stabilization process by storms in shear is exceptionally efficient relative to other types of convection. Specifically the storm in vertical shear makes use of the release of latent heat to form the moist updrafts

and force compensating subsidence in the environment, yet also manages to reverse the process and re-use the same moisture to cool the lower layers. Simply stated, a precipitating storm is most efficient from the standpoint of convective stabilization when the precipitation is evaporated in a moist downdraft, and there is a higher likelihood for this to occur in tilting systems in vertical shear.

Finally, since warming aloft on the order of several degrees centrigrade may do very little to stop convection (this can be checked on any thermodynamic diagram), it is likely that the moist downdraft in midlatitude convection does much, and probably more, to stabilize the atmosphere than the subsidence induced warming from the primary convective circulation.

#### 2.2. Dry downdrafts

2.2.1. Low latitude. Trade cumuli measurements by MALKUS (1954) indicated a general area of moderate lifting (1-3 amps) near the lower part of the clouds both in the clouds and in the clear areas around the clouds. Vertical motions at higher levels generally showed a continuation of rising motion within the cloud proper, however, areas of sinking air were apparent in the clear air adjacent to and between clouds. WARNER (1970), in a study of cumulus clouds along the eastern Australian coast also found substantial amounts of sinking air at intermediate levels in the clear areas adjacent to the clouds. In both of these cases dry downdraft velocities were on the order of one to three meters per second which was usually about twenty-five to fifty percent of the observed updraft speeds. In still another study of low-latitude cumulus, the Warm Rain Project in Hilo, Hawaii (LAVOIE, 1966), sinking motion in the clear air adjacent to cumulus clouds was observed using balloon flights. Downward velocities of up to 1.4 meters per second were recorded in the Hawaii case which for clear air is considered substantial for cumulus congestus in this region. Figure 2 (CUNNING-HAM, 1959) shows the water vapor mixing ratio structure in and around a cumulus congestus over Grand Bahama Island. Note the drop in mixing ratio at midlevels on both sides of the cloud.

Investigations of larger tropical cumulus clouds also indicate a significant region of clear air subsidence, on the order of meters per second, immediately adjacent to the clouds. Preliminary analyses of GATE data (BEAN, 1975) show instances of apparent dry downdrafts near tropical cumulus and cumulonimbus. WILLIS' (1972) study of a large cloud in an active tropical cloud line system showed a dry downdraft with at least a two and a half kilometer diameter (the area could possibly have been larger, but further information was not presented in the report). These and still other observations suggest the existence of substantial subsidence in the near vicinity of low-latitude moist-convection.

2.2.2. Mid-latitude. Vertical motion measurements around mid-latitude cumulus and cumulonimbus also display areas of sinking motion in the clear air adjacent to and between clouds. Fair weather Arizona cumuli, specifically cumulus humilis and

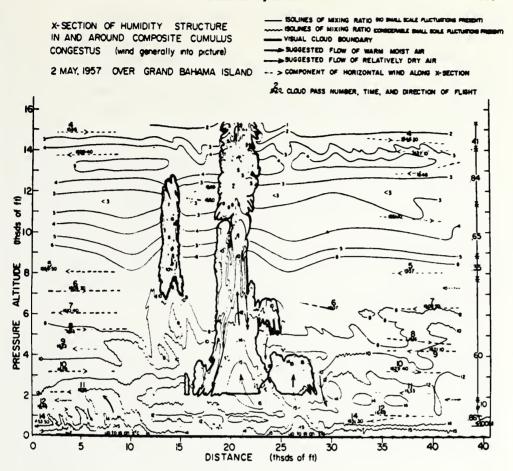


Figure 2
Cross section of humidity structure in an around composite cumulus congestus, over Grand Bahama Island, 2 May 1957. Wind generally into the picture. (From Cunningham, 1959; reproduced with permission of author.)

cumulus mediocris, were intensively studied by WEICKMANN and TEBO (1966). Aircraft observations revealed not only areas of substantial sinking motion in the clear air but anomalous warming in these sinking areas suggesting the possibility that the air was being forced to warm by adiabatic compression (warming was also apparent in many of the dry downdrafts around the low latitude clouds). Relatively high aerosol concentrations around these same clouds and much lower concentrations in the neighboring clear area showed that an additional downward circulation was occurring nearby (within 20 km) but not immediately adjacent to the clouds. It is not known whether this additional downward motion was part of an organized mesoscale circulation in response to the general area of convective updrafts or simply an area where large scale subsidence was not being blunted by active convection; WEICKMANN (1966)

indicated the former explanation and COTTON (1974) also alludes to the possibilities for this type of a circulation.

In addition to the temperature, aerosol, and vertical motion observations which indicate the presence of significant dry downdrafts, humidity observations clearly show areas of anomalously warm and dry air immediately adjacent to midlatitude clouds. Cunningham (1959) and Cunningham et al. (1956) penetrated numerous convective

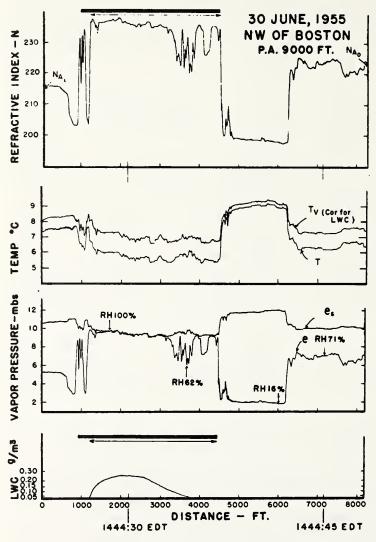
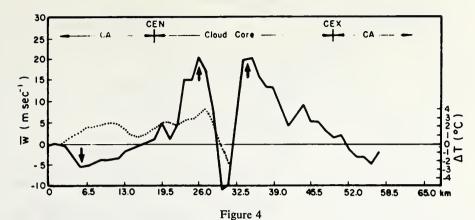


Figure 3

Cloud and environment parameters for cumulus penetrations northwest of Boston, 30 June 1955. Solid bars show periods when the aircraft was inside visible cloud and long arrows show the interior cloud region as deduced from the records. (From Cunningham, 1959; reproduced with permission of author.)



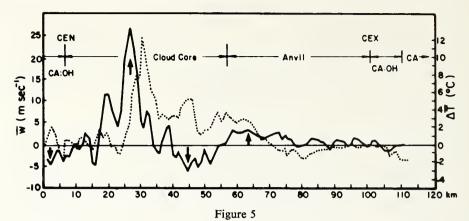


Mean vertical velocity and temperature variations near and within northeastern Colorado severe storm: 21 June 1972 at 9756 m MSL by F-101B aircraft. Solid line is vertical velocity and dotted line is temperature. Abbreviations are defined as follows: CEN and CEX  $\equiv$  visible cloud entrance and exit respectively; CA  $\equiv$  clear air; OH  $\equiv$  overhang. (From Sinclair, 1973; reproduced with permission of author.)

clouds and frequently found areas of dry, apparently sinking environmental air. Figure 3 (from Cunningham et al., 1956) shows the humidity and temperature for a flight through a relatively small cumulus which was penetrating an inversion and entering a more rapidly moving air-stream. Note the downdraft warming on the order of two to three degrees Centigrade at the same time that the relative humidity drops to less than a fourth of the environmental humidity. Although the presence of the inversion accentuates the effects of the compensating subsidence, similar profiles were observed for both large and small clouds under other atmospheric conditions.

Perhaps the most detailed information regarding the local return circulation around midlatitude convection is that given by SINCLAIR (1973). Using a T-33 and an F-101B aircraft, Sinclair has penetrated large convective storm cells over northeastern Colorado as well as Oklahoma squall-line storms. By design, observations were taken for a substantial distance outside the visible cloud boundaries in an attempt to obtain three dimensional turbulence data for the cloud system. Figures 4 and 5 (from SINCLAIR, 1973) show the vertical motion and temperature for flights near and within northeastern Colorado severe storms. Note the areas of clear air downdrafts (up to five meters per second and thirteen kilometers in width) on either side of the cloud in Fig. 4. Note also the relative warming in the clear air downdraft and the cooling in the moist downdraft (the temperature profile was terminated in the middle of the storm due to a sensor malfunction). The data in Fig. 4 were taken during a cross wind penetration of a severe storm while the data in Fig. 5 show a penetration along the axis of the mean wind. Note once again that there is a clear air downdraft (upwind of the storm) with a substantial moist downdraft within the visible cloud. Bear in mind that these observations are taken in the upper portions of the storms below the anvil cloud.

Sinclair states, 'These measurements, as well as other severe storm penetration



Mean vertical velocity and temperature variations near and within a northeastern Colorado severe storm: 28 July 1970 at 9146 m MSL by T-33 aircraft. See Fig. 4 for explanation of variables and symbols. (From Sinclair, 1973; reproduced with permission of author.)

cases, indicate that the descending sheath of air surrounding the updraft core(s) of the severe storm at these levels is warmer than the clear air environment in which the storm growth takes place. The presence of warm, dry air bordering the storm would appear to be an important thermodynamic factor in the turbulent mixing processes that take place along this boundary.' Observations of other midlatitude deep convective clouds by SAND (1975) also indicate clear air downdrafts on the order of ten to twenty-five percent of the updraft speeds.

Although the areas of updrafts and downdrafts quite likely fluctuated radically and rapidly in location, intensity and size, a conceptual model of an organized midlatitude convective storm which embodies these observations can still be constructed.

#### 3. Conceptual model

Figures 6 through 9 are schematics of a well-organized traveling midlatitude cumulonimbus in shear. Its structure is similar to the Browning and Ludlam (1962) and Newton (1963) models except that more detail is included for the vertical motion in the clear air and to some extent the directional shear with height (see Fig. 6). The vertical section shown in Fig. 7 is along the axis of the mean wind at anvil heights and depicts the vertical motion through the storm and its environment. Note the clear air sinking in the rear of the storm and the weak circulation ahead of the storm. The weak pre-storm circulation is based upon Sinclair's (1973) observations of weak ascending motion beneath the anvil and radiometric water vapor measurements by Kuhn et al. (1971), Shlanta and Kuhn (1973) and Kuhn and Stearns (1973). The water vapor measurements were taken at constant heights around several isolated and squall-line Colorado thunderstorms. It was observed that relatively high values of



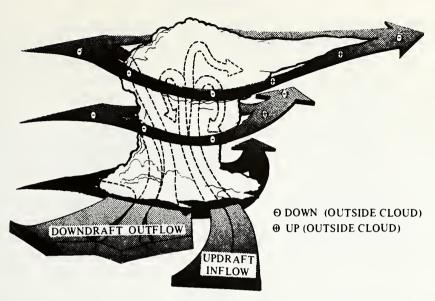


Figure 6

Conceptual model of traveling mid-latitude cumulonimbus in shear. Plus and minus signs indicate areas of up and down motion for airflow exterior to the cloud. Arrows bordered by dashed lines indicate airflow within the cloud.

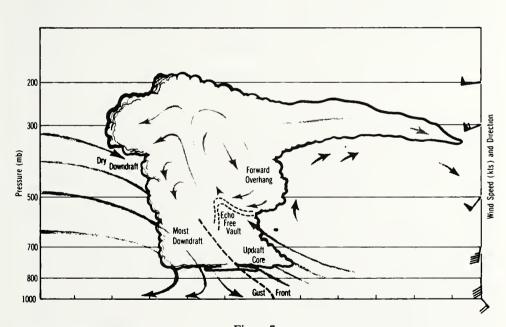


Figure 7

Conceptual cross section of vertical motion along the axis of mean wind. Wind barbs are shown in conventional notation.

water vapor downstream of the storms returned to upstream values within about fifty kilometers of the center of the storm. Since the observations were taken for about ninety minutes and the relative speed of the airflow away from the storm was approximately forty to fifty knots, it appears that sinking motion was occurring about twenty-five to fifty kilometers downstream from the primary updraft regions.

Figure 8 is a cross section perpendicular to the axis of mean wind and is simply intended to show the position of the dry downdraft areas relative to the moist up and downdrafts. Figure 9 is a conceptual schematic of the vertical motions through a horizontal plane at approximately 400 mb. The size of the plus and minus signs indicates the relative magnitude of the vertical motion.

These schematics are not meant to imply that organized midlatitude cumulonimbi generate a continuous circulation of the form shown here. Rather, they are intended to draw attention to the local 'direct' circulation of the storm both inside and outside of the visible cloud boundaries. To the best of the author's knowledge no information exists which definitely shows the mode through which the compensating downdrafts occur; that is, it is not known whether there is a continuous sheath of sinking air surrounding the updraft, broken zones of sinking air, or periodic sinking via small bubbles, etc. However, the data which is available does suggest some crude relationships between the moist updraft and the dry downdrafts. In general, the speed of the dry downdrafts was about twenty-five to fifty percent of the main updraft speeds (for middle and upper levels of the clouds) and the area affected by the dry downdrafts was about double the area of moist ascent. This means that for middle and upper levels, around fifty percent or more of the ascending mass was compensated for by local dry downdrafts. Caution should be used in using these estimates since the Cunningham

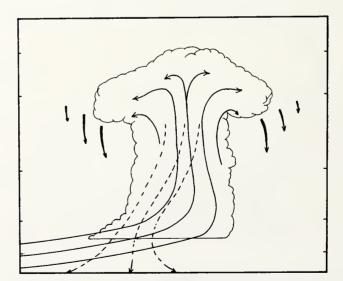


Figure 8

Conceptual cross section of vertical motion along an axis perpendicular to the mean wind.

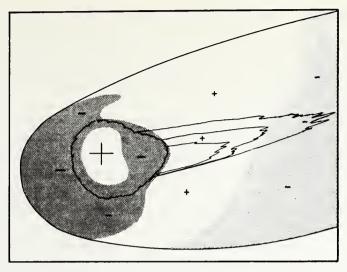


Figure 9

Conceptual schematic of vertical motion through a horizontal plane at 400 mb. Plus signs indicate up motion and minus signs down motion. The size of the plus and minus signs indicates the relative magnitude of the vertical motion and areas of down motion are shaded.

et al. (1956) data indicate that the degree of local subsidence may be strongly dependent upon large scale vertical motion.

#### 4. Discussion

#### 4.1. General considerations

In recent years, the role of moist convection in the earth's hydrologic cycle and general circulation has taken on increased stature. While the greatest emphasis has been on tropical convection (see, for example BATES, 1972), the importance of the effects of midlatitude convection on large scale circulation features has also been demonstrated (TRACTON, 1972). Even more recently, research emphasis on mesoscale weather systems has been increasing and has resulted in a re-evaluation of convective parameterization theories and hypotheses. In general, the objective of cumulus parameterization is to incorporate into the larger scale the interaction of a body of convective clouds with the larger scale without necessarily resolving the details of the individual convective elements. In order to develop a meaningful technique for parameterization, one must have a reasonable physical hypothesis which explains 'how much' convection will occur, what form(s) it will take, and how are the heat and momentum redistributed locally and 'upscale.' For example, some parameterization theories determine the amount of convection by relating it to the amount of vertical mass flux at the top of the boundary layer. Other techniques relate the amount of convection to the moisture

convergence within the boundary layer while still others use the moisture convergence integrated through the entire depth of the atmosphere. If the size(s) and type(s) of convective clouds were determined, say by using a simple cloud model, the number of clouds could also be determined. The final problem then, would be to distribute the momentum and heat carried by the clouds while allowing for cloud to cloud and cloud to environment interaction.

Consider now only the thermodynamic portion of the adjustment. Essentially there are two approaches to this problem (other than the direct convective adjustment described by Manabe et al., 1965). Basically, the first approach (e.g. Kuo, 1965) introduces the effects of the convective heating on the environment by simply area weighting the 'warmer' cloud air and the environmental air and assuming that complete mixing of the two produces the 'new' environmental air. The second approach (OOYAMA, 1969, and several others) assumes that warming occurs via compensating subsidence. In the case of hurricanes or well organized tropical storms, clearly compensating subsidence can not occur to any substantial degree in the inner wall region of the storm which is almost entirely an area of moist adiabatic ascent (SHEA, 1972). Logically then, warming by dry descent must occur outside the inner region (assuming small contribution in the storm's eye) and the warming of the wall region may be attributed to a gradual increase in equivalent potential temperature in the ascending towers. As OOYAMA (1969) pointed out, theoretical studies of disturbances in a conditionally unstable atmosphere by LILLY (1960), indicate that most of the compensating subsidence should occur outside the inner wall and surrounding convective bands and over an area which extends to about five inner core radii from the storm's center (about 300 to 600 km for most storms). It is important to note that Lilly's result is contingent upon having an inner region of essentially all moist ascent. Furthermore, Lilly found that for circular areas of moist convective ascent (without the surrounding convective bands), essentially all of the compensating subsidence occurs within a distance of about double the radius of the area of moist adiabatically ascending air. In both of these cases the subsidence is strongest immediately adjacent to the boundary of the ascending air or bands and gradually decreases with distance away from the updraft area. LILLY's results were derived for a 'no-vertical shear' situation (obviously not the case for hurricanes or midlatitudes convection), nevertheless, the observational evidence in Section I supports his results.

Theory and observations seem to indicate that compensating subsidence occurs on a scale on the order of one to five times the half-width (radius of the moist ascent only) of the disturbance, provided the half-width area is essentially all-moist ascent. Thus, the compensating subsidence for a cumulus ensemble should respond first to the individual areas of moist ascent within the ensemble rather than to the ensemble as a whole. This is contradictory to parameterization theories which require the compensating subsidence to occur on the scale of numerical model grid elements on the order of several hundred kilometers on a side. Since midlatitude moist convection rarely occurs in a form which exhibits large areas of essentially all moist ascent, this same problem of compensating

subsidence occurring rather locally also exists for parameterization of midlatitude convection.

#### 4.2. Model grid lengths and parameterization

In trying to deal with the problem of parameterization of cumulus convection, there are two primary considerations: 1) physically to understand how the convection actually produces an effect on the larger scale, and 2) how can the physical processes be realistically incorporated within the limitations of the numerical model. To some extent these considerations depend upon the size of the individual grid elements of the model. A natural grid length would be one which is small enough to incorporate the effects of the local moist and dry downdrafts yet large enough to avoid the microphysical cloud processes and still resolve the scale features under study. Consider, as an example of the problem involved, the typical midlatitude squall line. It is usually about ten to twenty kilometers in width suggesting that grid lengths should be on the order of a few kilometers at most. If one were only dealing with mature meso-systems with an already developed meso-low and high, then perhaps larger grid lengths could be used. However larger grid lengths would tend to spread over a broader area the strong stabilizing effects of the moist downdrafts thereby removing one of the primary mechanisms for formation and maintenance of the line-type convection. The point is, that the scale of the weather system to be simulated determines the size of the grid elements used in the model and the size of the grid elements strongly influences how the effects of convection can be incorporated. Small grid lengths on the order of five to ten kilometers would be a convenient size for directly incorporating the effects of the local moist and dry downdrafts. Larger grid lengths, however, may possibly require an intermediate parameterization step and the discussion below briefly considers this possibility.

#### 4.3. Intermediate circulation

If large scale compensating subsidence is not a direct result of convection, how then are the effects of convection physically transmitted up-scale for regions of convection composed of many smaller up-moist, down-dry circulations? There are several possibilities. Assume that there are no direct secondary circulations; that is after the adjacent environmental air is forced to sink locally, other environmental air is not forced to rise, sink, etc. In this situation the sinking environmental air may quickly become buoyant with respect to the ambient air and rise to some equilibrium point. In the process of sinking and rising, however, cloud material and ambient air will be mixed into the warm dry downdraft air producing evaporational cooling, and cooling by entrainment. Since the perimeter of the dry downdraft is fairly large (much larger than the moist updraft) and vertical velocities are smaller than in the updraft, it is reasonable that mixing effects may dominate and there is a minimum of buoyant recovery and

dissipation by gravity waves. Consider now the consequences of this process. Figure 10 shows a hypothetical area of moist convection (area A) and a larger environmental area without convection (area B). The up-moist, down-dry circulations in area A combine to produce a region of relative warming. One can envisage then an intermediate scale circulation between areas A and B (in some respects similar to CISK) in response to this relatively warmer region of cumulus convection. This would not only serve as a mechanism for development and intensification of mesoscale systems but would also provide a physical argument for compensating subsidence over a much larger surrounding area. Certainly it would be difficult to directly measure such an intermediate

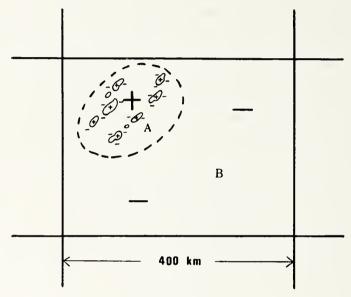


Figure 10

Hypothetical area of moist convection embedded within a numerical model grid element. Area A, enclosed by dashed line, represents an area of active convection with numerous individual convective elements. Local up and downdrafts for individual elements are indicated by small plus and minus signs. The large plus and minus signs indicate a mean vertical circulation between areas A and B.

circulation, however, an alternative approach is possible. As numerical modeling encroaches further into the mesoscale, it will become necessary to use grid lengths on the order of a few kilometers. Once grid lengths of this scale are used, direct effects of the moist downdrafts and local compensating subsidence can be incorporated and then the governing system of hydrodynamical equations can be left to develop the intermediate circulations. In this manner, the timing and magnitude of the intermediate circulation could be studied and its impact on the large scale could be measured directly.

Certainly the problem of parameterization of cumulus convection is difficult and complex and the observations to date only reveal enough about convective circulations

to show that they are not understood sufficiently well. Further observations are needed to clarify exactly how the convective up and downdrafts interact with the local environment and how then the resultant effects are transmitted upscale under different large scale conditions. Hopefully, research programs such as the proposed Severe Environmental Storms and Mesoscale Experiment (SESAME) may ultimately provide the observational information needed to clearly identify the physical mechanism which links the area of active convection to the larger scales. In the meantime, rather than having a single parameterization technique to handle all types of convection for all scales, it might be wiser to use a Richardson number or some other means to indicate the convective type and then call a parameterization scheme specifically designed for that particular type of convection.

#### REFERENCES

- A. H. Auer and J. D. Marwitz (1968), Estimates of air and moisture flux into hailstorms on the high plains, J. Appl. Meteor. 7, 196-198.
- J. R. Bates (1972), Tropical disturbances and the general circulation, Q. J. R. met. Soc. 98, 1-16.
- L. J. BATTAN and L. B. THIESS (1966), Observations of vertical motions and particle sizes in a thunderstorm, J. Atmos. Sci. 23, 78-87.
- ——(1970), Measurement of vertical velocities in convective clouds by means of pulsed Doppler radar, J. Atmos. Sci. 27, 293–298.
- B. Bean (1975), personal communication.
- L. Berkofsky (1974), Parameterization of cumulus convection for inclusion in a tropical operational forecasting model, AFCRL-TR-74-0089, Environmental Research Papers No. 467, 43 pp.
- A. K. Betts (1973), A composite mesoscale cumulonimbus budget, J. Atmos. Sci 30, 597-610.
- —— (1974), The scientific basis and objectives of the U.S. convective subprogram for the GATE, Bulletin of the A.M.S. 55, 304–313.
- K. A. Browning and F. H. Ludlam (1962), Airflow in convective storms, Q. J. R. met. Soc. 88, 117-135.
- H. R. BYERS and R. R. BRAHAM (1949), The thunderstorm; Report of the thunderstorm project, U.S. Air Force, U.S. Navy, U.S. National Advisory Committee for Aeronautics and U.S. Weather Bureau, Washington, D.C., 287 pp.
- A. J. Chisholm (1970), Alberta hailstorms: A radar study and model, Ph.D. Thesis, McGill University, Montreal, Canada, 237 pp.
- W. R. COTTON (1975), Data requirements for verification and development of models on the cumulus scale, Preprint of Third Symposium on Meteorological Observations and Instrumentation, 10-13 Feb. 1975, Washington, D.C. 1-4.
- R. M. Cunningham (1959), Cumulus Circulation, Recent Advances in Atmospheric Electricity, Pergamon Press, 361-367.
- R. M. CUNNINGHAM, V. G. PLANCK, and C. M. CAMPEN (1956), Cloud Refractive Index Studies, AFCRC-TR-56-210, Geophysical Research Paper No. 51, 106 pp.
- F. J. DUGAN (1973), The thermodynamic structure of the cumulus sub-cloud layer, Atmospheric Science Paper No. 205, Colorado State Univ., 97 pp.
- J. C. Fankhauser (1971), Thunderstorm-environment interaction determined from aircraft and radar observations, Mon. Wea. Rev. 99, 171-192.
- G. B. Foote and J. C. Fankhauser (1973), Airflow and moisture budget beneath a northeast Colorado Hailstorm, J. Appl. Meteor. 12, 1330-1353.
- T. Fujita (1959), Precipitation and cold air production in mesoscale thunderstorm systems, J. Meteor. 16, 454-466.

- W. M. Gray (1972) Cumulus convection and larger scale circulations, Part III, Atmos. Sci. Paper No. 190, Colorado State Univ., 67 pp.
- C. HARTSELL (1970), Case study of a traveling hailstorm, Report No. 70-1, Inst. Atmos. Sci., South Dakota School of Mines and Tech., Rapid City, S.D., 72 pp.
- G. A. Hookings (1965), Precipitation maintained downdrafts, J. Appl. Meteor. 4, 190-195.
- P. L. KAMBUROVA and F. H. LUDLAM (1966), Rainfall evaporation in thunderstorm downdrafts, Q. J. R. met. Soc. 92, 510-518.
- R. A. Kropfli and L. J. Miller (1975), Thunderstorm flow patterns in three dimensions, Mon. Wea. Rev. 103, 70-71.
- P. M. KUHN, M. S. LOJKO, and E. V. PETERSEN (1971), Water vapor: Stratospheric injection by thunderstorms, Science, 174, 1319–1321.
- P. M. Kuhn and L. P. Stearns (1973), Radiometric observations of atmospheric water vapor injection by thunderstorms, J. Atmos. Sci. 30, 507-509.
- H. L. Kuo (1965), On the formation and intensification of tropical cyclones through latent heat release by cumulus convection, J. Atmos. Sci. 22, 40-63.
- R. L. LAVOIE (1966), The warm rain project in Hilo, Hawaii, summer, 1965, Final Scientific Report, NSF Grant GF-192, Meteorology Division, Hawaii Institute of Geophysics, Univ. of Hawaii, HIG-66-5, 76 pp.
- D. K. LILLY (1960), On the theory of disturbances in a conditionally unstable atmosphere, Mon. Wea. Rev. 88, 1-17.
- F. H. LUDLAM (1966), Cumulus and cumulonimbus convection, Tellus 18, 687-698.
- J. S. MALKUS (1954), Some results of a trade-cumulus investigation, J. of Meteor. 11, 220-237.
- S. Manabe, J. Smagorinsky, and R. F. Strickler (1965), Simulated climatology of a general circulation model with a hydrologic cycle, Mon. Wea. Rev. 93, 769-798.
- J. D. MARWITZ (1972a), The structure and motion of severe hailstorms, Part III: Severely Sheared Storms, J. Atmos. Sci. 11, 189-201.
- —— (1972b), Precipitation efficiency of thunderstorms, Proc. Third Conference on Wea. Mod., Rapid City, S.D., 26-29 June 1972, 245-247.
- M. W. Moncrieff (1974), Structure and regimes of convection (unpublished manuscript).
- C. W. Newton (1963), Dynamics of severe convective storms, Meteor. Mono. 5, 33-58.
- (1966), Circulations in large sheared cumulonimbus, Tellus 18, 699-712.
- Y. OGURA (1972), Cumulus modeling and parameterization, (To be published in Rev. Geophys. Space Phys.)
- K. OOYAMA (1969), Numerical simulation of the life cycle of tropical cyclones, J. Atmos. Sci. 26, 3-40.
- W. SAND (1975), personal communication.
- D. J. Shea (1972), The structure and dynamics of the hurricane's inner core region, Atmos. Sci. Paper No. 182, Colorado State Univ. 134 pp.
- A. SHLANTA and P. M. KUHN (1973), Ozone and water vapor injected into the stratosphere from two isolated thunderstorms, J. Appl. Meteor. 12, 1375-1378.
- P. C. SINCLAIR (1973), Severe storm air velocity and temperature structure deduced from penetrating aircraft, Preprint Volume, Eighth Conf. on Severe Local Storms, 15-17 October 1973, AMS, Boston, Mass.
- T. Takeda (1965), The downdraft in convective shower cloud under the vertical wind shear and its significance for the maintenance of convective system, J. Meteor. Soc. Japan 43, 302-309.
- ——(1966), The downdraft in the convective cloud and raindrops: a numerical computation, J. Meteor. Soc. Japan 44, 1-11.
- M. S. TRACTON (1972), The role of cumulus convection in the development of extratropical cyclones, Dissertation, Dept. of Meteor., MIT, 157 pp.
- J. WARNER (1970), The microstructure of cumulus clouds, Part III. The nature of the updraft, J. Atmos. Sci. 27, 682-688.
- H. K. WEICKMANN and A. R. TEBO (1966), Temperature and humidity structure of cumulus mediocris, Flagstaff, Arizona 1963–1966. Unpublished manuscript. NOAA-APCL, Boulder, Colorado.
- —— (1966), Aitken nuclei as tracer in cloud physics research, J. de Recherches Atmospheriques 2, 154-157.

- P. T. WILLIS (1972), The morphology of tropical cumulus, Project Stormfury Annual Report, 1972, 61-90.
- M. Yanai (1972), A review of recent studies of tropical meteorology relevant to the planning of GATE experiment design proposal, WMO-ICSU, Vol. 2, Annex I.

(Received 9th April 1975)

P. Gloersen \*, R. O. Ramseier \*\*, W. J. Campbell \*\*\*, P. M. Kuhn \*\*\*\*, W. J. Webster, Jr.\*

# ICE THICKNESS DISTRIBUTION AS INFERRED FROM INFRARED AND MICROWAVE REMOTE SENSING DURING THE BERING SEA EXPERIMENT

#### Abstract

Remote sensing of the sea ice surface at wavelengths of 10 micrometers and 21 cm is investigated for the purpose of determining the feasibility of obtaining ice thickness from the radiometric measurements. Distinguishable radiometric signatures were obtained for thin ice at 21 cm, but the signatures do not follow a simple model consisting of a thin sheet of sea ice with parallel faces separating the ocean from the atmosphere. In fact, the signatures are distinguishable for ice thicknesses an order of magnitude larger than predicted on the basis of this simple model. It is speculated that the microwave signature pertains only to either the freeboard portion of the sea ice or the frazil layer. At 10 micrometers, the observations appear to fit the theoretical predictions rather well. The model consists of heat transfer from the ocean to the turbulent portion of the atmosphere through two layers, a slab of ice in which the heat transfer rate varies with temperature and the temperature varies with vertical position in the slab, and a nonturbulent boundary layer in the atmosphere directly above the ice in which the major heat transport is convective. Major difficulties in using infrared remote sensing for sea ice thickness determinations are found to be obscuration of the sea ice surface by ground haze and obtaining reliable values for the air temperature at the bottom of the turbulent atmosphere.

#### 1. Introduction

One of the most tantalizing of all objectives in remote sensing of sea ice is the possibility of determining the thickness of the ice. A number of investigators (Adey, 1971; Gloersen, et al. 1972) have observed microwave signatures of sea ice at long wavelengths that seemingly could be explained no other way than by assuming that the microwave radiometer was able to discern the sea surface

\*\* Department of the Environment, 562 Booth Street, Ottawa, Ontario, K1A OE7, Canada.

National Aeronautics and Space Administration, Goddard Space Flight Center, Greenbelt, Maryland 20771.

<sup>\*\*\*</sup> U. S. Geological Survey, Ice Dynamics Project, Tacoma, Washington 98416.
\*\*\*\* U. S. Department of Commerce, National Oceanic and Atmospheric Administration, Environmental Research Laboratories, Boulder, Colorado 80302.

through the sea ice. Unfortunately, no concurrent surface measurements were available to establish the actual sea ice thicknesses. Laboratory measurements of the complex dielectric constant (Hoekstra, 1971) and a simple layered dielectric model set the sensitivity of such determinations of sea ice thickness at about 1/10 of a wave-

length of the microwave radiation.

Another method for determining sea ice thickness that has been suggested (Ketchum, 1968) is based on measuring the surface temperature remotely by means of an infrared radiometer. The basis for this determination is that the sea ice layer is the main limitation for the transfer of thermal energy from the sea to the atmosphere in the Arctic environment. The rate of this transfer, then, depends on the thickness of the sea ice layer, and the surface temperature will vary accordingly. There are many difficulties associated with this sort of sea ice thickness determination, such as the variability with local weather conditions (ground haze, cloud cover, and surface winds) and the structure of the sea ice cover (snow cover, thickness, and ice concentration).

During the Bering Sea Experiment, we encountered a number of samples of thin sea ice with the infrared and 21 cm microwave radiometers which were also measured by the surface observations

team. The results of those observations are reported here.

## 2. The Microwave Model for Ice Thickness Determinations

A simple three-layer dielectric model has been used to demonstrate the sensitivity of microwave radiometry for the determination of sea ice thickness. The microwave wavelength chosen for this study was 15 cm, but the results are not very sensitive to wavelength and have therefore been represented in dimensionless terms. The following values (Table 1) have been assumed for dielectric constants of the three layers (Hoekstra, 1971). The computed emissivity of these three layers in shown in Figure 1. It can be seen that the results are remarkably uniform for the cases considered. The higher the imaginary part of the dielectric constant, the higher the surface reflectivity becomes, resulting in a decrease in the peak emissivity as the ice layer thickness increases. The oscillations in the emissivity (due to interference between the top and bottom of the ice) become more pronounced as the imaginary part of the dielectric constant becomes smaller, as one might expect. These results can

Table 1  $K_{alr} = 1.00$   $K_{sea\ water} = 70.5 - i36.0$   $K_{sea\ lce} = 4.0 - i5.2 \text{ at } 263 \text{ K}$  4.0 - i2.7 at 253 K 4.0 - i1.7 at 243 KSalinity =  $\frac{350}{00}$ Salinity =  $\frac{140}{00}$ 

283

now be qualitatively extended to sea ice with other values of salinity, keeping in mind that the imaginary part of the dielectric constant varies directly with salinity. In all cases (Figure 1) the maximum emissivity is first reached at an ice thickness of about 0.17 wavelengths in air (or 1/4 wavelength in the medium). This model implies that the limit of sensitivity of determination of ice thickness from microwave brightness temperature is not much more than 1/6 of a wavelength (in air) of ice thickness for a wide variety of salinities and sea ice temperatures.

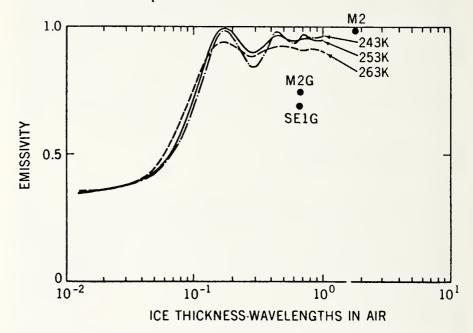


Fig. 1. Microwave emissivity of sea ice as a function of ice thickness in units of microwave wavelengths in air, based on a simple three—layer theory (see text). Experimental points have been added for the sake of comparison.

Рис. 1. Микроволновая излучательная способность морского льда как функция толщины льда в единицах микроволновых длин волн в воздухе, рассчитанная по простой трехслойной теории (см. текст). Экспериментальные точки добавлены для сравнения.

### 3. The Infrared Model for Sea Ice Thickness Determination

A two-layer model is used here to predict the surface temperature of thin sea ice. The heat transfer is assumed to take place between the ocean at 271 K and the turbulent atmosphere through a layer of sea ice in which: 1) the ice conductivity varies with temperature, 2) the ice temperature varies vertically within the slab, and through a non-turbulent atmospheric boundary layer above the slab in which the major heat transport is convective. Heat transfer through such

layers has been treated in textbooks (e. g. Jakob, 1949) and will not be repeated here. The heat transfer through sea ice has been measured (Schwerdtfeger, 1963) and found to vary inversely with the temperature in the medium. The constants measured for a salinity of 8 ppt have been incorporated in the following expression for the sea ice thickness:

$$\Delta Z_{\text{lce}} = \frac{k_{\text{alr}} \left[ 4.54 \times 10^{-3} \left( 271.5 - T_{\text{lce}} \right) - 1.89 \times 10^{-4} \ln \left( 272.5 - T_{\text{lce}} \right) \right] T_{\text{alr}}^{1/4}}{\left( T_{\text{lce}} - T_{\text{alr}} \right)^{6/4}}$$
(1)

where  $k_{\rm air}$  is a constant, containing such factors as the thickness of the convective boundary layer, the constant term in the thermal conductivity of the air, and the viscosity of air;  $T_{\rm lce}$  is the surface temperature (measured with the infrared radiometer); and  $T_{\rm air}$  is the temperature at the top of the convective boundary layer. The objective of this analysis was to provide a reasonable functional form for  $\Delta Z_{\rm lce}$ , rather than attempt to obtain a quantitative prediction. Thus  $k_{\rm air}$  was determined by curve-fitting to the experimental points.

#### 4. Observations

As a result of the aircraft navigational system malfunction on the 5 March flight and the corresponding lack of coincidence of the low pass aircraft track and the test points along the diagonal crossing the US test area, it is necessary to assume that the properties of the grey ice actually transversed by the aircraft are essentially the same as those for surface test point A3G on that date. This assumption is reasonable, since the grey leads were probably opened at about the same time, and the freezing rates are quite comparable over a large area. The data from the 20 and 28 February flights are in better coincidence, but the processing on the 28 February flight has not been completed since it was not included in the initially agreed exchange. The salinity and density profiles obtained on 5 March for the grey ice at A3G are typical of similar data taken on grey ice on other dates.

The surface data for A3G taken on 5 March are shown in Figure 2, illustrating both the aerial view of the test site and the physical data from the surface measurements of the grey ice. From this Figure, it can be seen that the salinity is approximately 8 ppt through most of the grey ice sample, which is the value used to develop Equation 1. This was also the case for the samples taken at test points M2G on 20 February and SE2G on 28 February. For reasons discussed in Paper (see p. 234—270), the salinity in the top few centimeters of the ice becomes very high; the thermal conductivity should drop correspondingly, but this has been neglected in this analysis since this layer is a small part of the total ice cover.

The infrared and microwave radiometer data acquired on the low-level passes on 20 February and 5 March are shown in Figures 3

and 4, where some of the points selected for this study are indicated. For the most part, the sharp spikes that occur result from open water in the leads. Some notable exceptions to this appear to occur early in the low altitude pass. The double spikes that occur at about 23h 28m 57s (Figure 4) decrease in amplitude as wavelength decreases, indicative of a thin ice signature. The fact that the spikes do not disappear at the shorter wavelengths may be attributable to the wet surface phenomenon described in Paper (see p. 234—270). The next sharp spike, appearing at about 23h 30m 00s, does decrease in amplitude more rapidly with wavelength, perhaps indicating a drier surface condition. It is interesting to note than the 10 micrometer infrared data (top of Figure 4) do not indicate open water in these leads, since the temperature recorded was less than 271 K. An exam-

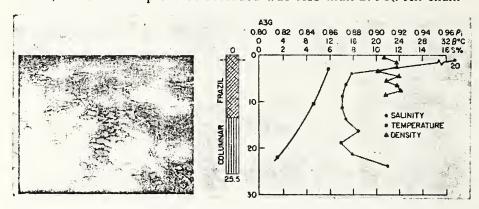


Fig. 2. Aerial view and surface test data for test point A3G. Рис. 2. Вид с вертолета и данные у поверхности для контрольной точки А3G.

ple of a fullyresolved open lead feature occurs near 23h 32m 22s (Lead 2, Figure 4), where the spike occurs at all wavelengths, and the infrared radiometer reads 27l K. An example of the wet-surface grey ice feature described earlier appears near 23h 40m 44s. Since this relatively wide feature seems to increase with a decrease in wavelength and does not appear at all at long wavelengths, one might infer that this particular grey ice area is relatively thick.

Two of the features observed on 5 March (Leads 2 & 3, Figure 4 and Table 2) are depicted as 10 micrometer infrared images in Figure 5. The temperatures indicated in Figure 5 are generally close to the actual values since the atmospheric contributions are small from that altitude, except when ground haze is encountered. Open water can be seen in part of Lead 2, but most of the ice in the lead appears to be uniform in thickness, as evidenced by the uniform surface temperature.

The 21 cm radiometer signal for the entire low-level passes on 20 February and 5 March, illustrated in Figures 3 and 4, were also recorded digitally and integrated for one second, so that two to

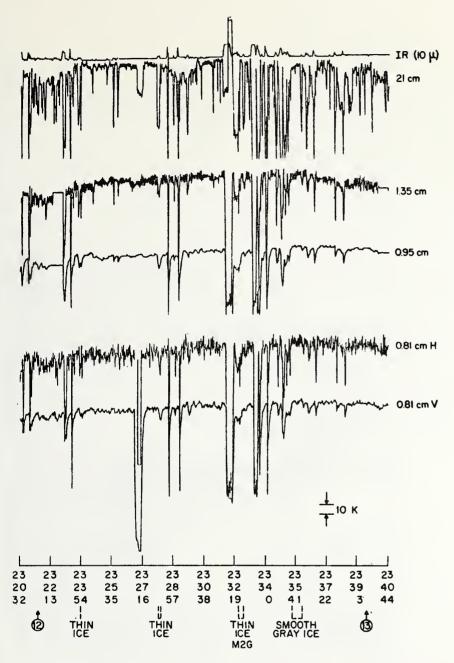


Fig. 3. Multiwavelength data obtained during the low pass of the aircraft over the US test area on 20 February, 1973.

Рис. 3. Даниые для различных длии волн, полученные во время прохода самолета на малой высоте над американским участком 20 февраля 1973 г.



Fig. 4. Multiwavelength data obtained during a low pass of the aircraft over the US test area on 5 March; 1973.

Рис. 4. Данные для различных длин волн, полученные во время прохода самолета на малой высоте над американским участком 5 марта 1973 г.

288

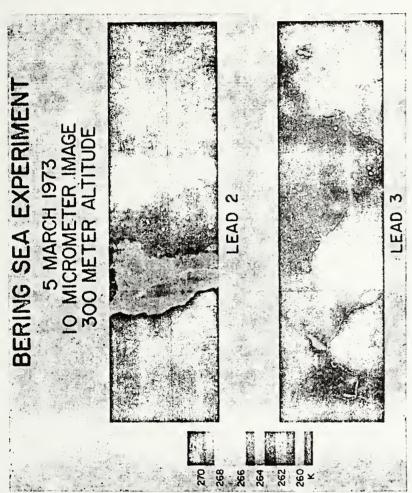


Fig. 5. Infrared images obtained during the low altitude aircraft pass over the US test area on 5 March, 1973. Leads 2 and 3 are indicated also on Figure 4.

Рис. 5. Инфракрасные изображения, полученые во время прохода само-лета на малой высоте над американским участком 5 марта 1973 г. Протоки 2 и 3 указаны также на рис. 4.

19 3ak. No 192

Table 2

2-20-73   M2   261   260.2   40   258   0.99   1.9 2-28-73   NW2   265.7   265.2   42   —   —   —	Date	Station	Tice	T <sub>air</sub>	ΔZ <sub>meas</sub>	T <sub>21 cm</sub>	€21 cm	<b>ΔZ</b> /λ
2-28-73     NW50     269.2     205.2     8     —     —       2-28-73     SE4G     269.2     264.2     19     —     —     —       2-28-73     SE0     266.2     264.2     87     —     —     —       2-28-73     SE1     266.2     263.7     74     —     —     —	2-20-73 2-20-73 2-28-73 2-28-73 2-28-73 2-28-73 2-28-73 2-28-73 3-5-73 3-5-73 3-5-73 3-5-73 3-5-73	M2O M2 NW2 NW5 NW5O SE4G SE0 SE1 SE1G A5 A1 A3O Lead 2 Lead 3 (18) Thick	263.2 261 265.7 269.2 269.2 266.2 269.2 261.2 263.6 266.2 269 265 261.7	260.2 260.2 265.2 265.2 264.2 264.2 263.7 263.7 256.2 257.2 258.2 253 253	14 40 42 65 8 19 87 74 14 71 65 25.5	258 	0.99	0.67 1.95    0.67   

three readings were obtained for each grey ice feature. Of course, there were many more readings for thick white ice. The averages of the digital data for each test point are listed in Table 2.

On 20 February an interesting feature was encountered with the aircraft on which surface measurements were also taken, corresponding to M2G (see Figure 1, p. 197, and Table 1, p. 198). In this case, the drop in brightness temperature decreases with wavelength. The data are listed in Table 2, and entered also in Figure 1 for comparison with the analysis.

#### 5. Discussion

The data for point SE1 were used to determine the constant  $k_{alr}$ in Equation 1.  $T_{lce}$  for this point was obtained while at low-level from the non-scanning 10 micrometer radionieter.  $T_{\rm air}$  for all points was obtained from Staten Island records and verified by measurements from the helicopters. The equation is plotted in Figure 6 using this value of  $k_{air}$  and several values of  $T_{air}$ , along with other experimental data obtained during the low-level data flight. The proximity of the points to the appropriate air temperature curves is remarkably good particularly at lower values of ice thickness,  $\Delta Z$ , when varying weather and surface conditions are taken into account. Some of the scatter of the experimental points might be accounted for by variation in the intervening ground haze, which would tend to lower the infrared radiometer reading. As a matter of fact, the haze on 20 February was sufficient to preclude producing a photomosaic from the high altitude photography. It is interesting that the points on Figure 6 (labeled 260) corresponding to data taken on 20 February show the poorest agreement with the curves.

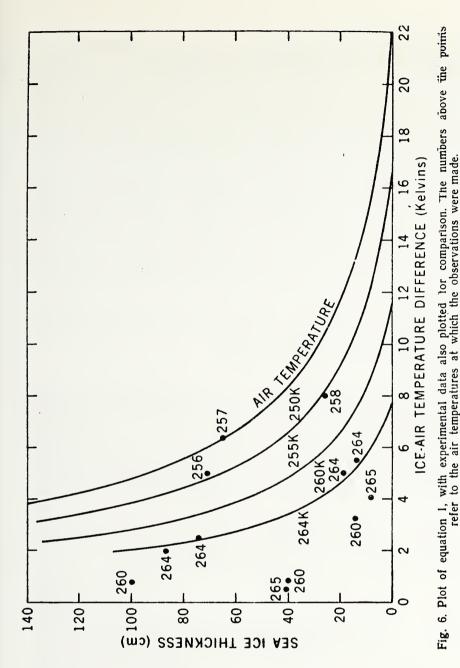


Рис. 6. График уравнения 1; для сравнения нанесеим также экспериментальные данные. Цифры пад точками — температура воздуха, при которой проводились наблюдения.

19\* 291

The 21 cm emissivities determined from the data taken near test points M2G and SEIG, listed in Table 2, are plotted in Figure 1 as a function of the ice thickness/wavelength ratio also determined from the Table 2 data. It is immediately apparent that our model for predicting the brightness temperature at 21 cm of sea ice for various thickness is grossly incorrect. We are led to conclude that something other than the semitransparency of thin ice to microwave radiation, as expressed in the curves of Figure 1, must be responsible for the observed variation in brightness temperature. The wet—surface phenomenon discussed in Paper (see p. 234-270) for 1.55 cm radiation also does not appear to fit the 21 cm observations in a consistent way. We are left, for the present time, with the unexplained observation that thin first-year ice (less than 0.20 m) tends to have lower brightness temperatures than thicker first-year ice, but the thickness scale involved does not fit any model at hand. Possibly the signatures are related to only the freeboard portion or the frazil ice portion of the thin sea ice; the thicknesses of these layers more closely fit the <sup>1</sup>/<sub>6</sub> wave thickness requirement of the simple model discussed earlier.

The data from 5 March (Leads 2 and 3) were not plotted on Figure 1 since they apparently do display the wet-surface phenomenon discussed in Paper (see p. 234-270).

#### REFERENCES

Adey, A. W. Theory and field tests of a microwave radiometer for determining sea ice thickness. Proc. ≠90, NATO Advisory Group for Aerospace Research & Development Conference, Colorado Springs (Technical Edition and Reproduction Limited, London 1971).

Gloersen, P., T. Wilheit and T. Schmugge. Microwave emission measurements of sea surface roughness, soil moisture, and sea ice structure. 4th Annual Earth Resources Program Review 1, 8—1 (1972) (NASA/JSC Document MSC-05937).

Hoekstra, P. and P. Cappilino. Dielectric properties of sea and so-dium chloride ice at UHF and microwave frequencies. J. Geophys. Res., 76, 4922 (1971).

Jakob, Max. Heat transfer, 1, 499 (Wiley, 1949).

Ketchum, R. D. and W. I. Wittmann. Infrared scanning the Arctic pack

ice, USN Internal Report 68-115 (1968).

Lane, J. A., and J. A. Saxton. Dielectric dispersion in pure polar liquids at very high radio-frequencies. Proc. Roy. Soc., A214, 400 (1952).

> П. Глоерсен, Р. Рамсайер, В. Кемпбелл, П. Кюн, В. Вебстер

#### РАСПРЕДЕЛЕНИЕ ТОЛЩИН ЛЬДА, ПОЛУЧЕННОЕ ПО ИК и микроволновым измерениям во время ЭКСПЕРИМЕНТА «БЕРИНГ»

Представлены результаты дистанционного зондирования ледяного покрова на длинах волн 10 мкм и 21 см с целью определения возможности оценки толщины льда по радиометрическим измерениям.

292

Анализ данных на длине волны 21 см позволил установить, что микроволновое излучение несет информацию лишь о тонком поверхностном слое льда. Однако расчеты, проведенные для простой трехслойной модели (вода—лед—воздух), не соответствуют экспериментальным данным.

Двухслойная модель переноса тепла от океана к атмосфере в инфракрасном диапазоне дала результаты, хорошо согласую-

щиеся с экспериментом.

Основные трудности в использовании ИК зондирования для определения толщины льда — влияние дымки на излучение и сложность получения надежных данных о температуре воздуха в нижнем слое турбулентной атмосферы.

# NOAA Technical Report ERL 300-0D 12

U.S. DEPARTMENT OF COMMERCE
NATIONAL OCEANIC AND ATMOSPHERIC ADMINISTRATION
Environmental Research Laboratories

# **Environmental Research Laboratories Radiation Programs - Requirements**and Recommendations

KIRBY HANSON, Editor
EDWIN FLOWERS
GARY HERBERT
DOUGLAS HOYT
PETER KUHN
SYUKURO MANABE
RUDOLF PUESCHEL
LOIS STEARNS

BOULDER, COLO.
MAY 1974



## ENVIRONMENTAL RESEARCH LABORATORIES RADIATION PROGRAMS - REQUIREMENTS AND RECOMMENDATIONS

#### SUMMARY

This report describes both the scientific aspects of the Environmental Research Laboratories (ERL) radiation programs and the requirement for measurement accuracy in these programs. The discussion in the following sections shows there are now requirements for accuracies which exceed present instrument technology. Table 1 summarizes the accuracies required.

The term accuracy has been used in this report for ease in communication. It means reproducibility to a known radiation scale value. It is not essential that this scale be the absolute radiation scale, but rather an established scale that does not change and is reproducible.

At present, the International Pyrheliometric Scale (IPS) is the internationally accepted radiation scale for pyrheliometric measurements. The scale is maintained by the World Meteorological Organization (WMO) sponsored World Radiation Center in Davos, Switzerland. This scale is reproduced in the United States by the Engineering Division of the National Weather Service (NWS), and the Eppley Laboratory. Presently, there appears to be a discrepancy of about 1 percent in the IPS depending on the type of standard used to define it. This discrepancy was determined only recently and is inherent in the definition of the IPS.

In the past few years, new types of absolute pyrheliometers have been produced by Kendall (1969), Willson (1973), and Geist (1972). These instruments promise to be useful absolute standards.

The ERL radiation scientists have been obtaining the Eppley Laboratory radiometers with calibrations linked to the IPS. As a result, previous ERL radiation measurements are traceable to the IPS through Eppley Laboratory standards. In a few cases, however, some research studies have used data from NWS network instruments, which have calibration traceability to the IPS through NWS standards. Recent studies show a discrepancy between the NWS and Eppley Laboratory pyranometer standards of 3.5 percent and in some (explainable) cases 10.5 percent (flanson et al., 1974).

Table 1. Accuracy Requirements for ERL Radiation Studies

Studies	Pyrheliometer (%)	Pyranometer (%)	Time Scale
Atmosphere Turbidity Regional Air Pollution Ocean Heat Transport	0.5	0.5 0.5	decades months years
Ocean Atmosphere Heat Exchange Atmospheric Absorption and Scattering Oceanic Attenuance	e	2.0 0.2 2.0	months minutes months

Present program requirements for accuracy (such as 0.5 percent over a period of decades) for the Geophysical Monitoring Program cannot be met by present instrument technology and measurement methods. Support for other ERL programs will require a great deal of effort by laboratory personnel to maintain a known radiation scale, to calibrate working standards and field radiometers, and to establish filter and sensor characteristics. Even with an extensive effort, it is uncertain that accuracy requirements can be met in all cases.

In view of the present need for laboratory support of ERL field programs, it is recommended that:

- 1. A central radiation facility be established to:
  - a) maintain (national) primary standard radiometers (with established calibration traceable to the internationally accepted pyrheliometeric scale) and provide facilities for calibrations of working standard radiometers;
  - b) provide facilities for evaluating commercially available pyrheliometers and pyranometers;
  - c) provide facilities for evaluating detectors, filters, and energy sources so their characteristics are known;
  - d) provide facilities for developing new sensors to improve the absolute accuracy and reproducibility of present radiation measuring instruments.
- 2. Such a central radiation facility be responsive to the technical needs of both the network programs of NOAA and the individual ERL radiation measurement programs.

Reprinted from Preprint Volume, Fifth Conference on Weather Forecasting and Analysis, March 4-7, 1974, St. Louis, Mo. Published by Amer. Meteor. Soc., Boston, Mass.

## USE OF NMC NUMERICAL GUIDANCE IN THE PREDICTION OF SEVERE DOWNSLOPE WINDSTORM

John F. Henz and Vincent R. Scheetz

Geophysical Research and Development Corporation Ft. Collins, Colorado 80521

J. Michael Fritsch

Environmental Research Lab, NOAA Boulder, Colorado

#### 1. INTRODUCTION

One of the most perplexing forecast problems facing the operational meteorologist near a mountain range is the accurate prediction of severe downslope windstorms. These windstorms frequently occur along the Front Range of the Rockies from Alberta to New Mexico along the Sterras in California and Nevada, and in the lee of the Wasatch Mountains in Utah. Wind gusts exceeding 90 knots are commonly observed as is wind damage in the hundreds of thousands of dollars. Exceptional cases, such as the January 1972 storm which raked foothills' communities from Cheyenne, Wyoming, to Pueblo, Colorado, produced millions of dollars of damage.

A study of these storms in Colorado from 1963-1972 identified two primary types of storms — the warm advection chinook associated with the strong subsidence field behind a jet stream maxima, and the cold advection bora associated with strong baroclinicity ahead of a jet stream maxima.

The accurate forecasting of these storms demands an integration of synoptic scale, meso-scale and microscale forecast techniques. Barotropic/baroclinic NMC vorticity progs, upper level wind charts, 500 mb chart, hourly surface chart and knowledge of local topography are among the essential data required. These forecasting parameters are interpreted in light of current physical hypotheses for producing the intense winds.

#### 1.1 <u>Definition of Severe Downslope Winds</u>

A severe downslope windstorm is one which has maximum gusts exceeding 64 knots and mean wind speeds greater than 32 knots which persist for at least one hour. Frequently, high velocity wind gusts and mean winds of over 32 knots are experienced for short time periods; however, the damaging windstorms, which are of greatest importance to the local public, are almost always of long duration.

#### 1.2 Location and Frequency of Events

The occurrence of hurricane-force winds at any given station located in the lee of a mountain range is a relatively infrequent event. A climatological study of strong downslope winds has been completed recently for the Boulder area. (Brinkmann, 1973). During three winter seasons, 1968-69, 69-70, 70-71, Brinkmann found a total of 20 windstorms with at least one gust exceeding 64 knots recorded by at least one wind station (out of a network of seven) in the area around Boulder, Colorado. Of these 20 storms, about half were associated with cooling in the free atmosphere (bora), approximately one-fourth were found to be accompanied by warming in the free air (chinook) and about onefourth showed little or no change in the free air temperature.

Boulder has received wide publicity on these violent winds, but that area is not unique in being affected by such storms. The weather station located on the Colorado State University Campus in Fort Collins, Colorado, some 60 miles north of Denver, recorded winds exceeding 64 knots on four occasions during the years 1964-71. (Riehl, 1971) (See Table 1.) Since that time two more such storms have occurred bringing the total to six in ten years. However, this station is located approximately four miles east of the base of the foothills and does not reflect the higher frequency and greater intensities experienced closer to the foothills. A new wind recording station has been in operation for two years at the base of the foothills west of Fort Collins. This new station indicates that the windstorms may occur twice as often close close to the foothills as the earlier records indicate.

Due to high winds, roads are frequently closed to all trailer and camper traffic in areas between wind recording stations, and no meteorological record is made of these high winds. Areas outside of metropolitan centers are sparsely populated in the west and consequently receive little publicity on the strong winds which also

Table 1
Frequency Distribution of Peak Gusts (mph)

	(after l	Riehl, 1971)	
	25-44	45-74	75-94
January	5	12	1
February	1	4	ī
March	5	4	ī
April	3	3	
May	4	3	
June	1	1	
July	2		
August	2	1	
September	1	1	
October		3	
November	2	2	1
December	2	10	
TOTAL	28	44	4
PERCENT	37	58	5

occur there.

#### 1.3.1 Chinook Downslope Windstorms

Chinook downslope windstorms in Colorado annually inflict the major windstorm damage. Figure 1 shows the "classical" severe chinook situation. Normally winds are west to northwest at all levels above mountain top. A strong negative vorticity advection field accompanies the velocity maxima as it reaches the Front Range of the Rockies. A surface pressure fall field is centered along the Colorado-Kansas border with large surface pressure rises occurring in western Colorado and Wyoming. Strong warm advection is occurring over the mountains in the layer from 700 - 500 mb in conjunction with an intense upper level subsidence field. The chinook begins as the velocity maxima aloft reaches the Continental Divide and ends as the strong negative vorticity advection aloft ceases, dependent of course on the movement of the jet. Occasionally severe snowstorm conditions follow this pattern due to deep cyclogenesis in southeastern Colorado.

#### 1.3.2 Bora Downslope Windstorms

Bora downslope windstorms, though just as common as the chinook, don't inflict nearly as much damage nor reach the intensity of severe chinooks. This may be due to the occurrence of the bora initially under an area of strong positive vorticity advection and upward vertical motion (Figure 2). This would work to destroy the subsidence type inversion needed for very strong winds. Again upper level winds attending the bora are west to northwest with strong cold advection occurring in the 700 - 500 mb layer. Normally the bora accompanies the passage of a Pacific front with surface pressure falls preceeding strong wind occurrence and strong pressure rises occuring during the strongest wind period. This is in direct opposition to the chinook which experiences its strongest winds while the pressure is falling.

#### 1.4 Property Losses

Because of the rapid increase in population along the entire Front Range, especially in Colorado, losses due to property damage caused by high winds have recently reached noteworthy numbers. Property losses from one storm have been estimated as high as \$2.5 million in the Boulder area alone. During a storm on January 7, 1969, 50 percent of the residences suffered some damage (City of Boulder, 1970).



Figure 1. Typical vorticity pattern, severe wind case — Chinook.



Figure 2. Typical vorticity pattern, severe wind case — Bora.

#### 2.0 THEORETICAL BACKGROUND

#### 2.1 Large Amplitude Lee Waves

Downslope mountain winds have been observed, studied, and written about for well over 100 years (see Brinkmann, 1973, for a comprehensive bibliography). There are several basic theories for their generation and probably the most common theoretical approach is to treat the winds as large amplitude lee waves. (Scorer and Klieforth, 1959; Boran, 1966). Long (1955) conducted several experiments in which he used fluids of different density in a closed channel to study the flow over a barrier. His work suggested two mechanisms which might produce downslope winds: (1) the fluid flow over a barrier was modified by the passage of a wave upstream from the barrier; and (2) when the lower fluid layers were blocked by the barrier, the upper layers descended to the surface on the leeward side. The importance of the first mechanism is that the wave upstream can influence the density gradient so that it might produce large amplitude lee waves. However, in order to obtain the large waves, a very stable layer with relatively light winds must be present. Although a stable layer is observed over the mountains in the strong downslope wind cases light winds in the stable layer are not usually evident. The second mechanism seems to fit the observed strong wind cases somewhat more closely since high momentum air could be brought down to the surface from middle layers of the atmosphere. However, it has been commonly observed that the peak gusts along the lee slopes in Boulder and Fort Collins, Colorado, sometimes greatly exceed the middle layer ( 500 mb) wind speeds. Indeed, in 1972 a lee slope windstorm occurred at Steamboat Springs, Colorado (on the western slope of the Rockies) in which northeasterly winds gusted to over hurricane force for several hours and 500 mb wind speeds were a scant 15 knots!

#### 2.2 Hydraulic Jump

Another theoretical approach, the "hydraulic jump" model (which allows for acceleration of the downslope winds), was suggested as a mechanism for downslope winds as early as 1953 by Schweitzer. In a hydraulic jump, fluid flow across a barrier can accelerate downslope to a velocity fast enough so that long surface waves cannot propagate upstream. In this situation a wave will steepen and break at the velocity point where upstream propagation ceases. For the atmosphere, Haughton and Isaacson (1968) developed a three-layer hydraulic jump model in which the lowest two layers had a constant wind speed and the upper layer had no mean wind speed. Each of the layers also had a constant potential temperature with inversions separating the layers. This model structure is not that similar to the observed atmospheric structure in strong downslope wind cases; nevertheless, the results of integrating the model revealed that lowering the inversion caused the hydraulic jump to move farther downslope. This is an important effect because it suggests a mechanism for producing the pauses which have been observed in the strong downslope winds.

Klemp and Lilly (1973) have generalized the Houghton-Isaacson model so that it is more representative of the observed atmospheric structure during the downslope windstorms. Their results have shown that the maximum surface wind is given by

$$v_{\text{max}} = \frac{(N_o V_o) (N_2 V_2)}{(N_1 V_1)^2} (N_o h)$$

where 0 = potential temperature g = gravitational acceleration h = height of the barrier U = mean wind speed Z = height ... g 30 1/2

 $N = \begin{bmatrix} g & \partial 0 \\ 0 & \overline{\partial 2} \end{bmatrix}$  and the subscripts 0, 1, and 2 refer to the bottom, middle, and upper model layers, respectively. This relationship very closely approximates the important controls and atmospheric conditions which are observed in the downslope windstorms. For a given mountain barrier of height h, equation (1) states that the maximum surface wind speed will increase with increasing wind speed and stability in the bottom and top layers and decreasing wind speed and stability in the middle layer. Observations (Brinkmann, 1973) indicate that the top of the lowest layer is usually around 650 mb; the second layer begins around 550 mb, and the upper layer starts around 300 mb. The fact that the observed inversion is around 650 mb indicates that it is most likely dynamically induced. The Klemp and Lilly model allows for the acceleration of the air downslope and should also produce lulls or pauses in the wind if the height of the inversion over the mountain rises. Furthermore, the hydraulic jump and associated turbulent dissipation of kinetic energy help explain why the winds dissipate so quickly to the east of the foothills.

## 3.0 SEVERE DOWNSLOPE WINDSTORM FORECASTING

From the standpoint of forecasting the <u>severe</u> downslope winds, both theory and observation require the forecast of a well-defined dynamically generated inversion. In addition relatively strong winds are required in the 650 to 550 mb layer and in the layer above 300 mb, while winds relatively constant with height are necessary in the 550 to 300 mb layer. These wind speed criteria are not too difficult to forecast using simple advection techniques, however, another procedure is needed to forecast the formation of the inversion.

#### 3.1 Current Forecast Techniques

Air Weather Service and National Weather Service have guidelines to follow in making forecasts of strong winds. In general the forecaster is required to measure or forecast surface pressure gradients across a known distance and then through the use of formulae or other forecast aids compute the probable maximum winds. This technique works reasonably well in areas with flat terrain where surface pressures reduced to mean sea level are consistent across

the area and give a fairly accurate picture of the pressure forces at work. In mountainous terrain during the wintertime "false" high pressure systems can produce apparent pressure gradients with little or no wind occurring at the surface. The forecast problem may be compounded by the presence of very cold stable air near the surface just to the lee of the mountains. Quite frequently the winds may be very strong just above the inversion but are unable to penetrate into the cold air near the ground. Consequently pure statistical techniques find poor correlation between surface winds and upper level winds.

Sangster (1972) in his statistical study concludes, "It would seem doubtful that any appreciable improvement by a statisticallyderived objective scheme over the skill shown by the technique of this memorandum can be achieved without additional insight based on experience or physical-dynamical reasoning". It is the purpose of this section to propose an alternate forecast technique based on physicaldynamical reasoning which achieves an operationally useful level of competence. Important forecast parameters are identified as well as their physical significance to the forecast. . A "windbox" or area wind forecast is described suitable for use by operational meteorologists working under real time deadlines.

#### 3.2 Important Meteorological Parameters

This study identified four essential meteorological parameters involved in the production of severe downslope windstorms. These parameters can be derived from standard synoptic analyses and their dynamic significance is briefly identified below.

#### 3.2.1 Vorticity Advection Field

Strong negative vorticity advection which indicates a dynamically induced subsidence inversion appears to be associated with the chinook windstorm. Strong positive and negative vorticity advection is associated with bora winds. The time rate of change and strength of the vorticity fields are important.

#### 3.2.2 Upper Level Relative Velocity Maxima

The velocity maximum is directly related to the vorticity field. Its strength, position, and vertical distribution relative to the surface topography determines the intensity of the mountain induced lee wave, subsidence field and maximum observed surface gusts.

## 3.2.3 <u>Temperature Advection Field at</u> 500-700 mb

The temperature advection identifies the type of windstorm, chinook or bora, and serves as a check on both the wind field and the vorticity advection pattern.

#### 3.2.4 Surface Pressure Field Changes

A strong surface pressure fall field on the plains accompanies a similar pressure rise field on the west side of the mountain barrier during important storms. From mass continuity considerations this must be the case and it is <a href="crucially">crucially</a> important for these fields to be present.

Classic synoptic situations depicting the "meshing" of all of these fields for both the chinook and bora windstorm configuration will be presented in the next section. These parameters are used to describe the issuance of a severe downslope "windbox".

#### 3.3 The Forecast Technique

The forecast technique employed uses the "box" or area forecast scheme which emphasizes the identification of areas of potential severe wind occurrence. Further refinements of the area forecast utilize knowledge of local terrain effects which act to enhance or diminish the expected winds. The critical limits of each significant parameter are summarized in Table 2. Use is made of standard facsimile pressure and vorticity charts for identifying the appropriate parameters. Figure 3 illustrates the composite chart identifying the severe wind warning area. This technique closely approximates the composite schemes utilized to predict severe thunderstorms though the emphasized parameters are different.

Table 2
Critical Limits of Significant
Meteorological Parameters

	Chinook	Bora
Temperature Advection °C/12 hr	+6	-6
Vorticity Advection x10 <sup>-5</sup> sec <sup>-1</sup> (12	-6 2 hr change)	<u>+</u> 6
Angle between Contour Field and Vorticity Field	60°-90°	60°-90°
Wind Direction	Within 45° of Perpendicular to mountain range	Within 45° of Perpendicular to mountain range
Isallobaric Field	-1 mb/hr	<u>+</u> 1 mb/hr

#### 3.3.1 Windbox Construction

The "windbox" (Figure 3) is constructed by assuming the 9000 foot contour of topography to be the western limit of the winds (Riehl, 1971). Superimposed on this is the surface pressure fall field of at least 1 mb per 3 hours, the appropriate vorticity advection field boundaries, the axis of the maximum upper level winds and the isotach field at the level of maximum winds every 20 knots beginning with 50 knots. The eastern limit is considered to be located 30 nm from the 6000 foot contour. Winds are forecast to occur within the area of 100% overlapping of all the parameters indicated by the checkerboard area (Figure 3). Maximum surface wind gusts are experienced within 10 nm of the 6000 foot contour and are decreased 30% for each successful 10 nm from the contour. This is in accordance with the observations.

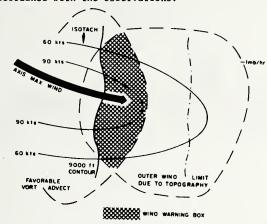


Figure 3. Construction of Composite Wind Box.

#### 3.3.2 Timing

The utility of any forecast is enhanced if the forecast event can be accurately timed. Success has been achieved by linearly interpolating the movement of the velocity maxima. This is accomplished by advecting the maximum at the speed of the difference in the wind speeds of the maximum and the winds within 200 nm downstream. This in turn cross-checked against the NMC vorticity fields advection timing. This technique provided at least a 6 hour area advance warning in all cases which is considered adequate for an area forecast. It allows ample time for preparation of all industry and community activities within the area to be affected.

#### 3.3.3 Verification

The forecast technique was applied to 22 windstorms which affected Fort Collins and Boulder during 1968-1972. It was found to work in all cases. The technique has been used daily operationally since December 1971 and has overforecast windstorm occurrence less than 5% of the time. In the overforecast situations vorticity field initializations, missing data and cloud cover appeared to be the direct cause of the missed forecast. A more thorough review of the verification will be presented at the conference.

#### 3.3.4 Local Topography

The most important nonsynoptic effect on the intensity of severe downslope windstorms is that of local topography. Along the Front Range of the Rockies in Colorado this effect can be related to the excessive winds reported in Boulder, the Rocky Flats Atomic Energy Plant near Golden, Monument Hill area north of Colorado Springs, the Raton Pass area near Trinidad and the foothills region west of Fort Collins. No doubt many other areas are similarly affected and it remains for the operational forecaster to explore these effects as the need arises for an accurate forecast.

#### 4.0 SUMMARY

The severe downslope windstorms which occur along the lee slopes of high mountain ranges are characterized by two basic types -- the warm advection chinook and the cold advection bora. Classical synoptic patterns which conform to observation and theory have been identified for each of these storm types. A forecasting procedure has been developed which is similar to weather forecast techniques used for severe thunderstorms and tornadoes. This study forecast technique provides a reliable 12 hour area or "windbox" forecast which identifies the area to be affected, peak wind gust expected in the area, and timing of the storm's initiation and end. The forecast technique combines the following parameters: magnitude of positive and negative relative vorticity advection, degree of 500 mb temperature advection, strength of the mid-upper level wind fields, and the surface pressure development patterns. The study also provides a coherent basis on which to explore the improvement of the mesoscale and microscale forecast for individual communities.

#### . REFERENCES

Beran, D.W., 1966: Large Amplitude Lee Waves and Chinook Winds. Atmospheric Science Technical Paper No. 75, Colorado State University, Fort Collins.

Brinkmann, W.A.A., 1973: A Climatological Study of Strong Downslope Winds in the Boulder Area. NCAR Cooperative Thesis No. 27.

City of Boulder, 1970: Analysis of Damage to
Residential Properties from High Winds Occurring
on January 7 and January 31, 1969 in Boulder
Colorado, City Manager's Office, Boulder.

Houghton, D.D., and Isaacson, E., 1968: Mountain Winds, Studies in Numerical Analysis. 2:21-52.

Klemp, J.B. and Lilly, D.K., 1973: A Mechanism for the Generation of Downslope Windstorms, <u>Royal Meteorological</u>, <u>Quarterly Journal</u> to be submitted.

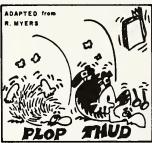
Long, R.R., 1955: Some Aspects of the Flow of Stratified Fields III. Continuous Density Gradients: Tellus, vol. 7, pp. 342-357.

Riehl, H., 1971: On the Climatology and Mechanisms of Colorado Chinook Winds. Unpublished Manuscript, Colorado State University, Fort Collins. Sangster, W.E., 1972: An Objective Forecast Technique for Colorado Downslope Winds, Technical Memorandum NWS CR-50, National Weather Service, United States National Oceanic and Atmospheric Administration, Kansas City.

Schweitzer, H., 1953: Versuch Einer Erklaerung des Fochns als Luftstroemung mit Ueberkritischer Geschwindigkeit, <u>Anchiv fuer Meteorologie</u>, <u>Geophysik</u> and <u>Bioklimatologie</u>, A, 5(3):350-371.

Scorer, R.S. and Klieforth, H., 1959: Theory of Mountain Waves of Large Amplitude, Royal Meteorological Society, Quarterly Journal, 85(364):131-143.







### Accelerated Decay of Thunderstorm Electric Fields by Chaff Seeding

#### F. JAMES HOLITZA and HEINZ W. KASEMIR

Atmospheric Physics and Chemistry Laboratory National Oceanographic and Atmospheric Administration Boulder, Colorado 80302

The field decay experiment conducted during the summer of 1972 in Colorado by the Atmospheric Physics and Chemistry Laboratory of the National Oceanic and Atmospheric Administration may be considered as the first experimental step to lightning suppression by chaff seeding. An airplane equipped with an electric field measuring system and a chaff dispenser flew underneath a developing thunderstorm, continuously monitoring the electric field. If the field exceeded 50 kV m<sup>-1</sup>, chaff was dispersed during the next two passes underneath the cloud, and the field decay was recorded until the storm dissipated. Each seeded storm was matched by a control (unseeded) storm to obtain the field decay rate under normal conditions. The field tests showed that chaff seeding in moderate fields of 50 kV m<sup>-1</sup> accelerated the field decay by a factor of 5. In one case a stronger field of 300 kV m<sup>-1</sup> was seeded, and the field decay rate was faster by a factor of 10 than that of the seeded storms having moderate fields. The physical background of this process, its limitations, and its significance to the problem of lightning suppression are discussed.

Experiments have been carried out to reduce the electric field growth in Colorado thunderstorms. They may be considered as the first step toward lightning suppression by chaff seeding. The physical concept of this method is based on the idea that corona discharge on a large number of chaff fibers releases so many ions into the cloud that the conductivity of the air is increased and consequently the field is decreased to such an extent that the high field value necessary to initiate lightning discharges is never reached. The physical principle of chaff seeding may be demonstrated by a simple laboratory experiment. If the spherical terminal of a high-voltage generator is placed above a grounded sphere (Figure 1a), spark discharge will occur between the two spheres if the breakdown field is reached. In our model the charged sphere represents the thunderstorm, the grounded sphere represents the earth, and the sparks represent cloud to ground lightning discharges. If a chaff fiber is put into the air gap between the spheres, the sparks will stop immediately but will start again as soon as the chaff fiber is removed. (The chaff fiber is attached to a teflon rod, well insulated from the ground and short enough so that it does not touch either one of the spheres.) This spark-suppressing effect can readily be explained. If the generator terminal is charged negatively, a large number of positive ions are liberated by corona discharge at the upper end of the chaff fiber and flow upward to the negatively charged terminal, and an equal number of negative ions are liberated at the lower end of the chaff fiber and flow down to the grounded sphere (Figure 1a). This ion flow provides a semiconductive path between the two spheres and loads down the generator so much that the high voltage necessary for a spark discharge cannot be maintained.

There are two important conditions that have to be fulfilled in this experiment. First, the corona discharge from the chaff fiber must begin at a field that is lower than the breakdown field. Second, the corona current produced by the chaff fiber should be of the same order of magnitude as or higher than the current delivered by the generator.

The field necessary for spark discharge is of the order of 3000 kV m<sup>-1</sup>. The field necessary to start corona discharge on the chaff fiber is about 30 kV m<sup>-1</sup>, which is about a factor of

100 lower than the breakdown field. Therefore in the laboratory experiment the first condition is certainly fulfilled. Transferring this requirement to thunderstorm conditions, we have to compare the 30 kV m<sup>-1</sup> corona onset field to the lightning igniting field of about 500 kV m<sup>-1</sup>. Here the corona onset field is lower than the lightning igniting field by about a factor of 17. This is less by a factor of 6 than the conditions of the laboratory experiment but still good enough for the chaff seeding method to work efficiently.

The second condition requires that the corona current be of the same order of magnitude as that produced by the generator. If in the laboratory experiment a Van de Graff generator is used, the generator current is of the order of 1  $\mu$ A. A corona current of 1  $\mu$ A is produced by the chaff fiber in a field of about 60 kV m<sup>-1</sup>. Therefore long before the flashover field of 3000 kV m<sup>-1</sup> is reached, the corona current will load down the generator. Even if the generator current is doubled, the corona current will increase with the square of the field and will match the doubled generator current in a field higher by a factor of 21/2 than 60 kV m<sup>-1</sup>, i.e., in a field of 85 kV m<sup>-1</sup>. Therefore in the laboratory experiment the second requirement is also fulfilled. The application of the second requirement to thunderstorm conditions encounters a number of presently unsolved problems. The generator current of the average thunderstorm is estimated to be of the order of 3 A, 2 A being dissipated by conduction current and 1 A in lightning discharges. If we assume that 30 C are destroyed by the average lightning stroke, the 1-A lightning current would provide the charge for one lightning stroke every 30s. If one of the more severe storms produces a lightning stroke every 5 s. the required lightning supply current would be 6 A. The thunderstorm generator current and the average lighning charge are only rough estimates and may vary within wide

The next uncertainty is connected with the conductivity inside the cloud. It is a fair assumption that the conductivity inside the cloud is less than the conductivity outside. This is caused by the fact that a certain percentage of the small ions are captured by the cloud elements and are very much reduced in their mobility. The same fate will meet the ions liberated by corona discharge; however, the percent captured by cloud elements and the distance of cloud penetration of the

Copyright © 1974 by the American Geophysical Union.

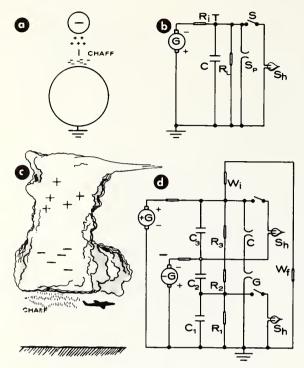


Fig. 1. (a) Corona discharge on a chaff fiber between charged spheres. (b) Circuit diagram to a. (c) Charge distribution in a thunderstorm. (d) Circuit diagram of a thunderstorm.

remaining ones are open questions. The ideal situation occurs when enough ions liberated from the chaff fibers can travel to the cloud charge centers and actively neutralize them. If this is not the case, chaff has to be dispersed throughout the cloud with such density that the region of influence of the individual chaff fibers overlaps, so that a conductive path between two opposite charge centers is established.

One may expect that a certain field concentration occurs at the boundary of the chaff seeded region in a manner similar to the field concentration at the surface of a conductive body in an electric field. This problem has been treated analytically by Kasemir [1973], who showed that when the vertical dimension of the seeded volume is not much greater than the horizontal dimension, the field concentration will be moderate and take a value of the order of 2. However, if the dimension of the seeded volume in the direction of the field is much larger than the dimension perpendicular to the field, then the field concentration may be high enough to trigger lightning discharges.

If it is assumed that the main direction of the fields in a thunderstorm is vertical, a horizontal line of chaff dispersed from an airplane would be the best way to avoid dangerous field concentration, whereas seeding from a dropsonde may cause elongated seeded volume with higher field concentration at the ends.

These problems, mentioned here briefly, have been discussed in more detail by Kasemir [1973]. However, this discussion is of necessity somewhat speculative, and for a decisive answer one has to wait until the necessary laboratory and field experiments can be performed. We may obtain a minimum estimate of the amount of chaff necessary to balance the average lightning supply current of 1 A by dividing it by the corona current of one chaff fiber. In a field

of 60 kV m<sup>-1</sup> the corona current of one chaff fiber is about 1  $\mu$ A. Therefore 1 million fibers could generate 1 A corona current. This amount is equivalent to about 100 g of chaff and can be dispersed in a few minutes. Inside the storm the fields are probably higher by a factor of 3 or more, and so the necessary chaff would be reduced. However, if volume seeding should be required, the amount would increase again, fast dispersion becoming an additional problem.

The value of the corona current of 1  $\mu$ A produced by a 10-cm-long chaff fiber in a field of 60 kV m<sup>-1</sup> has been obtained by extensive laboratory tests by B. Phillips and one of us. This value agrees well with the one we may calculate using the semiempirical formula published by *Chapman* [1958, equation 11]:

$$i = alkE^2/2 (1)$$

where i is the corona current in amperes; a is the empirical constant, equal to  $2 \times 10^{-11} \,\mathrm{m}^{-1}$ ; l is the length of chaff fiber, equal to  $0.1 \,\mathrm{m}$ ; k is the mobility of ions, equal to  $2 \times 10^{-4} \,\mathrm{m}^2$  V<sup>-1</sup> s<sup>-1</sup> at sea level and  $3.8 \times 10^{-4} \,\mathrm{m}^2$  V<sup>-1</sup> s<sup>-1</sup> at thunderstorm base altitude; and E is the thunderstorm field, equal to  $60 \,\mathrm{kV}$  m<sup>-1</sup>. Inserting the numerical values in (1), we obtain  $i = 0.72 \,\mu\mathrm{A}$  at sea level and  $i = 1.37 \,\mu\mathrm{A}$  at thunderstorm base altitude.

As a first step to lightning suppression the influence of chaff seeding on the electric field below a thunderstorm has been tested in the 1972 field decay experiment. Before we turn to a description of the test procedure and the discussion of the results, we will clarify the effect of chaff seeding on lightning and on the electric field below the storm by a circuit diagram that shows the important electrical properties of the thunderstorm (Figure 1d). As an introduction to the thunderstorm circuit let us first consider the circuit diagram of the laboratory experiment in Figure 1b. On the left side is the generator symbol G. The negative pole of the generator is connected through the internal resistor  $R_t$ , indicating a current source, to the capacitor C. In our laboratory experiment the short-circuit current was of the order of 1 µA. The capacitor C represents the capacitance between the two spheres. If there were no other load at the terminal point T connected to the generator, the voltage at T would rise with the time constant R<sub>i</sub>C to the open circuit voltage and remain at this value. However, there are three more paths in the circuit diagram through which charges delivered by the generator can bleed to ground. These are the load resistor  $R_L$ , the spark gap  $S_p$ , and, connected through switch S, the glow lamp Sh. All these circuit elements are connected in parallel to the capacitor C. The load resistor  $R_L$ represents the resistance of the air volume between the two spheres and any insulation resistance of the charged sphere to ground. In the laboratory experiment,  $R_L$  is assumed to be high in comparison with  $R_i$ , so that its voltage-reducing effect at the terminal T is negligible. In the thunderstorm this resistor is low enough to bleed away about 3/3 of the charge delivered by the thunderstorm generator. This is the resistor that should be drastically reduced by the corona discharge of the chaff fiber. This effect is represented in the circuit diagram by the glow lamp Sh. Finally, there is the spark gap  $S_p$ , which accounts for the spark in the laboratory experiment and for the lightning in the thunderstorm.

It is easy to understand the operation of this circuit. If the generator is switched on, the capacitor C is charged up until the voltage reaches the breakdown voltage of the spark gap  $S_p$ , if we assume that the switch S is open. The ensuing spark discharges the condenser C and stops if the charge of the con-

denser is exhausted. The condenser is then charged up again by the generator until the next spark occurs. This sequence of events will repeat itself as long as the generator is operating. If we now close the switch S, the glow lamp is ignited as soon as its breakdown voltage is reached and will continue to bleed away the charges delivered by the generator. The voltage at the terminal T will never reach the value for sparkover if the ignition voltage of the glow lamp is lower than the breakdown voltage of the spark gap. This is equivalent to the condition stated above that the corona onset field is lower than the lightning igniting field. The second condition, that the corona current should be of the same order of magnitude as the thunderstorm generator current, means that the glow lamp must be capable of absorbing as much current as the generator is able to produce. The closing and opening of switch S is equivalent to bringing the chaff fiber between the two spheres or taking it away.

The thunderstorm circuit diagram in Figure 1d is composed of two interconnected units of the circuit type shown in Figure 1b. Additional features are the two resistors  $W_i$  and  $W_f$  that connect the top of the thunderstorm to the ionosphere and the ionosphere to the earth. The current flow through these resistors represents the contribution of the individual storm to the maintenance of the fair weather field and current. Furthermore, the load resistor of the negative charge generator -G and the capacitor to ground is subdivided into the two parts  $R_1$ ,  $R_2$  and  $C_1$ ,  $C_2$  to represent the cloud volume from the negative charge center in the cloud to cloud base and the air volume from cloud base to ground. The purpose of this subdivision is to clarify the effect of chaff seeding below the cloud base, which will lead up to the field decay experiment discussed later on.

To facilitate relating the circuit diagram to the charge distribution in thunderstorms, Figure 1c shows a bipolar thunderstorm with positive charge in the top and negative charge in the base of the storm. The heights of the charge centers in Figure 1c are the same as the heights of the terminals of the positive or negative charge generator in the circuit diagram in Figure 1d. In Figure 1c an airplane is drawn below the cloud, and the released chaff fibers are shown as short vertical lines below the cloud base to demonstrate one of the seeding runs in the field decay experiment.

The spark gap marked C in Figure 1d between the positive and negative generator terminals symbolizes cloud discharges, and the spark gap G between the negative terminal and ground symbolizes ground discharges. The latter representation is incomplete insofar as the positive pocket charge in the base of the cloud and its corresponding generator are omitted from Figures 1c and 1d. This positive charge center in the base of the cloud is essential for the initiation of ground discharges and would have to be included if lightning suppression were discussed. However, the amount of the lower positive charge and its location in the cloud are not even approximately known. Furthermore, they are not essential for the discussion of the field decay experiment and thus are omitted here.

If it is assumed that the simple distribution of the positive and negative main charge centers is correct, chaff should be dispersed between the two charges to suppress cloud discharges. For ground discharge suppression the space between the negative and the elusive positive pocket charges in the base of the cloud should be seeded. In both cases the further assumption has to be made that either line or volume seeding will be effective in the cloud environment.

In the field decay experiment, seeding was done in the field of the negative space charge underneath the cloud. Therefore the glow lamp in Figure Id is connected at the junction of resistors  $R_2$  and  $R_1$ , and its influence on the spark gap G is reduced by the resistor  $R_2$ . A strong lightning suppression effect on ground discharges will not result from this type of seeding for the following reason. A necessary requirement for a lightning discharge is the high threshold field of about 500 kV m<sup>-1</sup> inside the cloud that produces the original breakdown. If this field is maintained over a short distance of the order of 100 m, the field concentration at the tips of the lightning channel is already so high that the lightning will continue to grow in a comparatively weak external field. This behavior is evidenced by the fact that a ground discharge is capable of penetrating toward the ground in spite of the weak fields closer to the ground, which are only of the order of 1-10 kV m<sup>-1</sup>. Chaff seeding underneath the cloud would merely increase the region of weaker fields between ground and cloud base, but it is doubtful that it can also significantly reduce the field inside the cloud. In other words, more of the potential energy required for the growth of a lightning discharge is furnished by the electric field inside the cloud than by the field underneath the cloud. However, a reduction of the voltage drop over the resistor  $R_1$  or its equivalent, a reduction of the field underneath the cloud base, can be expected. It was the purpose of the field decay experiment to investigate if such an accelerated field decay can be created by chaff seeding.

One of the favorable aspects of chaff seeding is the fact that corona discharge on the chaff fiber will start in a comparatively low electric field of about 30 kV m<sup>-1</sup> and that the corona current (ion production) increases with the square of the field. Therefore we may expect that high fields of the order of 120 kV m<sup>-1</sup> or more, which is 4 times the corona onset field, decay faster than lower fields of the order of 60 kV m<sup>-1</sup>, which is twice the corona onset field, and that for fields below 30 kV m<sup>-1</sup> there should be no effect from chaff seeding on the normal variation of the thunderstorm field.

#### EXPERIMENTS

The chaff is dispersed from an airplane making repeated passes under a thunderstorm. The airplane is equipped with a chaff dispenser, field mills [Kasemir, 1972], a corona indicator, and the necessary accessory equipment, such as a strip chart and magnetic tape recorder, altitude recorder, and so on. The test procedure was to select one growing cumulus cloud that already showed the emergence of light precipitation at the base. The electric field was then monitored during continuous passes underneath the stor ) If the field reached values of the order of about 50 kV ·n-1, two consecutive passes were seeded (or not seeded), and the field recording continued until the storm dissipated. The decision to seed or not to seed was based on the requirement that data should be collected for an equal amount of seeded and unseeded storms. With the clear-cut physical objective and the necessary monitoring equipment, no elaborate randomization process was required.

We define two categories of storms investigated, namely, category 1 for fields above 100 kV m<sup>-1</sup> and category 2 for fields between 30 and 100 kV m<sup>-1</sup>, and split each category into the seeded storms and the control storms, which were not seeded.

The following data have been collected and will be discussed: category 1, one seeded storm and no control storms; category 2, four seeded storms and four control storms. Fields

of 100 kV m<sup>-1</sup> or more are very seldom encountered below the storm. The data of the one seeded storm has been obtained in an earlier mission by Kasemir [1973] and is included here in the discussion. The graphs presented in Figures 2 and 3 show the field underneath the storm versus time. For each pass the maximum value of the negative vertical field component was listed with the corresponding time, and these peak values are connected in the graph by straight lines. The time interval between consecutive passes ranges from 3 to 9 min, the average being 4 min. In Figures 2a and 2b the average field of four category 2 storms is shown in the upper half of the figure, whereas the field of each individual storm is given with a reduced vertical scale in the lower half of the figure. To calculate the average field values, the seeded storms have been synchronized with respect to the first seeding run, and the control storms with respect to their maximum field value. Seeding events are marked on curves by the letter S.

It is evident from a comparison of Figures 2a and 2b that the field decay of the seeded storms after the second seeding run (Figure 2a) is much faster than the field decay of the control storms (Figure 2b). The accelerated field decay of the seeded storm is 6 kV m<sup>-1</sup> min<sup>-1</sup>, as compared with the decay of the control storm of 1.2 kV m<sup>-1</sup> min<sup>-1</sup>. If the field in the seeded storm is reduced to 34 kV m<sup>-1</sup>, the accelerated decay stops because the corona discharge on the chaff fibers stops, and further decay continues at a rate of 1.5 kV m<sup>-1</sup> min<sup>-1</sup>, which is about the value of the control storm. For the following discussion we will keep in mind that in category 2 storms the rate of field decay after seeding is about 6 kV m<sup>-1</sup> min<sup>-1</sup>, which is an increase by a factor of 5 over the average rate of field decay of the four control storms.

In the lower part of Figure 2a the field curves of the individual storms are arranged according to their maximum field values of 56, 62, 72, and 80 kV m<sup>-1</sup> in ascending order; i.e., the field curve with the lowest maximum field of 56 kV m<sup>-1</sup> is at the bottom, and the curve with the highest maximum field of 80 kV m<sup>-1</sup> is at the top of the four curves. Even though caution was taken not to overstress the significance of the data, there seems to be an indication that the field decay is faster for the higher maximum fields.

Storm 4 merits special attention because the field did increase after the first seeding run and started to decrease only after the second seeding run. Furthermore, the field increase before seeding is much faster than that in all other examples. Thus we are dealing here with a rapidly growing charge buildup that has not reached an equilibrium state. Therefore two seeding runs were necessary to reverse the sharp field increase to a field decrease. However, the most significant feature of this test was that seeding was done inside the cloud instead of below the cloud as it was in all the other cases. One has to expect that a large number of ions liberated by the corona discharge are captured by the cloud droplets, made immobile, and therefore removed from their role of increasing the conductivity of the cloud. From a purely theoretical consideration it is not possible to decide if this effect will completely counteract the purpose of chaff seeding or if it is only an insignificant side effect. This one test seems to indicate that chaff seeding causes an increase in conductivity inside the cloud in spite of the ion capture and consequently causes a decrease of the field.

Figure 3 shows the field decay caused by chaff seeding of a category 1 storm [Kasemir, 1973]. The field in this case had an extremely high value of 300 kV m<sup>-1</sup> and had maintained its high value for about 18 min when chaff seeding began. After 3 seeding runs, which required about 5 min, a dramatic field decay occurred at the high rate of 58 kV m<sup>-1</sup> min<sup>-1</sup>. The field dropped in about 8 min to a value below 30 kV m<sup>-1</sup> and remained below this value for the rest of the flight. This is about 10 times the decay rate of category 2 storms. Because the corona current increases with the square of the field, such

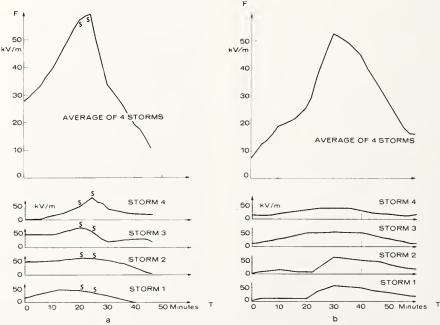


Fig. 2. Field F versus time T for (a) seeded cases and (b) control cases. Upper part shows average of four storms; lower part shows field pattern of the individual storms 1 through 4.

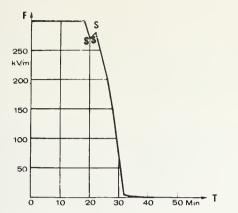


Fig. 3. Field decay after chaff seeding (S) of a category 1 storm.

a result could be expected from a theoretical point of view. However, it is very satisfying to see the fast decay happen in an actual experiment.

#### DISCUSSION

The data presented in the previous discussion indicate that chaff seeding has a discharging effect on the electric field of a thunderstorm. Since lightning is generated by an electric field, the same method also seems to be a good approach to lightning suppression. The pilot experiments in lightning suppression would follow a procedure similar to the field decay experiment with more extensive seeding and monitoring requirements. In the field decay investigation the difficult task of recording location and magnitude of each individual lightning stroke is not necessary, and seeding can be confined to the part of the storm where the field decay is investigated. The whole experiment can be carried out with a single airplane.

But even though our experiment is restricted to the part below the storm, the thunderstorm charge that generates the field at the monitoring airplane is spread out over several cubic miles, and still the data indicate that the field of such a charge can be reduced in the seeded area in a matter of minutes with two seeding runs. If we visualize that the chaff fibers emerge from the airplane in a very thin line compared to thunderstorm dimensions, this is truly a remarkable result and indicates a fast dispersion of the liberated ions and also the generation of an amount of charge comparable to the thunderstorm charge in a comparatively short time. The following discussion is devoted to these two points, dispersion and generated net charge.

There are two effects that may account for the fast dispersion, the mobility of ions and the movement of the chaff fibers themselves. Small ions have a mobility k of about  $k=4\times 10^{-4}$  m<sup>2</sup>  $V^{-1}$  s<sup>-1</sup> in the altitude where chaff seeding occurred. In an electric field E they travel with a velocity v=kE. If the field is for instance 50 kV m<sup>-1</sup>, as it is in the chaff seeding run of category 2 storms, positive ions would speed to the negative part of the cloud with a velocity of v=20 m s<sup>-1</sup>. This means that ions released at the beginning of the first run would have traveled in clear air a distance of 4.8 km in the time period of 4 min, when the second seeding run begins. Since the corona discharge is continuous, the stream of ions is also continuous, the result being that the volume of air

between the airplane path and the cloud is filled with positive ions. As soon as the ions reach the base of the cloud at least a certain percent are captured by the cloud droplets, and a surface layer of positively charged cloud droplets is formed. Other positive ions coming up will be deflected sideways, the result being a wider spread of the positive space charge. The attenuation of the field underneath the cloud will not be very different whether the ions accumulate at the cloud base or penetrate further into the cloud.

The second effect that may help to ionize the air of a larger air or cloud volume is the movement of the chaff fibers themselves [Kasemir, 1973]. Because negative corona discharge begins at a lower field than the positive corona discharge, the chaff fiber will initially lose negative charge and become positively charged until a balance between the positive and negative corona currents is reached. This leaves the chaff fiber with a positive net charge and subject to Coulomb force. Laboratory tests showed that gravity force pulling the chaff fiber down will be overcome by Coulomb force pulling the chaff fiber up if the field is greater than -60kV m<sup>-1</sup>. This force will cause the chaff fibers to move toward the negative charge centers in the cloud, especially inside the cloud where the fields are frequently larger than 60 kV m<sup>-1</sup>. In higher fields of 100 kV m<sup>-1</sup> or more the traveling speed of the chaff fiber may become several meters per second. The positively charged chaff fibers are repelled from positive charge centers. Therefore negative charge centers should be seeded from underneath and positive from overhead.

Coulomb forces may overcome gravitational forces, but they are not strong enough to overcome updrafts or downdrafts. Since the positive charge center is assumed to be in the upper part of the cloud, it may be possible to seed the positive charge center by releasing the chaff in a strong updraft.

The above discussion implies that the charge released by a thin line of chaff fibers may spread out in about 4 min in clear air over a volume of several cubic kilometers. We must next determine whether the amount of charge released in this time period is already an appreciable fraction of the average thunderstorm charge. The corona current on a single chaff fiber in a field of 60 kV m<sup>-1</sup> is about  $1 \times 10^{-6}$  A. During one chaff seeding run about 3 million chaff fibers are dispersed. The net current of all of these fibers is about 3 A. This results in a net charge of 720 C released in a 4-min period. During the second run again 3 million chaff fibers are dispersed, so that 4 min after the second run 2160 C of charge will be generated, if all the chaff fibers produce the I-µA corona current undiminished during this time period. This charge is considerably greater than the one in the negative charge centers, which is assumed to be of the order of -24 to -320 C. Therefore we may conclude, according to the estimates given above the net generated charge and the dispersion velocity, that the results of the field decay experiment are not in contradiction with physical principles.

#### REFERENCES

Chapman, S., Corona-point-discharge in wind and application to thunderclouds, in *Recent Advances in Atmospheric Electricity*, pp. 277-287, Pergamon, New York, 1958.

Kasemir, H. W., The cylindrical field mill, Meteorol. Rundsch., 25, 33-38, 1972.

Kasemir, H. W., Lightning suppression by chaff seeding, ERL Tech. Rep. ERL 284-APCL 30 Nat. Oceanic and Atmos. Admin., 1973.

(Received December 28, 1972; revised October 2, 1973.)

#### Reply

#### F. J. HOLITZA AND H. W. KASEMIR

Atmospheric Physics and Chemistry Laboratory, NOAA, Boulder, Colorado 80302

We are very grateful for the comments of L. Battan. They show us where we may have been too brief in our description of the experiment and analysis and give us an opportunity to explain more fully problems such as cloud selection and to present a brief statistical evaluation of the data.

We would start our test flights if strong cumulus development appeared in the sky, which usually occurred around noon, and the first cumulus congestus cloud inside a radius of about 80 km that showed icing at the top or the first thin streamers of precipitation at the bottom was selected as a candidate for our test. If the cloud did not produce electric fields above the 50 kV m<sup>-1</sup> threshold level within about 30 min, it was abandoned, and we hunted for another promising cloud. About half of the selected clouds had to be disregarded because of the lack of electrical development. Even now after some experience has been gained in thunderstorm research, we would not conjecture whether a cumulus congestus icing up or showing thin streamers of precipitation would generate fields above 50 kV m<sup>-1</sup> nor predict the storms natural field decay rate after it passed maturity. The chance of a bias in cloud selection with regard to field decay rate in the later part of the storm life is nil.

If the selected cloud reached the required field of 50 kV m<sup>-1</sup>, it would be seeded if data had been collected from an equal number of seeded and not seeded storms. It would not be seeded if the number of seeded storms exceeded the number of not seeded storms. The occurrence or absence of the 50 kV m<sup>-1</sup> threshold field provided a natural randomization. In addition, other events interfered randomly with our schedule. At one time our chaff dispenser did not work, and the anticipated seeded storm was by necessity a not seeded storm. At other times, permission to disperse chaff was not granted by the Federal Aviation Administration, because during the time it took for the field to reach the necessary 50 kV m<sup>-1</sup> the cloud had drifted too close either to an air traffic corridor or to the area reserved for the National Hail Research Experiment. These clouds too were then designated as not seeded clouds. If we would have used in addition to this inherent natural randomization some artificially introduced randomization procedure of our own, we would have probably obtained considerably fewer seeded storms than not seeded storms.

To determine whether the field decay rate of the seeded and not seeded storms is significantly different, we have applied one of the commonly used statistical tests to the data. We choose here the Wilcoxon rank-sum test [Bradley, 1968] because it doesn't require any assumption of the distribution function of the data. We tested the null hypothesis  $H_0$  that there is no significant difference between the decay rates of the seeded and not seeded storms against the alternative hypothesis  $H_1$  that the decay rates of the seeded storms are significantly higher than those of the not seeded storms.

Table 1 lists the decay rates of the seeded and not seeded

storms. Analysis of this data indicates that the null hypothesis is rejected at an observed significance level of 0.025, which implies that the difference between the decay rates of the seeded and not seeded storms did not occur by chance.

How do we know that this difference is caused by chaff seeding? To some extent this question is already answered by the statistical analysis because the only criteria used to divide the data into two groups was whether the storm was seeded. Further evidence pointing to the cause-effect relationship between chaff seeding and the accelerated field decay is the consistency between theory, laboratory experiments, and field experiments. If chance is excluded by the statistical analysis, it would be difficult to imagine any cause of the accelerated field decay other than chaff seeding.

The seeded storms were synchronized to the first seeding run for the following reason. The effect of chaff seeding should start right after the chaff release. It may not be strong enough to reverse immediately the field increase to a decrease. (See for instance storm 4 [Holitza and Kasemir, 1974] of the seeded storms, where a field decrease started only after the second seeding run.) However, the maximum field depends not only on chaff seeding but also on the behavior of the storm. The field decay after the maximum field is granted by definition. Therefore synchronization to the first seeding run reflects solely our treatment and is a more severe test of the chaff seeding effect. By synchronization to the maximum field of seeded storms we may be criticized for favoring chaff seeding by the synchronization method. However, we are happy to provide a composite plot drawn with synchronization to the peak field (Figure 1b).

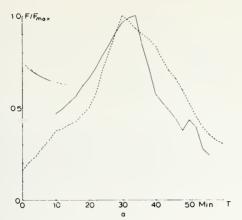
For better comparison we have normalized both the seeded and the not seeded composite plots to their peak field value. Figure 1a shows a plot of the field synchronized to the first seeding run, as has been done in the paper, and Figure 1b shows the field of the seeded storms synchronized to the peak field value, as has been suggested by Battan. In both figures the solid line is the composite field of the four seeded storms, and the dashed line the composite field of the four not seeded storms. In both plots the faster decay rate of the seeded storms as compared with the not seeded storms is evident. Synchronization to the peak field results in a more convincing

TABLE 1. Ranked Electric Field Decay Rates in Kilovolts per Meter per Minute of the Four Seeded and Four Not Seeded Storms

	Seeded		Not Seed	ed
Storm	Decay Rate	Rank	Decay Rate	Rank
1	-1.90	6	-1.277	3
2	-1.545	4	-1.247	2
3	-5.450	8	-1.127	1
4	-2.571	7	-1.70	5

Copyright © 1974 by the American Geophysical Union.

#### HOLITZA AND KASEMIR: COMMENTARY



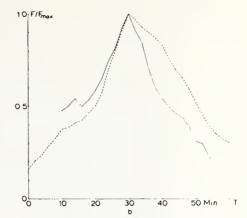


Fig. 1. Normalized composite plot of (a) four seeded storms (solid line) synchronized to their first seeding runs and four not seeded storms (dashed line) synchronized to their maximum field values and (b) four seeded storms (solid line) and four not seeded storms (dashed line) both synchronized to their maximum field values.

picture because of the similarity in the field increase and the marked difference in the field decrease.

We agree with Battan that the field tests should be continued in order to obtain a larger statistical sample. We are also aware of the fact that in 1972 we were favored by nature's providing single cell storms of the same type characterized by a simple field increase followed by a decrease. In more violent multicell storms with numerous field peaks the effect of chaff seeding may be more difficult to detect.

Finally, we agree with Battan's conclusion that 'The best that can be said of the field experiments is that the results were

consistent with their hypothesis.' This is probably the best that can be said of any weather modification experiment.

#### REFERENCES

Bradley, J. V., *Distribution-Free Statistical Tests*, pp. 105-111, Prentice-Hall, Englewood Cliffs, N. J., 1968. Holitza, F. J., and H. W. Kasemir, Accelerated decay of thunderstorm electric fields by chaff seeding, *J. Geophys. Res.*, 79, 425-429, 1974.

(Received June 4, 1974; accepted June 4, 1974.)

# DIURNAL VARIATIONS IN PLANETARY BOUNDARY-LAYER WINDS OVER LAND

#### LEE R. HOXIT\*

Atmospheric Science Dept., Colorado State University, Ft. Collins, Colo., U.S.A.\*\*

(Received 4 June, 1974)

Abstract. Windsonde data gathered over a nine-year period at three stations in the Southeast U.S. are stratified by season and by time of observation to provide average profiles depicting the diurnal variations in low-level winds. Significant variations are found (especially during the summer months) in wind speed, angle between wind direction and isobars, and the various terms of the kinetic energy budget equation.

A qualitative model of the diurnal variations in planetary boundary-layer winds (over land) is developed.

#### List of Symbols

α	Angle between the wind vector and isobars (positive for flow toward
	lower pressure)
$\alpha_0$	Angle between the surface wind vector and surface isobars (positive for
	flow toward lower pressure)
3	Kinetic energy dissipation
f	Coriolis parameter
g	Acceleration due to gravity
GMT	Greenwich Meridian Time
KE	Kinetic energy
LT	Local time
$\theta$	Potential temperature
t	Time
u"	Component of ageostrophic wind parallel to the isobars
v''	Component of the ageostrophic wind normal to the isobars (positive
	for flow towards lower pressure)
V	Wind vector
V''	Ageostrophic wind vector
$V_g$	Geostrophic wind vector
z	Height

#### 1. Introduction

Considerable effort has been devoted to investigating the effects of thermal stratification on the wind profile in the lowest 1-2 km. Observational studies include Mendenhall

Boundary-Layer Meteorology 8 (1975) 21-38. All Rights Reserved Copyright © 1975 by D. Reidel Publishing Company, Dordrecht-Holland

<sup>\*</sup> From a thesis submitted to the Graduate Faculty of Colorado State University in partial fulfillment of the requirements for the degree, Doctor of Philosophy.

<sup>\*\*</sup> Present Affiliation, Atmospheric Physics and Chemistry Laboratory, Environmental Research Laboratories, NOAA, Boulder, Colo., U.S.A.

22 LEE R. HOXIT

(1967) and Clark (1970) for land areas and Gordon (1952), Findlater et al. (1966), Cattle (1971) and Gray (1972) for ocean areas. Theoretical and/or modeling studies include those by Kurosaki (1968) and Yamamoto et al. (1968). In general, these studies have established the fact that the angle between the surface wind and surface isobar increases with increasing stability while the depth of the Ekman layer decreases.

Diurnal heating and cooling often produce rapid changes which complicate the relationship between the wind profile and thermal stratification. The change from adiabatic lapse rates in the afternoon to temperature inversions at night provides a mechanism for oscillatory changes in the winds even when the synoptic-scale flow is steady-state. Blackadar (1957), Blackadar and Buajitti (1957), and Bonner and Paegle (1970) have developed theoretical models of the diurnal oscillation in winds that are often observed in the 200–1500 m layer. They show that the ageostrophic winds which exist in this layer during the night are inertial oscillations resulting from the rapid change in eddy viscosity which takes place around sunset.

The goals of the present study are:

- (1) To define better the typical diurnal variations in wind speed and crossing angle.
- (2) To define how the diurnal variations change with different seasons.
- (3) To determine if these variations are large enough to invalidate the often utilized assumption that the kinetic energy generation and dissipation have approximately the same magnitude in the planetary boundary layer.

#### 2. Analysis Procedures

Prior to June, 1957, the standard times for United States winds aloft soundings were 0300, 0900, 1500 and 2100 GMT. During and after June, 1957, these times have been 0000, 0600, 1200 and 1800 GMT. For some stations, data are available for periods both before and after June, 1957. Combining the periods gives a total of eight observations per day.

TABLE I List of stations

Period of record	Elevation (m)
2/1/56- 7/30/64	101
1/11/56-12/31/64	79
1/1/56–12/31/64	62
	2/1/56- 7/30/64 1/11/56-12/31/64

Table I lists the three stations that were utilized in this study along with the elevations and periods of available data. These stations are located in the Southeast United States between 32 and 33°N. They have similar surface elevations and are mostly surrounded by flat terrain for at least 150 km. North and east of both Jackson and Montgomery are small areas of rolling hills with elevations of 200–400 m. Variations in the wind profiles due to local topography are expected to be small.

Wind data were obtained on magnetic tape from the National Climatic Center, Asheville, North Carolina. The 0600 and 1800 GMT observations for Shreveport were

pibal observations during 10/63-12/64. The other data were obtained by electronic tracking of windsondes and radiosondes.

Preliminary analyses suggested that the depth of the planetary boundary layer is frequently greater than the often quoted value of one kilometer. Consequently, this study included available data up to  $\sim 3$  km above the surface.

The data were at specified heights with levels at the surface and 150, 300, 500, 1000, 1500, 2000, 2500 and 3000 m. The first two levels (150 and 300 m) are heights above the surface while the remaining levels are heights above mean sea level (see Figure 1). Eighty meters was chosen as a representative surface elevation for all three stations so that the data could be combined. Thus, the 500-m data were applied to 420 m above the surface, 1000 to 920 m above the surface, etc. The total depth became 2920 m.

The data were stratified by time of observation (8 per day) and by season, with the seasons being defined as follows:

Winter – (December–February)

Spring - (March-May) Summer - (June-August)

Fall - (September-November).

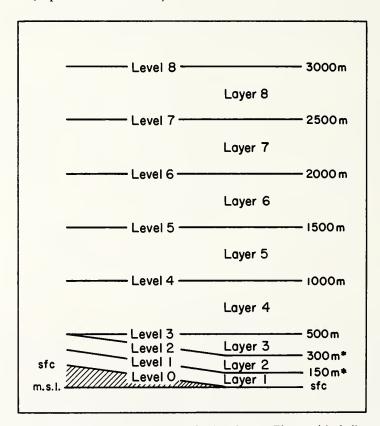


Fig. 1. Eight-layer model illustrating the data format. The asterisks indicate elevations above the surface.

24 LEE R. HOXIT

The change in wind direction was computed for each of the eight layers in Figure 1 for each observation. Mean values of this angle were then determined for each level for each stratification. The mean wind speed was also calculated for each level.

Though the lapse rates were not computed, the mean diurnal changes can be related to the typical heating and cooling of the lower atmosphere. Also, it is realized that many individual soundings indicate wind shears resulting from horizontal temperature gradients (geostrophic shear). However, with data samples of several hundred observations per stratification, we can assume that the thermal wind effects are largely eliminated. Also, the terrain surrounding these stations is fairly smooth and level, suggesting that the diurnal variation in the thermal wind would be small.

In about 5-10% of the observations, the data were missing for one or more of the levels. The change in wind direction could not be computed if the data for either of the two levels were missing, or a calm wind was reported. In conditions of light but nonzero wind speeds, the wind direction can change greatly from one level to another. In these cases, it is no longer obvious whether the wind is veering or backing with height. If the change in wind direction exceeded 60° in a given layer, the values were excluded. In this study, the computations were made for all possible layers where there were values, instead of discarding the entire observation.

#### 3. Results

#### 3.1. Variations in wind veering

The data from the three stations were combined to get the results presented here. Note that all three stations are located at or near 32.5° N. In the subsequent discussion it is assumed that the winds are in gradient or geostrophic balance at 2920 m above the surface.

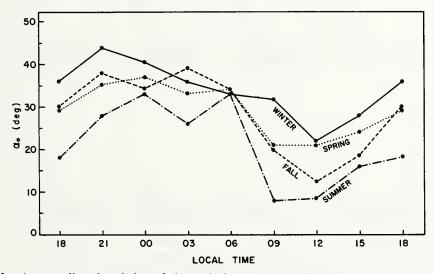


Fig. 2. Average diurnal variation of the angle between the surface wind and surface isobars.

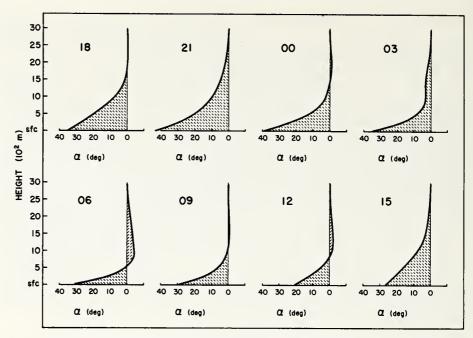


Fig. 3a. Average diurnal variation of the angle between wind and isobars as a function of height.

Times are Local Time. Season – Winter.

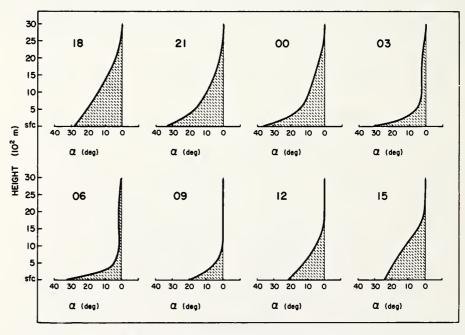


Fig. 3b. Same as Figure 3a. Season - Spring.

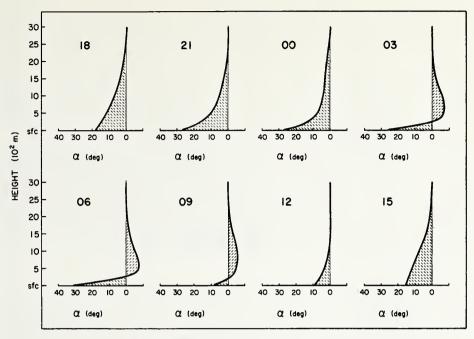


Fig. 3c. Same as Figure 3a. Season - Summer.

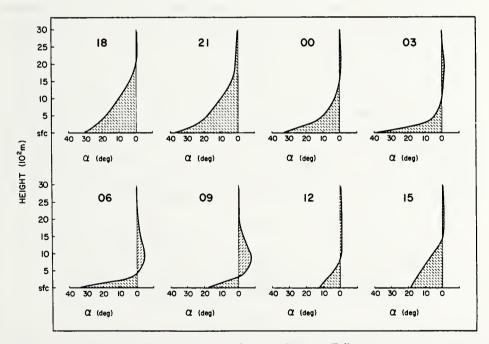


Fig. 3d. Same as Figure 3a. Season - Fall.

Figure 2 presents the diurnal variation of the surface crossing angle  $(\alpha_0)$  by season. In all seasons, the same basic pattern exists. The maximum values of  $\alpha_0$  persist from 2100 to 0600 LT while the minimum values occur between 0900 and 1200 LT. These results are very similar to those predicted numerically by Yamamoto *et al.* (1973). For all time periods the smallest values of  $\alpha_0$  occur during the summer season. The lower atmosphere is typically less stable then. Thus, the smaller surface crossing angles support the conclusion reached in the earlier studies mentioned in Section 1, – namely, the surface crossing angle decreases as the stability decreases.

Figures 3a-d show the diurnal changes of  $\alpha$  vs height for each season. The rate of decrease of  $\alpha$  in the lowest 500 m is maximum at 0600 LT, and minimum at 1500 LT. This corresponds to the typical times of maximum low-level stability and instability, respectively. The level at which  $\alpha$  first becomes zero typically increases from 300-500 m during the period from 0300 to 0900 LT to 1.5-2.0 km in the late afternoon. Note the tendency for flow toward higher pressure ( $\alpha$ <0) in the 1-2 km layer for the period 0300-0900 LT during the summer and fall seasons.

#### 3.2. VARIATIONS IN WIND SPEED

Figures 4a-b show the corresponding variations observed in the wind-speed profiles for the winter and summer seasons, respectively. The average wind speed at the surface is a maximum in the afternoon hours and a minimum late at night. In the 200-1500 m layer, an opposite oscillation exists. The maximum speeds occur near 0200 LT with no detectable phase shift with height. The minimum speeds occur in the early afternoon. For the summer season, the time of minimum speed changes with height. At 200 m, the minimum occurs near noon (1200 LT). At 1500 m, the minimum occurs near 1500 LT. The phase shift is approximately three hours or 2.5 hr km<sup>-1</sup>. This observed

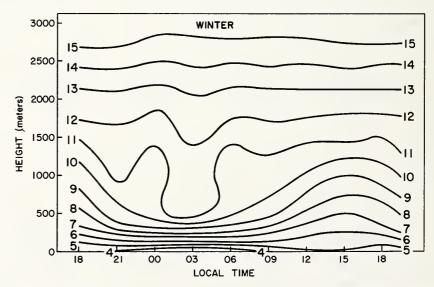


Fig. 4a. Average diurnal variation of the wind speed (m sec-1) vs height. Season - Winter.

28 LEE R. HOXIT

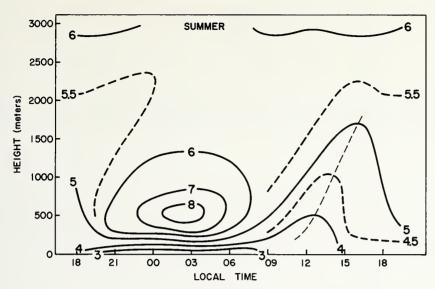


Fig. 4b. Same as Figure 4a. Season - Summer.

phase shift is opposite of that predicted numerically by Krishna (1968). His results suggested that both the maximum and minimum speeds are observed first at the higher levels with a phase shift of  $-2 \text{ hr km}^{-1}$  at 30°N and  $-8 \text{ hr km}^{-1}$  at 37°N.

During the night and morning hours, variations in both  $\alpha$  and wind speed above about 200 m appear to be independent of the changes in the lowest 200 m. The physical processes in the 200–1500 m layer are apparently not directly related to surface friction during this period. These observations suggest that the total layer of ageostrophic flow which we define as the Planetary Boundary Layer is made up of two sub-layers during the night and morning hours. The layer adjacent to the surface is the momentum boundary layer or Ekman layer. The top of this layer is the level at which the turbulent mixing induced by surface friction becomes negligible. At night the momentum boundary layer is only a few hundred meters thick. The second layer is formed shortly after sunset when the deep late-afternoon momentum boundary layer disappears. Blackadar (1957), and Blackadar and Buajitti (1957) have shown that variations in the ageostrophic wind in this layer correspond to inertial oscillations. We shall therefore refer to this layer as the inertial boundary layer.

#### 3.3. DIURNAL VARIATIONS IN THE KINETIC ENERGY BUDGET

The budget equation for the kinetic energy per unit mass can be written as:

$$\frac{\mathrm{d}(KE)}{\mathrm{d}t} = \mathbf{V} \cdot \nabla_p(gz) + \varepsilon,\tag{1}$$

where  $\varepsilon$  is the kinetic energy dissipation and  $\nabla_p$  indicates differentation on a constant pressure surface. This equation states that the total rate of change of kinetic energy is

equal to the generation plus the dissipation. Assuming that, in the mean, the advective terms are negligible, this equation reduces to

$$\frac{\partial (KE)}{\partial t} = \mathbf{V} \cdot \nabla_p (gz) + \varepsilon. \tag{2}$$

The generation term  $(\mathbf{V} \cdot \nabla_p(gz))$  can be written as  $fv''|\mathbf{V}_g|$ , where v'' is the wind component normal to the isobars. The mean cross-isobaric component was computed from the following approximation:

$$\overline{v''} \sim |\overline{V}| \sin \bar{\alpha},$$
 (3)

where the overbar indicates average quantities.

Since it was not feasible to obtain geostrophic winds corresponding to each observation, average values of  $|V_g|$  were estimated as follows. In a complementary study (Hoxit, 1973), average geostrophic winds speeds,  $(|V_g|)$  plus the average ratio of the geostrophic speed to the observed speed  $(|V_g|/|V|)$ , were computed for a combined data set taken from a 19-station rawinsonde network covering portions of the Central and Eastern United States. Computations were made for 7 levels in the lowest 250 mb of the atmosphere at 0000 and 1200 GMT for the winter and summer seasons. (Shreveport, Jackson and Montgomery were included in this network.) While the values of  $|V_g|$  obtained from this network are larger than those expected at the three stations considered here, the values of  $|V_g|/|V|$  are considered to be valid.

Fall and Spring values of  $\overline{|V_g|/|V|}$  were interpolated from the winter and summer values. Likewise, values were interpolated for the levels indicated in Figure 1. At 0000 GMT and 1200 GMT, average geostrophic speeds at each level were computed using the following

$$|\overline{\mathbf{V}_g}| \sim |\overline{\mathbf{V}}|(|\overline{\mathbf{V}_g}|/|\overline{\mathbf{V}}|),$$
 (4)

where  $|\overline{V}|$  was obtained from average wind speed profiles like those in Figures 4a and 4b. The final value of  $|\overline{V_g}|$  was set equal to the average of the 0000 and 1200 GMT values, then assumed to remain constant for all eight observation times. The generation term then became

$$V \cdot \nabla_p(gz) \sim f(|V| \sin \alpha) (|\overline{V_g}|).$$
 (5)

The total kinetic energy generation was obtained by integrating Equation (5) over the lowest 2.5 km. (Figure 3 indicated that the mean ageostrophic winds were negligible above this level.)

The total kinetic energy in the lowest 2.5 km was obtained by integrating over profiles of the kinetic energy per unit mass. Figures 5a and b provide sample profiles for Shreveport, Louisiana, for the winter and summer seasons, respectively. The local changes of kinetic energy are simply the differences between the consecutive 3-hr energy values.

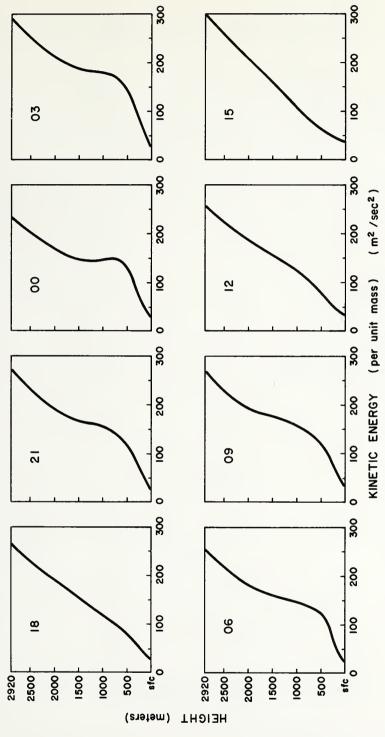
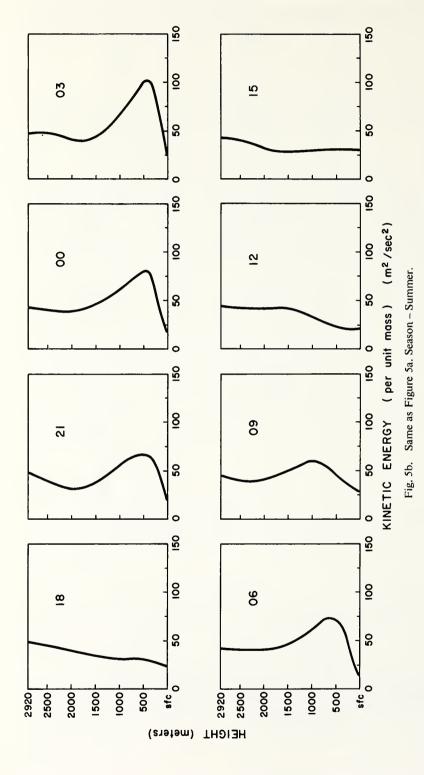


Fig. 5a. Average diurnal variation in the kinetic energy per unit mass for Shreveport, La. Season - Winter.



32 LEE R, HOXIT

The generation and tendency terms were computed for each of the three stations. The values were then combined. In order to obtain a smooth curve of the diurnal variation in these terms, the eight mean values were subjected to a  $\frac{1}{4}$ ,  $\frac{1}{2}$ ,  $\frac{1}{4}$  smoothing scheme.

The results for each season are plotted in Figures 6a and b. Again, the data for the three stations are combined. In all seasons, the generation term reaches a maximum near 2100 LT and a minimum near 0700 LT. The flow towards higher pressure in the inertial boundary layer (converting kinetic energy to potential energy) accounts for the negative generation values between 0400 and 1000 LT for the summer and fall seasons.

The local tendency curves indicate that the kinetic energy increases from about 1500 to 0200 LT. The maximum in total kinetic energy therefore occurs about 0200 LT, while the minimum occurs near 1500 LT. This means the kinetic energy variations in the inertial boundary layer dominate over the variations near the surface.

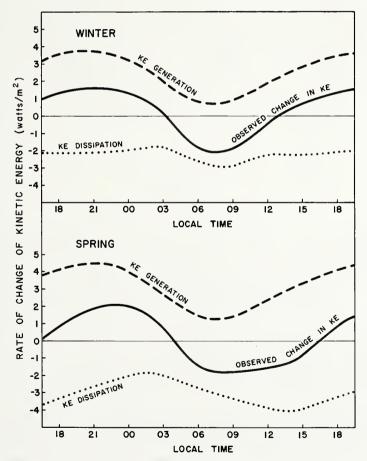


Fig. 6a. Average diurnal variations of kinetic energy generation, kinetic energy dissipation and change in kinetic energy for the lowest 2.5 km of the atmosphere. Seasons – Winter and Spring.

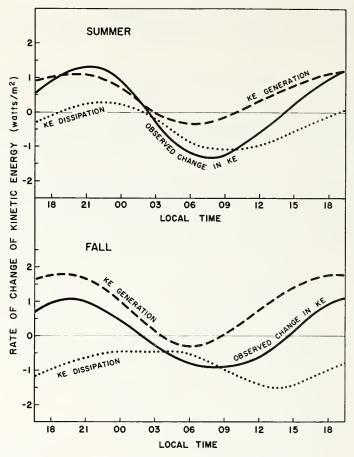


Fig. 6b. Same as Figure 6a. Seasons - Summer and Fall.

From Equation (2), the difference between the kinetic energy generation and observed change should be equal to the dissipation by turbulent processes. The resulting curves for the dissipation are also included in Figures 6a and b. Typically, the dissipation rate reaches a maximum between 1200 and 1500 LT. Minimum values occur between 0000–0600 LT. During the winter season, the diurnal variation in the dissipation curve is suppressed. This is attributed to the dominance of the synoptic-scale systems in determining the dissipation rates during winter.

Note that the dissipation curve for the night hours during the summer season becomes slightly positive. This is not physically realistic. The positive values result from the procedure of computing the dissipation as a residual. In this instance, the computed kinetic energy generation is less than the observed increase in kinetic energy. Remember that the kinetic energy is computed from the individual data values. The kinetic energy generation, however, is obtained from the mean crossing angle and speed curves. The inconsistencies in Figure 6b suggest that the mean kinetic energy generation has been underestimated.

34 LEE R. HOXIT

While the magnitudes of the generation and dissipation may contain errors, the basic features of the diurnal changes in Figures 6a and b are believed to be valid. They indicate that the often employed assumption of a balance between the kinetic energy generation and dissipation may lead to serious errors in the lowest 2 km. The present study shows that the magnitude of the tendency term is comparable to the magnitude of the dissipation especially during the period between 0600 and 0900 LT. Only when averaged over the entire day, will the magnitude of the generation and dissipation balance.

#### 4. Qualitative Model of Diurnal Wind Variations

The observed diurnal variations in the winds and the kinetic energy budget have been shown above. The reasons for these variations will now be associated with diurnal changes in stability. The typical diurnal variation in the potential temperature profile for the lowest 2.5 km is given in Figure 7. This diagram is representative of clear-sky conditions with no significant synoptic changes. The profiles in Figures 2–6, however, represent average diurnal changes, since data from both clear and cloudy conditions have been combined. The amplitudes of the wind variations in clear conditions are therefore somewhat suppressed. Nevertheless, the essential features of the daily variation in the  $\alpha$  and wind-speed profiles can be related to the potential temperature profiles of Figure 7.

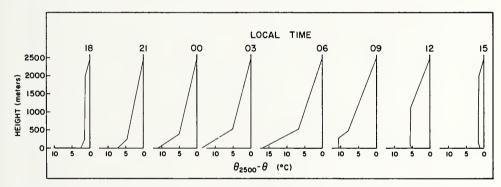


Fig. 7. Schematic profiles illustrating the typical diurnal variation in the potential temperature profile for the lowest 2.5 km under basically clear-sky conditions.

As indicated earlier, the data suggest that the lowest 2-2.5 km is made up of two layers – momentum boundary layer and the inertial boundary layer. A schematic diagram of the diurnal variation in the depths of these two layers is included in Figure 8.

The period of inertial motion is  $2\pi/f$ . The phase of the oscillation therefore depends on the latitude. The change of the ageostrophic wind components after the formation of the inertial boundary layer is demonstrated in Figure 9 for 33° N. In both Figures 8 and 9, the inertial boundary layer is developed around 1900 LT.

The discussion will begin with conditions during mid-afternoon (1500 LT). Surface heating and subsequent transfer of this heat to the lower atmosphere has produced

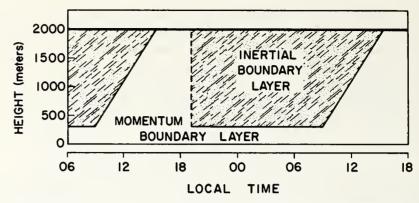


Fig. 8. Schematic diagram of the diurnal variation in the depths of the momentum and inertial boundary layers. Together these make up the planetary boundary layer.

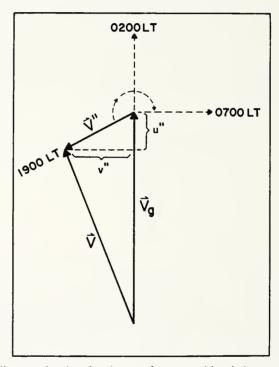


Fig. 9. Schematic diagram showing the change of ageostrophic wind components in the inertial boundary layer. Time of formation assumed to be 1900 LT. Latitude  $\approx 33^{\circ}$  N.

a deep layer with adiabatic lapse rate conditions. The momentum boundary layer is approximately 2 km thick. Both the kinetic energy generation and dissipation rates are large with an approximate balance between the terms. (Here and in the following paragraphs, similarity concepts relating the magnitude of the energy dissipation to the amount of turbulent mixing are utilized to indicate qualitatively the stability induced variations in  $\varepsilon$ .)

36 LEE R. HOXIT

Just after sunset, the surface cools rapidly. In turn, the lowest layers of the atmosphere are cooled while the temperature in the remainder of the layer remains essentially unchanged. The low-level cooling suppresses mechanical and buoyant mixing and leads to the formation of a new and much thinner momentum boundary layer. The wind direction and speed profiles in the new layer adjust with a time scale of the mixing processes (typically on the order of minutes). The dissipation of kinetic energy by the turbulence processes now becomes largely confined to the lowest few hundred metres. The total kinetic energy dissipation for the lowest 2 km decreases significantly. Above the developing ground-based stable layer, the turbulent mixing decreases rapidly. Frictional forces become insignificant. The adjustment time for the motion increases to that for large-scale motion (i.e., inertial motion). As a result, the kinetic energy generation in the layer remains significant for several hours. With the dissipation mechanism largely eliminated, the wind speeds increase rapidly. Eventually the Coriolis force becomes greater than the pressure gradient force and the flow towards lower pressure decreases to zero. The wind speeds typically reach maximum values 1 to 3 hr after midnight (see Figure 9).

An important consequence of the development of the inertial layer is that the flow at the top of the Ekman or momentum boundary layer will no longer be in geostrophic balance.

By sunrise, the low-level stable layer is well developed. The height of the momentum boundary layer is probably less than 300 m (in some cases less than 100 m) with the wind direction and speed changing rapidly with height. In the inertial layer, an ageostrophic component towards higher pressure has developed in response to the formation of the super-geostrophic wind speeds. This up-gradient flow produces negative kinetic energy generation values – conversion of kinetic energy to potential energy. As a result the wind speeds decrease.

After sunrise, surface heating eliminates the ground based stable layer. The mixing in the momentum boundary layer is enhanced by eliminating the restraining effects of a stable atmosphere. The rate of wind direction and speed changes with height are reduced.

Between 0900 and 1500 LT, the surface heating produces a deepening layer in which the lapse rates are essentially adiabatic. The adjustment of the depth of the Ekman or momentum boundary layer occurs on a time scale associated with the turbulent mixing processes. Thus, the depth of this layer will at all times correspond roughly to the depth of the adiabatic layer. As the mixing reaches higher and higher, the layer exhibiting inertial motion is eliminated. By mid-afternoon, the inertial layer has been completely destroyed and the boundary conditions for the top of the Ekman layer once again become that specified by gradient or geostrophic balance.

It should be pointed out that at 30-35°N the wind maximum in the inertial layer is destroyed by the combination of two separate processes:

- (1) Flow towards higher pressure (reducing kinetic energy),
- (2) Dissipation by turbulent-scale processes as the momentum boundary layer replaces the inertial layer during the period from 0900 to 1500 LT.

#### 5. Summary

Diurnal changes in the lapse rates in the lowest 2 km under basically clear conditions typically lead to:

- (a) the formation of an inertial boundary layer shortly after sunset,
- (b) an order of magnitude variation in the depth of the momentum boundary layer. Corresponding to these events are significant variations in wind speed and the angle between the wind direction and the isobars.

The existence of inertial oscillations eliminates the feasibility of parameterizing low-level winds in terms of existing lapse rates. Only in the afternoon hours does a balance exist among the Coriolis, pressure gradient and frictional forces throughout the lowest 2 km. Likewise, the geostrophic departure method for computing surface stress is valid only in the afternoon hours.

Large changes in the total kinetic energy generation and the total kinetic energy of the lowest 2 km were also found. At 32.5° N the maximum and minimum generation values are observed near 2100 and 0700 LT. The maximum and minimum total kinetic energy is observed near 0200 and 1500 LT. The dissipation of kinetic energy by turbulent-scale processes reaches a maximum in mid-afternoon and a minimum during the late night hours. The often employed assumption of the kinetic energy generation being of the same magnitude as the dissipation is shown to be invalid during most of the 24-hr cycle.

#### Acknowledgements

The author gratefully acknowledges the guidance and encouragement of Dr William M. Gray of Colorado State University who served as his advisor during the course of this research. Special thanks are also expressed to Drs Alan K. Betts, Elmar R. Reiter and Virgil A. Sandborn for their helpful suggestions.

Mr Edwin Buzzell did most of the programming work; Mr Larry Kovacic drafted the figures; Mrs Barbara Brumit and Mrs Cheryl Brown aided in the data reduction and Mrs Barbara Brumit also typed the manuscript.

This research was supported by the National Science Foundation under Grant GA-32589xl.

#### References

Blackadar, A. K.: 1957, 'Boundary Layer Wind Maxima and Their Significance for the Growth of Nocturnal Inversions', Bull. Am. Meteorol. Soc. 38, 283-290.

Blackadar, A. K. and Buajitti, K.: 1957, 'Theoretical Studies of Diurnal Wind Variations in the Planetary Boundary Layer', Quart. J. Roy. Meteorol. Soc. 83, 486-500.

Bonner, W. D. and Paegle, J.: 1970, 'Diurnal Variations in Boundary Layer Winds Over the South-Central United States in Summer', Monthly Weather Rev. 98, 735-744.

Cattle, H.: 1971, The Terrestrial Low Latitude Boundary Layer, Ph.D. Dissertation, Dept. of Meteorol., Imperial College of Science and Tech., 201 pp.

Clark, R. H.: 1970, 'Observational Studies in the Atmospheric Boundary Layer', Quart. J. Roy. Meteorol. Soc. 96, 91-114.

Findlater, J., Harrower, T. N. S., Hawkins, G. A., and Wright, H. L.: 1966, Surface and 900 mb Wind Relationships, Sci. Paper No. 23, Meteorol. Office, London, 41 pp.

38 LEE R. HOXIT

- Goraon, A. H.: 1952.: 'Angle of Deviation Between the Winds at 50 ft and 2000 ft over the North Atlantic Ocean', *Meteorol. Mag.* 81, 59.
- Gray, W. M.: 1972, A Diagnostic Study of the Planetary Boundary Layer Over the Oceans, Atmos. Sci. Paper No. 179, Dept. of Atmos. Sci., Colo. State Univ., Ft. Collins, Colo., 95 pp.
- Hoxit, L. R.: 1973, Variability of Planetary Boundary Layer Winds, Atmos. Sci. Paper No. 199, Colo., State Univ., Ft. Collins, Colo., 157 pp.
- Krishna, K.: 1968, 'A Numerical Study of the Diurnal Variation of Meteorological Parameters in the Planetary Boundary Layer. I Diurnal Variations of Winds', *Monthly Weather Rev.* 96, 269–276.
- Kurosaki, A.: 1968, Numerical Calculation of the Structure of Ekman Boundary Layer, Presented at the WMO/IUGG Symposium on Numerical Weather Prediction, Tokyo, Japan.
- Mendenhall, B. R.: 1967, A Statistical Study of the Frictional Wind Veering in the Planetary Boundary Layer, Atmos. Sci. Paper No. 116, Colo. State Univ., Ft. Collins, Colo., 57 pp.
- Yamamoto, G., Yasuda, N., and Shimanuki, A.: 1968, 'Effect of Thermal Stratification on the Ekman Layer', J. Meteorol. Soc. Japan 46, 442-455.
- Yamamoto, G., Shimanuki, A., Aida, M., and Yasuda, N.: 1973, 'Diurnal Variation of Wind and Temperature Fields in an Ekman Layer, J. Meteorol. Soc. Japan 51, 377-387.

#### Planetary Boundary Layer Winds in Baroclinic Conditions

LEE R. HOXIT<sup>1,2</sup>

Dept. of Atmospheric Science, Colorado State University, Fort Collins 80521 (Manuscript received 11 November 1973, in revised form 29 January 1974)

#### ABSTRACT

Systematic stratifications and analyses of low-level radiosonde data are performed for portions of the eastern half of the United States. The procedures are designed to specify changes in the planetary boundary layer wind profile resulting from variations in baroclinicity. The angle between the winds and isobars, the ageostrophic wind components, the surface stress, and the surface wind speeds are all shown to be functions of the orientation of the thermal wind vector relative to the surface geostrophic wind. These variations are consistent with a mixing-length model of the additional turbulent momentum transport initiated by the vertical shear of the geostrophic wind.

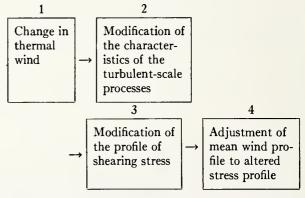
#### 1. Introduction

The modification of the basic Ekman spiral in baroclinic conditions has been realized by numerous investigators. Several of these, including Blackadar (1965), Ching (1964), Kovetz et al. (1963), Lettau (1967), Cattle (1971), Ellison (1956), MacKay (1971), Utina (1962) and Zaitsev (1966), have modified the theory of the basic Ekman spiral to include baroclinic effects. Bernstein (1959), Mendenhall (1967), Utina (1966), Gray (1972) and others, have investigated the effects of baroclinicity on observed wind veering profiles. The thermal wind relationship indicates that the magnitude of the modification depends on the relative magnitude of the temperature gradient while the sign depends on the orientation of this gradient relative to the surface isobars. Basically, the thermal wind reduces the veering of the wind in cases of cold air advection and increases the veering in cases of warm air advection.

A second and potentially more important effect in baroclinic flow has been suggested by Sheppard et al. (1952). The baroclinicity modifies the vertical shears of the horizontal winds in the planetary boundary layer (PBL) which in turn modify the turbulent transport of momentum and the stress profiles.

The present study examines the effects of this modified momentum transport on the PBL winds. Specifically, we seek to define the variations in the wind profiles from those expected in barotropic conditions. The direct thermal wind effects (change of pressure gradient with height) are subtracted from the observed data. In addition, the data are stratified into three stability and five speed categories. The remaining dependence of the

The sequence of events which occurs due to changes in baroclinicity is visualized as follows:



The details of the processes in steps 2 and 3 cannot be defined explicitly due to closure problems in classical turbulence theory. In seeking alternative methods, it is hypothesized that a model of the role of baroclinicity can be obtained by ignoring steps 2 and 3, thereby looking only for cause and effect relationships between steps 1 and 4. In this type of approach, the physical processes in step 2 are parameterized in terms of variables defining changes in the thermal wind.

#### 2. Experiment design and analysis procedures

This study is based on analyses of large amounts of regular radiosonde data. This section presents in detail

NOAA, Boulder, Colo. 80302.

wind profiles on the magnitude and orientation of the thermal wind is attributed to the momentum transport initiated by geostrophic shear. It is postulated that the momentum transport due to geostrophic shear (like the change in the pressure gradient with height) is a linear function of the magnitude of the thermal wind, and is dependent on the orientation of the thermal wind relative to the low level winds.

<sup>&</sup>lt;sup>1</sup> From a thesis submitted to the Graduate Faculty of Colorado State University in partial fulfillment of the requirements for the degree of Doctor of Philosophy.

<sup>2</sup> Present affiliation: Atmospheric Physics and Chemistry,

the station locations, times of observation, periods of record, data formats, and vertical coordinates. Included also are descriptions of the methods used in computing the parameters defining the speed, stability and baroclinicity for each wind sounding; plus the parameters used to define the observed wind profiles. The criterion used in the various data stratifications are presented. Finally, the advantages and limitations of averaging radiosonde and windsonde data to depict PBL winds are discussed.

#### a. List of symbols3

#### 1) GEOMETRIC VARIABLES

#### Lengths

n horizontal axis of a natural coordinate system
 s horizontal axis of a natural coordinate system

x distance in the east-west direction (positive to the east)

y distance in the north-south direction (positive to the north)

z distance in the vertical (positive upward)

#### Angles

 $\alpha_T$  angle between the wind direction at the top level and the wind direction at some level below (positive for wind veering with height)

angle between the wind vector and isobars (positive for flow toward lower pressure)

angle between the surface wind vector and surface isobars (positive for flow toward lower pressure)

α' angle between the wind vector 100 mb above the surface and the surface wind vector

angle between the wind vector 100 mb above the surface and the surface geostrophic wind angle measured clockwise from the direction of

the surface geostrophic wind to the direction of the mean thermal wind in the lowest 100 mb

γ direction from which wind is blowing (0° is a north wind with values increasing clockwise)

angle measured clockwise from the direction of the wind 100 mb above the surface to the direction of the mean thermal wind in the lowest 100 mb

#### 2) Dynamic variables

#### Winds

S average speed in the lowest 100 mb

V wind vector

V<sub>0</sub> surface wind vector

 $V_0(B)$  surface wind vector for barotropic conditions

 $egin{array}{ll} V_{g} & ext{geostrophic wind vector} \ V_{u_0} & ext{surface geostrophic wind vector} \ V_{T} & ext{thermal wind in the lowest } 100 \text{ mb} \ \Delta V_{g} & ext{shear of the geostrophic wind} \ \end{array}$ 

#### Wind components: Meteorological coordinates

u east-west wind component (west wind positive)
 v north-south wind component (south wind positive)

#### Wind components: Natural coordinates

- (i) Positive s axis oriented along the observed wind vector at the lower of two defined levels.
- u' component of the observed wind along the positive s axis
- v' component of the observed wind along the positive n axis
- $\Delta u_{T}'$  component of the observed wind shear along the positive s axis
- $\Delta v_{T}'$  component of the observed wind shear along the positive n axis
- $\Delta u_{\theta}'$  component of the geostrophic shear along the positive s axis
- $\Delta v_{y}'$  component of the geostrophic shear along the positive n axis
- $\Delta u'$  component of the wind shear along the positive s axis after the geostrophic shear is eliminated from the observed shear
- $\Delta v'$  component of the wind shear along the positive n axis after the geostrophic shear is eliminated from the observed shear
- (ii) Positive s axis oriented along the geostrophic wind vector
- u" ageostrophic component of the wind parallel to the geostrophic wind (positive when the wind component along the isobar is less than the geostrophic wind speed)
- v" ageostrophic component of the wind perpendicular to the geostrophic wind (positive for flow toward lower pressure)
- (iii) Positive s axis oriented along the surface geostrophic wind vector
- $u_s$  component of the wind parallel to the surface geostrophic wind (positive if in the same direction as the geostrophic wind)
- $u_{s_y}$  component of the geostrophic wind parallel to the surface geostrophic wind
- v<sub>n</sub> component of the wind normal to the surface geostrophic wind (positive for flow toward lower pressure)
- $v_{n_{\boldsymbol{\theta}}}$  component of the geostrophic wind normal to the surface geostrophic wind

#### Stress components

stress component along the *s* direction stress component along the *n* direction

Tzx

Tzn

<sup>&</sup>lt;sup>3</sup> In the text, vectors are printed in **bold** face type; in the figures vectors are indicated by wavy underlining.

 $au_{z_{s_0}}$  surface stress component along the s direction surface stress component along the n direction surface stress produced by momentum transfer in the z direction

#### Others

 $C_d$  drag coefficient

Coriolis parameter  $[=2\Omega \sin \phi]$ , where  $\Omega$  is the angular velocity of the earth and  $\phi$  is the latitude

 $z_0$  the surface roughness parameter

#### 3) THERMODYNAMIC VARIABLES

p pressure

 $p_0$  surface pressure

T temperature

 $T_0$  surface temperature

 $\bar{\Gamma}$  average lapse rate in the lowest 100 mb  $\lceil {}^{\circ}\text{C} (100 \text{ mb})^{-1} \rceil$ 

ρ density

#### 4) Constants

g acceleration due to gravity
 R gas constant for dry air

#### 5) Miscellaneous

Ro surface Rossby number

#### b. Station network

To obtain horizontal derivatives of temperature for computing thermal winds in the PBL, it is desirable to have a network with relatively high radiosonde station density in an area of fairly smooth terrain. The network which best satisfies these criteria is shown in Fig. 1. Thermal winds were computed only for the 19 stations in the interior of the network.

The data source for the network analyses was routine radiosonde data in a specified pressure level format (Deck 645). These data were obtained on magnetic tape from the National Climatic Center, Asheville, N. C. Data were available for the standard observation times of 0000 and 1200 GMT. (These times correspond approximately to 1800 and 0600 local time for the 19 interior stations.) This deck contains winds, temperatures, relative humidities and heights for the surface

TABLE 1. Period of record included in the analyses.

	Nov.	Dec.	Jan.	Feb.	Mar
1965	X	X			
1966	X	X	X	X	X
1967	X	X	X	X	X
1968	X	X	X	X	X
1969			X	X	X

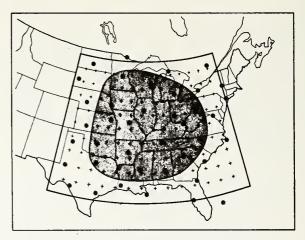


Fig. 1. Radiosonde network. Data from stations outside the shaded area were utilized only to calculate the horizontal derivatives of temperature for the 19 interior stations. The superimposed 2° latitude by 2° longitude grid was used in all horizontal analyses.

and specified pressure levels. For pressures greater than 200 mb, the data are available at 50-mb intervals beginning at 1000 mb.

The period of record treated in the network analyses is shown in Table 1. A total of 20 winter months were utilized. With 19 stations in the interior of the network and approximately 30 days per month, the total data sample included approximately 11,400 radiosonde observations for both 0000 and 1200 GMT.

#### c. Vertical coordinates

The major drawback to using data for specified pressure levels is that the height above the surface varies from one station to another due to different station elevations. Likewise, these heights vary in time due to the passage of high and low pressure systems. This height variability required that the specified pressure level radiosonde data be converted to a reference frame which would better indicate the height above the surface. The reference frame which was utilized is shown in Fig. 2. This system accounts for both station elevation differences and the time changes associated with moving pressure systems by specifying the different levels above the surface in terms of the surface pressure.

The analyses are restricted to the lowest 250 mb of the atmosphere (approximately to the lowest 2.5 km). The 250-mb layer is subdivided by seven levels into a six-layer model. Linear interpolation between the wind and temperature data in the specified pressure format provided wind and temperature data at each of the seven levels.

#### d. Computation of external parameters

The external factors considered in this study are thermal stratification (stability), the magnitude of the flow (speed), and baroclinicity. Of these, only the mag

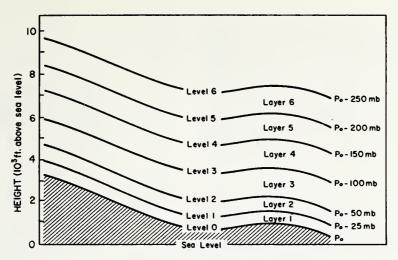


Fig. 2. Vertical reference frame.

nitude of the flow can be computed directly from the wind data. The stability can be parameterized by the lapse rate of temperature. Lapse rates can be estimated from the radiosonde temperature data, although some detail is lost in interpolating temperature values for specified levels. The thermal wind (baroclinicity) requires analysis of the horizontal temperature gradients. The procedures used to compute these parameters are discussed below.

#### 1) STABILITY

The stability parameter selected was the average lapse rate in the lowest 100 mb. Lapse rates were computed from the interpolated temperatures in the surface pressure based reference frame (Fig. 2). The temperature at the upper level  $(T_{p_0-100})$  was subtracted from the temperature  $(T_0)$  at the surface. With this convention, positive lapse rates correspond to decreasing temperatures with height.

#### 2) Speed

The speed parameter used in this study was the average speed in the lowest 100 mb. This was obtained by weighting the wind observations for the first four levels in Fig. 2 according to the depth of the layer for which they were representative, i.e.,

$$S = 0.25(|\mathbf{V}_{p_0-100}|) + 0.375(|\mathbf{V}_{p_0-50}|) + 0.25(|\mathbf{V}_{p_0-25}|) + 0.125(|\mathbf{V}_{0}|). \quad (1)$$

#### 3) THERMAL WIND

The thermal wind computations were made utilizing the expressions for pressure coordinates as given by

$$\Delta u/\Delta p = (R/fp)(\Delta T/\Delta y)_{\mu}, \tag{2}$$

$$\Delta v/\Delta p = -(R/fp)(\Delta T/\Delta x)_{p}. \tag{3}$$

Two temperature analyses were made for each observation time. The first analysis utilized the average of the 950- and 900-mb temperatures as the initial data. In cases where the surface pressure was less than 950 mb, the surface temperature was substituted for the 950-mb temperature to arrive at an initial data value. The second analysis was made using the average of the 850-, 800- and 750-mb temperatures as the initial data. The value of p in Eqs. (2) and (3) was set equal to 925 mb and 800 mb for the first and second analysis, respectively.

Computing the thermal wind for a layer instead of at a given level smooths the effects of the height variation of temperature (inversions, etc.) on the value of the thermal wind. The decision not to use surface temperature in the analysis (except when required at stations with higher station elevations) is based on the fact that the surface temperatures are greatly affected by the immediate surroundings and often are not representative of the overall temperature pattern.

The horizontal temperature fields were analyzed by a modified version of an objective analysis program developed by Fritsch (1969). The 2° latitude×2° longitude grid shown in Fig. 1 was used. Initial values for each grid point were obtained by weighting the data for the five closest stations. The grid values were then adjusted by two successive cubic spline interpolations. The horizontal temperature derivatives were evaluated by applying the centered finite-difference approximation to the final grid values.

The station elevations of the inner 19 stations varied from 62 m at Montgomery to 432 m at Omaha. This implied a typical variation of only 35–40 mb in surface pressure. Therefore, the thermal winds given by the first analysis were considered as representative for the first three layers in the surface pressure reference model given in Fig. 2. Similarly, the thermal winds from the second analysis were assigned to the upper three layers

of the model. Using this scheme any changes in the thermal wind with height were reflected between the third and fourth layer. Usually, these differences were small. Exceptions were found near air mass boundaries and in the Great Plains where a significant diurnal variation in the direction of the thermal wind exists due to radiational heating and cooling on a sloping terrain.

As suggested earlier, the modifications due to baroclinicity should be proportional to the magnitude and orientation of the thermal wind relative to the low-level wind. The parameter selected to define the magnitude is  $|\mathbf{V}_T|/S$  where  $\mathbf{V}_T$  is the thermal wind vector in the lowest 100 mb and S the average speed in the lowest 100 mb. The parameter selected to define the orientation is the angle  $\psi$ , where  $\psi$  is defined as the angle measured clockwise from the wind direction 100 mb above the surface to the direction of  $\mathbf{V}_T$  (see Fig. 3). Both  $|\mathbf{V}_T|/S$  and  $\psi$  were computed for each individual observation.

#### e. Computations of dependent parameters

The parameters which define the observed wind profile are treated as dependent parameters. From the wind data (wind speed and direction at each level), the following were computed.

## 1) The change in wind direction $(\alpha_{T_j})$ in each of the layers defined in Fig. 2

The direction for the lower level was subtracted from the direction at the upper level such that positive differences indicate wind veering with height. The subscript T indicates the veering due to the thermal wind has not been eliminated from the data. The subscript j indicates the layer number.

#### 2) WIND SHEAR IN EACH LAYER

Wind components in meteorological coordinates (coordinates aligned with the north-south and east-west directions) were converted to components in a natural coordinate system. The natural coordinates were oriented so the positive *s* axis coincided with the wind vector at the lower level. The transformation equations are

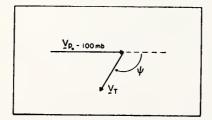
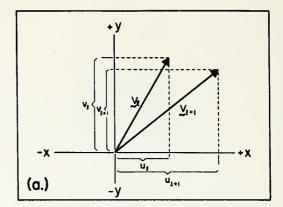
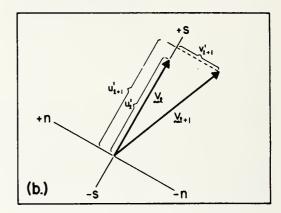


Fig. 3. Schematic diagram defining the angle  $\psi$ .





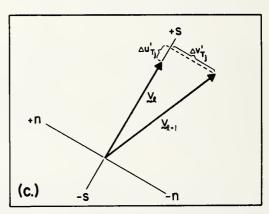


Fig. 4. Schematic diagram illustrating the method used to compute the wind shear between levels l and l+1. (a) Wind vectors and components in the meteorological coordinate system. (b) Wind vectors and components in the natural coordinate system. (c) Wind vectors and components of the wind shear in the natural coordinate system.

$$u'_{l+1} = -u_{l+1} \sin \gamma_l - v_{l+1} \cos \gamma_l v'_{l+1} = u_{l+1} \cos \gamma_l - v_{l+1} \sin \gamma_l$$
(5)

for the lower and upper levels, respectively. Here u and v are the wind components in the meteorological coordinate system; u' and v' are the wind components in the natural coordinate system;  $\gamma$  is the wind direction; and

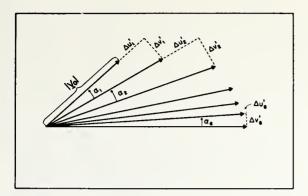


Fig. 5. Procedure employed in constructing hodographs.

the subscript l corresponds to the level number as defined in Fig. 2. The observed wind shear along  $(\Delta u_T')$  and perpendicular  $(\Delta v_T')$  to the flow at the lower level are

$$\Delta u_{T_i}' = u'_{l+1} - u_{l}', \tag{6}$$

$$\Delta v_{T_i}' = v'_{l+1}. \tag{7}$$

Fig. 4 provides a schematic diagram illustrating how this calculation was made. The values of  $\alpha_{T_j}$ ,  $\Delta u_{T_j}$  and  $\Delta v_{T_j}$  were computed for each layer for each observation.

In about 5-10% of the observations, the data were missing for one or more of the levels. The change in wind direction and the wind shear could not be computed if the data for either of the two levels was missing. Computations were made for all possible layers instead of discarding the entire observation.

Additional criteria were established for cases of calm or light winds. When calm conditions were reported for a level, the angle  $(\alpha_T)$  could not be computed for the two adjacent layers. In these instances the wind shear vector was not computed so that averages of the two parameters would be based on the same data sample. In conditions of light but non-zero wind speeds, the wind direction can change greatly from one level to another. In these cases, it is no longer obvious whether the wind is veering or backing with height. If  $\alpha_T$  exceeded  $60^\circ$  in a given layer, the values of  $\alpha_T$ ,  $\Delta u_{T}'$ , and  $\Delta v_{T}'$  were discarded, maintaining the same data sample for these parameters.

## 3) Elimination of the Geostrophic shear from the observed wind data

The thermal wind vectors for each of the six layers in Fig. 2 were transformed into the natural coordinate system used to compute the observed shear (see Fig. 4). The resulting components of the geostrophic shear defined as  $\Delta u_g$  and  $\Delta v_g$  were subtracted from the observed shear:

$$\Delta u_j' = \Delta u_{T_j}' - \Delta u_{g_j}', \tag{8}$$

$$\Delta v_i' = \Delta v_{T_i}' - \Delta v_{g_i}'. \tag{9}$$

Again j refers to the layer number in Fig. 2. The resulting values of  $\Delta u'$  and  $\Delta v'$  along with the magnitude of the observed surface wind were utilized to construct wind hodographs with the geostrophic shear eliminated. Assuming geostrophic balance 250 mb above the surface, new veering angles were obtained from this hodograph. These angles, identified by the symbol  $\alpha$ , are the angles between the isobars and the observed wind. Fig. 5 illustrates how the hodographs were constructed and how the values of  $\alpha$  were obtained.

#### f. Data stratifications

Initially the role of the three external factors was assumed to be unknown. The proper methodology needed to establish the dependence of the PBL winds on any of these factors is to hold two of the factors constant and let the third vary. This means we must allow for all possible combinations of the three factors. Stratifications A and B are designed to satisfy these criteria.

#### STRATIFICATION A

(Five speed, three stability, and nine baroclinicity categories)

The dependent parameters defining the observed wind profiles  $(\Delta u_T', \Delta v_T', \alpha_T)$  are stratified using the categories of external parameters defined below. This scheme results in 135 possible combinations of speed, stability and baroclinicity.

Speed categories {based on the average speed  $[m \sec^{-1}]$  in the lowest 100 mb}

- 1. *S* ≤ 5
- 2.  $5 < S \le 10$
- 3.  $10 < S \le 15$
- 4. 15<*S* ≤ 20
- 5. S > 20

Stability categories {based on the average lapse rate  $\lceil {^{\circ}} C (100 \text{ mb})^{-1} \rceil$  in the lowest 100 mb}

- Γ≤0
- 2.  $0 < \overline{\Gamma} \leqslant 5$
- 3.  $\bar{\Gamma} > 5$

Baroclinicity categories [based on magnitude and direction of the thermal wind in the lowest 100 mb]

- 1.  $\psi = 1-45^{\circ}$  ;  $|V_T|/S \ge 0.2$
- 2.  $\psi = 46-90^{\circ}$ ;  $|V_T|/S \ge 0.2$
- 3.  $\psi = 91-135^{\circ}$ ;  $|V_T|/S \ge 0.2$
- 4.  $\psi = 136-180^{\circ}$ ;  $|V_T|/S \ge 0.2$
- 5.  $\psi = 181-225^{\circ}$ ;  $|V_T|/S \ge 0.2$
- 6.  $\psi = 226-270^{\circ}$ ;  $|V_T|/S \ge 0.2$
- 7.  $\psi = 271 315^{\circ}$ ;  $|V_T|/S \ge 0.2$
- 8.  $\psi = 316 360^{\circ}$ ;  $|V_T|/S \ge 0.2$
- 9.  $|V_T|/S < 0.2$  (negligible thermal wind)

The data combinations are identified by the three numbers corresponding to the speed, stability and thermal wind categories. For example, the combination (3, 1, 7) includes those observations with S=10-15 m sec<sup>-1</sup>,  $\bar{\Gamma} \leq 0$ C (100 mb)<sup>-1</sup>, and  $\psi = 271-315$ ° with  $|V_T|/S \geq 0.2$ . Note that this scheme combines data from all of the 19 radiosonde stations.

#### STRATIFICATION B

(Five speed, three stability, and nine baroclinicity categories—geostrophic shear eliminated from the wind data.)

The categories of speed, stability and baroclinicity are identical to those defined in Stratification A. The dependent parameters  $(\Delta u', \Delta v', \alpha)$  are those obtained after the geostrophic shear was eliminated from the observed data.

The results of Stratification B were used to obtain average values for two additional quantities. These are the geostrophic wind speed and the ageostrophic winds. Values were obtained at each of the seven levels defined in Fig. 2 for each of the 135 possible combinations.

- 1) Average geostrophic wind speeds. Mean wind hodographs for each combination of speed, stability and thermal wind were constructed. The magnitude of the surface wind vector was set equal to the average surface speed. Vectors for successively higher levels were obtained by adding the average shear ( $\Delta u'$  and  $\Delta v'$ ) to the existing vectors. The procedure is illustrated in Fig. 6. Since the geostrophic shear is eliminated from the values of  $\Delta u'$  and  $\Delta v'$ , the magnitude of the vector of 250 mb is considered to be equal to the average surface geostrophic wind speed  $|\overline{V_{g_0}}|$ . The average geostrophic speed at the top level  $|\overline{V_{g_6}}|$  was set equal to the average observed speed at level six. The geostrophic speeds at the remaining levels were then obtained by linear interpolation between the values for the surface and the top level.
- 2) Average ageostrophic wind components. The deviation of the wind vector from the geostrophic wind vector is the ageostrophic wind. The average ageostrophic components parallel  $(\overline{u''})$  and perpendicular

Table 2a. Standard deviations (deg) of the observed wind veering.

	l.	ayers [h	eight (n	ıb) abov	e surfac	e]	
Time (GMT)	0-25	26-50	51-100	101-150	151-200	201-250	0-250
0000 1200	16.0 19.3	11.8 12.5	18.5 19.1	18.7 18.9	17.2 17.0	14.9 17.0	61.3 61.5

Table 2b. Average standard deviations (deg) for selected categories from Stratification B.

0000	9.6	4.4	8.5	9.2	10.0	9.5	28.4
1200	16.1	7.7	11.3	11.2	10.8	10.7	31.0

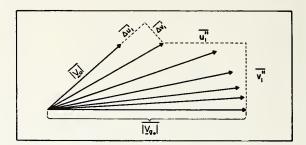


Fig. 6. Procedure employed in obtaining components of the ageostrophic wind.

 $(\overline{v''})$  to the geostrophic wind were taken from the mean wind hodographs as shown in Fig. 6. In this study, v'' is positive for ageostrophic flow toward lower pressure, and u'' is positive when the wind component along the isobar is less than the geostrophic speed.

Much of the variation in the magnitudes of u'' and v'' are due to variation in the magnitudes of the geostrophic wind. For this reason, the dimensionless quantities  $u''/|V_{\sigma}|$  and  $v''/|V_{\sigma}|$  were computed. These two dimensionless quantities, plus the angle between the wind and isobars  $(\alpha)$ , are used to define the characteristics of the wind profile.

#### g. Analysis of variance

An indication of the variability in the wind profiles for the winter season is given in Table 2. This table lists the standard deviations of the observed veering for the 19 interior U. S. stations. From a statistical viewpoint, the variability results from a combination of errors in the data and real differences. In the following paragraphs the sources of the observed variability are discussed.

#### 1) Observational errors

In the data making up any individual sounding, the possibility of errors exists due to the accuracy limitations of the observing system. In addition, errors may be introduced in the data reduction procedure or in any subsequent handling of the data. While these errors may contribute to the variability of the wind veering, it seems reasonable to assume that these errors are random. The methodology used in this study, namely, averaging the data from many soundings to obtain composite or average profiles, will minimize the effects of these random errors.

#### 2) Local variations

At any time, the actual wind may be considered to be made up of a mean and a perturbation. In the PBL these perturbations are most commonly associated with the turbulent eddies. At other times perturbation arises due to mesoscale features such as thunderstorms. While these variations are real and contribute to the variability in the wind profiles, they should be eliminated in a study of the mean wind profiles. Like observational errors, the variations due to gust-scale turbulence and mesoscale systems are considered to be random in their occurrence. I nus, we assume that the effects of local variations are minimized in the averaging process.

#### 3) Topographical effects

At some stations, the local topography modifies the PBL wind profile. Since these modifications may be systematic at any one station, averaging the data does not eliminate these effects. If, however, the data from several stations are combined, as is the case here, the probability of the topographical effects being largely eliminated from the average value is good.

#### 4) VERTICAL RESOLUTION OF WIND DATA

The wind data provided in either the specified height or pressure format are actually average winds for a layer of the atmosphere. For all altitudes considered in this study, the horizontal displacement of a balloon for a 2-min period is converted to a wind speed and direction. The average rate of rise of the balloons is near 300 m min<sup>-1</sup>. The derived wind data are therefore averages for a layer ~600 m thick. This wind is then assigned to the height corresponding to the balloon elevation at the intermediate time. In the data reduction procedures, the 2-min average wind is computed at 1-min intervals in an overlapping fashion.

The data assigned to the specified pressure levels in Deck 645 are obtained by linear interpolation between elevations of the 1-min interval wind data. Due to the limits in the vertical resolution, the details existing in the actual wind profile are suppressed or smoothed in the resulting wind data. The result of this smoothing is to suppress the variability in the observed data. The true variability in the wind profiles may therefore be larger than those given in Table 2. If the details, which are lost by smoothing, are random variations, the averaging process will still yield an accurate profile of the true mean wind. If, however, certain systematic but detailed features exist in the true mean wind profiles, these features cannot be preserved in the average profiles. The limited vertical resolution and subsequent smoothing in the collected data are the most serious drawbacks to a statistical treatment of routine radiosonde and windsonde data for the PBL. Nevertheless, the qualitative aspects of the major features in the actual wind profiles should still exist in the average profiles.

#### 5) VARIABILITY CAUSED BY EXTERNAL FACTORS

The characteristics of the wind profile in the PBL are influenced by (i) baroclinicity, (ii) stability, (iii) magnitude of the wind velocity, (iv) accelerating or

non-steady flow, and (v) changes in surface roughness. The present study considers only the first three factors. Since data for all stations were combined, the results are representative of a mean surface roughness for the network area.

Accurate computations of the synoptic-scale accelerations could not be made because of limited accuracy of the wind data (i.e., while thermal winds can be obtained from horizontal temperature gradients, several nonlinear terms must be evaluated to obtain accelerations). Therefore, it was not possible to establish the variations in the PBL winds caused by synoptic-scale accelerations nor the correlations between these accelerations and the thermal winds. Hopefully, these correlations are not significant and the variations are mostly eliminated in the averaging processes. However, the accelerations which produce the often observed nocturnal wind maximum in the 300-1500 m layer are fairly systematic in their time of occurrence. These variations are retained in the averages and produce differences in the 0000 and 1200 GMT average wind profiles (see Fig. 13 for example).

Table 2 also provides standard deviations of the wind veering for selected combinations from Stratification B [0000 GMT: the nine thermal wind categories with speed category 3 and stability category 3; 1200 GMT: the nine thermal wind categories with speed category 3 and stability category 1] The differences between the standard deviations provide an estimate of how much of the total variability is explained by variations in the first three factors listed above. (One would expect an even greater reduction if the number of categories for each factor were increased.) For the individual layers the standard deviations decrease from 30–50%. This implies a 50–75% reduction in the variance.

The standard deviation for the total veering in the lowest 250 mb is reduced from near 60° to near 30°. This corresponds to about a 75–80% reduction in the variance. This comparison suggests that a majority of the observed variability in the wind profiles for the lowest 2.5 km is related to changes in speed, stability, or the direction and magnitude of the thermal wind.

#### 3. Direct effect of geostrophic shear

Only those combinations of speed and stability categories that had more than 25 observations for each of the nine thermal wind categories were considered in the subsequent discussion. Table 3 lists these combinations and the respective number of observations. Figs. 7–10 and 12–15 and Tables 4–7 are based on data from these combinations. In obtaining average values for each thermal wind category, the combinations were weighted equally, thereby eliminating any systematic trends related to speed or stability.

Average magnitudes of  $|V_T|/S$  for each thermal wind category are given in Table 4. These values indicate that the magnitudes of the thermal winds are somewhat

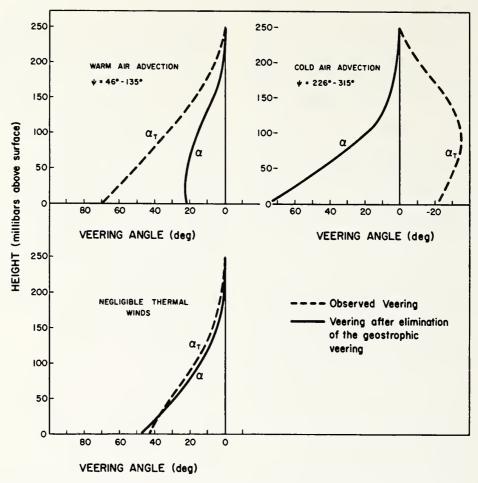


Fig. 7. Comparison of the average veering angles at 0000 GMT prior to and after the elimination of the geostrophic veering.

larger for the cold air advection cases. For the total data sample, the values of  $|V_T|/S$  was  $\geqslant 0.2$  in 85% of the 0000 GMT observations and  $\geqslant 0.2$  in 81% of the 1200 GMT observations.

In Fig. 7, the average observed veering angle at 0000 is plotted as a function of height for cases of significant warm air advection ( $\psi=46^{\circ}-135^{\circ}$ ,  $|V_T|/S \ge 0.2$ ), significant cold air advection ( $\psi=226^{\circ}-315^{\circ}$ ,  $|V_T|/S$ 

TABLE 3. Combinations of categories from Stratifications A and B which were used to obtain the values shown in Figs. 7-10 and 12-15. The number of observations is given for each combination. In obtaining average values for each thermal wind category, the combinations were weighted equally.

Categories						r of obser il wind ca				
Speed	Stability	1	2	3	4	5	6	7	8	9
			a. (	0000 GMT	Γ					
2	2	223	232	205	171	122	132	201	255	18
3	$\overline{2}$	92	95	88	46	32	40	63	90	23
2	3	310	198	165	204	203	228	457	625	39
3	3	135	62	61	99	58	64	237	336	4(
			ь.	1200 GMT	Γ					
2	1	335	323	255	166	148	234	334	429	33
3	ĺ	158	124	98	34	34	61	115	166	38
2	2	169	123	86	101	156	232	363	322	2-
3	2	120	52	37	36	69	88	160	187	36

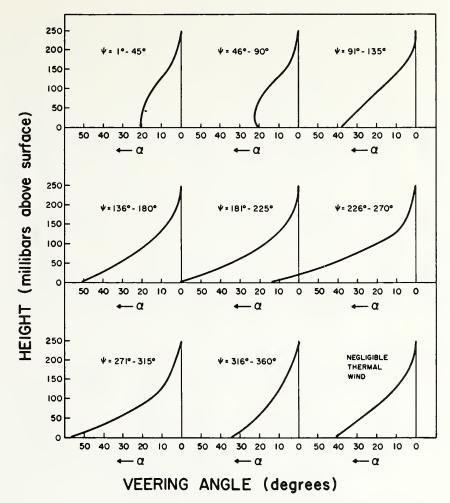


Fig. 8. Height profiles of the angle between wind and isobars at 0000 GMT for the nine thermal wind categories. Geostrophic veering has been eliminated from the data.

 $\geqslant$  0.2), and negligible thermal wind ( $|V_T|/S < 0.2$ ). In Fig. 7 and elsewhere, the veering angles are plotted as deviation of wind direction from the direction 250 mb above the surface. Large differences are found in the observed veering for the warm and cold air advection cases. Contrast, for example, surface values of  $\alpha_T$  of 70°

Table 4. Average values of  $|V_T|/S$  during the winter season for the nine thermal wind categories.

Thermal wind category	1200 GMT	0000 GMT
$1^{\circ}-45^{\circ}   \mathbf{V}_T /S \geqslant 0.2$	0.49	0.49
$46^{\circ}-90^{\circ}  V_T /S \geqslant 0.2$	0.46	0.45
$91^{\circ}-135^{\circ}  V_T /S \geqslant 0.2$	0.48	0.47
$136^{\circ}-180^{\circ}  V_T /S \geqslant 0.2$	0.56	0.51
$181^{\circ}-225^{\circ}  V_T /S \geqslant 0.2$	0.57	0.58
$226^{\circ}-270^{\circ}  V_T /S \geqslant 0.2$	0.61	0.63
$271^{\circ}-315^{\circ}  \mathbf{V}_{T} /S \geqslant 0.2$	0.58	0.61
$316^{\circ} - 360^{\circ}  V_T /S \geqslant 0.2$	0.55	0.55
$ \mathbf{V}_T /S < 0.2$	0.13	0.13

and  $-21^{\circ}$  for warm air and cold air advection, respectively. The geostrophic veering is positive for warm air advection and negative for cold air advection. The negligible thermal wind case portrays the more typical profile of observed veering.

As expected, the geostrophic shear resulting from horizontal temperature gradients has a profound effect on the observed PBL wind veering. The next problem is to determine if the existence of geostrophic shear modifies the angle between the isobars and the winds, or ageostrophic wind components.

#### 4. Indirect effects of geostrophic shear

#### a. Variations of wind veering

Fig. 7 also shows the veering as a function of height after the geostrophic veering has been subtracted from the observed veering. The veering angle is now the angle between the observed wind and the isobars  $(\alpha)$ . As expected, the profile for the negligible thermal wind cases remains essentially the same. However, large

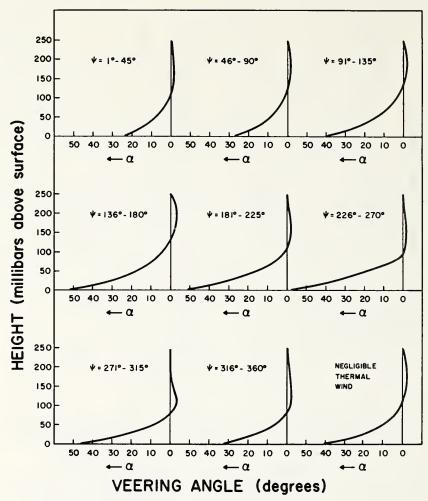


Fig. 9. As in Fig. 8 except for 1200 GMT.

changes occurred in the other two classes. The important result is that, in the lowest 100-mb layer, the angles between the wind and isobars for the cold air advection cases are significantly greater than the angles for warm air advection. This is completely opposite to the observed veering comparisons.

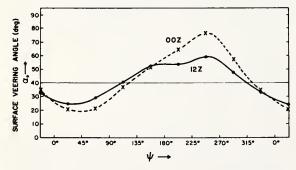


Fig. 10. Angle between the surface wind and surface isobars as a function of the angle between the wind vector 100 mb above 'he surface and the thermal wind vector in the lowest 100 mb.

Figs. 8 and 9 show in more detail the dependence of the angle between wind and isobars on the direction of the thermal wind in relation to the wind at  $\sim 1$  km above the surface. Values of  $\psi$  from approximately  $330^{\circ}-150^{\circ}$  represent warm air advection; and values from  $150^{\circ}-330^{\circ}$ , cold air advection. At both 0000 and 1200, we see that the profiles are strongly dependent on the value of  $\psi$ . Again the veering angles are significantly larger in cases of cold air advection. In Fig. 10, the angle between the surface wind and surface isobars from Figs. 8 and 9 is shown as a function of  $\psi$ . The range amounts to 56° for the 0000 GMT cases and 35° for the 1200 GMT cases. Minimum and maximum values of  $\alpha_0$  occur at  $\psi \approx 45^{\circ}$  and 245°, respectively.

The surface geostrophic wind is often more easily obtained than the actual wind 100 mb above the surface. Therefore, it is desirable to have the information shown in Fig. 10 expressed as a function of the angle  $(\beta)$  between the direction of the surface geostrophic wind and the thermal wind in the lowest 100 mb (see Fig. 11). In the analysis procedures, surface pressure

TABLE 5. Average values of the geostrophic wind speed, and the normalized ageostrophic wind components, for eight categories of  $\psi$  (or  $\beta$ ) and for conditions with negligible thermal winds. Time 0000 GMT.

	(01	β) and for conditi	one men neg		11 WINGS: 1 IIII						
				Heigh	t (mb above	surface)					
		0	25	50	100	150	200	250			
4	β			Average geo	strophic wind	speed, $ V_{o} $					
(deg)	(deg)		(m sec <sup>-1</sup> )								
01-45	06-70	9.1	10.0	10.0	12.7	14.4	16.2	18.0			
46-90	71-112	12.1	12.6	13.0	14.0	14.9	15.8	16.7			
91-135	113-142	14.4	14.4	14.4	14.3	14.3	14.2	14.2			
136-180	143-168	14.7	14.4	14.1	13.4	12.9	12.3	11.8			
181-125	169-190	14.3	13.9	13.4	12.5	11.6	10.6	9.6			
226-270	191-230	12.8	12.8	12.7	12.7	12.6	12.5	12.4			
271-315	231-297	9.8	10.6	11.4	12.9	14.4	15.8	17.2			
316-360	298-05	7.8	9.0	10.1	12.3	14.6	16.8	18.9			
$ V_T /2$	S<0.2	12.2	12.4	12.6	13.0	13.4	13.8	14.2			
4	β										
(deg)	(deg)			Avera	age value of $v$	"/ V <sub>0</sub>					
01-45	06-70	0.30	0.32	0.38	0.25	0.08	0.03				
46-90	71-112	0.21	0.30	0.34	0.26	0.11	0.03	_			
91-135	113-142	0.22	0.31	0.35	0.27	0.11	0.03				
136-180	143-168	0.23	0.33	0.35	0.27	0.12	0.03	_			
181-225	169-190	0.28	0.38	0.41	0.29	0.15	0.08	_			
226-270	191-230	0.43	0.55	0.58	0.35	0.13	0.06	_			
271-315	231-297	0.51	0.60	0.55	0.28	0.10	0.04	_			
316-360	298-05	0.53	0.57	0.52	0.29	0.12	0.04	_			
$ V_T /.$	S<0.2	0.32	0.41	0.43	0.29	0.12	0.04				
	β					S . // /   37					
(deg)	(deg)			AV	erage value o	[ 11 /   V <sub>0</sub>					
01-45	06–70	0.59	0.32	0.15	0.04	0.00	0.00	-			
46-90	71-112	0.67	0.40	0.23	0.07	0.01	0.00				
91-135	113-142	0.70	0.46	0.25	0.05	-0.01	-0.01	_			
136-180	143-168	0.71	0.47	0.26	0.03	-0.01	0.00	_			
181-225	169-190	0.72	0.49	0.32	0.06	0.00	0.00	_			
226-270	191-230	0.80	0.57	0.36	0.06	0.01	0.01	_			
271-315	231-297	. 0.76	0.52	0.30	0.04	0.00	-0.01	_			
316-360	298-05	0.62	0.33	0.15	0.03	0.00	0.00	-			
$ V_T /S$	S < 0.2	0.69	0.44	0.27	0.04	-0.01	-0.01	_			

data reduced to sea level were not available and the surface geostrophic winds were not computed. However, the average difference between the angles  $\psi$  and  $\beta$  can be obtained as follows. For the eight categories of  $\psi$ , the average direction difference ( $\alpha'$ ) between the surface wind and the wind at 100 mb above the surface can be obtained from the average observed veering angles. Values of  $\alpha'$  were obtained from the results of Stratification A. The directional difference ( $\alpha_0$ ) between the surface wind and the surface geostrophic wind is given in Fig. 10 (from Stratification B). The average difference ( $\alpha''$ ) between the surface geostrophic wind

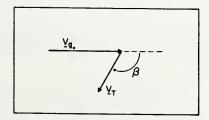


Fig. 11. Schematic diagram defining the angle  $\beta$ .

direction and the wind direction at 100 mb above the surface is then

$$\alpha'' = \alpha' - \alpha_0. \tag{10}$$

Therefore, the angle  $\beta$  is given by,

$$\beta = \psi + \alpha''. \tag{11}$$

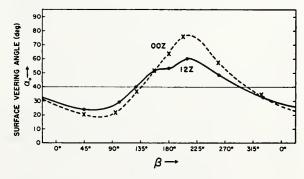


Fig. 12. Angle between the surface wind and surface isobars as a function of the angle between the surface isobars and the thermal wind.

Table 6. Average values of the geostrophic wind speed, and the normalized ageostrophic wind components, for eight categories of  $\psi$  (or  $\beta$ ) and for conditions with negligible thermal winds. Time 1200 GMT.

				gine thermal w			<del></del>	
				0	(mb) above s			
		0	25	50	100	150	200	250
$_{ m (deg)}^{m \psi}$	β (deg)			Average geo	strophic wind (m sec <sup>-1</sup> )	speed, $ V_g $		
01-45	08-72	8.4	9.2	9.9	11.4	13.0	14.5	16.0
46-90	73-115	9.9	10.4	10.9	11.8	12.8	13.7	14.6
91-135	116-142	11.8	11.8	11.9	11.9	11.9	12.0	12.0
136-180	143-167	12.2	11.9	11.6	11.1	10.5	9.9	9.3
181-225	168-192	11.6	11.3	11.0	10.3	9.7	9.0	8.3
226-270	193-232	10.5	10.8	11.1	11.6	12.2	12.7	13.2
271-315	233-300	8.6	9.4	10.4	11.9	13.6	15.2	16.9
316-360	301-07	7.0	8.1	9.2	11.5	13.6	15.9	18.0
$ V_T /2$	S<0.2	10.3	10.5	10.7	11.1	11.6	12.0	12.4
<i>\psi</i>	β			A	== value of s''	/137 1		
(deg)	(deg)			Avera	ge value of v''	/   V ø		
01-45	08 - 72	0.24	0.26	0.16	0.00	-0.02	-0.01	_
46-90	73-115	0.22	0.21	0.14	0.00	-0.05	-0.02	_
91-135	116-142	0.22	0.25	0.20	0.04	-0.03	-0.02	.—
136-180	143-167	0.25	0.28	0.21	0.05	-0.02	-0.05	_
181-225	168-192	0.28	0.29	0.20	0.00	-0.03	-0.01	_
226-270	193-232	0.31	0.31	0.19	0.00	-0.03	-0.02	_
271-315	233-300	0.35	0.32	0.19	-0.03	-0.02	0.00	_
316-360	301-07	0.36	0.30	0.16	-0.04	-0.03	-0.01	_
$ V_T /$	'S < 0.2	0.27	0.26	0.18	0.00	-0.03	-0.01	
Ψ.	β				, , ,	///** /		
(deg)	(deg)			Avera	ge value of u'	7   V <sub>0</sub>		
01-45	08-72	0.63	0.13	-0.12	-0.16	-0.08	-0.01	_
46-90	73-115	0.67	0.23	-0.08	-0.17	-0.08	-0.04	_
91-135	116-142	0.69	0.30	-0.01	-0.16	-0.08	-0.02	_
136-180	143-167	0.70	0.30	-0.02	-0.17	-0.09	-0.03	_
181-225	168-192	0.66	0.24	-0.07	-0.17	-0.10	0.00	_
226-270	193-232	0.66	0.23	-0.04	-0.11	-0.05	-0.01	_
271-315	233-300	0.65	0.19	-0.06	-0.13	-0.05	-0.03	_
316-360	301-07	0.59	0.12	-0.13	-0.12	-0.05	-0.01	-
$ V_T /$	'S<0.2	0.66	0.23	-0.06	-0.15	-0.08	-0.02	_

Fig. 12 shows  $\alpha_0$  as a function of  $\beta$ . The amplitudes obviously remain the same as those in Fig. 10. Note, however, that the minimum values of  $\alpha_0$  now occur at  $\beta \approx 65^{\circ}$  and the maximum values of  $\alpha_0$  occur at  $\beta \approx 210^{\circ}$ .

#### b. Variation in ageostrophic winds

Tables 5 and 6 give the average values of  $|V_{g}|$ ,  $v''/|V_{g}|$  and  $u''/|V_{g}|$  at each level for each of the nine thermal wind categories for 0000 and 1200, respectively. Remember that v'' is the ageostrophic wind component perpendicular to the isobar while u'' is the component parallel to the isobar. Fig. 13 provides a comparison of the normalized ageostrophic components for cold and warm air advection. In the lowest 1 km there is significantly more cross isobaric flow in the cold air advection cases. Also note the large difference between the values for 0000 and 1200. The major reason for this difference is the more stable lapse rate categories associated with the 1200 GMT data.

The negative values of  $v''/|V_{\mathfrak{g}}|$  and  $u''/|V_{\mathfrak{g}}|$  at 1200 above about 300 m are reflections of the inertial motions which produce the well-known nocturnal wind maxi-

mum. These inertial oscillations are usually triggered shortly after sunset and persist through the mid-morning hours. The deviations in the ageostrophic winds are negligible at 0000 but significant at 1200. For further discussions concerning this phenomena see Blackadar (1957), Bonner and Paegle (1970), Lettau (1967) and Hoxit (1973).

At 0000 GMT, Fig. 13 shows greater values of  $u''/|V_{\sigma}|$  in the lowest 100 m for the cold air advection cases. The difference, however, is not as great as for the  $v''/|V_{\sigma}|$  values. At 1200, there is no significant difference between cold and warm air advection.

#### c. Variations in surface stress

Assuming no accelerations, the equation of motion in pressure coordinates for the wind components along and perpendicular to the surface geostrophic wind can be written as

$$fv_n - g(\partial z/\partial s) - g(\partial \tau_{zs}/\partial p) = 0, \tag{12}$$

$$-fu_s - g(\partial z/\partial n) - g(\partial \tau_{zn}/\partial p) = 0, \tag{13}$$

where the positive s axis coincides with the direction of

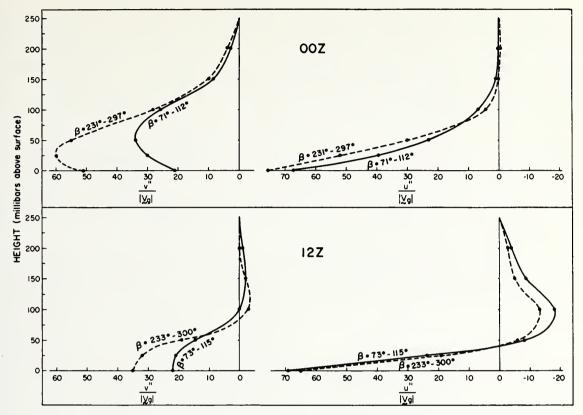


Fig. 13. Comparison of the normalized ageostrophic wind components for cases of warm and cold air advection.

the surface geostrophic wind, and  $u_s$  and  $v_n$  are the wind components parallel and perpendicular to the s axis. Utilizing the geostrophic wind relationship and integrating from the surface to a level where the stress becomes negligible, we obtain the geostrophic departure formulation for computing the surface stress. Assuming the stress is zero 250 mb above the surface, the components of the surface stress are

$$\tau_{:s_0} = -(f/g) \int_{p_0}^{p_0 - 250 \text{ mb}} (v_n - v_{n_0}) dp, \qquad (14)$$

$$\tau_{:\eta_0} = (f \cdot g) \int_{p_0}^{p_0 - 250 \text{ mb}} (u_s - u_{s_g}) dp.$$
 (15)

The assumption of no accelerations is not valid for the individual observations. Eqs. (14) and (15) are applied

to average values, however, and we assume that the accelerations produced by moving synoptic systems are largely climinated in the averaging process. The accelerations and corresponding changes in the ageostrophic winds associated with the development of nocturnal wind maximums are systematic (see Fig. 13). Therefore, the geostrophic departure method cannot be used to compute the surface stress at 1200.

Values of  $\tau_{z_{0}}$ ,  $\tau_{z_{0}}$  and  $\tau_{z_{0}}$  were computed for 0000 for each of the nine thermal wind categories using the data combinations given in Table 3. The resulting values are given in Table 7. The effect of the thermal wind in modifying the stress in the PBL is demonstrated in Fig. 14. The surface stress values have been normalized by dividing by the average surface geostrophic wind speed. The variations of this ratio are shown as a function of the angle  $\beta$ . Note the similarity between the

Table 7. Average values of the surface stress and components of surface stress (dyn cm<sup>-2</sup>) for 0000 GMT.

	β (deg)							Negligible thermal	
	06-70	71-112	113 142	143-168	169-190	191-230	231-297	298-05	winds
$ au_{z\sim_0} \  au_{z_{10}} \  au_{z_{20}} \  au_{z_{20}}$	5.2 2.0 5.6	6.2 2.4 6.7	6.6 3.8 7,6	6.5 4.5 7.9	5.9 6.6 8.9	5.2 9.2 10.5	6.3 6.4 9.0	6.5 2.9 7.1	6.6 3.8 7.6

curve for  $\tau_{z_{n_0}}/|V_{g_0}|$  and the curve for  $\alpha_0$  given by Fig. 12. The minimum value of  $\tau_{z_{n_0}}/|V_{g_0}|$  is found at  $\beta \approx 180^\circ$ , while the maximum value is near 325°. These angles correspond closely to conditions with the thermal wind opposing  $(\beta \approx 180^\circ)$  and increasing  $(\beta \approx 325^\circ)$  the surface wind vector. Combining the stress components gives rise to significantly larger ratios of  $\tau_{z_0}/|V_{g_0}|$  for cold air advection conditions.

#### d. Variations in surface speed

Average surface wind speeds at 0000 were also obtained from the data combinations listed in Table 3. The curve of  $|\mathbf{V}_0|/|\mathbf{V}_{g_0}|$  vs  $\beta$  is shown in Fig. 15. Note that the greatest values of this dimensionless quantity are associated with cold air advection with the shape of the curve being similar to that for  $\tau_{z_0}/|\mathbf{V}_{g_0}|$  presented in Fig. 14. Indeed, these curves should be similar if the geostrophic departure method and drag coefficient method for computing surface stress are to yield comparable values. [The formulation for the drag coefficient method is  $\tau_{z_0} = \rho C_d(\mathbf{V}_0)^2$ , where  $C_d$  is the bulk drag coefficient.]

#### e. Interpretation of results

The amount of mechanical turbulence near the surface is determined primarily by the magnitude of the flow near the surface and the roughness characteristics of that surface. To a large extent, the vertical distribution of the turbulence is determined by the thermal stratification. Mixing-length theory states that the vertical momentum transport is proportional to the shear of the horizontal wind vector. When geostrophic shear exists in the PBL, the vertical momentum transport is modified from that expected in barotropic conditions. This modifies the stress profile as shown in Fig. 14. This in turn modifies the mean wind profiles in the lower layers.

The mechanism is portrayed schematically in Fig. 16. Examples are shown for (a) warm air advection

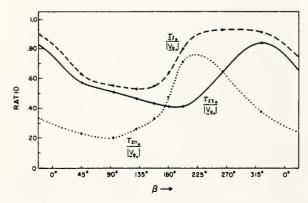


Fig. 14. Normalized values of the surface stress at 0000 GMT as a function of the angle between the surface geostrophic wind and the thermal wind in the lowest 100 mb. The units are (dyn cm<sup>-2</sup>)/(m sec<sup>-1</sup>).

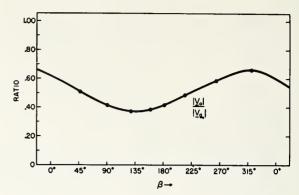


Fig. 15. Normalized values of the surface wind speed as a function of the angle between the surface geostrophic wind and the thermal wind in the lowest 100 mb.

 $(\beta = 70^{\circ})$  and (b) cold air advection ( $\beta = 210^{\circ}$ ). In addition, examples are shown for cases of (c) the thermal wind blowing in the same direction as the surface geostrophic wind  $(\beta = 0^{\circ})$ , and (d) the thermal wind opposing the surface geostrophic wind ( $\beta = 180^{\circ}$ ). In each case, the additional downward momentum transfer induced by the geostrophic shear is added schematically to the surface wind vector that would exist in a barotropic atmosphere. For  $\beta = 70^{\circ}$ , the additional momentum transported from above opposes the flow toward lower pressure in the region near the surface. The result is a smaller surface crossing angle and less ageostrophic flow toward lower pressure. When  $\beta = 210^{\circ}$ (cold air advection), the flow toward lower pressure is increased and  $\alpha_0$  becomes larger than the value for similar conditions in a barotropic atmosphere. Intuitively, it is expected that the greatest modification of  $\alpha_0$  occurs when the additional momentum transport is perpendicular to the surface wind vector that would exist in barotropic conditions. This statement is consistent with the results given in Fig. 10.

In cases where  $\beta = 0^{\circ}$ , the effect is to increase the surface wind speed and slightly decrease the crossing angle. This would result in an increase of the surface stress in the direction of the surface geostrophic wind. When the thermal wind opposes the geostrophic wind vector, the result is a decreased value of the surface stress along the geostrophic wind and an increase in the surface crossing angle.

Sheppard et al. (1952) were the first to suggest that this mechanism could modify the PBL wind profile. Recently, Blackadar (1965), MacKay (1971) and Cattle (1971) have developed theories expressing this effect quantitatively. For neutral conditions  $\lceil |V_T|/S \approx 0.5 \rceil$  and  $z_0=1$  cm, Blackadar's model gave values of  $\alpha_0$  of  $18.4^\circ$ ,  $17.7^\circ$ ,  $26.3^\circ$  and  $26.8^\circ$  for  $\beta$  equal to  $0^\circ$ ,  $90^\circ$ ,  $180^\circ$  and  $270^\circ$ , respectively. While these model variations in  $\alpha_0$  are in qualitative agreement with the present study, the amplitudes are much smaller than those given in Fig. 12. However, greater variations would be expected if the values of  $z_0$  were increased. Cattle presented

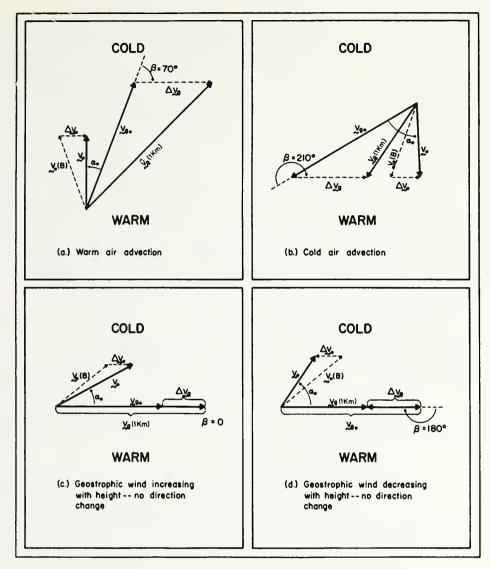


Fig. 16. Schematic examples of how the additional downward momentum transport, resulting from geostrophic shear in the turbulent boundary layer, modifies the surface crossing angle from that expected in a barotropic atmosphere. See Section 2a for definitions of symbols.

theoretical values of  $\alpha_0$  for  $\beta = 0^\circ$ , 90°, 180° and 270°. He showed large values of  $\alpha_0$  for  $\beta = 180^\circ$  as opposed to  $\beta = 0^\circ$ . Cattle's theoretical results are also in qualitative agreement with the observational results of the present study. MacKay shows maximum and minimum values of  $\alpha_0$  at  $\beta = 135^\circ$  and 315°, respectively. This does not agree with Cattle's theoretical results or the observational results shown in Fig. 12. The phase angle between MacKay's curves and those in Fig. 12 is very near 90°. The explanation for this difference is not clear, but may result from MacKay's modeling the magnitude of the thermal wind as an exponential function decreasing with height as opposed to the more general case of the magnitude being approximately constant with height.

## 5. The role of geostrophic shear in selected atmospheric processes

#### a. Movement of cold air masses

The effects just described can frequently be observed in synoptic analysis. Fig. 17 provides a good example. Here the surface analysis over the eastern United States for 0000 GMT 24 December 1970 is shown. A strong cold front is advancing through the area. The region of cold air advection is indicated by the stippled area behind the cold front. In this region, the value of  $\beta$  as given by the angle between the isobars and surface isotherms is between 200° and 270°. The average value of  $\alpha_0$  is 60°. Ahead of the front there is an area of weak warm air advection indicated in a second stippled area.

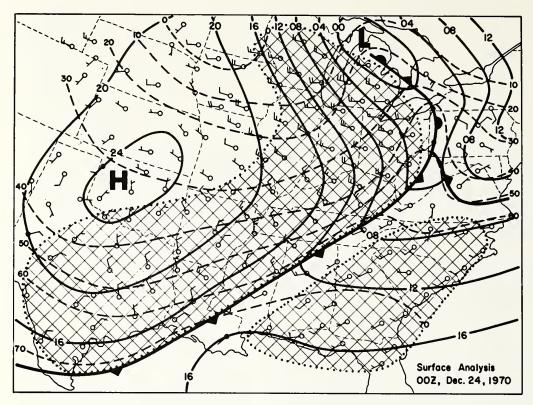


Fig. 17. Surface analysis showing the modification of the angle between the surface winds and surface isobars. Surface pressure (mb, using last two digits only) is given by the solid lines, and temperature (°F) by the dashed lines. The observed winds are plotted for each station. In the stippled area behind the cold front the average value of  $\alpha_0$  is 60°. In the stippled area ahead of the cold front the average value of  $\alpha_0$  is 33°.

In this region, the values of  $\beta$  range from 0°-50° and the average value of  $\alpha_0$  is 33°.

The momentum transport initiated by the geostrophic shear in the strong baroclinic zones behind cold fronts results in an increase in the cold air advection at the surface. This allows the surface air to flow almost directly away from the center of the cold anticyclones. The cold air then moves very rapidly eastward and southward (in the Northern Hemisphere) allowing little time for air mass modification.

#### b. Transport of angular momentum

Conservation of angular momentum arguments lead to the fact that westerly momentum must be transported from the atmosphere to the earth in mid-latitudes. This obviously is the case in regions where the average surface geostrophic winds are from the west. However, in much of the Northern Hemisphere, the synoptic pressure systems are cellular. Alternating high and low pressure systems move across a region and the resultant surface geostrophic wind may have a negligible westerly component. Fig. 18 shows such a pattern in schematic form. Here the typical case of a sinusoidal temperature field existing in a cellular pressure pattern is shown. The winds with a northerly component are associated with cold air advection (increas-

ing the angle between surface winds and surface isobars). Likewise, the winds with a southerly component are associated with warm air advection (decreasing the surface veering angles). As shown in Fig. 16, the westerly component is also increased in the areas of east and west winds. The effect of the momentum transport initiated by the geostrophic shear, therefore, systematically increases the westerly component of the surface

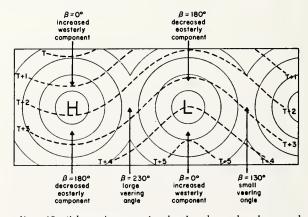


Fig. 18. Schematic example showing how the downward momentum transport by the geostrophic shear can systematically increase the westerly component of the surface winds.

wind over the entire region. Priestley (1967) has suggested that the geostrophic shear may provide an important mechanism for the downward transport of westerly angular momentum.

Eighty-three percent of the approximately 22,800 winter observations in the United States network had ratios of  $|V_T|/S \ge 0.2$ . The average surface geostrophic wind speed was about 10 m sec-1. If we assume that the basic temperature pattern is similar to that in Fig. 18, then from Tables 5 and 6 the increase in the westerly component of the mean surface wind is  $\sim 1.5$  m sec<sup>-1</sup>. We further assume that this is representative of the mid-latitude land areas and that the modification is only half as great over the mid-latitude oceans due to weaker temperature gradients and the decrease in surface roughness. At 40N the ratio of land to ocean area is near 1, so the estimate for the average increase in the surface westerly wind component around the latitude belt would be near 1 m sec<sup>-1</sup>. The hemispheric average of the observed surface westerly component at 40N during January is only about 2 m sec<sup>-1</sup> (Crutcher et al., 1966). Though the 1 m sec-1 increase is only an estimate, it appears that Priestley's suggestion is correct and that a significant proportion of the westerly momentum which is transferred from the atmosphere to the earth in the mid-latitudes reaches the surface through downward turbulent transport maintained by geostrophic shear in the PBL.

#### 6. Conclusions

In baroclinic conditions, geostrophic shear modifies the vertical transport of horizontal momentum from that which would exist in barotropic conditions. The way in which the additional momentum transport modifies the stress profiles depends on the direction and magnitude of thermal wind in the PBL relative to the direction and magnitude of the surface geostrophic wind. The effect is to increase (decrease) the ageostrophic wind components toward lower pressure in cold (warm) air advection. In conditions with a basic north-south temperature gradient, the geostrophic shear produces a systematic transport of westerly angular momentum from the atmosphere to the earth's surface. This increases the westerly component of the average surface wind.

Acknowledgments. The author gratefully acknowledges the guidance and encouragement of Dr. William M. Gray of Colorado State University who served as his advisor during the course of this research. Special thanks are also expressed to Drs. Alan K. Betts, Elmar R. Reiter and Virgil A. Sandborn for their many helpful suggestions.

Mr. Edward Buzzell did most of the programming work; Mr. Larry Kovacic drafted the figures; Mrs. Barbara Brumit and Mrs. Cheryl Brown aided in the data reduction; and Mrs. Margaret K. Larabee typed the manuscript.

This research was supported by the National Science Foundation under Grant GA-32589 X1.

#### REFERENCES

- Bernstein, A. B., 1959: The effect of a horizontal temperature gradient on the surface wind. M.S. thesis, Pennsylvania State University.
- Blackadar, A. K., 1957: Boundary layer wind maxima and their significance for the growth of nocturnal inversions. Bull. Amer. Meteor. Soc., 38, 283-290.
- —, 1965: A single layer theory of the vertical distribution of wind in a baroclinic neutral atmospheric boundary layer. AFCRL 65-531, Final Report Contract AF(604)-6641, Pennsylvania State University, 22 pp.
- Bonner, W. D., and J. Paegle, 1970: Diurnal variations in boundary layer winds over the south-central United States in summer. *Mon. Wea. Rev.*, 98, 735-744.
- Cattle, H., 1971: The terrestrial low latitude boundary layer. Ph.D. dissertation, Imperial College of Science and Technology, 201 pp.
- nology, 201 pp.
  Ching, J. K. S., 1964: A theory of wind distribution in a single-layered diabatic baroclinic turbulent boundary layer of the atmosphere. M.S. thesis, Pennsylvania State University, 65 pp.
- Crutcher, H. L., A. C. Wagner and J. S. Arnett, 1966: Components of the 1000 mb winds (or surface winds) of the Northern Hemisphere. NAVAIR 50-1C-51, Published by Direction of the Chief of Naval Operations, Govt. Printing Office, Washington, D. C., 80 pp.
- Ellison, T. H., 1956: Atmospheric turbulence. Survey in Mechanics, G. I. Taylor Anniversary Vol., Cambridge University Press, 400-430.
- Fritsch, J. M., 1969: Objective analysis of a two-dimensional data field by the cubic spline technique. Mon. Wea. Rev., 99, 379-386.
- Gray, W. M., 1972: A diagnostic study of the planetary boundary layer over the oceans. Atmos. Sci. Paper No. 179, Colorado State University, 95 pp.
- Hoxit, L. R., 1973: Variability of planetary boundary layer winds.
   Atmos. Sci. Paper No. 199, Colorado State University,
   182 pp.
- Kovetz, A., J. Neumann and R. Suzi, 1963: Extension of Ekman's spiral to conditions of near-neutral static stability and a constant horizontal temperature gradient. *Beitr. Phys. Atmos.*, 36, 201–212.
- Lettau, H., 1967: Small-to-large-scale features of boundary layer structure over mountain slopes. Proc. Symp. Mountain Meteorology, E. R. Reiter and J. L. Rasmussen, Eds., Atmos. Sci. Paper No. 122, Colorado State University, 1-74.
- MacKay, K. P., 1971: Steady-state hodographs in a baroclinic boundary layer. Boundary-Layer Meteor., 1, 161-168.
- Mendenhall, B. R., 1967: A statistical study of the frictional wind veering in the planetary boundary layer. Atmos. Sci. Paper No. 116, Colorado State University, 57 pp.
- Priestley, C. H. B., 1967: Handover in scale of the fluxes of momentum, heat, etc., in the atmospheric boundary layer. *Phys. Fluids*, 10, Pt. 2, S38-S46.
- Sheppard, P. A., H. Charnock and J. R. D. Francis, 1952: Observations of the westerlies over the sea. Quart. J. Roy. Meteor. Soc., 78, 563-582.
- Utina, Z. M., 1962: Effect of horizontal temperature inhomogeneity on the structure of the boundary layer of the atmosphere. Tr. Gl. Geofiz. Observ., 127, 134-144.
- —, 1966: Wind distribution in the boundary layer. Tr. Gl. Geofiz. Observ., 187, 146-148.
- Zaitsev, A. S., 1966: Effects of non-homogeneity of temperature on the wind field in the boundary layer. Tr. Gl. Geofiz. Observ., 187, 139-145

#### AN ANALYSIS OF THE MESOSCALE CIRCULATIONS WHICH

PRODUCED THE APRIL 3, 1974 TORNADOES IN NORTHERN INDIANA

Lee R. Hoxit Charles F. Chappell

National Oceanic and Atmospheric Administration Atmospheric Physics and Chemistry Laboratory Boulder, Colorado

#### INTRODUCTION

During the afternoon and evening of April 3, 1974 a massive outbreak of severe storms occurred over a wide area of the United States east of the Mississippi River. During the three-hour period from 1500 CST to 1800 CST a squall line moved rapidly across portions of Illinois, Indiana, Lower Michigan and Ohio. Imbedded in this line was a well-defined mesoscale low pressure system that produced a swath of tornadoes extending from East Central Illinois northeastward to Southeast Michigan. Certain characteristics of this mesoscale weather system are examined, and processes that may have contributed to its formation and propogation are discussed. A hypothesis for the genesis and maintenance of such mesoscale low pressure systems is presented.

#### 2. METEOROLOGICAL ANALYSES

A brief review of the synoptic scale conditions that existed during the afternoon of April 3, 1974 is given in Figures 1 to 4. The surface analysis is valid for 2100 GMT (1500 CST), while the 500 mb

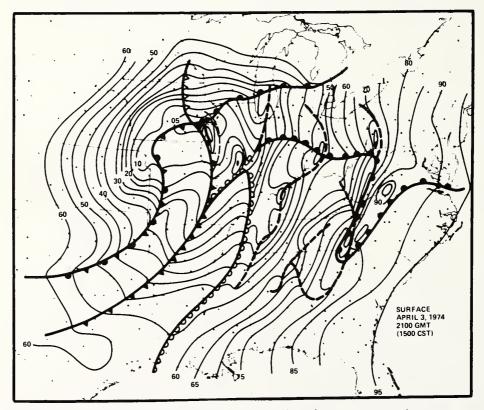


Figure 1. Surface analysis for 2100 GMT (1500 CST) April 3, 1974. Surface pressures hundredths of inches of mercury in excess of 29.00 inches.

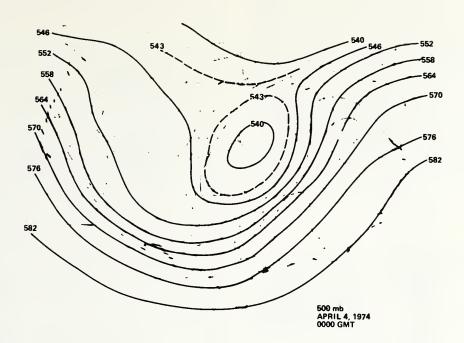


Figure 2. 500 mb analysis for 0000 GMT April 4, 1974. Contours - 60 meter intervals; Isotherms -  $2^{\circ}C$  intervals.

analysis (Figure 2), vertical motion analysis (Figure 3), and lifted index analysis (Figure 4) are valid for 0000 GMT, April 4 (1800 CST, April 3). It is evident from these charts that the atmosphere over Northern Indiana and Southeastern Michigan is only slightly unstable, but the region is experiencing the maximum of synoptic scale forcing.

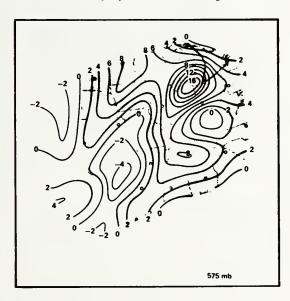


Figure 3. Vertical motion at 575 mb (cm/sec).
For 0000 GMT April 4, 1974. Computed using the Kinematic method.



Figure 4. Lifted index analyses for 0000 GMT April 4. 1974.

Of the observations routinely included in a surface report, only the pressure tendency provides an indication of a net change in the atmospheric mass above the station. Assuming hydrostatic equilibrium, changing surface pressure can also be interpreted as a change in the mean temperature of the atmospheric column above.

Figure 5a shows an analysis of the changes in surface pressure from 1400C to 1500C over the Ohio Valley and southern Great Lakes Region. The station network shown provides a subjective guide to the size of the phenomena that can be resolved. The pattern indicates the presence of several isallobaric centers with characteristic dimensions of 100-400 km. This analysis, however, reflects the combined effects of both synoptic scale and mesoscale changes.

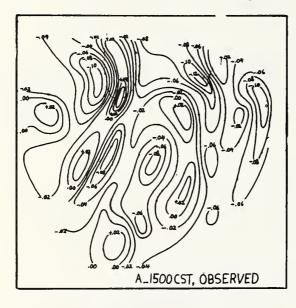


Figure 5a. One hour pressure tendencies. For period ending at 1500 CST April 3, 1974. Units are in inches of mercury.

In order to more clearly delineate mesoscale features, an estimate of synoptic scale pressure tendencies is obtained and subtracted from the total isallobaric field. This is accomplished as follows. Utilizing an 80-km grid, pressure tendencies at three observation times (1400 CST, 1500 CST and 1600 CST) were averaged to get a mean hourly tendency. Next, the mean hourly values were smoothed spatially using a five point equal-weight smoothing scheme. The resulting synoptic scale tendencies are shown in Figure 5b. The combined time- and space-smoothing appears to have successfully eliminated most of the mesoscale features. Next, the synoptic scale pressure tendencies (Figure 5b) were subtracted from the total isallobaric field (Figure 5a), the resulting difference (Figure 5c) being an indication of the pressure tendencies produced by the mesoscale circulations. Figure 6a-c and Figures 7a-c show similar analyses valid for 1600 CST and 1700 CST, respectively.

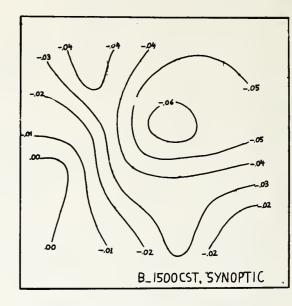


Figure 5b. One hour synoptic scale pressure tendencies. For period ending 1500 CST. April 3, 1974. Units are in inches of mercury.

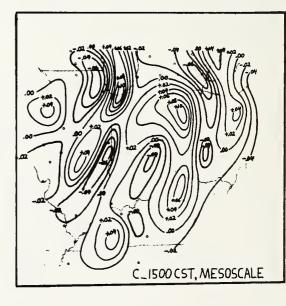
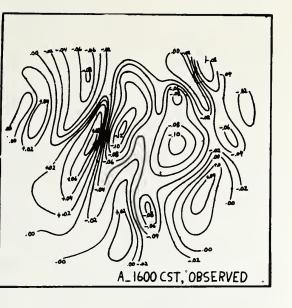


Figure 5c. One hour mesoscale pressure tendenci For period ending at 1500 CST April 1974. Units are in inches of Mercury.



C\_1600 CST, MESOSCALE

Figure 6a. Same as Figure 5a but for period ending at 1600 CST.

Figure 6c. Same as Figure 5c but for period ending at 1600 CST.

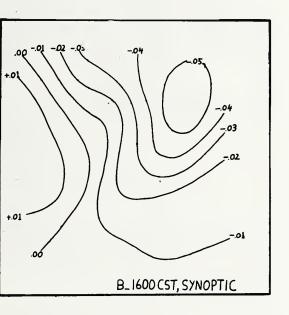


Figure 6b. Same as Figure 5b but for period ending at 1600 CST.



Figure 7a. Same as Figure 5a but for period ending at 1700 CST.

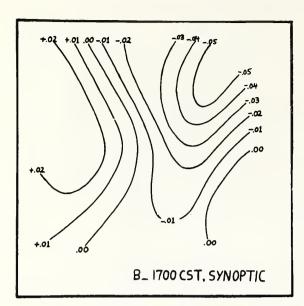


Figure 7b. Same as Figure 5b but for period ending at 1700 CST.

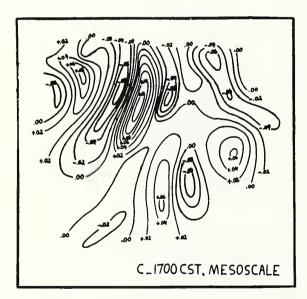


Figure 7c. Same as Figure 5c but for period ending at 1700 CST.

The evolution of most isallobaric features can be followed from 1500 CST through 1700 CST. The pattern reveals a combination of line-type phenomena (characteristic length of 300-800 km) and cellular phenomena (characteristic dimensions of 100-400 km).

The system which produced the Northern Indiana tornadoes was already in existence at 1500 CST and is identified by the pressure fall/rise couplet over Southeast Illinois. During the next two hours the system moved northeastward at

about 120 km/hour. The greatest pressure falls (greather than 0.10 inches of mercury per hour or about 3 1/2 mb/hour) were present at 1600 CST (Figure 6c), as the severe storms were passing just north of Lafayette, Indiana. Figure 8 presents an analysis of the surface pressures at 1600 CST. Note that the meso-low/bubble-high system is quite apparent over Western Indiana. After 1700 CST the meso-low moved into Southern Michigan and gradually lost its identity.

Figure 9 shows the track of the pressure fall center from 1500 CST to 1700 CST, along with tornado tracks for Northern Indiana as presented by Fujita (1975). The 1535 CST radar summary is also shown and indicates an almost continuous line of convection from Southern Michigan to Southern Illinois, approximately 600 km in length. It is of interest that tornado occurrence is confined to the relatively small portion of this line that coincides closely with the track of the mesoscale pressure-fall center.

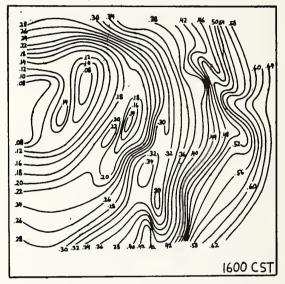


Figure 8. Surface pressure analysis valid at 1600 CST April 3, 1974. Units are in inches of mercury in excess of 29.00 inches.

This phenomenon points to the existence of a smaller scale weather system (meso- $\beta$  scale or 20 km<1.200 km, See Orlanski, 1975) that organizes the convection in such a manner as to provide a more favorable local environment for tornado occurrence.

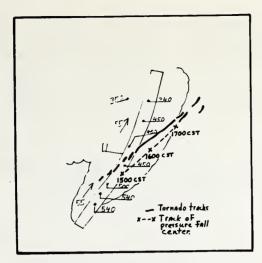


Figure 9. Radar summary valid at 1535 CST for the Illinois, Indiana region. Also included are tracks of the tornadoes produced by the squall line as reported by Fujita (1975) and the track of the mesoscale pressure Fall Center.

#### GENERATION AND MAINTENANCE OF SQUALL-LINES AND MESO-LOWS

The mechanism producing the mesoscale pressure rises, i.e., the meso- or bubble-high, has been documented by Fujita (1959). He showed that cold air produced by evaporation is a major factor in their genesis. However, mechanism(s) responsible for producing mesoscale pressure-fall centers have proven more difficult to define.

An atmospheric column may be warmed by any, or combinations, of the following processes; 1) warm air advection, 2) solar insolation either through absorption at the ground and subsequent transfer to the atmosphere, or absorption directly into the atmosphere, 3) release of latent heat, or 4) adiabatic warming via sinking motion.

#### 3.1 Solar Insolation and Latent Heat Release

The qualitative role of surface heating and low-level warm air advection in priming and triggering cumulus convection has been known for some time by forecasters and researchers alike. These processes, along with the release of latent heat, can also contribute to intensification of cyclones on the larger synoptic scale.

In the particular case presented here, the area ahead of the meso-low was covered with broken to overcast cirrus and scattered low and middle clouds. There is reason to believe, therefore, that solar insolation and latent heat release played only minor roles in producing the net warming and surface pressure falls. Thus, major contributions to the net warming appear to be either from warm air advection, warming due to adiabatic compression, or both.

At 1600 CST (Figure 6c), mesoscale surface pressure falls as large as 0.10 inches of mercury per hour are indicated over North-Central Indiana. This is equivalent to a net

warming of approximately 0.4C/hour for the atmospheric column below 100 mb, or about 1.0C/hour for the atmospheric column below 500 mb.

#### 3.2 Warm Air Advection

The 0000 GMT (1800 CST) 850 mb and 700 mb synoptic analyses show winds 25 to 50 meters per second oriented nearly perpendicular to temperature gradients of nearly 5C/400 km over the Indiana region. If not compensated by other processes, this synoptic scale temperature advection is sufficient to produce a 1C/hour warming in the lower troposphere. Since it is possible for mesoscale circulations to produce horizontal temperature advections of comparable or even greater magnitudes, the observed mesoscale pressure falls could be accounted for through strong warm air advection. However, it is not clear how horizontal temperature advection can initiate such an organized mesoscale circulation even though it appears it may contribute importantly to their subsequent maintenance and motion.

#### 3.3 Adiabatic Warming

Figure 10 presents a conceptual cumulonimbus cloud model proposed by Fritsch (1975). This model synthesizes several observational studies of clouds existing in moderate to strong vertical shear. Note the sinking that occurs in the middle and upper levels of the troposphere and lower stratosphere well downwind of the main updraft. Kuhn (1975) recently observed sinking motion at elevations near 13 km as far as 50 to 60 km downwind of a cumulonimbus core. Two-dimensional model simulations of deep convection in moderate and strong environmental shear by Schlesinger (1973a, b) have also yielded sinking motions 40 to 80 km downwind of the main updraft.

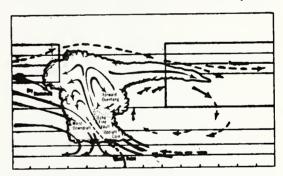


Figure 10. Schematic model of the vertical circulations in and near large cumulonimbus clouds in moderate to strong shear.

(Adapted from Fritsch (1975)). Boxes enclose regions for which few observations of the vertical circulations are available. Solid arrows based on observations. Dashed arrows based on suppositions.

Table I shows estimates of sinking rates necessary to produce a net temperature increase of near 0.4C/hour below 100 mb, or a 3 1/2 mb surface pressure fall/per hour. The calculations are based on the 1200 GMT (0600 CST) April 3 sounding for Nashville, Tennessee, which produces an indication of the general thermodynamic structure over

Indiana during the afternoon.

Table 1

Sinking rate necessary to produce 0.4C/hour warming in an atmospheric column below 100 mb.

Level	Vertical Motion			
700 mb	-10 cm/sec			
500 mb	-10 cm/sec			
300 mb	- 4 cm/sec			
150 mb	- 2 cm/sec.			

Note that the required subsidence is not unreasonably large. Also, in this case, sinking is much more efficient as a warming mechanism in the upper troposphere and lower stratosphere.

In the case of the Indiana squall line, the axis of maximum pressure falls are estimated to lie about 60 km ahead of the actual convective line, though an accurate displacement is difficult to define with the station density available. The pressure falls downwind of the line extend up to 150 km. The position and movement of these mesoscale pressure falls, relative to the convection, suggests that they may result from warming produced by mesoscale sinking downwind of the existing convection.

The possibility that this sinking is on a scale larger than that of an individual cloud is of major significance. If mesoscale subsidence is responsible for producing the downwind pressure falls, it follows, then, that this sinking could contribute significantly to mesoscale organization and the downwind propogation of severe convection. In addition, this sinking would probably act to thermodynamically suppress convection several tens of kilometers ahead of the severe convection. This could occur through a reduction of available buoyant energy, or by a short-term generation, or enhancement, of a stable layer separating this subsiding air from the boundary layer airmass (See Figure 10). This boundary layer airmass must be lifting and cooling in response to the convergence of the low-level isallobaric wind. Thus, mesoscale circulations could contribute first to a capping, and then a sudden release of the convective instability. Release of the convective instability would occur as the stable layer lifts in response to decreasing subsidence in upper tropospheric levels (eventually lifting appears) and continued strong convergence and lifting in the lowest levels as the convective line approaches.

#### 4. CONCLUSIONS

It is hypothesized that downwind subsidence directly forced by deep convection in a sheared environment is a major factor in the formation and propogation of severe weather producing squall-lines and meso-lows. Major warming is believed to occur in the upper troposphere and lower stratosphere. The exact location and intensity of this return-type circulation appears to be a function of the intensity and density of existing convective cells, as well as such environmental parameters as wind direction and speed,

wind shears and thermal stratification. Intrusion of convective updrafts into the stable lower stratosphere appears to create imbalances that ultimately contribute to the downwind sinking.

It is further hypothesized that the occurrence of many tornadoes, especially the large, long-lived ones, are a result of complex interactions involving several scales of atmospheric motion. The general evolution of events leading to such tornado occurrences appears to be as follows. The synoptic scale acts to prime the atmosphere over a wide area by destabilizing the atmosphere and developing vertical wind shears. This is likely to occur ahead of synoptic scale baroclinic waves, where horizontal advective processes and vertical lifting patterns normally work in harmony toward these ends.

Shorter atmospheric waves, dry lines, frontal systems, and other features of the meso- $\alpha$  (200 $\alpha$ / $\alpha$ ) scale trigger the first individual storms of the meso- $\alpha$  scale (2.0 $\alpha$ / $\alpha$ ). These individual storms grow and subsequently extend to tropopause and jet stream levels, where they perturb and interact with environmental features.

Along the convective lines at certain intervals, individual storms concentrate to form large cumulonimbus systems. This focusing of convection and development of large cumulonimbus systems is not well understood, but the number of such systems that can be supported on a given day apparently depends on the strength and concentration of synoptic scale forcing.

In order to concentrate pressure falls to obtain an isallobaric fall center at the surface, the shape or laplacian of warming in the upper troposphere and lower stratosphere is important, and therefore mesoscale sinking must take on a particular configuration. This in turn requires a focusing of the sinking motion in a favored area ahead of the convective line, and the mechanism for producing this has not been determined. An answer to this question seems to lie in understanding how large cumulonimbus systems interact with synoptic and meso-Y scales of motion, as well as among themselves. Knowledge of how these large convective systems block, divert, and otherwise change the character of environmental air streams, especially in the upper troposphere and lower stratosphere, seems vital to the solution of this problem.

Whether, or at what point in time, a mesoscale low pressure system develops in response to a particular cumulonimbus system continues to be unknown. Assuming its genesis is a result of concentrated mesoscale sinking in the upper troposphere and lower stratosphere, it would seem to depend upon the juxtaposition of several individual storms into certain preferred orientations. The individual storms, in turn, probably must contain updrafts of a certain size, strength and height. Once meso-cyclogenesis has occurred, mesoscale advective processes can then contribute to its maintenance. The meso-low may continue for a few hours in a quasi-steady state, nurturing the severe convection that gave it birth, until interrupted by significant changes on the synoptic scale.

It is hoped that future experiments, such as SESAME, will obtain the important "out-of-cloud" measurements necessary to address and understand the vital scale interactions that lead to tornado genesis. Mesoscale models for forecasting the evolution of the severe storm environment in greater detail will also require this same data for realistic parameterizations of organized mid-latitude convection.

#### References

- Fritsch, J. M., 1975: Cumulus dynamics: Local compensating subsidence and its implications for cumulus parameterization.

  <u>Pure and Appl. Geophysics</u> (to be published).
- Fujita, T., 1959: Precipitation and cold air production in mesoscale thunderstorm systems. J. Meteor., 16, 454-466.
- Fujita, T. (1975): "Super outbreak tornadoes of April 3-4, 1974," University of Chicago Publication, (map with related statistics).
- Kuhn, P., 1975: Personal Communication
- Orlanski, I., 1975: A rational subdivision of scales for atmospheric processes.

  <u>Amer. Meteor. Soc.</u>, 56, 527-530.
- Schlesinger, R. E., 1973a: A numerical model of deep moist convection: Part I. Comparative experiments for variable ambient moisture and wind shear. J. Atmos. Sci., 30, 835-856.
- Schlesinger, R. E., 1973b: A numerical model of deep moist convection: Part II. A prototype experiment and variations upon it. J. Atmos. Sci., 30, 1374-1391.

**NOAA Technical Report** 

# Tornado Outbreak of April 3-4, 1974; Synoptic Analysis



LEE R. HOXIT
CHARLES F. CHAPPELL

BOULDER, COLORADO OCTOBER 1975

U.S. Department of Commerce Rogers C.B. Morton, Secretary

National Oceanic and Atmospheric Administration Robert M. White, Administrator

Environmental Research Laboratories Wilmot Hess, Director

#### TORNADO OUTBREAK OF APRIL 3-4, 1974; SYNOPTIC ANALYSIS

### Lee R. Hoxit and Charles F. Chappell

#### **ABSTRACT**

Synoptic scale analyses of the intense spring cyclone that produced the widespread tornado outbreak on April 3-4, 1974, are presented for the period from 1200 GMT April 2 to 1200 GMT April 4. The dynamics and kinematics creating the severe storm environment in the Ohio and Tennessee River Valleys on the afternoon and evening of April 3 are emphasized.

#### Introduction

The worst tornado outbreak of this century occurred on April 3-4, 1974. Figure 1\* shows the tracks of 148 tornadoes that occurred in the 24-hour period from noon CST April 3 to noon CST April 4. The combined path length of these storms was 2598 miles. Additional tornadoes occurred the night of April 2 and the afternoon of April 4. Numerous wind and hailstorms were also reported with this system.

The statistics (table 1) prepared by the National Oceanic and Atmospheric Administration (1974) demonstrate the storm's impact both in terms of human suffering and material damage.

During the afternoon and evening of April 1, a strong baroclinic wave at upper levels moved onto the northern California and

Oregon coasts, with the associated Pacific cold front advancing through Nevada and Idaho. This system eventually produced over the eastern U.S. the severe weather on April 3-4 whose evolution is discussed in this report:

#### Table 1

April 3-4, 1974, Disaster Survey Statistics

sorm related fatalities — 315

Storm related injuries — 6,142

Families suffering losses — 27,590

Damage Estimate — \$600,000,000

<sup>\*</sup>A larger version of this map in color is available from the University of Chicago Press for a handling fee of 30¢.

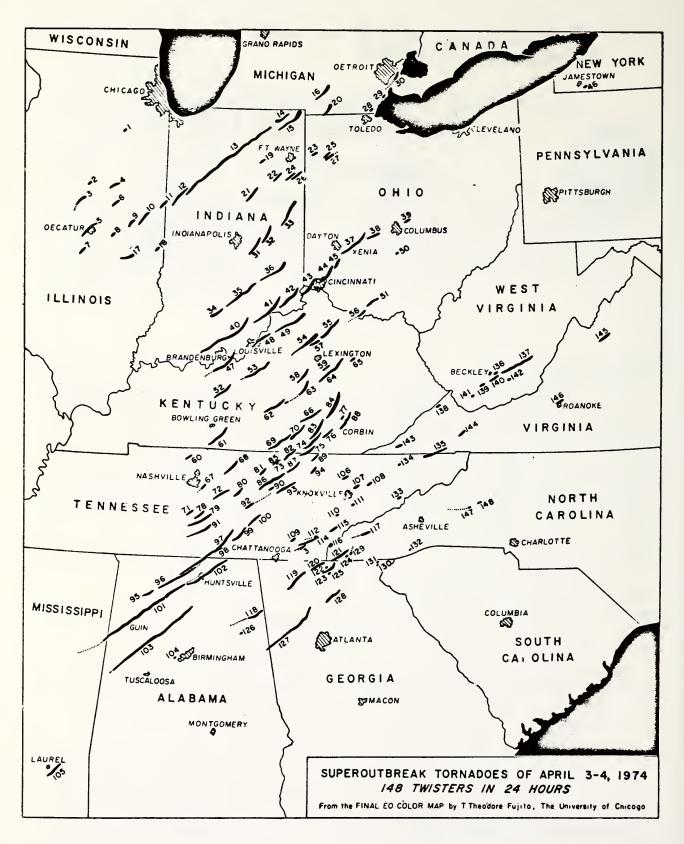


Figure 1 Tornado tracks for the period 1200 CST, April 3 to 1200 CST, April 4, 1974 [Fujita (1975)].

## NOAA Technical Report ERL 319-APCL 33

U.S. DEPARTMENT OF COMMERCE
NATIONAL OCEANIC AND ATMOSPHERIC ADMINISTRATION
Environmental Research Laboratories

# Zonal Profiles of Atmospheric Water Vapor

P. M. KUHN

BOULDER, COLO. MARCH 1975



#### ZONAL PROFILES OF ATMOSPHERIC WATER VAPOR

#### P. M. Kuhn

Water vapor burden and in situ mixing ratios at high altitude flight levels were inferred from observations in the rotational water vapor spectral band (19.0-35.0  $\mu$ m). Flight levels averaged approximately 14.0 km during twenty-two zonal traverses aboard the NASA Ames Research Center's Airborne Infrared Observatory. The method of radiance observations to infer water vapor burden and concentration, while radiometric, involved emission observations rather than absorption spectra analysis employed by McKinnon and Morewood [1970]. The east-west flights were made during the February through December, 1974, period. They provided profiles of lower stratospheric and upper tropospheric water vapor from 30° to 50° North latitude between 90° and 140° West longitude.

The objective of the research is to describe the method of recovery of the water vapor burden and in situ mixing ratio by inference from infrared emission observations and to present typical results.

#### 1.0 INTRODUCTION

Previous aircraft and balloon borne observations of lower stratospheric water vapor give an average concentration of 2.5 parts per million. Most of the measurements have been obtained from single locations. Mastenbrook [1971, 1974] has, perhaps, acquired the largest number of balloon observations. Brewer and Tomson [1972] have inferred water vapor infrared emission by observations made from a balloon platform. Recently Harries, et al. [1974] observed water vapor burden and in situ concentrations from high altitude aircraft over moderately restricted traverses. However, it was McKinnon and Morewood [op. cit.] who accomplished the first stratospheric water vapor burden observations along an extended traverse from infrared observations. Kuhn, et al. [1971] followed with long traverses around large thunderstorm systems. This work describes a similar set of observations but with a different infrared inference technique.

#### Antarctic infrared radiation budget

P. M. KUHN and L. P. STERNS
Atmospheric Physics and Chemistry Laboratory
National Oceanic and Atmospheric Administration
Boulder, Colorado 80302

The 1973 austral winter marked the 15th season of ballon-borne radiometersonde flights at Anundsen-Scott South Pole Station. From the inception of the program, the number of stations making measurements increased to five in 1963. These scattered stations enabled a longwave radiation budget for Antarctica to be established with South Pole Station as a central point. Then the number of stations was decreased to two: Byrd and South Pole. In the 1967 winter one balloon was launched per 24 hours at each of these two stations (187 flights per station). This intensive program, then, set a sound basis for future comparisons of the continent's infrared budget.

The radiometer used is the Suomi-Kuhn (1958) economical net radiometer. An important feature of the research has been the continued use of the same design and material fabrication of the radiometer-sonde since its 1959 introduction to antarctic research.

It has been observed that changes have occurred in the observations of radiative cooling,  $\Delta T/\Delta t$ (°C. day<sup>-1</sup>), a function of the one-dimensional divergence with height of the net radiant flux. Since 1963 this quantity has increased noticeably in the mean. But we should consider our noise equivalent observational response or minimum detectable change in the radiative contribution, for a single observation, to atmospheric cooling, which is calculated to be  $\pm 0.4$ °C. from the expression for atmospheric radiative cooling through the first law of the thermodynamics. The mean, winter antarctic (Pole Station) columnar cooling from 550 through 100 millibars increased by 0.25°C. per day from 1963 through 1972. Subsequent data has verified this. Since our standard error  $(\sigma N^{-1/2})$ , where  $\sigma$  is the root mean square error or ininimum detectable signal, ±0.4°C. day<sup>-1</sup> and N is the mean number of observations of the same atmospheric layer equal to approximately 10) is approximately ±0.126°C. day-1, the increase in cooling by 0.25°C. day is statistically significant.

Monitoring of the profiles of radiant flux and derived parameters over Antarctica shows that calculations of downward flux and observations indicates a decreasing divergence (observed ininus calculated) when the atmospheric transmission model

is employed with the same spectral resolution, 10.0 centimenter<sup>-1</sup>. In all cases aerosol contributions to the downward flux are omitted; but mean cloudiness for cirrus and altostratus clouds are included, employing a volume absorption coefficient of  $1.0 \times 10^{-5}$  centimeter<sup>-1</sup>. By adjusting the cloud volume absorption coefficient and assuming a droplet or particle distribution, we could conclude approximate figures on changing liquid water content through Mie theory computations. This will be attempted. A possible radiative feedback due to carbon dioxide increase is being investigated.

The inference from both observational conclusions is that cloud or moisture "contamination" has decreased from 1963 through 1973 over Antarctica. Observations and related calculations are planned to continue through at least 1976 to validate this apparent change in the antarctic atmosphere through changes in its infrared transmission.

#### Reference

Suomi, V. E., and P. M. Kuhn. 1958. An economical net radiometer. Tellus, 10: 160-163.

# antaccic Journal of the Journal States

National Science Foundation

September/October 1975

Vol. X-No. 5

# Changes in the antarctic thermal radiation budget

P. M. Kuhn and L. P. STEARNS
Environmental Research Laboratories
National Oceanic and Atmospheric Administration
Boulder, Colorado 80302

Vertical profiles of the thermal infrared radiation budget over Antarctica have been made during 16 austral winters. These profiles include upwardand downward-directed radiant fluxes, which yield data on net irradiance and layer cooling. An economical net radiometer (Suomi-Kuhn, 1958) is carried aloft piggyback on a standard radiosonde until the balloon bursts. The homogeneous terrain surrounding antarctic stations and the continued use of the same design and material fabrication since the program's inception have enabled exceptionally meaningful profile comparisons.

Radiative cooling, which is a function of the onedimensional divergence of the net radiant flux with height, has changed through the years. At Amundsen-Scott South Pole Station the columnar cooling from 575 through 125 millibars during the deepest

cold period (June through August) increased from 1963 through 1967 by 0.31°C per day. After 1967 the cooling change is small. This is based on a total of 430 ascents in 10 years; with a minimum of 19 and a maximum of 88 flights per year.

Similarly, Byrd Station showed a steady increase in cooling from 1963 through 1968, with no leveling off in 1967. The Byrd observations were discontinued after 1968. The increase noted here was 0.41°C per day. This average was based on a total of 298 flights, in 6 years. The standard error for this number of flights and values was computed to be 0.095°C per day for South Pole Station and 0.11°C per day for Byrd Station. Such statistics indicate that the increases shown were all significant.

Further, calculations were made with a radiative transfer equation to determine the influence of altostratus and cirrus clouds on the observed radiant flux. A value of  $1.0 \times 10^{-5}$  per centimeter was used for the bulk absorption coefficient. The tentative conclusion is that cloud (most likely moisture) contamination decreased over this period. The possibility of radiative feedback due to a carbon dioxide increase is nonetheless being investigated.

sen-Scott South Pole Station the columnar cooling of the studies are being made to determine the from 575 through 125 millibars during the deepest thermal energy balance at the ice-air interface, using a total net radiometer and a dew point scale.

Observations will continue through 1976.

Field support for this research is provided by National Science Foundation grant OPP 74-19485.

#### References

Suomi, V. E., and P. M. Kuhn. 1958. An economical net radiometer. Tellus, 10: 160-163.

September/October 1975

227

### P. M. Kuhn and L. P. Stearns

Atmospheric Physics and Chemistry Laboratory National Oceanic and Atmospheric Administration Boulder, Colorado 80302

### 1. INTRODUCTION

The SKYLAB field phase in June, August and September of 1973 in the Houston area, White Sands and Phoenix areas provided a unique opportunity to conduct infrared observations and subsequent calculations of the transmission and absorption properties of haze and middle altitude clouds. This was accomplished using both an 8.0 to 13.0µm downward looking chopper radiometer and an upward-downward looking radiometer (4.39 to 40µm) attached to a standard radiosonde.

One aspect of this research was to experimentally observe and analyze a volume absorption coefficient together with related optical properties of dust and middle tropospheric clouds to permit a simple solution for bulk radiation transfer phenomena. Since a detailed, moderately high resolution (1.0 cm-1 resolution) radiative transfer approximation program, RADIANCE (1970) has been in use by the authors for several years, and since it is being continuously updated, it is only necessary to add these additional absorbers to the existing solution once their radiative character is determined. It is believed that this in situ method of determining the haze and cloud optical properties is different from other methods and therefore can provide interesting comparisons.

For the radiometric transfer calculations, the simultaneous radiometersondes provided profiles of the free air temperature and humidity profiles. In each site the measurements were made over nearly homogeneous surfaces in order to provide a nearly uniform interface.

The upwind and downwind locations chosen from some large source such as Phoenix enabled a determination of the IR transmission of both dust and altostratus clouds. In each case, the bases and tops were distinct.

### SOME IR RADIATIVE PROPERTIES OF HAZE AND CLOUDS

Platt (1973, 1974) as well as Kuhn, Weickmann and Stearns (1974) and Kuhn (1970) have investigated and reported their results concerning some of the optical properties of cirrus, contrails and middle altitude clouds. Preceding much of this work were the efforts of Hall (1968) in determining a physical model of radiative transfer in cirrus. The general agreement, at least insofar as the volume absorption coefficient is concerned, is very good. The investigation of middle altitude cloud radiative properties was prompted

by a desire to compare these results with previously reported results of Platt (op. cit.) on middle latitude clouds.

The emissivity of a haze layer or a cloud layer on the basis of continuity is defined as

$$\varepsilon = 1. -\tau -\rho,$$
 (1)

where  $\tau$  is the transmission and  $\rho$  the IR reflectivity. From (1) we may write, ignoring  $\rho$ ,

$$\ln \tau = \ln (1-\epsilon) = (-K\Delta Z), \qquad (2)$$

where K  $(km^{-1})$  is the volume absorption coefficient and  $\Delta Z(km)$  is the cloud thickness or depth.

To facilitate comparisons, Table 1 lists the haze and/or cloud physical properties with the symbols employed by the authors on the left and those of Platt (1974) on the right.

TABLE 1. Physical Properties of Atmospheric Absorbers

This wo	Platt		
Optical Thickness :	$\Delta u = \int_{z=0}^{z} K\Delta z$	$\tau_{A} = \int_{h=0}^{h} dh$	
Vol. Absorp. Coef.:	K(km <sup>-1</sup> )	$\sigma$ $(km^{-1})$	
Cloud Thickness :	ΔZ(km)	h (km)	
Thickness vs. $\epsilon$ :	$K\triangle Z = \ln(1-\varepsilon)$	$\tau_{A} = \ln(1-\epsilon)$	

### 3. METHODS OF ANALYSES

Consider a haze or cloud layer of thickness,  $\Delta Z_{\star}$  and optical thickness, KdZ, as in Figure 1.

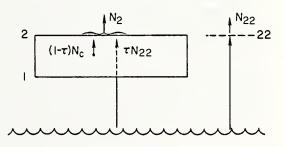


Figure 1. Symbolic atmospheric haze layers with arrows depicting upwelling IR radiance.

The radiance transmission (1- ) is given by

$$\tau = \frac{N_2 + N_c + -\rho(N_2 + N_c)}{N_{22} + N_c +}$$
(3)

and the radiance emissivity is given by

$$\varepsilon = \frac{N_2 + N_2 + \rho (N_2 + N_c)}{N_c + N_2 + N_c}$$
(4)

The errors in the determination of the absorption coefficient are based on a radiometer noise equivalent radiance of  $2.35 \times 10^{-6} \text{ w cm}^{-2} \text{ sr}^{-1}$ . This results in an average error of  $\pm .05$  in the transmission or emissivity,  $\tau$  and  $\epsilon$ , respectively. The error in the volume absorption coefficient from (2) is given by

$$dK = \frac{1}{\Lambda Z} \frac{d\tau}{\tau} \tag{5}$$

From Eq. (5) and from an average error or  $\pm 0.05$  in transmission, the average error in the volume absorption coefficient, K, is  $\pm .009$  km<sup>-1</sup>. The flux or irradiance emissivity is required in place of the zenity emissivity for radiative flux transfer and IR cooling calculations. Elsaesser (1940) shows that the flux emissivity,  $\epsilon_f$ , is approximately equal to the zenith emissivity,  $\epsilon$  (our observations), of unidirectional radiance from a column of optical depth, K $\Delta Z$ , 1.66 (K $\Delta Z$ ).

In these equations N† is the upwelling radiance (w cm $^{-2}$  sr $^{-1}$ ),  $\rho$  the layer IR reflectivity and the subscript, "c", is the black body radiance at the mean temperature of the layer. Subscripts 1, 22 and 2 refer to layer levels (Fig. 1). "22" is the same level as "2" but is the upward radiance in a dust-free or cloudless atmosphere. For shallow layers N1† may be used in place of N22† in Eq. (3) with only a small error. However, in deeper layers (>1.5 km) N22† must be employed. This necessitated a profile in a haze or dust-free area or outside of the cloud.

### 4. RESULTS

### a. Haze

Average values of the haze transmission calculated from observations entered in Eq. (3), the volume absorption coefficient, K, and the optical depth,  $K\Delta Z$ , are summarized in Fig. 2.

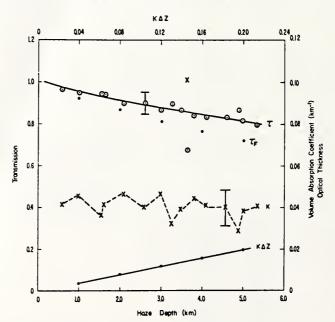


Figure 2. Haze transmission, volume absorption coefficient relative to haze depth and optical depth using White Sands, New Mexico, 11, 12 August 1973.

These observations through Eq. (2) provide the curve of K. The optical thickness, KdZ, is calculated and appears at integer values of the geometric depth of the dust. The mean value of K is .042  $\pm$ .009  $\rm km^{-1}$ . However, the rms deviation is only .0035  $\rm km^{-1}$ .

The smooth nature of the transmission and more important of the absorption coefficient suggests a uniform distribution of the atmospheric dust load. Error limits of observation and calculations are given by the vertical arrows. The narrow range of variations in these optical properties is in contrast to the much wider range of variation in clouds. Haze IR properties are an order of magnitude less, numerically, than those of middle clouds. The assumption is further made that the dust particles are uniformly less than a micron in diameter. Their effect on bulk radiative transfer and cooling is discussed subsequently.

### b. Middle Clouds

Table 2 lists the observed and derived optical properties of tropical middle altitude clouds and may be compared with the prior research of Platt (1974). In fact the cloud observations and calculations were made as a result of Platt's excellent work with his lidar.

TABLE 2. Observed and Derived Cloud Optical Properties

Cloud Type	Depth (km)	Mean Height (km)	Mean Temp (°C)	τ*	€ <sub>N</sub>	K
As-Ac	1.5	21.0	-11.8	.42	.58	.58
As	.6	20.5	-11.0	. 3	.37	.77
Аs	2.0	21.0	-11.8	.25	.75	.69
As-Ac	2.0	20.0	-10.0	.23	.77	.73
As	0.4	18.7	- 7.0	.04	.96	8.06
As	0.3	16.7	- 4.5	.07	.93	8.86

Calculated f  $\sim$  F<sub>1</sub>. (3) as an average of ten observations of N<sub>2</sub> N<sub>22</sub> $\uparrow$  and N<sub>2</sub>.

 $K(km^{-1})$  is determined from observations by Eq.(2).

The last two values of As are of shallow depths, large values of K and high emissivity apparently are strong absorbers and would appear to be composed of a large number of supercooled water droplets. It is also evident that a mixture of ice crystals and water as well as various particle densities causes the range in the values of K. However, there is tendency to relate moderately deep, ice crystal clouds with K values <1.0 km<sup>-1</sup> and shallow dense altostratus, water droplet clouds with K values >7.0 km<sup>-1</sup>. They are apparently composed mainly of ice particles with some supercooled water droplets evidenced by their lower values of K (K < 1.00 km) as suggested by Platt (op. cit.).

### 5. CALCULATED COOLING RATES

### a. Atmospheric Haze

The NOAA RADIANCE program discussed in Section

1 has provisions for computations involving various aerosol layers such as cloud or haze providing the volume absorption coefficient is known.

To calculate cooling rates through a haze layer, a temperature, pressure, humidity profile over White Sands, New Mexico, for 11 August 1973 was input to the RADIANCE solution. Fig. 3 is a plot of the results, providing calculated IR cooling rates at the midpoints of each layer in the haze and a corresponding haze-free and cloudless cooling rate profile.

The computations of infrared cooling show the cooling to average only .009C  $hr^{-1}$  throughout the haze layer employing an absorption coefficient of .042  $km^{-1}$  as determined from observations. This cooling may be easily balanced by solar warming in the layer. This cooling rate would hardly alter the dynamics of the haze layer.

### b. Middle Clouds

-Padicmetersorde profiles through middle altitude aftostratus and altocumulus clouds furnished the RADIANCE calculation input to determine cooling rates through these clouds. Absorption coefficients from Table 2 were employed in two examples with calculated cooling rate curves appearing in Fig. 4, both the flight of 8 August 1973 over Rosenburg, Texas. The curves are labeled, cloudless, K = .77 and K = .8. Cloud bases and tops are indicated for the two calculations.

Moderately deep clouds with K < 1.00 exhibit calculated cooling rates of up to 0.23C hr<sup>-1</sup>, not enough to alter the cloud stability. In contrast shallow dense clouds of water droplets with K≈8.0 display calculated cooling rates of approximately 0.15C hr<sup>-1</sup>. Such a cooling rate could have an effect on cloud stability

### 6. CONCLUSION

It would appear important now to combine IR cooling rates for atmospheric absorbers with solar heating to complete the radiation budget analyses for both cloudless and cloudy and hazy atmospheres. Also the bulk radiative transfer approach employing a volume absorption coefficient determined in the atmosphere for non-gaseous absorbers and combined with a mass absorption coefficient (cm2g-1) for the gaseous absorbers provides a simple and rapid computer solution. Admittedly in cloud or in haze scatter of radiant emission was assumed negligible but the nature of the observations would appear to validate the use of the experimentally determined absorption coefficient in the presence of haze or cloud. A classification of absorption coefficient in relation to various cloud types and depths as well as to various haze or dust layers could now be attempted from the large amount of data available. Further, sufficient simultaneous haze and cloud composition and IR observations exist to attempt this classification as input to radiative transfer calculations for future improved input to numerical weather models.

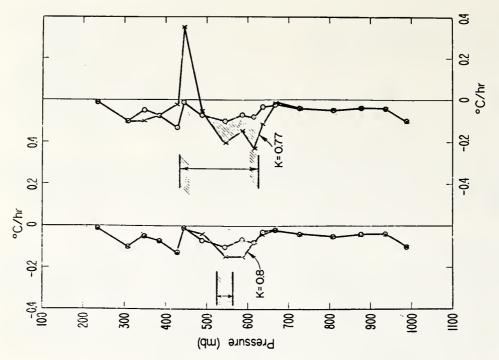
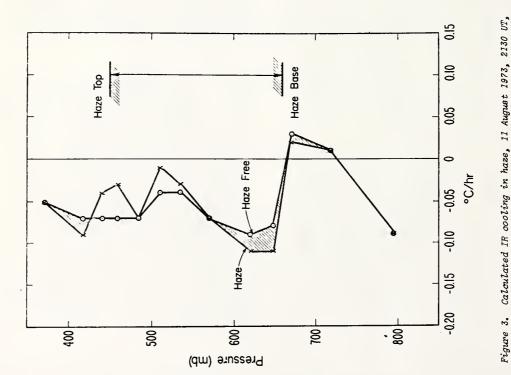


Figure 4. Calculated IR cooling through thin and deep middle clouds, 8 August 1973, 1937 UT over Rosenburg, Texas, oil fields.



Calculated IR cooling in haze, 11 August 1973, 2130 UT. White Sands, over sand Ames, New Mexico.

### REFERENCES

- Davis, P. A., 1971: Applications of an airborne ruby lidar during a BOMEX program of cirrus observations. J. Appl. Meteor., 10, 1314-23.
- Hall, F. F., Jr., 1968: A physical model of cirrus 8 $\mu$ m to 13 $\mu$ m sky radiance, Appl. Opt. 7, 2264-2269.
- Kuhn, P. M., 1970: Airborne observations of contrail effects on the thermal radiation budget. J. Atmos. Sci., 27, 337-342.
- Kuhn, P. M., H. K. Weickmann and L. P. Stearns, 1974: Transfer of infrared radiation through clouds. Appl. Opt., <u>13</u>, 512-517.
- Platt, C. M. R., 1973: Lidar and radiometric observations of cirrus clouds. J. Atmos. Sci., 30, 1191-1204.
- \_\_\_\_\_, 1974: Structure and optical properties of some middle-level clouds. J. Atmos. Sci., 31, 1079-1088.

### LATITUDINAL PROFILES OF STRATOSPHERIC WATER VAPOR

P. M. Kuhn and L. P. Stearns

Atmospheric Physics and Chemistry Laboratory National Oceanic and Atmospheric Administration Boulder, Colorado 80302

M. S. Lojko

Computer Services
National Oceanic and Atmospheric Administration
Boulder, Colorado 80302

Abstract. Water vapor burden and in situ mixing ratios above and at high altitude flight levels were inferred from observations in the rotational water vapor spectral band (19.0-35.0  $\mu m$ ). Flight levels ranged from 15.3 to 20.0 km during 12 meridional traverses of a W-B57-F jet. The method of radiance observation, while radiometric, involved emission observations rather than absorption spectra analyses employed by McKinnon and Morewood [1971]. The flights made during September, October, November 1973 and January 1974 provide profiles of lower stratospheric water vapor by overlapping tracks from 50°S latitude to 75°N latitude.

The objective of the research is to describe the method of recovery of the water vapor burden and in situ mixing ratio by inference from infrared emission observations and to present the results as a latitudinal profile.

### Introduction

Previous aircraft and balloon-borne observations of lower stratospheric water vapor give an average concentration of 2.5 parts per million. Most of the measurements have been obtained from single locations. Mastenbrook [1971, 1974] has, perhaps, acquired the largest number of balloon observations. Brewer and Thomson [1972] have also inferred water vapor via infrared emissions from observations aboard a balloon platform. Recently Harries et al. [1974] observed water vapor burden and in situ concentrations from high altitude aircraft over moderately restricted traverses. However, it was McKinnon and Morewood [op. cit.] who accomplished the first stratospheric water vapor burden observations along an extended north-south traverse over North and South America from infrared absorption observations. This work describes a similar set of observations but with a different infrared inference technique.

### Instrumentation

The radiometer employed in these observations (Fig. 1) is a blackened chopper system with a speed of response of 20 ms. The electronic signal is AC from a temperature controlled, deuterated triglycine sulfate pyroelectric detector, referenced to the black chopper. The tempera-

Copyright 1975 by the American Geophysical Union

ture of the chopper blade is monitored by a thermistor bead embedded in the chopper. Connections to the thermistor are made through redundant sliprings.

The radiometer forward lens is silicon. The aft interference filter is an optical flat of coated silicon with a cut-on frequency of 512 cm and a peak transmission of 0.58 decreasing to 0.0 at 266 cm<sup>-1</sup>. The noise equivalent radiance (N.E. $\Delta$ N.) of the radiometer system was measured to 2.1 x 10<sup>-7</sup> w cm<sup>-2</sup> sr<sup>-1</sup> at the detector. Electronic output is -10.0 to +10.0 VDC.

To ascertain the minimum water vapor burden at a flight level of 19.0 km (60 mb) a reference to Table 1 calculations is necessary. These data represent a calculation of downward radiance for the spectral interval of the radiometer employed. Recalling the instrument N.E. $\Delta$ N. of 2.1 x  $10^{-7}$ 

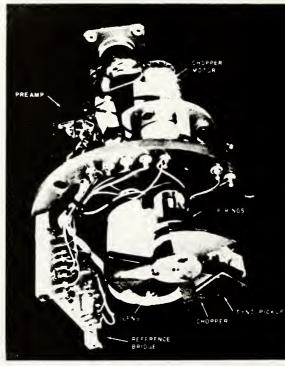


Fig. 1. Water vapor radiometer optical head.

Table 1 Calculated Radiation and Water Vapor Profiles

	Calculated Radiation and Water Vapor Profiles									
STATION.	OAK	U.	ATE + 31-12	2-74					CALCULATED.	01/03/75
	GTH HEGIUN VE NUMBERS		19.23 270.00		MICHONS WITH F	FILTER = 14	<b>+-33</b> 0	DOWNWARD RAI	DIANT POWER FOR 3	0 LAYERS
4E55URE	TEMP.		MIX RATIO	DELU	IRHAUIANCE W/SU CM	ANGLE	RADIANCE W/SQ CM SR	CO 2 GM/SQ CM	H2O GM/SG CM	
0.1	-274.0		-0.0000	0.000+000	0.000000+000	0.00	1.2409-151	0.0000	0.000+000	
0.6	1.0		U•0024	6.122-007	1.349998-008	0.00	1.2311-007	0.1240	6.122-007	
17.0	-50.3		0.0024	4.016-005	2.408028-007	0.00	2.1959-006	4.1912	4.078-005	
۵۰۰0	-47.7		0.0024	7.347-006	2.161551-007	0.00	1.9711-006	4.9352	4.812-005	
23.0	-54.9		0.0024	7.347-006	2.21/953-007	0.00	2.0226-006	5.6792	5.547-005	
30.0	-51./		0.0024	1.714-005	2.417073-007	0.00	2.2042-006	7.4152	7.261-005	
34.0	-5>.5		0.0024	y.796-006	2.529962-007	0.00	2.3071-006	8.4072	8.241-005	
50.1	-5/.9		0.0024	3.918-005	2.907017-007	0.00	2.7239-006	12.3752	1.216-004	
70.0	-50.7		0.0024	4.878-005	3.591708-007	0.00	3.2753-006	17.3352	1.706-004	
77.0	-50.5		0.0024	1.714-005	J.832866-007	0.00	3.4952-006	19.0712	1.877-004	
. 94.0	-64.9		0.0024	4.163-005	4.355262-007	0.00	3.9716-006	23.2872	2.293-004	
100.0	-50.5		0.0024	1.467-005	4.523515-00/	0.00	4.1250-006	24.7752	2.440-004	
112.0	-50.7		0.0036	3.673-005	5.054570-007	0.00	4.6093-006	27.7512	2.808-004	
				1.237-004	6.878026-007	0.00	6.2721-006	33.7032	4.044-004	
136.0	-47.5		0.0005			0.00	7.5275-006	37.1752	5.080-004	
150.0	-53.3		0.0080	1.036-004	8.254621-007	0.00	7.6435-006	37.6712	5.245-004	
135.0	34.3		0.0005							

and comparing the water vapor burden and radiance at 50.0 and 70.0 mb reveal a radiance differential of 5.5 x  $10^{-7}$  w cm<sup>-2</sup> sr<sup>-1</sup> corresponding to a water vapor burden differential of 0.49 x  $10^{-4}$  g cm<sup>-2</sup>. This demonstrates a minimum detectable water vapor burden differential of approximately  $\pm$  0.2 x  $10^{-4}$  g cm<sup>-2</sup>. If we arbitrarily double this "error" response, arriving at  $\pm$  0.4 x  $10^{-4}$  g cm<sup>-2</sup>, it is evident that our percentage error for observations at 60 mb is 20% (0.4/2.0).

### Applied Theory: Water Vapor Burden

The following five equations with appropriate directions are the technique by which we proceed from observed radiance, to calculated radiance, to inferred water vapor burden. Before following the plan of the inference we should state three basic assumptions:

- A temperature profile above the aircraft but based on an observed flight level temperature is assumed from the nearest sounding station.
- The latest water vapor transmission functions [Wark et al., 1974] are employed as valid for the atmosphere.
- The water vapor mixing ratio lapse with height above observational level follows a power law [Smith, 1966].

$$(N_c + N_o +)_{\Delta v} \le N.E.\Delta N.(2.1 \times 10^{-7} \text{ w cm}^{-2} \text{ sr}^{-1}),(1)$$

where  $\Delta v$  is the radiometer response frequency interval, 266 - 512 cm<sup>-1</sup>.

Calculated or observed downward radiance may be expressed as

$$N \downarrow = \int_{V} \int_{p} \Phi(v) B(v, T(p) \dots) \frac{\partial \tau(u(p), v)}{\partial p}$$

$$dp dv (w cm^{-2} sr^{-1}) \qquad (2)$$

where p is pressure (mb),

- is radiometer system transmission,
- B is the Planck function,
- $\tau$  is the transmission function of water vapor (266-512 cm<sup>-1</sup>)
- u is the optical mass of water vapor (g cm<sup>-2</sup>), and,
- T is the absolute temperature (°K),
- v is the frequency (cm<sup>-1</sup>).

Defining the temperature profile above flight level it is possible to vary the downward radiance, N+ by varying u(p), since,

$$\tau = \tau(u,k) . \tag{3}$$

Here k is the water absorption coefficient  $(\mbox{cm}^2\mbox{ g}^{-1})\,.$ 

The optical mass, u, is varied by changes in the flight level mixing ratio,  $q_0$  in the mathematical approximation for u (g cm<sup>-2</sup>),

$$u = \frac{1}{g} \int_{p} \overline{q} dp \simeq \frac{1}{g p_{o}^{\lambda}} \sum_{i} q_{o} p_{i}^{\lambda} \Delta p(g cm^{-2}) \qquad (4)$$

Where g is the acceleration of gravity (cm  $sec^{-2}$ ), q is the water vapor mass mixing ratio (g  $g^{-1}$ )

"o" subscript refers to flight or reference level, and

 $\lambda$  is a power law exponent [Smith, op. cit.]. The choice of a non-zero value for  $\lambda$  eliminates the assumption of a uniform mixing ratio with height. To satisfy eq. (1) by use of eq. (2) and (4), a value of  $\lambda = 0.33$  in eq. (4) was empirically determined from previous in-situ observational values of water vapor burden at 180 mb [Kuhn, 1975] at 212 mb [Kuhn et al., 1971] and current observations of the burden as illustrated in Figure 2. If one assumes a uniform mixing ratio above flight level,  $\lambda = 0.0$ , then the analyses of Figure 3 employing a value of 0.33 for  $\lambda$  result in mixing ratios approximately 33% less than those of the figure. This is not a drastic departure from an assumption of a constant mixing ratio with height and yet does reflect a  $\lambda$  determined from actual observations. Thus eq. (4) reduces to

$$u = q_0 C (5)$$

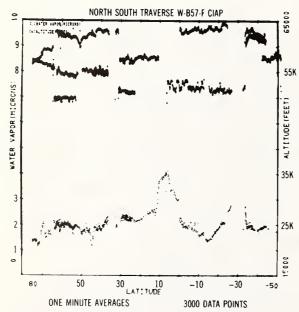


Fig. 2. Averages of water vapor burden (ordinate is g cm<sup>-2</sup> x 10<sup>4</sup>). Water vapor data cover lower portion of figure while altitude data comprise the broken line segments of the upper portion of the figure.

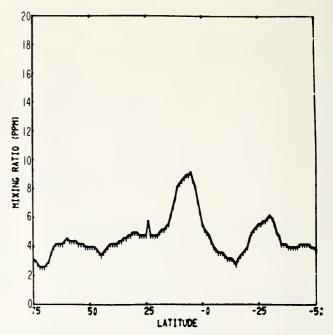


Fig. 3. Average water vapor mixing ratio (parts per million by mass) from same data as Figure 2.

where  $\lambda$ ,  $\Delta p$  and  $p_0$  are fixed. In effect,  $\Delta p$  is fixed as one assigns 10 mb intervals to  $\Delta p$  upward to 0.1 mb from the pressure, p, at flight level. It is therefore necessary to change only  $q_0$  as part of an iterative convergence routine for  $N_c +$  and  $N_0 +$ . The technique used is a modified Newton-Raphson routine (to alter u from the i-th to i+1-th iteration). It is described by Traub [1967].

In essence, then, one defines a temperature profile above radiometer flight level, makes an educated guess of  $q_0$  at flight level, p, and proceeds to minimize the difference between  $N_C^+$  and  $N_O^+$  via the iterative calculation to which we alluded.

Applied Theory: Water Vapor Concentration

The water vapor concentration is an automatic output from the solution of eq. (5). It appears as a solution of this equation along with the total water vapor and as stated does not imply a constant mixing ratio above the aircraft.

### Discusssion of the Observations

In 1972 and 1973 a series of CIAP (Climatic Impact Assessment Program, Department of Transportation) high altitude missions to observe the water vapor burden in the stratosphere at approximately 60 mb were flown between 75°N latitude and 50°S latitude. These 12 meridional flights between 70°W longitude and 150°W longitude with a W-B57-F aircraft were accomplished at altitudes ranging from 15.2 to 19.7 km. They were completed during September, October, and November, 1973 and January 1974 and provided latitudinally overlapping segments for the north to south track.

Observations were made at a 1-Hz rate. Figure 2 is a computer plot of 1-minute observation averages of water vapor burden (g cm $^{-2}$  x  $10^{-4}$ ), which are averaged as a five-data-point moving mean and assigned to the mean latitude for the set. Statistics for each small set of five data points are meaningless. However, in the section on instrumentation, the error in the water vapor inference of from  $\pm$  0.2 to  $\pm$  0.4 x  $10^{-4}$  g cm $^{-2}$  was calculated.

Notable in the figure is the doubling of the vapor burden over the intertropical convergence zone spanning some 15° of latitude. The observations also show a slight negative gradient in the burden from 29°N to 75°N, apparently due to the autumn to winter seasonal observation period. This probably does not indicate an annual maximum. The indicated peaking from 26° to 33° latitude is presumably due to thunderstorms over the flight track over South America. There is just a hint of a negative gradient southward from 35° south since these observations at the southern end of the austral late spring and summer may represent a seasonal maximum.

Figure 3, illustrating the average mixing ratio (g g<sup>-1</sup>) of water vapor obtained by solving for q<sub>0</sub> in (5), was plotted only for each degree of latitude. Weickmann and Van Valin [1974] compare these observations here discussed with those of McKinnon and Morewood [op. cit.], concluding that they are not contradictory but rather represent "approximate limits of an annual cycle." Certainly the difference in the observational techniques (infrared emission in this report and infrared absorption in the case of McKinnon and Morewood [op. cit.]) speaks well for the modest agreement.

### References

Brewer, A.W., and K.P.B. Thomson, A radiometersonde for observing stratospheric emission due

- to water vapour in its rotational band, Quart. J. Royal Met. Soc., 98, 187-192, 1972.
- Harries, J.E., D.G. Moss, and N.R. Swann, H<sub>2</sub>O, O<sub>3</sub>, N<sub>2</sub>O and HNO<sub>3</sub> in the Arctic stratosphere, Nature, 250, 475-476, 1974.
- Kuhn, P.M., Zonal profiles of atmospheric water vapor, NOAA Tech. Report, ERL 319-APCL 33, U.S. Dept. of Commerce, Boulder, Colo., 11 pp, 1975.
- Kuhn P.M., M.S. Lojko, and E.V. Petersen, Water Vapor: Stratospheric injection by thunderstorms. Science. 174, 1319-1321, 1971.
- storms, Science, 174, 1319-1321, 1971.

  Mastenbrook, H.J., The variability of water vapor in the stratosphere, J. Atmos. Sci., 28, 1495-1501, 1971.
- Mastenbrook, H.J., Water-vapor measurements in the lower stratosphere, Canadian J. Chem., 52, 1527-1531, 1974.
- McKinnon, D., and H.W. Morewood, Water vapor distribution in the lower stratosphere over North and South America, <u>J. Atmos. Sci.</u>, <u>27</u>, 483-493, 1970.
- Traub, J.F., The solution of transcendental equations, Mathematical Methods for Digital Computers, vol. 2, p. 171, edited by A. Ralston and H.S. Wilf, John Wiley & Sons, New York, 1967.
- Smith W.L., Note on the relationship between total precipitable water and surface dewpoint, <u>J. Appl. Met.</u>, <u>5</u>, 726-727, 1966.
- Wark, D.Q., J.H. Lienesch, and M.P. Weinreb, Satellite observations of atmospheric water vapor, Appl. Optics, 13, 507-511, 1974.
- Weickmann, H.K., and C.C. Van Valin, The sources and sinks of water vapor in the stratosphere, Tech. Rept. ERL 307-APCL 32, 34 pp. 1974.

(Received March 17, 1975; accepted April 9, 1975)

## NOAA Technical Report ERL 331-APCL 34

U.S. DEPARTMENT OF COMMERCE
NATIONAL OCEANIC AND ATMOSPHERIC ADMINISTRATION
Environmental Research Laboratories

# Airborne Infrared Imagery of Arctic Sea Ice Thickness

P. M. KUHN

L. P. STEARNS

R. O. RAMSEIER

BOULDER, COLO. MAY 1975



P. M. Kuhn, L. P. Stearns, and R. O. Ramseier<sup>1</sup>

The paper presents an empirically observed correlation between ice thickness and infrared brightness ice temperature, based on heat transfer and heat flux at the sea-ice and sea-air interfaces. During the February-March 1973 NASA-USSR Bering Sea Ice Experiment (BESEX), simultaneous surface coring data were combined with infrared imagery in the 840-1237 cm<sup>-1</sup> spectral band, acquired from the NASA Convair 990 Jet Laboratory. From the combined data, we inferred ice thicknesses from ±5 cm for thin ice to ±17 cm for thick ice. Coldest sea ice temperatures during BESEX, approximately -22 to -24C, occurred at the tops of the pressure ridges, exhibiting a singular vein-like structure clearly discernible in the highly detailed color enhanced imagery. Freshly refrozen leads and polynyas exhibited the highest brightness temperatures, averaging -3.0 and -0.5C respectively.

### 1. INTRODUCTION

Research results from the BESEX expedition over the Arctic Ocean and Bering Sea in February and March 1973 indicated that infrared (IR) thermal emission from sea ice varies significantly with ice thickness. The ice thickness is inversely proportional to the radiant emission and convective heat transfer at the surface, and directly proportional to the difference between ice surface temperature and the sea temperature at the base of the ice layer.

An areal presentation of sea ice thickness, as determined by high speed airborne IR imagery, can be applied in several important ways. For example, with such a presentation ice thickness can be estimated as a function of time. Questions on rates of freeze and thaw associated

<sup>&</sup>lt;sup>1</sup>Department of the Environment, Ottawa, Ontario, Canada.

with ice thickness can be resolved for shipping and sub-surface marine activities. Insight can be acquired into the thermodynamics of the rates of ice formation and dissipation, a key consideration in the theoretical basis of this study. Our research uses the areal presentations to develop a usable relationship between IR remotely sensed ice thermal emission and sea ice thickness.

Sea ice brightness temperatures converted to physical ice temperatures were related to simultaneous surface corings of ice thickness. The IR imagery was false color enhanced by amplitude-slicing techniques to highlight the ice thickness pattern. The physical temperature of ice is obtained by "calibrating" the atmosphere during ascent and descent.

NASA's Convair 990 Jet Laboratory supporting the research efforts carried an IR line scanning mapper during the 1972 and 1973 experiments. Flight operations over the ice were conducted at elevations ranging from 300 m to 11.5 km. Due to frequent (50% of the time) interspersion of cirriform clouds between flight level and the surface, the 11.5 km altitude did not yield as good IR imagery as did the 3.3 km and 300 m altitudes. However, uniform cirrus coverage allowed good imagery ice thickness inferences from 10 km. The 3.3 km altitude with its wide scan track, 6.6 km, furnished excellent false color enhanced imagery with a spatial, elemental resolution of approximately 2.0 m. The adjustment of the brightness temperature of the ice to obtain the physical temperature is approximately +1.5C at 3.3 km and +4.0C at 11.5 km in the 840-1237 cm<sup>-1</sup> window channel employed.

### **Transfer of Infrared Radiation Through Clouds**

P. M. Kuhn, H. K. Weickmann, M. J. Lojko, and L. P. Stearns

Calculations of radiative through and resulting ir cooling of cloud forms is certainly more difficult than observations. Based on observations, a radiative transfer model has been developed for absorption in clouds employing an observationally determined volume absorption coefficient, ranging from 0.0005 to 0.0007 cm<sup>-1</sup>. This model does not require any assumption of cloud blackness or thickness and permits clouds to remain partially transparent or opaque as their thickness and absorption dictate. Agreement within a standard deviation of 12.0 W m<sup>-2</sup> between observation and calculation has been maintained in approximately twenty profiles through clouds. The standard deviation was determined from some 140 observations.

### I. Introduction

The transfer of total radiant thermal (infrared) power in and through cloud forms is more easily observed than calculated. This is so, since infrared (ir) wide band heat budget radiometers can readily be calibrated to include responses to all methods of radiative transfer through clouds, while calculations of such transfers are enormously complex (Refs. 1 and 2, among several authors on the subject). A critical consideration is that of cloud blackness.

One approach to a bulk property solution of ir transfer through clouds and the resulting atmospheric cooling or warming due to such transfer is to observe the atmospheric transmission first and then follow with calculations adjusted to observations by inferring the atmospheric attenuation coefficient. This assumes an accurate wide band (NE $\Delta$ N = 1 × 10<sup>-7</sup> W cm<sup>-2</sup> sr<sup>-1</sup>) radiometer and a suitable transfer model. Our purpose is always to provide a transfer model for ir radiation through cloud that is sufficiently accurate and yet is conservative as to computer time requirements. Relative to accuracy, we wish to be able to compute ir cooling rates to ± 0.15°C day<sup>-1</sup>. The purpose of this reported research is to provide a simple computer model for ir transfer through clouds based on real atmospheric cloud observations from aircraft radiometers through parameterizing.

### II. Instrument

The radiometer is a wide band pyroelectric detector bolometer sensing in the spectral region 5.0-35.0  $\mu m$  with a noise equivalent radiance of  $1 \times 10^{-7}$  W cm<sup>-2</sup> sr<sup>-1</sup>. This corresponds to a minimum equivalent blackbody temperature resolution of  $0.05^{\circ}$ C.

The radiometer observed radiance at a zenith angle of 52.5° indicates the total downward hemispheric flux when multiplied by  $\pi$ .<sup>3</sup> This has often been demonstrated and eliminates zenith scanning. The filtered spectral sensitivity of the radiometer  $\phi(\nu)$  over the band 5.0-35.0  $\mu$ m (286-2000 cm<sup>-1</sup>) has an average relative response of 0.55. The response of the detector appears in Fig. 1. Altitude scans were accomplished to verify the  $\pi$  ( $N_{52.5^{\circ}}$ ) relation. The radiometer sampling rate is 10 sec<sup>-1</sup>, which is then electronically averaged for 1-sec intervals. (Fig. 2) is pressure-sealed to the hull of the NASA jet laboratory with the chopper external to all optics. Figure 3 illustrates the mirror system with zenith-to-nadir scan capability, normal to the flight track.

### III. Basic Equations

The upward radiance (W cm<sup>-2</sup> sr<sup>-1</sup>) observed by the wide band radiometer or calculated at aircraft level is represented by the radiative transfer approximation

$$\begin{split} N \uparrow &= - \int_{\nu_1}^{\nu_2} \int_{\rho}^{\rho_s} \phi(\nu) B[\nu, T(p)] \frac{d}{dp} \tau(\nu, p) dp d\nu \\ &+ \int_{\nu_s}^{\nu_2} \phi[\nu] B[\nu, T(p_0) \tau(\nu, p_0) d\nu, \quad (1) \end{split}$$

where  $B[\nu, T(p)]$  is the Planck function (W cm<sup>-2</sup> sr<sup>-1</sup> cm); T(p) is temperature (K) at pressure p (mb);  $\phi(\nu)$  is the spectral sensitivity of the radiometer; and  $\tau(\nu,p)$  is the total transmission of the atmosphere for all radiators along a path from p to  $p_a$ , a function of the pressure, temperature, water vapor, mass, and the spectroscopic data for the 5.0-35.0- $\mu$ m band. Subscript a refers to the aircraft pressure level;  $p_0$  is the surface pressure. Similarly, the downward radiance may be represented by the expression,

$$N \downarrow = -\int_{\nu_1}^{\nu_2} \int_{p}^{p_o} \phi(\nu) B[\nu, T(p)] \frac{d}{dp} \tau(\nu, p) dp d\nu \qquad (2)$$

The authors are with NOAA/ERL, Boulder, Colorado 80302. Received 18 June 1973.

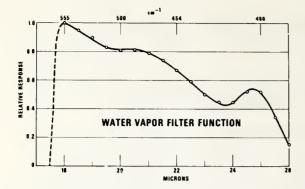


Fig. 1. Relative response of detector-filter system.

Observed or calculated fluxes (w cm-2) are given by

$$F = \pi N(52.5^{\circ}).$$
 (3)

The transmission model employed in the radiative flux calculations is basically the Elsasser<sup>4</sup> periodic model. The absorption coefficients for water vapor and carbon dioxide are those of Möller and Raschke (1964), incorporating data from Yamamoto<sup>5</sup> covering the 6.3- $\mu$ m band of water vapor, 1160-2120 cm<sup>-1</sup>, and the rotational band of water vapor, 200-800 cm<sup>-1</sup>. The absorption coefficients are listed in the cited reference. They are not the absorption coefficients upon which the Elsasser chart data are based. The absorption coefficients for the continuum  $k_1$  (foreign broadening portion) and  $k_2$  (e-type absorption) are taken from Ref. 6.

In the spectral regions where active absorption bands of two or more absorbers overlap each other 520-800 cm<sup>-1</sup> for carbon dioxide and water vapor, and 840-1140 cm<sup>-1</sup> for ozone and the water vapor window, the multiplicity formulation is employed to determine the total transmissivity. The spectral transmissivity  $\tau$  is determined by the product of the spectral transmissivities of the individual constituents,

$$\tau_{\nu} = \tau_{\nu_1} \cdot \tau_{\nu_2} \cdot \tau_{\nu_3} \cdots \tau_{\nu_n}, \tag{4}$$

$$d_{c} = 1 - \epsilon_{r} \tag{5}$$

where the subscripts refer to the specific transmission function of the n active gasses in the spectral interval  $\nu$ .

One of the n transmissivities, in line with the purpose of the study, that of modeling transfer of ir radiation through clouds, will be the transmissivity of the cloud. Stratus decks, where the size distribution of the droplets peaks at approximately  $10.0~\mu m$ , are the primary input to the cloud transfer model. Stratified cirrus sheets and possibly thunderstorm anvil ice blowoff are next in the modeling. In the following section we consider parameterizing of a cloud transfer model.

### IV. Parameterizing ir Transfer Through Clouds

### A. Band Spectral Transmissivities

The cloud radiation transfer model employs the same basic equations, Eqs. (1), (2), (3), (4) and (5), employed in Sec. III to describe radiative transfer processes. Primary emphasis is placed on Eq. (4) in that we are adding a spectral transmissivity for cloud with a representation of various cloud absorption coefficients based on direct flux observations.



Fig. 2. Radiometer system.

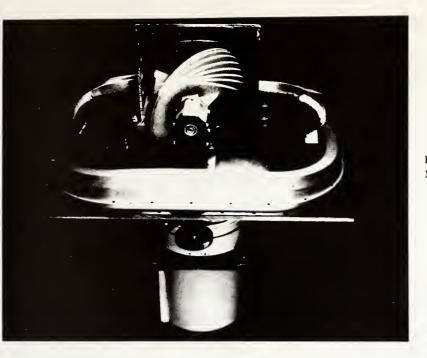


Fig. 3.
Mirror system, external for radiometer.

Table I summarizes the spectral distribution of the optically active gases employed in the model calculation.

### B. Cloud Transmission Function and Absorption Coefficients

The cloud absorption coefficient K (cm<sup>-1</sup>) is identified in the expression for the transmission function for clouds  $\tau_c$ ,

$$\tau_{c_{\lambda \nu}} = \exp[-K(z)\beta \Delta Z],\tag{6}$$

where  $\Delta Z$  is cloud depth (cm),  $\beta$  is sec  $\theta$ (zenith angle). K (cm<sup>-1</sup>) is equal to the product of the liquid water content (g cm<sup>-3</sup>),  $\rho_{cld}$  and the mass absorption coefficient (cm<sup>2</sup> g<sup>-1</sup>). K is then determined by equating observed upward and downward flux with calculated flux [Eq. (4)]. K is assumed independent of wavelength. To determine K, only its value in the expression for total transmission, Eq. (6), is ad-

Table I. Spectral Distribution of Optically Active
Gases Employed in Model

Gas (cloud)	Frequency range (cm <sup>-1</sup> )	Wavelength range $(\mu m)$
Ozone	605-800	12.5-16.5
	960-1180	8.5-10.4
Carbon dioxide	550-820	12.2 - 18.2
	2247-2392	4.18-4.45
Water vapor	280-2280	4.4-35.0
Water vapor, window	680-1200	8.3-14.7
Continuum $k_1$	750-1100	9.0-13.3
Continuum $k_2$	750~1100	9.0 - 13.3
Cloud	280-2280	4.4-35.0

justed until  $|F\uparrow_c - F\uparrow_0| \le \text{N.E.}\Delta F_{\text{radiometer}}$  and  $|F\downarrow_c - F\downarrow_0| \ge \text{N.E.}\Delta F_{\text{radiometer}} = 5.0 \text{ W cm}^{-2}$ .

We should note that this model does not assume that the cloud is black ( $\tau=0$ ) or grey ( $\tau=0.50$ ), but rather it evaluates the transmission for various cloud thicknesses as observed and the absorption coefficient. For example, let us assume that  $K=0.0001~{\rm cm}^{-1}$  and the cloud deck is 200 m deep. From Eq. (6) we have,

$$\tau_{c_{\Delta\nu}}=0.135.$$

If the cloud depth is 300 m, the value of the transmission drops to 0.05 and at 500 m the cloud is black. Thus, in calculating upward and downward fluxes it is necessary to monitor the transmission function to determine the depth at which the cloud is black as a new background for the upward or downward directed ir flux.

### C. Calculation Scheme

- (1) Vertical profile observations are made of the following parameters: air temperatures, humidity (%), upward flux (W cm<sup>-2</sup>), downward flux (W cm<sup>-2</sup>), atmospheric cooling (°C day<sup>-1</sup>), interface temperature (°C), cloud top (mb), and cloud base (mb).
- (2) Specify the top and base of the cloud as well as the cloud absorption coefficient *K*.
- (3) Employing Eqs. (1) and (3), calculate upward power with a true surface temperature  $T(p_0)$  as background.
- (4) Monitor  $\tau_c$  at some frequency  $\nu$  (recall that it is independent of wavelength) to ascertain at what

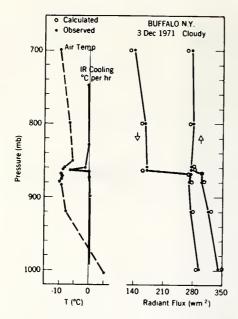


Fig. 4. Buffalo, N. Y., aircraft radiometric profile, cloudy, 3 December 1971, •—• calculated flux; O—O, observed flux; ●—•, ir cooling; ---, air temperature.

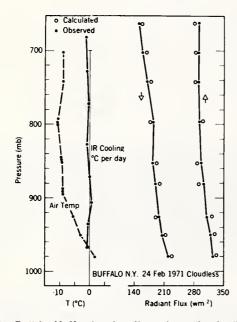


Fig. 5. Buffalo, N. Y., aircraft radiometric profile, cloudless, 24 February 1971, symbols as in Fig. 4.

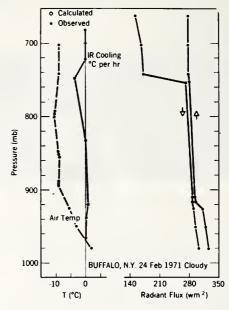


Fig. 6. Buffalo, N. Y., aircraft radiometric profile, cloudy, 24 February 1971, symbols as in Fig. 4.

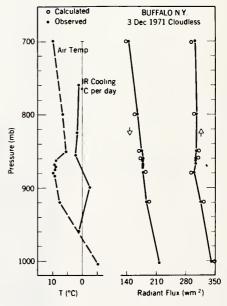


Fig. 7. Buffalo, N. Y., aircraft radiometric profile, cloudless, 3 December 1971, symbols as in Fig. 4.

March 1974 / Vol. 13, No. 3 / APPLIED OPTICS 515

pressure level it becomes zero or if it reaches zero. This is accomplished only in the cloud layer.

- (5) If  $\tau_c$  becomes zero, discard this calculation and repeat calculation with  $T(p_0)$  in Eq. (1) set equal to the cloud temperature at level where  $\tau_c = 0$ .
- (6) Repeat for all succeeding layers within the cloud.
- (7) Repeat entire integrating procedure in Eqs. (2) and (3) in calculating the downward power flux.
- (8) Compare observed upward and downward directed radiant flux with calculated flux from 1 km above cloud top through and to 1 km below cloud base.
- (9) Repeat calculations with new K until calculated and observed radiances for the cloud region are within  $\pm 10.5$  cm<sup>-2</sup> of each other.

By way of a preview, values of K (cm<sup>-1</sup>) determined from stratus observations ranged from 0.0005 to 0.0007 cm<sup>-1</sup>. It is clear that with varying cloud depth and varying K's, clouds in this parameterization are not black per se. The computer program for this cloud radiative transfer model, RADIANCE, is on file at the National Oceanic and Atmospheric Administration offices in Boulder, Colorado, by the authors.

### V. Observations and Calculations

During the Great Lakes snow redistribution program in January and December of 1971, several flight hours accrued with the instrument described in Sec. II. Many of these hours involved ascents through cloudy as well as cloudless atmospheres during which upward and downward radiative flux profiles were observed. Since pressure, temperature, and humidity profiles were also obtained, calculations through cloudy and cloudless atmospheres were also obtained for the same time.

Figure 4 for the Buffalo-Lake Erie area, and over the Lake, illustrates the observed and calculated profile of upward and downward flux  $(W m^{-2})$ , ir cooling (°C h<sup>-1</sup>), and air temperature in °C.

The atmospheric temperature change due to radiative divergence or convergence is given by,

$$\partial T/\partial t = -(g/c_p)|\partial F_N/\partial P_{ir}|, \tag{7}$$

where  $c_P$  is the specific heat of air, g the acceleration of gravity, p pressure, t time, and  $F_N$  is the net flux of ir radiation noted by subscript ir. Employment of a value of  $0.0005~{\rm cm^{-1}}$  for K results in good agreement between observed and calculated upward and downward flux. From observations and calculations, slight warming at the cloud base and strong cooling at the cloud top are typical of all observed radiometric profiles through such stratiform clouds. The thickness in this instance is only 142 m. However, the substantial value of K resulted in ir opacity for the stratus cloud by the third level, whether the approach is from top or bottom. At least at this level the transmissivity of the cloud was  $0.00 \pm 0.03$ , our criterion for opacity. The strong cooling at 862

mb and the resulting overturning tends to maintain the cloud.

Figure 5 for the same profiles as in Fig. 4 but over a cold snow-covered surface illustrates radiative transfer in a cloudless atmosphere away from the lake stratus. This illustrates typical midlatitude cooling profiles over a snow surface. Observations and calculations are in reasonable agreement through 700 mb. Cooling rates are in °C day-1.

On 24 February 1971 (Fig. 6), the aircraft (with radiometer) profiled a very deep cloud layer, principally stratocumulus, extending from a base at 925 mb to a top at 740 mb. The value of K chosen for this thick cloud, which gave best agreement between calculated and observed flux, was 0.0006 cm<sup>-1</sup>. Cloud transmissivities at the base and top reached zero after a penetration of 700 m into the cloud in the model. This agreed with the radiometric flux observations. It was evident, however, that the observations responded to the cloud in a shorter distance of penetration than the calculations. This is due to the instability that occurs in flux calculations and subsequent ir cooling computations for a very shallow atmospheric layer. Again, one notes the strong cooling, 3.7°C h<sup>-1</sup>, at cloud top; no radiative temperature change within the cloud; and substantial warming, 0.7°C h<sup>-1</sup>, just into the cloud

As in Fig. 5, Fig. 7 is a calculated profile of radiant flux and ir cooling for an ascent after cloud seeding, assuming cloudless conditions and a saturated air mass through 740 mb.

### VI. Conclusion

It appears that a satisfactory simplified model to include parameterizing ir radiative transfer through stratus cloud layers has been developed on the basis of observations. A volume absorption coefficient for stratus clouds K (cm<sup>-1</sup>) was determined by adjusting upward and downward flux calculations to coincide with those observed at each level through the cloud by  $|F_c - F_o| \leq 10.5 \text{ W m}^{-2}$ , where  $F_c$  and  $F_o$  are the calculated and observed fluxes.

Table II. Volume Attenuation Coefficients for Clouds Stratus and Strato Cumulus ( $\overline{\Delta z}=0.3-1.0$  km)

Researcher	K (cm <sup>-1</sup> )	Spectral region (µm)
Mc Clatchey®	0.00020	1.0-10.0
Feigel'son <sup>1</sup>	0.00013	10
	0.00027	12
	0.00034	18
Shifrin <sup>8</sup>	0.00048	8.0-12.0
	0.00052	12.0 - 16.0
	0.00068	16.0 - 20.0
Yamamoto <sup>5</sup>	0.00060	10.0-20.0
	0.00100	8.0-10.0
This study	0.00010-0.00050	5.0 – 35.0
	Cirrus Clouds	
	$(\overline{\Delta z} = 0.8 \text{ km})$	
This study	0.00008-0.00010	5.0 - 35.0

Table II summarizes values of the volume absorption coefficient by various researchers for stratus or stratocumulus clouds together with the results of this study. In some instances, values were derived from the mass absorption coefficient  $k \pmod{g^{-1}}$ . Future work will deal with cumulus-type clouds, their anvil ice sheets, and other cirriform clouds.

### References

 E. M. Feigelson, Light and Heat Radiation in Stratus Clouds (translated from Russian, U. S. Dept. Commerce, Wash. D. C., 1964).

- G. Korb and F. Möller, Theoretical Investigation on Energy Gain by Absorption of Solar Radiation in Clouds, Final Tech. Rept., U. S. Dept. of the Army (1962).
- 3. G. D. Robinson, Quart. J. Roy. Meteorol. Soc. 76, 17 (1950).
- 4. W. M. Elsasser and M. F. Culbertson, Atmospheric radiation tables, Meteorological Monographs (American Meteorological Society, Boston, 1960), vol. 4, No. 23.
- G. Yamamoto, M. Tanako, and S. Asamo, J. Quant. Spectrosc. Rad. Transfer 11, 697, (1971).
- 6. K.S. Bignell, Quart. Roy. Meteorol. Soc. 96, 390 (1970).
- R. M. Goody, Atmospheric Radiation (London, Clarendon Press, 1964), vol. 1.
- K. S. Shifrin, Thermal Radiation Transfer in Clouds, Trudy GGO, No. 46. (1955).
- R. A. McClatchey, R. W. Fenn, F. E. Volz, J. S. Garing and J. E. A. Selby, Optical Properties of the Atmosphere (Revised) Rept. A.F.C.R.L (1971).

### Longwave Radiation Effects of the Harmattan Haze

P. M. KUHN, H. K. WEICKMANN, AND L. P. STEARNS

Atmospheric Physics and Chemistry Laboratory, National Oceanic and Atmospheric Administration Boulder, Colorado 80302

Infrared (IR) in situ radiance observations,  $8.0-14.0~\mu m$  ( $714-1250~cm^{-1}$ ) and  $9.5-11.5~\mu m$  ( $870-1052~cm^{-1}$ ), of the West African Harmattan haze during the 1974 Global Atmospheric Research Project Atlantic Tropical Experiment field phase made possible the determination of some of the radiative properties of this tropospheric phenomenon. This in turn permitted development of a simple calculation model for radiative transfer through the haze. Radiometric observations of the dust haze, reaching from 600 m to 6.25 km, were analyzed for haze IR transmission. A transfer model incorporating these transmission properties gave an average calculated IR cooling rate of  $0.09^{\circ}C~h^{-1}$  for the entire haze layer compared to a haze-free cloudless troposphere cooling rate of  $0.06^{\circ}C~h^{-1}$  for the same levels. The haze volume absorption coefficient was approximately  $0.042~km^{-1}$  for layers of all depths. This uniformity of the haze transmission was further evident in the direct correlation of its transmission and optical depth.

### INTRODUCTION

The Global Atmospheric Research Project Atlantic Tropical Experiment (Gate) field phase in the summer of 1974 out of Dakar, Senegal, West Africa, provided a unique opportunity to conduct airborne infrared (IR) observations and subsequent calculations of the transmission and absorption properties of the well-known Harmattan haze. The vertical profile observations were made in the 8.0- to 14.0- and 9.5- to 11.5-\mu m spectral region 'looking' downward with a 2° field-of-view chopper radiometer with a noise equivalent radiance of  $2.35 \times 10^{-6}$ W cm<sup>-2</sup> sr<sup>-1</sup>. There were no filters or windows exterior to the chopper. Consequently, the radiometer is completely outside of the cabin of the jet aircraft that is the airborne platform. Because of Gate, NASA's Convair 990 laboratory was available for the research. The details of the IR radiometer employed in this research are described by Kuhn et al. [1974]. The only addition to the instrument described was a calibrating reference source for the chopper radiometer system.

The intent of this research was to experimentally observe and analyze some of the long-wave radiative effects of the Harmattan haze and to develop thereby a simple model to calculate vertical profiles of the radiance and irradiance in a dusty atmosphere. Specifically, it was to determine the haze total extinction coefficient to permit a simple solution for bulk radiative transfer phenomena including radiative cooling. Since a detailed moderately high resolution (1.0 cm<sup>-1</sup>) radiative transfer approximation model (P. M. Kuhn et al., unpublished report, 1975) had been in use for some time, it was only necessary to add this additional absorber to the existing solution once the haze radiative properties were determined.

To provide backup data, a CO<sub>2</sub>, Q branch IR radiometer installed to observe outward ahead of all engine nacelles provided profiles of the free air temperature aboard the Convair 990 and operated simultaneously with the downward-looking IR radiometer. Calculations required the humidity profiles taken either from the 1200 or 0000 UT Dakar-Yoff, Senegal, sounding, which was never more than 200 n. mi. (370 km) to the east of the radiation profiles or from the Gate ship radiosonde nearest to the flight profile area.

Copyright © 1975 by the American Geophysical Union.

Observations made over the generally uniform temperature of the Atlantic, between 8° and 14° north, provided the best data during the numerous Gate Convair 990 radiation profile missions. (The temperature was found to be uniform by the downward-looking radiometer which continuously monitored sea surface temperature. This radiometer was calibrated for brightness sea surface temperature versus surface physical temperature by at least two flight profiles for each mission.)

Although clouds below the Convair 990, if they were intercepted by the acceptance cone of the radiometer, could alter the results, the narrow (2°) field of view of the radiometer insured satisfactory observations except in solid undercast. Fortunately, there were numerous areas with scattered to cloudless conditions during the dust profile missions.

The dust, sweeping off the Sahara from the northeast and visible in SMS satellite imagery (Figure 1), appeared most intense during Gate phase 1, from June 24 through July 10, 1974, and on the average in the layer from 980 mbar as a base through 520 mbar. There were frequent opportunities to determine the IR transmission of the dust when the Convair 990 penetrated the dust-laden atmosphere. The boundaries between the dust layer and the relatively clean transparent air above or below the dust layer were easy to see from the air-craft moving through the dust layer. The yellowish veil against a light background formed a definite haze horizon. In addition, the IR air temperature usually indicated an inversion at the top of the haze horizon. Radar altimetry together with inertial navigation and real time data acquisition and display systems made boundary identification instantaneous.

### PHYSICAL CONSIDERATIONS

By determining a physical model of radiative transfer in cirrus and aerosols, *Hall* [1968], *Fleming and Cox* [1974], and *Grassl* [1973] laid the groundwork for our determination of a bulk total extinction coefficient in the atmosphere.

In order to avoid cumbersome in-text definitions of physical parameters a list of mathematical and physical symbols employed with their appropriate dimensions is presented.

- T total transmission;
- R reflection or scattering;
- A absorption;
- 1. T extinction;
  - N long-wave radiance, W cm<sup>-2</sup> sr<sup>-1</sup>;

### 12:00 181:74 01-A-2 0200 VIS 2 MI



Fig. 1. SMS visible satellite image of June 30, 1974, at 1200 UT showing Dakar, the Sahara, and the Eastern Atlantic.

- q mixing ratio, g g-1;
- k mass absorption coefficient, cm<sup>2</sup> g<sup>-1</sup>;
- Z limits of integration on height, cm;
- σ mean bulk total extinction coefficient for dust including continuum, km;
- $\theta$  absolute temperature;
- ν wave number, equal to  $1.0/\lambda$  cm<sup>-1</sup>;
- $\Delta \nu$  increment of wave number, cm<sup>-1</sup>;
- λ wavelength, cm;
- $\rho$  density, g cm<sup>-3</sup>;
- Δ finite difference operator;
- 1 base of dust layer;
- 2 top of dust layer;
- 11 base of dust free layer;
- 22 top of atmospheric dust free layer;
- downward radiance or transmission;
- upward radiance or transmission;
- D haze or dust;
- E extinction;
- n particular layer;
- 0 surface.

The principal of conservation of energy or power requires that

extinction ≡ scattering + absorption

for energy traversing an absorbing and scattering medium. Symbolizing extinction, scattering, and emission, one may write

$$1.0 - T_{\nu} = R_{\nu} + A_{\nu} \tag{1}$$

Equation (1), expressing the conservation of energy in terms of monochromaticity, is exact. However, we will define a bulk form of total extinction in radiant power traversing a medium

$$1.0 - T_{\Delta \nu} = R_{\Delta \nu} + A_{\Delta \nu} \tag{2}$$

Here the extinction  $1.0-T_{\Delta\nu}$  covering a to-be-specified wave number interval  $\Delta\nu$  also implicitly includes the effects of emission by the medium, in this case the Harmattan dry haze, and scattering by the haze particles. Beers law permits us to repeat

$$T_{\Delta\nu D} = \exp\left(-\hat{\sigma}_{E\Delta\nu}\Delta Z\right) = \exp\left(-\rho k_{E\Delta\nu}\Delta Z\right)$$
  
= 1.0 -  $R_{\Delta\nu D}$  +  $A_{\Delta\nu D}$  (3

Here  $T_{\Delta\nu D}$  is a 'bulk transmission' and  $\bar{\sigma}_{\Delta\nu E}$ , the bulk total extinction coefficient, is determined by

$$\tilde{\sigma}_{\Delta\nu E} = -(\ln T_{\Delta\nu D}/\Delta Z) \tag{4}$$

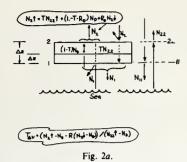


Fig. 2. Symbolic atmospheric haze layer with arrows depicting upwelling and downward IR radiance. Symbols are defined in text.

where  $\bar{\sigma}_{\Delta\nu E}$  is measured per kilometer. Equation (4) is determined solely from radiance and temperature observations but does include effects of scattering, however small. This then is the reason for using the term bulk. Subsequent determination of  $T_{\Delta\nu D}$  must include an assumption about the scattering  $R_{\Delta\nu D}$ .

In line with our purpose of analyzing and modeling bulk long-wave radiative transfer through the Sahara dust we required a bulk total extinction coefficient  $\tilde{\sigma}_{\Delta\nu E}$  as input to the model transfer solution. To accomplish this, it was necessary to obtain observations of  $T_{\Delta\nu D}\uparrow$  for evaluation by (4). These were obtained by the aircraft radiometric observations in the following manner looking downward.

Consider the radiometric profiling of a haze layer of thickness  $\Delta Z$  as in Figure 2. Further, consider the power budget at the top of the haze layer, denoted by the level symbol 2 and at the same top of a haze-free layer in the adjacent atmosphere, denoted by the level symbol 22. The arrows indicate the direction of propagation of the radiant power, dashed arrow shafts indicating transmission and solid shafts indicating emission or reflection. In each case we consider the vertical or radiance component of the power transfer.

Now the radiant power balance at the top of the haze layer may be written as [Davis, 1971; Kuhn, 1970]

$$N_2 \uparrow = T_{\Delta \nu D} \uparrow N_{22} \uparrow + (1.0 - T_{\Delta \nu D}) \uparrow - R_{\Delta \nu D} N_D + R_{\Delta \nu D} N_2 \downarrow$$
 (5)

But to ascertain the influence of a different (colder) spectral source or background region on the haze transmission, we used an upward-looking radiometer aboard the Convair 990 to observe downwelling power. The balance at the base of the haze layer may be written similarly as

$$N_1 = T_{\Delta\nu D} [N_{11}] + (1.0 - T_{\Delta\nu D}] - R_{\Delta D} N_D + R_{\Delta\nu D} N_1$$
 (6)

The  $N_D$  in (5) and (6) is evaluated from direct observations (CO<sub>2</sub> band radiometer) of the dust layer temperature. Best agreement between observed and calculated radiance was achieved when employing a dust layer transmission obtained from radiance observations and calculations utilizing a dust layer temperature one third of the depth into the layer from the observing level. By profiling upward or downward through the haze layer it was possible to obtain transmissions of several layers of increasing thickness as are required for a solution of the bulk total extinction coefficient  $\hat{\sigma}_{\Delta\nu E}$  from (4).

Equations (5) and (6) may now be rewritten to give transmission as

$$T_{\Delta\nu D} \uparrow = [N_2 \uparrow - N_D - R_{\Delta\nu D} (N_2 \downarrow - N_D)]/(N_{22} \uparrow - N_D) \quad (7)$$
 and

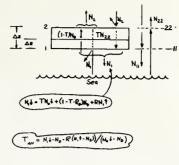


Fig. 2b.

$$T_{\Delta\nu_D} \downarrow = [N_1 \downarrow - N_D - R_{\Delta\nu_D}(N_1 \uparrow - N_D)]/(N_{11} \downarrow - N_D) \quad (8)$$

In the absence of observations on the scattering  $R_{\Delta\nu D}$  the IR transmission is determined neglecting the scattering term. However, the effects of scattering are included in what we have termed a bulk transmission. Actually, the subsequent close agreement between observed radiance and calculated radiance employing a bulk total extinction coefficient determined from this transmission validates the assumption. Davis [1971] also was forced to omit scattering in his work on cirrus transmission observations.

Before the results of haze transmission and extinction observations and calculations are discussed, it appears appropriate to tidy up the references to test and error limits alluded to in prior discussion. They are summarized in the following:

- 1. Noise equivalent radiance (N.E. $\Delta$ .N.) of radiometers employed was ascertained in a laboratory calibration against blackbody sources controlled to  $\pm 0.05$  °C. The N.E. $\Delta$ .N. was  $2.35 \times 10^{-6}$  W cm $^{-1}$  sr $^{-1}$ .
- 2. From (4) the error in  $\bar{\sigma}_{\Delta\nu E}$  for an error in the  $T_{\Delta\nu D}$  observation is given by

$$d\bar{\sigma}_{\Delta\nu E} = \frac{dT_{\Delta\nu D}}{T_{\Delta\nu D}\Delta Z} \tag{9}$$

3. The error in  $T_{\Delta\nu D}$ , from (5), is given by

$$dT_{\Delta,D} = \frac{N_{22} \int dN_2 \int -N_2 \int dN_{22}}{(N_{22} \int)^2}$$
 (10)

A 2% error in the downward radiance, averaging  $2.5 \times 10^{-3}$  W cm<sup>-2</sup> sr<sup>-1</sup>, in the 8.0- to 14.0- $\mu$ m band, produces approximately a 0.2% error in  $T_{\Delta\nu D}$ , which in turn results in an error of  $\pm 0.0011$  in  $\bar{\sigma}_{\Delta\nu E}$  from observation 2 above. It is clear that radiance errors are more critical when  $\bar{\sigma}_{\Delta\nu E}$  is determined from upward radiance, since upward radiance averages 4.3  $\times$  10<sup>-3</sup> W cm<sup>-2</sup> sr<sup>-1</sup>. The error in  $\bar{\sigma}_{\Delta\nu}$  when upward radiance is employed could reach  $\pm 0.010$ .

### TRANSMISSION CALCULATIONS FROM RADIANCE OBSERVATIONS

Observations of  $T_{\Delta\nu\rho}$  were accomplished on one mission, that of June 30, 1974. Observations of  $T_{\Delta\nu\rho}$  were made on the Gate mission of June 30 and July 3 and 29, 1974. Of course such observations necessitated a profile in a haze-free area immediately adjacent to the Harmattan haze. On all of our missions the north or south edge of the haze was strikingly visible. Figure 3 illustrates typical profiles of upward and downward radiance N and N at two spectral passbands, 9.5-11.5 and

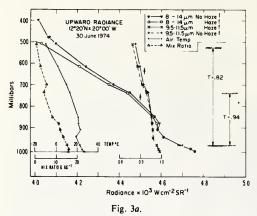


Fig. 3. Upward and downward radiance, air temperature, and mixing ratio on June 30, 1974. Haze layer boundaries are indicated by cross hatching. Transmission, indicated by T, represents both 9.5–11.5 and 8.0–14.0  $\mu$ m. Vertical arrows denote the extent of haze layers. Symbol T in the figure represents  $T_{\Delta\nu D}$  in text.

 $8.0-14.0 \mu m$ , and for two layer depths, 510-980 and 737-980 mbar. The observations were conducted within and outside of the haze at approximately 1200 UT at 12°20'N, 20°00'W. Each plotted circle, triangle, plus sign, or cross represents a mean of 30 radiometric observations, computer averaged over a 30-s interval. The plotted curves are also typical of the missions on July 4 and 29, 1974.

The transmissions in both passbands (Figure 3) obtained from the equivalent radiance N by means of (7) and (8) and over the two layers shown, employing the aircraft observed temperature (CO<sub>2</sub> thermometer) and humidity profiles are virtually identical at 0.82 and 0.94. This is because the haze emission and transmission do not vary to any degree across the spectral region 7.0-15.0.

The slope of the curve of transmission calculated from up-

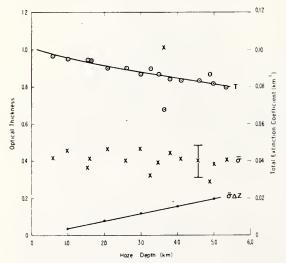
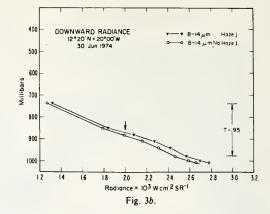


Fig. 4. Haze radiance transmission T and total extinction coefficient  $\tilde{\sigma}$  relative to haze geometric depth  $\Delta Z$  and optical depth  $\tilde{\sigma}\Delta Z$ . Data are from June 30 and July 3 and 29, 1974, depicting the Atlantic 100 km west of Dakar, Senegal. Symbol  $\tilde{\sigma}$  in the figure represents  $\tilde{\sigma}_{\Delta\nu E}$  in text.



welling radiance suggests layer structure in the haze such as that at 850 mbar down to that at 950 mbar. Here a more dense layer may be inferred from the almost zero gradient. The slope change in the transmission calculated from the downward radiance at 850 mbar further substantiates the suggestion of the more dense layer with the increase of the power gradient.

The computation of  $T_{\Delta\nu D}$  from upward or downward transmission for the layer 980-737 mbar over the 9.5- to 11.5- $\mu$ m region for a mission at 1200 UT on June 30, 1974, at 12°20′N, 20°W resulted in a difference of less than 0.005. Here  $T_{\Delta\nu D}$ ! =  $T_{\Delta\nu D}$ ! = 0.94 (Figures 3a and 3b). Background radiance changes over the spectral band 9.5-11.5  $\mu$ m were thus obviously not significant and justify the use of a common bulk total extinction coefficient for both upwelling and downwelling haze radiance.

In the IR haze cooling computations to be discussed subsequently the radiance effects of the haze covered only the 8.0- to 14.0- $\mu$ m spectral band. In fact all the radiators, carbon dioxide, ozone, water vapor, continuum, and dust are restricted to their optically active regions. *Grassl* [1973] demonstrates that 'the aerosol contribution below 8 and above 13 microns was negligible because the absorption coefficient of water vapor far exceeded the aerosol absorption coefficient.'

### **BULK TOTAL EXTINCTION COEFFICIENT**

Average values of the Harmattan haze transmission calculated from observations entered in (7), the total extinction coefficient  $\bar{\sigma}_{\Delta\nu E}$  from (4), and the optical depth  $\bar{\sigma}_{\Delta\nu E}\Delta Z$  are summarized in Figure 4 for profiles of June 30 and July 3 and 29, 1974. Each transmission data point (circled dots) is the mean of 300 radiometric observations. The solid curve is a least squares fit to the data excluding the data point with a transmission of 0.64. These transmission observations entered in (4) provide the data for curve of  $\bar{\sigma}_{\Delta\nu E}$ . The optical thickness  $\bar{\sigma}_{\Delta\nu E}\Delta Z$  is calculated and appears at integer values of the geometric depth of the dust. The mean value of all observations of  $\bar{\sigma}_{\Delta\nu E}$  is 0.042 km<sup>-1</sup>.

The smooth nature of the transmission curve and the uniformity of the magnitude of the absorption coefficients, through layers from 1.0 to 5.0 km deep, suggest a very well-mixed haze layer. The error limit of individual observations of  $\bar{\sigma}_{AVE}$  is shown by the vertical bars.

### CALCULATED RADIANCE AND COOLING RATES

Upon determination of the total extinction coefficient  $\bar{\sigma}_{\Delta\nu E}$  the upward radiance N was calculated from the transfer approximation given as

$$N \uparrow_{\Delta_{\nu}} = - \int_{1.0}^{\tau_{\Delta_{\nu}}} B_{\Delta_{\nu}}(\theta) dT + B_{\Delta_{\nu}}(\theta) T_{0} \qquad (11)$$

Here.

$$T = T_{\text{HeO}} \cdot T_{\text{CO}_2} \cdot T_{\text{O}_3} \cdot T_D \uparrow \tag{12}$$

where  $T_D$  is given in (3) as

$$T_{\Delta\nu D} = \exp\left(-\bar{\sigma}_{\Delta\nu E}\Delta Z\right) \tag{13a}$$

and

$$dT = T_n - T_{n+1} \tag{13b}$$

In calculations the use of  $T_{\Delta\nu D}$  in place of an additional continuum transmission term eliminates a double contribution in the water vapor continuum. The bulk total extinction coefficient in (13a) does not include a scattering coefficient and therefore is used through  $T_{\Delta\nu D}$  in (11).

Calculations of the upward radiance for the missions of June 30, 1974, and July 4 and 29, 1974, resulted in a root mean square (rms) difference from observations of  $1.3 \times 10^{-4}$  W cm<sup>-2</sup> sr<sup>-1</sup> for an upward profile averaging  $4.4 \times 10^{-3}$  W cm<sup>-2</sup> sr<sup>-1</sup>. This agreement supports not only the addition of dust transmission to the model calculations in (12) but also the method of observations.

Finally, we noted an interesting result of the radiance observations and calculations that has direct applications in the solution of this transfer model for haze if not for similar models. We obtained best results in the evaluation of haze transmission  $T_{\Delta\nu D} \mid$  or  $T_{\Delta\nu D} \mid$  when we used the air temperature from a level approximately one third of the distance into the haze from the observing level at the top, base, or within the layer for calculating the haze radiance  $N_D$  in (5) and (6). Calculations involving either upward or downward radiances were improved by use of that air temperature over a mean layer temperature.

To illustrate calculated cooling rates through the haze layer, a temperature-pressure-humidity profile 100 km southwest of Dakar for July 4, 1974, was input to the long-wave radiance transfer model. Figure 5 is a plot of the results, illustrating calculated cooling rates at the midpoints of each layer in the haze and a corresponding haze-free and cloudless cooling rate profile for a layer depth of 4.6 km over the spectral range 4 3-4 0 m

The calculation of IR cooling in (11) using the bulk total extinction coefficient of 0.042 km<sup>-1</sup> as determined from observations shows the cooling to average 0.09°C h-1 throughout the haze layer. In contrast, the haze-free cooling rate average is 0.06°C h<sup>-1</sup> for the aerosol optical depth of 0.2. This cooling increase is not large and may be balanced by solar warming in the layer. Grassl [1973] calculated the wavelength dependence of radiative cooling rates in the presence of aerosol for a standard maritime atmosphere in the 5.0- to 100.0-\mu m spectral region and with an optical depth of 0.2. This average computed IR cooling rate increase due to maritime aerosol was 0.022°C h<sup>-1</sup>. This compares well with our calculated cooling rate increase of 0.03°C h-1 for the Harmattan haze. At the surface there is little or no effect on the 1R cooling. Consequently, a decrease in the solar input at the surface may cause a net cooling. However, subsidence heating in the high-pressure area over the northwest Sahara may be one factor compensating for any net cooling. It is clear that short-wave radiant power budgets for the Gate area when they are available must

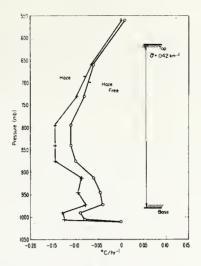


Fig. 5. Calculated IR cooling in Harmattan haze. Data are from July 4, 1974. Vertical arrow denotes depth of layer in degrees Centigrade per hour.

be investigated and combined with the IR to obtain a total radiation budget.

### Conclusions

Transmission calculations from upward- and downward-directed radiance ranged from 0.92 to 0.80 for 1.0- to 5.0-km haze layers for the 8.0- to 14.0- and 9.5- to 11.5- $\mu$ m spectral bands. These transmission values were essentially the same whether they were inferred from upward or downward radiance observations. The uniformity of the transmission over the wider band (8.0-14.0  $\mu$ m) suggests little change in the radiative properties of the dust over broader spectral regions.

A bulk radiative transfer approach, employing a bulk total extinction coefficient determined in situ in the atmosphere for haze and combined with mass extinction coefficients for the gaseous absorbers, gives a simple and rapid computer solution for IR radiative transfer. The in situ nature of the observations in the Gate experiment would appear to validate the use of the experimentally determined total extinction coefficient in the presence of haze for calculations of radiance. This addition to the transfer equation model predicts haze radiance that agrees well with observed radiance in the 9.5- to 11.5- and 8.0- to 14.0- $\mu$ m windows.

The use of the in situ determined haze total extinction coefficient in a broad band radiative transfer model for 1R atmospheric cooling produces results that are physically reasonable when they are compared with haze-free atmospheric cooling rates. The calculated cooling also agrees with preliminary results of Gate radiometersonde cooling observations. It would appear important now to combine IR cooling rates for atmospheric absorbers with Gate observations of solar heating when they are available to complete the total radiation budget analyses for hazy atmospheres.

Acknowledgments. The research reported in this publication was supported by the NOAA Gate Project Office, the Office of Applications of the National Aeronautics and Space Administration and by the Atmospheric Physics and Chemistry Laboratory, National Oceanic and Atmospheric Administration.

### REFERENCES

Davis, P. A., Applications of an airborne ruby lidar during a Bomex program of cirrus observations, J. Appl. Meteorol., 10(6), 1314-1323, 1971.

Fleming, J. R., and S. K. Cox, Radiation effects of cirrus clouds, J. Atmos. Sci., 31(8), 2182-2188, 1974.

Grassl, H., Aerosol influence on radiative coding, Tellus, 25(4), 386-395, 1973.

Hall, F. F., Jr., A physical model of cirrus 8-13 microns infrared radiance, Appl. Opt., 7(11), 2264-2269, 1968.

Kuhn, P. M., Airborne observations of contrail effects on the thermal radiation budget, J. Aimos. Sci., 27(6), 937-942, 1970.

Kuhn, P. M., H. K. Weickmann, and L. P. Stearns, Transfer of infrared radiation through clouds, Appl. Opt., 13(3), 512-517, 1974

(Received January 2, 1975; revised March 17, 1975; accepted March 17, 1975.)

By Peter M. Kuhn, National Oceanic & Atmospheric Administration, Boulder, Colorado Victor S. Whitehead, NASA Johnson Space Center, Houston, Texas and William E. Marlatt, Colorado State University, Fort Collins, Colorado

### **ABSTRACT**

The Skylab field phase in June, August and September of 1973 for the SCARP (Skylab Concentrated Atmospheric Radiation Project) provided a unique opportunity to conduct infrared and solar observations and subsequent calculations beneath the orbiting space vehicle during EREP overpasses. Infrared and solar transmission and absorption properties observed within the atmosphere were compared with EREP experiments, notably the S-191 and S-192. These same observations were later employed in the development and comparison of various atmospheric infrared and solar radiative transfer approximations. Solar radiation observations and calculations in the scattering atmosphere included the 0.4 to 1.1 cm spectral range while infrared observations and calculations covered the spectral band and portions thereof within the 5.0 to 40.0 cm region. Principal conclusions drawn from the solar radiation research are:

- More sophisticated models yield more accurate results when compared with observations.
- 2. The models, on the whole, overestimate the actual surface albedo.

Principal results of the infrared radiation research are:

- 1. Semimaritime atmospheres (Houston) haze transmission ranges from 0.80 to 0.95 with a "bulk" absorption coefficient for the spectral interval, 870 to 1050 cm<sup>-1</sup>, averaging 0.04 km<sup>-1</sup> (-0.009 km<sup>-1</sup>).
- Cooling due to infrared radiation divergence or convergence in the haze layer averages only 0.009C hr<sup>-1</sup> with an rms error of one third to one half of this value.
- 3. Infrared transfer models tend to over-compute atmospheric attenuation.
- 4. Transfer of radiation in the water vapor continuum developed by Bignell resulted in more attenuation than was actually observed.
- 5. Total infrared extinction coefficients for the Phoenix and surrounding desert areas were observed to be 0.30 km $^{-1}$  and 0.052 km $^{-1}$ , respectively.

### INTRODUCTION

The purpose of the research described was and is during its final compilation to arrive at a more complete description of radiative transfer within the atmosphere with emphasis on the contribution of aerosols to this transfer both in the

infrared and solar spectral regions. It was further a defined objective to determine the accuracy and applicability of a variety of models of radiative transfer through air masses of differing characteristics including varying amounts of wet and dry aerosols.

### **TECHNIQUES**

Radiative data were collected primarily by onboard aircraft radiometric sensors, balloon-borne radiometric sensors and ground based sensors observing both radiation and aerosol properties of the atmosphere. At Phoenix, helicopters were employed to profile radiation and aerosol content of the atmosphere from the surface to 2.7 km above sea level reference. In all instances EREP S-191, S-192 and S-190 data were integrated into the evaluation of the various models when possible.

The formulas employed in the research in the development of the various transfer models are given by Kuhn, Weickmann and Stearns (1975), Renne and Marlatt (1974), Reeser and Marlatt (1974) and by Pueschel and Kuhn (1975).

### **RESULTS**

Figure 1 symbolizes the atmospheric infrared radiative transfer in a non-scattering atmosphere. Figure 2 presents an average set of values for the haze transmission and total extinction calculated from data observed in the Phoenix area. The expression for this calculation is given by,

$$T = N_2 \mathbf{1} - N_c \mathbf{1} - e(N_2 \mathbf{I} - N_c)/(N_{22} \mathbf{1} - N_c).$$

The formula is valid for the spectral interval 870 - 1050 cm<sup>-1</sup> and should be referred to Figure 1. Figure 3 typifies cooling in haze.

It is evident from Figures 4 through 8, which show comparisons between observed and calculated radiation (infrared) profiles that better agreement was achieved between observation and models for some test sites than for others. Two major factors contribute to a failure of agreement—the thermal nonuniformity of the test sites, where the surface observation of the interface temperature may not be representative of the site, and changes of the surface or interface temperature with time due to changes in the intensity of solar radiation and cloud cover. One should recall that at least one third of the upwelling radiation at levels above the surface by some 3 to 10 kilometers is due to transfer in the atmospheric window region.

In Figure 9, typical results determined with the doubling solar transfer model for White Sands, N.M., aerosol data are shown. To determine the target albedo, only the solar zenith angle and the planet albedo are required. For many situations the albedo determined can be substituted for spectral reflectivity. Figure 10 shows the calculated target albedo vs. planet albedo curves. These are the expected extremes between the different models as far as sophistication is concerned. Figure 11 provides the aerosol size distribution for Phoenix, Arizona, and vicinity on September 6, 1973.

### REFERENCES

- 1. Kuhn, P. M., H. K. Weickmann and L. P. Stearns: Radiative effects of the Harmattan haze. Accepted for publication, JGR, Oceans & Atmospheres, 1975.
- 2. Renne, D. S. and W. E. Marlatt: A comparison of several atmospheric infrared radiation transfer models, Sixth Conference on Aerospace and Aeronautical Meteorology, American Meteorological Society, Boston, Mass., Nov., 1974.
- 3. Reeser, W. K. and W. E. Marlatt: A test and comparison of radiation transfer models through scattering atmospheres, Sixth Conference on Aerospace and Aeronautical Meteorology, American Meteorological Society, Boston, Mass., Nov., 1974.
- 4. Pueschel, R. F. and P. M. Kuhn: Planetary radiation budget: Effects of urban aerosols. Accepted for publication, JGR, Oceans & Atmospheres, 1975.

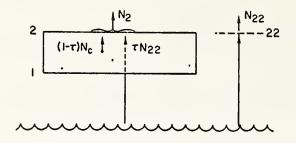


Figure 1. Symbolic atmospheric haze layers with arrows depicting upwelling IR radiance.

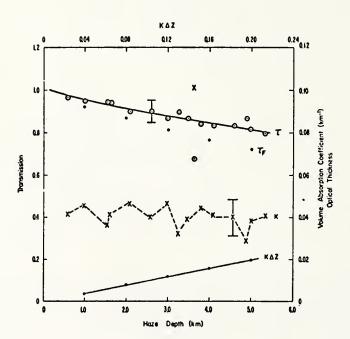


Figure 2 Haze transmission, volume absorption coefficient relative to haze depth and optical depth using White Sands, New Mexico, 11, 12 August 1973.

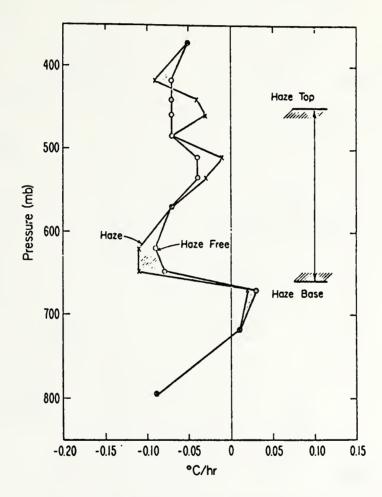
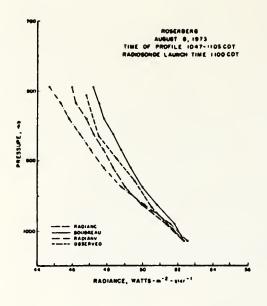
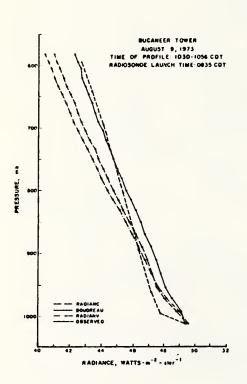
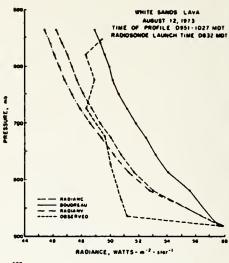


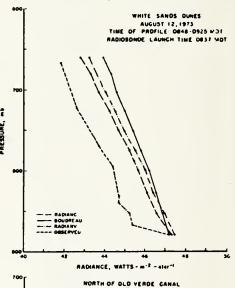
Figure 3. Calculated IR cooling in haze, 11 August 1973, 2130 UT, White Sands, over sand dunes, New Mexico.

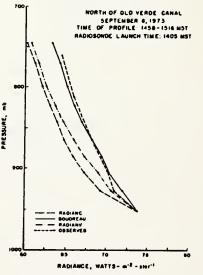




Figures 4 through 8, Upper left to lower right







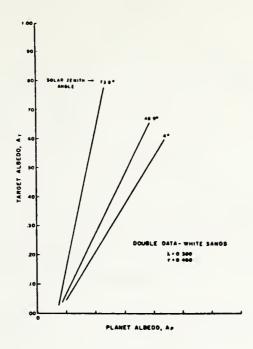


Figure 9

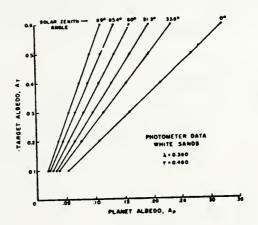


Figure 10

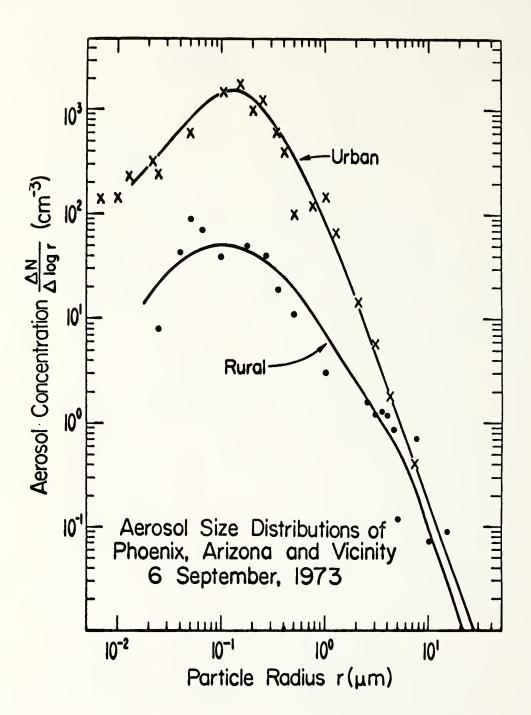


Figure 11

### Hawaiian Volcanos—A Source of Ice Nuclei?

G. LANGER AND C. J. GARCIA

National Center for Atmospheric Research, Boulder, Colorado 80302

B. G. MENDONCA AND R. F. PUESCHEL<sup>1</sup>

National Oceanic and Atmospheric Administration Mauna Loa Observatory, Hilo, Hawaii 96720

C. M. FULLERTON

Cloud Physics Observatory, University of Hawaii, Hito, Hawaii 96720

The possibility that ice nuclei are associated with or generated by volcanic eruptions is of long-standing interest. Studies of Hawaiian volcanos to examine such a possibility have been undertaken by several investigators with controversial results. This study reviews and interprets past findings and adds some new results. The new results involved continuous monitoring of ice nuclei with an NCAR counter during a 1971 eruption and membrane filter sampling for ice nuclei at the ground and in the air during a 1972 eruption. Also, laboratory research was conducted on ice nucleus generation from lava and brush burned during eruptions. No clear indication was found that ice nuclei are directly generated during the eruptions, but ice nucleus activity did increase during these periods.

The possibility that ice nuclei are associated with or generated by volcanic eruptions is of long-standing interest. Aerosols from volcanos often are ejected to high altitudes, even into the stratosphere, and hence they may travel for long distances and produce effects on a global scale. Volcanic eruptions, frequent in Hawaii, are not of a violent nature and so are amenable to closeup study. Several experiments have been performed on the island to monitor ice nucleus trends (Price and Pales [1964], using an expansion chamber; Droessler and Heffernan [1965], using membranes; Hobbs et al. [1971], using an NCAR counter). Elsewhere, Isono et al. [1959] have concluded that volcanic eruptions in Japan are a source of ice nuclei, and Ishizaka [1972] observed volcanic particles in Japan in rainwater from clouds reaching high altitudes. However, the subject is more complex than was first anticipated, and the correlation between ice nuclei and volcanic activity on Hawaii remains largely inconclusive. This note presents a review of our current thinking about Hawaiian volcanos as a source of ice nuclei.

Most ice nucleus measurements on the island of Hawaii have been made either at the Mauna Loa Observatory (MLO), near the summit of one of the two 4000-m mountains that dominate the island, or within the coastal city of Hilo. Although the arrival of fresh volcanic effluent at the sampling site definitely can be established by total aerosol and Aithen nucleus measurements and the presence of SO<sub>2</sub>, concurrent ice nucleus measurements at MLO show differing results. The concentration of ice nuclei may decrease [*Price and Pales*, 1964], remain the same [*Pueschel and Mendonca*, 1972a], or increase [*Hobbs et al.*, 1971].

Any ice nucleus measurements must be interpreted with proper consideration of the activation processes employed by the nucleus detection technique in question. Different instruments respond differently to changes in supersaturation. For example, the results of the Second International Ice and Condensation Nucleus Workshop in Fort Collins, Colorado [Langer, 1973a], have revealed an anomaly in the Bigg-Warner expansion chamber used extensively by Price and Pales [1964] and others in Hawaii. It was found that the counter does not respond to ice nuclei that require a relatively high supersaturation when a high concentration of condensation nuclei is present that prevents condensation on these ice nuclei. Volcanic effluent certainly contains large numbers of such condensation nuclei [Pueschel and Mendonca, 1972b], and these findings may explain why Price and Pales [1964] measured a decrease of ice nuclei during eruptions. Similarly, the membrane technique does not respond well if large numbers of cloud condensation nuclei are present. The NCAR ice nucleus counter permits control of supersaturation [Langer, 1973b], and the data must be interpreted accordingly.

Another major variable involves the transport of volcanic smoke, which may travel some distance out over the ocean or up into the atmosphere before reaching the sampling site. The source of the ice nuclei may be difficult to identify if mixing has occurred with air containing ice nuclei from other sources on the island. To ascertain what the local sources might be, ice nucleus samples were collected near the Halemaumau vent in Kilauea caldera, the location of active vulcanism at the time on Hawaii. Results from the NCAR counter and membrane filters showed a reduction in count (from 2.5 to 0.3 per liter at -20°C) when the sampled air had mixed with the fumes, suggesting that the fumes may deactivate ice nuclei passing over the vent. Sulfurous materials have been reported to deactivate ice nuclei [Georgii, 1963], and part of the aerosol emitted by Halemaumau is ammonium sulfate particles [Cadle et al., 1967, 1969].

Other major sources of aerosols on the island gave the following results when tested for the presence of ice nuclei.

1. Fires during harvesting of sugar cane were found to be a strong source of ice nuclei (the fires are a necessary part of the harvesting procedure to remove the leaves before cutting the stalks) [Pueschel and Langer, 1973].

Now with NOAA-APCL, Boulder, Colorado 80302.

Copyright © 1974 by the American Geophysical Union.

- 2. Kline [1960] pointed out that ocean water may be a source of ice nuclei. Therefore the surf at Kumukahi Point, the most easterly point on the island, exposed much of the time to the trade winds, was studied as a possible source of ice nuclei. Some increase in ice nucleus activity (from 0.3 to 1.0 per liter at -20°C) was measured, both with an NCAR counter and with membranes, when wind direction was toward the sampling site from the surf.
- 3. Price and Pales [1964], using an expansion counter, reported strong local sources of ice nuclei from aircraft operations at the Hilo airport. It should be noted that the frequent rainfall on the windward side of the island (over 7.6 m per year at an elevation of 915 m, about 9.7 km upslope from the Hilo city limits) may effectively scavenge ice nuclei from local sources. However, convection from cane fires may penetrate a weak inversion, and volcanic eruptions are known to eject aerosols above even a strong trade wind inversion.

The authors had the opportunity to sample aerosols directly from eruptions during the period of the present study in 1971-1972. Sampling was done with membrane filters, exposed initially as close as possible to the eruption and then at increasing distances. Aircraft samples also were taken in the smoke plume. Volcanic smoke was not a prolific source of ice nuclei. Many of the smoke samples contained abundant hygroscopic material; i.e., drops readily formed on the membranes upon activation. This action interferes with ice nucleus measurements that use the membrane technique. The ice nucleus count from membranes exposed to cane fire smoke plumes [Pueschel and Langer, 1973] was almost an order of magnitude higher. On the other hand, during periods of volcanic activity, ice nucleus measurements at MLO showed enhanced nucleus activity. Data from the eruption of August 14, 1971, are presented to illustrate this contention. Figure 1 gives the ice nucleus count from two NCAR counters operated at MLO. The duration of the eruption is shown on the plot; it was brief but spectacular. Relevant aerosol data collected at MLO [Pueschel and Mendonca, 1972b] showed that the effluent from the midday eruption reached MLO that evening after penetrating the trade wind inversion; there was a sudden increase in Aitken nucleus count and total aerosol

content of the air which was measured by a nephelometer. No concurrent sudden increase in ice nucleus concentration, such as that observed by *Hobbs et al.* [1971], was noted.

Two observations, however, appear to relate the enhanced ice nucleus activity to the eruption. Although the lowest nucleus concentration normally is found around midnight (August 13-14), after the eruption of August 14 the midnight count increased (August 14-15) and remained higher than the normal background for more than a week (until August 21-22). Furthermore, for the next several days the nucleus count in the daytime upslope air advected to MLO showed pronounced peaks. This pattern was observed for other eruptions and at present may be interpreted as a delayed process of ice nucleus formation in the residual smoke from the eruption, resulting from SO<sub>2</sub> decay, aerosol coagulation, etc., as suggested by *Hobbs et al.* [1971]. This appears to be as tenable a hypothesis as the one that suggests that the nuclei were advected to MLO from island cane fires.

The differing responses of the two counters are of interest. One unit, operated at a lower supersaturation, shows only a slight increase in nucleus count. The effect of supersaturation on the activation of certain types of ice nuclei was demonstrated (as was mentioned earlier) at the Second International Condensation and Ice Nucleus Workshop [Langer, 1973a].

During the 1969 eruptions the periods of high counts developed at night during downslope flow, the reverse of the presently observed pattern. This result may imply that in the 1971–1972 eruptions the haze was largely confined to the levels of the trade wind inversion. The 1969 effluent may have reached higher levels and then subsided at night. The fact that the high counts in 1969 were limited to a few periods of 10-hour duration during downslope flow indirectly supports the idea that this effluent reached above the trade wind inversion. Some of it intersected Mauna Loa and then moved on instead of being trapped in the island atmosphere. In the 1971–1972 episodes, peak nucleus counts continued for weeks in the upslope air advected to MLO. The other difference noted is that the 1969 eruptions were of short duration and the lava flowed for long distances toward the ocean from the Kilauea area at

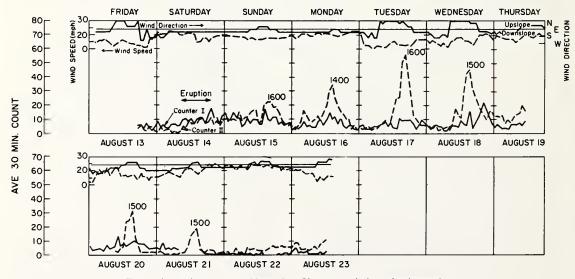


Fig. 1. Ice nucleus counts at Mauna Loa Observatory during volcanic eruption.

1200-m elevation, at times entering the water. These differences may indicate different mechanisms of incorporating the smoke into the atmosphere.

Some laboratory work was done to clarify future areas of research that may be of importance. Volcanic ice nuclei may come from smoke particles that originate from lava. The active ingredient could be copper sulfide, an active ice nucleant, which is present generally in lava but has not been identified specifically in Hawaiian lavas. To test this theory, some samples of clinker-type lava (aa) from Mauna Loa were crushed and dispersed into an NCAR ice nucleus counter at -20°C. About 1% of the particles nucleated. The material was similarly tested in the NCAR counter with a weak cloud; i.e., the humidifier was cooled to 16°C so that the moisture supply in the cloud chamber was insufficient to allow ice crystal growth. In this case the counter ceased to respond to the lava dust; i.e., the lava particles were not mistakenly counted as ice crystals. Next, dust particles generated as described above were allowed to settle on a membrane filter, counted, and then allowed to nucleate. It was found that I out of 1000 particles visible in the microscope produced ice crystals. Therefore, it would appear that lava dust has icenulleating properties.

The next logical step was to heat a lava sample in a quartz tube and test the resulting aerosol, if any, in an NCAR counter. There was no evidence of any smoke from the lava; it simply melted into a smooth structure, and no ice nuclei were noted. Fresh lava may act quite differently from reheated old material. In an eruption, fountaining produces lava aerosol particles, i.e., particles produced by mechanical disruption rather than by vaporization-condensation. Lava may burn surrounding scrub vegetation and trees and generate nuclei in that manner. Nuclei from the latter process would depend on the amount of vegetation in the path of the lava. Typical vegetation samples from the volcano surroundings were burned and the smoke sampled for ice nuclei. Only ohia-lehua branches were an active source of nuclei at -20°C.

In conclusion, the above discussion indicates that ice nuclei are potential in volcanic activity but their incorporation into atmospheric aerosols remains to be defined. Future work should include studies on the hypothesis of *Hobbs et al.* [1971] on the delayed activation of ice nuclei from smoke. Emphasis

must also be placed on air trajectory studies of the haze and aircraft sampling at varying distances from the island. Data are needed on haze activity both during eruptions and during the extended periods of quiescence between eruptions.

Acknowledgments. The continued interest and assistance of R. Hansen of the NCAR solar observatory at MLO is appreciated. R. Cadle of NCAR assisted generously in obtaining aerosol and SO<sub>2</sub> samples at MLO and helped to interpret the results

#### REFERENCES

Cadle, R. D., A. F. Wartburg, E. R. Frank, and J. P. Lodge, Particles in volcanic fumes, *Nature*, 213, 581, 1967.

Cadle, R. D., A. L. Lazrus, and J. P. Shedlovsky, Comparison of particles in the fume from eruptions of Kilauea, Mayon, and Arenal volcanos, J. Geophys. Res., 74, 3372-3378, 1969.

Droessler, E. G., and K. H. Heffernan, Ice nucleus measurements in Hawaii, J. Appl. Meteorol., 4, 442-445, 1965.

Georgii, H. W., Investigations on the deactivation of inorganic and organic freezing nuclei, Z. Angew. Math. Phys., 14, 503-510, 1963. Hobbs, P. V., C. M. Fullerton, and G. C. Bluhm, Ice nucleus storms in Hawaii, Nature, 230, 90-91, 1971.

Ishizaka, Y., On materials of solid particles contained in snow and rain water, 1, J. Meteorol. Soc. Jap., 50, 362-375, 1972.

Isono, K. M., M. Komobayashi, and A. Ono, Volcanos as a source of atmospheric ice nuclei, *Nature*, 183, 317-318, 1959.

Kline, D. B., Recent observations of freezing nuclei variations at ground level, in *Physics of Precipitation, Geophys. Monogr. Ser.*, vol. 5, edited by H. Weickmann, pp. 240-246, AGU, Washington, D.C., 1960.

Langer, G., Analysis of Second International Ice Nucleus Workshop results with emphasis on expansion chambers, NCAR counters, and membrane filters, J. Appl. Meteorol., 12, 991-999, 1973a.

Langer, G., Evaluation of NCAR ice nucleus counter, 1, Basic operation, J. Appl. Meteorol., 12, 1000-1011, 1973b.

Price, S., and J. C. Pales, Ice nucleus counts and variations at 3.4 km and near sea level in Hawaii, *Mon. Weather Rev.*, 92, 207-221, 1964.

Pueschel, R. F., and G. Langer, Sugar cane fires as a source of ice nuclei in Hawaii, J. Appl. Meteorol., 12, 549-551, 1973.

Pueschel, R. F., and B. G. Mendonca, The dispersion into the higher atmosphere of effluents during an eruption of Kilauea volcano, J. Rech. Atmos., 6, 439-446, 1972a.

Pueschel, R. F., and B. G. Mendonca, Sources of atmospheric particulate matter on Hawaii, *Tellus*, 24, 139-142, 1972b.

(Received June 22, 1973; revised September 14, 1973.)

Reprinted from Preprint Volume, Conference on Cloud Physics, Tucson, Ariz. Oct. 21-24,1974. Published by Amer. Meteor. Soc., Boston, Mass.

#### SOLUTIONS TO THE DROPLET COLLECTION EQUATION FOR POLYNOMIAL KERNELS

#### Alexis B. Long

CIRES, University of Colorado, Boulder, Colorado 80302

#### 1. INTRODUCTION

Satisfactory inclusion of droplet collision and coalescence in a theoretical cloud model requires knowing their effect on the spectral distribution function n(x,t)dx. This gives at time t the mean number density of droplets with individual volumes x to x+dx. n(x,t) is obtained by solving a scalar transport "collection" equation of the form

$$\frac{\partial n}{\partial t} \frac{(x,t)}{\partial t} = \int_{0}^{x/2} n(x-y,t) K(x-y,y) n(y,t) dy$$

$$- n(x,t) \int_{0}^{\infty} K(x,y) n(y,t) dy.$$
(1)

The stochastic nature of the droplet collection process enters (1) through the collection kernel K(x,y). This quantity is related to the probability that in a given interval of time there will be in a cloud a collection event involving two particular droplets of volumes x and y.

Solutions to (1) have been either numerical or analytic depending upon the form of K(x,y). Numerical solutions have been based upon a gravitational collection mechanism, for which the kernel is

where R(x) is the radius of the larger (spherical) collector droplet, and r(y) is the radius of the smaller collected droplet; E(x,y) is the collection efficiency of the two droplets and is given by the product of their collision efficiency 
$$E_C(x,y)$$
 and coalescence efficiency  $E_C(x,y)$ ; V is the droplet terminal fall velocity. Analytic solutions to (1) have been obtained, principally by Scott (1968) and Drake and Wright (1972) for ap-

- (**)// **		(/
P(x,y) = B(x+y)		(3Ъ)
P(x,y) = Cxy		(3c)
P(x,y) = A + B(x+y)		(3d)
P(x,y) = B(x+y) + Cxy	•	(3e)
P(x,y) = A + B(x+y) + Cxy	$(A = B^2/C).$	(3f)

proximations to K given by the polynomials

This paper examines how well these and certain other polynomials approximate K(x,y) and how well solutions to (1) based on them correspond to numerical solutions based on K. A close correspondence would justify replacing the numerical solutions by analytic solutions based on the polynomials.

Numerical solutions to (1) have a limited utility, especially if combined with the predictions of other cloud physical equations into an overall description or model of a cloud. We note,

for instance, that the numerical computation time required to obtain n(x,t) throughout a cloud model will be prohibitive since it equals the time required at any point in the model (~0.1-10% real time) multiplied by the number of its grid points (~10 $^3$ -10 $^6$ ).

These drawbacks to numerical solutions have led to alternative methods for solving (1). Bleck (1970) has developed an approximate numerical method for solving (1) which is supposed to require less computer time than a direct numerical solution. It is doubtful, however, whether the solutions obtained are accurate descriptions of droplet growth, especially in the "tail" of the distribution where we find those large drops which are all-important in the development of precipitation. Drake (1972) has discussed a method for solving (1) by expressing n(x,t) in terms of its statistical moments  $M_1(t)$ , i = 0,1,2,... This, in principle, yields a closed expression for n(x,t) even for a kernel as complicated as that in (2), once the time-dependence of a number of the moments is obtained. The number of moments required to reproduce the distribution is not known. but for an accurate description of the tail region it may be so high as to require the moments to be obtained numerically. This takes us back to the computational problems associated with numerical solutions to (1).

Up to now analytic solutions to (1) have not been proposed as possible replacements to numerical solutions because the "polynomial" kernels in (3) for which they are valid do not seem close approximations to the actual kernel. Nevertheless, these analytic solutions are all algebraic functions of x and t and are simply evaluated by performing certain straightforward sums. This suggests they might be usefully incorporated into cloud models, provided they correspond closely with numerical solutions.

This paper examines whether there is a close correspondence. First, we determine how well each polynomial P(x,y) in (3) matches K(x,y) in (2). We obtain those values of the coefficients A, B and C which minimize the deviation (defined in a certain sense) between K and the respective polynomial P. Comparing this minimum deviation for the various polynomials will tell us which are closest to the actual kernel and most likely to lead to realistic analytic solutions to (1) as compared to actual, numerical solutions. Numerical integration of (1), using in place of K the best polynomials in (3), will show how realistic these solutions are.

Certain polynomials other than those in (3) are also considered. These turn out to be closer to K, and it will be suggested that analytic solutions to (1) be sought for them.

#### 2. EVALUATION OF K(x,y)

The first step in obtaining the coefficients A, B and C in the polynomials P(x,y) is to evaluate the actual kernel K(x,y) in (2).

The collision efficiency for any droplet pair is computed using interpolation and extrapolation techniques from the efficiencies for particular droplet pairs calculated by Shafrir and Gal-Chen (1971) and by Klett and Davis (1973).

The coalescence efficiency is taken as unity because present knowledge of it is still uncertain and covers only a limited range of droplet pairs.

The terminal velocity is evaluated using the approximate formula developed by Long and Manton (1974). This formula is based on the data of Gunn and Kinzer (1949) and Beard and Pruppacher (1969) for 1013 mb and 20C atmospheric conditions. The formula is corrected for altitude because the collision efficiencies of Klett and Davis and Shafrir and Gal-Chen are for 900 mb, OC conditions.

Figure 1 displays representative values of the collection kernel evaluated in the above manner.

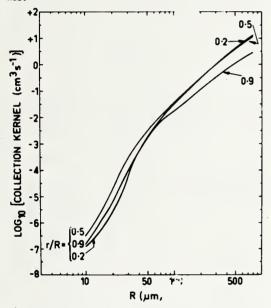


Figure 1. Actual droplet collection kernel K(x,y).

In judging how well the various polynomials approximate K(x,y) it will be useful to have estimates of its x- and y-dependence. From the collision efficiencies and terminal velocities referred to above it can be shown (see Long (1974)) that  $K(x,y) \approx 9 \times 10^9 [x^{1/3} + y^{1/3}]^2 [x^{2/3} (1 - k_1 y^{-1/3})] [x^{2/3} - y^{2/3}]$ 

$$K(x,y) \approx 9 \times 10^9 [x^{1/3} + y^{1/3}]^2 [x^{2/3} (1 - k_1 y^{-1/3})] [x^{2/3} - y^{2/3}]$$
(4)

for  $R \lesssim 50 \mu m$ ,

where  $k_1 \approx 4.8 \times 10^{-4} \text{cm}$ , and  $K(x,y) \approx 6.4 \times 10^3 \left[ x^{1/3} + y^{1/3} \right]^2 \left[ x^{1/3} - k_2 y^{\Omega/3} \right]$  (5) for 50 µm  $\lesssim R \lesssim 400$  µm.

In (5) the quantities  $k_2$  and  $\alpha$  are both approximately unity for  $r\gtrsim 50~\mu m$ , but for smaller r they are approximately  $80~cm^{-1}$  and 2, respectively. Eqs. (4) and (5) show that K increases roughly as  $x^2$  for small droplets and as x for larger ones. K increases less strongly with y and, in fact, decreases as y approaches x. Coefficients of y and

 $y^2$  in a polynomial approximating K should thus be smaller than those for x and  $x^2$ . It can thus be expected that even if the deviation between K(x,y) and the symmetric polynomials in (3) is minimized by optimizing their coefficients, this minimum will only be relative, compared to that attainable with unrestricted (not symmetric) coefficients. For this reason we have here also approximated K(x,y) by polynomials with independent coefficients. Perhaps analytic solutions to (1) may some day be found for them.

#### 3. OBTAINING THE APPROXIMATING POLYNOMIALS

There have been two previous determinations of the coefficients A, B and C in (3). Golovin (1963) evaluated the quotient K(x,y)/(x+y), found it held fairly constant at a value  $B\approx 6000~{\rm s}^{-1}$  for a wide range of R  $\gtrsim 50~{\rm \mu m}$ , and concluded that for these droplets B(x+y) is a reasonable approximation to K(x,y). For smaller R, the technique (Scott, 1968) has been to require the coefficients in any approximating polynomial to be such that it coincides with K for R = 30  ${\rm \mu m}$  and r = 10  ${\rm \mu m}$ .

The coefficients in each approximating polynomial are here obtained by requiring that the rms deviation D(P;K) between the logarithm of P(x,y) and the logarithm of K(x,y) be a minimum. In particular it is required that

$$D(P;K) \equiv \left[ \frac{\int_{S} \int [\ell n P(x,y) - \ell n K(x,y)]^{2} d(\ell n y) d(\ell n x)}{\int_{S} \int d(\ell n y) d(\ell n x)} \right]_{(6)}^{1/2}$$

be a minimum.

The integration domain S will depend on when in the history of a droplet population the polynomial P(x,y) is approximating K(x,y). Inasmuch as P(x,y) is limited in how well it approximates K(x,y) it seems advisable when obtaining a solution to (1) based on P(x,y) to use for small t when all droplets are small a version of the polynomial fitted to values of the kernel for these droplets alone, and to use for longer t when there are more large droplets a version of the polynomial taking more into account their kernel. Figure 2 displays the five domains S used here over which distinct versions of each polynomial P(x,y) are fitted to K(x,y). For small t the solutions to (1) are based on the domain I version of P(x,y), but as time passes and large droplets are created the solutions are based on versions for domains II, III, ....

The criterion for changing from one version of P to the next derives from the requirement that the solution to (1) give a good description of the size of the 100th-largest drop per cubic meter of cloud. Since there are around 100 drops per cubic meter in moderate rain, the size of the smallest of these,  $x_{100}(t)$ , will tell us how fast precipitation is being produced by collision and coalescence. Furthermore, because the larger drops have the greatest effect on the entire distribution, accurate knowledge of their sizes will in turn improve the overall solution to (1). Since the 100th-largest drop grows approximately continuously, at the rate

$$\frac{dx_{100}(t)}{dt} = \int_{0}^{x_{100}(t)} yP[x_{100}(t), y]n(y, t)dy, \qquad (7)$$

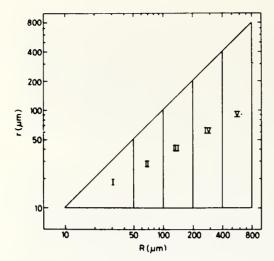


Figure 2. The five droplet pair domains over which the polynomials P(x,y) approximate the collection kernel K(x,y). Domain I is as outlined, domain II includes domain I plus the additional area denoted by the roman numeral II, domain III includes domain II plus the additional area denoted by the roman numeral III, etc.

it will be best described if we change from that version of P(x,y) for one domain to that for the next as  $x_{100}(t)$  grows from the one domain into the next. This is the procedure followed here.

Each polynomial P(x,y) is fitted to K(x,y) as follows. Because P(x,y) can be written as

$$P(x,y) = \sum_{\substack{m=0\\n=0}}^{\infty} c_{mn} x^{m} y^{n}$$
(8)

the condition that it minimize D(P;K) and the additional stipulation that it have x-y symmetry like the polynomials in (3) together imply that any potentially non-zero coefficients  $C_{mn}$  satisfy

$$\frac{\partial D(P;K)}{\partial C_{mn}} + \frac{\partial D(P;K)}{\partial C_{nm}} = 0, \qquad m \neq n$$
 (9a)

$$\frac{\partial D(P;K)}{\partial C_{mm}} = 0. {(9b)}$$

The potentially non-zero coefficients would be A, B, and C in (3).

Applying (9a) and (9b) to (6) and using (8) yields

$$C_{mn} = \exp \frac{\int_{S} \frac{x^{m}y^{n} + x^{n}y^{m}}{P(x,y)} \ln \left[ \frac{K(x,y)}{P_{mn}(x,y)} \right] d(\ln y) d(\ln x)}{\int_{S} \frac{x^{m}y^{n} + x^{n}y^{m}}{P(x,y)} d(\ln y) d(\ln x)}$$
(10a)

$$C_{mm} = \exp \frac{\int_{S} \int \frac{x^{m}y^{m}}{P(x,y)} \ln \left[\frac{K(x,y)}{P_{mm}(x,y)}\right] d(\ln y) d(\ln x)}{\int_{S} \int \frac{x^{m}y^{m}}{P(x,y)} d(\ln y) d(\ln x)}$$
(10b)

The polynomial  $P_{mn}(x,y)$  in Eqs. (10) is defined by

$$P_{mn}(x,y) = P(x,y)/C_{mn}$$

If x-y symmetry is not required or if symmetry is retained but the polynomial in Eq. (3f) is fitted to K, then in place of (10a) and (10b) there will appear other equations.

In using Eqs. (10) to evaluate each coefficient  $C_{mn}$  an iterative procedure is followed. Beginning with estimates for all of the potentially non-zero coefficients in the polynomial, the right-hand sides of (10a) and (10b) are numerically evaluated for all values of m and n corresponding to the non-zero coefficients. The new estimates obtained for each  $C_{mn}$  are then used to re-evaluate the right-hand sides of (10a) and (10b) to obtain another estimate for each coefficient. Iteration continues until each coefficient is stationary to at least three significant figures. D(P;K) is at the same time observed and is found to decrease rapidly to a stationary value.

The starting estimate for each coefficient  $C_{mn}$  (or  $C_{mm}$ ) in P(x,y) is obtained from the requirement that the factor  $C_{mn}x^my^n + C_{nm}x^ny^m$  (or  $C_{mm}x^my^n$ ) when evaluated for  $R=30~\mu m$  and  $r=10~\mu m$  be equal to the fraction (1/N) times the actual value of the kernel for these two droplets. The integer N is chosen equal to the number of distinct coefficients in P(x,y) that are initially assumed to be non-zero (e.g., N = 2 in (3e)).

#### 4. THE APPROXIMATING POLYNOMIALS

Tables 1 and 2 display the approximating polynomials for domains I to V.  $\label{eq:continuous} % \begin{array}{c} T_{i}(t) & T_{i}(t) \\ T_{i}$ 

a. Symmetric volume polynomials
The first five polynomials in Table 1 are
those for which (1) can presently be solved analytically. Approximating polynomials of degrees
2, 3, 4, and 5 also were considered, and it was
found that they all converge to the sixth polynomial in Table 1 of degree 2. Third-, fourth-, and
fifth-degree terms evidently play an insignificant
role in an approximation to the collection kernel,
if domains as large as those considered here are
used.

The parenthetical numbers in Table 1 give exp[D(P;K)] for each polynomial. The figure (4.8) for example means that over the indicated domain there is a 480% rms deviation between P(x,y) and K(x,y). The significance of an error of such magnitude cannot really be assessed without comparing solutions to (1) based on P with those based on K. Section 5 will make this comparison, but an error of a few hundred per cent may not be important since Figure 1 indicates about a 1000% variation in K itself for a fixed R and varying r.

The results in Table 1 are consistent with our discussion in section 2 of the x-dependence expected for K. Polynomial 6 increases with  $\mathbf{x}^2$  for small droplets; as the approximation domain includes larger droplets it increases more as the first power of x. Similarly, the coefficient B for the linear terms in polynomials 4 and 5 increases relative to A and C as the approximation domain includes larger droplets. For domain I the coefficient  $\mathbf{C}_{20}$  in polynomial 6 is similar to the prefactor in Eq. (4). For large domains B in

polynomials 2 and 5 is similar to the prefactor in Eq. (5). B is smaller for the polynomials, however, because each allows for collector droplets smaller than 50 µm.

TABLE 1. Six symmetric polynomials P(x,y) approximating the actual collection kernel K(x,y)

	pproximating	Coefficients minimizing D(P;K) for each droplet pair domain						Units of	
	polynomial, P(x,y)	I		II III		IV	v	coefficient	
1	A	A	= 1.20 x 10 <sup>-4</sup> (12)	1.10 x 10 <sup>-3</sup> (17)	6.46 x 10 <sup>-3</sup> (22)	3.14 x 10 <sup>-2</sup> (28)	1.35 x 10 <sup>-1</sup> (38)	cm <sup>3</sup> s <sup>-1</sup>	
2	A+B(x+y)	A B	= 0 = 8.83 x $10^2$ (4.8)	$0$ 2.15 x $10^3$ (4.2)	$0$ 3.28 x $10^3$ (3.4)	0 $4.10 \times 10^3$ $(2.9)$	$04.48 \times 10^3$ (2.6)	cm <sup>3</sup> s <sup>-1</sup>	
3	Сжу	С	$= 5.49 \times 10^{10}$ (4.7)	6.27 x 10 <sup>10</sup> (5.3)	4.60 x 10 <sup>10</sup> (7.7)	2.80 x 10 <sup>10</sup> (13)	1.50 x 10 <sup>10</sup> (22)	cm <sup>-3</sup> s <sup>-1</sup>	
4	A+B(x+y)+Cxy $(A = B2/C)$	A B C	= $4.41 \times 10^{-7}$ = $1.36 \times 10^{2}$ = $4.18 \times 10^{10}$ (4.6)	$7.75 \times 10^{-6}$ $5.05 \times 10^{2}$ $3.29 \times 10^{10}$ (4.8)	$6.93 \times 10^{-5}$ $9.51 \times 10^{2}$ $1.30 \times 10^{10}$ (5.6)	$4.07 \times 10^{-4}$ $1.23 \times 10^{3}$ $3.70 \times 10^{9}$ (6.7)	2.55 x 10 <sup>-3</sup> 1.45 x 10 <sup>3</sup> 8.23 x 10 <sup>8</sup> (8.3)	cm <sup>3</sup> s <sup>-1</sup> s <sup>-1</sup> cm <sup>-3</sup> s <sup>-1</sup>	
5	A+B(x+y)+Cxy	A B C	= 0 = 4.16 x 10 <sup>2</sup> = 2.24 x 10 <sup>10</sup> (4.5)	0 1.62 x 10 <sup>3</sup> 6.33 x 10 <sup>9</sup> (4.0)	0 3.24 x 10 <sup>3</sup> 8.80 x 10 <sup>7</sup> (3.4)	0 4.10 x 10 <sup>3</sup> 0 (2.9)	0 4.48 x 10 <sup>3</sup> 0 (2.6)	cm <sup>3</sup> s <sup>-1</sup> s <sup>-1</sup> cm <sup>-3</sup> s <sup>-1</sup>	
6	$\sum_{m,n=0}^{2} C_{mn} x^{m} y^{n}$	C <sub>0</sub> 1	a = 0 $a = C_{10}$ $a = 9.44 \times 10^{9}$ $a = C_{20}$ $a = C_{20}$	3.46 x 10 <sup>1</sup> C <sub>10</sub> 5.28 x 10 <sup>9</sup> C <sub>20</sub> (2.4)	1.42 x 10 <sup>3</sup> C <sub>10</sub> 5.05 x 10 <sup>8</sup> C <sub>20</sub> (2.9)	$3.04 \times 10^{3}$ $C_{10}$ $3.33 \times 10^{7}$ $C_{20}$ $(2.8)$	$4.04 \times 10^{3}$ $C_{10}$ $1.70 \times 10^{6}$ $C_{20}$ $(2.6)$	s <sup>-1</sup> s <sup>-1</sup> cm <sup>-3</sup> s <sup>-1</sup>	

For polynomial 6 those coefficient values not explicitly included in Table 1 were found to converge rapidly toward zero. The parenthetical numbers give exp[D(P;K)] for each polynomial-domain combination. For example, for polynomial 1 - domain I the figure (12) means that throughout domain I polynomial 1 is in rms terms within a factor of 12 of the actual kernel.

TABLE 2. Three polynomials P(x,y) approximating the actual collection kernel K(x,y)

Approximating polynomial.	Coefficients minimizing D(P;K) for each droplet pair domain					Units of	
P(x,y)	I	II III		IV V		coefficient	
1 A+B <sub>1</sub> x+B <sub>2</sub> y	$ \begin{array}{rcl} A & = 0 \\ B_1 & = 1.15 \times 10^3 \\ B_2 & = 0 \\ & (4.1) \end{array} $	0 2.63 x 10 <sup>3</sup> 0 (3.6)	0 3.86 x 10 <sup>3</sup> 0 (3.0)	0 4.68 x 10 <sup>3</sup> 0 (2.6)	0 5.02 x 10 <sup>3</sup> 0 (2.3)	cm³ s- s-	
2 A+B <sub>1</sub> x+B <sub>2</sub> y+Cxy	A = 0  B1 = 7.91 x 102  B2 = 0  C = 1.10 x 1010  (4.0)	0 2.06 x 10 <sup>3</sup> 0 4.86 x 10 <sup>9</sup> (3.5)	0 3.73 x 10 <sup>3</sup> 0 1.78 x 10 <sup>8</sup> (3.0)	0 4.68 x 10 <sup>3</sup> 0 0 (2.6)	0 5.02 x 10 <sup>3</sup> 0 0 (2.3)	cm <sup>3</sup> s- s- cm <sup>-3</sup> s-	
$\begin{array}{ccc} & & & & \\ \Sigma & & & \\ & & & \\ m, & & & \\ \end{array} \qquad \begin{array}{ccc} & & & \\ & & & \\ & & & \\ \end{array} \qquad \begin{array}{cccc} & & & \\ & & & \\ & & & \\ \end{array} \qquad \begin{array}{cccc} & & & \\ & & & \\ & & & \\ \end{array} \qquad \begin{array}{ccccc} & & & \\ & & & \\ & & & \\ \end{array} \qquad \begin{array}{ccccc} & & & \\ & & & \\ & & & \\ \end{array} \qquad \begin{array}{ccccc} & & & \\ & & & \\ & & & \\ \end{array} \qquad \begin{array}{cccccc} & & & \\ & & & \\ & & & \\ \end{array} \qquad \begin{array}{ccccccccccccccccccccccccccccccccccc$	$C_{10} = 0$ $C_{20} = 1.10 \times 10^{10}$ $(1.9)$	1.17 x 10 <sup>2</sup> 5.39 x 10 <sup>9</sup> (2.2)	1.93 x 10 <sup>3</sup> 4.57 x 10 <sup>8</sup> (2.6)	$3.67 \times 10^3$ $2.91 \times 10^7$ (2.5)	$4.67 \times 10^3$ $1.26 \times 10^6$ (2.3)	cm <sup>-3</sup> s <sup>-3</sup>	

For polynomial 3 those coefficient values not explicitly included in Table 2 were found to converge rapidly toward zero.

Focusing on polynomial 2, one of the better kernel-approximations in Table 1, we note that A+B(x+y) in Eq. (3d) fits K(x,y) best when A is zero. Thus, no improvement to the B(x+y) approximation (in Eq. (3b)) is obtained by adding to it a non-zero constant factor. This is expected since the dominant power of x in any domain considered here lies between  $x^1$  and  $x^2$  and not between  $x^0$  and  $x^1$ . Table 1 shows how B(x+y) varies with approximation domain and indicates that Scott's (1968) choice for B of 1.56 x  $10^3$  s<sup>-1</sup> happens to be appropriate for a domain intermediate to I and II. Figure 3 indicates that for each domain B is smaller than the value of 6000 s<sup>-1</sup> proposed by Golovin (1963a). This is because here smaller collector droplets (R<50  $\mu$ m) are also taken into account.

Of all those polynomials in Eqs. (3) for which analytic solutions to (1) exist polynomial 5 is closest to the actual kernel, at least for domains I, II, and III. For domains IV and V it is equalled by B(x+y)

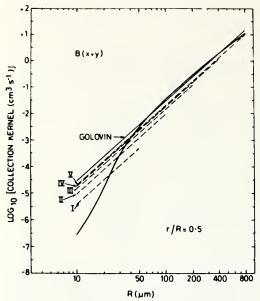


Figure 3. Comparison of the approximating polynomial B(x+y) and the actual collection kernel K(x,y). Heavy solid line denotes the actual kernel. Light solid line denotes B(x+y) as proposed by Golovin (1963a). Dashed lines denote polynomial determined in this paper and labelled according to domain of approximation.

as the best polynomial. Analytic solutions to (1) based on polynomial 5 should be the most realistic.

Polynomial 6 in Table 1, second degree in x and in y, improves upon the others, most dramatically for domains I, II, and III. Figure 4 shows the relative extent to which it and polynomials 1 and 5, of degree 0 and 1 respectively, approximate K(x,y).

b. Volume polynomials

Table 1 indicates y plays the same role as x in any polynomial approximating K(x,y). This is only because of the imposed x-y symmetry. Section 3 showed that the smaller droplet actually has a secondary influence on the kernel and suggested that a better approximation to K(x,y) should result if symmetry is not required. Removing x-y symmetry led to the polynomials in Table 2. In every case they approximate K(x,y) better than their counterparts (2, 5, and 6) in Table 1.

This does not imply no y-dependence in the kernel but simply indicates that on the scale of the approximation domains used here and to within the resolution provided by integer powers of x and y, the behavior of K(x,y) is determined only by the size of the larger, collector droplet. This is not surprising, since Figure 1 indicates the kernel changes by several orders of magnitude as x varies over its natural range but changes by only about one order of magnitude as y varies over its range.

c. Piecewise approximations to K

Figures 3 and 4 indicate K(x,y) may be closely approximated by two separate polynomials, one for domain I where K behaves as x<sup>2</sup> and another for that portion of domain V exterior to domain I where it behaves as x. Polynomial 6 in Table 1

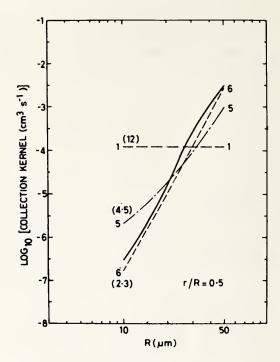


Figure 4. Comparison for domain I of the actual kernel and the polynomials 1, 5, and 6 in Table 1 of orders 0, 1, and 2, respectively. Parenthetically attached to each graph is its rms deviation exp[D(P;K)] from the actual kernel.

or polynomial 3 in Table 2 can serve as the domair I approximation. The Golovin polynomial would be suitable for the larger droplets but can be improved slightly using the techniques of Section 3. The following two piecewise approximations to K have been obtained.

 $P(x,y)=9.44x10^{9}(x^{2}+y^{2}); exp[D(P;K)]=2.3 \text{ for } R \le 50\mu\text{m}$ (11a)

 $P(x,y)=5.78x10^{3}(x+y)$ ; exp[D(P;K)]=1.6 for R>50µm (11b)

ıd

 $P(x,y)=1.10x10^{10}x^2$ ; exp[D(P;K)]=1.9 for  $R \le 50 \mu m$  (12a)

 $P(x,y)=6.33x10^3x$  ; exp[D(P;K)]=1.4 for R>50 $\mu$ m (12b)

The approximation in (11) is displayed in Figure 5. Whether the collection equation can be solved analytically using these piecewise approximations is an open question because some of the mathematical techniques heretofore used are not applicable. Nevertheless, the small values of exp[D(P;K)] for both approximations indicate the merit in searching for such solutions.

#### 5. SOLUTIONS TO THE COLLECTION EQUATION

Solutions to (1) have been obtained using several of the better approximations in Tables 1 and 2. This section compares these solutions with those based on the actual kernel in (2). The polynomials used are 2, 5, and 6 in Table 1, all those in Table 2, and those in Eqs. (11) and

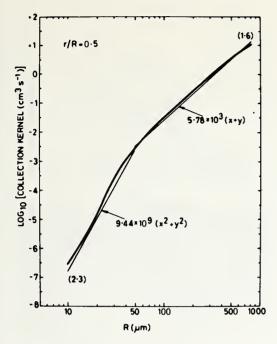


Figure 5. Comparison of the approximating polynomial in (11) and the actual kernel. The parenthetical numbers give  $\exp[D(P;K)]$  for the two parts of the polynomial, fitted over domain I and over that portion of domain V exterior to domain I. (12). Analytic solutions to (1) have been found to date only for 2 and 5 in Table 1. The remaining polynomials more closely approximate K(x,y), however, and on the basis of the results in this section it will be suggested that analytic solutions be sought for some of them.

The collection equation is solved by numerical integration in every case inasmuch as analytic solutions exist for only two of the polynomials. As already stated, when solving (1) using any given polynomial (except (11) and (12)) we change from one version to the next according to the size of the 100th-largest drop. When using polynomials 6 in Table 1 and 3 in Table 2, liquid water was not conserved in the maritime cloud after about 350 s and in the continental cloud after about 650 s. These polynomials thus yield valid solutions to (1) only in the early stages of a cloud's evolution. This is due to the presence in these polynomials of an xy term predicting too rapid growth for the large cloud drops. The result is a solution which becomes meaningless after a given time (see Long (1974)). Even though the domain I versions of polynomials 6 and 3 are partly incorporated in (11) and (12), for these approximations liquid water is conserved at all times. This is because (11) and (12) better describe the kernel at large droplet sizes.

In each case the initial distribution has the well-known form

$$n(x,t_0) = \frac{N^2(t_0)}{L} \frac{(v+1)^{V} + 1}{\Gamma(v+1)} \left[ \frac{x}{x_0} \right]^{V} e^{-(v+1)x/x_0}$$
(13)

In (13)  $N(t_0)$  is the initial number density of droplets of all sizes and equals 50 cm<sup>-3</sup> (maritime clouds) or 200 cm<sup>-3</sup> (continental clouds). L is the liquid water content of all the droplets taken

together and equals  $10^{-6}~\text{cm}^3$  of water per cubic centimeter of air. The parameter  $\nu$  is given '…

$$v = p_x^{-2} - 1,$$

where  $D_X$  is the relative dispersion in x. A value of  $\nu$  = 2 is used here, for which  $D_X \approx 0.58$  and  $D_T \approx 0.20$ .

#### . Continental cloud

Figures 6-8 show how the distribution of liquid water among the droplets,  $g(2nR,t)\equiv 3x^2n(x,t)$ , changes with time and how the 100th-largest drop grows. There is little meaningful difference between predictions based on the symmetric polynomials in Table 1 and Eq. (11) and on their slightly better counterparts in Table 2 and Eq. (12). There is a significant difference, which is now discussed, between the predictions based on the linear polynomials and those containing an xy term and the predictions based on (11), (12) and the polynomials having  $x^2$  terms.

The linear polynomials and those containing xy predict a general collapse of the distribution into a smaller number of larger droplets. This occurs because these polynomials are 10-20 times too large at just those radii (~10 µm) where most cloud droplets are initially located (cf. Figs. 3, 4, and 6). Following the initial collapse, the distribution moves to the right and for some time maintains a tail extending beyond that of the actual distribution (see Fig. 8). Eventually, however, the predicted kernel for the droplets in the tail becomes smaller than the actual kernel (see Figs. 3 and 4), their growth rate is slowed compared to the droplets in the tail of the actual distribution, and these droplets become as large.

distribution, and these droplets become as large.

The polynomials containing x<sup>2</sup> and the approximations in (11) and (12), on the other hand, predict a liquid water distribution remarkably similar to the actual distribution. This can be attributed to the much better approximation to K in domain I where all the droplets initially lie. The development of the distribution is thus not biased by an initial collapse and instead proceeds in the expected manner. The initial peak in the distribution slowly decreases, a tail is formed toward the larger sizes, and there is only a few minutes' difference in the time needed for  $R_{100}(t)$  to equal 100 um, the size of a fine drizzle droplet. similarities exist even though there is a 100-150% error in the approximations in domain I and a 40-60% error for larger droplets. A breakdown of K(x,y) into quadratic and linear parts apparently retains most of the physics originally contained in the collision efficiencies and terminal velocities.

#### b. Maritime cloud

Figure 9 shows, for this cloud and for the linear polynomials and those containing xy, a smaller relative collapse of the spectrum. This is expected because, first, there are now fewer droplets initially, thus fewer collection events, and second, the droplets that do exist initially are located around 18 µm, where the polynomials are less in error (see Figs. 3 and 4).

As in the continental cloud there is a better correspondence between the actual distribution and that predicted by the polynomials in (11) and (12). The second maximum in  $g(\ln R)$  appears for the approximating polynomials as well (Fig. 10) and the 100th-largest drop takes only 10-15% longer to reach any given size (Figure 11). Once again, an  $x^2$ -(small collector droplet) and x-(large collector droplet) dependence in K describes its essential features.

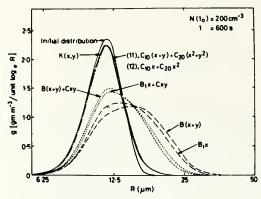


Figure 6. Liquid water distribution at 600 sec in a typical continental cloud, as predicted by the actual collection kernel K(x,y) in (2) and as predicted by various polynomials approximating K.

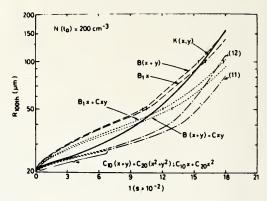


Figure 8. The radius of the 100th-largest droplet per cubic meter of a typical continental cloud, as predicted by the actual collection kernel K(x,y) in (2) and as predicted by various polynomials approximating K. Vertical strokes on graphs denote the time when a change is made from one version of a polynomial to the next. Braces show period of validity of results (short-dashed lines) obtained using the indicated polynomials. These results are here virtually identical to those obtained using (11) and (12).

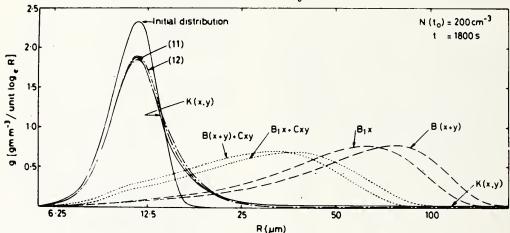


Figure 7. As in Figure 6 except at 1800 sec.

#### 6. CONCLUSIONS

Numerical solutions to the droplet collection equation, using certain polynomial approximations to the gravitational collection kernel, have been examined to learn whether they usefully describe the evolution of a cloud droplet distribution. The results for typical continental and maritime clouds (Figs. 6-11) show that the distribution is closely described if the actual kernel K(x,v) is replaced by

9.44 x  $10^9$  ( $x^2+y^2$ ),  $R \le 50$  µm; 5.78 x  $10^3$  (x+y), R > 50 µm (see Eq. (11) and Fig. 5) or by

1.10 x 10  $^{10}$  x  $^2$  ,  $R \leqslant 50~\mu m$  ; 6.33 x 10  $^3$  x,  $R > 50~\mu m$ 

(see Eq. (12)). R is the radius of the larger droplet, x is its volume in cubic cendineters, and y is the volume of the smaller droplet.

From the standpoint of including droplet collection in multi-dimensional cloud models, an analytic solution to the collection equation is desirable. An attempt should be made to find such solutions based upon either of the above approximations. If these cannot be found because of the piecewir nature of the approximations, then solutions based on the portions for  $R \leqslant 50~\mu m$  still would describe the first few hundred seconds of droplet growth. A comparatively poor description of the droplet distribution comes from the most physically realistic analytic solution presently existing, based on the kernel approximation B(x+y)+Cxy.

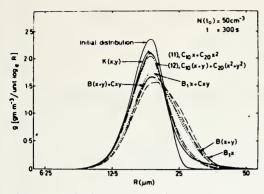


Figure 9. Liquid water distribution at 300 sec in a typical maritime cloud, as predicted by the actual collection kernel K(x,y) in (2) and as predicted by various polynomials approximating K.

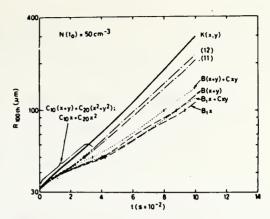


Figure 11. The radius of the 100th-largest dro let per cubic meter of a typical maritime clou. Legend is otherwise identical to that in Fig. c.

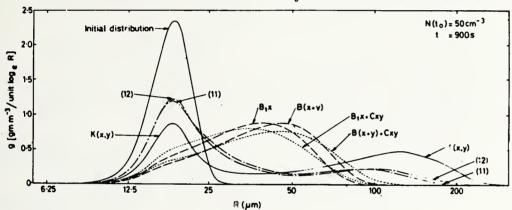


Figure 10. As in Figure 9 except at 900 sec.

Acknowledgments. The research reported here was initially supported at CSIRO, Division of Cloud Physics, by a National Science Foundation Postdoctoral Fellowship.

#### REFERENCES

Beard, K.V., and H.R. Pruppacher, 1969: A determination of the terminal velocity and drag of small water drops by means of a wind tunnel. J. Atmos. Sci., 26, 1066-1072.

Bleck, R., 1970: A fast, approximative method for integrating the stochastic coalescence equation.

J. Geophys. Res., 75, 5165-5171.

Drake, R.L., 1972: The scalar transport equation of coalescence theory: Moments and kernels.

J. Atmos. Sci., 29, 537-547. , and T.J. Wright, 1972: The scalar transport equation of coalescence theory: New families of

exact solutions. J. Atmos. Sci., 29, 548-556.
Golovin, A.M., 1963: The solution of the coagulation equation for cloud droplets in a rising air current. Bull. Acad. Sci. USSR, Geophys. Ser., No. 5, 482-487.
Gunn, R., and G.D. Kinzer, 1949: The terminal velocity of fall for water droplets in stagnant air.

J. Meteor., 6, 243-248.

Klett, J.D., and M.H. Davis, 1973: Theoretical collision efficiencies of cloud droplets at small Rey-

droplets. J. Atmos. Sci., 31, 1053-1057.
Scott, W.T., 1968: Analytic studies of cloud droplet coalescence. I. J. Atmos. Sci., 25, 54-65.

Shafrir, U., and T. Gal-Chen, 1971: A numerical study of collision efficiencies and coalescence parameters for droplet pairs with radii up to 300 microns. J. Atmos. Sci., 28, 741-751.

#### Surface Layer and Energy Budget Parameterizations for Mesoscale Models

EVERETT C. NICKERSON<sup>1</sup> AND VIRGINIA E. SMILEY

Environmental Protection Agency, Meteorology Laboratory, Research Triangle Park, N. C. 27711 (Manuscript received 15 October 1974, in revised form 9 December 1974)

#### ABSTRACT

A transcendental equation is presented for the Monin-Obukhov length L based upon (i) the Businger-Dyer surface layer formulations, (ii) parameterizations of the moisture flux, ground storage, and radiation terms in the surface energy budget; and (iii) the wind and temperature at 10 m above a surface characterized by a roughness length zo. The surface temperature, friction velocity and sensible heat flux are obtained from the computed value of L.

#### 1. Introduction

Horizontal inhomogeneities in surface roughness, temperature and heat flux can lead to significant perturbations in an undisturbed air flow. An understanding of the meteorological effects of these varying surface conditions or "urban fabric" (Myrup and Morgan, 1972) is necessary to improve the simulation of transport and dispersion of pollutants, especially for periods of light wind, or for morning and evening hours when significant changes occur in the mixing depth. One-dimensional models such as those of Estoque (1963) and Sasomori (1970) provide insight into the effects of those varying conditions on the structure of the atmospheric boundary layer as it progresses through a diurnal cycle. Knowledge gained from urban field experiments (McElroy, 1973) can improve parameterization of the important physical processes in one-dimensional models. In the following section, we present such a parameterization procedure that may be used to incorporate physical processes at the earth's surface into a mesoscale model.

#### 2. Sensible heat flux

Deardorff (1972) used an integrated form of the Businger-Dyer equations (Businger et al., 1971) given by Paulson (1970) to specify the vertical variation of wind and temperature within the surface layer. The wind and temperature profiles for the unstable case were expressed in a form that is especially convenient for examining the effects of departures from neutral stability:

$$\frac{ku}{u_*} = \ln\left(\frac{z}{z_0}\right) - \left[\ln\left(\frac{1+\zeta^2}{2}\right) + 2\ln\left(\frac{1+\zeta}{2}\right) - 2\tan^{-1}\zeta + \frac{\pi}{2}\right], \quad (1)$$

$$kF = \ln\left[\frac{(\zeta-1)(\zeta_0+1)}{(\zeta+1)(\zeta_0-1)}\right] + 2\left[\tan^{-1}\zeta - \tan^{-1}\zeta_0\right],$$

$$kF = \ln\left[\frac{(\gamma-1)(\gamma_0+1)}{(\gamma-1)(\gamma_0+1)}\right] + 2\left[\tan^{-1}\zeta - \tan^{-1}\zeta_0\right],$$

$$\frac{(\theta - \theta_0)u_*k}{(\overline{-w'\theta'})_0R} = \ln\left(\frac{z}{z_0}\right) - 2\ln\left(\frac{1 + \eta^2}{2}\right),\tag{2}$$

$$\zeta = \left(1 - \frac{\gamma z}{L}\right)^{\frac{1}{4}}$$
 and  $\eta = \left(1 - \frac{\gamma''z}{L}\right)^{\frac{1}{4}}$ ,

and  $\gamma$ ,  $\gamma''$ , k, R are constants. We have followed Deardorff (1972) and used the values  $\gamma = 15$ ,  $\gamma'' = 9$ , k=0.35, R=0.74.

Eqs. (1) and (2) involve the approximation of an integral between  $z_0$  and z (where  $z_0$  is the surface roughness) by an integral from 0 to z. In most situations, the resulting error caused by the approximate treatment of the lower boundary condition is negligible. However, for flow over large roughness lengths in the presence of a large upward heat flux (i.e.,  $z/L\ll 0$ ), Eqs. (1) and (2) are incorrect in that they imply that the wind speed at height h, and the potential temperature difference between the surface and h reverse their signs.

The exact expressions corresponding to (1) and (2)

$$\frac{u}{u_*} = F\left(\frac{z}{L}, \frac{z}{z_0}\right),\tag{3}$$

$$\frac{(\theta - \theta_0)u_*}{(-w'\theta')_0} = G\left(\frac{z}{L}, \frac{z}{z_0}\right),\tag{4}$$

where for the unstable case

$$kF = \ln \left[ \frac{(\zeta - 1)(\zeta_0 + 1)}{(\zeta + 1)(\zeta_0 - 1)} \right] + 2\left[ \tan^{-1} \zeta - \tan^{-1} \zeta_0 \right], \quad (5)$$

$$\frac{kG}{R} = \ln \left[ \frac{(\eta^2 - 1)(\eta_0^2 + 1)}{(\eta^2 + 1)(\eta_0^2 - 1)} \right], \tag{6}$$

Present affiliation: Atmospheric Physics and Chemistry laboratory, NOAA, Boulder, Colo. 80302  $\frac{kG}{R} = \ln \left[ \frac{(\eta^2 - 1)(\eta_0^2 + 1)}{(\eta^2 + 1)(\eta_0^2 - 1)} \right],$ 

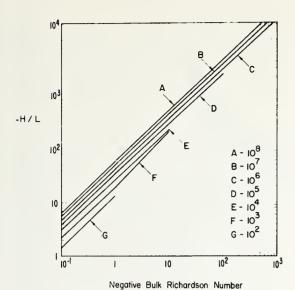


Fig. 1. Stability parameter -H/L as a function of  $-\mathrm{Ri}_B = hg(\theta_h - \theta_0)/\theta_h U_h^2$  for  $10^2 \leqslant H/z_0 \leqslant 10^8$  with an upward sensible heat flux. Calculations were made with the unmodified expressions (1) and (2).

and where

$$\zeta_0 = \left(1 - \frac{\gamma z_0}{L}\right)^{\frac{1}{4}}, \quad \eta_0 = \left(1 - \frac{\gamma'' z_0}{L}\right)^{\frac{1}{4}}.$$

For the stable case,

$$kF = \ln X + \beta Y, \tag{7}$$

$$kG = R \ln X + \beta Y, \tag{8}$$

where  $X=z/z_0$ , Y=z/L,  $\beta=4.7$ . Some caution should be exercised in the use of (7) and (8), however, since the value of the constant  $\beta$  may be considerably influenced by the nature of the underlying terrain.

Eqs. (5) and (6) become identical with Faulson's results in the limit of neutrally stratified flow. Differences between the two formulations may be seen in Figs. 1 and 2 where the relationship between h/L and the bulk Richardson number, i.e.,

$$Ri_{B} = \frac{hg(\theta_{h} - \theta_{0})}{\theta_{h}U_{h}^{2}} = \frac{G}{kF^{2}}\frac{h}{L},$$
(9)

is shown for  $h/z_0$  ranging between  $10^2$  and  $10^8$ . Here  $\theta_h$  and  $U_h$  represent the wind speed and potential temperature at a height h which is within the surface layer. In Fig. 1 the curves terminate because the original expressions for the function F and G become zero. Fig. 2 shows the new expressions obtained from (5) and (6). The corresponding plot for the stable case is shown in Fig. 3.

An expression for the sensible heat flux may be obtained by combining Eqs. (3) and (4) to give

$$Q_0 = \frac{-U_h^3 \theta_h Y}{kgh F^3}. (10)$$

For simplicity, we specify the latent heat flux in terms of a Bowen ratio (i.e.,  $Q_B = Q_0/B$ ).

#### 3. Surface storage

The storage term for the one-dimensional models previously mentioned was computed from a Fickian diffusion term and subsurface temperatures. Such a direct approach is not practical, however, for an urban area having an irregular surface texture. Surface storage must be parameterized and we have chosen to express it in terms of the net radiation. The O'Neal data (Lettau and Davidson, 1957) are compatible with surface storage directly proportional to net radiation (i.e.,  $S=\lambda R$ ), with different constants appropriate for nighttime and daytime. During morning and evening transition periods, the storage is often sufficiently small that such an approximation does not seriously affect the surface energy budget calculations. The constant  $\lambda$  was set equal to 0.19 when the net radiation was positive (daytime conditions) and to 0.32 when the net radiation was negative.

#### 4. Surface energy budget model

The energy budget at the earth's surface may be expressed as

$$R - Q_s - Q_E - S = 0,$$
 (11)

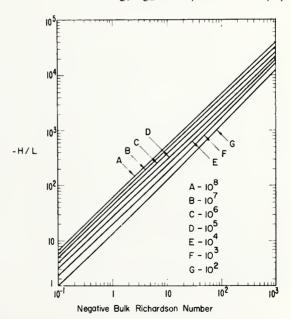
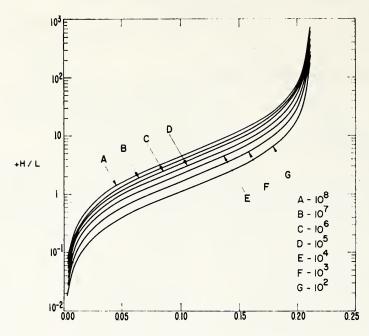


Fig. 2. As in Fig. 1 except that calculations were made with the modified expressions (5) and (6).



Positive Bulk Richardson Number

Fig. 3. Stability parameter H/L as a function of Ri<sub>B</sub> for a downward sensible heat flux.

where R is the net radiation,  $Q_s$  the sensible heat flux,  $Q_B$  the latent heat flux, and S the surface storage. The net radiation R is written as

$$R = -\epsilon \sigma \theta_s^4 + F_s \downarrow + F_L \downarrow, \tag{12}$$

where  $\theta_s$  is the surface temperature,  $\epsilon$  the emissivity,  $\nu$  the Stefan Boltzman constant, and  $F_s \downarrow$  and  $F_L \downarrow$  represent the downward shortwave and longwave radiation respectively.

A knowledge of the heat transfer within the viscous sublayer is necessary for an accurate specification of the temperature difference between the earth's surface and the height  $z_0$ . Heat transfer within the viscous sublayer is included in the model developed by Sasamori (1970), but a more rigorous treatment may be found in Yaglom and Kader (1974) where an expression for  $\delta\theta = \theta_s - \theta_0$  is derived. And yet, it is not clear that such treatments are especially useful in the context of mesoscale models with varying surface conditions and with horizontal grid spacings on the order of 1-10 km. At the present time, then,  $\theta_s$  in Eq. (12) is replaced by  $\theta_0$ .

Upon combining the parameterizations of the previous section, we may then write (11) as

$$C_{1}\left(1-C_{2}\frac{h}{L}\right)^{4}-C_{3}\frac{h}{L}-C_{4}=0, \tag{13}$$

where

$$C_{1} = \epsilon \sigma \theta_{h}^{4}$$

$$C_{2} = \frac{U_{h}^{2}G}{khgF^{2}}$$

$$C_{3} = \frac{U_{h}^{3}\theta_{h}\left(1 + \frac{1}{B}\right)}{khg(1 - \lambda)F^{3}}$$

$$C_{4} = F_{s} \downarrow + F_{L} \downarrow$$

Given the winds and temperature at a height h, together with the surface roughness  $z_0$ , and the incoming solar radiation; we may use (13) to compute the Monin-Obukhov length L. The heat flux, surface temperature and friction velocity may then be obtained from (1) and from

$$\theta_0 = \theta_h \left( 1 - \frac{U_h^2 G}{k h g F^2} \right) \frac{h}{L}$$

$$U_* = \frac{U_h}{F}$$

The method of successive bisection was used to solve the transcendental equation (13). CFU time on an IBM 370-165 was on the order of a few tenths of a second. Computational time could be considerably reduced, however, by the use of a more efficient iteration procedure (McCalla, 1967). If  $F_1$  and  $F_2$  represent two successive estimates of the function F(z/L)=0, then the iteration procedure was terminated when the absolute value of  $(F_1-F_2)$  was less than  $10^{-4}$  times  $(F_1+F_2)/2$ .

#### 5. Summary and conclusions

The parameterized surface energy budget equation expressed by (13) was tested on the O'Neil data using a one-dimensional model similar to that of Sasamori (1970). The first grid point was located at a height of 10 m. The calculated temporal distributions of the surface energy budget components, surface temperature, and wind and temperature fields above the ground were similar to those of Sasamori and therefore need not be presented here. The test case demonstrated that the presented parameterization procedure provides a reasonable description of the surface energy balance. More data on the energy budget components over representative land use categories for all seasons of the year will be required, however, before the parameterization procedure can be used in an operational mode.

Acknowledgments. The authors wish to thank the reviewers for their helpful suggestions, especially for

the Yaglom and Kader reference and for the definition of new variables that allowed Eqs. (5) and (6) to be written in a more compact form.

#### REFERENCES

- Businger, J. A., J. C. Wyngaard, Y. Izumi and E. F. Bradley, 1971: Flux-profile relationships in the atmospheric surface layer. J. Atmos. Sci., 28, 181-189.
- Deardorff, J. W., 1972: Parameterization of the planetary boundary layer for use in general circulation models. *Mon. Wea. Rev.*, 100, 93-106.
- Estoque, M. A., 1963: A numerical model of the atmospheric boundary layer. J. Geophys. Res., 68, 1103-1113.
- Lettau, H. H., and B. Davidson, 1957: Exploring the Atmosphere's First Mile. Pergamon Press, 578 pp.
- McCalla, T. R., 1967: Introduction to Numerical Methods and Fortran Programming. Wiley, 359 pp.
- McElroy, J. L., 1973: A numerical study of the nocturnal heat island over a medium-sized mid-latitude city (Columbus, Ohio). Boundary Layer Meteor., 3, 442-453.
- Myrup, L. O., and D. L. Morgan, 1972: Numerical model of the urban atmosphere, Vol. 1, The city-surface interface. Contrib.
- Atmos. Sci., No. 4, University of California, Davis.

  Paulson, C. A., 1970: The mathematical representation of wind speed and temperature in the unstable atmospheric surface layer. J. Appl. Meteor., 9, 857-861.
- Sasamori, S., 1970: A numerical study of atmospheric and soil boundary layers. J. Atmos. Sci., 27, 1122-1137.
- Yaglom, A. M., and B. A. Kader, 1974: Heat and mass transfer between rough wall and turbulent fluid flow at high Reynolds and Peclet numbers. J. Fluid Mech., 62, 601-623.

AGI ICE NUCLEI: PHYSICAL AND CHEMICAL PROPERTIES DEPENDING ON THEIR GENERATING PROCEDURE

F. P. Parungo, E. Ackerman and R. F. Pueschel Atmospheric Physics and Chemistry Laboratory NOAA, Boulder, Colorado 80302

#### 1. INTRODUCTION

Since the discovery of silver iodide (AgI) as a cloud seeding agent, its physical and chemical properties have been widely studied (Vonnegut, 1949; Mason and Hallett, 1956; Pena and Caimi, 1967; Mossop and Tuck-Lee, 1968). However, the knowledge of AgI aerosol is still inconclusive and controversial. The properties of AgI particles depend not only on the generating methods, but also on the generating environments and sampling procedures. To accurately determine the properties of an AgI aerosol, one must produce and collect the particles under actual or simulated seeding conditions.

The Atmospheric Physics and Chemistry Laboratory of ERL/NOAA conducted the Modification of the Great Lakes Winter Storms Project (Weickmann, 1973) and used Patten-Mark series airborne flame generators (Patten et al., 1971). The NOAA/ERL Experimental Meteorology Laboratory (Simpson and Woodley) has used airborne pyrotechnic cloud seeding systems (Olin-Mathieson K-1050). This investigation studied the physical and chemical properties of AgI aerosols produced by these two methods at simulated airborne conditions.

For these experiments, we chose the FAA wind tunnel at Atlantic City, New Jersey (National Aviation Facilities Experimental Center). It is an open-circuit, induction-type tunnel with a 2 m diameter test section and 50 m length. Two Pratt and Whitney J-57-F19W turbojet engines are capable of simulating an air speed up to 650 mph.

#### 2. AIRBORNE FLAME GENERATOR

The airborne flame generator was designed to be mounted on the wing-tip of an aircraft flying at approximately 200 mph. Thus, in the wind tunnel this wind speed was simulated. Acetone was used as fuel and the solvent for AgI. Because AgI is only slightly soluble in acetone, an iodide salt, such as KI, NaI, or NH4I is usually added to form a complex with AgI and to yield a homogeneous solution. We used a 2 percent AgI solution with two different additives, NaI and NH4I. In both cases, the molar ratio between AgI and NaI was 2 to 1. The combustion rate was 0.6 £ solution per min yielding 12 g min of AgI.

The generator is designed to produce AgI crystals by a vapor-solid transition. Our first aim was to measure the quenching rate of the exhausting AgI vapor at 200 mph wind speed. To measure ne temperature profile, twelve chromel-alumel thermocouplers were set in a row from 0 to 34 inches away from the generator's exhaust cone. When acetone solution was injected into the generator

and ignited, the flame temperature was approximately 1000°C. There was practically no temperature difference between the solutes being either AgI-NaI or AgI-NH.I. Fig. 1 shows the cooling rate of the flame; the exhaust plume reached 147°C ( $\beta$ -AgI formation point) within 6 milliseconds and cooled to ambient temperatures in 10 milliseconds.

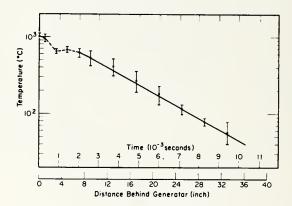


Figure 1. Temperature profile of the generated aerosol.

#### PYROTECHNIC

In airborne pyrotechnic systems, cartridges containing mixtures of chemicals are dropped from aircraft and flare in midair to deliver the AgI aerosol. The terminal fall velocity at igniting point is approximately 150 mph. We conducted the experiment on pyrotechnic in the wind tunnel at the same wind speed. The cartridges tested were Olin-Mathieson X-1050 pyrotechnic flares. The composition is listed in Table 1 and the expected product at ambient temperature is given in Table 2 (Simpson and Woodley, 1970).

Table 1. Composition of Olin-Mathieson X-1050

Percent by Weight		
53.0		
8.0 5.6		
12.9		
10.5		
10.0		

Table 2. Expected exhaust products

Compound	Amount	gm (100 gm	of mix <sup>-1</sup> )
Silver iodide (AgI)		44.0	
Potassium iodide (KI)		6.1	
Magnesium oxide (MgO)		9.5	
Aluminum oxide (Al <sub>2</sub> O <sub>3</sub> )	)	24.1	
Strontium oxide (SrO)		7.2	
Nitrogen (N <sub>2</sub> )		1.4	
Carbon dioxide, water,	etc.	31.7	

#### 4. AEROSOL SAMPLING

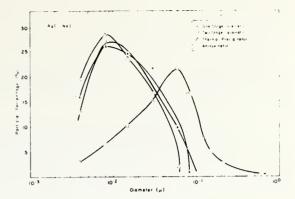
Sampling aerosol from a high airstream flow having anisokinetic flow conditions at the sampling orifice can cause serious errors. (Watson, 1953). To obtain sufficient data of isokinetic and anisokinetic samples and to compare their results, we used four different sampling techniques: (1) anisokinetic sampler; (2) one-stage decelerating isokinetic sampler; (3) two-stage decelerating isokinetic sampler; (4) thermal precipitator. In the first three methods, aerosols were collected on Millipore or Nuclepore filters; in the thermal precipitator, electron-microscope sampling screen coated with Formvar was used. The detail was described by Weickmann (1974).

#### 5. SIZE DISTRIBUTION OF THE GENERATED AEROSOLS

All the collected samples were brought to Boulder, Colorado, for study at the Atmospheric Physics and Chemistry Laboratory. Our laboratory (APCL) has a Scanning Electron Microscope (SEM) with a resolution of 250Å; we also used NCAR's transmission electron microscope (TEM) which has a resolution of 20Å. For the TEM, specimens must be on transparent film which is mounted on the electron-microscope screen. Aerosol samples collected on the screens with the thermal precipitator can be directly observed and photographed by the TEM. The samples on Nuclepore or Millipore filters must be replicated with a layer of silicon monoxide (SiO) coating and transferred to the TEM screen by dissolving off the filter with a certain solvent (Frank et al., 1970). The transparent SiO film with aerosol replicas set on the screen can then be examined with the TEM.

The results of particle size distribution show no statistical difference between one stage and two stages of isokinetic sampling; samples collected by thermal precipitator also yield a similar distribution. However, the open filters that collected the aerosols anisokinetically showed the distribution shifted to larger sizes than for the other three methods (Fig. 2). This result agrees with a tentative semiempirical theory developed by Watson (1953) concerning errors due to anisokinetic sampling of aerosols.

Fig. 3(a) shows the size distribution and concentration of the AgI aerosol produced by the flame generator. The mediam diameter of AgI-NaI aerosol is  $0.008~\mu$  and the median diameter of AgI-NH $_{4}I$  aerosol is  $0.004~\mu$ . Thus, we estimate that 1 g of AgI can produce  $6.4\times10^{17}$  AgI-NaI particles and  $5.1\times10^{18}$  AgI-NH $_{4}I$  particles. The aerosols have 90 percent of their populations in the  $3\times10^{-3}\mu$  to  $3\times10^{-2}\mu$  range, which is one order of magnitude smaller than the results from previous investigations using a similar generator at lower wind speed (Davis et al., 1973; Mossop and Tuck-Lee,



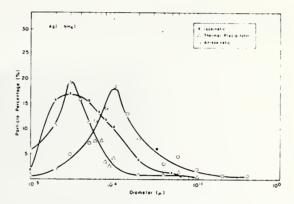


Figure 2. Size distribution of AgI aerosols which were collected by different methods.

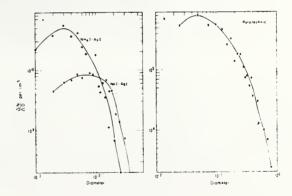


Figure 3. Size distributions of the aerosols (a) AgI-NaI and AgI-NH<sub>4</sub>I; (b) pyrotechnic.

1968). This may be caused by the high air flow rate to disperse the exhausted vapor thinner; the high quenching rate to prevent diffusional losses and thereby to increase the supersaturation; and immediate sampling to prevent particle coagulation.

Fig. 3(b) shows the size distribution and concentration of AgI particles produced by the pyrotechnic flares; the median diameter is 0.09  $\mu$  which is approximately one order of magnitude larger than the aerosols produced by the flame gene-

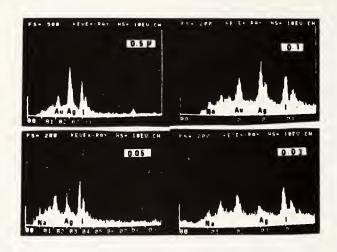
rator. Consequently, the aerosol concentration is three orders of magnitude less than the AgI-NaI or AgI-NH4I aerosol.

#### 6. ELEMENTAL ANALYSIS OF INDIVIDUAL PARTICLES

AgI aerosols produced by both airborne techniques are tested for their nucleation ability. However, what are these particles that result from combustion with different additives at high temperatures and formed in such strong air flow? To attack this basic important problem, we studied the chemical composition of the individual particles.

An X-ray Energy Spectrometer (XES) which is interfaced with a scanning electron microscope (SEM) was used for chemical analysis. The X-ray radiation is a characteristic identification of the elements of the specimen, and the intensity of the radiation is a measure of this element's quantity. By using the combination of SEM-XES, we can observe the individual particle—its size, shape, and surface structure; at the same time, we can identify the elements present in it. However, this powerful instrument has three limitations at present: (1) the diameter of the particle must be >250A; (2) atomic number (Z) must be >10; (3) the analysis is only semiquantitative.

Since the SEM-XES restricts the particle diameter to larger than 0.02  $\mu$ , it is unfortunate that approximately 90 percent of AgI-NaI aerosol produced by the generator is smaller than this limitation and they cannot be identified by this method. We could only study the larger particles (d >0.02  $\mu$ ); their X-ray spectra are in Fig. 4. When AgI-NaI solution was used, the generated aerosol showed no presence of



Pigure 4. X-ray energy spectra of AgI-NaI aerosol with different sizes.

NaI in the particles >0.5  $\mu$ . However, when d <0.5, a low intensity of X-ray at 1.07 eV (Na K $\alpha\beta$ ) can be detected. Furthermore, as the size of the particles decreases, the iodine peaks get stronger, indicating more NaI present; however, no pure NaI particles were detected. Fig. 5 shows the relationship between X-ray intensity of AgI-NaI particles and their size. The X-ray intensity depends not only on the specimen's quantity, but also on its topography and matrix, which are unknown factors here. Therefore, the analysis is semiquantitative; the data points on the graph are the average value and the range is only 80 percent of confidence. However, from these experimental data, we can draw a general conclusion that the detectable surface of large particles (d >0.5  $\mu$ ) are covered with only AgI while smaller particles (d <0.5  $\mu$ ) consist of both AgI and NaI. To explain these results, we must examine the thermodynamic properties of all the compounds involved. Fig. 6 shows the relationship of vapor pressure P and temperature T, according to Clausius-Clapeyron equation  $\Delta\log P = \frac{\Delta H}{R\Delta T}$  where  $\Delta H$  is either heat of evaporation or heat of

formation. The saturation vapor pressure of NaI is only slightly lower than that of AgI at a given temperature. Thus, AgI and NaI would probably solidify simultaneously to form a solid solution. However, AgI partially decomposes above its melting point, free Ag and I<sub>2</sub> vapor are products of the exhaust plume and upon cooling they will recombine to form AgI vapor. Because the vapor pressure of AgI formation is so much higher than both AgI and NaI's vaporization pressure that Ag and I<sub>2</sub> can recombine later and only at a cooler temperature. The freshly formed AgI vapor then deposits on the already existing AgI-NaI particles by heterogeneous nucleation and envelopes them. Thus, the large particles whose pure AgI coating is thick enough to prevent electron beams penetrating through fail to give rise to X-ray radiation of the enclosed NaI, while small particles showed X-ray radiation of both AgI and NaI.

When we used the AgI-NH<sub>4</sub>I solution, the generated particles were uniformly smaller than those from the AgI-NaI systems. Again, 95 percent of the particles were too small to be detected by XES. The

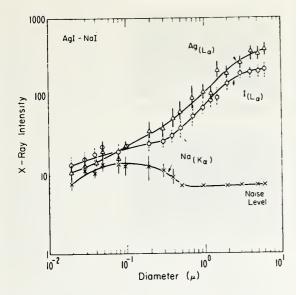


Figure 5. X-ray intensity of AgI-NaI particles.

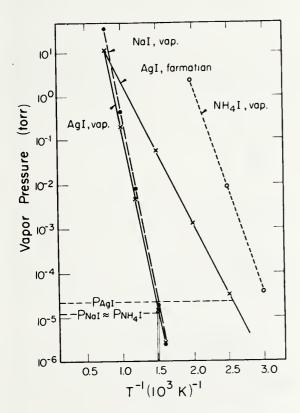


Figure 6. Vapor pressure of the iodides at various temperatures.

relationship between the particle size (d >0.02  $\mu$ ) and X-ray intensity is shown in Fig. 7. Unfortunately, N and H are not detectable by XES (Z <10); thus, the ammonium contribution to the particles is unmeasureable. However, we can observe there

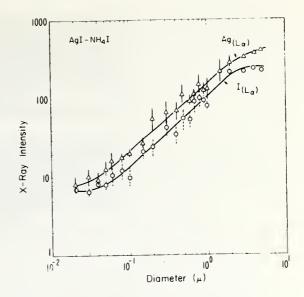


Figure 7. X-ray intensities of AgI-NH<sub>4</sub>I particles.

is no sudden change in the ratio between the X-ray intensity of Ag and I. It is therefore justified to assume that large and small particles have a similar surface composition. Figure 6 shows that NH4I vapor saturates at a cooler temperature than AgI. When the exhausting plume cools down, first AgI solidifies by homogeneous nucleation to form fine particles; then the NH4T vapor deposits on the AgI surface. Since we used less NH<sub>4</sub>I than AgI (mole ratio 1 to 2) and NH<sub>4</sub>I is a thermally unstable compound that decomposes into NH3 and HI and loses portions in the flow, we can expect that NH4I was insufficient to give as thick a coating on the surface of the initial AgI particles as AgI did to NaI in the AgI-NaI system. The aerosol produced by AgI-NH4I systems are AgI particles that were covered with either a thin layer or spots of NH4I.

We also used X-ray energy spectrometry (XES) to determine the elemental composition of individual particles produced by the pyrotechnics. From the analysis of 500 particles having a diameter from 0.02  $\mu$  to 10  $\mu,$  we found only 25 percent were pure AgI (Fig. 8).; the majority (55 percent) were mixtures of Ag, I, Mg, Al, K, and Sr which were the elements of the compounds in the flare. In addition, 15 percent of the particles were an iodide mixture without silver, and 5 percent were silver particles without iodine. The use of silver iodate (AgIO3) in a pyrotechnic mixture requires complete thermal decomposition to liberate Ag and I2, which recombine to form AgI upon cooling. Evidently Ag and I2 not only react to each other, but also are mixed with the other combustion Table 2 lists the expected exhaust products and their quantitative yield; these were hypothetical values based on the thermodynamics of the flare's stoichiometric mixture. If these compounds were produced in the exhaust, they did not exist as individual particles. They were mixed or compounded with one another. The qualitative and quantitative analysis of individual particles would be a very complicated problem because there were five or six compounds that passed through high heat

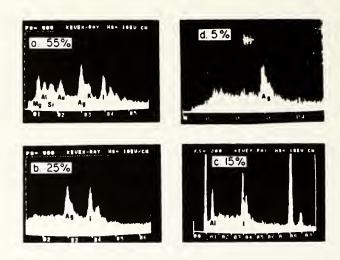


Figure 8. X-ray energy spectra of the particles produced by pyrotechnic.

and rapid cooling. Reactions such as evaporation, decomposition, gas phase reaction, and gas-solid transition had taken place in a high ventilation. The real composition of the exhaust products apparently varies a great deal from the theoretical prediction.

#### 7. PHOTO-STABILITY OF THE AgI AEROSOLS

In the photographic industry, AgI has been used as a photo detector because of its sensitivity to the photons that decompose it into silver and iodine. When used as a cloud secding agent, Reynolds et al. (1951) found that AgI's ice nucleation ability was deactivated by irradiation. To study photo-decomposition of AgI aerosols, we first used freshly ground pure AgI (reagent grade) and measured the ratio of the X-ray intensities between Ag and I; the result is shown in Fig. 9(a).

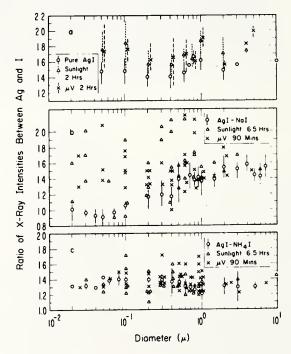


Figure 9. Ratio of X-ray intensities between Ag and I, effected by radiation: (a) AgI; (b) AgI-NaI; (c) AgI-NH,I

The ratio is within a range of  $1.5\pm0.2$  and appears to be independent of the particle size. If it was decomposed by radiation, the produced iodine would evaporate and Ag would remain; as a result, the ratio of X-ray intensity between Ag and I should increase. This is indeed what we found when we irradiated AgI particles with sunlight or ultraviolet (UV) light (2573 Å) for two hours. The average increase in the ratio was approximately 15 percent.

Next we used the same method to study the aerosol that was produced by AgI-NaI generator (Fig. 9(b)). As we have mentioned previously, the ratio between Ag and I decreases as the particle size decreases, because the small particles have a thin AgI coating and the larger ones have a thick AgI coating. As these particles are subjected to irradiation of sunlight or UV light, Ag to I ratio increased for all sizes; however, the degree of decomposition seems more intensive in the fine particles than the coarse ones.

When AgI-NH,I aerosols were investigated for their photostability (Fig. 9(c)), no significant increase in the ratio of Ag to I was observed. If we apply our findings to the aerosols of AgI-NH,I which are covered partially or completely with NH,I, it is easy to understand that AgI may be shielded from the radiation; furthermore, even if the photons penetrate through the NH,I cover, the decomposed I<sub>2</sub> may not escape easily and recombination of Ag and I<sub>2</sub> could occur. Therefore, any change in ratio of Ag to I is undetectable.

No attempt was made to investigate the photostability of the aerosol produced by pyrotechnic because it was found as mixtures of multi-elements; the Ag and I content in a particle varies from 0 to 100 percent. The method of comparing the X-ray intensities between Ag and I is unsuitable for them.

#### 8. HYGROSCOPIC PROPERTIES OF THE AgI AEROSOLS

Silver iodide is a hydrophobic substance; its solubility in water is approximately 2 parts per trillion (2  $\times$  10<sup>-9</sup> g ml^-1). An AgI particle with a diameter of 0.01  $\mu$  and weight of 2  $\times$  10<sup>-18</sup> g will dissolve completely in a water drop whose diameter is larger than 15  $\mu$ . However, the hydrophobic character of the surface of AgI particles could cause high surface tension, and it would need time to reach solubility equilibrium. Thus, fine AgI particles are often suspended in water in a colloidal state for an indefinite time.

To test the hygroscopic properties of the AgI aerosols, we carried out two experiments using the particles collected on the electronmicroscope screen, which was coated with a thin Formvar film. In the first experiment, the screens were placed in a small chamber over water for one hour and examined by an electron microscope. AgI -NaI particles showed little effect from the water vapor. AgI-NH4I and pyrotechnic aerosols absorbed moisture to form a drop; after drying out they left a ring of dissolved residue and insoluble particles within. The experiment indicates that AgI-NH4I and pyrotechnic particles whose surfaces were enriched with hydrophilic components are hygroscopic and can act as condensation nuclei. However, AgI-NaI particles are coated with AgI and show less affinity toward water vapor. In the

second experiment, the screens were floated sample side down on the water for one hour. Almost all the AgI-NH4I particles were washed away; but one-third of AgI-NaI and two-thirds of pyrotechnic particles remained. This may be explained by their size. The pyrotechnic particles were largest and they survived in water best, while AgI-NH4I particles were smallest, and they dissolved quickest.

#### 9. ICE NUCLEATION EFFECTIVENESS OF AgI AEROSOLS

There are many techniques for measuring nucleation ability. Because the aerosol samples obtained in the wind tunnel experiments were collected on filters, we were limited to detecting the nucleation activity with a membrane ice nucleus counter.

Langer and Rodgers (1974) at NCAR constructed a new ice crystal developing unit, where ice nuclei on a membrane filter are activated at a controlled temperature and humidity to produce ice crystals. Two kinds of humidifiers are used. One is a "condensation development humidifier." Clean air is saturated at the vapor pressure of ice which is cooled to a well-controlled temperature to provide a continuous source of water vapor. The other is called a "cloud development humidifier." Moist air is expanded to form supercooled cloud droplets which provide a strong source of moisture. The ice crystals grown on the membrane filter under these controlled conditions are counted with an optical microscope.

The ice nucleation process can be classified as (A) sublimation: at ice supersaturation, water vapor deposits on a nucleus to form ice; (B) condensation freezing: at water supersaturation water condenses on the nucleus and then freezes; (C) contact: supercooled water droplets freeze by contact with a nucleus.

When the humidity in the ice nucleus counter was regulated to 95 percent of water saturation (water subsaturation) while at ice supersaturation, we should obtain the count of sublimation ice nuclei. Fig. 10 indicates no ice nucleus was observed at temperatures warmer than -8°C. At -12°C and -16°C, nuclei produced by all three methods-pyrotechnic, AgI-NaI, and AgI-NH4I--were beginning to be active as sublimation nuclei, but all in very small amounts.

When the humidity was 103 percent, nuclei would act as condensation freezing nuclei. At  $-6^{\circ}$ C, AgI-NH<sub>4</sub>I and pyrotechnic began to be active, but not AgI-NaI. At  $-8^{\circ}$ C and  $-16^{\circ}$ C, AgI-NH<sub>4</sub>I and pyrotechnic were more active than AgI-NaI. These results agreed with our interpretation of composition and properties of the aerosols (section 8).

When the cloud development humidifier was used, supercooled cloud droplets were introduced on the sample filters to produce ice crystals. The nuclei would act essentially as freezing nuclei through two mechanisms: condensation-freezing and contact-freezing. We do not believe that the freezing mechanism of these two processes is much different except for the fact that a nucleus embedded in a drop may become dissolved before it is able to nucleate while a freezing nucleus which just makes contact with a droplet may not experience this disadvantage. No method exists to date to test this

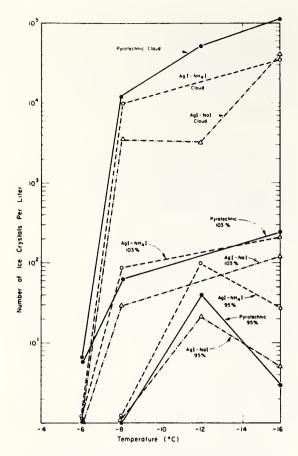


Figure 10. Effectiveness of ice nuclei produced by the different methods determined by membrane filter ice nucleus counter.

hypothesis. Because of the strong increase in the ice crystal counts when cloud drops were introduced, we believe that contact nucleation played an important part here. At a temperature warmer than -12°C, AgI-NH<sub>\*</sub>I was more active than AgI-NaI, but at -16°C their activities were approximately equal. Generally, aerosols from the pyrotechnic were more active than the flame generator products at this cloud condition.

The result may be explained by the difference in size of the three types of aerosols. Based on our measurement, 90 percent of AgI-NH,I particles had a diameter  $\leq 0.01 \,\mu$ , and 90 percent of AgI-NaI particles had a diameter <0.02 μ. These very small particles could be most active as contact nuclei. However, they may penetrate in between the filter fiber (0.1  $\mu$  pore) or coagulate on the surface. Thus, some of them did not have an opportunity to contact water droplets and failed to be counted as ice nuclei. On the other hand, aerosols produced by the pyrotechnic were one order of magnitude larger than the flame generated products. They stayed on the surface of the filter  $(0.1 \mu)$  to be in contact with water droplets. The ice nuclei count in this case should therefore be closer to the real concentration.

#### 10. CONCLUSION

We collected the AgI aerosols produced by the flame generator and by pyrotechnic at a simulated airborne conditions and studied their physical and chemical properties in relation to their nucleation activities. The following results were obtained:

- 1. The quenching rate was such that the aerosols sublimed within one millisecond and reached ambient temperature within 10 milliseconds.
- 2. The size distribution of AgI aerosols depended on generating methods, air speed and isokinetic sampling. The median diameters of the particles were AgI-NaI, 0.008  $\mu$ ; AgI-NH<sub>4</sub>I, 0.004  $\mu$ ; pyrotechnic, 0.09  $\mu$ .
- 3. The surface of AgI-NaI particles was coated with pure AgI; AgI-NH, I particles were coated with NH, I. Pyrotechnic aerosols were a mixture of exhaust products.
- 4. AgI-NH<sub>4</sub>I and pyrotechnic aerosols were more hyrgoscopic than AgI-NaI particles. However, their rate of solution in water was: phrotechnic aerosol < AgI-NaI < AgI-NH<sub>4</sub>I.
- 5. AgI-NH<sub>4</sub>I aerosol was more photo-stable than AgI-NaI aerosol.
- 6. Pyrotechnic and AgI-NH4I aerosols were better condensation freezing nuclei than AgI-NaI. All three were most active as contact ice nuclei in the presence of supercooled cloud droplets. less active as condensation-freezing ice nuclei at water supersaturation, and least active as sublimation ice nuclei at ice supersaturation.

#### Acknowledgment

This research was under the direction of Dr. H. K. Weickmann. We thank Mr. D. Eyre, Mr. B. T. Patten and Mr. R. A. Proulx for their technical assistance in carrying out the experiments. Dr. R. I. Sax and Mr. J. Wisniewski of EML, NOAA, provided us with pyrotechnic cartridges and many valuable suggestions. We are very grateful to Mr. G. Langer and Mr. J. Rodgers of NCAR for the measurement of ice nuclei on membrane filter.

#### References

- Davis, B. L., L. R. Johnson and R. J. Moeng, 1973:
  Particle size of cloud seeding aerosols obtained by wide-angle and small-angle X-ray scattering. Nerelco Rept., 20, 15-20.
- Frank, E. R., K. R. Spurny, D. C. Sheesley and J. P. Lodge, Jr., 1970: The use of nuclepore filter in light and electron microscopy of aerosols. J. du Microscopie, 9, 735-740.
- Langer, G. and J. Rodgers, 1974: An experimental study of the detection of ice nuclei on membrane filter and other substrata. In press.
- Mason, B. J., and J. Hallett, 1956: Artificial ice-forming nuclei. Nature, 177, 681-683.

- Mossop, S. C., and C. Tuck-Lee, 1968: The composition and size distribution of aerosols produced by burning solutions of AgI and NaI in acetone. J. Appl. Meteor., 1, 234-240.
- Patten, B. T., J. D. McFadden and H. A. Friedman, 1971: Airborne cloud seeding system developed and utilized by Research Flight Facility. Proc. Int. Conf. on Weather Modification, Canberra, Australia, p. 358.
- Pena, R. G. and E. A. Caimi, 1967: Hygroscopicity and chemical composition of silver iodide smoke used in cloud seeding experiments. J. Atmos. Sci., 24, 383-386.
- Reynolds, S. E., W, Hume and M. McWhirter, 1951: Effects of sunlight and ammonia on the action of silver-iodide particles as sublimation nuclei. Bull. Am. Meteor. Sci., 33, 26-31.
- Simpson, J., and W. L. Woodley, 1970: An air-borne pyrotechnic cloud seeding system and its use. J. Appl. Meteor., 9, 109-122.
- Vonnegut, B., 1949: Nucleation of supercooled water clouds by silver iodide smoke. *Chem. Rev.*, 44, 277-289.
- Watson, H. H., 1953: Errors due to anisokinetic sampling of aerosols. Report of Symposium V, Aerosols, 31-44. Army Chemical Center.
- Weickmann, H. K., 1973: The Modification of Great Lake Winter Storms. NOAA Tech. Rept., ERL-265-APCL 26, 103 pp.
- Weickmann, H. K., 1974: Physical and chemical properties of AgI aerosols formed at simulated cirborne conditions. NOAA Tech. Rept. in press.

## NOAA Technical Report ERL 337-APCL 36

U.S. DEPARTMENT OF COMMERCE
NATIONAL OCEANIC AND ATMOSPHERIC ADMINISTRATION
Environmental Research Laboratories

# Physical and Chemical Properties of Agl Aerosols Formed at Simulated Airborne Conditions

F. P. PARUNGO R. F. PUESCHEL B. T. PATTEN D. EYRE

BOULDER, COLO.

DECEMBER 1975



#### **ABSTRACT**

AgI cloud-seeding nuclei were produced in a wind tunnel by both a flame generator and a pyrotechnic at simulated aircraft speeds (150 to 200 mph). These aerosols were collected with isokinetic and anisokinetic samplers. By using an electron microscope combined with an X-ray energy spectrometer, we determined the particles' size, shape, chemical composition, photostability, and hygroscopicity. We also studied the relationship between these properties and the AgI aerosols' effectiveness as sublimation, condensation-freezing, and contact nuclei. All the aerosols' properties depend on the generating techniques, the additives mixed with AgI before combustion, and the quenching rate of the exhaust plume.

From our study of the existing aerosol-generating methods, we developed a new method: combusting solid AgI in a flame generator. We found the aerosol's size distribution, chemical arrangement, and physical properties can be controlled by mixing another salt with the solid AgI; this promotes heterogeneous nucleation or modifies the surface characteristics during the vapor-to-particle transition. This new method has the potential of delivering an AgI aerosol having the properties required for ice nuclei in a particular cloud seeding operation.

#### Solar Radiation: Effects of Atmospheric Water Vapor and Volcanic Aerosols

RUDOLF F. PUESCHEL

Atmospheric Physics & Chemistry Laboratory, NOAA, Boulder, Colo. 80302

CHARLES J. GARCIA AND RICHARD T. HANSEN

National Center for Atmospheric Research, High Altitude Observatory, Hilo, Hawaii 96720

(Manuscript received 29 October 1973)

#### ABSTRACT

Atmospheric water vapor attenuates normal incidence solar radiation received on Mauna Loa, Hawaii, by up to 10%. During periods of active fountaining, aerosols from Kilauea Volcano at times obscure global trends in atmospheric turbidity. Corollary measurements such as precipitable water and the aureole are necessary in order to evaluate the effects upon solar radiation of global trends in atmospheric turbidity.

#### 1. Introduction

Long-term, "benchmark" measurements of solar radiation are recognized as being of great value for monitoring the properties of the earth's atmosphere (see, for example, Roberts, 1970). Variations in the flux of incoming solar radiation to the surface of the earth may be due either to natural causes (such as increased atmospheric turbidity caused by volcanic eruptions) or induced by man's activities (including industrial pollution, burning of fossil fuels, and dust storms resulting from dry land farming). Particularly useful are measurements of solar radiation made at locations remote from known sources of pollution; the Mauna Loa Observatory is exceptionally well situated in this regard (Price and Pales, 1963).

The purpose of this report is to present an evaluation of the two principal causes of day-to-day variations in solar radiation at Mauna Loa. These are absorption by atmospheric water vapor and absorption plus scattering by aerosol particles expelled from nearby volcanic eruptions (Kilauea). Both of these effects can be quite large, producing attenuations of the order of 10%. However, when due compensation is made for these natural effects, we believe that the sensitivity of ground-based solar radiation instruments on Mauna Loa for monitoring the atmosphere for possible effects due to human activities can be greatly improved.

#### 2. Results and discussion

The study is based upon measurements over a  $9\frac{1}{2}$  month period, 15 August 1971 through 31 May 1972. Recognizing that even at Mauna Loa the surrounding environment is often "contaminated" during the afternoon by the upward convection of marine air

(Mendonca, 1969a,b), we limited ourselves to data collected only during early morning periods, when the sun's altitude was at 30° (varying between 0801 and 0933 local time). Thus, in essentially all cases the air surrounding the mountain was descending (several notable exceptions will be described later), i.e., the observations were performed when the Observatory was upwind from local pollution sources.

Three parameters were measured, as follows:

- 1) Direct solar radiation with an Eppley normal-incidence pyrheliometer. No correction was made for ambient temperature dependence (-0.15% per degree Celcius) because at this time of day the temperature range at Mauna Loa is only about 6C.
- 2) Total atmospheric precipitable water based upon the relative intensities of the sun in a water vapor band (0.935  $\mu$ m) and a nearby reference region (0.880  $\mu$ m) (Foster *et al.*, 1964).
- 3) Solar aureole at  $0.38^{\circ}$  from the center of the sun, in the red spectral region ( $0.6200 \mu m$ ). These measurements were made with a coronal photometer, similar to the K-coronameter (Wlerick and Axtell, 1957).

Results from the  $9\frac{1}{2}$  month period are shown in Fig. 1, where daily values are plotted of solar radiation (middle), precipitable water (bottom) and aureole (top). The most immediate and striking conclusion from this figure is the nearly perfect (inverse) tracking between the total solar radiation and water vapor content of the atmosphere on a day-to-day basis. This is shown again in Fig. 2 in the form of a scatter diagram; highest incidence of direct radiation occurs when the intervening terrestrial atmosphere is dry. Excluding the eleven dates indicated, the correlation coefficient between the two parameters is 0.95. We should empha-

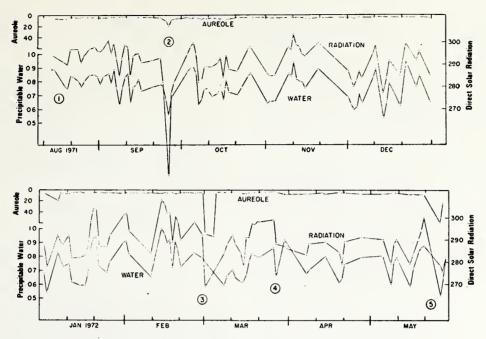


Fig. 1. Day-to-day variations at Mauna Loa Observatory of direct solar radiation and precipitable water ratio at sun's altitude of 30° (corresponding to an airmass of 2). In all cases, the sky was cloud-free in the direction of the sun. At the top are measurements of the aureole made on the same mornings but not necessarily at the same time. Note the almost perfect tracking between solar radiation and precipitable water except during the five periods indicated by 1-5.

size at this point that only measurements made when the sky was completely cloud-free in the direction of the sun at 30° altitude (corresponding to an airmass of 2) are included in these figures. Considering just the highest measurement of total solar radiation (308 ordinate units on 14 February) and the lowest value (277 on 14 December) during this period, we conclude that the direct solar radiation measurements with a wavelength-integrating Eppley pyrheliometer may vary by as much as 10%, depending upon the amount of precipitable water vapor along the sun-earth path at a given time. This is due to the very broad spectral response of the thermopile, 0.35 to 2.5 µm, which encompasses many of the prominent infrared water vapor absorption bands (see, for example, Gates, 1966).

Calibration curves for a similar spectral hygrometer were obtained in Arizona several years ago by comparing the measured ratio of energies received through the two interference filters (0.935 and 0.880 µm) with the total vertical atmospheric water vapor content determined from radiosondes, using standard evaluation techniques (King and Parry, 1964). In addition, Mueller (1968) placed a searchlight at various horizontal distances (between 3 and 72 m) from the hygrometer to find the instrumental response to smaller precipitable water contents (less than 1.5 mm). Unfortunately, neither of these earlier calibrations are any longer valid for the instrument in use at Mauna Loa

because of several electronic modifications. Therefore, a comparison was made of the daily hygrometer ratio (at sun elevation of 30°) with the water vapor content above the elevation of Mauna Loa Observatory (3400 m) determined from the radiosondes launched from Hilo airport by the National Weather Service at 0200. The results (Fig. 3) showed a linear relationship between the logarithm of the precipitable water content and the hygrometer ratio between sun and earth. The correlation coefficient was 0.63 with a standard deviation of 30%. Much of the scatter is undoubtedly due to the imperfect humidity measurements by the radiosondes and differences in atmospheric paths and times of the hygrometer and radiosonde samplings, plus, of course, the inherent limitations of the spectral hygrometer technique (Foster et al., 1964; King and Parry, 1964). Nonetheless, it became clear that the total precipitable water above Mauna Loa during the observation period varied, on the average, within the range of low values of 0.9 mm and high values of 7 mm. Based on published water vapor absorption coefficients (McDonald, 1960), this agrees with the observed 10% solar radiation changes.

In Fig. 2, eleven dates are specifically noted, all of which fall below the least-squares fit line. The details of the special circumstances at these times are given in Table 1. We consider the radiation measurements of 30 and 31 March 1972 as being invalid because of the

strong likelihood that the sensors were affected by blowing snow at the station. Three of the remaining four periods followed substantial increases in volcanic action at Kilauea (new major eruptions began on 14 August, 24 September and 25 February) so that the magnitude of local atmospheric pollution— due to both volcanic haze and burning vegetation—was greatly increased. Generally, this pollution is carried away from the island by the prevailing northeast trade winds. However, in the instances reported here, including the period in late May, the volcanic haze extended to elevations above the Mauna Loa Observatory even during the early morning hours. Accordingly, as shown in Fig. 2, the direct solar radiation was attenuated to lower values than expected from consideration of only the precipitable water absorption. The aureole measurements (top curve of Fig. 1) provide a further indication that these low values of direct solar radiation are due to volcanic haze. Note that with the exception

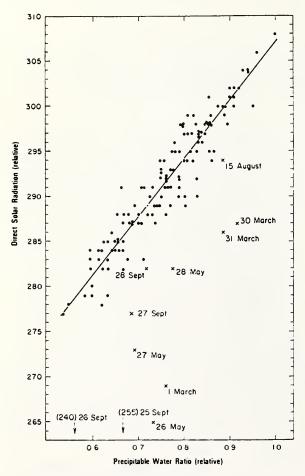


Fig. 2. Comparison of direct solar radiation and the precipitable water ratio at Mauna Loa Observatory from 15 August 1971 to 31 May 1972. The solid curve is the least-squares fit of the dots; the eleven dates were omitted from calculation of this curve and from the correlation coefficient (0.95).

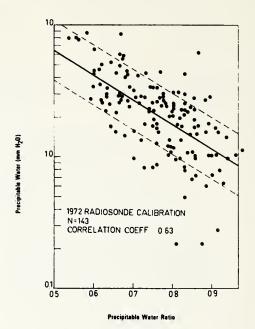


Fig. 3. Comparison of precipitable water ratio from the infrared hygrometer and absolute units from radiosonde soundings. The solid curve is the least-squares fit of the dots; the dashed curves show the standard derivation.

of these few dates, the brightness of the sky in the near vicinity of the sun remained essentially constant but became enhanced (presumably due to forward scattering by the volcanic dust particles) on 25 September, 1 March and 26 May.

These results of local volcanic eruptions upon solar radiation measurements may be compared with the global effects found by Dyer and Hicks (1965) following the eruption of Mount Agung on the Island of Bali in 1963. Typical Mauna Loa values taken from Table 1 show a 5-15% decrease of direct solar radiation and an associated tenfold increase in brightness of the aureole (at 0.38° from the center of the sun in the red spectral region), lasting for a few days, immediately after new eruptions of Kilauea and with unusual atmospheric circulation around the island. In contrast, following Mount Agung's eruption, near Melbourne, Australia, there was a 25% decrease in the monthly average of direct radiation and a 100% increase in diffuse sky radiation, lasting for several years. A similar persistence in turbidity of smaller magnitude apparently due to the intrusion of Agung's dust into the stratosphere has already been found by Ellis and Pueschel (1971) from analysis of the monthly averages of Mauna Loa's solar radiation measurements.

#### 3. Summary and conclusions

In summary, we believe that the principal result of this study is the demonstration that with auxiliary measurements of precipitable water and the aureole,

TABLE 1. Periods of unusually low direct solar radiation.

Time period	Diminution of direct solar radiation $(\%)$	Enhancement aureole $(\%)$	Apparent pollution source
1. 14-15 August 1971	2	50	Volcanic eruption at Halemaumau from about 0900-1900, 14 August
2. 25-28 September 1971	14	375	Volcano eruption at Mauna Ulu, began 1920, 24 September
3. 26 February-4 March, 1972	8	1800	New volcanic eruption at Mauna Ulu, started 25 February.
4. 30–31 March 1972	5	100	Blowing snow at Mauna Loa following storm of 29 March.
5. 26–28 May 1972	9	900	Mauna Ulu eruption con- tinuing. Trade winds absent.

it is possible to evaluate solar radiation data more sensitively, eliminating those variations due to natural causes (atmospheric water content and local pollution, such as Hawaii's volcano) and thereby better monitor long-term trends in turbidity of our earth's atmosphere. In order to cause solar radiation attenuations to exceed 10% due to aerosols, particulate mass changes of 770 gm hectare-1, or 39×106 metric tons, are required (Barrett, 1971). At a presently existing annual production rate of pollutant particulate material of 296×106 tons (Robinson and Robbins, 1971) and with a tropospheric aerosol retainment factor of the order of 10-3 (Weickmann and Pueschel, 1973), a 130 times greater pollutant aerosol output is required to be unequivocally detectable at Mauna Loa, Hawaii. If we assume that the present power consumption is compatible with the existing aerosol production, and that the annual incremental increase of power requirements levels off at 10% (Cook, 1971), then simple arithmetic shows that in 49 years we will be able to detect manmade changes in atmospheric turbidity. Improved emission control techniques will certainly extend this limit further into the future.

On the natural scale, volcanic eruptions of the caliber of Krakatoa (1883) are required to cause atmospheric dust loadings that would affect solar radiation in excess of the day-to-day variations due to water vapor and local volcanic effluents.

We conclude that elaborate methods are required to correct solar radiation data with respect to water vapor before it is possible to monitor presently existing trends in atmospheric turbidity with wavelength-integrating pyrheliometers. A correlation coefficient of 0.44 was established between precipitable water and surface mixing ratio measured with the infrared hygrometer and a dewpoint hygrometer, respectively. A similarly poor correlation was found to exist between aureole

observations and aerosol light scattering at the surface. Hence, surface observations at Mauna Loa reflect only poorly the conditions in space.

In view of the findings reported above, it becomes obvious that the evaluation procedure for solar radiation data proposed by Ellis (1970, personal communication) is an excellent way to provide meaningful results. Although the selection of extremely dry days with excellent optical homogeneity reduces the sample population to about 10%, it was possible to show the effects upon solar radiation of volcanic eruptions such as Agung (1963), Taal (1965) and Awu (1966); however, no human-derived turbidity trend could be detected. It is suggested that by eliminating all "wet" days from solar radiation records dating back much farther than 1958, such as the Smithsonian record which was initiated in 1902 by C. Abbott, worldwide turbidity trends might be recovered.

Acknowledgment. We are indebted to H. T. Ellis of the Mauna Loa Observatory for providing the solar radiation data for this study.

#### REFERENCES

- Barrett, E. W., 1971: Depletion of short-wave irradiance of the ground by particles suspended in the atmosphere. *Solar Energy*, 13, 323-337.
- Cook, E., 1971: The flow of energy in an industrial society. Sci. American, 225, 135-144.
- Dyer, A. J., and B. B. Hicks, 1965: Stratospheric transport of volcanic dust inferred from solar radiation measurements. *Nature*, 208, 131-133.
- Ellis, H. T., and R. F. Pueschel, 1971: Solar radiation: Absence of air pollution trends at Mauna Loa. *Science*, 172, 845-846.
- Foster, N. B., D. T. Volz and L. W. Foskett, 1964: A spectral hygrometer for measuring total precipitable water. *Humidity and Moisture*, Vol. 1, New York, Reinhold, 455-464.
- Gates, D. M., 1966: Spectral distribution of solar radiation at the earth's surface. *Science*, 151, 523-529.

- King, R. L., and H. D. Parry, 1964: Field tests and calibration of the total atmospheric water vapor hygrometer. *Humidity* and Moisture, Vol. 2, New York, Reinhold, 450-457.
- McDonald, J. E., 1960: Direct absorption of solar radiation by atmospheric water vapor. J. Meteor., 17, 319-238.
- Mendonca, B. G., 1969a: The trade wind inversion at the slopes of Mauna Loa, Hawaii. J. Appl. Meteor., 8, 213-219.
- —, 1969b: Local wind circulation on the slopes of Mauna Loa. J. Appl. Meteor., 8, 533-541.
- Mueller, J., 1968: A spectral hygrometer developed for the Mauna Loa geophysical research sitation. ESSA Internal Report, 7 pp.
- Price, S., and J. C. Pales, 1963: Mauna Loa Observatory: The first five years. Mon. Wea. Rev., 91, 665-680.
- Roberts, W. O., 1970: Benchmark stations for the measurement of presently missing parameters. *Meteor. Monogr.*, 11, No. 33, 412-420.
- Robinson, E., and R. C. Robins, 1971: Emissions, concentrations and fate of particulate atmospheric pollutants. Final Report, Project SCC-8507, Stanford Research Institute.
- Weickmann, H. K., and R. F. Pueschel, 1973: Atmospheric aerosols: Residence times, retainment factors and climatic effects. Contri. Atmos. Phys. 46, 112-118.
- Wlerick, G., and J. Axtell, 1957: A new instrument for observing the electron corona. Astrophys. J., 126, 253-258.

### Infrared Absorption of Tropospheric Aerosols: Urban and Rural Aerosols of Phoenix, Arizona

R. F. PUESCHEL AND P. M. KUHN

Atmospheric Physics and Chemistry Laboratory, Environmental Research Laboratories NOAA, Boulder, Colorado 80302

Infrared in situ radiance measurements in the 9.5- through 11.5-\mu spectral region resulted in a direct determination of the IR volume extinction coefficient. Aerosols were collected for an analysis of size distributions and chemical composition. Mie calculations based on these data show that at 10-\mu wavelength more than 95% of the IR extinction is caused by absorption. A comparison of the calculated with the measured aerosol absorptivity resulted in values for the imaginary part of the IR refractive index of 0.47 and 0.19 for the urban and rural aerosols, respectively.

To evaluate the effects of the interaction of atmospheric particulate matter with long-wave radiation, we must know the infrared optical aerosol properties. Of primary concern is the influence of the particle on infrared radiation in the 8- to 13-\mu wavelength spectral window. Extinction of 1R radiation in these wavelengths could result in a possible warming of the atmosphere [Idso, 1974] and could cause inaccurate measurements of radiometric data, e.g., surface temperature measured from earth-orbiting satellites [Jacobowitz and Coulson, 1973]. For these reasons the Report of the Study of Man's Impact on Climate [1971] recommends 'increased research on the refractive index (including absorption) of atmospheric particles in relation to their composition, design, size and shape and its change with increasing pollution for short and long wave radiation.'

In the past, values of the IR refractive index [Volz, 1972a, b, 1973] were determined by the potassium-bromide pellet technique [Kendall, 1966]. Samples of rainwater and/or snow water solubles or dust collected by sedimentation were mixed and pressed with the powdered halide under vacuum into a clear glassy disc. Transmission spectra of these samples were obtained in standard IR spectrographs.

There are several disadvantages associated with the potassium-bromide method. First, the particulate matter collected in precipitation does not accurately represent the optically important parameters of the aerosol, e.g., size, size distribution, and chemical composition. Second, interference with the physical aerosol properties occurs during the mixing and pressing process. Third, the aerosol particles are concentrated in the pellets, this concentration creating a possibility of multiple scattering and absorption effects that would not occur naturally. These factors can influence the accuracy of results.

Ivlev and Popova [1973] evaluated the optical characteristics of a model aerosol by assuming a linearity between the optical constants of the particle bulk constituents and the particle surface chemical composition. Because the surface chemistry of aerosols varies strongly in both time and space, however, we feel that in situ measurements are mandatory in order to evaluate properly the radiative effects of aerosols.

To get a more representative effect of the natural aerosol size distribution, we chose to compute the 1R absorption and scattering properties of aerosols collected over Phoenix, Arizona, and vicinity. The aerosol was collected on membrane

Copyright © 1975 by the American Geophysical Union.

filters at 500 m msl that had air aspirated through them at a controlled rate. Thermal convection during the sampling period assured homogeneity in the aerosol number concentration within the 1000-m-deep boundary layer. This was confirmed by cloud nuclei measurements with a Gardner fine particle counter.

After collection the aerosol deposit was analyzed for particle sizes by a scanning electron microscope. The inorganic elemental composition of the particles was determined by an X ray energy dispersive analyzer. Figure 1 shows the size distributions of the urban and rural aerosols that were investigated. The elemental composition of the rural aerosol closely resembled that of the Arizona soil. Consequently, we chose a value of 1.6 for the scattering index n' (real part of the refractive index) because of its close relationship with the inorganic aerosol composition. The urban aerosol was found to be richer in the elements Mg, Pb, S, Cl, and Fe. It is documented in the literature [Bullrich, 1964], however, that this composition changes the scattering index n' insignificantly.

While n' was kept constant, we calculated the aerosol absorption coefficient for the wavelength  $\lambda=10~\mu m$  and an interval 0 < n'' < 0.5 for the absorption index n'' (imaginary part of the refractive index), using Mie theory [Van de Hulst. 1957]. While we realize that this theory is strictly valid only for particles of ideal shape, the case in point here is a comparison between two types of aerosols. We believe that the error introduced by the fraction of particles that have irregular shapes is of similar magnitude in both cases.

While the aerosols were being sampled, we also measured the upward infrared in situ radiance in the 9.5- to  $11.5-\mu m$  spectral region with a 2° field of view chopper radiometer through the aerosol layer from the surface to the top. This provided an independent experimental method for determining the aerosol volume absorption coefficient [Kuhn and Stearns, 1974].

To analyze long-wave radiative transfer through the Phoenix aerosol layer, it was necessary to determine the bulk total extinction coefficient  $K_{\Delta\nu}$  (per centimeter). To accomplish this, we obtained observations of  $T_{\Delta\nu}$ , the aerosol layer transmission. These were acquired in the following manner by aircraft radiometric observations 'looking' downward.

Consider the radiometric observation of a haze layer of thickness  $\Delta Z$  (Figure 2) by examining the power budget at the

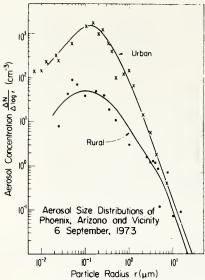


Fig. 1. Number frequency distributions as a function of size for aerosols collected in the urban and rural atmospheres of Phoenix, Arizona.

top of the haze layer, denoted by the level symbol 2, and at the same top of a haze-free layer in the adjacent atmosphere, denoted by the level symbol 22. The arrows indicate the direction of propagation of the radiant power, dashed arrow shafts indicating transmission and solid shafts indicating emission or reflection. In each case we refer to the vertical, or radiance, component of the power transfer.

The radiant power balance at the top of the aerosol layer may be written [Davis, 1971; Kuhn, 1970] as

$$N_2 \uparrow = T_{\Delta \nu} \uparrow N_{22} + (1.0 - T_{\Delta \nu} \uparrow - R_{\Delta \nu}) N_A + R_{\Delta \nu} N_2 \rfloor \quad (1)$$

where N is the radiance (watts per square centimeter per steradian),  $T_{\Delta\nu}$  is the transmission in the spectral interval  $\Delta\nu$  (per centimeter),  $R_{\Delta\nu}$  is the reflection in the spectral interval  $\Delta\nu$  (per centimeter), the subscript 2 designates the top of the aerosol layer (Figure 2), the subscript 22 denotes the top of the atmospheric aerosol-free layer, and the subscript A indicates the aerosol layer.

Radiance  $N_A$  in (1) is evaluated from direct observations with the  $CO_2$  band radiometer of the aerosol layer temperature. By profiling upward through the aerosol layer it was possible to obtain transmissions of several layers of increasing thickness, which are required for a solution of the

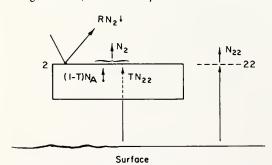


Fig. 2. Symbolic atmospheric haze layer with arrows depicting upwelling IR radiance.

bulk total extinction coefficient  $K_{\Delta\nu}$ . From (1) a determination of  $T_{\Delta\nu}$  by aircraft radiometric techniques must include at least an assumption or postulation of the value of the reflectance  $R_{\Delta\nu}$ .

In what follows we postulate a maximum value of  $R_{\Delta\nu}$  of 0.03 [Davis, 1971]. Equation (1) may now be rewritten to give transmission as

$$T_{\nu} = [N_2 - N_A - R_{\Delta \nu}(N_2 - N_A)]/(N_{22} - N_A)$$
 (2)

The principle of conservation of energy or power requires that

for energy traversing an absorbing and scattering medium. Symbolizing extinction, scattering, and emission, we may write

$$1.0 - T_{\nu} = R_{\nu} + A_{\nu} \tag{3}$$

where  $T_{\nu}$ ,  $R_{\nu}$ , and  $A_{\nu}$  are the monochromatic transmission, reflection, and absorption. Equation (3), expressing the conservation of energy in terms of monochromaticity, is exact. However, we will define a bulk form of total extinction in radiant power traversing a medium as

$$1.0 - T_{\Delta \nu} = R_{\Delta \nu} + A_{\Delta \nu} \tag{4}$$

Here the extinction,  $1.0 - T_{\Delta\nu}$ , covering the wave number interval  $8.0-12.0~\mu m$  for  $\Delta\nu$  also implicitly includes the effects of emission by the medium, in this case the aerosol haze, and scattering by the aerosol particles.

Beer's law permits us to state from (4) that

$$T_{\Delta\nu} = \exp\left(-K_{\Delta\nu}\Delta Z\right) = 1.0 - R_{\Delta\nu} + A_{\Delta\nu} \tag{5}$$

Here, as is stated,  $K_{\Delta\nu}$  is the bulk total extinction coefficient (per centimeter), and  $K\Delta Z$  is the optical thickness.

Then

$$K_{\Delta\nu} = \ln T_{\Delta\nu}/\Delta Z \tag{6}$$

is the solution for the total extinction coefficient, where  $\Delta Z$ , the aerosol scale height, was found to be about 1000 m deep by vertical profiling from a helicopter.

We now compare the calculated absorption values  $b_{aba}$ , the measured absorption values K, and the derived values n'' for the urban and rural aerosols of Phoenix, Arizona (Figure 3). This approach is justified because our calculations show that more than 95% of the IR extinction at 10  $\mu$ m is caused by absorption. Table 1 gives the result.

It follows from Figures 1 and 3 that a variation in the aerosol mass loading has a pronounced effect on the IR absorption index and hence on the aerosol absorptivity. On the

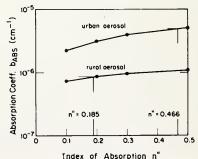


Fig. 3. Absorption coefficients as a function of the absorption index calculated for the size distributions shown in Figure 1.

TABLE 1. Measured Volume Absorption Coefficient K and Calculated Absorption Index n" for Urban and Rural Aerosols

Parameter	Urban Aerosols	Rural Aerosols		
K	$(4.98 \pm 0.05) \times 10^{-6} \mathrm{cm^{-1}}$	$(8.63 \pm 0.09) \times 10^{-7} \text{ cm}^{-1}$		
n"	$0.47 \pm 0.03$	0.19 ± 0.05		

other hand, Figure 3 shows that for a given aerosol size distribution a change in the absorption index has only a small effect on the aerosol absorptivity if n'' > 0.1.

Kuhn et al. [1975] discuss on theoretical grounds the error that is involved in IR extinction measurements using the chopper radiometer. They conclude that the absolute error in K is of the order of 0.01 when upward radiance is measured. Because of this accuracy in the radiometric measurements it follows from Table 1 that the rms error in  $n^m$  is still tolerable in spite of the flat slope of the  $b_{abo}$  equals K versus  $n^m$  curve.

The value of n'' in Table 1 for the rural aerosol is of the same magnitude as that reported by Volz [1972a] for water soluble aerosols and dust collected in precipitation. We have not found in the literature an absorption index of urban aerosols to compare with our value determined for the Phoenix aerosol on September 6, 1973. However, the relatively high absorptivity that we found would support Idso's [1974] conjecture that the warming trend in Phoenix since 1946 is caused by thermal blanketing.

The IR in situ measurements result in a wavelength-integrated value over the spectral range 8.0  $\mu$ m  $< \lambda < 12.0$   $\mu$ m of the total extinction coefficient. Therefore it does not resolve the spectral variation in n'' that exists within this spectral region. However, we feel that by the described method we derive a value of n'' that is representative for correcting IR measurements performed over the same wavelength interval.

Acknowledgments. We thank Evelyn Ackerman and Farn Parungo for performing the aerosol size and chemical analyses and Lois Stearns and Dick Proulx for their help in the fieldwork.

#### REFERENCES

Bullrich, K., Scattered radiation in the atmosphere and the natural aerosol, Advan. Geophys., 10, 88-260, 1964.

Davis, P. A., Applications of an airborne ruby lidar during a Bomex program of Cirrus observations, J. Appl. Meteorol., 10, 1314-1323, 1971.

Idso, S. B., Thermal blanketing: A case for aerosol-induced climatic alteration, *Science*, 186, 50-51, 1974.

Ivlev, L. S., and S. I. Popova, The complex refractive indices of substances in the atmospheric aerosol dispersed phase, *Izv. Acad. Sci. USSR Atmos. Oceanic Phys.*, no. 9, 1034-1043, 1973.

Jacobowitz, H., and K. L. Coulson, Effects of aerosols on the determination of the temperature of the earth's surface from radiance measurements at 11.2 μm, Tech. Rep. NESS 66, NOAA, Suitland, Md., 1973.

Kendall, D. M., Applied 1R Spectroscopy, 560 pp., Reinhold, New York, 1966.

Kuhn, P. M., Airborne observations of contrail effects on the thermal radiation budget, J. Atmos. Sci., 27, 937-942, 1970.

Kuhn, P. M., and L. P. Stearns, Infrared radiation observations vs. calculations in the atmosphere during Skylab, paper presented at 6th Conference of Aerospace and Aeronautical Meteorology, Amer. Miner. Soc., El Paso, Tex., 1974.

Kuhn, P. M., H. K. Weickmann, and L. P. Stearns, Long-wave radiation effects of the harmattan haze, J. Geophys. Res., 80, in p. ess, 1975.

Report of the Study of Man's Impact on Climate, 308 pp., MIT Press, Cambridge, Mass., 1971.

Van de Hulst, H. C., Light Scattering by Small Particles, 453 pp., John Wiley, New York, 1957.

Volz, F. E., Infrared absorption by atmospheric aerosol substances, J. Geophys. Res., 77, 1017-1031, 1972a.

Volz, F. E., Infrared refractive index of atmospheric aerosol substances, Appl. Opt., 11, 755-759, 1972b.

Volz, F. E., Infrared optical constants of ammonium sulfate, Sahara dust, volcanic pumice and flyash, Appl. Opt., 12, 564-567, 1973.

(Received January 30, 1975; accepted February 14, 1975.)

#### ARTIFICIAL ICE NUCLEI PRODUCTION BY EVAPORATION AND SUBLIMATION OF SALTS IN A FLAME

R. F. Pueschel and F. P. Parungo Atmospheric Physics and Chemistry Laboratory NOAA, Boulder, Colorado 80302

and

B. T. Patten Research Flight Facility NOAA, Miami, Florida 33148

#### 1. INTRODUCTION

In cloud seeding experiments, airborne ice nuclei are usually generated by the burning of either pyrotechnics at terminal fall velocities of the cartridges, or acetone solutions of AgI mixed with other iodide salt in generators operated at aircraft speeds. There are apparent disadvantages associated with either method. In the first case, the aerosols formed are relatively large and chemically only poorly defined (Parungo et al., 1974). This excludes these particles from being efficient contact nuclei; they have to act via the condensation-freezing process which uses up large amounts of seeding material. In the second case, the aircraft need to be equipped with sophisticated automated generators.

The particles produced by both methods are chemically of a mixed nature and quite hygroscopic. Consequently, they will easily dissolve in cloud droplets, limiting their lifetime appreciably.

It was for reasons of circumventing one or more of these problems that we attempted an injection of solid AgI, and mixtures of AgI with NaI, into a flame. Measurements of size and chemical composition of these aerosols proved the feasibility of this method of ice nuclei production. In the following discussion we will show that we were able to produce pure AgI nuclei with a narrow size spectrum. The addition to AgI of NaI prior to injection resulted in a change of the size distribution and the hydrophobicity of the nuclei produced.

#### EXPERIMENTAL SET-UP

The salts were finely crushed prior to feeding them through a metering system into the nose cone of the Patten generator (Patten et al., 1971). The rate of injection could be varied from 0.5 to 360 grams per minute. Injection took place near the axis of the burner, where the salt crystals mixed readily with the air-fuel mixture. Evaporation took place in the combustion chamber of the burner, and re-condensation occured at a supersaturated state somewhere in the exhaust fumes. Sampling and analysis was done in the same way as reported elsewhere (Parungo et al., 1974).

#### 3. RESULTS AND DISCUSSIONS

Figure 1 shows the cumulative distribution curves, determined from transmission electron-micrographs, for pure AgI aerosols (curve 1), and mixtures of AgI with NaI in the weight ratios 1 to 1 (curve 2) and 1 to 2 (curve 3). The straight lines of the graph are some evidence, even though no strict mathematical proof, that each aerosol distribution is governed by the lognormal law. More important, however, are the following physical and chemical features partly apparent from the graphs, and partly gained from subsequent investigations.

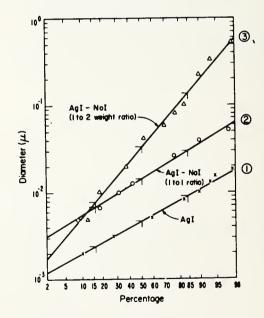


Figure 1. Cumulative size distribution of aerosols formed by the condensation of pure AgI vapor (case 1), and vapor mixtures with weight ratios of AgI to NaI of 1 to 1 (case 2) and 1 to 2 (case 3).

#### 3.1 Control of Hydrophobicity of Ice Nuclei

It follows from Figure 1 that injection of pure AgI salt into the flame results in a nuclei

distribution that has a geometric mean of about  $5\times 10^{-3}~\mu m$ , and a geometric standard deviation of about 50% of the mean. Both these features, viz., the small mean particle size and small polydispersity, are ample proof that the nuclei have been formed by a gas-to-particle conversion process. (No mechanical disintegration process could provide the energies that would be necessary to produce particles of such a small size.)

According to Fletcher (1962), AgI aerosols of diameters less than  $1\times 10^{-2} \mu m$  are inefficient sublimation nuclei. An increase in average particle size can possibly be achieved by an increase of the salt injection rate, hence particle concentration and coagulation rate. (An injection rate of 360 gm min<sup>-1</sup> has proved feasible, while the data in Figure 1 resulted from an injection rate of about 10 gm min<sup>-1</sup>.)

We would like to point out, however, that we are mainly interested in the aerosol size which is conducive to the freezing process in general, since the smaller particle size required for these processes makes for a more efficient use of the seeding agent. Moreover, if contact freezing is desired, this process benefits from the high mobility of small particles.

The small particle size achieved in the experiments reported here provided also an opportunity of investigating the water solubility of submicron AgI ice nuclei. This important property determines life time and thereby efficiency of the nuclei in seeding attempts of clouds with a high water content. Mathews and St.-Amand (1972) calculated the rate of solution of AgI particles in water and predicted that nuclei with radii smaller than 0.01  $\mu$  will dissolve in less than 400 sec. in water drops having radii of 40 μ. If this prediction is true, small AgI particles will be lost due to dissolving in cloud drops and remain ineffective as nuclei in any sub-cloud seeding. To test this theory, the sampling screens that had collected AgI aerosols were floated on water, sample side up, for 30 min. and subsequently re-examined in the transmission electron microscope. No change of particle size, shape, or concentration by this treatment has been observed. Then, the sampling screens were soaked thoroughly for an additional two hours and reexamined in the electron microscope. It was observed that most of the particles remained on the film with spots and stains around them. These important results imply that after prolonged contact on the interface with water dissociation of AgI had occurred; however, the diffusion of the solution from the interface into the water was incomplete. Although our experimental conditions deviated in two aspects from the principles underlying Mathews and St.-Amands calculations, i.e., attachment to the substratum protected a portion of the particle surface from contact with water and the prevention of Brownian motion to enhance the diffusion rate, it appears from these tests that the rate of solution of even small pure AgI nuclei in water is slow enough to preserve their efficiency in sub-cloud seeding over the time of several hours.

#### 3.2 Control of Size Distribution of Ice Nuclei

It follows from Figure 1 that the injection of salts consisting of mixtures of AgI with NaI results in an increase of the geometric mean

diameter of the nuclei size distribution. Furthermore, it is evident from Figure 1 that the mean particle size increases in direct proportion to the amount of NaI added to the mixture. These observations suggest the interesting possibility of a control of the nuclei size distribution and hygroscopicity by the addition to AgI of the proper salt in specified amounts.

In order to understand the processes involved in these size changes, it is necessary to look into the solid-vapor relationships as functions of temperature, pressure and concentration. Figure 2 shows the equilibrium vapor pressure as function of temperature of sodium iodide (upper curve) and silver iodide (lower curve) (Handbook of Chemistry and Physics, 1973). Clearly the

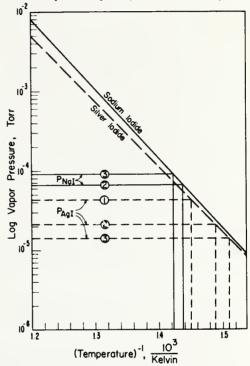


Figure 2. Equilibrium vapor pressure of AgI and NaI as function of salt concentration and temperature.

equilibrium vapor pressure depends on the partial pressures of the salts that are added to the flame. For example, if we vaporize pure AgI at a rate of 10 g min  $^{-1}$  into an air flow rate of 1.6  $\times$  10  $^{4}$  m  $^{3}$ per minute (corresponding to an air speed of 320 km per hour through a duct of cross section  $3.14~\text{m}^2$ ), the resulting partial pressure, P(AgI,) amounts to  $4.3~\times~10^{-5}$  torr (case 1). In the virtual absence of any foreign nuclei, the AgI particles form by homogeneous nucleation and have the small-size spectrum shown in Figure 1 (curve 1). The addition to the same air volume of a salt mixture with a ratio of AgI to NaI of 1 to 1 by weight, at the same rate results in the partial pressures of 2.2  $\times$   $10^{-5}$  torr and 6.7  $\times$   $10^{-5}$ torr for AgI and NaI, respectively (case 2). Clearly, the NaI reaches vapor-solid equilibrium at a higher temperature than does AgI. Based on the temperature profiles reported by Parungo et al. (1974), NaI crystallizes at an earlier point

in time than does AgI. The NaI particles now can serve as centers around which AgI forms by heterogeneous nucleation, resulting in a size distribution that has a larger geometric mean than is found by the homogeneous nucleation of AgI in case 1. The conditions for the formation of still larger particles by heterogeneous nucleation are given if a salt mixture with an AgI to NaI ratio of 1 to 2 is injected into the flame. In this case, the precrystallization of NaI takes place at a still earlier point in time with the possibility that larger NaI crystals serve as nuclei for the AgI vapor condensation (case 3).

#### 3.3 Tests with lead iodide

Lead iodide aerosols were formed and tested under identical experimental conditions as was silver iodide. The results agreed qualitatively with those for silver iodide and can be summarized as follows: (1) The geometric mean of the size distribution of an aerosol composed of pure PbI2 was  $2 \times 10^{-2} \mu m$ . The standard deviation amounted to four times the mean; (2) The addition to PbI2 of NaI in a weight ratio of 1 to 1 increased the geometric mean by a factor of about three; (3) Water treatment resulted in a dissolution of only the smallest PbI2 particles; (4) A dissolution of the mixed PbI2-NaI particles could not be detected. Apparently, their hydrophobicity is increased due to their larger sizes. Thermodynamic consideration indicates that chemically this aerosol forms by heterogeneous nucleation and consists of a rather pure PbI2 shell around a NaI core.

#### 4. SUMMARY AND CONCLUSIONS

The results can be summarized as follows:

- Pure AgI ice nuclei can be produced by the injection into a gasoline flame of finely crushed AgI crystals.
- 2. The rate of solution of even small (<0.01  $\mu m$  diameter) pure AgI nuclei is too small to cause significant losses by collision and coagulation with cloud droplets.
- 3. A control over the size distribution of a seeding aerosol is possible by adding to AgI a salt with proper vapor pressure in specified amounts.
- 4. By the same process it is possible to alter the water solubility of the generated ice nuclei.

These results permit the following important conclusions:

- 1. Sub-cloud seeding into warm clouds is possible without encountering appreciable losses of ice nuclei, provided seeding is done with pure AgI nuclei.
- 2. The control of both size and water solubility provides a means of promoting one or more of the modes of action of ice nuclei, viz., sublimation, contact freezing, or freezing following condensation.
- 3. A better control of the heterogeneous nucleation of AgI on NaI should result in

well defined nuclei in which a large portion of (expensive) AgI is replaced by (inexpensive) NaI.

#### Acknowledgment

We thank Dr. Helmut Weickmann for stimulating and supporting the study, Dave Eyre and Dick Proulx for their help in conducting the experiments, and Evelyn Ackerman for performing aerosol size and chemical analyses.

#### References

- Fletcher, N. H., 1962: The physics of rainclouds, Cambridge University Press, Cambridge, U.K., 386 pp.
- Handbook of Chemistry and Physics, 1973: The Chemical Rubber Co. Press, Cleveland, Ohio, D-182 ff.
- Mathews, L. A. and P. St.-Amand, 1972: The contribution of interfacial kinetics and of diffusion to the rate of solution of AgI particles and its effect on nucleation. Preprint, 3rd Conf., Weather Mod., Rapid City, S. D., 1-4.
- Parungo, F. P., et al., 1974: AgI ice nuclei; Physical and Chemical properties depending on their generating procedure, preprint, 4th Conference on Weather Mod., Ft. Lauderdale, FL, 18-21 November 1974.
- Patton, B. T., et al., 1971: Airborne cloud seeding system developed and utilized by RFF, Proc. Int. Conf. Weather Mod., Canberra, Australia, p. 358.

# THE MIXED NATURE OF LABORATORY-PRODUCED AEROSOLS FROM SEAWATER

by

#### R.F. PUESCHEL and C.C. VAN VALIN

Atmospheric Physics and Chemistry Laboratory
National Oceanic and Atmospheric Administration
Boulder, Colorado, U.S.A.

#### RÉSUMÉ

Des mesures effectuées dans l'air par diffusion de la lumière et pour des hygrométries variables montrent un retard dans l'accroissement de taille des gouttelettes d'aérosols pour des degrés hygrométriques excédant 70 %. Ce phénomène dépend de l'origine géographique de l'eau de mer à partir de laquelle les aérosols sont produits par éclatement de bulles. Les analyses par chromatographie en phase gazeuse et par spectrométrie de masse portant sur les solvants extraits de l'eau marine montrent l'existence d'une relation directe entre ce retard d'accroissement de la gouttelette et la quantité de matière organique présente dans l'eau de mer. Des procédures analytiques sont décrites, qui ont été utilisées pour : a) démontrer le départ de matière organique de l'eau de mer sous l'action du pétillement, b) montrer qu'une partie de la matière organique est transportée sous forme d'aérosols, c) décrire l'effet de la matière organique sur l'accroissement des gouttelettes. Ce phénomène d'accroissement a des conséquences sur les processus de développement des nuages et sur les échanges dynamiques, conséquences dues aux effets combinés de la réduction des tailles, de la différence dans les quantités de chaleur latente libérée et d'un changement dans les caractéristiques de surface des gouttelettes au sein des nuages.

#### ABSTRACT

Light scattering measurements at varying relative humidities on aerosols show a retarded droplet growth at humidities exceeding 70 % depending on the geographic origin of the seawater from which they were produced by the bursting-bubble process. Gas chromatographic and mass spectrometric analyses of solvent extracts of the ocean water show a direct relationship between the effect of retarded droplet growth and the quantity of organic matter in seawater. Procedures are described which were used a) to demonstrate the removal of organic material from seawater by the bursting-bubble process, b) to show that some of the organic matterial is transported as an aerosol, and c) to describe the effect of the organic matter on droplet growth. The observed phenomenon has implications in regard to cloud development and dynamics through the combined effects of a reduced size, a different amount of liberated latent heat, and a change in surface characteristics of the cloud droplets.

#### I. — Introduction.

A reduced droplet growth on sea-salt particles at relative humidities exceeding 70 percent, as compared with salt particles resembling the inorganic composition of seawater, was postulated [1] from light scattering measurements on aerosols produced over the Pacific Ocean off the Washington coast. The cause of this effect was sought in a change of the condensation coefficient due to surface active organic matter. This interpretation was subsequently challenged by Winkler and Junge [2]. They concluded from mass determinations as functions of relative humidity of aerosol impactor samples and brine residues that the different proportions of hydrates in the solutes alter the particle hygroscopicity and hence the droplet growth. Although this concept deserves attention, particularly in light of the inorganic ion fractionation that takes place during the bursting-bubble process [3], other reports [4, 5, 6, 7] produce evidence of a direct cause-effect relationship between surfactants and droplet growth.

A retarded droplet growth, whatever its cause, has the following important implications for cloud development and dynamics: a) The droplet growth on sea-salt nuclei due to the combined effects of a reduced size, a different amount of liberated latent heat, and a change in surface tension might be too slow to make the sea-salt hypothesis an adequate basis for explaining a mechanism of maritime rain formation [8]; b) a retarded droplet growth would reduce the amount of liberated latent heat, which could effect the earth's heat budget; c) once a steady state is reached, at a given supersaturation the colloidal stability within the cloud will be altered due to a change of the collision-coalescence processes determined by the size and surface properties of the droplets [9]; d) the scavenging efficiency of cloud drops for gases and aerosols could be altered.

In view of these implications, the deliquescence experiments [1] were repeated and extended to maritime aerosols produced from ocean waters having different geographic origins. We found that growth of condensation nuclei from samples taken from Hawaii and Florida coastal waters, and from Puget Sound, Washington, is inhibited above a relative humidity of 70 percent when compared with the growth of nuclei produced by an identical process from a synthetic (inorganic) salt solution resembling the ionic composition of seawater. The extent of the droplet retardation depends on the geographic origin of the seawater producing the condensation nuclei. Puget Sound and Atlantic coastal waters exhibit a larger effect than do mid-Pacific waters. Gas chromatographic and mass spectrometric analyses of ocean water from each of the three locations show a direct relationship between the effect of retarded droplet growth and the quantity of organic matter in seawater.

#### II. — EXPERIMENTAL.

The bursting-bubble process, as a source for the maritime aerosol, was simulated in the laboratory by forcing filtered air through a fritted glass sparger held 10 cm below a 700 cm² surface area of a seawater sample contained in a 12 l flask. This aerosol generator was identical to the one used previously [1] resulting in the same particle size distribution, which was of the Junge type with a slope of -3 and a median particle size of 0.1  $\mu$ m. Additional experimental procedures were designed: a) to demonstrate the removal of organic material from seawater by the bursting-bubble process, b) to show that some of the organic material is transported as an aerosol, either alone or in association with sea-salt particles, and c) to describe the effect of the organic matter on droplet growth. These procedures were applied to seawater samples that were obtained at various locations by submerging a 3.8 l jug so that filling was done from the upper  $\sim$  2 cm of water. No further effort was made to quantify the ratio of « surface » to « subsurface » water.

In the first instance [part a)], filtered air was forced through the sparger at a rate of 1.5 l min<sup>-1</sup>. Compressed air used for sparging was found to be free of organic gases by a test involving passing the air directly into a hexane trap for 16 hours, followed by concentration and chromatography. The air was then conducted into deionized water contained in a second flask. From the deionized water flask the air passed into a solvent trap containing n-hexane. The water samples were extracted with n-hexane, and the extracts and the hexane trap material were evaporated to a small volume and subjected to electron capture and flame ionization gas chromatography [10]. Response of the electron capture detector used for the chromatograms shown in figures 1, 2 and 3, was linear within the range employed.

For part b), in order to show that during the bursting-bubble process part of the organics are released in particulate form, we employed an impactor instead of the deionized water trap. The dimensions of the impactor were such that at a flow rate of  $2 \, l \, min^{-1}$  all particles of radius larger than  $0.1 \, \mu m$  are deposited on an 18 mm microscope slide cover glass. The cover glass was then crushed and mulled in a small volume (1 ml) of n-hexane and analyzed by gas chromatography.

In part c), the seawater was sparged with 1 l min<sup>-1</sup> of air, and the exiting air was diluted with 14 l min<sup>-1</sup> of dry (RH < 30 percent) air. This aerosol-containing airstream was then rehumidified under controlled conditions to a relative humidity of from 30 to 95 percent. Humidity was provided by passing the sample airstream through a temperature-controlled copper water tank with an evaporative surface of 500 cm<sup>2</sup>. The relative humidity was measured with a dry-bulb wet-bulb psychrometer at the outlet of the nephelometer, with adequate air velocity provided by the aspiration blower. Aerosol measurements were performed with a recording Aitken nucleus counter and an integrating nephelometer.

#### III. — RESULTS AND DISCUSSIONS.

Determination of dissolved solids in the deionized water trap revealed about 0.1 percent salt after 39 hours. With a 3 percent salinity in 6 l of initial seawater exposing a surface area of 700 cm², this corresponds to a particle production rate of  $1.7 \times 10^{-9}$  g cm<sup>-2</sup> sec<sup>-1</sup>. With an average mass of  $10^{-12}$  to  $10^{-13}$  g per nucleus (or particle), the corresponding nuclei production rate is  $1.7 \times 10^3$  to  $1.7 \times 10^4$  nuclei cm<sup>-2</sup> sec<sup>-1</sup>. This figure is well within the range of the numerous values of production rates of the open ocean found in the literature.

The sea-to-air transfer of organic matter during the bursting-bubble process is demonstrated in figures 1 and 2. Figure 1 shows the gas chromatograms from a seawater sample which was collected in Puget Sound near Seattle, Washington. The upper chromatogram represents an extract of 3 l of seawater as collected. The next chromatogram is from 6 l of seawater after aeration for 39 hours; the third chromatogram is the deionized water trap after aeration, and the bottom chromatogram is the hexane trap.

The large peak following No. 17 in the chromatogram of fresh seawater probably is from accidental contamination of the aliquot withdrawn for analysis, since it was not repeated in any of the other fresh seawater samples. The contaminant here is one of the phthalate ester group of plasticizers. In all other respects, this chromatogram is typical of the fresh seawater extracts and was used because it represents an aliquot of the same water sample used for the other chromatograms in this figure.

Figure 2 shows the chromatograms from a seawater sample which was collected at Gray's Harbor, Washington. From the top, the chromatograms represent 1.5 l of seawater as collected, 6 l of seawater after aeration, the deionized water trap after aera-

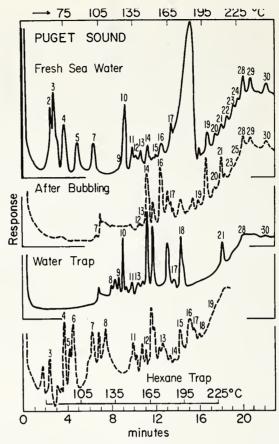


Fig. 1. — Temperature programmed gas chromatograph traces for water from Puget Sound, Washington, prior to treatment (top), after sparging with dry filtered air at the rate of 1.5 l min-1 for 39 hours (second), the deionized water trap after 39 hours (third), and the hexane trap at the same time (bottom). The large peak in the top chromatogram, following No. 17, is an artifact and was not repeated in other aliquots of the same sample. The temperature scale at the top refers to a 4-minute isothermal run at 75 C followed by a linear rise to 225 C, and pertains to the upper three chromatograms. The temperature scale at the bottom, pertaining only to the hexane trap sample, was for a 2-minute isothermal run, followed by a 150 C linear program.

tion, and the hexane trap after aeration. The temperature programmed chromatograms of the original seawater samples show several relatively volatile organic compounds of low retention times in the chromatographic columns (Figs. 1 and 2). They are absent, or nearly so, from the next two chromatograms, representing the original sample after bubbling and the deionized water trap. They do reappear in the hexane trap, however, as shown by the bottom chromatogram.

This demonstration of the sea-to-air transfer of n-hexane soluble organic matter during the bursting-bubble process was substantiated by the following experiment, which also proved that some of the organic substances participate in atmospheric photochemical reactions while airborne. The aerosol light scattering coefficient and the particle number concentration were measured with an integrating nephelometer and a continuous Aitken counter, respectively. A 2.5 W Hg quartz lamp with a peak spectral output of 2536 A was used to irradiate the aerosol. The result was that exposure

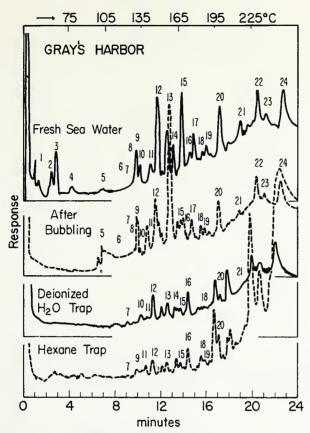


Fig. 2. — Temperature programmed gas chromatograph traces for water from Gray's Harbor, Washington, prior to treatment (top), after sparging with dry filtered air at the rate of 1.5 l min<sup>-1</sup> for 26 hours (second), the deionized water trap (third), and the hexane trap (bottom) at the same time. All chromatograms were made with a 4-minute isothermal period at 75 C followed by a 16-minute linear rise to 225 C.

of the aerosol to UV light increases the Aitken nuclei concentration by a factor of 3 and enhances the aerosol light scattering coefficient by about 9 percent. The contribution of this photochemically produced aerosol to maritime visibilities and to the oceanic cloud nuclei budget remains to be investigated.

The chromatogram from a 12 hour aerosol impactor sample is shown in curve B of figure 3. Curve A is the chromatogram from 1 l of original seawater from Puget Sound, however, a different sample than the seawater used for the chromatogram of figure 1. Curve C is the chromatogram from pure solvent condensed to the same extent as in the sample extracts, i.e., at a ratio of about 3000 to 1. The major peak at the high temperature end of the aerosol impactor extract is recognizable as having been transferred from the seawater, and is completely lacking in the solvent blank.

To show qualitative and quantitative differences with geographic locations of the ocean-dispersed organic substances, we subjected hexane extracts to mass spectrometric analyses. Figure 4 shows the mass spectra of seawater from Florida (top), Puget Sound (middle), and Hawaii (bottom). The peaks at the left ends of the spectrograms which are tipped with arrows were offscale and the response could only be approximated. Relative concentrations of organic materials in these samples are in the ratio of roughly

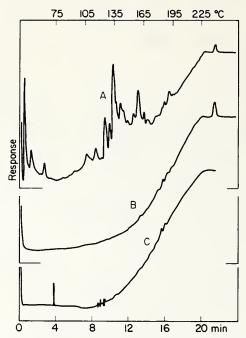
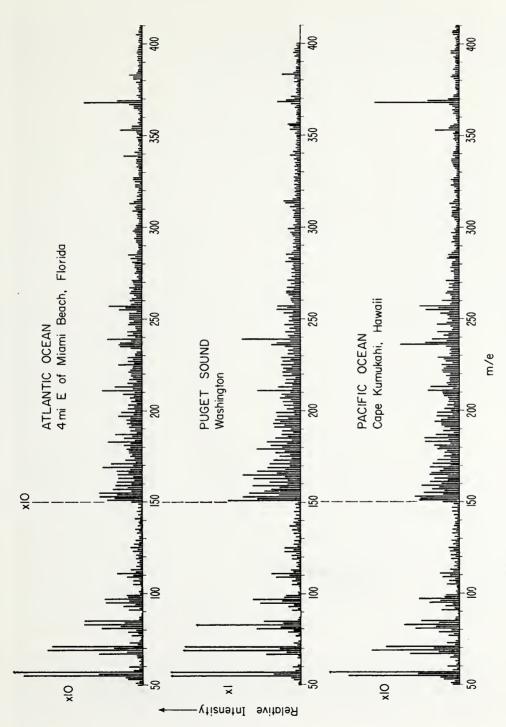


Fig. 3. — Chromatograms of extract from 1 liter of seawater from Puget Sound (Curve A), from the impactor extract (Curve B) in which the airstream from the seawater bubbling flask was directed against an 18 mm microscope cover slide, and from a concentrate of the extraction solvent (Curve C).

1:3:10 for Hawaii, Florida and Puget Sound, respectively, as estimated from mass spectrometer ion current and from gas chromatography detector response. Estimated total organics content is of the order of 1 part in  $10^{10}$  to 1 part in  $10^{9}$ . Mass spectrometric and gas chromotographic analyses of samples from the three locations are remarkably similar qualitatively. All contain saturated, monounsaturated, and diunsaturated hydrocarbons ( $C_nH_{2n+2}$ ,  $C_nH_{2n}$ ,  $C_nH_{2n-2}$ ) through C=29, which represents the upper limit of mass spectrometer operating conditions. Judging from the progression of the 14 mass unit cycles, these series continued to much higher carbon numbers. Fragments of these three series, or from the alkyl moiety of substituted aromatics, dominate the low mass range of the spectrum.

In the higher mass range the more intense response was obtained from polycyclic hydrocarbons of the general formulae  $C_nH_{2n-8}$ ,  $C_nH_{2n-22}$ ,  $C_nH_{2n-10}$ , and  $C_nH_{2n-24}$ . The m/e (mass to charge) responses at 384, 368, 314 and 264, probably representing parent molecules, are accompanied by secondary responses at 1 and 15 mass units lower, corresponding to loss of a proton and a methyl group. These are not accompanied by responses 14, 16 or 17 units lower which would correspond to loss of N, O or OH. The peak at m/e 236 is accompanied by m/e 219, suggesting loss of OH.

Further interpretation of these spectra will be reported later. The preliminary evaluation presented here has not indicated man-made pollution of seawater, although mass spectrometric and gas chromatographic analyses of some of the other samples from Puget Sound and Biscayne Bay, Florida, have revealed the presence of butyl carbobutoxymethyl phthalate and dioctyl phthalate in concentrations of about one part in 10<sup>13</sup>. These compounds are plasticizers used in synthetic rubber and plastics production.



— Mass spectrograms obtained from 1 liter extracts of seawater. The peaks at the left ends of the spectrograms which are tipped with arrows were offscale and the response could only be approximated. Starting at m/e (mass to charge ratio) of 50, the Puget Sound trace was taken from the lowest amplification instrument scale, the other two were from the factor-of-10 instrument scale. At m/e > 150, all traces were amplified by 10. Fig. 4.

The extinction coefficient, b, due to scattering can be related to particle radius r with the b  $\alpha$  r<sup>p</sup> dependence. Because p  $\approx$  2 for the aerosol size distribution as obtained here, even small differences in the size of the particles can be detected.

Figure 5 summarizes the responses of light scattering to relative humidity for the several different aerosols. The upper curve corresponds to the variation in the light scattering coefficient with humidity for a pure NaCl solution aerosol. The lower curves give the variations for light scattering with humidity for laboratory produced seawater aerosols from water samples off the shores of Hawaii, Florida, and Washington.

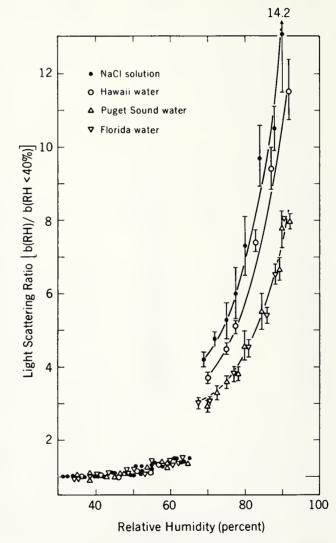


Fig. 5. — The light scattering ratio as a function of humidity for a 3.2 percent NaCl solution, and seawater samples from Cape Kumakahi, Hawaii, Puget Sound, Washington, and Biscayne Bay, Florida. The discontinuity in the curves represents the onset of droplet growth at RH of 65 to 68 percent. This low deliquescence point is caused most likely by those particles that are smaller than 0.1  $\mu m$  radius. The vertical bars represent the limits of experimental error in multiple runs.

It has been demonstrated [1] that the addition to the pure NaCl solution of MgCl<sub>2</sub> and MgSO<sub>4</sub> salts, i.e., Mg<sup>++</sup> and SO<sub>4</sub><sup>--</sup> ions which are second to Na<sup>+</sup> and Cl<sup>-</sup> in abundance in seawater, does not influence the droplet growth indicated by light scattering. This would mean that inorganic ions are not responsible for the phenomenon of retarding growth relative to growth on pure NaCl particles. Other investigators [2], however, found differences in the mass change with relative humidity of salt deposits that depended on their ionic composition. This was attributed to the different amounts of crystal water in different solute mixtures. Furthermore, it has been reported [2] that no difference exists in the condensation efficiencies of either maritime aerosols sampled by impactors, or of brine residues of seawater from different geographic locations. The data of figure 5, on the other hand, clearly point toward the dependence of the amount of condensed water on sea salt particles on the point of the origin of the latter. The explanation of such discrepancies can probably be sought in the different methods of aerosol and seawater sampling, the differences in depths in the ocean from which the samples were taken, and different methods of analyses, viz., mass determinations of salt deposits on substrates versus in situ observations by optical means. Whatever the cause, a connection between anomalous deliquescence of sea spray aerosols and organic matter dissolved or suspended in that part of the ocean from which they originate is strongly suggested by the data of figure 5 in conjunction with the organics analyses reported in figures 1-4. The effect is the strongest at coastal waters on both sides of the North American Continent; they contain larger numbers of organic substances in higher concentrations than do mid-oceanic waters typified by the Hawaii samples.

The natural production of aerocolloidal systems consisting of both organic and inorganic materials is significant in the development of maritime and continental clouds. It has been demonstrated that natural sea-salt particles produced from coastal waters are less hygroscopic than synthetic sea-salt crystals. Apparently, some of the organic molecules attach themselves to natural sea-salt particles and are surface active in the sense that they replace water molecules at the surface due to their smaller dipole moment (sometimes caused by deformation and polarization only). The thereby reduced Coulombic attraction to the solvent molecules lowers the surface energy. Once a monomolecular surface layer is formed, the accommodation coefficient for water vapor is reduced by the same electrostatic effects. Reduced droplet growth is a logical consequence.

Consequences for in-cloud processes can be postulated based on the data in figure 5. The light scattering ratio between a synthetic inorganic solution and natural ocean water off the North American Coast is 1.6 at relative humidities approaching 100 percent. Assuming a b  $\alpha$  r² dependence of the light-scattering coefficient b and cloud droplet radius r, this corresponds to a volume ratio of 2 with the following implications: a) Given an average water content of 0.5 g m $^{-3}$  and a specific heat of air of 300 cal m $^{-3}$ , the difference in latent heat released during a retarded condensation process amounts to a cooling off of the atmosphere by 0.5 C. b) Assuming the results found at slightly undersaturated conditions can be extrapolated to the supersaturated state, the rate of change of supersaturation of an air parcel during adiabatic lifting will be increased by about 12 percent from its value at unaffected droplet growth. c) The collision efficiency for the same collector drop radius will be reduced to 50 percent of its value for an unaffected drop. Subsequent coalescence could be altered by the presence of monolayers on the droplet surfaces.

#### IV. — SUMMARY AND CONCLUSIONS.

We have demonstrated that seawater near the continental coasts contains organic matter with a great variety of molecular weights and structures, and that midocean water samples (Hawaii) contain lesser, but still significant, amounts of organic

substances. This organic material, dissolved or dispersed in seawater, is collected by diffusion or coalescence on the surface of air bubbles as they rise to the surface. The bursting-bubble mechanism releases this organic material into the air in the form of both vapor and particulate matter. Part of the organic material is attached to the seasalt particles produced by the same process, either during their formation or by coagulation and diffusion while airborne.

The fractionation of inorganic ions during the bursting of bubbles at the ocean surface unquestionably will affect the deliquescence of the resulting sea-salt particles. However, the results reported here are strongly indicative of an effect of naturally occurring dissolved or suspended organic materials on the sea aerosol hygroscopicity. If inorganic composition alone influenced droplet growth [2], the hygroscopicity of sea-salt aerosols should be independent of geographic origin. But the results reported here (Fig. 5) show such dependence. This dependence of droplet growth on origin is inescapably due to dissolved or suspended organic matter in surface waters. Moreover, if the ocean dissolved or suspended material is thought of as being associated with inorganic ions, an effect on the fractionation during oceanic nuclei production is to be expected.

Our mass spectrometric and gas chromatographic analyses have shown that occasionally the coastal water contains trace amounts of phthalate ester plasticizers. Hence, although naturally occurring organic substances are preponderant in coastal ocean waters, the possibility exists that man can inadvertently affect atmospheric phenomena by polluting coastal ocean waters.

#### ACKNOWLEDGEMENTS.

We thank Dr. Helmut Weickmann, NOAA, for many interesting and helpful discussions, and Mr. Robert Pressey, Denver Research Institute, for his assistance in performing the mass spectrometric analyses.

#### REFERENCES

- [1] PUESCHEL R.F., CHARLSON R.J. and AHLQUIST N.C. (1969). On the anomalous deliquescence of sea spray aerosols. J. Appl. Meteor., 8, pp. 995-98.
- [2] Winkler P. and Junge C.E. (1971). Comments on « Anomalous deliquescence of sea spray
- aerosols ». J. Appl. Meteor., 10, pp. 159-63.
  [3] GLASS S.J., Jr., and MATTESON M.J. (1973). Ion enrichment in aerosols dispersed from bursting bubbles in aqueous salt solutions. Tellus, 25, pp. 272-80.
- [4] STOROZHILOVA A.I. (1971). Passivation of hygroscopic condensation nuclei by surfactant adsorption from gas phase. Advances in Aerosol Physics, no 1 (V.A. Fedoseev, Ed.), pp. 47-52, Israel Program for Scientific Translations, Jerusalem.
- [5] LEONOV L.F., PROKHOVOV P.S., EFANOVA T.A. and ZOLOTAREV I.A. (1972). Passivation of condensation nuclei by cetyl alcohol vapor. Advances in Aerosol Physics, nº 2 (V.A. Fedoseev, Ed.), pp. 12-20, Israel Program for Scientific Translations, Jerusalem.
- [6] SILAEV A.V., IVANCHENKO L.V. and BAKHANOVA R.A. (1972). Passivation of ammonium chloride nuclei by cetyl alcohol vapor. Advances in Aerosol Physics, no 2 (V.A. Fedoseev, Ed.), pp. 59-65, Israel Program for Scientific Translations, Jerusalem.
- [7] CHALENKO V.G., GEL'MAN L.A. and PESTUN T.S. (1972). The effect of surfactant monolayers on the rate of evaporation of water. Advances in Aerosol Physics, nº 2 (V.A. Fedoseev, Ed.), pp. 21-32, Israel Program for Scientific Translations, Jerusalem.
- [8] WOODCOCK A.H. (1952). Atmospheric salt particles and raindrops. J. Meteor., 9, p. 200.
- [9] VAN VALIN C.C. and Allee P.A. (1971). Water cloud stabilization with chlorinated silanes. J. Atmos. Sci., 28, pp. 1076-78.
- 10] DAL NOGARE S. and JUVET R.S., Jr. (1962). Gas-Liquid Chromatography, Theory and Practice, John Wiley and Sons, New York.



#### EFFECTS OF AIR POLLUTANTS ON CLOUD NUCLEATION

Rudolf F. Pueschel, Charles C. Van Valin, Farn P. Parungo

NOAA, Atmospheric Physics and Chemistry Laboratory, Boulder, CO 80302

Abstract. The nucleation efficiency of an urban aerosol is closely related to its chemical composition, which is strongly affected by human activities. Sulfates and leadbromochloride have been found to temporarily increase the surface solubility and capillarity of naturally produced insoluble clay particles. This phenomenon alters the atmospheric nuclei budget and affects the natural mechanisms that remove pollutants from the atmosphere.

Concern exists that man's activities that enhance the contamination rate of the atmosphere might have detrimental effects on weather and climate. Numerous examples of inadvertent weather modification have been reported in the literature [e.g., Schaefer, 1969; Changnon, 1969, 1971; Hobbs et al., 1970; Weickmann, 1972]. However, additional information is needed in order to discuss the complex problems of how anthropogenic nuclei are generated, what their turnover times are, on what trajectories they travel through the atmosphere, and by what mechanisms they convert water vapor into the liquid or solid phases.

The aerosol parameters that determine particle efficiency in atmospheric water phase transitions are chemical composition, water solubility, size, and surface structure [Pruppacher, 1973]. Examples of inadvertent weather modification can be postulated if human activities can be shown to affect one or more of these characteristics. Scanning electron microscopy combined with energy dispersive X-ray analysis [Fitzgerald and Gantzel, 1971] provides a sufficiently sensitive method for simultaneous evaluation of aerosol composition, size, and surface structure. Aerosols sampled on membrane filters in metropolitan Denver were subjected to this type of analysis. The aerosol sampling was performed in a mobile laboratory which also has been equipped with standard aerosol measuring equipment, i.e., recording Aitken, cloud condensation and ice nuclei counters, and an integrating nephelometer, providing a continuous record of variations in the nuclei population.

As a case study, we present here data of 8 June 1973 when the mobile laboratory was located within the South Platte River valley on the northeast edge of Denver, Colorado, at an elevation of ~1700 m msl. This was within the area affected by the pollution episode which occurred on that day. The temperature was ~16°C at 0600 MDT with a thin cloud deck at 4500 m (est.), and a low-level inversion (~300 m). The cloud deck evaporated at about 0915 MDT resulting in exposure of the polluted layer to solar irradiation with the UV intensity comparable with that which is usually experienced above the boundary layer. This was fol-

Copyright @1974 by the American Geophysical Union

lowed almost immediately by the disintegration of the inversion. By noon the temperature had risen to  $\sim\!\!29\,^\circ\text{C}$ . In a fashion typical of Denver area inversions, the air movement was light from the south-southwest carrying the polluted urban atmosphere across the laboratory site. When the inversion broke, the air movement became very light northerly to calm, and for several hours thereafter was characterized by vertical mixing rather than organized horizontal motion.

Results typical of Denver pollution episodes are shown in Fig. 1, 2, and 3. Fig. 1 shows the variation with time of the chemical composition of the Denver aerosol. Plotted for sequential time periods are the percentages of aerosols containing the elements aluminum, silicon, calcium, sulfur, lead, chlorine. The graphs show that the high proportion of particles containing the elements Al, Si and Ca does not vary significantly with time. This is proof of the strong clay mineral character of the background aerosol formed in and around Denver, Colorado. On the other hand, the fraction of particles containing Pb, S, and Cl are subject to strong variations with time and have apparent peaks during the rush hours. Unquestionably, during pollution episodes, the primary source of these three elements is human activity. Pb and Cl, for example, are found in PbBrCl a component of particulate automobile exhaust. Sulfur-containing particles are probably sulfates from a  $SO_2 \rightarrow SO_4^{\frac{\pi}{4}}$  gas-to-particle conversion process. The data in Figure 1 resulted from the analyses of several hundred particles. These

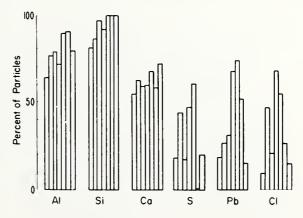


Figure 1. Variation with time of the elements Al, Si, Ca, S, Pb, and Cl contained in Denver aerosol on 8 June 1973. The bars correspond in sequence from left to right to the time (MDT) 0706-0735, 0736-0809, 0811-0856, 0858-0952, 0954-1112, 1113-1214, and 1217-1232 respectively.

were selected at random and in each instance varied in size between 0.1 $\mu$ m and 20 $\mu$ m diameter. Whereas slight changes in the size distribution of the aerosols sampled at different times were observed, these size changes were too small to cause the changes in the nucleation properties of the particles that were observed.

It is illuminating to look into the cloud and ice nucleating properties that are associated with chemical changes. Figure 2 shows temporal variations of light scattering (measured with the Charlson integrating nephelometer), Aitken nuclei (measured at 300 percent supersaturation), cloud condensation nuclei (measured in a thermal diffusion cloud chamber at 0.5 percent supersaturation), and ice nuclei (measured with the NCAR acoustic counter). Of interest here is the large increases in light scattering, cloud condensation nuclei, and ice nuclei at about 0940 MDT. The ice nuclei concentration declined to previous levels almost immediately, whereas cloud condensation nuclei concentration and aerosol light scatter remained elevated for approximately 15 minutes longer. After ~1000 MDT, all four parameters gradually declined as nearby traffic subsided to midday levels and atmospheric mixing continued.

The large increase in light scattering at 0930 MDT could represent a coagualtion process having taken place, which created particles of lightscattering size at the expense of Aitken nuclei. The sudden onset, however, of a visibility reduction suggests the advection to the measuring site of an optically different aerosol owing to the chemical changes shown in Figure 1. Many of the newly created particles were also active as cloud condensation nuclei, by means of increased surface solubility from adsorbed H2SO4 or (NH4)2SO4 and/or increased surface capillarity. McDonald (1964) has shown that, to act as a cloud condensation nucleus, a mineral dust particle must satisfy the relation D > 2r\*, where r\* is the Kelvin radius at a given supersaturation, and D is the greatest transverse dimension of a nonspherical wettable particle. Adding a water soluble substance to the particle surface has the effect of lowering r\*. This implies that smaller, and therefore more, dust particles can now act as cloud condensation nuclei, as was actually observed. (Note that the adsorption of organic matter on silicate particles would have the opposite effect. Organic matter lowers the water solubility and increases the contact angle, thus decreasing the nucleating capability of the particle.)

The increased ice nuclei activity that was observed (Figure 2) is attributed to adsorption on the mineral particle surface of lead halide particles. The rapid decline in ice nuclei activity that occurred before the atmosphere became diluted would then be attributable to photolytic decomposition [Pierrard, 1969] with the products being gaseous halogens plus solid PbO. That such a pathway is likely was borne out by the more rapid decline (Figure 1) of the incidence of Cl on aerosol particles than that of Pb following the most heavily polluted time period. Such a conversion of lead halides to PbO would account for a concomitant decrease in cloud condensation nuclei activity because of the PbO having two

orders-of-magnitude lower solubility in water.

An investigation of individual particles illuminates to some degree the previous discussion. Figure 3 shows a typical example of a mixed particle. While the center of the particle (part b) contains Si only, and probably consists of the insoluble SiO<sub>2</sub>, other portions of the same particle (parts a and c) contain many more elements with a multitude of possible compound formations. Section (a) contains only the elements Pb, Br, Cl and thus is uniquely identified as leadbromochloride.

The findings reported here have implications for the removal of aerosol particles from the at-

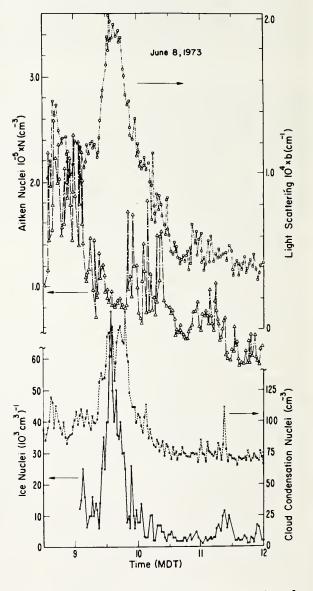


Figure 2. Time variation of the concentration of Aitken nuclei ( $\Delta$ ), cloud condensation nuclei (X), ice nuclei (0), and light scatter ( $\Box$ ) on 8 June 1973 in Denver.

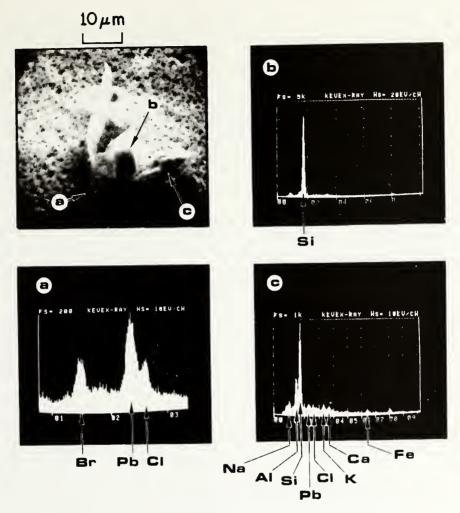


Figure 3. Size, shape and chemical composition of a mixed nucleus in the Denver atmosphere.

mosphere by precipitation scavenging. Greenfield (1957) showed that two distinctly different mechanisms can produce the scavenging effect. Much of the giant sized particulate matter, with radii > 5 to 10µm, are removed by inertial impaction with raindrops, while the smaller particles are removed by Brownian diffusion of aerosols of radii < 0.01µm into cloud droplets. Therefore, a gap occurs in the particle size distribution, extending from about  $r\approx 0.05 \mu m$  to about  $r\approx 5 \mu m,$  where neither aerodynamic impaction by raindrops nor Brownian capture by cloud droplets can remove aerosols with appreciable efficiency. Slinn and Hales (1970) showed that thermophoretic and diffusophoretic effects narrow this "Greenfield gap" somewhat, but do not eliminate it. The width of the scavenging gap of the optically most active aerosol sizes should be significantly reduced during pollution episodes, when increased solubility and capillarity enhance the rainout mechanism.

In summary, the city aerosol has a mixed nature which is caused by an interaction of natural clay

particles with anthropogenic aerosols and gases. Because the rates of production, interaction, reactions, and decomposition change with time, both the concentrations and the chemical composition of the metropolitan aerosol are subject to strong temporal fluctuations due to human interference. Consequently, the cloud nucleating capability of the aerosol in metropolitan atmospheres varies strongly with time owing to these chemical changes. In this study, we found that compounds containing PbBrCl and S are examples of air pollutants that convert otherwise inert mineral dust particles into active cloud nuclei. Such a causeeffect relationship probably also exists between other types of pollutants and the atmospheric cloud nuclei budget.

Acknowledgment. We thank Dr. Helmut K. Weickmann for providing the logistics to make these investigations possible. His valuable suggestions in many discussions to this phase of the work are greatly appreciated. Richard A. Proulx deserves special thanks for his dedication and effectiveness toward success of the field work reported here.

#### References

- Changnon, S., Recent Studies of Urban Effects on Precipitation, <u>Bull. Amer. Meteorol. Soc.</u>, <u>50</u>, 411-421, 1969.
- Changnon, S., Comments on the Effect of Rainfall of a Large Steelworks, <u>J. Appl. Meteorol.</u>, <u>10</u>, 165-168, 1971.
- Fitzgerald, R., and P. Gantzel, X-ray Energy Spectrometry in the 0.1 to 10A Range in Energy Dispersion X-ray Analysis: X-ray and Electron Probe Analysis, <u>ASTM STP 485</u>, Am. Soc. Testing and Materials, Philadelphia, Pa., 3-35, 1971.
- Greenfield, S. M., Rain Scavenging of Radioactive Particulate Matter from the Atmosphere, <u>J.</u> Meteorol., <u>15</u>, 115-125, 1957.
- Hobbs, P. V., L. F. Radke, and S. J. Shumway, Cloud Condensation Nuclei from Industrial Sources and their Apparent Influence on Precipitation in Washington State, <u>J. Atmos. Sci.</u>, <u>27</u>, 81-89, 1970.
- McDonald, J. E., Cloud Nucleation on Insoluble Particles, <u>J. Atmos. Sci.</u>, <u>21</u>, 109-116, 1964.

- Pierrard, J. M., Photochemical Decomposition of Lead Halides from Automobile Exhaust, Env. Sci. and Technol., 3, 48-51, 1969.
- Pruppacher, H. R., The Role of Natural and Anthropogenic Pollutants in Cloud and Precipitation Formation, Chemistry of the Lower Atmosphere, chap. 1, S. I. Rasool, Ed., Plenum Press, New York, 1973.
- Schaefer, V. J., The Inadvertent Modification of the Atmosphere by Air Pollution, <u>Bull. Amer.</u> <u>Meteorol. Soc.</u>, <u>50</u>, 199-206, 1969.
- Slinn, W. G., and J. M. Hales, Phoretic Processes in Scavenging, in <u>Precipitation Scavenging</u>, <u>AEC Symp. Ser.</u>, 22, 1970.
- Weickmann, H. K., Man-made Weather Patterns in the Great Lakes Basin, <u>Weatherwise</u>, <u>25</u>, 260-267, 1972.

(Received February 25, 1974; revised March 29, 1974; accepted April 2, 1974.)

# Approximations to diffusion in a random veiocity field

M. L. Thiebaux

National Oceanic and Atmospheric Administration, Boulder, Colorado 80302

(Received 30 May 1973)

The diffusion of a marked fluid particle is considered in a random incompressible, isotropic velocity field, stationary in space and time. The integrodifferential equations proposed earlier by Bourret and Saffman, for the time evolution of the probability density of marked fluid particles, are introduced and solutions are found for a Gaussian Lagrangian covariance function. An improved equation is derived by including the effects of higher-order moments. Solutions are found to be in good agreement with independent results based on fluid particle diffusion in a multivariate-normal field.

#### I. INTRODUCTION

The diffusion of marked fluid particles in a turbulent flow is described by a density function that satisfies a linear stochastic equation. Statistical properties of the motion of the particles can be related to the statistical properties of the turbulent flow, but since the general relation appears mathematically intractable, it is not surprising that a satisfactorily complete solution has not been found. In this paper, we shall test some simple approximations to the diffusion problem by comparing with independent results based on computer simulation and the direct-interaction approximation. The goal of the approximations used or referred to in this paper is to take as input information some basic statistics of the velocity field, and derive the probability density function for the concentration of marked fluid particles.

We shall be concerned with diffusion in an incompressible random velocity field  $\mathbf{u}(\mathbf{x},t)$  that is stationary in space and time, and isotropic. We assume there exists a length scale defined as the reciprocal of some characteristic wave number in the velocity spectrum. Dimensionless space and time units will be used throughout this paper by measuring distance in units of this length scale, and by measuring velocity in units of the root-meansquare of one Cartesian component of the velocity field Accordingly, the unit of time may be thought of as a characteristic eddy circulation time.

Let G(x,t) denote the probability density that a marked fluid particle starting at x = 0, t = 0 arrives at x at time t. The characteristic function or Fourier transform is given by

$$\tilde{G}(\mathbf{k},t) = \int G(\mathbf{x},t) \exp(-i\mathbf{k} \cdot \mathbf{x}) d\mathbf{x}. \tag{1}$$

Since G(x, t) is a probability density and  $G(x, 0) = \delta(x)$ , we have

$$\tilde{G}(0,t) = \tilde{G}(\mathbf{k},0) = 1$$
, for all  $\mathbf{k}$  and  $t$ . (2)

The dispersion in the  $x_1$  direction is the moment

$$X(t) = \int x_1^2 G(\mathbf{x}, t) d\mathbf{x} = -\lim_{\mathbf{k} \to 0} \frac{\partial^2}{\partial k_1^2} \tilde{G}(\mathbf{k}, t). \tag{3}$$

Other important statistics derivable from  $\tilde{G}(\mathbf{k},t)$  are the effective eddy diffusivity,<sup>3</sup>

$$\kappa(t) = \frac{1}{2} \frac{dX(t)}{dt},\tag{4}$$

and the Lagrangian velocity covariance,4

$$R_L(t) \equiv \langle u_1(t)u_1(0)\rangle_L = \frac{1}{2}\frac{d^2}{dt^2}X(t).$$
 (5)

Assuming that as  $t \to \infty$ , the eddy diffusion process behaves more and more like classical (thermal or molecular) diffusion,<sup>4</sup> then we expect

$$\kappa(t) \to \kappa(\infty), \quad \text{a finite limit,}$$

$$\tilde{G}(\mathbf{k}, t) \to \exp(-k^2 \kappa(\infty)t), \quad \text{for } k \ll 1, \quad (6)$$

and hence,

$$X(t) \to 2\kappa(\infty)t.$$
 (7)

For  $t \ll 1$ , a fluid particle moves such a short distance that any realization of  $\mathbf{u}(\mathbf{x},t)$  may be considered approximately constant in space and time. Constant velocity field realizations, with multivariate-normal statistics, yield the exact solution<sup>2</sup>

$$\tilde{G}(\mathbf{k},t) = \exp(-\frac{1}{2}k^2t^2), \tag{8}$$

in which case

$$X(t) = t^2. (9)$$

The result (9) is also the short time behavior of the dispersion under less restrictive conditions.<sup>4</sup>

In Sec. II, we introduce an integrodifferential equation for  $G(\mathbf{x}, t)$ , derived earlier and containing a second-order moment of the velocity field as a kernel function. An analytical study is made of the Laplace transformed solution when  $R_L$  is Gaussian and comparisons with earlier computer experiments are exhibited. In Sec. III, we derive an improved integrodifferential equation based on the inclusion of simulated effects of higher velocity moments. Solutions are tested against the computer experiments.

# II. SECOND-MOMENT INTEGRODIFFERENTIAL EQUATION

The density  $\theta(x,t)$  of marked fluid particles advected by a velocity field  $\mathbf{u}(x,t)$  evolves according to

$$\frac{\partial}{\partial t}\theta(\mathbf{x},t) = -\mathbf{u}(\mathbf{x},t) \cdot \nabla \theta(\mathbf{x},t). \tag{10}$$

A stochastic (Wiener-Hermite)<sup>5</sup> expansion of Eq. (10)

.

Copyright @ 1974 American Institute of Physics

509

about the Gaussian parts of  $\theta$  and u yields an integrodifferential equation of infinite order,  $^{6,7}$  involving Eulerian velocity field moments, for the ensemble mean  $\bar{\theta}(\mathbf{x},t)$ . The probability density  $G(\mathbf{x},t)$ , which is the Green's function for  $\bar{\theta}$ , satisfies the same equation. Saffman's first isolated the lowest-order term in the expansion, thereby obtaining an approximate linear integrodifferential equation that reduces to

$$\frac{\partial G}{\partial t}(\mathbf{x},t) = \int_0^t dt' A(t-t') \nabla^2 G(\mathbf{x},t'), \qquad (11)$$

for the velocity field considered here. The above derivation gives  $A(t-t') = R_E(t-t')$ , where the latter is the (isotropic) Eulerian one-point covariance function. The Fourier transform version of Eq. (11) is

$$\frac{\partial \tilde{G}}{\partial t}(\mathbf{k}, t) = -k^2 \int_0^t dt' A(t - t') \tilde{G}(\mathbf{k}, t'). \tag{12}$$

Applying (2)-(5) to (12), we find

$$X(t) = 2 \int_0^t (t - t') A(t') dt', \qquad (13)$$

$$\kappa(t) = \int_0^t dt' A(t'), \tag{14}$$

$$R_L(t) = A(t). (15)$$

The identity (15) which follows from the approximate equation (11) suggests that the approximation can be improved by replacing A(t-t') by  $R_L(t-t')$ . The resulting equation was earlier hypothesized and discussed by Bourret.<sup>9</sup> An independent justification of Bourret's equation will be presented in Sec III.

An intermediate approach is taken in this section. The form of Eq. (12) will be preserved, while A(t - t') will be considered an adjustable function that approximates  $R_L(t - t')$ .

The solution of Eq. (12) may be obtained in closed form in terms of Laplace transforms. Letting

$$H(\mathbf{k}, p) = \int_0^\infty \exp(-pt)\tilde{G}(\mathbf{k}, t) dt$$
 (16)

and

$$S(p) = \int_0^\infty \exp(-pt)A(t)\,dt,\tag{17}$$

then, after some manipulation, we find the Laplace transformed solution

$$H(\mathbf{k}, p) = [p + k^2 S(p)]^{-1}$$
 (18)

Consequently, the solution is given by the integral representation

$$\tilde{G}(\mathbf{k},t) = \frac{1}{2\pi i} \int_{\gamma - i\infty}^{\gamma + i\infty} \frac{\exp(pt) dp}{p + k^2 S(p)},$$
 (19)

where the contour of integration lies to the right of all singularities of  $H(\mathbf{k}, p)$  in the complex p plane.

For Gaussian or exponential A(t), the singularities of  $H(\mathbf{k}, p)$  are simple poles at locations  $p = p_i(k^2)$ , i = 1, 2,

..., such that  $Re[p_i(k^2)] < 0$  if  $k^2$  is real and positive. The solution for exponential A(t) has been presented and discussed elsewhere. Here, we shall first discuss some properties of the solution for Gaussian A(t) and then compare with independent results for which  $R_E$  is Gaussian and  $R_L$  is approximately Gaussian.

The Laplace transform of

$$A(t) = \exp(-a^2t^2) \tag{20}$$

is

$$S(p) = (\sqrt{\pi}/2a) \exp(p^2/4a^2)[1 - \operatorname{erf}(p/2a)].$$
 (21)

With  $z \equiv p/2a$ , Eq. (19) becomes

$$\tilde{G}(\mathbf{k},t) = \frac{1}{2\pi i} \int_{\gamma - i\infty}^{\gamma + i\infty} \frac{\exp(2azt) dz}{z + (k^2/2a^2)\chi(z)},\tag{22}$$

where

$$\chi(z) = \int_{-\infty}^{\infty} \exp(z^2 - w^2) dw. \tag{23}$$

If  $z_n$  is a zero of  $z + (k^2/2a^2)\chi(z)$ , then the residue of the corresponding pole in (22) is

$$\exp(2azt)\bigg/\frac{d}{dz}[z+(k^2/2a^2)\chi(z)]\tag{24}$$

evaluated at  $z_n$ . From the properties of (23), the denominator in (24) reduces to

$$1 - 2\left(z_n^2 + \frac{k^2}{4a^2}\right),\tag{25}$$

and hence we have the representation

$$\tilde{G}(\mathbf{k},t) = \sum_{n} \frac{\exp(2az_n t)}{1 - 2[z_n^2 + (k^2/4a^2)]}.$$
 (26)

Figure 1 shows the trajectories of the poles,  $z_n = z_n(k^2/4a^2)$ , in a portion of the upper half of the complex z plane. The usefulness of representation (26) follows from the observation that the trajectory of the leading pole, which lies farthest to the right, controls the dominant term in the sum as  $t \to \infty$ .

For  $k^2$  in the neighborhood of zero, it follows from (21) that the trajectory of the leading pole is given approximately by

$$z_0 \approx -\sqrt{\pi} \, k^2 / 4a^2$$
 for  $k^2 \ll a^2$ , (27)

and hence

$$\tilde{G}(\mathbf{k},t) \approx \exp(-\frac{1}{2}\sqrt{\pi} k^2 t/a)$$
 (28)

This is in agreement with the expected classical behavior (6) since from (14) we find

$$\kappa(\infty) = \int_0^\infty A(t') dt' = \sqrt{\pi/2}a. \tag{29}$$

As  $k^2$  increases from zero, the leading pole is joined by another pole moving along the negative real axis, and for

510

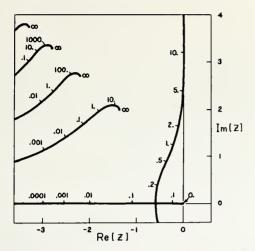


FIG. 1. Complex z plane showing some trajectories of poles  $z_s(k^2/4a^2)$ . Values of  $k^2/4a^2$  are indicated on trajectories. Leading trajectory lies on negative real axis and asymptotically approaches imaginary axis.

 $k^2 > 0.589 \ a^2$ , the poles move off the real axis to form a complex conjugate pair. As  $k^2 \to \infty$ , the poles recede to  $\infty$  according to

$$z_0 = -(\sqrt{\pi} k^2 / 8a^2) \exp(-k^2 / 4a^2)$$
  

$$\pm i [k^2 / 4a^2) + \frac{1}{2} ]^{1/2} \quad \text{for } k^2 \gg 4a^2, \quad (30)$$

which leads to the large t, large  $k^2$  behavior

$$\tilde{G}(\mathbf{k},t) = \exp\left[-\sqrt{\pi} \, at \left(\frac{k^2}{4a^2}\right) \exp\left(\frac{-k^2}{4a^2}\right)\right] \cos(kt). \quad (31)$$

Thus, for a fixed, large value of  $k^2$ ,  $\bar{G}(\mathbf{k},t)$  decays to zero as  $t\to\infty$ . For a fixed large value of t, the exponential factor attains its minimum value  $\exp(-0.652at)$  at  $k^2=4a^2$ , but then increases again to unity as  $k^2/4a^2\to\infty$ . The large  $k^2$  behavior thus approaches  $\bar{G}(\mathbf{k},t)\approx\cos(kt)$ . Although (31) is bounded by unity and formally corresponds to a finite modal relaxation time that vanishes as  $k^2\to\infty$ , this unphysical sinusoidal behavior is peculiar to the nearly wave-like character of Eqs. (11) or (12). On the other hand, if the corresponding Green's function is applied to an initially spread-out distribution  $\bar{\theta}(\mathbf{x},0)$  of particles such that the Fourier transform of  $\bar{\theta}$  cuts off sufficiently rapidly for  $k^2\gg 4a^2$ , then the time evolution of the large k modes, however mistreated, would not appreciably affect the determination of  $\bar{\theta}(\mathbf{x},t)$ .

The small t behavior of  $\tilde{G}(\mathbf{k},t)$  is easily found by deriving its Taylor series in t. Assuming only that  $\partial A(0)/\partial t = 0$ , a straightforward iteration of Eq. (12) yields

$$G(\mathbf{k},t) = 1 - \frac{1}{2}k^{2}t^{2} + \frac{1}{24}\left(k^{4} - k^{2}\frac{\partial^{2}A}{\partial t^{2}}(0)\right)t^{4} + O(t^{6})$$
(32)

which is consistent with (9) and also with (8) to order  $t^2$ .

This section is concluded with a comparison of numerically evaluated solutions of Eq. (12) with computer

Phys. Fluids, Vol. 17, No. 3, March 1974

experiments of diffusion in a random velocity field. The latter results, due to Kraichnan, were based on constructing particle trajectories in a two-dimensional, incompressible, isotropic, multivariate-normal velocity field. In terms of the dimensionless units introduced in Sec. I, the comparison is made with Kraichnan's results for an Eulerian time correlation function  $\exp(-\frac{1}{2}t^2)$  and an energy spectrum  $\delta(k-1)$ . In this particular case, his computations of the Lagrangian velocity correlation, both by the computer simulation and by the direct-interaction approximation, are well-fitted by a Gaussian curve  $\exp(-a^2t^2)$  where  $a\approx 1.0$ . Accordingly, in Fig. 2, we display  $\tilde{G}(\mathbf{k},t)$  computed from (12) using the Gaussian form (20) for several values of a in the neighborhood of unity.

The agreement between  $\tilde{G}(\mathbf{k},t)$ , derived from Eq. (12) with parameter a=1, and the computer experiment points reproduced in Fig. 2 is good for the smaller values of k, but an appreciable wave-like departure is already seen at k=1. Kraichnan's direct-interaction approximation curves are also reproduced in Fig.2.

# III. HIGHER-ORDER INTEGRODIFFERENTIAL EQUATION

The unsatisfactory high-k behavior in the second moment equation can be improved by considering the effects of the higher-order moments that were neglected in Eq. (11). The infinite-order integrodifferential equation, of which Eq. (11) is the lowest-order part, is

$$\frac{\partial G}{\partial t}(\mathbf{x},t) = \int_0^t dt' \{ \langle \mathbf{u}(\mathbf{x},t) \cdot \nabla \mathbf{u}(\mathbf{x},t') \cdot \nabla \rangle + \sum_{n=1}^{\infty} (-1)^n \int_{t'}^t dt_n \int_{t_n}^t dt_{n-1} \int_{t_{n-1}}^t dt_{n-2} \cdots \int_{t_2}^t dt_1 \times \langle \langle \mathbf{u}(\mathbf{x},t) \cdot \nabla \mathbf{u}(\mathbf{x},t_1) \cdot \nabla \mathbf{u}(\mathbf{x},t_2) \rangle \cdot \nabla \cdots \mathbf{u}(\mathbf{x},t_n) \cdot \nabla \mathbf{u}(\mathbf{x},t') \cdot \nabla \rangle \} G(\mathbf{x},t').$$
(33)

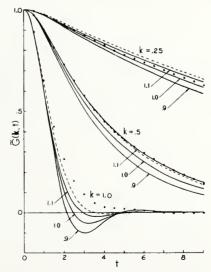


FIG. 2. Plots of  $\tilde{G}(\mathbf{k},t)$  vs time. Solid curves are computed from Eq. (12) with a Gaussian kernel function and are labeled with parameter a=0.9, 1.0, 1.1. Points are computer experiment values. Dashed curves are direct interaction approximation values.

The notation  $\langle\langle \cdots \rangle\rangle$  stands for a certain finite linear combination of products of Eulerian moments very similar to a cumulant of order n+2. The precise definition is immaterial here. All that we need to know is that each  $\mathbf{u}$  in each term in the linear combination is coupled to a  $\nabla$ , which operates on everything to its right. Hence, assuming stationarity, the bracketed kernal  $\{\cdots\}$  in (33) is an infinite-order differential operator of the form

$$\sum_{n=0}^{\infty} \sum_{m=1}^{n+2} F_{i_1 i_2 \cdots i_m}^{(n)}(t-t') \nabla_{i_1} \nabla_{i_2} \cdots \nabla_{i_m}, \qquad (34)$$

or, after combining terms of the same order, of the form

$$\sum_{m=1}^{\infty} H_{i_1 i_2 \cdots i_m}(t-t') \nabla_{i_1} \nabla_{i_2} \cdots \nabla_{i_m}.$$
 (35)

Each tensor  $H_i \cdots I_n$  is an infinite sum of time integrals of Eulerian moments. Isotropy further reduces (35) to

$$\sum_{m=1}^{\infty} A^{(m)}(t-t')(\nabla^2)^m, \tag{36}$$

so that the Fourier transform version of (33) is

$$\frac{\partial \tilde{G}(\mathbf{k},t)}{\partial t} = \sum_{m=1}^{\infty} \int (-k^2)^m A^{(m)}(t-t') \tilde{G}(\mathbf{k},t') dt'_{\delta} \quad (37)$$

It is now possible to evaluate the kernel functions  $A^{(m)}(t-t')$ , each of which contains Eulerian moments of arbitrarily high order, in terms of Lagrangian moments by comparing (37) with the formally exact power series expansion of  $\tilde{G}(\mathbf{k},t)$  in the components of  $\mathbf{k}$ ,

$$\bar{G}(\mathbf{k},t) = 1 + \sum_{m=1}^{\infty} \frac{(-1)^m}{(2m)!} k_{i_1} k_{i_2} \cdots k_{i_{2m}} \times \int_0^t dt_1 \int_0^t dt_2 \cdots \int_0^t dt_{2m} \langle u_{i_1}(t_1) u_{i_2}(t_2) \cdots u_{i_{2m}}(t_{2m}) \rangle_L.$$
 (38)

The expression  $\langle \cdots \rangle_L$  denotes the Lagrangian moment of order 2m. With isotropy and stationarity, the second time derivative of (38) reduces to

$$\frac{\partial^{2} \tilde{G}}{\partial t^{2}}(k,t) = -k^{2} \langle u_{1}(t)u_{1}(0) \rangle_{L} 
+ \frac{1}{2}k^{4} \int_{0}^{t} dx \int_{0}^{t} dy [\langle u_{1}(t)u_{1}(0)u_{2}(x)u_{2}(y) \rangle_{L} 
+ 2 \langle u_{1}(t)u_{1}(x)u_{2}(y)u_{2}(0) \rangle_{L}] + O(k^{6}).$$
(39)

On the other hand, from (37) we find

$$\lim_{k \to 0} \frac{\partial^2}{\partial k^2} \frac{\partial^2 \tilde{G}(\mathbf{k}, t)}{\partial t^2} = -2A^{(1)}(t), \tag{40}$$

$$\lim_{k \to 0} \frac{\partial^4}{\partial k^4} \frac{\partial^2 \tilde{G}(\mathbf{k}, t)}{\partial t^2} = 24 A^{(2)}(t) + 24 \int_0^t dx \int_0^t dy A^{(1)}(x) A^{(1)}(y), (41)$$

and so establish that

$$A^{(1)}(t) = \langle u_1(t)u_1(0)\rangle_L \equiv R_L(t) \tag{42}$$

and

512

$$A^{(2)}(t) = -\int_0^t dx \int_0^{t-x} dy \, R_L(x) \, R_L(y)$$

$$+ \int_{0}^{t} dx \int_{0}^{t} dy \left[ \frac{1}{2} \langle u_{1}(t)u_{1}(0)u_{2}(x)u_{2}(y) \rangle_{L} + \langle u_{1}(t)u_{1}(x)u_{2}(y)u_{2}(0) \rangle_{L} \right].$$
(43)

The derivation of (42) is the independent justification, mentioned in Sec. II, of Bourret's hypothesis concerning the nature of the kernel function in Eq. (12). The derivation corroborates a previous conjecture? that the Bourret equation can be derived by selectively summing those parts of the right-hand side of (33) that contain second-order derivatives of  $G(\mathbf{x}, t)$ .

The kernel function sum in (37) may be written as

$$\sum_{m=1}^{\infty} (-k^2)^m A^{(m)}(t-t')$$

$$= -k^2 A^{(1)}(t-t') \exp[-g(k^2, t-t')], \quad (44)$$

where  $g(k^2, t - t')$  is to be determined approximately. The basis for the approximation is to conjecture that  $g(k^2, t - t')$  is effectively well-represented by its leading term in an expansion of (44) in powers of  $k^2$  and t - t'. To carry this out we need the leading term in (43). Isotropy requires

$$\langle u_1(0)u_1(0)u_2(0)u_2(0)\rangle_L = \frac{1}{3}\langle u_1^4\rangle,$$
 (45)

true in both two and three dimensions, so that (43) yields

$$A^{(2)}(t-t') = \frac{1}{2}(\langle u_1^4 \rangle - 1)(t-t')^2 + \cdots, \quad (46)$$

and we find

$$g(k^2, t - t') = \frac{1}{2}(\langle u_1^4 \rangle - 1)k^2(t - t')^2 + \cdots$$
 (47)

Hence, the proposed approximation to (37) is

$$\frac{\partial \tilde{G}(\mathbf{k},t)}{\partial t} = -k^2 \int_0^t R_L(t-t') \times \exp\left[-\frac{1}{2}(\langle u_1^4 \rangle - 1)k^2(t-t')^2\right] \tilde{G}(\mathbf{k},t')dt'. \tag{48}$$

The exponential factor in the kernel of (48) is a device intended to simulate the presence of the higher-order moments by cutting off the divergent  $k^2$  behavior of the first term of the sum in (44). The exponential cutoff chosen is not unique by any means, but it does introduce a new parameter, the fourth-order moment  $\langle u_i^4 \rangle$ , in a simple way.

The small t behavior of the solutions of (48) is given by (32) with the replacement

$$\frac{\partial^2 A(0)}{\partial t^2} \rightarrow \frac{\partial^2 R_L(0)}{\partial t^2} - k^2 (\langle u_1^4 \rangle - 1), \tag{49}$$

and hence the solutions are again consistent with (8) to order  $t^2$ . The large t, small k behavior in (48) may be extracted by updating t' in  $\tilde{G}(\mathbf{k},t')$  to t, solving the resulting trivial differential equation, and letting  $k \ll 1$ . The classical diffusion behavior (6) is still obtained.

In the remainder of this section, Eq. (48) is tested against the computer experiments referred to in Sec. II. For a multivariate-normal field, where  $\langle u_i^4 \rangle = 3 \langle u_i^2 \rangle^2 = 3$ , Eq. (48) becomes

$$\frac{\partial \tilde{G}}{\partial t}(\mathbf{k}, t) = -k^2 \int_0^t R_L(t - t') \times \exp(-k^2(t - t')^2) \tilde{G}(\mathbf{k}, t') dt'. \tag{50}$$

Numerical solutions of (50), using  $R_L(t-t') = \exp(-(t-t')^2)$ , are displayed in Fig. 3 together with the same computer experimental points and direct-interaction approximation curves reproduced in Fig. 2. The improvement over the corresponding solutions from (12) is evident. In fact, the agreement is as good as or better than the direct-interaction approximation.

Comparisons with another case treated by Kraichnan are displayed in Figs. 4 and 5. The computer experiment was carried out on a three-dimensional frozen Eulerian field with an energy spectrum  $\frac{1}{2}\delta(k-1)$ . The Lagrangian velocity correlation, reproduced in Fig. 6, has a substantial negative region for  $2.5 \le t \le 5.5$  and does not fit a Gaussian curve. A piecewise interpolative curve was fitted to  $R_L$  and used in the numerical solution of (50). Again the agreement with the computer experiment seems at least as good as the direct-interaction approximation curves.

The direct-interaction approximation applied to the diffusion problem takes as input information the Eulerian velocity covariance and derives the characteristic function of the full probability density  $G(\mathbf{x},t)$  as well as the Lagrangian velocity covariance  $R_L(t)$ . These are considerably more difficult tasks than that of calculating  $G(\mathbf{x},t)$  given  $R_L(t)$  as is done in the integrodifferential equations, since the Lagrangian velocity is the more natural description of marked particle motion. Although Eq. (33), a formally exact starting point for the derivation of (12) or (48), contains Eulerian moments, we were able to carry out indirectly some infinite sums of the Eulerian moments and thereby obtain an equation containing Lagrangian moments. The spectrum and dimensionality of the velocity field do not appear explicitly in the resulting equations, but are buried in the structure of  $R_L$ .

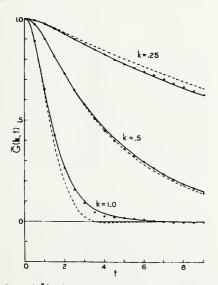


FIG. 3. Plots of  $\bar{G}(\mathbf{k},t)$  vs time. Solid curves are computed from Eq. (50) with a Gaussian-Lagrangian correlation function. Points and dashed curves are the same as in Fig. 2.

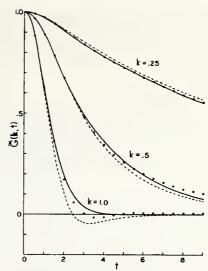


FIG. 4. Plots of  $\tilde{G}(\mathbf{k},t)$  vs time. Solid curves are computed from Eq. (50) using Lagrangian correlation function derived from computer experiment values for frozen Eulerian field. Dashed curves are direct interaction approximation values.

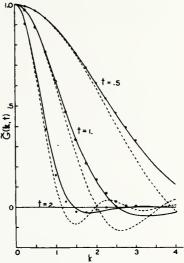


FIG. 5. Plots of  $\tilde{G}(\mathbf{k},t)$  vs k. Solid curves are computed from Eq. (50) using Lagrangian correlation function derived from conputer experiment. Points and circles are computer experiment values for frozen Eulerian field. Dashed curves are direct interaction approximation values.

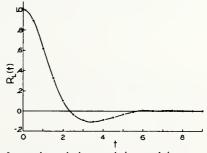


FIG. 6. Lagrangian velocity correlation used in computing solid curves in Figs. 4 and 5. Interpolative curve is drawn through the computer experiment points.

An interesting possibility that remains to be studied is that of taking Eq. (12) with  $A(t-t') = R_E(t-t')$ , as derived in Ref. 8, and then trying to improve it by including the effects of the higher-order Eulerian moments in (33).

## **ACKNOWLEDGMENTS**

I am grateful to Dr. R. H. Kraichnan for providing me with his computer experiment and direct-interaction approximation data reproduced in this paper.

This work was performed while the author held a

National Research Council Resident Research Associateship.

- <sup>1</sup> R. H Kraichnan, Phys. Fluids 13, 22 (1970).

  <sup>2</sup> P. H. Roberts, J. Fluid Mech. 11, 257 (1961).

  <sup>3</sup> G. I. Taylor, Proc. London Math. Soc. 20, 196 (1921).

  <sup>4</sup> G. I. Taylor, Proc. R. Soc. Lond. A 151, 421 (1935).

  <sup>5</sup> W. C. Meecham and D.-t. Jeng, J. Fluid Mech. 32, 225 (1968).

  <sup>6</sup> M. L. Thiebaux, Phys. Rev. A 5, 1444 (1972).

  M. J. Thiebaux, Phys. Phys. Fluids 16, 1305 (1973).
- <sup>1</sup> M. L. Thiebaux, Phys. Fluids 16, 1395 (1973).
- P. G. Saffman, Phys. Fluids 12, 1786 (1969).
- 9 R. Bourret, Can. J. Phys. 38, 665 (1960).

# On the application of quasi-Lagrangian coordinates to random shear flows\*

#### M. L. Thiebaux

National Oceanic and Atmospheric Administration, Boulder, Colorado 80302 (Received 17 April 1973; revised manuscript received 5 November 1973)

An ensemble of homogeneous random shear flows with steady linear mean velocity profiles is considered from a purely kinematical point of view. Quasi-Lagrangian coordinates (advected by the mean flow) are used so that a proper orthogonal decomposition of the fluctuation velocity field is possible and periodic boundary conditions can be imposed. The conditions of stationarity in time and incompressibility take on special forms when applied to wave-vector moments. A simple application of the methodology is presented in the construction of a two-dimensional random shear flow.

#### 1. INTRODUCTION

A turbulent incompressible fluid in a shear flow is a dynamically interesting system because the turbulent energy can be directly drawn from the kinetic energy of the mean flow. The attempt to understand the mechanism of this energy transfer under the simplest conditions has compelled experimental and theoretical investigators to consider the idealized case of turbulence in a homogeneous shear flow.

Nearly homogeneous turbulent shear flows, have been generated and studied in the laboratory. 1,2 One significant feature emerging from the experimental studies is evidence that such flows, although very nearly homogeneous in some ways, are not strictly stationary in time in an Eulerian frame advected by the mean velocity. Also it has been demonstrated analytically that time scales must monotonically increase in homogeneous shear flows.3 However, such flows may be considered quasistationary if the statistical properties of primary concern are only weakly dependent on time displacements. The notion of temporal stationarity is clearly a useful one for analytical purposes and can be applied to mathematically idealized systems. For example, in studies of the dispersion of passive quantities in randomly generated velocity fields (e.g., see Ref. 4), which already have idealistic properties such as specified probability laws, the assumption of temporal stationarity is not only convenient and harmless, but also may be essential for clarity.

In this paper, we shall consider an ensemble of shear flows with homogeneous, random velocity fluctuations and a steady linear mean velocity profile. We wish to develop a kinematic description of the ensemble that satisfies statistical notions of spatial homogeneity and temporal stationarity. A central feature in this development will be the use of quasi-Lagrangian coordinates. In general, the quasi-Lagrangian frame, as defined by Gifford<sup>5</sup> in connection with atmospheric turbulence, is a time-dependent nonorthogonal coordinate system that is advected (and distorted) by the mean flow. Quasi-Lagrangian coordinates  $(\xi^1,\xi^2,\xi^3)$  may then be defined by the requirement that a point in real space moving with the mean velocity maps into a fixed point in  $\xi$ -space.

The usefulness and significance of quasi-Lagrangian coordinates in the case of a homogeneous shear flow will be discussed in this paper and are first briefly summarized here: (i) The advection and distortion of the velocity fluctuation field by the large-scale mean flow is an intrinsic property of the quasi-Lagrangian methodology. Thus, the sweeping effect that larger scales of motion have on the smaller scales is partly taken into account by the formalism. (ii) The com-

bined statements of homogeneity, incompressibility, and stationarity in terms of quasi-Lagrangian coordinates take on simple forms that are relatively easy to satisfy simultaneously when synthesizing random realizations of shear flows. An example of such a synthesis is given in Sec. 5. (iii) In both random syntheses and dynamical numerical computations, the simultaneous constraints of homogeneity and periodic boundary conditions are possible with quasi-Lagrangian coordinates.

#### 2. STATIONARY HOMOGENEOUS SHEAR FLOWS

Let  $\mathbf{x} = (x_1, x_2, x_3)$  denote coordinates in a Cartesian frame labeled I in which the mean velocity is

$$\langle \mathbf{V} \rangle = \omega x_2 \mathbf{e}_1,$$

where  $\omega$  is the constant rate of shear and  $\mathbf{e}_1$  is the unit vector in the  $x_1$  direction. Now consider a second moving Cartesian frame II, with axes parallel to those of I, but with a different origin. Frame II is moving with the mean velocity  $\langle \mathbf{V} \rangle$  at its origin. Hence, the mean flow as seen by an observer in II appears identical to that seen by an observer in I. If all other statistical properties of the ensemble of velocity fields appear identical to the two observers, then the shear flow is homogeneous. In this paper we shall consider only second-order Eulerian moments of the velocity field, i.e., the autocorrelation tensor. If only the autocorrelations are observed and appear identical to the two observers, the shear flow is said to be covariance homogeneous.

To be specific, we write the total velocity  ${\bf V}$  as the sum of its ensemble mean part and a fluctuating part  ${\bf v}$ ,

$$\mathbf{V} = \langle \mathbf{V} \rangle + \mathbf{v}$$
.

and suppose that measurements of the components of  $\mathbf{v}$  are made in I at two space-time points denoted  $(I,\mathbf{x}^{(k)},l^{(k)})$ , for k=1,2. Then the ensemble average of the product of the observed velocity components is the second-order moment, or autocorrelation tensor,

$$\langle v_i(I, \mathbf{x}^{(1)}, t^{(1)}) v_i(I, \mathbf{x}^{(2)}, t^{(2)}) \rangle$$
. (2.1)

A similar moment can be determined in  $\Pi$  where velocity fluctuations are measured at the same times  $t^{(1)}$ ,  $t^{(2)}$  and at points whose locations relative to the origin of  $\Pi$  are the same vectors  $\mathbf{x}^{(1)}$ ,  $\mathbf{x}^{(2)}$ . This moment we denote

$$\langle v_i(H, \mathbf{x}^{(1)}, t^{(1)}) v_j(H, \mathbf{x}^{(2)}, t^{(2)}) \rangle$$
. (2.2)

The statement of covariance homogeneity is that moments (2.1) and (2.2) are identical.

It is possible to rewrite (2.2) as a moment defined in frame I. If at time t the origin  $\mathbf{x}_0$  of II is given in I by the equation

$$\mathbf{x}_0 = \mathbf{a} + \omega t a_2 \mathbf{e}_1,$$

where a is some constant vector, then (2.2) is the same as

$$\langle v_i(I, \mathbf{a} + \omega t^{(1)} a_2 \mathbf{e}_1 + \mathbf{x}^{(1)}, t^{(1)} \rangle v_j(I, \mathbf{a} + \omega t^{(2)} a_2 \mathbf{e}_1 + \mathbf{x}^{(2)}, t^{(2)} \rangle$$
. (2.3)

The equality of (2.1) and (2.3) is the covariance statement of the extension to shear flows of the definition of instantaneous homogeneity discussed by Batchelor.<sup>6</sup>

A set of quasi-Lagrangian coordinates suitable for the shear flow is given by

$$\xi^1 = x_1 - \omega t x_2, \quad \xi^2 = x_2, \quad \xi^3 = x_3.$$

Then, with the notation

$$v_i(\xi, t) \equiv v_i(I, \mathbf{x}, t),$$

where  $\xi$  stands for the three contravariant components  $\xi^1$ ,  $\xi^2$ ,  $\xi^3$  of the position vector  $\mathbf{x}$  as described in the quasi-Lagrangian frame, the equality of (2.1) and (2.3) is equivalent to

$$\langle v_i(\xi^{(1)}, t^{(1)})v_j(\xi^{(2)}, t^{(2)}) \rangle$$

$$= \langle v_i(\xi^{(1)} + \mathbf{a}, t^{(1)})v_i(\xi^{(2)} + \mathbf{a}, t^{(2)}) \rangle$$
 (2.4)

for any a.

The great advantage of the form (2.4) (identical to the conventional statement of covariance homogeneity) over the equality of (2.1) and (2.3) is that the expansion of the velocity fluctuation field in orthogonal Fourier modes defined with respect to the quasi-Lagrangian coordinates then results in second-order moments that are diagonal in the corresponding wave-vector space. Furthermore, it is easily seen that the imposition of periodic boundary conditions consistent with homogeneity, of much convenience in numerical and theoretical investigations, is possible in quasi-Lagrangian coordinates, and impossible in Cartesian coordinates.

Another view of this expansion was elucidated by Lumley.7 It can be shown that the expansion in quasi-Lagrangian Fourier modes is the proper orthogonal decomposition in the sense of Loève.8 Lumley used this decomposition, identified as the set of eigenfunctions of the autocorrelation tensor, as the basis for defining the "big eddies" in a nonhomogeneous flow. In our application, we are giving "proper" treatment to the effect of the largest component of the motion, namely the mean flow. Since the autocorrelation tensor is homogeneous in the components of  $\xi$ , its eigenfunctions are harmonic functions of  $\xi$ . A harmonic function (Fourier mode) defined with respect to the quasi-Lagrangian coordinates feels the effect of the mean flow by being advected and distorted by it. In contrast, a conventional Cartesian Fourier mode would be simply superimposed on the mean flow and would ignore its advective effect.

To complete this section, we exhibit the familiar statement of Eulerian covariance stationarity in frame I. For any time interval b,

$$\begin{aligned} \langle v_i(I, \mathbf{x^{(1)}}, t^{(1)}) v_j(I, \mathbf{x^{(2)}}, t^{(2)}) \rangle \\ &= \langle v_i(I, \mathbf{x^{(1)}}, t^{(1)} + b) v_j(I, \mathbf{x^{(2)}}, t^{(2)} + b) \rangle. \end{aligned}$$

In the remainder of this paper, the terms homogeneous and stationary will be used to mean covariance homogeneous and covariance stationary, respectively.

#### 3. STRUCTURE OF AUTOCORRELATION TENSOR

Assuming periodicity in  $\xi^1$ ,  $\xi^2$ , and  $\xi^3$ , we can Fourier analyze the velocity fluctuation field according to

$$v_i(\xi, t) = \sum_{\mathbf{p}} A_i(\mathbf{p}, t) \exp(i\mathbf{p} \cdot \xi)$$
 (3.1)

where  $\mathbf{p} \cdot \boldsymbol{\xi} = p_i \, \boldsymbol{\xi}^i$ , summed over the repeated indices. Without loss of generality, it can be supposed that at t=0, all members of the ensemble of velocity fields have a rectangular periodic lattice as observed in frame I. The periodic lattice in  $\boldsymbol{\xi}$ -space, which for convenience may be visualized with the three  $\boldsymbol{\xi}^i$  axes drawn mutually perpendicular, can then be considered rectangular for all times. For simplicity, we suppose that a periodic element at t=0 is a cube of volume  $L^3$ . Hence, the covariant components  $p_i$  of wave vector p are  $(2\pi/L)n_i$ , i=1,2,3, where the  $n_i$  are integers, and the sum in (3.1) is over all integers.

The inverse of (3.1) is

$$A_{i}(\mathbf{p},t) = L^{-3} \int d\xi \, \exp(-i\mathbf{p} \cdot \boldsymbol{\xi}) v_{i}(\boldsymbol{\xi},t),$$

where the region of integration is any periodic element in  $\xi$ -space.

As a consequence of (2.4), the covariance function of  $A_i$  reduces to

$$\langle A_i(\mathbf{p}, t)A_i(\mathbf{p}', t')\rangle = \Delta(\mathbf{p} + \mathbf{p}')\alpha_{ij}'(\mathbf{p}, t, t'), \qquad (3.2)$$

where

$$\Delta(\mathbf{p}) = 1,$$
 if  $\mathbf{p} = 0$ ,  
= 0, otherwise,

and

$$\begin{aligned} \alpha_{ij}'(\mathbf{p},t,t') &= L^{-3} \int F_{ij}(\xi-\xi',t,t') \\ &\times \exp[-i\mathbf{p} \cdot (\xi-\xi')] d(\xi-\xi'). \end{aligned}$$

We have set

$$F_{ij}(\xi - \xi', t, t') = \langle v_i(\xi, t) v_j(\xi', t') \rangle,$$

which follows from (2.4). Conversely, it is the  $\Delta(p+p')$  structure of the covariance function that assures and therefore is equivalent to homogeneity.

We shall now derive the condition on  $\alpha_{ij}$  that is equivalent to stationarity. Reverting to frame I coordinates and imposing stationarity, we have

$$\begin{split} F_{ij}(\xi-\xi',t,t') &= F_{ij}(\xi^1-\xi'^1,\xi^2-\xi'^2,\xi^3-\xi'^3,t,t') \\ &= \langle v_i(I,\mathbf{x},t)v_j(I,\mathbf{x}',t') \rangle \\ &= \langle v_i(I,\mathbf{x},t+b)v_j(I,\mathbf{x}',t'+b) \rangle \\ &= \langle v_i(\xi^1-\omega b\xi^2,\xi^2,\xi^3,t+b) \\ &\times v_j(\xi'^1-\omega b\xi'^2,\xi'^2,\xi'^3,t'+b) \rangle \\ &= F_{ij}(\xi^1-\xi'^1-\omega b(\xi^2-\xi'^2),\xi^2-\xi'^2,\xi^3-\xi'^3,t+b,t'+b). \end{split}$$

Hence,  $F_{ij}$  must be invariant under the substitutions

$$t \to t + b, \quad t' \to t' + b,$$
  
 $\xi^1 - \xi'^1 \to \xi^1 - \xi'^1 - \omega b(\xi^2 - \xi'^2),$ 
(3.3)

for any b.

615

We have written  $F_{ij}$  as a function of the five independent space-time variables  $\xi^1-\xi'^1$ ,  $\xi^2-\xi'^2$ ,  $\xi^3-\xi'^3$ , t, and t'. It is clear that we could have used, just as well, the five independent variables

$$\xi^{1} - \xi'^{1} + \frac{1}{2}\omega(t + t')(\xi^{2} - \xi'^{2}),$$
  

$$\xi^{2} - \xi'^{2}, \qquad \xi^{3} - \xi'^{3},$$
  

$$t - t', \qquad t + t'.$$
(3.4)

Of these, only t+t' changes under the substitutions (3.3). It follows that  $F_{ij}$  must depend only on the other four variables in (3.4). Hence, stationarity is equivalent to the statement that

$$\begin{split} F_{ij}(\xi^1 - \xi'^1, \xi^2 - \xi'^2, \xi^3 - \xi'^3, t, t') \\ &= G_{ij}(\xi^1 - \xi'^1 + \frac{1}{2}\omega(t + t')(\xi^2 - \xi'^2), \xi^2 \\ &- \xi'^2, \xi^3 - \xi'^3, t - t'). \end{split}$$

Equation (3.2) then becomes

$$\alpha'_{ij}(\mathbf{p}, t, t') = L^{-3} \int G_{ij}(\xi''^{1} + \frac{1}{2}\omega(t + t')\xi''^{2}, \xi''^{2}, \xi''^{3}, t - t') \times \exp(-i\mathbf{p} \cdot \xi'')d\xi''.$$
(3.5)

The region of integration in (3.5) can be a cube of volume  $L^3$  with edges parallel to the  $\xi''$  axes. For the moment, we choose a cube (ABCD) in Fig. 1) centered at  $\xi'' = 0$ , which incidentally lies in the neighborhood of the maximum contours of  $G_{ij}$ .

Since  $G_{ij}$  is defined as the covariance function of fields periodic in the components of  $\xi$  and  $\xi'$ , it is clearly periodic in the components of  $\xi'' = \xi - \xi'$ . Periodicity in  $\xi''^1$  allows the  $\xi''^1$ ,  $\xi''^2$  region of integration to be distored into a parallelogram (A'B'C'D) in Fig. 1) as long as A'D' = B'C' = L. If we let the independent variables in  $G_{ij}$  be

$$\eta_1 = \xi''^1 + \omega T \xi''^2,$$
 $\eta_2 = \xi''^2, \quad \eta_3 = \xi''^3,$ 
 $\tau = t - t',$ 
(3.6)

where  $T = \frac{1}{2}(t + t')$ , and take  $A'A = \frac{1}{2}\omega TL$ , then (3.5) becomes

$$\begin{split} \alpha'_{ij}(p,t,t') &= L^{-3} \int_{-L'/2}^{L/2} d\eta_1 \int_{-L'/2}^{L/2} d\eta_2 \int_{-L'/2}^{L/2} d\eta_3 \\ &\times \exp[-i\eta_1 p_1 - i\eta_2 (p_2 - \omega T p_1) - i\eta_3 p_3] \\ &\times G_{ij}(\eta_1,\eta_2,\eta_3,\tau). \end{split} \tag{3.7}$$

The right-hand side of (3.7) is a function only of the four independent variables  $p_1,p_2-\omega T p_1,p_3, \text{ and } \tau.$  An equivalent choice of independent variables is  $p_2-\omega t p_1,$   $p_2-\omega t' p_1,p_3,$  and t-t'. Hence, a necessary condition for stationarity is that  $\alpha'_{ij}$  be of the form

$$\alpha'_{ij}(\mathbf{p}, t, t') = \alpha_{ij}(p_2 - \omega t p_1, p_2 - \omega t' p_1, p_3, t - t').$$
 (3.8)

That (3.8) is not sufficient for stationarity will now be demonstrated. An additional, but almost trivial, condition is required on the covariance function. Given an  $\alpha'_{ij}$  that satisfies (3.8), we can take the Fourier inverse of (3.5) to obtain the function  $G_{ij}$ . The latter will be periodic on the boundaries of ABCD. On the other hand, inverting Eqs. (3.6), we have

$$\begin{split} \xi''^{1} &= \eta_{1} - \omega T \eta_{2} \\ \xi''^{2} &= \eta_{2}, \quad \xi''^{3} = \eta_{3}, \\ t - t' &= \tau. \end{split} \tag{3.9}$$

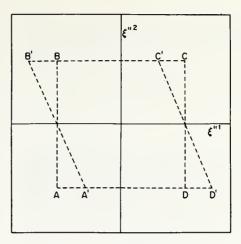


FIG. 1. Permissible regions of integration in Eq. (3. 5) projected onto the  $\xi''^1$ ,  $\xi''^2$  plane.

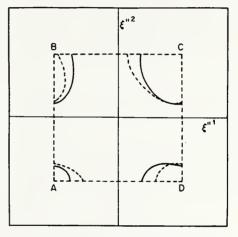


FIG. 2. Periodicity violating contours of  $G_{ij}$  for fixed  $\xi''^3$ .

Constant values of  $\eta_1, \eta_2, \eta_3$ , and  $\tau$  imply constant values of  $G_{ij}$  for any T, if stationarity is to hold. Suppose that at T=0, a contour of  $G_{ij}$  for fixed  $\xi''^3$  is located as shown by the solid curves in Fig. 2. The way the contours evolve with T is determined by the condition of stationarity, embodied in Eqs. (3. 9). In particular, for a slightly greater value of T, the contours will have shifted and distorted into the dotted curves indicated in Fig. 2, and periodicity is destroyed. It is clear that periodicity and stationarity can be rigorously compatible inside the square only if no contour of  $G_{ij}$  crosses the boundaries AD or BC.

A sensible extension of this condition is that  $G_{ij}$  is zero along the planes  $\xi''^2=\pm\frac{1}{2}L$ . For if  $\xi''^2=\pm\frac{1}{2}L$ , then  $|x_2-x_2'|=\frac{1}{2}L$ . Hence a physically reasonable form for the additional condition is that L must be large enough so that the velocity covariance is zero (or nearly zero in practice) for spatial separations of  $\frac{1}{2}L$  in the  $x_2$  direction.

# 4. CONTRAVARIANT COMPONENTS OF v: INCOMPRESSIBILITY

Up to this point we have not dealt with the transformation of the velocity field components into the quasi-Lagrangian frame. For applications involving dynamical equations of motion, turbulent advection of passive field, or simply the statement of incompressibility, it is analytically advantageous to introduce the transformed components. The contravariant components of  ${\bf v}$  in the quasi-Lagrangian coordinate system are

$$u^{1}(\xi, t) = v_{1}(\xi, t) - \omega t v_{2}(\xi, t),$$

$$u^{2}(\xi, t) = v_{2}(\xi, t),$$

$$u^{3}(\xi, t) = v_{3}(\xi, t).$$
(4.1)

While we shall not discuss the transformed Navier-Stokes or passive field advection equations, it is well to point out that the field  $\mathbf{u}=(u^1,u^2,u^3)$  has the following two essentially self-evident properties:

(a) The form of the substantial derivative D/Dt is preserved in quasi-Lagrangian coordinates. Thus,

$$\frac{\partial}{\partial t} + \sum_{i=1}^{3} V_i \frac{\partial}{\partial x_i} = \frac{\partial}{\partial t} + \sum_{i=1}^{3} u^i \frac{\partial}{\partial \xi^i},$$

where  $x_i$  and t are the independent variables on the left-hand side, while  $\xi^i$  and t are the independent variables on the right-hand side.

(b) The form of the incompressibility condition is preserved. If  $\nabla^\bullet V=0$  in frame I,then

$$\sum_{i=1}^{3} \frac{\partial}{\partial \xi^{i}} u^{i} = 0. \tag{4.2}$$

A simple physical interpretation of the contravariant velocity components can be made. Consider a wave in quasi-Lagrangian coordinates

$$u_0^j(\xi, t) = C^j(t) \exp(i\mathbf{p} \cdot \xi)$$

with  $C \cdot p = 0$  so that the wave is formally transverse in quasi-Lagrangian space. Using (4.1), and reverting to frame I coordinates, we have

$$\mathbf{v}_0(\xi, t) = \mathbf{v}_0(I, x, t) = \mathbf{A}(t) \exp[i\mathbf{q}(t) \cdot \mathbf{x}], \tag{4.3}$$

where

616

$$A_1(t) = C^1(t) + \omega t C^2(t),$$
  

$$A_2(t) = C^2(t), \quad A_3(t) = C^3(t),$$
(4.4)

and

$$q_1 = p_1, q_3 = p_3,$$
  
 $q_2 = p_2 - \omega t p_1.$  (4.5)

Equation (4.4) gives the rule for transforming contravariant components in the quasi-Lagrangian frame back into frame I components. Similarly, (4.5) applies to covariant components. Then, since  $\mathbf{A}(t) \cdot \mathbf{q}(t) = \mathbf{0}$ , (4.3) is a transverse wave in real space as well. The wave vector  $\mathbf{q}(t)$  is time-varying in such a way that, in addition to their normal propagation, planes of constant phase are advected or rotated by the shear mean flow. Conversely, if the mean flow has a linear profile, a transverse wave in real space is observed as a transverse wave in  $\xi$ -space.

Modes of this type were derived by Moffat<sup>9</sup> in a study of plane wave perturbations in an otherwise laminar uniform shear flow. Linearized Navier-Stokes dynamics led to explicit solutions for the  $C^{j}(t)$ , but such considerations are beyond the scope of this paper.

It should be clear that the definition of homogeneity in Sec.1 applies equally well to the contravariant

components of the velocity fluctuation. Thus, any  $v_i$  in (2.4) may be replaced by a  $u^i$ . Moments defined on one type of field are linear combinations of moments of the other type, with time-dependent coefficients. A velocity fluctuation field can then be defined by the contravariant components

$$u^{j}(\xi, t) = \sum_{\mathbf{p}} C^{j}(\mathbf{p}, t) \exp(i\mathbf{p} \cdot \xi)$$

and homogeneity is satisfied if

$$\langle C^i(\mathbf{p},t)C^j(\mathbf{p}',t')\rangle \sim \Delta(\mathbf{p}+\mathbf{p}').$$

Incompressibility is assured if we let

$$C^{i}(\mathbf{p}, t) = \epsilon^{ijk} B_{i}'(\mathbf{p}, t) p_{k}, \tag{4.6}$$

where  $\epsilon^{ijk}$  is the permutation symbol and B' is any complex-valued vector function of p and t. Without loss of generality, we may write

$$B_{1}' = B_{1}(\mathbf{p}, t),$$
  
 $B_{2}' = B_{2}(\mathbf{p}, t) + \omega t B_{1}(\mathbf{p}, t),$  (4.7)  
 $B_{3}' = B_{3}(\mathbf{p}, t).$ 

The components of B' may be considered the covariant components of B transformed into the quasi-Lagrangian Fourier space. Then, using (4.1) and (3.1), we find

$$\mathbf{A}(\mathbf{p}, t) = \mathbf{B}(\mathbf{p}, t) \times \mathbf{q}(t), \tag{4.8}$$

where the components of  $\mathbf{q}$  are given by (4.5). Equation (4.8) is the incompressibility condition for the Fourier modes in (3.1). The real-space field with Fourier mode coefficients  $\mathbf{B}(\mathbf{p},t)$  is the vector potential for the velocity fluctuation field.

The component of B parallel to q does not contribute to A (or to C). It is, therefore, appropriate to decompose B into perpendicular and parallel parts,

$$\mathbf{B} = \mathbf{B}_{\perp} + \mathbf{B}_{\parallel}.$$

Equation (4.8) can now be solved for the perpendicular part.

We find

$$B_{\perp}(\mathbf{p}, t) = q^{-2}\mathbf{q}(t) \times A(\mathbf{p}, t),$$
 (4.9)

an immediate consequence of which is that the covariances of the components of  $\mathbf{B}_{\perp}(\mathbf{p},\,t)$  and  $\mathbf{B}_{\perp}(\mathbf{p}',\,t')$  are all proportional to  $\Delta(\mathbf{p}+\mathbf{p}')$ . Since the statistical properties of  $\mathbf{B}_{\parallel}$  are immaterial, we can then write

$$\langle B_i(\mathbf{p}, t)B_j(\mathbf{p}', t')\rangle \sim \Delta(\mathbf{p} + \mathbf{p}')$$
 (4.10)

as the statement of homogeneity suitable for an incompressible velocity field.

Again, from (4.9), it is seen that the covariances of the components of  $\mathbf{B}_{\perp}(\mathbf{p},t)$  and  $\mathbf{B}_{\perp}(-\mathbf{p}',t')$  are linear combinations of the covariances  $\alpha_{ij}$  with coefficients [functions of  $\mathbf{q}(t)$  and  $\mathbf{q}(t')$ ] that depend only on the independent variables  $p_1, p_2 - \omega t p_1, p_2 - \omega t' p_1$ , and  $p_3$ . Since

$$p_1 = [(p_2 - \omega t' p_1) - (p_2 + \omega t p_1)] / \omega (t - t'), \quad (4.11)$$

and stationarity requires the  $\alpha_{ij}$  to depend only on  $p_2 - \omega t p_1, p_2 - \omega t' p_1, p_3$ , and t - t', it follows that the covariances of the components of  $\mathbf{B}_t$  depend only on

these same variables. It is obviously convenient to choose the statistical properties of  $B_{\parallel}$  to be the same as those of  $B_{\perp}.$  Hence, stationarity for the incompressible field is equivalent to the statement that

$$\langle B_{i}(\mathbf{p}, t)B_{j}(-\mathbf{p}, t') \rangle = \beta_{ij}(p_{2} - \omega t p_{1}, p_{2} - \omega t' p_{1}, p_{3}, t - t').$$
 (4.12)

A field B(p, t) satisfying (4.10) and (4.12) gives the Fourier modes for an incompressible, homogeneous, and stationary velocity fluctuation field according to (4.8), or the corresponding contravariant modes according to (4.7) and (4.6).

#### 5. A TWO-DIMENSIONAL RANDOM VELOCITY FIELD

In this section we shall construct a two-dimensional example of an incompressible random velocity fluctuation field in a mean shear flow, satisfying homogeneity and stationarity. The example serves as a concrete demonstration of the methodology and may be a useful model in numerical simulations of random shear flows. The extension to three dimensions is not difficult,

Suppose g is a random complex function of  $\mathbf{p}$  and t such that

$$g(\mathbf{p}, t) = -g^*(-\mathbf{p}, t) \tag{5.1}$$

and

617

$$\langle g(\mathbf{p}, t)g(\mathbf{p}', t')\rangle = -\Delta(\mathbf{p} + \mathbf{p}')\phi(t - t'). \tag{5.2}$$

Property (5.1) assures that the velocity is real. Two-dimensionality of A follows if we take

$$B_1(\mathbf{p}, t) = B_2(\mathbf{p}, t) = 0$$

but let

$$B_3(\mathbf{p}, t) = b(p_1, p_2 - \omega t p_1)g(\mathbf{p}, t)$$

where  $b(\cdot\cdot\cdot)$  is a real nonrandom even function of its two arguments. Combining the above properties, we have

$$\begin{split} B_{3}(\mathbf{p}, t)B_{3}(\mathbf{p}', t') \\ &= -\Delta(\mathbf{p} + \mathbf{p}')b(p_{1}, p_{2} - \omega t p_{1})b(p_{1}, p_{2} - \omega t' p_{1})\phi(t - t'). \end{split}$$

Recalling (4.11), we see that (4.10) and (4.12) are satisfied by this B. The corresponding components of C and A are, respectively,

$$C_{1}(\mathbf{p},t) = -\,p_{2}b(p_{1},p_{2}-\omega t p_{1})g(\mathbf{p},t),$$

$$C_2(\mathbf{p}, t) = p_1 b(p_1, p_2 - \omega t p_1) g(\mathbf{p}, t),$$

and

$$A_1(\mathbf{p}, t) = -(p_2 - \omega t p_1)b(p_1, p_2 - \omega t p_1)g(\mathbf{p}, t),$$

$$A_2(\mathbf{p}, t) = C_2(\mathbf{p}, t).$$

An example of a random function satisfying (5.1) and (5.2) is

$$g(\mathbf{p}, t) = \gamma(\mathbf{p}) \exp[i\Omega(p)t + i\delta(p)] - \gamma(-\mathbf{p})$$
$$\times \exp[-i\Omega(-p)t - i\delta(-p)]$$

where  $\gamma(p)$ ,  $\Omega(p)$ , and  $\delta(p)$  are real random variables with the following properties:

(a)  $\gamma(\mathbf{p})$ ,  $\Omega(\mathbf{p}')$ , and  $\delta(\mathbf{p}'')$  are independent random variables for any  $\mathbf{p}$ ,  $\mathbf{p}'$ ,  $\mathbf{p}''$ .

- (b)  $\delta(\mathbf{p})$  and  $\delta(\mathbf{p}')$  are independent for any  $\mathbf{p} \neq \mathbf{p}'$ .
- (c)  $\delta(\mathbf{p})$  is uniformly distributed in the interval  $[0, 2\pi]$  for all  $\mathbf{p}$ .
- (d)  $\langle \gamma^2(\mathbf{p}) \rangle = \frac{1}{2}$  for all  $\mathbf{p}$ .
- (e) The probability distribution of Ω(p) is the same for all p.

The function  $\phi$  is given by

$$\phi(\tau) = \langle \cos \Omega \tau \rangle \,. \tag{5.3}$$

We may note that the probability laws of  $\gamma(\mathbf{p})$  and  $\Omega(\mathbf{p})$  are essentially unspecified. However, two important special cases of (5.3) are (i)  $\phi(\tau)$  is a symmetric Gaussian function of  $\tau$  if  $\Omega$  has a symmetric normal distribution, and (ii)  $\phi(\tau)$  is an exponential function of  $|\tau|$  if  $\Omega$  has a symmetric Cauchy distribution.

To be specific, let us suppose that

$$\begin{split} b(p_1, p_2 - \omega t p_1) &= (2\pi)^{1/2} v_0 L^{-1} Q^{-2} \\ &\times \exp\{-[p_1^2 + (p_2 - \omega t p_1)^2]/4Q^2\}, \quad (5.4) \end{split}$$

where Q is a cutoff parameter in wave-vector space and  $v_0$  is the root-mean-square of one component of the fluctuation velocity, and that  $\Omega$  is Cauchy-distributed with the probability density function

$$f(\Omega) = (1/\pi)\tau_{\Omega}/(1 + \tau_{\Omega}^{2}\Omega^{2}), \quad -\infty < \Omega < \infty,$$

so that

$$\phi(\tau) = \exp(-|\tau|/\tau_0).$$

Then, we find

$$\begin{split} \langle C_i(\mathbf{p},t)C_j(\mathbf{p}',t')\rangle &= \Delta(\mathbf{p}+\mathbf{p}')(\delta_{ij}p^2 - p_ip_j)E, \\ \langle A_i(\mathbf{p},t)A_j(\mathbf{p}',t')\rangle &= \Delta(\mathbf{p}+\mathbf{p}')(\delta_{ij}\mathbf{q}'\cdot\mathbf{q} - q_i'q_i)E, \end{split}$$

where

$$E = 2\pi v_0^2 L^{-2} Q^{-4} \cdot \exp(-|t - t'|/\tau_0)$$

$$\times \exp\{-\frac{1}{2} p_1^2 Q^{-2} [1 + \frac{1}{4} \omega^2 (t - t')^2] - \frac{1}{2} Q^{-2} [p_2 - \frac{1}{2} \omega (t + t') p_1]^2\},$$

$$q_1 = q_1' = p_1,$$

$$q_2 = p_2 - \omega t p_1,$$

$$q_2' = p_2 - \omega t' p_1.$$

The velocity fluctuation moments are

Using the prescription

$$\sum_{\mathbf{p}} \rightarrow (L/2\pi) \int d\mathbf{p},$$

we find

$$\langle v_i(\xi, t) v_j(\xi', t') \rangle = v_0^2 S^{-5} \exp[-\frac{1}{2}Q^2 (\eta_1^2 S^{-2} + \eta_2^2) - |t - t'| / \tau_0] \rho_{ii}$$
 (5.5)

vhere

$$\begin{split} \rho_{11} &= Q^2 \big[ \tfrac{1}{4} \, \omega^2 (t-t')^2 \eta_1^2 - S^4 \eta_2^2 \big] + S^2, \\ \rho_{12} &= Q^2 S^2 \eta_1 \eta_2 + \tfrac{1}{2} \, \omega (t-t') (S^2 - Q^2 \eta_1^2), \\ \rho_{21} &= Q^2 S^2 \eta_1 \eta_2 - \tfrac{1}{2} \, \omega (t-t') (S - Q^2 \eta_1^2), \end{split}$$

$$\begin{split} &\rho_{22} = S^2 - Q^2 \eta_1^2, \\ &S = \big[1 \, + \tfrac{1}{4} \omega^2 (t - t')^2\big]^{1/2}, \\ &\eta_1 = \xi^1 - \xi'^1 \, + \tfrac{1}{2} \omega (t + t') (\xi^2 - \xi'^2), \\ &\eta_2 = \xi^2 - \xi'^2. \end{split}$$

Although the space-time structure of  $\langle v_i v_j \rangle$  in (5.5) appears complicated and artificially contrived from ad hoc premises, the assumptions that led to this structure are actually very simple. With some redundance, the essential ingredients are summarized below:

- (a) homogeneity, stationarity, and incompressibility.
- (b) decomposition of the fluctuation field into plane waves of statistically independent amplitudes, frequencies, and phases. Only the probability law of the phases needs to be specified completely, and this is dictated by homogeneity.
- (c) the form of the spectrum  $b(\cdots)$  in (5.4). This model spectrum would appear to be the most artificial

assumption, but it is also perhaps the simplest extension to a shear flow, consistent with the stationarity requirement (4.12), of a commonly used Gaussian spectrum.

- \*This work was performed while the author held a National Research Council Resident Research Associateship.
- W. G. Rose, J. Fluid Mech. 25, 97 (1966).
- <sup>2</sup>F. H. Champagne, V. G. Harris, and S. Corrsin, J. Fluid Mech. 41, 81 (1970).
- <sup>3</sup>J. L. Lumley, J. Fluid Mech. 41, 413 (1970).
- <sup>4</sup>R. H. Kraichnan, Phys. Fluids 13, 22 (1970).
- <sup>5</sup>F. A. Gifford, Proc. USAEC Meteorological Information Meeting (AECL-2787), 485 (1967).
- <sup>6</sup>G. K. Batchelor, *The Theory of Homogeneous Turbulence* (Cambridge U. P., Cambridge, 1953).
- <sup>3</sup>J. L. Lumley, Proc. of the International Colloquium on Atmospheric Turbulence and Radio Wave Propagation, Moscow (edited by A. M. Yaglom and V. I. Tatarsky), 166 (1967).
- <sup>6</sup>M. Loève, *Probability Theory* (Van Nostrand, Princeton, N. J., 1963), p. 478.
- <sup>9</sup>H. K. Moffat, in Ref. 7, 139 (1967).

# RADIONUCLIDE DECAY IN STEADY STATE RESERVOIRS

MARTIAL L. THIEBAUX, JR.\*

Environmental Research Laboratories, National Oceanic and Atmospheric Administration

and

#### H. JEAN THIEBAUX

Department of Mathematics, University of Colorado and National Center for Atmospheric Research, Boulder, Colorado 80302, U.S.A.

(Received 20 November 1973)

Abstract—The natural decay of a radionuclide during detainment in a reservoir by large scale circulation processes is considered under steady state conditions. It is shown that when the residence time distribution is a step function, a one-parameter model is defined with the least possible effluent radioactivity. A second one-parameter model, yielding significantly greater radioactivity, is defined if the reservoir contents are uniformly mixed. Reservoir models of higher complexity may be constructed by a systematic linking together of the one-parameter models. Effluent radioactivities determined by the only possible two-parameter models are less than or equal to that of the uniformly mixed model. This fact is demonstrated by several specific examples.

#### 1. INTRODUCTION

Locating nuclear power plants near bodies of water for cooling purposes inevitably leads to some radio-active contamination of the water through leakage and routine releases of radioactive wastes (Logsdon and Chissler, 1970). If the cooling water enters a freshwater lake, or reservoir, the risk of serious contamination of a public water supply must be assessed, along with other detrimental effects.

Let us consider a particular radionuclide residing in a public water supply such as a reservoir. Its concentration in a parcel of water can be diminished to an allowable level by natural decay only if the residence time of the parcel in the reservoir is sufficiently large in comparison to the half life of the radionuclide. Although other important methods of removal of radioactive wastes are in use (International Atomic Energy Agency, 1963), we will confine our attention here to the natural decay history of low-level radioactivity that enters and is detained in a reservoir.

The basic scheme is as follows. Water enters a reservoir of volume V at a volumetric rate S. The influent carries a radionuclide of concentration  $c_i$ . The effluent, considered to be a uniform mixture of parcels

of water that have traversed the reservoir in many different paths, leaves the reservoir at the same rate S and carries the radionuclide at the reduced concentration  $c_e$ . The mean lifetime of the radionuclide is R (= 1.443 times the half life); the reciprocal mean lifetime  $\lambda = 1/R$  is the radioactive decay rate; and the ratio  $\rho = c_e/c_i$  is a useful quantity which we shall call the reduction factor. We wish to determine  $\rho$  as a function of  $\lambda$  and the parameters that characterize the circulation of water in the reservoir.

The complications of additional sources or sinks, transient modes of reservoir operation, stochastic parameterizations (Aitsam, 1969), sedimentation and biological concentration or removal (National Technical Advisory Committee, 1968), and decay product radioactivity are not considered in this paper, although it is recognized that some or all of these must be included in more exact reservoir models. The scope of this paper is limited to identifying large-scale internal circulation parameters and principles that are relevant in determining  $\rho$ . Our approach is based on a simple parameterization procedure in contrast to detailed hydrodynamical modelling such as that of Stanislav and Mohtadi (1971).

# 2. THE RESIDENCE TIME DISTRIBUTION FUNCTION AND THE UNIFORM FLOW MODEL

The residence time of a parcel of fluid is the length of time it resides in the reservoir between

<sup>\*</sup> This author held a National Research Council Resident Research Associateship while work was performed.

entering and leaving. The distribution of the residence times for all parcels passing through the reservoir is clearly an important factor in determining  $c_e$ . For any steady state reservoir, this distribution is characterized by a distribution functon F(t). The fraction of water that passes through the reservoir with a residence time t in the interval  $t_1 \le t \le t_2$  is just  $F(t_2) - F(t_1)$ . Hence F(t) is a non-decreasing function satisfying

$$1 = \int_0^\infty dF(t) \text{ and } 0 \le F(t) \le 1 \text{ for } 0 \le t < \infty.$$

A useful parameter in this distribution is the "flushing time"

$$T \equiv V/S, \tag{1}$$

which is the time it would take to fill or empty the reservoir at the rate S. Significantly, T is also the mean residence time of the water that has passed through the reservoir, assuming all the water in the reservoir eventually does leave.

To confirm this assertion, we can imagine that the distribution of (finite) residence times is discretized and takes on values  $t_1, t_2, \ldots$ . Let  $V_i$  be the total volume, at some instant, of those parcels in the reservoir that will have a residence time  $t_i$ . This water leaves the reservoir at the rate  $V_i/t_i$  under steady state conditions; and so  $S = \sum_i V_i/t_i$ . The mean residence time,  $\overline{T}$  say, is the average of  $t_i$  weighted not by  $V_i$ , but by the part of  $V_i$  that leaves the reservoir in some arbitrary time interval  $\Delta t$ . This part is  $(V_i/t_i)\Delta t$ . Hence

$$\overline{T} = \frac{\sum_{i} (V_i/t_i)\Delta t \ t_i}{\sum_{i} (V_i/t_i)\Delta t} = \frac{V}{S} = T.$$
 (2)

In terms of the (continuous) distribution function, we have

$$T = \int_0^\infty t \, \mathrm{d}F(t). \tag{3}$$

The effluent value of the concentration of a radioactive species carried by a parcel of residence time thas been reduced by radioactive decay to a fraction  $e^{-\lambda t}$  of the influent value. Hence, any distribution F(t)of residence times produces a mixed effluent concentration such that the reduction factor is

$$\rho = \int_{0}^{\infty} e^{-\lambda t} dF(t).$$
 (4)

It is proved below that, for a reservoir with mean residence time T, the reduction factor can be no less than  $e^{-\lambda T}$ . Furthermore, the latter is the result of the special case of what we shall call the uniform flow (u.f.) model in which the residence time for all parcels of water is the constant T.

For all distributions satisfying  $T = \int_0^\infty t \, dF(t)$ ,

$$\int_0^\infty e^{-\lambda t} dF(t) \ge e^{-\lambda T}$$

with equality only for the step function

$$F(t) = \begin{cases} 0, & \text{if } t \leq T \\ 1, & \text{if } t > T \end{cases}$$

The proof of this statement will use the integral representation

$$\int_{0}^{\infty} e^{-\lambda t} dF(t) = \lim_{\substack{\max |t_{j-1}| \to 0 \\ j \neq 1}} \sum_{j=1}^{n} e^{-\lambda \xi_{j}} [F(t_{j}) - F(t_{j-1})]$$

where each  $\xi_j \in (t_{j-1}, t_j)$  and the limit is taken over all partitions such that  $0 = t_0 < t_1 < \cdots < t_{n-1} < t_n = \infty$ .

Since F is a bounded non-decreasing function, then the integral is the limit of the sum, as written above, for any scheme which selects the  $\xi_j \in (t_{j-1}, t_j)$ ,  $j = 1, \ldots, n$ .

For successive partitions the mean value theorem for integrals may be invoked for selection of the  $\xi$ 's. That is, it is possible to require that each  $\xi_i \in (t_{i-1}, t_i)$  satisfy

$$\int_{t_{j-1}}^{t_j} t \, \mathrm{d}F(t) = \xi_j [F(t_j) - F(t_{j-1})],$$

with their existence guaranteed by the mean value theorem.

Now we have

$$\sum_{j=1}^{n} \xi_{j} [F(t_{j}) - F(t_{j-1})] = \sum_{j=1}^{n} \int_{t_{j-1}}^{t_{j}} t \, dF(t)$$
$$= \int_{0}^{\infty} t \, dF(t) = T.$$

Restricting ourselves to the use of mean-value  $\xi$ 's and noting that, for  $p_j = F(t_j) - F(t_{j-1})$ , j = 1, ..., n,

$$\sum_{1}^{n} p_{j} = 1 = \int_{0}^{\infty} \mathrm{d}F(t),$$

we shall seek the minimum, with respect to the p's and  $\xi$ 's of

$$p_1 e^{-\lambda \xi_1} + \cdots + p_n e^{-\lambda \xi_n}$$

subject to the constraints

$$T = p_1 \xi_1 + \dots + p_n \xi_n$$

and

$$1 = p_1 + \cdots + p_n$$

To do this, we shall use the method of Lagrange's for any  $(p_1, \ldots, p_n)$  and  $(\xi_1, \ldots, \xi_n)$  satisfying multipliers. Since

$$0 = \frac{\partial}{\partial \xi_{v}} \left| \sum_{i=1}^{n} p_{i} e^{-\lambda \xi_{j}} - A \left( T - \sum_{i=1}^{n} p_{j} \xi_{j} \right) - B \left( 1 - \sum_{i=1}^{n} p_{j} \right) \right|$$
$$= -\lambda p_{v} e^{-\lambda \xi_{v}} + A p_{v}$$

and

$$0 = \frac{\partial}{\partial p_{v}} \left| \sum_{1}^{n} p_{j} e^{-\lambda \xi_{j}} - A \left( T - \sum_{1}^{n} p_{j} \xi_{j} \right) - B \left( 1 - \sum_{1}^{n} p_{j} \right) \right|$$
$$= e^{-\lambda \xi_{v}} + A \xi_{v} + B_{v}$$

for all  $v = 1, \ldots, n$ , imply

$$A = \lambda e^{-\lambda \xi_v}$$
 and  $B = -(1 + \lambda \xi_v)e^{-\lambda \xi_v}$ ,

then  $\xi_{\nu}$  must be constant with respect to  $\nu$ . Say  $\tau = \xi_{\nu}$ for v = 1, ..., n. Using the constraints to evaluate  $\tau$ , we get

$$T = \sum_{1}^{n} p_{\nu} \xi_{\nu} = \tau \sum_{1}^{n} p_{\nu} = \tau \times 1 = \tau.$$

Finally, the type of extreme point is determined if we define

$$\phi = \sum_{j=1}^{n} p_{j} e^{-\lambda \xi_{j}} - A \left( T - \sum_{j=1}^{n} p_{j} \xi_{j} \right) - B \left( 1 - \sum_{j=1}^{n} p_{j} \right)$$

and examine

$$\begin{bmatrix} \left(\frac{\partial^{2}\phi}{\partial\xi_{v}}\frac{\partial\xi_{\mu}}{\partial\xi_{\mu}}\right) & \left(\frac{\partial^{2}\phi}{\partial\xi_{v}}\frac{\partial\rho_{\mu}}{\partial\rho_{\mu}}\right) \\ \left(\frac{\partial^{2}\phi}{\partial\rho_{v}}\frac{\partial\xi_{\mu}}{\partial\xi_{\mu}}\right) & \left(\frac{\partial^{2}\phi}{\partial\rho_{v}}\frac{\partial\rho_{\mu}}{\partial\rho_{\mu}}\right) \end{bmatrix} \\ = \begin{vmatrix} (\delta_{v\mu}(-\lambda)^{2} p_{v}e^{-\lambda\xi_{v}}) & (\delta_{v\mu}[-\lambda e^{-\lambda\xi_{v}} + A]) \\ (\delta_{v\mu}[-\lambda e^{-\lambda\xi_{v}} + A]) & (0) \end{vmatrix} \\ = \begin{pmatrix} D & O \\ O & O \end{pmatrix}$$

since we know  $A = \lambda e^{-\lambda \xi_v}$ , for all v. The non-zero elements of the diagonal matrix D are  $(-\lambda)^2 p_x e^{-\lambda \xi_x} > 0$ . Hence the extreme point is the (unique) minimum.

Since we have shown that

$$\sum_{1}^{n} p_{j} e^{-\lambda \xi_{j}} \ge \sum_{1}^{n} p_{j} e^{-\lambda T} = e^{-\lambda T} \sum_{1}^{n} p_{j} = e^{-\lambda T}$$

$$T = \sum_{1}^{n} p_{j} \xi_{j}$$
 and  $1 = \sum_{1}^{n} p_{j}$ ,

then for any of our integral-approximating sums it follows that

$$\sum_{j=1}^{n} e^{-\lambda \xi_{j}} [F(t_{j}) - F(t_{j-1})] \ge e^{-\lambda T}.$$

Furthermore, equality can only be achieved if all the  $\xi_i$ 's are equal to T. Due to the restrictions of the limiting process, namely that the  $\xi_i$ 's be elements of consecutive disjoint intervals, they can only be equal if  $F(t_i)$  $-F(t_{j-1})=0$  for all but one j, say j\*. Also  $\xi_{j^*}=T$ means  $(t_{i^*-1}, t_{i^*}) \ni T$ . We have  $0 = F(0) = F(t_0)$  and  $1 = F(\infty) = F(t_n)$ ; and these facts, together with  $F(t_j) - F(t_{j-1}) = 0$ , for all  $j \neq j^*$ , impose the conclusions:

$$F(t_1) - F(t_0) = F(t_1) = 0$$

$$\vdots$$

$$F(t_{p-1}) - F(t_{p-2}) = F(t_{p-1}) = 0$$

and

$$1 - F(t_{n-1}) = F(t_n) - F(t_{n-1}) = 0 \text{ or } F(t_{n-1}) = 1$$

$$\vdots$$

$$1 - F(t_{j^n}) = F(t_{j^n-1}) - F(t_{j^n}) = 0 \text{ or } F(t_{j^n}) = 1.$$

The above, together with  $\xi_{r} = T$ , dictate

$$F(t) = \begin{cases} 0, & \text{if } t \leq T \\ 1, & \text{if } t > T \end{cases}$$

For this F,

$$\int_0^\infty e^{-\lambda t} dF(t) = e^{-\lambda T} [1 - 0] = e^{-\lambda T}.$$

Although the u.f. model is highly idealistic in that there is no molecular diffusion or turbulent mixing on any scale, it possesses the unique distinction of yielding the least possible effluent radioactivity. Hence it provides a yardstick for defining the effectiveness of radioactivity-reduction by detainment in a reservoir. To be precise, we define the reduction efficiency  $\varepsilon$  of a real or model reservoir with reduction factor  $\rho$  by

$$\varepsilon = e^{-\lambda T}/\rho.$$
 (5)

In particular, therefore, the u.f. model is 100 per cent efficient. It should be noted that  $\varepsilon$  is a function of the mean lifetime of the radionuclide under consideration, as well as the reservoir characteristics.

Another distinctive property of the u.f. model is that it is determined by the single parameter T, which is undoubtedly the most readily available parameter describing the large scale flow characteristics of a reservoir.† It is tempting to apply T as a characteristic

<sup>†</sup> In counting the number of parameters to define a model, we do not include mean lifetime of the radionuclide.

time scale to get a rough estimate of the reduction of radioactivity of a radionuclide passing through the reservoir. However, to say that the reduction factor is  $e^{-\lambda T}$  is then to make the most optimistic assumption of 100 per cent efficiency. That such an estimate, even in the order-of-magnitude sense, can be grossly misleading will be demonstrated in Section 3.

#### 3. THE UNIFORMLY MIXED MODEL

An alternative and commonly used, one-parameter reservoir model with an intuitively reasonable physical basis is one in which the contents are steadily and uniformly mixed (Harte and Socolow, 1971; Carlson et al., 1968). This may be considered the complement of the u.f. model, since now diffusion and turbulent mixing completely dominate the internal flow. In this case, which we call the uniformly mixed (u.m.) model,  $T^{-1}$  is the constant probability per unit time that any parcel of fluid leaves the reservoir. This is similar to the exponential radioactive decay law in which there is a constant probability per unit time that a nucleus undergoes decay. Hence the residence time distribution function is

$$F_{u.m.}(t) = (1 - e^{-t/T}).$$
 (6)

From (4), we find the reduction factor

$$\rho_{\rm u.m.} = [1 + \lambda T]^{-1} \tag{7}$$

and so

$$\varepsilon_{\rm u.m.} = (1 + \lambda T) e^{-\lambda T}$$
.

Table 1 lists u.m. model reduction efficiencies for several radionuclides commonly occurring in fission reactor releases (Kahn, 1971). Reservoirs of flushing times 3 yr and 10 yr are assumed in the examples. The table shows how inefficient a reservoir can be in reducing short-lived radionuclide concentrations; or, equivalently, how incorrect it can be to assume the reduction factor is  $e^{-\lambda T}$ . For example,  $Co^{58}$ , an appreciable component of nuclear power plant wastes, has a reduction factor 0.086 in a uniformly mixed reservoir with a 3 yr flushing time. This is 1/0.000306

or about 3300 times larger than the least possible reduction factor  $e^{-\lambda T}$  (= 2.6 × 10<sup>-5</sup>).

#### 4. TWO-PARAMETER MODELS

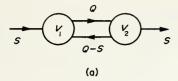
While the one-parameter models introduced in Sections 2 and 3 have the virtue of very simple physical interpretations and correspondingly simple mathematical forms, the great discrepancy between their reduction efficiencies or relatively short-lived radionuclides is disturbing. It is possible; however, that there are classes of more realistic reservoir models for which a one-parameter model is still a good approximation. To investigate this possibility we shall construct more complex models based on physically sensible large-scale circulation patterns and then make comparisons of their reduction efficiencies. The complex models may of course be intrinsically interesting and useful by themselves.

The procedure that we shall follow for building up complex models is the linking together of units that are themselves either u.f. or u.m. models. The complexity of a model increases with the number of parameters required in its definition. A hierarchy of reservoir models of increasing number of parameters can be constructed by this procedure. Thus, denoting the u.f. model by a square and the u.m. model by a circle, it turns out that the only two-parameter models are those shown in Fig. 1. Some three-parameter models are displayed in Fig. 2, for the interested reader. However, we shall study only the one- and two-parameter models in this paper.

Figure 1(a), the two-cell (t.c.) model, corresponds to a reservoir consisting of two cells which are independently and uniformly mixed, a separation that could be caused by topography and prevailing winds. The influent enters one cell, the effluent leaves the other, and there is a steady transfer between the two cells. Figure 1(b), the recirculating (r.c.) model, corresponds to a case where there is negligible turbulent mixing, but there is a steady circulation due to a single large eddy. Similar physical interpretations can be found for the higher order models. In particular,

Table 1. Reduction efficiencies for some radionuclides based on the uniformly mixed model.

Radionuclide	Half-life	Decay rate (yr - 1)	$\varepsilon_{\text{u.m.}}, T = 3 \text{ yrs}$	$\varepsilon_{\text{u.m.}}$ , T = 10 yr
Ba <sup>140</sup>	12.8 days	19.8	$1.1 \times 10^{-24}$	$3 \times 10^{-84}$
Co <sup>58</sup>	72 days	3.51	$3.06 \times 10^{-4}$	$2 \times 10^{-14}$
Co <sup>60</sup>	5.27 yrs	0.131	0.94	0.62
H <sup>3</sup>	12.3 yrs	0.0563	0.99	0.89



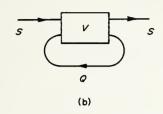


Fig. 1. The two-parameter models.

Fig. 2(b) is the model for a uniformly mixed epihimnion undergoing steady transfer with an unmixed hypolimnion. The influent and effluent connect only with the epilimnion.

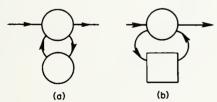
#### Two-cell model

In Fig. 1(a)  $V_1$  and  $V_2$  are the volumes of the cells connected to the influent and effluent, respectively. The flow rate from 1 to 2 is Q, while that from 2 to 1 is Q - S, where  $Q \ge S$ . Let x = radionuclide concentration in cell 1. Applying (7) to cells 1 and 2 separately, we find

$$\frac{Qx}{Sc_i + (Q - S)c_e} = \left(1 + \lambda \frac{V_1}{Q}\right)^{-1}, \frac{c_e}{x} = \left(1 + \lambda \frac{V_2}{Q}\right)^{-1}$$
(8)

Eliminating x between these equations gives

$$\rho_{\text{t.c.}} = \left[1 + \lambda T + \lambda^2 B\right]^{-1} \tag{9}$$



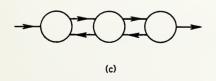


Fig. 2. Some three-parameter models.

where the two parameters are

$$T = \frac{V_1 + V_2}{S} = \frac{V}{S} \text{ and } B = \frac{V_1 V_2}{QS}.$$
 (10)

To provide a uniform basis for later comparisons it is preferable to relate B to the variance of the residence time distribution, and take the latter divided by  $T^2$  to be the second parameter  $\omega$ . The variance is given in general by

$$\lim_{\lambda \to 0} \frac{\partial^2}{\partial \lambda^2} \ln \rho. \tag{11}$$

For the t.c. model, we obtain

$$\omega = 1 - 2\frac{B}{T^2}, \quad \frac{1}{2} \le \omega \le 1;$$
 (12)

and hence

$$\rho_{1c} = \left[1 + \lambda T + \frac{1}{2}\lambda^2 T^2 (1 - \omega)\right]^{-1}.$$
 (13)

The smallest variance  $(\omega = \frac{1}{2})$  and hence the greatest reduction efficiency possible in the model occurs when the two cells have equal volumes and Q = S. The largest variance  $(\omega = 1)$  occurs either when one of the cell volumes = 0 or when  $Q \to \infty$ , in which case the model reduces to the u.m. model.

It should be pointed out that although  $\rho_{\text{t.c.}}$  is well defined for  $0 \le \omega \le \frac{1}{2}$  in Eq. (13), a corresponding residence time distribution function for this range of  $\omega$  does not exist.

#### Recirculating model

The time required for fluid to move uniformly from left to right in the square of Fig. 1(b) is V/(Q+S), where the recirculation rate Q satisfies  $0 \le Q < \infty$ . The rate of radionuclide entering on the left side is  $Sc_i + Qc_e$ , while the rate it leaves on the right side is  $(Q+S)c_e$ . Hence we have

$$\frac{(Q+S)c_e}{Sc_i+Qc_e} = e^{-\lambda V/(Q+S)}$$
 (14)

or

$$\rho_{\rm r.c.} = \left| \left( 1 + \frac{Q}{S} \right) e^{\lambda V/(Q+S)} - \frac{Q}{S} \right|^{-1}$$
 (15)

We find

$$\omega = \frac{Q}{Q+S}, \quad 0 \le \omega \le 1, \tag{16}$$

so that we can write

$$\rho_{\rm r.c.} = \frac{1 - \omega}{e^{\lambda T (1 - \omega)} - \omega}.$$
 (17)

When the recirculation rate  $Q \to 0$ , when  $\omega = 0$ , and the model reverts to the u.f. model. On the other hand, as  $Q \to \infty$ ,  $\omega \to 1$ , and  $\rho_{\rm r.c.} \to \rho_{\rm u.m.}$ . This is an understandable limit because a very large recirculation rate effectively stirs up the reservoir to uniformity.

### 5. RESULTS AND DISCUSSION

Although the risks of radioactivity in the environment show a record of having undergone very careful scrutiny and control, some of the basic assumptions are controversial and may be at fault. It now seems that even very low concentrations of radioactivity are suspect (Gofman and Tamplin, 1970; Holcomb, 1970). In planning for the public use of water with radioactive contamination, safety considerations are accordingly of the utmost importance; and so it is good planning policy to take a conservative approach in estimating  $c_e$ . Such a policy generally implies assuming pessimistic operating conditions, such as a maximum expected rate of release of radioactive wastes, and a maximum expected rate of use of reservoir water. Therefore, it would be inconsistent with this policy to assume, trivially, the least possible reduction factor in estimating the effect of the reservoir detainment process. On the other hand, it is not such a trivial matter to estimate a sensible upper limit for  $\rho$ . An upper bound on  $\rho$  is 1, corresponding to a swift narrow channel connecting influent to effluent in an otherwise stagnant reservoir. We shall conclude by presenting and discussing some numerical results, which shed light on the problem of estimating a sensible upper limit for  $\rho$ .

Reduction factors for the two-parameter models are plotted as functions of T in Figs. 3-6. These are

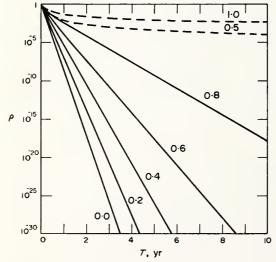


Fig. 3. Reduction factors for Ba<sup>140</sup>

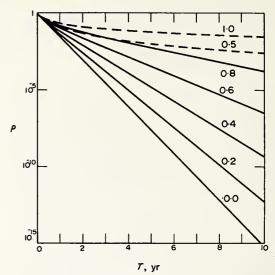


Fig. 4. Reduction factors for Co58.

computed for the four radionuclides listed in Table 1. The dashed curves give  $\rho_{\rm t.c.}$  while the solid curves give  $\rho_{\rm r.c.}$ . The number above each curve is the value of  $\omega$ . The curves generally indicate (i) the agreement between the u.f. and u.m. limits ( $\omega=0.0$  and 1.0, respectively) as  $T\to 0$ , and (ii) the pronounced divergence between these limits as  $T\to \infty$ .

Figure 7 displays the contours of constant values of  $\varepsilon_{\text{t.c.}} = \rho_{\text{u.f.}}/\rho_{\text{t.c.}}$  (dashed curves) and of the ratio  $\rho_{\text{t.c.}}/\rho_{\text{u.m.}}$  (solid curves). The abscissa and ordinate of the plots are the dimensionless parameters R/T and  $\omega$ , respectively. The contour values are printed next to the contours. At any point to the right of a curve, the value of  $\varepsilon_{\text{t.c.}}$  or  $\rho_{\text{t.c.}}/\rho_{\text{u.m.}}$  is larger than the contour value and approaches unity as  $R/T \to \infty$ . In particular,

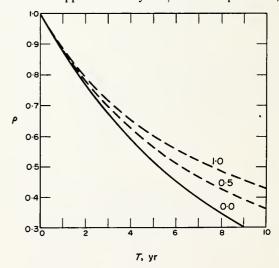


Fig. 5. Reduction factors for Co<sup>60</sup>.

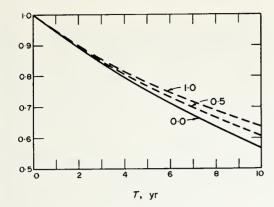


Fig. 6. Reduction factors for H<sup>3</sup>.

for any point to the right of the solid contour marked 0.85, the u.m. model is a "good" approximation (within 15 per cent) to the t.c. model. In this respect, the u.m. model is always better than the u.f. model; and, furthermore, it gives an upper bound on the reduction factor, assuming the t.c. model itself is a good approximation to the actual reservoir.

Figure 8 similarly displays the contours of constant values of  $\varepsilon_{\rm r.c.} = \rho_{\rm u.f.}/\rho_{\rm r.c.}$  (dashed curves) and of the ratio  $\rho_{\rm r.c.}/\rho_{\rm u.m.}$  (solid curves). In this case, for values of  $\omega > 0.45$ , the u.m. is again better than the u.f. model, assuming the r.c. model is valid. However, for  $\omega \leq 0.45$  the upper bound on  $\rho$  given by the u.m. model is relatively inaccurate in comparison to the u.f. model.

The step from one-parameter to two-parameter models is peculiar in that the former establish the extreme limits of the latter. It is necessary to resort to three-parameter models to find reduction factors lying above the curves labelled 1.0 in Figs. 3-6. Thus, a principle result we wish to report here may be stated as follows: Among the low-complexity steady state reservoir models (number of parameters < 3),

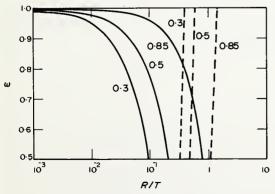


Fig. 7. Contours of  $\varepsilon_{t,c}$  and  $\rho_{t,c}/\rho_{u,m}$ .

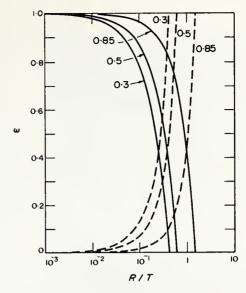


Fig. 8. Contours of  $\varepsilon_{\rm r.c.}$  and  $\rho_{\rm r.c.}/\rho_{\rm u.m.}$ 

the u.m. model stands out in that it gives a rigorous upper bound on the reduction factor. Although the simplicity and usefulness of this fact are self-evident, we might restate this by observing that it enhances (and establishes limits on) the credibility of a calculation based on the assumption that the contents of a reservoir are uniformly mixed.

#### REFERENCES

Aitsam A. (1969) Advances in Water Pollution Research, pp. 837-844. Pergamon Press, New York.

Carlson C. A. et al. (1968) Radioactivity and a Proposed Power Plant on Cayuga Lake, Fernow Hall, Cornell University.

Gofman J. W. and Tamplin A. R. (1970) Testimony presented at Hearings of the Joint Committee on Atomic Energy, U.S. Congress, Jan. 28, 1970.

Harte J. and Socolow R. H. (1971) Patient Earth, pp. 132-134. Holt, Rinehart & Winston, New York.

Holcomb R. W. (1970) Radiation risk: a scientific problem? Science N.Y. 167, pp. 853-855.

International Atomic Energy Agency (1963) Disposal of Radioactive Wastes into Fresh Water, Vienna (Safety Series No. 10).

Kahn B. et al. (1971) Radiological Surveillance Studies at a Boiling Water Nuclear Power Reactor, BRH/DER 70-1, U.S. Environmental Protection Agency.

Logsdon J. E. and Chissler R. I. (1970) Radioactive Waste Discharges to the Environment from Nuclear Power Facilities, BRH/DER 70-2, U.S. Dept. of Health, Education and Welfare.

National Technical Advisory Committee (1968) Water Quality Criteria, pp. 49-51. Federal Water Pollution Control Administration, Washington, D.C.

Stanislav J. and Mohtadi M. F. (1971) Mathematical simulation of dispersion of pollutants in a lake with ice cover. *Water Res.* 5, pp. 401-412.

## Formation of Cloud and Ice Nuclei by the Combustion of Crude Oil

C. C. VAN VALIN, R. F. PUESCHEL AND F. P. PARUNGO

Environmental Research Laboratories, NOAA, Boulder, Colo. 80302 2 October 1974 and 10 March 1975

#### ABSTRACT

Aitken nuclei and ice nuclei concentrations in the smoke plume from an oil well fire near Glenrock, Wyo., on 14 December 1973, were found to be elevated by at least an order of magnitude as compared with the surrounding atmosphere. The composition of most particles in the plume was suggestive of the clay minerals; these could account for the increased ice nuclei concentrations.

#### 1. Introduction

On 5 December 1973 the newly drilled Patterson No. 1 oil well near Glenrock, Wyo., caught fire. For several weeks it burned about 200 barrels of crude oil per hour. The smoke plume was visible for at least 50 km downwind and presented an opportunity for measurement of some of the characteristics of crude oil combustion products in an otherwise clean atmosphere.

### 2. Sample collection

On 14 December 1973, one of us (RFP), along with a pilot and an assistant, flew from Boulder, Colo., to the well site to measure Aitken nuclei concentrations

 $(N_A)$  and obtain membrane filter samples for subsequent measurement of deposition ice nuclei concentrations  $(N_I)$  and analysis of collected particles for their elemental composition and surface characteristics. Values of  $N_A$  were measured *in-situ* with a Gardner Small Particle Counter. A Cessna Model 205, single engine, six place airplane was used. Samples were collected while the plane crossed the plume, turned, and crossed again, as shown in Fig. 1. Sampling was done from 5 to 50 km downwind from the well; position keeping was within  $\pm 1$  km of the distance shown. The time consumed in turning and repositioning for another crossing was estimated at from 45 s to 1 min; at the greater plume distances a Gardner Counter reading  $(N_A)$ 

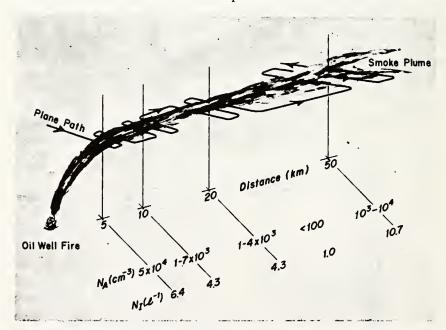


Fig. 1. Aitken nuclei  $(N_A)$  and ice nuclei  $(N_I)$  concentrations downwind from the Patterson No. 1 oil-well fire 14 December 1974. An  $N_A$  of <100 cm<sup>-3</sup> was measured in the adjacent undisturbed atmosphere. The  $N_I$  of 1.0  $\ell^{-1}$  was measured by Allee (1974) at Lander, Wyo., on this date.

indicative of background was obtained before the turn was accomplished. Since the time required to cross the plume varied from 15 s to 1 min, from half to three-quarters of the sampling time was spent outside the plume, with the consequence that  $N_I$  (Fig. 1) is proportionately understated.

Aerosols were collected by drawing outside air through a 0.45  $\mu$ m pore size, mixed cellulose ester membrane filter. Flow rate was 10  $\ell$  min<sup>-1</sup>, sampling time was 5 min per filter. Ice nuclei collected on half of the filter were measured in the laboratory by the method of Bigg et al. (1963), at  $-20^{\circ}$ C, in an atmosphere saturated with respect to water. Another part of the filter was used for elemental and surface characterization of individual particles on the filter by scanning electron microscopy with energy dispersive x-ray analysis (SEM-EDX).

The smoke from the burning oil formed a well-defined plume at an elevation of 3000 m MSL (surface elevation, 1550 m). The pilot estimated the vertical thickness to be 300–400 m, with a horizontal width of 1 km at 10 km downwind, and 4 km at a downwind distance of 50 km. As viewed from  $\sim$ 70 km away and perpendicular to its axis, at least 50 km of the plume length was visible as it extended from west to east. In the surrounding atmosphere  $N_A$  varied from 200 cm<sup>-3</sup> to fewer than 100 cm<sup>-3</sup>; within the smoke plume  $N_A$  was from one to several times an order of magnitude higher, even at the maximum sampling distance of 50 km downwind from the fire.

### 3. Discussion and conclusions

According to Allee<sup>1</sup>, the 14 December 1973 24 h average  $N_I$ , and the December 1973 monthly average  $N_I$  at Lander, Wyo., were 1.0 and 1.2  $\ell^{-1}$  respectively, as measured by the same procedure as used here (Allee, 1974).

We consider the Lander sample of 14 December 1973 to be representative of the same air mass present at the site of the oil well fire on the same day. Hence, the background concentration of  $1.0 \, \ell^{-1}$  is shown in Fig. 1. As mentioned earlier, the ice nuclei measurements in the plume and vicinity probably understate the  $N_I$  in the plume by factors of 2-4, with the smaller factor occurring at the greatest distance. On this basis,  $N_I$  in the plume is seen to be elevated by more than an order of magnitude.

The energy dispersive x-ray analyses of two particles, collected 5 and 10 km downwind from the fire, are shown in Fig. 2. These are representative of the majority of particles found on the collection filters in the sense that they contain a variety of elements suggestive of mixed mineral origin. Silicon, oxygen and aluminum are the most abundant elements in the earth's crust, and the lower x-ray spectrograph is typical of our analyses of clay mineral particles (elements lighter

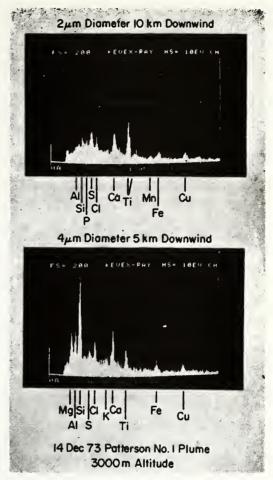


Fig. 2. Energy dispersive x-ray analyses of particles collected on 0.45 μm membrane filters.

than sodium do not respond in our x-ray energy spectrometer). These are hydrous aluminum silicates, with magnesium, iron, sodium, potassium and calcium often present as essential constituents (Hurlbut, 1971).

Several investigators have attempted to assay the ice nucleating effectiveness of various natural mineral dusts (e.g., Fukuta, 1958; Mason and Maybank, 1958; Mason, 1960). In general, the silicate minerals of the clay and mica groups were most active. Laboratory studies have also shown that many metallic oxides are capable of ice nucleation at rather high temperatures, i.e., above —10°C (Mason, 1971). Ice nucleation appears to depend upon a suitable crystalline substrate for initiating ice crystal growth either by contact or by deposition (Fletcher, 1970).

In the upper x-ray spectrograph of Fig. 2, the prominent signal for titanium is suggestive of rutile  $(TiO_2)$ , or along with the calcium, of perovskite  $(CaTiO_3)$ . Both of these, according to their crystal lattice dimensions, might be effective as ice nuclei at -10 to  $-8^{\circ}C$ .

<sup>&</sup>lt;sup>1</sup> Private communication.

TABLE 1. Elemental composition of particles.

Approximate distance downwind (km)	5	10	20	50	Total	Percent occurrence in plume	Percent occurrence in Lander,
Number of particles within 1 mm <sup>2</sup>	27	19	22	21	89	piae	Wyo.
Element detected							
Na	1	3	4	1	9	10	20
Mg	5	2	3	1	11	12	20
Al	24	11	9	9	53	60	70
Si	16	14	19	18	67	75	90
P	7	10	8	10	35	39	15
S	18	15	11	14	58	65	35
Cl	9	13	8	11	41	46	30
K	4	8	5	6	23	26	50
Ca	6	6	6	6	24	27	50
Ti	4	9	3	6	22	25	5
V	6	7	3	8	24	27	
Fe	7	7	5	4	23	26	40
Cr	1				1	1	
Ni		2 °			2	2	
Со		1	1	1	3	3	
Ag		1	3	2	6	7	
Cu*				1	1	1	

<sup>\*</sup> When the Cu mounting stud is used, the estimation of sample Cu is very uncertain.

For the elemental analyses, we evaluated all particles on 1 mm<sup>2</sup> of each filter. The findings are summarized in Table 1.

By far the most abundant organometallic compounds in crude petroleum are the vanadium-containing porphyrins (Baker, 1969), and the vanadium in these samples is probably from this source. (Vanadium was not detected in the samples collected at Lander.) Although the higher oxides of vanadium, that would be produced during the combustion of petroleum, are slightly soluble in water, their crystal spacings appear to be suitable for ice deposition. Therefore they may be active as ice nuclei. The higher incidence of sulfur, chlorine and phosphorus in these samples, as compared with their occurrence in the Lander samples, indicates that the petroleum was an important source of these elements. Combustion of the petroleum carrier would result in soluble products. Such water-soluble products would not be active as ice nuclei, and in fact, would probably deactivate otherwise active mineral particles by forming a water-soluble surface coating (Pueschel et al., 1974).

In eleven oil wells in the state of Wyoming, nickel was the metal next in abundance to vanadium, occurring at an average of one-fifth the concentration of vanadium (Ball et al., 1960). However, nickel was found in only two of the examined particles from our samples, and therefore cannot be considered as significant here in terms of possible ice nucleating sites.

The other elements found in the particles sampled are abundant and widespread in the earth's crust, and probably represent minerals resident in the petroleum deposit or eroded from the bore hole. Of the minerals that may be represented here, some have fairly high-temperature thresholds of ice nucleating ability, e.g., kaolinite [Al<sub>4</sub>(Si<sub>4</sub>O<sub>10</sub>)(OH)<sub>8</sub>], tridymite (SiO<sub>2</sub>), magnetite (Fe<sub>3</sub>O<sub>4</sub>, which often contains significant quantities of Ti), hypersthene [(Mg,Fe)<sub>2</sub>(Si<sub>2</sub>O<sub>6</sub>), often containing Al], and calcite (CaCO<sub>3</sub>) (Mason, 1971).

It is also appropriate to comment on the probable contribution of these particles to the cloud condensation nuclei (CCN) budget, even though our lack of a suitable instrument made it impossible to measure CCN within the smoke plume. CCN activity appears to depend upon surface capillarity or surface solubility (Pueschel et al., 1974); the high incidence of sulfur, chlorine and phosphorus in particles from the oil-well fire suggests the presence of soluble sulfates, chlorides and phosphates on the particle surface, and consequently, a high CCN activity.

### 4. Summary

We have shown that the smoke plume from an oil-well fire contains at least an order of magnitude more Aitken and ice nuclei per unit volume than the surrounding atmosphere, and the particles remain airborne for considerable distances downwind. An elemental analysis of individual particles by SEM-EDX has identified elements in abundances and combinations suggestive of minerals that are known to be active ice nucleators. On the other hand, the relatively high concentrations of sulfur, chlorine and phosphorus suggest the presence

of other substances that are inactive as ice nuclei, but which may be effective as CCN.

Acknowledgments. We thank Helmut K. Weickmann for suggesting and assisting in the preparation for this research flight. We also take this opportunity to thank Robert S. Lawrence of the Wave Propagation Laboratory, NOAA, and Richard A. Proulx for their participation as pilot and technician, respectively.

#### REFERENCES

- Allee, P. A., 1974: Ice nuclei concentration measured by a benchmark network. Preprints Fourth Conf. Weather Modification, Ft. Lauderdale, Amer. Meteor. Soc., 242-245.
- Baker, F. W., 1969: Porphyrins. Organic Geochemistry, G. Eglinton and M. T. J. Murphy, Eds., Springer-Verlag, 464-497.
  Ball, J. S., W. J. Wenger, H. J. Hyden, C. A. Horr and A. T.

- Myers, 1960: Metal content of twenty-four petroleums. J. Chem. Eng. Data, 5, 553-557.
- Bigg, E. K., S. C. Mossop, R. T. Mead and N. S. C. Thorndike, 1963: The measurement of ice nucleus concentrations by means of Millipore filters. J. Appl. Meteor., 2, 266-269.
- Fletcher, N. H., 1970: The Chemical Physics of Ice. Cambridge University Press, 271 pp.
- Fukuta, N., 1958: Experimental investigations on the ice-forming ability of various chemical substances. J. Meteor., 15, 17-26.
- Hurlbut, C. S., Jr., 1971: Dana's Manual of Minerology, 18th ed. Wiley, 579 pp.
- Mason, B. J., 1960: Ice-nucleating properties of clay minerals and stony meteorites. Quart. J. Roy. Meteor. Soc., 86, 552-556. -, 1971: The Physics of Clouds. Oxford, Clarendon Press, 671
- pp. , and J. Maybank, 1958: Ice-nucleating properties of some natural mineral dusts. Quart. J. Roy. Meteor. Soc., 84, 235-
- Pueschel, R. F., C. C. Van Valin and F. P. Parungo, 1974: Effects of air pollutants on cloud nucleation. Geophys. Res. Lett., 1,

SESSION: WMO-5

MODIFICATION OF SNOW ACCUMULATION BY CLOUD SEEDING

by

H.K. Weickmann

WMO - 5: Modification of Snowfall, Snowcover, and Ice Cover

International Symposia on the Role of Snow and Ice in Hydrology

Symposium on Measurement and Forecasting

# MODIFICATION OF SNOW ACCUMULATION BY CLOUD SEEDING IN THE GREAT LAKES BASIN

Helmut K. Weickmann
Atmospheric Physics and Chemistry Laboratory
Environmental Research Laboratories
National Oceanic and Atmospheric Administration
Boulder, Colorado 80302

The Great Lakes Basin encloses an area of more than 750,000 km² and has a water surface of 250,000 km². Thirty-two million people live within the lake boundaries - twenty-eight million of them take their water requirements directly from the hydrological system of the Great Lakes Basin. This makes a daily total water consumption for industrial and private use of 15,600 million gallons. It is interesting to note that the average amount of snow falling from a typical Lake Erie "lakestorm" is 250,000 millions of gallons, or a 16 day supply of water for the population. During the period 4 November 1966 through 25 January 1969, 23 storms occurred; this was a water supply for 1 year. As the hydrology of all lakes is delicately balanced, it is obvious that the artificial manipulation of atmospheric resources over lakes may have a very significant influence on various human activities.

For the past 5 years NOAA has studied the weather modification potential of the Great Lakes Region. Numerous observations of artificial rain and snowfall have been made in the Buffalo region of Lake Erie (see Table 1.) Climatologically, the Great Lakes region is peculiar in that its numerous relationships between the water surfaces and the air exert particularly strong influences in the atmospheric boundary layer. In winter the entire Great Lakes Basin has a high frequency of shallow cloud layers which, upon travelling across the still unfrozen and warm lakes, form the basic ingredient for the development of lake storms. The Basin is the seat of many industries whose pollution potential not only affects the hydrology and ecology but also the weather. For instance, large concentrations of highly effective freezing

nuclei have been formed downwind of the Bethlehem Steel Plant in Lackawanna near Buffalo. These nuclei have released downwind snow showers on several occasions. Of course, the famous La Porte, Indiana anomaly is another case of a possible pollution effect.

Table 1.

## INITIATION OF PRECIPITATION TABLE

	CONVECT	VE LAYER	STRATIFOR	M LAYER	SEEDING	
	8ASE	TOP	8ASE	TOP	TYPE	RESULT
13 NOV 68	900' -7°C	2000' -9°C			650lbs Dry Ice Racetrack	# 35min V A.S.
25 NOV 68		1800 -9.5 •	2100' -10°C	2400' -10.8*0	2501bs Dry Ice Circle	* <sup>I</sup> 26min ∇ A.S.
29 NOV68		1800 -10.8			450 lbs Dry ice 3 Legs	<sup>*¹</sup> ½³⁄hr
2 DEC 68		2400 -11			550 lbs Dry Ice Racetrack	• Over ∇ Lake
3 DEC 68	1000 +1.5	2600 -8	2700 -11.3	2900 -12.3	2400g Ag I Fusees	Over  ∇ Lake
6 DEC 68	300	1500 -10.3	1800	2100 -11.7	2400g Ag I Fusees 700lbs Dry Ice	1-2 • Over ∇ 1-2 Lake • 36 min A.S.

The tightly controlled lake hydrology causes problems with the water supply of the City of Chicago which has a water allotment from Lake Michigan of 1700 cubic feet/sec (CFS) while its needs are 3200 CFS. Cost of 1700 CFS to the water user amounts to more than \$3,000,000.00 in 10 days!

Field experience and climatological studies in the Great Lakes Basin indicate the frequency occurrence of shallow supercooled cloud layers within the boundary layer. These cloud layers are generally 1700 - 1800 m thick and often have cloud top temperatures warmer than -15°C. Few natural freezing nuclei are active at these warm temperatures and consequently there is a poor natural release of precipitation. Precipitation from these clouds can be significantly increased through artificial seeding. The areal extent of these cloud systems should be the subject of future studies. Precipitation potential can be estimated from the rate of condensation in convective cloud

layers based upon updraft speeds measured with a doppler radar. Table 2 gives hourly values of induced precipitation for various conditions of cloud thickness and temperature. On at least two occasions in our seeding experiments, once over Lake Michigan and once over Lake Erie, we accidentally created and observed the artificial formation of a miniature squall line consisting of several heavy rain squalls. A 20 km wide squall line of 5 hours duration, extending the length of Lake Michigan, would sustain the water needs of Chicago for 30 days! Such a squall line would essentially "recycle" water that has evaporated upwind of the Lake back into the Lake and would decrease winter precipitation over the eastern shore areas of Lake Michigan - an area which has a winter precipitation surplus.

Table 2

ESTIMATE OF INDUCED PRECIDITATION - 50% FEFICIENCY

ESTIMATE OF TRESCENT TRAITER - 30% ETTERENT				
GEOGRAPHIC AREA	STRATUS CLOUD THICKNESS (Meters)	TEMPERATURE RANGE (°C)	UPDRAFT VELOCITY (cm/sec)	INDUCED PRECIPITATION (mm/hr)
	3000	0 to -22	10	1.73
GREAT LAKES	3000	0 to -22	50	8.05
	2000	0 to -15	50	4.50

NOAA's research objective in the Lake Erie program was to mitigate the effects of intensive lake storms in the Buffalo industrial and metropolitan areas. The seeding concept called for over-seeding of the cloud system thus changing the type of precipitation particles from the natural forms - graupel and rimed snowflakes - to a crystal habit that forms by diffusion only, falls. slower and is therefore carried further inland. Another concept called for

snowout over the Lake prior to reaching land. This second concept has been tested by using the Lavoie Numerical Model for the lake storms on Erie and by studying the distribution of precipitation with and without seeding. This model has been tested on a number of storms and it has been found to represent realistically the development of the cloud system and precipitation patterns for Lake Erie and Ontario. It has been expanded to include precipitation processes for the formation of snowflakes. For a fictitious lake winter storm developing along the long axis of Lake Erie at a wind velocity of 15 m/sec, air temperature of  $-4^{\circ}$ C, water temperature of  $+8^{\circ}$ C, up-stream depth of atmospheric boundary layer of 1.25 km, the steady state precipitation area is shown in Figure 1. Here the hatched parts means growth of precipitation elements due to vapor diffusion, stippled signifies growth through diffusion and riming. It is evident that the snow falls over the eastern lake area with one maximum over the Buffalo metropolitan area.

Figure 2 shows what happens for the same case when the storm system is seeded along the indicated line for one hour, so that the crystal concentration reaches  $100/\Omega$ . The Figure indicates that most of the snow falls into the water in form of snowflakes. While this may not be the only solution that nature may find, it is certainly a realistic solution and a very interesting one during times of low water level, indeed. (It is a most encouraging result, similar studies will have to be carried out for other lakes in the Great Lakes Basin.)

The artificial precipitation potential for other types of cloud systems has not yet been studied by NOAA but there can be no question that the peculiar land and lake distribution in the Basin will cause natural convergences in the boundary layer which should lead to preferred locations for cloud developments. We are convinced that the time has come for a thorough exploration of the artificial precipitation potential of the entire Great Lakes Basin and specifically for Lake Michigan and Lake Erie.

Also, climatic amelioration through dissipation of super cooled stratus clouds has already been accomplished on a small basis—there is no reason, except logistic ones, why this should not be carried out on a large scale.

## Future Plans:

A comprehensive study of the potential of weather modification in the Great Lakes Basin is planned along the following areas:

- (1) a climatology of cloud populations and their areal extent;
- (2) a study of the natural convergence mechanisms within the boundary layer as well as the effects of modification of the boundary layer as well as the effects of modification of the boundary layer flow due to urban developments;
- (3) a study of the hydrological and ecological problems connected with weather modification in the Great Lakes Basin;
- (4) an evaluation of the legal and international implications of precipitation modification;
- (5) an investigation of inadvertent weather modification caused by industrial air pollution;
- (6) a study of the socio-economic impact of weather modification activities on various interest groups (skiing areas, shipping, New York Thruway Authority, power production);
- (7) an evaluation of the effects of nuclear power plants on lake temperature, rate of evaporation and cloud formation;
- (8) a study of the influence of pollutants scavenged by artificial precipitation on lake ecology.

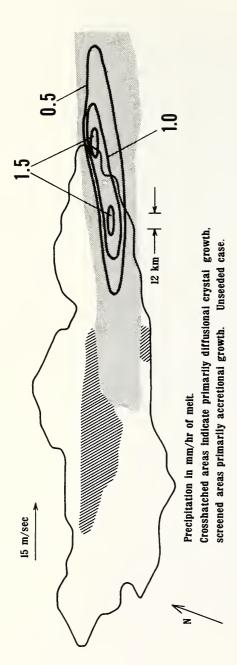


FIGURE 1

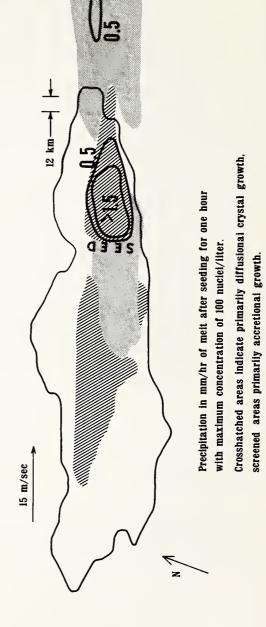


FIGURE 2

In and thous Conference on Weather Modification Tashkent, USSR HELMUT WEICKMANN AND PETER V. HOBBS Reprinted from Bulletin of the American Meteorological Society, Vol. 55, No. 4, April 1974

The first truly international conference on weather modification, sponsored by the World Meteorological Organization and the International Association of Meteorology and Atmospheric Physics and hosted by the Hydrometeorological Science of the USSR, was held from 1–7 October 1973, in Tashkent, USSR. The Conference was attended not only by scientists from those countries actively engaged in weather modification but also by many observers from nations throughout the world interested in advances in this subject. The importance which the USSR places on weather modification was indicated by the large number of Soviet scientists present at the Conference: 70% of the 270 participants were from the Soviet Union and of the 60 papers presented at the Conference 24 were authored by Soviet scientists.

The Conference was sub-divided into the following sessions: fog dispersal, rain enhancement, snow enhancement, hail suppression, modification of tropical storms and thunderstorms, technical and operational aspects of weather modification, physical, statistical and economic evaluations of weather modification, and ice nucleus technology. Six to ten papers, including invited review papers, were presented in each session and some 42 papers were read by title only. In this summary we can only highlight the interesting topics discussed during the Conference and indicate the trend of some of the more spirited discussions. For details on the many papers presented the reader is referred to the Proceedings of the Conference to be published by the WMO. (Regrettably, these Proceedings will not contain the discussions and comments from the floor.)

The most firmly established weather modification technique is the dispersal of cold fogs through glaciation by dry ice or propane. Many airports throughout the world employ this technique operationally for the improvement of visibility. Indeed, the technique is so sufficiently well established that only two papers were presented on the subject. Krasnovskaya et al. (USSR) reported on the use of propane for the dispersal of supercooled fogs near, and even slightly above, 0C. Propane reacts with water to form clathrate compounds with equilibrium water vapor pressures lower than saturation relative to either water or ice at -3 to 0C. Hicks and Vali (USA) presented the results of field and laboratory tests on cloud glaciation by liquified propane

spray. The field tests showed production efficiencies from  $2 \times 10^{11}$  to  $5 \times 12^{12}$  ice crystals per gram of propane. A direct relationship was found between the production efficiency and the rate of supply of water vapor to the glaciated zone as determined by wind velocity and cloud liquid water content.

Cold fogs, however, account for only 5% of fogs throughout the world. Consequently, considerable efforts are being expended to develop techniques for the dissipation of warm fogs. Methods reported at the Conference included the use of surface active agents to reduce the growth rates of fog droplets (Bakhanova and Silayev-USSR; Derjaguin et al.-USSR) and the dispersal of hygroscopic substances to enhance droplet growth rates and fallout (Derjaguin et al.—USSR). These esoteric techniques, although appealing to the cloud physicists, have yet to be proven operationally successful. "Brute force" techniques, such as the use of helicopter downwash, jet engine exhausts, and groundbased heating, can be used to dissipate warm fogs but they are expensive. Silverman (USA) described a thermal fog dissipation system under consideration by the United States Air Force. Costs of capital equipment are estimated at \$6,500,000 per airport with a cost-tobenefit ratio of 6:1 in 1973 and 22:1 in 1981 (assuming one aircraft landing per 5-minute burn). Fortunately, the fuel used to run the ground-based heaters is less than that which would be used were the aircraft to be diverted! Facy (France) described a French system for warm fog dispersal in which the exhausts from jet engines installed alongside the runway is vented upwards. The system uses 600 and 2,500 liters of gasoline per hour per engine for standby power and full power, respectively.

In a review paper on rain enhancement, Warner (Australia) set the scene for a topic which was to be a subject of controversy throughout the Conference, namely, the evaluation of weather modification experiments. He listed five criteria which he thought should be met in order to fully evaluate any weather modification experiment: 1) good statistical design and analysis, 2) long-term continuity, 3) uniformity in cloud characteristics, 4) clouds susceptible to modification techniques, and 5) background knowledge of the microphysics and dynamics of the clouds. Examples of "good" and "bad"

cloud seeding experiments were given. In the ensuing discussion from the floor, the point was made that while statistical techniques are valuable in evaluating weather modification experiments, they cannot replace sound physical concepts. It is interesting to note that the most successful weather modification technique (the dissipation of cold fogs) has never been subjected to strict statistical evaluation. Unfortunately, many weather modification projects have been carried out without either good physical or statistical evaluation.

Furmen et al. (USSR) described the results of seeding cumulonimbus clouds in the Ukraine with silver iodide dispersed from an aircraft into updraft regions at cloud base. Evaluation was carried out by comparing rainfall at the ground and radar observations from 17 seeded clouds with that predicted from a multivariate regression line for rainfall established from measurements on 99 unseeded clouds. The average rainfall from the seeded clouds was twice that computed from the regression line. Questions were raised as to the statistical significance of these results.

Gagin (Israel) discussed cloud and precipitation processes which operate in the cloud systems over Israel which statistical analysis has shown exhibit substantial increases in precipitation following seeding with silver iodide. Anomalously high ice particle concentrations (which have been observed in some clouds in other parts of the world) are not observed in these clouds. Clouds with top temperatures above —14C have ice crystal concentrations less than 1 liter-1, and ice is not detectable in clouds warmer than —10C. About 35% of the total number of clouds on a rainy day have radar echo top temperatures of —14C or higher. These observations appear to provide the already impressive statistical evaluation of the Israeli cloud seeding experiments with a sound physical basis.

Theoretical studies in which cloud sceding was simulated in numerical models were presented by Orville et al. (USA) and Stalevich et al. (USSR). Orville's twodimensional, time-dependent mountain cumulus cloud model indicated that, compared to natural clouds, heavy continuous ice-nucleus seeding should yield less rain and graupel, light continuous ice-nucleus seeding, more rain for the shallower clouds and less for the deeper clouds, and seeding with hygroscopic particles should yield more rain for a broad range of cloud sizes. It transpired in discussion that the Bergeron ice crystal process for precipitation development is not included in this model but that microphysical processes appear to be secondary in importance to dynamical processes, particularly in marginal situations. Stalevich et al., described a timedependent model of convective clouds which has been used to predict the time at which precipitation particles due to artificial seeding should first appear, the duration and intensity of the precipitation, time variations in precipitation rate and sizes of the precipitation particles.

The review paper on snow enhancement was given by Weickmann (USA) who emphasized Bergeron's original ideas on the releaser (or seeder) cloud and spender (or feeder) cloud which, in addition to occurring together, can also occur independently. Recent measurements have indicated that releaser clouds (Cs or As) furnish between 5 and 40 crystals per liter. When spender clouds (St or Sc) occur alone and with top temperatures sufficiently high that the natural production of ice crystals is deficient for effective snowout, the potential exists for snow enhancement by seeding with artificial ice nuclei. The structure of winter cloud systems and their potential for modification were reviewed in the light of these concepts. Leskov (USSR) discussed the results of dry ice seeding of winter frontal clouds in the steppe of the Ukraine. The abstract to this paper states "Seventy-seven experiments were carried out during 1960-72. Sixty-one precipitating Ns-As were seeded, of which in 16 experiments the precipitation was stimulated." However, in notes taken during the simultaneous Russian-to-English translation of this paper we recorded that there were 77 experiments on seeding frontal clouds of which 61 precipitated after seeding and 16 did not precipitate. The mean relative increase in precipitation attributed to seeding was stated to be about 100%, provided the cloud layers were not less than 250 m thick and the cloud top temperatures no higher than -4C. There was no evidence for redistribution of precipitation due to the seeding. No randomization or other means for statistical evaluation appear to have been employed in these experiments. However, some interesting physical measurements were obtained. Measurements from aircraft showed that artificial seeding with 700 gm of dry ice per km increased the concentrations of ice crystals in the clouds by factors of 10 to 100, although crystal concentrations in the unseeded Ns and As were already as high as 1,000 liter-1.

Kapoor et al. (India) reported on a cloud seeding experiment, using ground-based AgI generators at Delhi, which has been in progress every winter since 1968. Results from the first four years of the program suggest a net increase of 52% in rainfall in the target area. However, the increase is not statistically significant. Strict randomization has been observed only since the third year of the experiment.

Hobbs and Radke (USA) discussed the results of a detailed physical evaluation of the effects on cloud and snowfall of overseeding with AgI in a mountainous region (the Cascade Project). In many case studies simultaneous airborne, ground, and radar measurements of up to a dozen cloud and precipitation variables have shown that under certain conditions snowfall can be diverted from the windward to the leeward slopes of a large mountain range by overseeding. Statistical analysis was not employed in this project.

Juisto (USA) discussed the seeding requirements for the rapid glaciation of supercooled clouds and applied his results to different cloud systems. A new weather modification project in Nevada—the *Pyramid Pilot*  Cloud Seeding Project—was discussed by Warburton (USA). It is planned to last for three years with strict randomization.

The review paper on hail suppression was given by Burtsev et al. (USSR). An excellent account was given of our present understanding of hailstorms and their precipitation mechanisms. The USSR hail suppression projects were described. At the present time 3,770,000 hectares in the USSR are under "protection" from hail by cloud seeding techniques. It is believed that this "protection" resulted in a reduction in hail fall over this area of from three to four times in 1972. However, the authors of this paper acknowledged the difficulties of evaluating the effectiveness of hail modification experiments and they were of the opinion that "only the first step has been made" in hailstorm investigations.

Zaitchenko et al. (USSR) reported on observations of hailstorms and the results of hail suppression experiments in Moldavia. Temperature, humidity and wind conditions have been studied when hailstorms develop. A relationship between the intensity of hailstorms and the rate of horizontal airflow in the upper cloud levels was observed. Four hundred thousand hectares are being "protected" by cloud seeding in Moldavia. Statistical data collected since 1966, using two controlled areas and one target area, indicate reduction in hail damage by a factor of 10 to 30 within the "protected" area.

Lominadze et al. (USSR) described the hail suppression activities of the Transcaucasian Hydrometeorological Institute. Potential hailstorms are seeded by injecting NaCl into their lower regions and by injecting AgI into the upper levels (the NaCl is hypothesized to remove liquid water from the lower regions of the hailstorm by rainout). In 1973 250,000 hectares were "protected" by cloud seeding. The total quantity of seeding agents used over this area in 1973 was 377.12 kg of NaCl and 58.42 kg of AgI. The "protection" technique was claimed to have been reliable and highly efficient during the past five years of operation, but details of the techniques used for evaluation were not given.

Kachurin et al. (USSR) discussed a numerical model for cumulonimbus clouds which allows calculation of the vertical and horizontal boundaries of the cloud, vertical air motions, supersaturations, liquid water content, crystallization, and the growth of droplets, ice crystals and hail. Model calculations indicate that under certain conditions seeding with artificial ice nuclei should decrease the size and concentration of the solid precipitation particles.

The Soviet papers on hail suppression stimulated lively discussions from the floor, particularly on the question of verification. Soviet scientists have, in the past, favored physical rather than statistical evaluation of their weather modification experiments. However, it appears that the physical evaluations have been confined largely to measurements of radar reflectivity. No response was received from the Soviet delegates following a request from the floor for the results of any physi-

cal evaluation based on airborne measurements in hailstorms before, during, and after artificial seeding.

Admirat (France) presented an interesting paper on the structure and distribution of hail based on observations from 400 hailpads in southern France. Ten observations in unseeded hailstorms showed that the hail fell around a zone (the "hailcore") in which all parameters reached peaked values. The number of concentrations of hailstones and their maximum dimensions increased simultaneously and, at any one place, the number of hailstones of a given size was in inverse ratio to the size.

The results of climatological and synoptic studies of hailstones in Japan were described by Omoto (Japan). In the eastern-central portion of Honshu there is a close relation between orography and the formation and movement of hailstorms. A relatively high correlation between hail occurrence and the 500 mb temperature was also noted. Radar data from the area north of Tokyo showed that supercell-type hailstorms were rare. In most cases hail fell in the right flank and within a small area of multicell-type storms.

The lack of any report from the United States' National Hail Research Experiment, which began in 1971, was regrettable.

Session 5 contains a potpourri of papers. Gentry (USA) presented a comprehensive review on hurricane dynamics, numerical models of hurricanes, and attempts at hurricane modification. The rationale for seeding the wall clouds as well as the radial cloud bands for reducing maximum winds in hurricanes was discussed along with future plans for the United States experiments.

Vulfson and Levin (USSR) described the use of artificially-induced vertical jets of air for modifying convective clouds. Following the original idea behind Dessens' "meteotron," 12 jet engines are being used with a power of 500,000 kW to generate updraft velocities of 350 m sec-1 and an initial air temperature of 450C (in 1974 the power will be increased by 20% to produce updrafts of 600 m sec-1 and temperatures of 1100C). Field experiments carried out in the Ukraine during the period 1967-1969 indicated that for condensation levels about 1 km above the ground, clouds were produced above the jets and under favorable conditions these sometimes precipitated (artificial ice nuclei were sometimes injected into the jets). Experiments to induce downdrafts and dissipate clouds were also described. Four techniques have been investigated: horizontal aircraft flights through the clouds, dropping powders (such as Portland cement) or water into the clouds, jet aircraft flying vertically in the clouds, and detonating explosives in the upper parts of clouds. It was stated that -based on more than 100 experiments between 1961 and 1965-both warm and supercooled clouds can be partially or completely destroyed through the use of these techniques. This conclusion received strong criticism from the floor where it was pointed out that randomization had not been used in evaluating the results

and, in the case of the powders, a plausible physical mechanism had not been advanced.

Artsybashev et al. (USSR) described work carried out by the Main Geophysical Observatory and the Research Institute of Forestry in their attempts to extinguish forest fires by artificially seeding convective clouds with ice nucleating materials dispersed from aircraft. It was claimed that during the period 1970–1972, 121 forest fires were extinguished over an area of 180,000 hectares by the use of this technique. Again, questions were raised from the floor concerning the lack of statistical control in their experiments. In reply it was mentioned that seedable convective clouds gave three times more rain and that indeed even weak precipitation will extinguish a forest fire.

Randomized experiments carried out in Moldavia involving the seeding of thunderstorms with PbI and also with cement were described by Gaivoronsky et al. (USSR). These substances were introduced into the clouds using large (Oblako) rockets. The results obtained with PbI indicated that clouds with top temperatures above -30C increased in altitude after seeding but clouds with top temperatures below -30C did not grow. The frequency of lightning flashes (detected with lightning sensors sensitive to frequencies from 52 to 62 hertz and with a range of 21 km) from the unseeded clouds was 2.5 times that from the seeded clouds. Dissipation of convective thunderstorms was attempted using 30 kg of cement. The authors stated that the evolution of convective clouds can be controlled with this technique, the average time required for the complete dissipation of an air mass cumulus cloud being 15 minutes. Although the experiments were randomized, the statistical significances of the results attributed to artificial modification were not given.

Khorguany and Kalov (USSR) reported on measurements of the downdrafts produced by falling powders (Polymethyl-methacrylat and cement). Ten kg of cement powder released from balloons at an elevation of 50 to 160 m on a calm day were found to generate downdrafts of several meters per sec. A lively discussion arose on the physical mechanisms which might be responsible for any dissipation of convective clouds by the relatively small quantities of cement dust used in the Soviet field experiments. Following a request from the floor, Seregin (USSR) reiterated that in a few hundred field experiments on clouds 5 to 6 km thick, the clouds were always dissipated by 10 kg of cement per cloud under unstable lapse rate conditions. In some 60 experiments on clouds more than 9 km thick, which also included clusters of storm clouds, clouds were dissipated on 80% of the occasions by introducing cement powder. Seventéen of the 60 cases consisted of frontal clouds and most of these were not dissipated by the cement.

Djachuk (USSR) discussed corona discharges from small ice crystals in the tops of cumulonimbus clouds. It was observed that in electric fields of one to two thousand volts per cm the orientation of needles and plates are changed from a horizontal to a vertical position. It was suggested that corona discharge generated on the long ice particles after their reorientation might trigger the lightning discharge.

Kasemir (USA) reported on his experiments to initiate corona discharge for lightning suppression using metallized chaff fibers. At field strengths of about 60 kV m<sup>-1</sup> a corona current of 1  $\mu$ A is generated at the ends of each fiber. If two million fibers are injected into a thunderstorm they should discharge a current of about two amperes which is compatible with the charge generation of an average thunderstorm. In field experiments it was observed that the electric fields measured near the bases of thunderclouds decayed faster by a factor of about 5 to 6 after chaff had been released.

Sax (USA) reported on NOAA's cumulus "dynamic" seeding experiments carried out in Florida in 1973. These involved the coordination of surface, radar, and airborne measurements. Seeding activities were strictly randomized. Results from the experiments were not available.

The session on Technical and Operational Aspects of Weather Modification contains several excellent and detailed reviews of the wide-range of techniques and equipment being used in the Soviet Union for their cloud, fog, and hail modification projects.

Seregin et al. (USSR) described techniques used for the generation and delivery of seeding agents into clouds and fogs. Pyrotechnics (AgI and PbI) are in widespread use. Ground-based dispersal systems with remote control are used for the dispersal of supercooled fogs. Heat sources together with hygroscopic particles have been found the most effective means for dispersing warm fogs. The equipment used produces hygroscopic particles with a controlled size distribution. Rockets, which can be fired from moving vehicles, are widely used for carrying materials into clouds in those areas from which aircraft are excluded. Ground-based "Oblaka" rockets are used to carry up to 7 kg of powder materials into clouds where they are dispersed by explosion. Larger quantities of material are dispersed from rockets launched from aircraft.

The rockets and shells used in the Soviet Union for hail modification projects were described by Bibilashvili (USSR). Pyrotechnics with AgI and PbI which generate  $3 \times 10^{12}$  to  $10^{13}$  particles gm<sup>-1</sup> have been widely used in the "anti-hail" rockets. The early rockets (PGI), designed in 1959, reached a maximum altitude of 4 km and carried 172 gm payload. The more recent rocket "Oblako" reaches 9 km and can carry 6 liters of pyrotechnics, dry ice or other reagent. A new two-stage rocket "Alazan" reaches 9 km and can carry 1 kg of material. Artillery shells are also used for the delivery and dispersal of chemicals into hailstorms. The "antihail" shells "Elbrus," with 100 and 130 mm calibers, can be used up to distances of 13 and 18 km respectively. The large amounts of explosive used in these shells break the low-strength

359 321

plastic material of the shell body into small safe fragments.

Radar methods and equipment used in the Soviet hail suppression projects were described by Abshaev and Kartsivadze (USSR). Radars are used for identifying the main hail-producing zones in cumulonimbus and they have played a crucial role in the evaluation of Soviet weather modification activities. (In a subsequent paper by Kartsivadze and Salukvadze, a series of 90,000 measurements of radar parameters on 8,500 cumulonimbus clouds, of which 3,000 were seeded, were described!) The use of a single wavelength radar (optimum 10 cm) to detect hail is based on either complex measurements of the geometric and temperature characteristics of the clouds, maximum cloud reflectivity and on a hail-occurrence probability calculation, or on radar reflectivity and depolarization ratio measurements. Hail is also detected through measurements of the radar-echo power ratio at 3.2 and 10 cm wavelengths together with estimates of the scattering power of particles of different sizes. It has also been established that the radar-echo power logarithm difference on PPI, RHI, and A-scans, obtained through simultaneous and coincident observations at two wavelengths, permits the identification of hail in clouds and estimates of the sizes of hailstones.

In a review paper on the engineering and operational aspects of weather modification, Dennis and Schleusener (USA) emphasized experience gained in South Dakota, which in 1972 began the first large scale weather modification program in the USA to be supported by state funds. The principal objectives of the program are to increase rainfall from summer convective clouds and to suppress hail damage. Airborne seeding with AgI will be used in both programs. The 1972 program covered about 10,000,000 acres and used two radars and eight aircraft. The 1973 program was expanded to cover 27,000,000 acres with six radars and 17 aircraft. Details of the results of the program were not given.

Ozawa and Omoto (Japan) described a two-stage rocket for delivering AgI into clouds which has been developed for hail suppression in Japan. The rocket is ejected from a mobile launcher and it burns up before reaching the ground. It attains a maximum altitude of 7 km and carries 200 gm of AgI pyrotechnic.

The first paper in the session on Physical, Statistical, and Economic Evaluations of Weather Modification was given by Changnon (USA) who reviewed methods for evaluating precipitation modification experiments. The statistical method of the adjacent crossover design was considered to be the most powerful technique for evaluation provided that the effects of seeding do not persist or spread.

Bujkov and Kornienko (USSR) described methods for estimating the physical and economic effectiveness of weather modification. "Anti-hail" programs in the USSR have been evaluated mainly on the basis of reductions in the area of crops damaged by hail and improvements of crop-plan fulfillments. Some statistical techniques

have been used (e.g., comparison of target and control areas, historical regression) but randomization of the seeding has not been employed.

Stout (USA) discussed the potential benefits which could accrue from precipitation augmentation over the Great Lakes. When the level of Lake Michigan is low, a 10% increase in the autumn and winter snowfall should produce economic benefits in excess of 5 million dollars.

The important subject of possible downwind effects from cloud seeding activities was discussed by Brier et al. (USA). In statistical analyses of several randomized rain augmentation experiments carried out in the United States and Israel, no evidence has been found for decreases in rainfall downwind of the intended target area. On the contrary, it has been observed in several cases that precipitation increases downward are greater than in the target area.

A lively paper on the statistical design and evaluation of rain modification experiments was given by Neyman and Scott (USA). The necessity of randomization was stressed, although there is no statistical technique presently available for coping with the full complexity of weather modification efforts. Statistical analyses of two rain modification experiments, intended to increase rainfall in localized areas, have indicated that precipitation was affected at distances 100 miles or more away after time lags of several hours.

Tsykunov and Poluektova (USSR) discussed physical and economic methods for determining the effectiveness of "anti-hail" projects. The weaknesses of the crop-yield method based on target-control areas or historical regression were pointed out.

The final session of the Conference was concerned with ice nucleus technology. Allee (USA) described the instrumentation of a network for measuring ice nuclei which consists of 19 stations spread over the Western United States. Millipore filters are being used for the measurements and the air is being sampled for five minutes in each hour during a 24-hour period at each station. The filters are then sent to a control center for analysis. Preliminary results indicate a general increase in the concentration of ice nuclei from the Pacific coast-line to the Central United States. An ice nucleus production rate over the land of 2 m<sup>-2</sup> min<sup>-1</sup> was estimated from this increase. An opinion was expressed from the floor that the project will be subject to uncertainties in the technique used for measuring ice nuclei.

Church et al. (USA) emphasized the ecological advantages of using biodegradable organic chemicals for cloud seeding. Metaldehyde seems particularly desirable from this point of view. The current status of ice nucleus generator technology was reviewed by Fukuta (USA).

An interesting paper on the removal of a pyrotechnically-generated tracer (metallic indium) placed in a convective updraft was given by Dingle (USA). The tracer was detected at the ground out to distances of some 50 km from the point of release.

A few final remarks: One of the most interesting and useful features of the Conference was the lively discussions which repeatedly highlighted the proceedings and produced a healthy cross-fertilization of ideas. In particular, the difficult problem of evaluating the effectiveness of weather modification activities was hotly debated. The Soviet approach has been based mainly on apparent economic effectiveness together with some physical (mainly radar) evaluation. Interestingly, it became increasingly apparent as the Conference progressed that not all of the Soviet scientists are satisfied with these techniques. In other countries, the statistical evaluation of weather modification experiments has received more emphasis but often the physical evaluations have been poor. Ideally, of course, both detailed physical evaluation and strict randomized statistical controls should be emphasized.

The scope of activities in weather modification of the host country was impressive. Clearly, in the USSR there are many more scientists working in this field than in the United States, the scope of the USSR activities is greater, with a more diverse array of equipment for delivering seeding agents into clouds. The subject is receiving a high level of support from a number of branches of the Soviet government as it does in the USA.

Many professional contacts and friendships were made and renewed during the Conference and these bode well for future international cooperation in weather modification.

In the concluding Conference session the motion was accepted to make these conferences a regular international endeavor. The Second Conference, to be sponsored jointly by the WMO and IAMAP, is planned for 1976 in Boulder, Colorado, in close coordination with the IAMAP International Conference on Cloud Physics which is scheduled for the same year in the same location.

Acknowledgment: The attendance of one of us (P. V. H.) at this Conference was made possible by a travel grant from the National Science Foundation. H. K. Weickmann attended also as President, International Commission on Cloud Physics, IAMAP.

#### THE SKYLAB CONCENTRATEO ATMOSPHERIC RADIATION PROJECT - AN OVERVIEW

Victor S. Whitehead NASA-Johnson Space Center, Houston, Texas

Peter M. Kuhn NOAA-Environmental Research Laboratories, Boulder, CO

William E. Marlatt Colorado State University, Oepartment of Earth Resources Fort Collins, Colorado

> L. Edwin Williamson Atmospheric Science Laboratory White Sands Missile Range, New Mexico

In this presentation I hope to provide the background and continuity for the five papers to follow in this session. The Skylab Concentrated Atmospheric Radiation Project (SCARP) is one of almost 150 experiments utilizing the Earth Resources Experiment Package flown onboard Skylab. The Principal Investigator for SCARP is Or. P.M. Kuhn of the NOAA Environmental Research Laboratories; Co-Investigators in the initial proposal were W.E. Marlatt of the Oepartment of Earth Resources, Colorado State University, and V.S. Whitehead of NASA/JSC, Earth Observations Oivision. These three were joined by L. E. Williamson of the Atmospheric Sciences Laboratory and R.F. Pueschel also of NOAA after the project commenced.

The Skylab SCARP was conceived in the Spring of 1972 as a step in arriving at a more complete description of radiation transfer within the atmosphere, with emphasis on the contribution of aerosols to this transfer. The defined objective of this study was to determine the accuracy and applicability of a variety of models of radiation transfer through air masses of differing characteristics including varying amounts of wet and dry aerosols.

### The approach used was:

- a. To acquire a comprehensive description of the atmospheres structure and composition over sites of differing radiation properties for a variety of air masses in conjunction with the Skylab observations of these sites and supporting observations of the radiation transfer at the surface and at levels between the surface and the spacecraft,
- b. To acquire and implement several models of radiation transfer for both visible and thermal regions; and to test these models against observations.

c. To apply the results of these tests to descriptions of where the models may be applied effectively.

It was anticipated that other investigations could make use of the data base acquired in this approach, hence the experiment was declared an open one in which other investigators could participate on an exchange of data basis. In addition to Williamson and Pueschel who are presenting two of the following five papers, data exchanges occurred with EPA which provided a Lidar in the first field effort, with the Texas Air Control Board for data acquired in the Houston area, and with other Skylab investigators.

To acquire the desired variety in the data base, sites were selected and data acquired onshore and offshore in the vicinity of Houston, Texas, to provide a warm moist clean and a warm moist dirty atmosphere: over White Sands Missile Range, N.M., both sands and the mal pais were acquired to provide extremes of surface characteristics for a clean dry atmosphere and Phoenix, Arizona to provide hot dry clean and hot dry dirty atmosphere. Other sites were surveyed for use (San Francisco, Four-Corners, and St. Louis) but were not acquired due to operational constraints, primarily caused by weather.

Each field effort differed somewhat from the other in the type of data acquired as the investigators attempted to apply the experience of the preceding effort. A typical exercise however would consist of:

a. Movement of personnel and equipment to facilities nearest to the points of the field effort about three days prior to the scheduled Skylab overflight. Last minute changes to the operation plans were made.

- b. Two days prior to the Skylab overflight a low key field effort was initiated primarily to check out equipment and procedures. During this day one or more radiometersonde releases would be made by P.M. Kuhn and Associates. Surface meteorological and radiometric measurements would be made at more than one site by the groups from NOAA and ASL. The Colorado State Aircraft would fly at least one multiple level pattern between sites with sensor operating for general familiarity, timing and instrument test. This days' effort would be concluded by a general debriefing on problems and re-planning where desirable.
- c. On the day prior to the Skylab overpass, a schedule was followed identical to that planned for the day of the overpass. These consist of hourly or continuous measurements of:
  - (1) Downwelling and upwelling solar flux.
  - (2) Direct beam solar radiation.
  - (3) Net radiation at the surface.
  - (4) Radiation temperature of the surface, sky, and cloud.
  - (5) Wind, temperature, and dew point.
  - (6) Sky cover (photographs)
  - (7) Radiometersonde profiles (temperature, dew point, and upand downwelling thermal radiation) each three hours.
  - (8) Aircraft profiles from near surface to above the haze layer (profiles of aerosol number density and size distribution, upwelling and downwelling solar flux, and profiles of temperature and dew point). Three times daily: early morning, at time of day of Skylab over pass and late afternoon. If the time of day of Skylab overpass differed greatly from the time of maximum surface heating another flight would be attempted at that time.
- d. On the day of the overpass the only difference in schedule from the day preceding was the participation of the Skylab crew. The crew had been provided photographs of all those sites acquired to aid in recognition and acquisition of sites by the S-191 spectrometer. Requirements for data acquired using the \$190A multispectral camera. the \$1908 mapping camera, the \$-191 spectrometer and the \$192 multispectral scanner were satisfied with less than thirty seconds of data for each of the field exercises. The camera and scanner system were pointed at nadir in the Z-local vertical mode, the spectrometer, however, could be directed to point at a specific site by the operator to acquire several spectral scans. It should be noted, that late in the planning stages for SCARP the opportunity to use a helicopter mounted \$191 spectrometer was offered and profiles from near surface to 12,000 feet were acquired for the same sites as were acquired by Skylab.
- e. It was initially planned to maintain the same observation schedule the day following

the Skylab overpass as on the two days preceding in order to take advantage of the established field deployment to acquire more varied air masses. This was discontinued about midway through the field program for efficiency in scheduling. Exercises were then terminated about 24 hours after the Skylab overpass with only a single, or at most, two flights by the Colorado State University aircraft and one or two radiometersonde releases on that day. The exercise was concluded with a review of the effort and suggestions for planning of the next field exercise.

Early in the program an effort was made by the Colorado State University graduate students working on the project to survey available radiation transfer models and to acquire working programs of examples of models different types from their developers. Most model programs requested were acquired and implemented on Colorado State and/or Johnson Space Center computers.

### ASSESSMENT OF PERFORMANCE

In a field program as compelx and as time critical as this, it would be surprising if all operations went according to plan. The usual problems of, tape change required at a critical moment, lost balloons, site obscured by clouds or not discernible by Skylab crew, occurred (one particularly notable unforeseen failure was the melting of one of P.M. Kuhn's net radiometers in the Arizona desert). On the positive side, in spite of these and other shortcomings, a good set of field data were acquired. These consisted of one partial data set over rangeland at Rosenburg (West of Houston) in August 1973 and a simultaneous data set acquired from the Buccaneer Tower 25 miles off-shore from Galveston. The Skylab crew was not able to identify Rosenburg for \$191 acquisition due to scattered clouds in the area but \$190 and \$-192 data were acquired. Clouds obscured the Buccaneer Tower from view at overpass time and operational difficulties prevented a successful radiometersonde release from the tower. The aircraft and surface observations were successful, including radiometersondes from Rosenburg, providing good examples of moist clean and moist moderately dirty atmospheres.

Again in August through a clean dry atmosphere, the sands and lava beds at the White Sands Missile Range were observed from Skylab with corresponding surface, balloon and aircraft observations (including the helicopter S191 system) were acquired at each site. The sands were out of the field-of-view of the S-193 scanner due to orbital drift but both sands and lava beds were acquired by the multispectral cameras and the spectrometer. The field program here was also much smoother than in the Houston effort due to experience gained there, more favorable weather and access of White Sands Missile Range support facilities.

The final field exercise (although it was not known to be such at the time) occurred in the vicinity of Phoenix, Arizona, in early September. Three sites were operated from the surface and aircraft (including two helicopters, one with the S-191 spectrometer, the other with new aerosols monitoring instrumentation). All three sites were acquired by the Skylab S191 spectrometer and S190A multispectral

camera. One site was located several miles upwind of Phoenix, one several miles downwind providing examples of hot dry clean and hot dry dirty atmospheres.

In the modeling activities for the visible region, 10 scattering models have been acquired and implemented. Tests have been made against the data available and models have been compared. In the thermal region while fewer models have been considered, the work has also progressed satisfactorily. On the negative side, plans were made to acquire data from San Francisco area, Four-Corners area, St. Louls area and Houston areas during Skylab IV. In every case weather or conflicts in schedules prevented this acquisition, thereby excluding cool season atmospheric samples from consideration.

In concluding these introductory remarks, I would like to note that a compliation of the data sets will be performed and made available as technical reports to others wishing to further the testing and comparison of radiative transfer models.

# NOAA Technical Report ERL 336-APCL 35

U.S. DEPARTMENT OF COMMERCE
NATIONAL OCEANIC AND ATMOSPHERIC ADMINISTRATION
Environmental Research Laboratories

# An Historical Climatology of Damaging Downslope Windstorms at Boulder, Colorado

C. DAVID WHITEMAN JOHANNA G. WHITEMAN

BOULDER, COLO.
NOVEMBER 1974



# AN HISTORICAL CLIMATOLOGY OF DAMAGING DOWNSLOPE WINDSTORMS AT BOULDER, COLORADO

## C. David Whiteman and Johanna G. Whiteman

A climatology is developed for damaging downslope windstorms at Boulder, Colorado, based on newspaper accounts since 1869. One hundred and fifty-one documented windstorms provide the data on which statistical and climatological calculations are based. The area affected by downslope windstorms is described, information on the temporal distribution of the windstorms is given, including annual, monthly, and diurnal distributions, and windstorm characteristics are discussed. Wind-related damage is classified by severity and areal extent.

### 1. INTRODUCTION

## Heavy Storm in Boulder

Last Wednesday night [17 November] our town was visited with the heaviest wind experienced here for the last five or six years. The storm commenced brewing about 9 o'clock in the evening and lasted till morning. From 12 to 1 o'clock it blew the hardest. At this time different parties were up, bracing their buildings, to prevent their being blown away or broken to pieces. Several new structures on the eve of completion were torn down, or moved off their foundations. The large frame building being put on Pearl Street by Mr. Andrews, was leveled to the ground entirely. It will take some hundreds of dollars to repair its damages. Eggleston's new drug store was writhed [sic] and twisted to one side, and had not Mr. G. feared some damage, and commenced bracing it up, his building would have fallen, demolishing another in its fall. A portion of the projecting brick gable on the store occupied by Tourtellot &

Squires was blown upon the roof, crushing it in, and doing other damage. Had the weight been much heavier, it would have gone through to the ground, to the great damage of the goods in store. Mr. Sullivan's new frame dwelling, partly enclosed, was slid nearly off its foundation, and sundry other small structures about town were turned over, or otherwise damaged. At Valmont the storm did not rage as furiously, only overturning a few haystacks, etc. We have not heard the amount of damages estimated. Nearly every building the storm reached was more or less shaken, and our citizens may congratulate themselves on escaping as well as they did, and take warning to build more solidly in the future. Were the air as dense here as at sea level, it is probable the town would have been razed to the ground.

**Boulder County News** 







PENN STATE UNIVERSITY LIBRARIES

ACCOUNTY ACCOUN